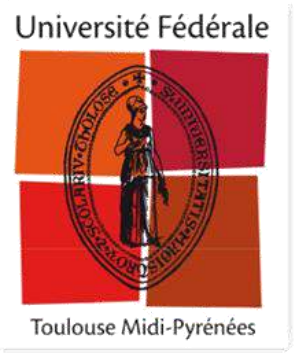

THÈSE

En vue de l'obtention du

DOCTORAT DE L'UNIVERSITÉ DE TOULOUSE

Délivré par :

Université Toulouse III - Paul Sabatier (UT3 Paul Sabatier)

Présentée et soutenue par :
Morgane STECKIEWICZ

Le Mardi 26 Septembre 2017

Titre :

L'ionosphère du côté nuit de Mars dévoilée par les déplétions d'électrons suprathermiques

École doctorale et discipline ou spécialité :
ED SDU2E : Astrophysique, Sciences de l'Espace, Planétologie

Unité de recherche :
IRAP

Directeur/trice(s) de Thèse :

Christian MAZELLE	**Directeur de Recherches**	**Directeur de thèse**
Nicolas ANDRÉ	**Chargé de Recherches**	**Co-directeur de thèse**
Philippe GARNIER	**Maître de conférences**	**Encadrant de thèse**

Jury :

François LEBLANC	**Directeur de Recherches**	**Président du jury**
Dominique DELCOURT	**Directeur de Recherches**	**Rapporteur**
Viviane PIERRARD	**Maître de Recherches**	**Rapporteur**
Sébastien BOURDARIE	**Maître de recherches**	**Examinateur**
Dominique FONTAINE	**Directrice de Recherches**	**Examinateur**

The nightside Martian ionosphere unveiled by suprathermal electron depletions

Morgane Steckiewicz

‘*La plus utile et honorable science et occupation*
A une femme, c’est la science du ménage.’

Montaigne (1533-1592)

Acknowledgements

I would like first to thank MAVEN, which achieved with success its insertion around Mars and records for more than three years now wonderful data without which this PhD would not have occurred. We began our research life together and I hope its will last much longer. Through this acknowledgement I obviously want to thank the operation and instrument teams, as well as the science team which welcomed me among them. Among others I would like to thank Bruce Jakosky, Dave Brain, Jasper Halekas, Jared Espley, Jim McFadden, and Jack Connerney for the help they gave me all along this PhD. A special acknowledgement to Janet Luhmann, Dave Mitchell, Rob Lillis and Laïla Andersson who followed my work from the beginning, helped me write my papers and are always good advisors in the way to carry on studies. I would also like to thank Shannon Curry, Gina DiBraccio, Yasir Soobiah, Yuki Harada, Shaosui Xu, Yaxue Dong, Yuni Lee, Scott England, Zachary Girazian, Christopher Fowler, Matt Fillingim and Meridith Elrod for the interesting discussions and the moments spend together.

Je remercie profondément Dominique Fontaine et Sébastien Bourdarie d'avoir accepté de participer à mon jury, François Leblanc de l'avoir présidé, ainsi que les rapporteurs Viviane Pierrard et Dominique Delcourt pour leurs lectures attentives, leurs remarques et leurs conseils. Merci infiniment à tous. I also want to thank Dave Mitchell for his coming, his kindness and his picky questions. Je remercie également Dorine Roma pour avoir organiser les déplacements des différents membres du jury.

Je remercie mes directeurs de thèse pour m'avoir donné l'opportunité de faire ce doctorat et tout particulièrement Philippe, qui a accepté de faire partie de cette aventure périlleuse et qui m'a suivie, épaulée, encouragée et soutenue tout au long de ces trois années. Merci pour ton temps et tes conseils, et surtout pour avoir donné une chance à cette thèse. Je tiens aussi à remercier Ronan et François pour leur gentillesse et leur bienveillance, mais aussi pour le temps qu'ils ont consacré à mes travaux.

Cette thèse a été effectuée au sein de l'IRAP et je tiens à remercier ses directeurs successifs Martin Giard et Philippe Louarn pour m'avoir accueilli dans leur laboratoire. J'ai ainsi pu profiter de toute l'infrastructure du laboratoire pour mener à bien ce travail. Je suis profondément reconnaissante à tous les membres de l'équipe PEPS pour m'avoir acceptée

parmi eux et encouragée tout au long de ces trois années. Merci notamment à Benoit, Aurélie, Jérémie, Christian J., Matthieu, Andréi, Frédéric, Alexis, Pierre-Louis, Iannis, Lionel, Vincent et Jeannot. Je remercie en particulier Jean-André Sauvaud pour avoir été ma voix quand celle-ci n'était pas à la bonne fréquence, et pour m'avoir permis de publier mon premier article. Merci à Dominique Toublanc pour son soutien et ses conseils tout au long de ma thèse et de mon parcours dans l'enseignement. Merci à Arnaud pour m'avoir soutenue dans les premiers mois de ma thèse et mes premières missions. Merci à Myriam et Elena pour avoir sauvé je ne sais combien de Time Tables et plus globalement merci aux équipes de développement informatique pour m'avoir facilité l'accès aux données tout au long de ma thèse.

Dans un ordre non représentatif : Merci à UniverSCiel et à tous ses membres pour leur dynamisme, leur enthousiasme, leur gentillesse et tous les projets passionnants qu'ils portent et auxquels j'ai pu participer pour faire briller un peu plus les yeaux des enfants (et des grands enfants). Merci en particulier à Marina, Wilhem, Vincent, Philippe, Edoardo, Damien, Tata, Minus et Cortex pour ces moments passés ensemble. Merci aux Etoiles brillents pour tous et à Thierry, Pieter, Cécile, Armelle, Emmy, Simon, Julie, Mélanie et Hélène pour cette expérience unique ! Merci à Geneviève pour m'avoir suivie et aidée dans les divers choix difficiles que j'ai été amené à prendre depuis quatre ans. Merci à Marie Brut et à Jean-François Georgis de m'avoir fait découvrir l'enseignement. Merci à Natasha, Benjamin, Thomas et Mika d'avoir partagé mon bureau tout au long de ces trois années. Merci pour ces moments et rires partagés. Merci à Myriam, Gaëlle, Elsa et David pour toutes les pauses café que nous avons partagées. Merci à Merlin pour sa participation à l'écriture de ma thèse. Merci à Agnès pour m'avoir aidé à préparer ma soutenance et pour son soutien. Je suis très heureuse d'avoir pu faire ces conférences sur Mars avec toi ☺ Merci à Issaad pour m'avoir nourrie de gateaux délicieux ! Merci à Mikel, Mickaël, Nathanaël, Maxime, Anna, Norberto, Yoann, Eduardo et Jérémy pour votre écoute votre gentilesse, et les moments passés ensembles. Merci également à Zonta International pour avoir reconnu la valeur de mes travaux à travers la bourse Amelia Earhart.
Je suis très heureuse que cette thèse m'ait permi de tous vous rencontrer.

Enfin, merci à ma famille, mes parents, mes grands-parents, mes sœurs, mon neuveu et mes nièces, mais surtout merci à Arthur pour avoir été là tous les jours de ma thèse, pour m'avoir soutenu et permis d'arriver jusqu'au bout de cette épreuve.

Abstract

The nightside ionosphere of Mars still remains an unfamiliar and mysterious place. Nightside suprathermal electron depletions are specific features of this region which have been observed at Mars by three spacecraft to date: Mars Global Surveyor (MGS), Mars EXpress (MEX) and the Mars Atmosphere and Volatile EvolutioN (MAVEN) mission. Their study enables the observation of the nightside ionosphere structure and dynamics as well as the underlying neutral atmosphere, the specific Martian magnetic topology, and possible conduits for atmospheric escape. Structures as different as magnetic cusps, current sheets or the UV terminator can be investigated through suprathermal electron depletions, due to the processes leading to their observation on the nightside of Mars.

The main goal of my PhD has been to use the complementarity of the three missions MGS, MEX, and MAVEN to understand the different mechanisms at the origin of suprathermal electron depletions and their implication on the structure and the dynamics of the nightside ionosphere. In this context, three simple criteria adapted to each mission have been implemented to identify suprathermal electron depletions from 1999 to 2017.

A statistical study reveals a transition region near 170 km altitude separating the collisional region where suprathermal electron depletions are directly due to electron absorption by atmospheric CO_2 and the collisionless region where they are mainly due to electron exclusion by closed crustal magnetic field loops. Understanding of these phenomena enables me to estimate the location of the UV terminator. It appears to be located ~120 km above the optical terminator, though this location is different between the dawn and dusk terminator and is expected to vary throughout the different Martian seasons.

Résumé

L'ionosphère du côté nuit de Mars reste encore à ce jour une zone mystérieuse et peu connue de l'environnement Martien. Les déplétions d'électrons suprathermiques sont des structures spécifiques à cette région, observées jusqu'à présent par trois satellites : Mars Global Surveyor (MGS), Mars EXpress (MEX) et Mars Atmosphere and Volatile EvolutioN (MAVEN). Leur étude permet aussi bien l'observation de la structure et de la dynamique de l'ionosphère du côté nuit que celle de l'atmosphère neutre, de la topologie magnétique martienne, ainsi que l'étude de l'échappement atmosphérique de Mars. Des structures aussi différentes que les cornets magnétiques, les couches de courants ou encore le terminateur ultra-violet peuvent être examinées à travers les déplétions d'électrons suprathermiques, de par les mécanismes à l'origine de leur présence du côté nuit de Mars.

Le but principal de ma thèse a été de tirer parties des trois jeux de données offerts par les satellites MGS, MEX et MAVEN pour mieux comprendre les mécanismes à l'origine des déplétions d'électrons suprathermiques observées du côté nuit ainsi que leur impact sur la structure et la dynamique de l'ionosphère du côté nuit. Dans cette optique, trois critères simples adaptés à chaque mission ont été développés pour identifier les déplétions d'électrons suprathermiques dans une base de données allant de 1999 à 2017.

Une étude statistique a révélé la présence d'une région de transition autour de 170 km d'altitude séparant la région collisionnelle dans laquelle les déplétions d'électrons suprathermiques sont directement dues à l'absorption des électrons par le CO_2 atmosphérique, et la région non-collisionnelle dans laquelle elles sont principalement dues aux boucles fermées de champs magnétique d'origine crustale. La compréhension de ces mécanismes m'a permis d'estimer la localisation du terminateur ultra-violet. Celui-ci est situé en moyenne ~120 km au-dessus du terminateur optique. Cette altitude varie entre le côté soir et le côté matin, et une variation saisonnière est prédite par les modèles atmosphériques.

Table of Contents

Introduction

The nightside ionosphere of Mars is still poorly investigated compared to the dayside one. One of the main observational properties of this region is the presence of recurrent structures characterized by significant depletions in electron fluxes and hence called "nightside suprathermal electron depletions" (hereinafter referred to as **electron depletions**). The first observations of these structures were obtained during the 400 km mapping orbit of Mars Global Surveyor (**MGS**) by the Electron Reflectometer instrument that detected on Mars' optical shadow pronounced decreases of the electron count rates up to three orders of magnitude at all energies [*Mitchell et al.*, 2001]. The same structures were then detected by the Mars Express (**MEX**) Electron Spectrometer [*Soobiah et al.*, 2006]. The statistical analysis of their geographical distribution suggested that the observation of electron depletions is due to the passage of the spacecraft inside closed crustal magnetic field loops preventing plasma coming from the dayside or the magnetotail from populating these regions. [*Mitchell et al.*, 2001; *Soobiah et al.*, 2006; *Soobiah*, 2009]. However, studies on electron depletions made with MGS and MEX are both restricted in altitude and instrumentation. They cannot observe the phenomenon at altitudes below 250 km with a complete suite of plasma instruments.

On September 21, 2014, a new spacecraft get inserted around Mars to complement the Martian fleet: the Mars Atmosphere and Volatile EvolutioN (**MAVEN**) mission. It is designed to study the structure, composition, and variability of the upper atmosphere and ionosphere of Mars, its interaction with the Sun/solar wind, and the Martian atmospheric escape [*Jakosky et al.*, 2015a]. For this purpose, it carries onboard a complete suite of plasma and field instruments including a magnetometer, two ion and one electron spectrometers, and a Langmuir probe. The spacecraft since then reached its mapping orbit which is a highly elliptical precessing orbit with a nominal periapsis at 150 km, a period of 4.5 h and an inclination of 75°. This periapsis can periodically be lowered down to ~125 km for 5 days periods known as "**deep-dips**", which allows measurements of suprathermal electron depletions at previously unsampled altitudes.

Contrary to MGS and MEX observations, during most MAVEN periapsis passages in the nightside ionosphere suprathermal electron depletions are detected, even in regions with nearly no crustal magnetic field. Hence, MGS and MEX only observed the tip of the iceberg. Other processes than the interaction with crustal magnetic fields must occur for suprathermal electron depletions to be observed.

Suprathermal electron depletions are interesting structures as they are recurrently observed on the nightside ionosphere and can be used to characterize its structure and dynamics. *Mitchell et al.*, [2007] and *Brain et al.*, [2007] for example used electron depletions to determine the magnetic topology of Mars thanks to electron spectrometers. However, a clear comprehension of the processes at the origin of the observation of these structures is lacking and needed to carry out such studies.

In this work I want to take advantage of the different datasets offered by MGS, MEX and MAVEN to better understand the structure and dynamics of the nightside ionosphere through the study of electron depletions. MGS data are therefore used from 1999 to 2006 to take advantage of the mapping **circular orbit** at a roughly constant altitude (~400 km) of the spacecraft, allowing observations of the phenomenon every 2 h over the whole range of possible latitudes [-90°, 90°]. MEX data are used from 2004 to 2014, which gives us an unparalleled **long-term view** of the phenomenon at both relatively low (down to ~250 km) and high altitudes. Finally, MAVEN data are used from October 2014 to March 2017. During this time period the spacecraft covered both hemispheres except the poles, but due to this short duration and MAVEN orbital parameters, all latitudes are not yet covered at all possible altitudes. Even though the coverage and duration of this data set are much lower than those of MGS and MEX, MAVEN reached during this time period **altitudes down to 110 km**, which are unsampled by MGS nor MEX. Added to MAVEN instrument suite, this coverage enable a finer study of the structure of suprathermal electron depletions. This huge data set gathering observations made over 18 years by different instruments reaching different altitude regimes enables us to compare events observed in similar conditions (several spacecraft in the same region) and enrich this joint vision with new observations closer to the surface (with MAVEN).

So as to present the work carried out during my PhD, this manuscript is divided into five chapters:

- In **Chapter 1** is described the global environment of Mars: what characterizes the Martian obstacle, how it interacts with the solar wind, what are the regions and boundaries we are likely to encounter when looking at plasma data, to finally focus on the nightside ionosphere and its suprathermal electron depletions.
- In **Chapter 2** are described the different datasets used in this manuscript: we browse the different missions and their associated orbitography and instruments, the analysis tools I have used to process the data, the frames and definitions that I will use in the rest of the manuscript and the model of crustal magnetic field that I have chosen.

- **Chapter 3** is dedicated to the identification of suprathermal electron depletions. These structures have already been identified by several spacecraft and instruments but the MAVEN payload offers new highlights on their properties. This enables me to create criteria able to automatically detect suprathermal electron depletions in the different electron spectrometers data.
- In **Chapter 4** I use the catalogs obtained after application of the three criteria to characterize the different processes at the origin of suprathermal electron depletions in the nightside ionosphere of Mars. Geographical and altitudinal distributions are used in association with pressure balance and plasma composition analysis in order to derive an updated scenario of creation of electron depletions.
- In **Chapter 5** I focused on the dynamics of the nightside ionosphere. The flux spikes regularly observed between suprathermal electron depletions are structures of interest to observe the dynamics of the nightside ionosphere. The observation of electron depletions in unexpected regions or the absence of observation in regions where they should cover the whole surface regarding the previously established scenario remind us that other processes are at work in the nightside ionosphere. The location of the UV terminator, and its variability with seasons and dusk/dawn side are investigated.

Conclusions and perspectives finally put an end to my manuscript.

Introduction

L'ionosphère du côté nuit de Mars est une partie assez peu connue de l'environnement martien, comparée à l'ionosphère du côté jour. Une des principales caractéristiques observationnelles de cette région est la présence de structures récurrentes caractérisées par une déplétion significative du flux d'électrons. Elles sont pour cette raison appelées « déplétions d'électrons suprathermiques du côté nuit » (nous les appellerons par la suite **déplétions d'électrons** pour ne pas alourdir le texte). La première observation de ces structures a été réalisée par le satellite Mars Global Surveyor (**MGS**) dont l'orbite était circulaire à ~400 km. Son spectromètre à électrons détecta de fortes diminutions du taux de comptage d'électrons jusqu'à trois ordres de grandeur à toutes les énergies quand le satellite passait dans l'ombre de la planète [*Mitchell et al.*, 2001]. Le même type de structures a ensuite été détecté par le spectromètre à électrons du satellite Mars Express (**MEX**) [*Soobiah et al.*, 2006]. Une étude statistique de leur distribution géographique suggéra que l'observation de déplétions d'électrons est due au passage du satellite dans des boucles fermées de champ magnétique crustal excluant le plasma venant du côté jour ou de la queue [*Mitchell et al.*, 2001; *Soobiah et al.*, 2006; *Soobiah*, 2009]. Cependant, les études menées sur les déplétions d'électrons à l'aide des données de MGS et de MEX sont à la fois restreintes en altitude et au niveau instrumental. Ces satellites ne peuvent en effet observer ce phénomène qu'à des altitudes supérieures à 250 km, avec une instrumentation ne permettant qu'une étude partielle de ses caractéristiques.

Le 21 Septembre 2014 un nouveau satellite est entré en orbite autour de Mars, complétant ainsi la flotte martienne : la mission Mars Atmosphere and Volatile EvolutioN (**MAVEN**). Cette mission a pour but d'étudier la structure, la composition et la variabilité de la haute atmosphère et de l'ionosphère martienne, leurs interactions avec le Soleil et le vent solaire ainsi que l'échappement atmosphérique de Mars [*Jakosky et al.*, 2015a]. Dans cette optique, MAVEN a embarqué à son bord un ensemble cohérent d'instruments plasma, dont deux magnétomètres, deux spectromètres à ions et un à électrons, et une sonde de Langmuir. Le satellite est sur une orbite fortement elliptique, précessant naturellement, avec un périapse nominal à 150 km, une période de 4,5 h et une inclinaison de 75°. Ce périapse peut périodiquement être abaissé pour atteindre une altitude de ~125 km pendant une période de cinq jours appelée « **deep dip** ». Ces périodes permettent d'effectuer des observations de déplétions d'électrons à des altitudes jamais atteintes précédemment.

Jusqu'à présent, des déplétions d'électrons ont été observées avec MAVEN au cours de tous ses passages à basses altitudes du côté nuit, sauf quelques rares exceptions, et ce même dans les régions où le champ magnétique d'origine crustale est très faible. Ainsi, il semble que MGS et MEX n'aient pu observer que la partie émergée de l'iceberg. L'interaction du plasma avec le champ magnétique crustal ne peut pas être le seul mécanisme à l'origine de la création de déplétions d'électrons.

Les déplétions d'électrons sont des structures intéressantes de par leur observation récurrente dans l'ionosphère du côté nuit de Mars. Elles peuvent ainsi être utilisées pour caractériser sa structure et sa dynamique. *Mitchell et al.*, [2007] et *Brain et al.*, [2007] les ont par exemple utilisées pour déterminer la topologie magnétique de Mars à l'aide des données issues des spectromètres à électrons. Cependant, une bonne compréhension des processus à l'origine de la formation des déplétions d'électrons manque et est nécessaire pour mener à bien de telles études.

A travers ce doctorat j'ai souhaité tirer au maximum profit des différents jeux de données offerts par MGS, MEX et MAVEN pour mieux comprendre la structure et la dynamique de l'ionosphère du côté nuit de Mars à travers l'étude des déplétions d'électrons. Dans cette optique, les données de MGS ont été utilisées de 1999 à 2006, de sorte à tirer profit de son orbite **circulaire**, permettant une observation du phénomène toutes les deux heures sur toute la gamme de latitude possible [-90° ; 90°]. En ce qui concerne MEX, j'ai utilisé les données obtenues entre 2004 et 2014, ce qui donne une **vue à long terme** du phénomène, à la fois à relativement basses altitudes (jusqu'à ~250 km) et à hautes altitudes. Finalement, les données de MAVEN ont été utilisées d'Octobre 2014 jusqu'à Mars 2017. Pendant cette courte période le satellite a couvert les deux hémisphères à l'exception des pôles. Cependant, cela n'est pas encore suffisant pour couvrir toutes les latitudes à toutes les altitudes possibles. Bien que la couverture et la période étudiée soit bien plus faible que pour MGS et MEX, MAVEN est descendu pendant cette période jusqu'à des **altitudes de 110 km**, altitudes non couvertes ni par MGS ni par MEX. Cette couverture, associée aux capacités instrumentales de MAVEN, permet une étude plus fine des déplétions d'électrons suprathermiques. Cette immense base de données, regroupant plus de 18 années d'observations par différents instruments couvrant différentes gammes d'altitudes, nous permet de comparer des événements observés dans des conditions similaires (plusieurs satellites dans la même région) et d'enrichir cette vision commune avec de nouvelles observations plus proches de la surface (avec MAVEN).

Afin de présenter le travail que j'ai mené au cours ma thèse, ce mémoire a été divisé en cinq parties:

- Dans le **Chapitre 1** est décrit l'environnement global de Mars : ce qui caractérise l'obstacle martien, comment celui-ci interagit avec le vent solaire, quelles sont les régions et les frontières qui sont susceptibles d'être rencontrées en étudiant les données des instruments plasma, pour finalement se focaliser sur l'ionosphère du côté nuit et ses déplétions d'électrons suprathermiques.
- Dans le **Chapitre 2** sont décrits les différents jeux de données utilisés au cours de ma thèse : nous parcourons les différentes missions avec leur orbitographie et les instruments qui leur sont spécifiques, les outils d'analyse de données que j'ai été amenée à utiliser, les repères et différentes définitions qui seront utilisés par la suite et le modèle de champ magnétique crustal que j'ai choisi.
- Le **Chapitre 3** est dédié à l'identification des déplétions d'électrons suprathermiques. Ces structures ont déjà été identifiées par différents satellites et instruments mais MAVEN et sa suite d'instruments nous offre un nouvel éclairage sur leurs propriétés. Cela m'a permis de créer trois critères capables de détecter automatiquement les déplétions d'électrons suprathermiques au sein des données de chaque spectromètre à électrons.
- Dans le **Chapitre 4** j'utilise les catalogues obtenus après application des trois critères pour mettre en évidence les différents processus physiques à l'origine de la présence de déplétions d'électrons dans l'ionosphère du côté nuit de Mars. Nous étudirons pour cela les distributions géographiques et en altitude des déplétions d'électrons, conjointement à une analyse de l'équilibre de pression et de la composition du plasma contenue dans ces structures. Cela m'a permis de mettre à jour le scénario de création des déplétions d'électrons suprathermiques.
- Dans le **Chapitre 5**, je me focalise sur la dynamique de l'ionosphère du côté nuit. Les pics de flux qui sont observés entre deux déplétions d'électrons sont des structures privilégiées pour étudier cette dynamique. L'observation de déplétions d'électrons dans des régions inattendues ou même l'absence d'observation là où elles devraient recouvrir l'ensemble de la surface selon le scénario précédemment établi nous rappelle que d'autres processus sont aussi à l'œuvre dans l'ionosphère du côté nuit. La localisation du terminateur UV ainsi que sa variabilité saisonnière et entre le côté soir ou le côté matin seront ensuite étudiées.

Une conclusion et des perspectives viendront clore ce manuscrit.

1. The Martian environment

Mars is a fascinating planet, sometimes called 'twin planet of the Earth' due to its neighborhood and its history. It is hence one of the most visited objects of the Solar System since humanity achieved escaping Earth's gravity. However, the Martian environment, structured by the interaction of Mars with the solar wind, is not yet fully understood. It lays between the Earth one, whose atmosphere is shielded by a strong internal magnetic field, and the Venus one, which has no proper magnetic field but a very dense atmosphere. It even has common features with comets.

The different types of interactions existing between the solar wind and the different bodies of the Solar System is discussed in section 1.1. We then focus on the nature of the Martian obstacle in section 1.2. Finally, our current knowledge on the interaction of Mars with the solar wind is developed in section 1.3.

1.1. Interaction of the solar wind with the different bodies of the Solar System

All the bodies present in the Solar System, from the biggest planets to the smallest dust particles, are immersed in the solar wind. All these objects interact with the solar wind, but each of these interactions is unique as each object has its own specificities. However, the interactions with the solar wind can be gathered into different classes, which are detailed in section 1.1.2 after a short description of the solar wind (section 1.1.1).

1.1.1. The solar wind

The solar wind is a flow of ionized solar plasma particles carrying a frozen-in magnetic field — a remnant of the solar magnetic field — which streams outward through interplanetary space [*Kivelson and Russel*, 1995]. This ejection of plasma is due to the difference of gas pressure existing between the solar corona and the interplanetary space, which is large enough to balance the solar gravity. The existence of the solar wind was conjectured in the 50s and it has directly been observed by space probes in the mid-60s.

The composition of this plasma is the same as the one of the solar corona: 95% of **hydrogen** (H^+), 4% of **helium** (He^{++}), and 1% of heavy ions. The solar wind is very **tenuous** (~ 40 amu. cm^{-3} near the orbit of Mercury and ~ 0.001 amu. cm^{-3} near the orbit of Pluto), **supersonic** ($\sim 250 - 800$ km. s^{-1}), and **dynamic**. It typically travels a Mars diameter in 15-20 seconds and changes on timescales as short as minutes.

Embedded in this plasma is a weak magnetic field oriented in a direction nearly parallel to the ecliptic plane (the plane of the Earth's orbit around the Sun). It is called the Interplanetary Magnetic Field (**IMF**). However, due to the radial movement of the particles and the rotation of the Sun, the magnetic field lines form the Parker spiral [*Parker*, 1958], as sketched in Figure 1. Hence, the IMF reaches Mercury with an angle of ~20° with respect to the planet-Sun line, ~45° for the Earth, and ~56° for Mars [Brain et al., 2006].

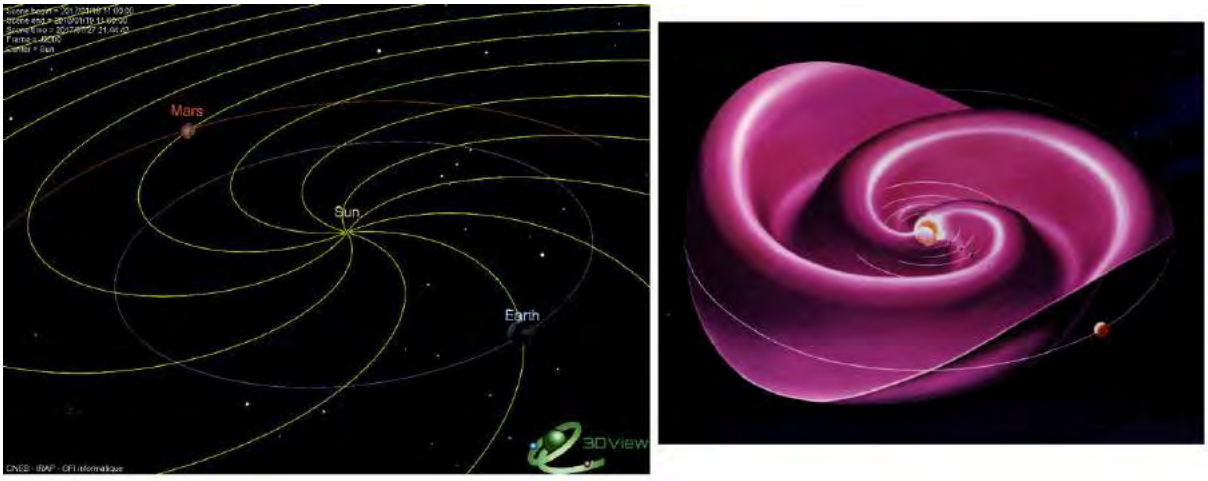

Figure 1. Illustration of the Parker spiral.

Left: Illustration of the Parker spiral made with 3D view (see section 2.4.1) and the orbit of the Earth and Mars.

Right: 3D representation of the Parker spiral with the orbit of Mercury, Venus, the Earth, Mars and Jupiter.

As it expands into the solar system, the solar wind evolves in terms of density, temperature, and strength of its IMF, so that the incident plasma at Mars has properties intermediate between those experienced by inner and outer planets. Several properties of the solar wind at the average distance of the Earth [*Kivelson and Russel*, 1995], and of Mars [*Brain*, 2006; *Fränz et al.*, 2006], from the Sun are gathered in Table 1. The average distance of the Earth from the Sun is defined as 1 Astronomical Unity (1 AU$\sim 150 \times 10^6$ km). Mars is at an average distance of 1.5 AU from the Sun.

For the different bodies embedded in the solar wind, the boundary between where sunlight is received and where it is not is called the **terminator** (see section 5.3.1.2).

Property	Earth orbit (1 AU)	Mars orbit (1.5 AU)
Proton density	$6.6\ \mathrm{cm}^{-3}$	$1-3\ \mathrm{cm}^{-3}$
Flow speed	$450\ \mathrm{km.s}^{-1}$	$300-400\ \mathrm{km.s}^{-1}$
Proton temperature	10 eV	10 – 20 eV
Electron temperature	12 eV	2 – 10 eV
Magnetic field	7 nT	2 – 4 nT

Table 1. Typical properties of the solar wind observed at the orbit of the Earth [Kivelson and Russel, 1995] and at the orbit of Mars [Brain, 2006; Fränz et al., 2006]

The different bodies embedded in the solar wind are all obstacles on its course toward the limits of the Solar System. The solar wind plasma flow is then modified in the vicinity of the planets, satellites or comets which slow down its progression. The environment of the bodies are in return shaped by the passage of the solar wind.

1.1.2. Four different classes of interaction

Though the different bodies present in the Solar System possess various characteristics, it is possible to sort their interaction with the solar wind into different classes. These interactions depend mostly on the presence or absence of an atmosphere, and therefore of an ionosphere, and on the presence or absence of an intrinsic magnetic field strong enough to deflect the solar wind flow. These characteristics set which kind of obstacle interacts with the solar wind (solid body, ionosphere, intrinsic magnetic field…) and hence the kind of the resulting interaction. There are many different ways of sorting these interactions and the sorting presented below is one among others. However, it allows to get a good idea of the different possible interactions and what makes them different.

The four general classes presented here are the following: **(1) magnetospheres**, **(2) cometary and Moon-like interactions**, **(3) induced-magnetospheres**, and **(4) mini-magnetospheres**. These different groups are showing up in the M-B diagram presented in Figure 2 (adapted from *Barabash,* [2012]). In this figure is compared the total mass of the neutral gas present around an object (**M**) and the magnetic field (**B**) at this object. For the bodies lacking of an intrinsic magnetic field, B corresponds to the value of the interplanetary magnetic field at the distance of the body from the Sun.

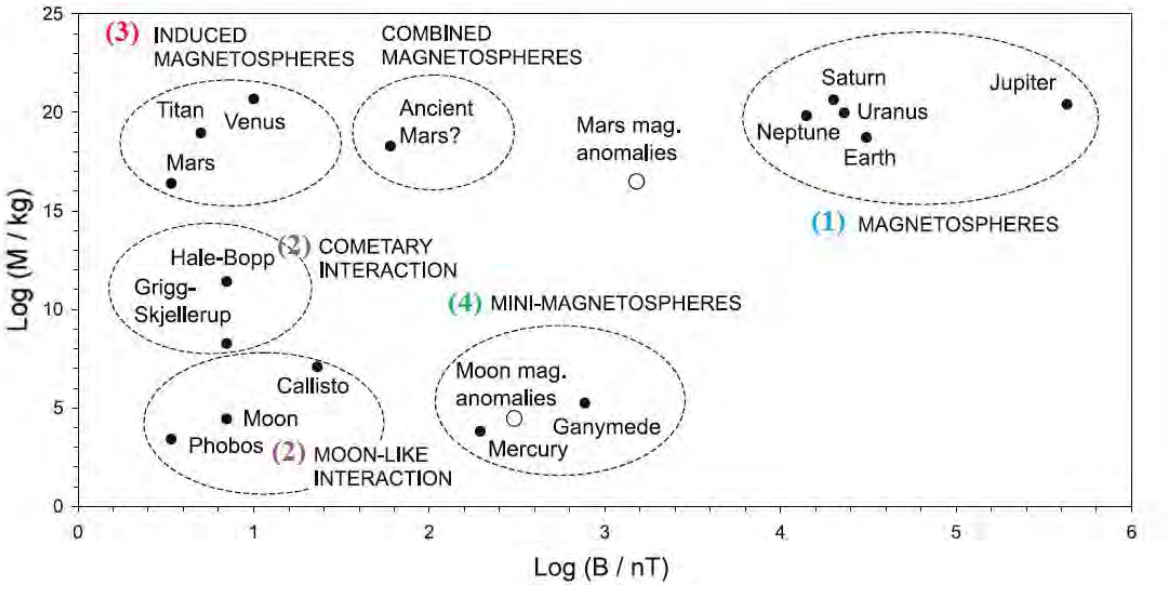

Figure 2. M-B diagram [Barabash et al., 2012].

M corresponds to the total mass of the neutral gas present around an object and B corresponds to the magnetic field at this object (intrinsic or interplanetary magnetic field).

- **(1) Magnetospheres** (Saturn, Neptune, Uranus, Earth, Jupiter)

This is the most familiar interaction of an object with the solar wind. The bodies concerned are those which own a **strong intrinsic magnetic field**. The planetary magnetic field provides in this case the effective obstacle to the solar wind plasma. A simplified sketch of the Earth magnetosphere is drawn in Figure 3 [adapted from *Luhmann et al.*, 1991].

The solar wind pressure compresses the internal magnetic field lines on the dayside, distorting and confining them inside a magnetospheric cavity. As the solar wind is supersonic, this encounter creates a shock upstream the planet, called the **bow shock**. The solar wind is then slowed down and reaches a subsonic speed in a region called the **magnetosheath**. The magnetosheath acts like a buffer region between the interplanetary medium where the solar wind plasma is dominant and the near planetary environment where the planetary plasma is dominant. Hence, this transition region is filled with shocked, deflected, heated and high density solar wind plasma with its draped, frozen-in magnetic field (the draping of the IMF is discussed in more details in section 1.3.1.2)

As the solar wind is a conductive fluid, a current layer called the **magnetopause** exists to isolate the magnetic field of the planet from the IMF. The magnetopause is the outer boundary of what is called the **magnetosphere**, which is defined as the region of space where the magnetic field lines have at least one end connected to the source of the internal magnetic field.

Only a small amount of solar wind particles finally go through the magnetopause, particularly in the cusp regions, more or less sporadically.

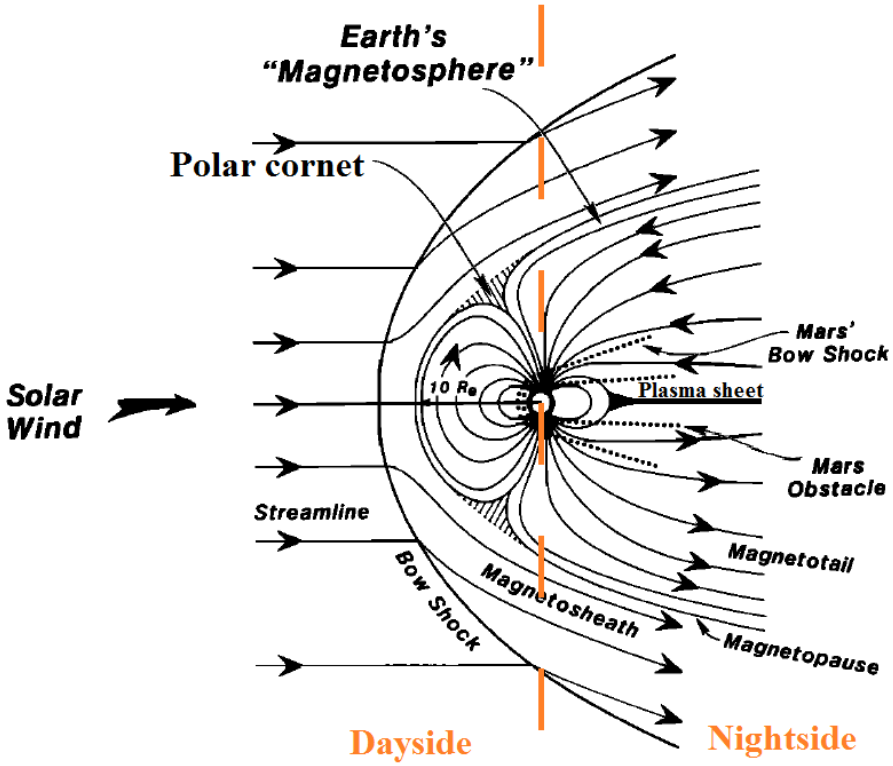

Figure 3. Illustration of the general features of the interaction of the solar wind with the Earth magnetic field. Superimposed in dotted lines are the main features of the Mars-solar wind interaction. The sizes of the planets have been normalized for the purpose of comparison [adapted from Luhmann et al., 1991].

Though on the dayside the planetary magnetic field lines are compressed by the solar wind pressure, on the nightside they are pinched into a long **magnetotail**. The magnetotail is composed of two lobes of opposite polarity, depending of the inner magnetic field polarity, and extending in the anti-solar direction. They are isolated from each other by a **plasma sheet**, at which the radial component of the magnetic field reverses.

- **(2) Cometary and Moon-like interactions** (Callisto, Moon, Phobos, comets, …)

The bodies concerned in this category do not possess an internal magnetic field nor a consistent atmosphere (the active comets at small heliocentric distances being excluded from this category). In this case, the obstacle to the flow of the solar wind is an **incompressible conducting body**, such as an iron core or a salt-water ocean. The solar wind particles then travel without being disturbed until they reach the surface of the obstacle, where they are

absorbed. This creates a **plasma-absorption wake** left in the plasma behind the body, which is characteristic for this kind of interaction. At the same time, the IMF diffuses into the low conducting outer layers of the obstacle at a rapid rate, so that it is barely perturbed from its upstream orientation. Contrary to different configurations (such as the magnetospheres detailed previously), neither the magnetic field nor the particles accumulate on the dayside.

An illustration of this interaction at the Moon is presented on the left side of Figure 4, adapted from *Luhmann et al.*, [2004]. We clearly see that the IMF is hardly affected by the passage of the obstacle but that a wake cavity is formed downstream. In the case of the Moon, there is no bow shock upstream the body because the diversion of the magnetic field occurs inside the absorbing body.

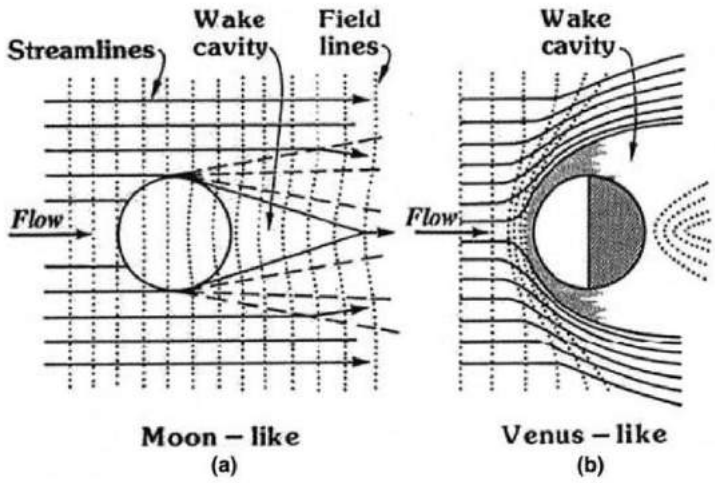

Figure 4. Illustration of two different interactions of the solar wind with unmagnetized obstacles. Left: the Moon interacts mainly with the solar wind plasma, while le IMF is hardly disturbed. Right: in the case of Venus, the presence of a substantial ionosphere produces a relatively impenetrable obstacle. Adapted from [Luhmann et al., 2004].

- **(3) Induced-magnetospheres** (Titan, Venus, Mars)

This class of interaction contains bodies that do not possess an intrinsic magnetic field at large scale but that possess a dense atmosphere. The word 'induced' used here refers to the general processes of creating an effective magnetic obstacle through plasma interactions [*Luhmann et al.*, 2004]. The induced magnetic fields include the field perturbations resulting from electromagnetic induction, but also from the flow interaction.

In this case, the atmosphere of the bodies is partially ionized by the ultraviolet solar photons which create an ionosphere (see section 1.2.1.1 for more details). The obstacle to the solar wind is then an electrically conducting, compressible **ionospheric shell** which balances

the external plasma pressure at a boundary generally called **ionopause**. As in the case of the magnetospheres, the solar wind slows down upstream the obstacle and becomes subsonic when it crosses the bow shock upstream the body. At the same time, the interplanetary magnetic field lines pile up in front of the obstacle and drape around it, as shown on the right side of Figure 4 for the case of Venus. The so-formed induced magnetosphere also includes a magnetosheath and an induced tail which is essentially the extension of the magnetosheath into the wake.

In Figure 5 is shown a simplified scenario of the creation of an induced magnetosphere. The intrinsic neutral environment of a planet (step 1) is ionized through different processes by the ultraviolet solar photons (step 2). The so-formed ionosphere is a conductor (step 3). The incoming magnetic fields generate induced currents in the ionosphere that keep the IMF from penetrating through the body by generating a canceling field (step 4). This situation persists as long as the external magnetic field keeps changing its orientation and/or magnitude [Luhmann, 1995].

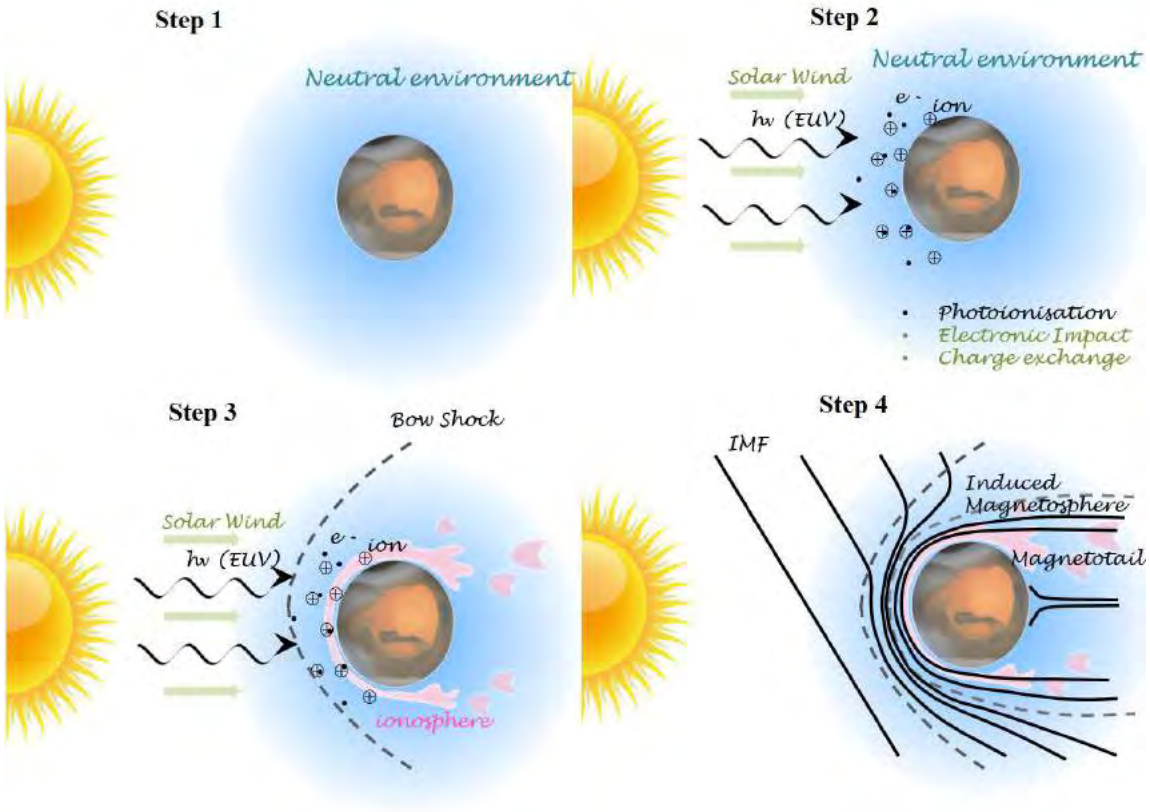

Figure 5. Illustration of the steps leading to the formation of an ionospheric obstacle in the solar wind flow. Adapted from Kivelson and Russel [1995].

The induced magnetosphere interaction will be discussed in more details in section 1.3.1, for the specific case of Mars.

- **(4) Mini-magnetospheres** (Ganymede, Mercury, Moon magnetic anomalies)

This last class gathers bodies with no significant atmosphere but with a magnetic field (intrinsic or remnant) two or three orders of magnitude weaker than in the magnetosphere class. This class appears like an intermediate case between bodies with low or no magnetic field and planets with strong intrinsic magnetic fields.

The solar wind plasma directly interacts with the surface of the body, as for the Moon, since no atmosphere can shield it. This interaction contributes to the creation of a thin atmosphere: an **exosphere** (see section 1.2.1.1), whose composition reflects the composition of the surface. In the case of Mercury, other processes like thermal desorption and meteorit bombing are also to be considered. The low gravity of the planet added to its high surface temperature due to its vicinity to the Sun facilitate the creation of such an exosphere.

In addition, there is a magnetosphere-like interaction with the formation of a magnetosphere, a magnetopause, cusps, a magnetotail, etc. However, there is no coupling with an ionosphere, with no creation of ionospheric currents like at Earth, but there is a coupling with the core. An illustration of the magnetosphere of Mercury is given in Figure 6.

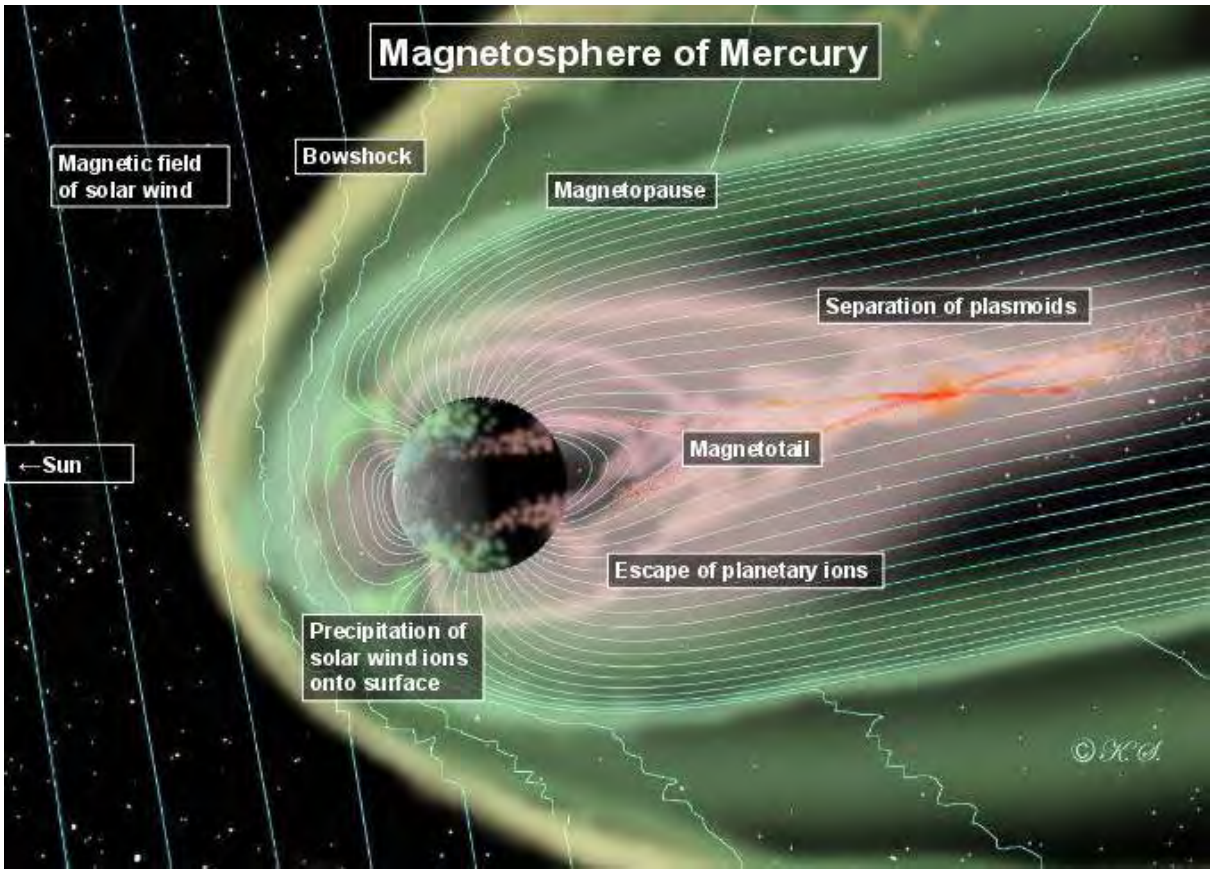

Figure 6. Illustration of the magnetosphere of Mercury. The solar wind comes from the left side.

Much remains to be discovered about these types of magnetospheres, and future missions, such as Bepi-Colombo at Mercury or JUICE at Ganymede, will help understanding this kind of interaction.

As observed in Figure 2, the Martian interaction with the solar wind cannot be restricted to one category, due to its magnetic and atmospheric history. The global interaction can be similar in some extent to that of induced magnetospheres, such as Venus or Titan, but the presence of strong crustal magnetic sources induces localized mini-magnetospheres. Understanding the Martian interaction with the Sun hence begins by understanding the nature of the Martian obstacle. The current atmospheric and magnetic environment of Mars are described respectively in section 1.2.1.1 and 1.2.1.2. We then propose in section 1.2.2 an overview of the Martian history, which enables a better understanding of the current observations. This finally leads us to the description of the Martian interaction with the solar wind in section 1.3.

1.2. The Martian obstacle

Mars is the fourth planet of our solar system and the last telluric one. It orbits around the Sun on an elliptic orbit with a maximum distance to the Sun (aphelion) of 1.67 AU and a minimum distance to the Sun (perihelion) of 1.38 AU, which imply an eccentricity of 0.0935, much higher than the Earth one (0.0167). Mars inclination on its orbital plane is $25{,}19°$, which is comparable to the Earth ($23{,}44°$) and implies the presence of **seasons**.

The length of the day on Mars is quite comparable to the Earth one: $\sim 24\text{h}37\text{min}$, and the planet makes a revolution around the Sun in ~687 days, a little less than two Earth years. With an average radius of $3386{,}2\ km$, Mars is twice as small as the Earth and the gravity at its surface is three times smaller. The temperature at its surface can vary from -3°C to -133°C.

1.2.1. Mars today

Mars has been visited by more than twenty spacecraft - landers - rovers to date (see section 2.1 for more details). These in-situ measurements have allowed a better knowledge of the Martian object, its current atmosphere (1.2.1.1) and magnetic field (1.2.1.2), which both are important to understand the interaction of Mars with the Solar wind.

1.2.1.1. Atmosphere - Exosphere - Ionosphere: who is who?

Atmosphere

Based on the nomenclature used for the terrestrial atmosphere, the Martian atmosphere can be divided into several layers according to the mechanisms involved (turbulence, molecular diffusion, photoionization, heating by absorption of UV rays). Taking the collisional point of view, the atmosphere can be divided into two parts: the barosphere and the exosphere (Figure 7). These two layers are characterized by a dimensionless number, the **Knudsen number** (Kn):

$$\text{Kn} = \frac{\lambda}{H}$$

The **mean free path** λ can be defined as follows, in the case of a gas composed of a single species, where n is the density of the species, and $\pi\sigma^2$ the cross section :

$$\lambda = \frac{1}{\pi n \sigma^2 \sqrt{2}}$$

The **scale height** H — corresponding in every point to the altitude to be raised for the pressure to be decreased by a factor of e — can be defined as follows:

$$H = \frac{k_B T}{M g}$$

Where M is the mean molecular mass, g the local acceleration of gravity, k_B the Boltzmann constant and T the medium temperature.

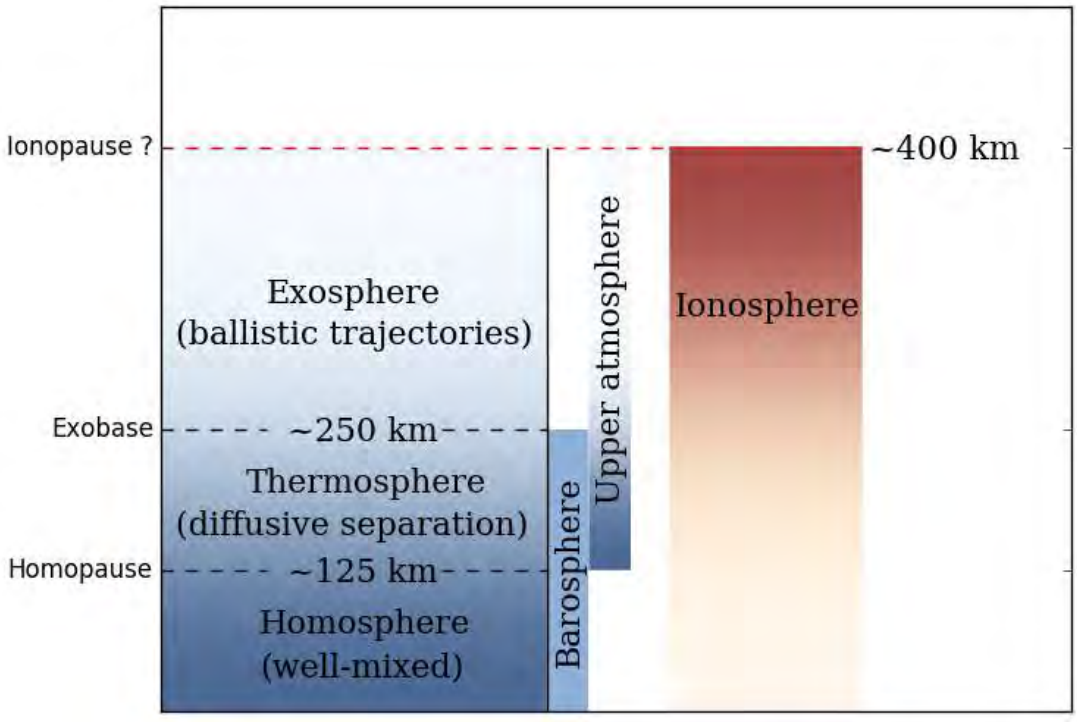

Figure 7. Altitudinal extension of the different atmospheric regions and boundaries discussed in section 1.2.1.1 and of the ionosphere.

Regarding the Knudsen number, the barosphere and the exosphere can be defined as follows:

- The **barosphere** is a region of low Knudsen number ($Kn \ll 1$). This is the inner part of the atmosphere, with the highest density. The dynamics is dominated by collisions between molecules and atoms, which result in a collisional medium, dominated by diffusion processes.

- The **exosphere** is a region of high Knudsen number ($Kn \gg 1$). It corresponds to the external layer of the atmosphere and hence the less dense. The dynamics is here dominated by external forces, especially gravitation. It is characterized by a very high Knudsen number, which means that there are very few collisions, and that the trajectories of the particles are essentially ballistic. The exosphere is an exchange area between the lower atmosphere and the interplanetary medium.

The transition between the collisional and non-collisional medium is called the **exobase**. It has been estimated at 250 km by *Anderson and Hord* [1971], after Mariner 6 and 7 observations.

The barosphere can be divided into two layers, regarding the mixing of the atmospheric components: the homosphere and thermosphere (see Figure 7). The homosphere and thermosphere are separated by a layer called the **homopause** (located at ~125 km mean altitude on the dayside).

- The **homosphere** is the lower layer, characterized by atomic and molecular constituents which are well mixed by winds and dissipative turbulence [*Stewart*, 1987; *Bougher* 1995; *Bougher et al.*, 2000; 2009; 2014]. The relative proportion of each species stays quasi-constant, no matter the molecular mass.
- The **thermosphere** corresponds to the region where the atomic/molecular diffusion dominates. Individual species begin to separate according to their unique masses and scale heights. The low mass species have higher scale height and will then be more abundant at higher altitude regarding heavier species whose density will decrease more quickly with altitude. The first in situ measurements of the thermosphere composition were obtained by the Viking 1 and 2 entry probes in 1976 [*Nier and McElroy*, 1976; *Nier et al.*, 1976]. The measurements recorded along the descent of the landers highlighted the presence of $CO_2, N_2, {}^{40}Ar, O_2, NO$ and maybe CO in the Martian atmosphere.

More recently, measurements made with the Mars Atmosphere and Volatile EvolutioN (MAVEN) spacecraft down to the homopause improved our knowledge of the composition of the atmosphere and its variation with altitude. On the left panel of Figure 8 is plotted the neutral composition obtained during one orbit down to 133,8 km, near the equator at noon, and on the right panel is plotted the average vertical neutral profiles obtained at 45° solar zenith angle [*Mahaffy et al.*, 2015b]. We clearly observe that the lower atmosphere is dominated by $\mathbf{CO_2}$ whereas the higher atmosphere is dominated by **O**, with significant amount of O_2, N_2 and N.

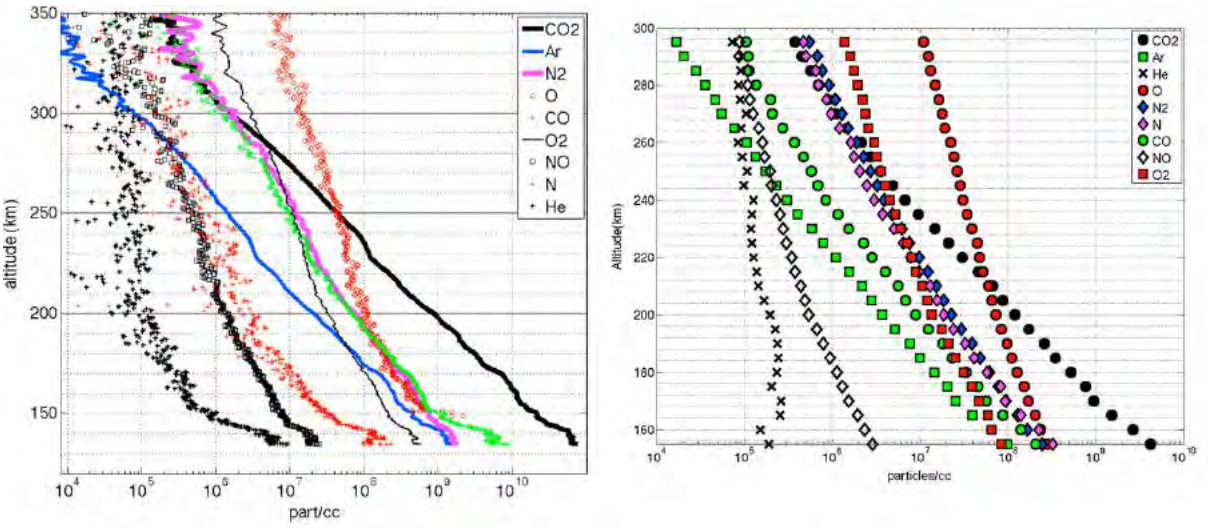

Figure 8. Neutral profiles obtained with the NGIMS instrument on MAVEN [Mahaffy et al., 2015]. Left panel: an example of the variation with altitude of nine atomic and molecular species during a passage down to 133.8 km. Right panel: the average vertical profiles for nine upper atmosphere species at 45° solar zenith angle.

Ionosphere

The upper neutral atmospheric region includes the thermosphere and the exosphere (also sometimes referred to as the corona). The upper neutral atmosphere interacts directly with the solar wind particles and photons, modifying the plasma neighboring the planet and creating an **ionosphere** (i.e. a part of the atmosphere that is ionized). While the thermosphere extends from ~100 to ~250 km altitude, the ionosphere can extend from ~100 to ~400 km altitude [*Bougher et al., 2014*].

The process of ionization involving photons is called photoionization, and the process involving energetic-particles is often called impact ionization. While photons mainly come from the Sun, the ionizing particles can come from the Sun, but also from the galaxy (cosmic rays), or from the ionosphere itself. The only requirement for the photons and energetic particles to ionize the neutral atmosphere is that their energy exceed the ionization potential or binding energy of a neutral. Atmospheric ionization is usually attributable to a mixture of these various sources, but one often dominates.

The three predominant ionization processes at Mars are the following (but there are several other mechanisms which play an important role in the dynamics and the escape of the ionosphere, see section 1.2.2.2):

- Photoionization:

Solar photons arriving on Mars mainly interact with O and CO_2 by the following mechanisms:

$$CO_2 + h\nu \rightarrow CO_2^+ + e^-$$
$$O + h\nu \rightarrow O^+ + e^-$$

These two reactions are both associated with an ionization threshold near 90 nm: 91,1 nm for oxygen and 89,9 nm for carbon dioxide. This means that only photons with lower wavelengths can photoionize O and CO_2. This corresponds to solar photons in the "extreme" ultra-violet (EUV) and ultraviolet (UV) wavelength ranges. Photoionization is the most important ionization process at Mars, in particular to create the **dayside ionosphere**.

- Ionization by electronic impact:

It corresponds to the interaction of electrons coming from the solar wind or the magnetosheath with the atmospheric neutrals thus producing ions. This process is the dominant ionization process producing the **nightside ionosphere**. Following is an example of such ionization by electronic impact with a neutral (M):

$$e^- + M \rightarrow M^+ + e^- + e^-$$

- Charge exchange reactions

The plasma of the solar wind or of the induced magnetosphere interacts with the neutrals of the atmosphere. The incident ions can extract an electron from the atmospheric neutrals and transfer them their positive charge, thus producing a new ion and an energetic neutral atom. This process plays an important role in the production of ions (and associated cyclotron waves) at high altitudes in the **Martian corona**, due to the solar wind incident protons. Following is an example of such charge exchange reaction:

$$H^+ + O \rightarrow O^+ + H$$

In Figure 9 are plotted the altitude profiles of the main ions of the Martian ionosphere, obtained by *Benna et al.*, [2015] during the first eight months of the MAVEN mission in 2014-

2015. We can observe that the dominant ion is O_2^+ below 300 km, with a smaller but significant amount of O^+ and CO_2^+, depending on the altitude.

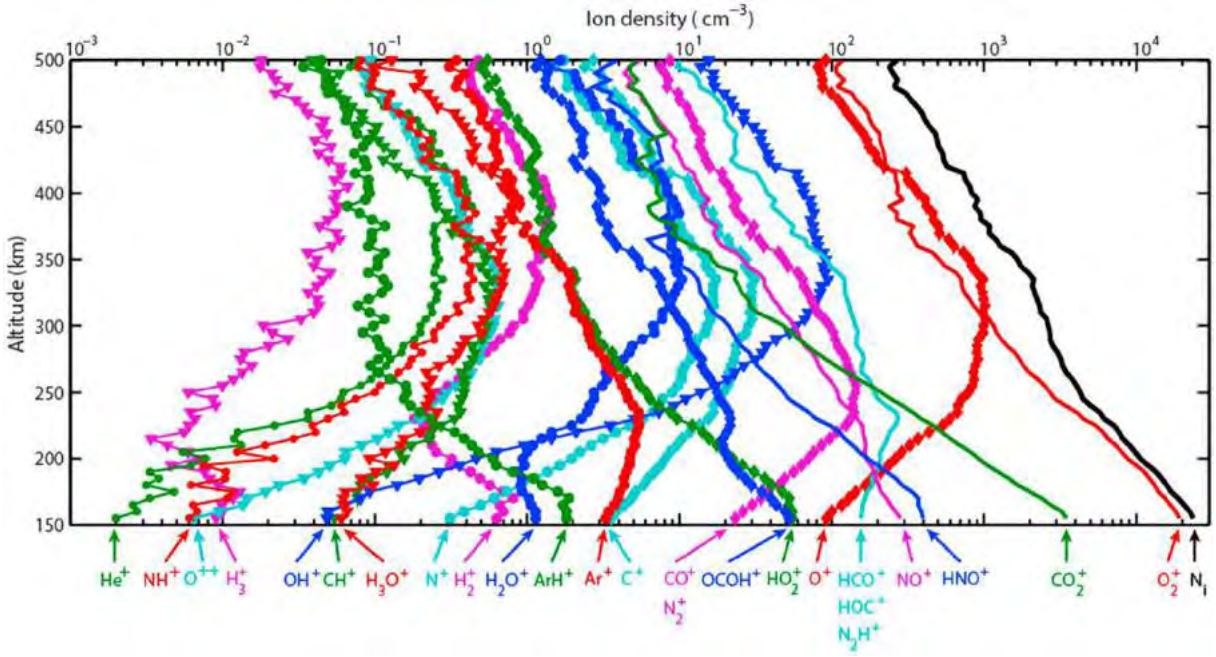

Figure 9. Altitude profiles of the averaged density of ionospheric ions measured by NGIMS onboard MAVEN. Measurements were made at a solar zenith angle of 60° and at altitudes between 150 and 500 km. The vertical profile of the total ion density N_i is also plotted in black. [Benna et al., 2015]

The altitude profile of ion production shows a peak at some altitude (the so-called Chapman layer), because the rate of ionization depends on both the neutral density (which decreases with altitude) and the incoming solar photons or precipitating plasma intensity (which decreases towards the surface due to absorption by the atmosphere). The altitude of this peak is specific to each ionization source. Hence, we usually observe three peaks on the Martian ionospheric profiles on the dayside: one for the EUV-UV, one for the X-ray and one for the meteoroids. Those peaks are different on the nightside.

1.2.1.2. The Martian magnetic field

The question of the Martian intrinsic magnetic field remained unanswered until the end of the 90s, when it was proved that, at the present time, **Mars does not possess any global magnetic field** generated by an internal dynamo.

The first observations of the Martian magnetic field in the near Martian environment had been made by the Mariner 4 spacecraft in 1965 when it passed within 13 200 km of the planet.

The lack of detectable magnetic field signature attributable to Mars led to the conclusion that the Martian magnetic moment could not exceed 3×10^{-4} that of the Earth dipole moment, equivalent to an equatorial field of less than 100 nT [*Smith et al.*, 1965]. Additional measurements were made by Mars 2, 3 and 5 in the early 1970s and by Phobos 2 in 1989. Even the Phobos 2 spacecraft, whose lowest altitudes were at 850 km from the surface, did not measure any magnetic field providing evidence of an intrinsic magnetic field. The scientific community was then divided between those claiming the presence of a small intrinsic dipole moment [*Dolginov and Zhuzgov*, 1991; *Slavin et al.*, 1991; *Verigin et al.*, 1991a; *Möhlmann et al.*, 1991] and those claiming the absence of any intrinsic magnetic field [*Russell et al.*, 1995; *Gringauz et al.*, 1993].

Mars Global Surveyor (MGS) was the first spacecraft to obtain magnetic field observations beneath the ionosphere (~170 to 200 km) in 1997-1998. It provided 83 periapsis passes with altitudes between 100 and 170 km. This region is particularly interesting since it is shielded from the confounding effects of the solar wind interaction with the Martian atmosphere and ionosphere. The induced magnetic fields resulting from this interaction can indeed reach levels similar to those arising from a planetary field of internal origin (see section 1.3.1.3). *Acuña et al.* [1998] showed that on several orbits reaching the underside of the ionosphere, relatively weak magnetic fields ($\leq 5nT$) were observed. They hence conclude that Mars does not possess a global intrinsic magnetic field on a large scale, and therefore **no dynamo** at present.

However, on some other orbits, like the one presented in Figure 10, the magnetometer recorded large magnetic fields near the periapsis. The amplitude of the magnetic field plotted on the right panel is projected on the MGS orbit on the left panel, so that the highest amplitude of the magnetic field (~400 nT) is observed at the closest point of the spacecraft orbit, while no significant magnetic field can be observed on the remaining part of the orbit. For these kind of orbits, it was found that the observed magnetic fields were restricted to a segment of the spacecraft trajectory that passed close to the Martian crust. Hence, the observed magnetic signatures are not of global scale, as it would necessarily be if they were generated in the deep interior, for example by a dynamo. It was thus discovered that the magnetic field of Mars is dominated by **intensely magnetized sources**, distributed non-randomly in its crust [Acuña et al., 1998, 1999].

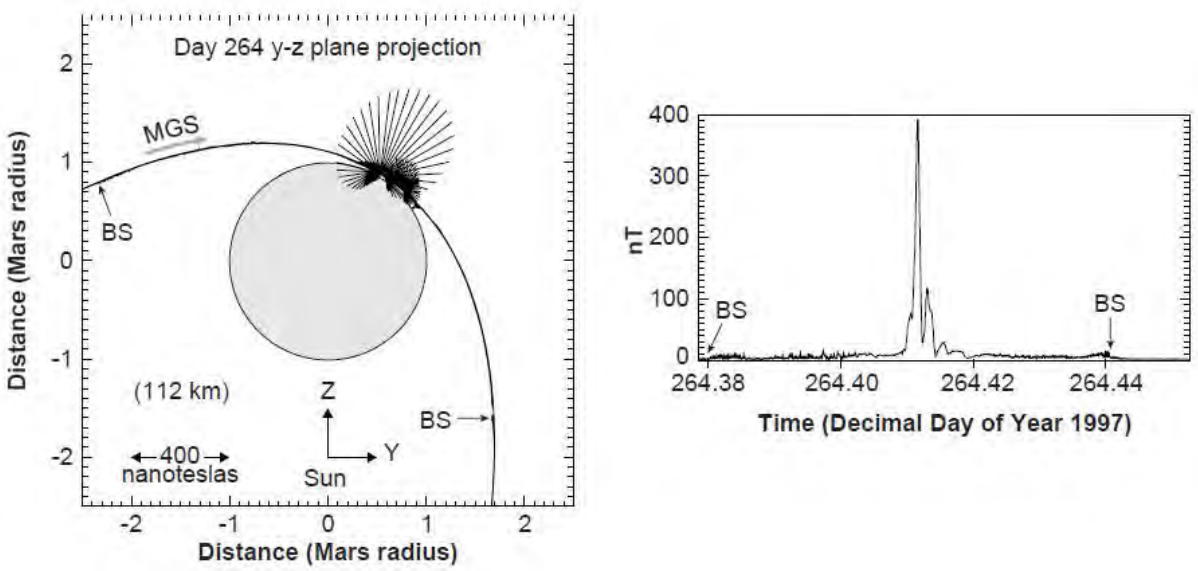

Figure 10. Illustration of the magnetic field measured by MGS [Acuña et al., 1998].
Left panel: projection of the MGS spacecraft trajectory and observed magnetic field onto a plane perpendicular to the Mars orbit plane and the Mars-Sun line for a specific periapsis. The field observed along the trajectory at 3-s intervals is represented by a scaled vector projection of B originating from the position of the spacecraft at such times. Field vectors are scaled to $400\ nT\ =\ 1\ R_{Mars}$. *Right panel: magnitude of the observed magnetic field as a function of time for the time interval represented on the left panel.*

Compiling the data obtained by MGS during two full Martian years at its 400 km-mapping altitude, Connerney et al., [2005] presented a global map of the magnetic fields due to remnant magnetism in the Martian crust. Figure 11 is an updated version of this map [Connerney et al., 2015]. It is a global map of the filtered radial magnetic field (ΔB_r), color contoured over two orders of magnitude variation in signal amplitude. The map is superimposed on the Mars Orbiter Laser Altimeter shaded topography map.

The **crustal magnetic sources**, mainly located in the southern hemisphere, can be considered as small dipoles located under the Martian crust. They form closed magnetic field loops (see section 1.3.2.1), which extends beyond 120 km altitude over 70% of the surface, and can extend up to 1500 km altitude over the strongest southern sources. The crustal magnetic field can reach intensities exceeding 200 nT at 400 km in the southern hemisphere [Acuña et al., 2001]. The largest crustal magnetic field strength ever measured at Mars is ~1600 nT near 100 km altitude. This value can be compared to the typical strength of the Earth's global magnetic field and magnetic anomalies measured at 400 km: 26000 nT and 10 nT, respectively.

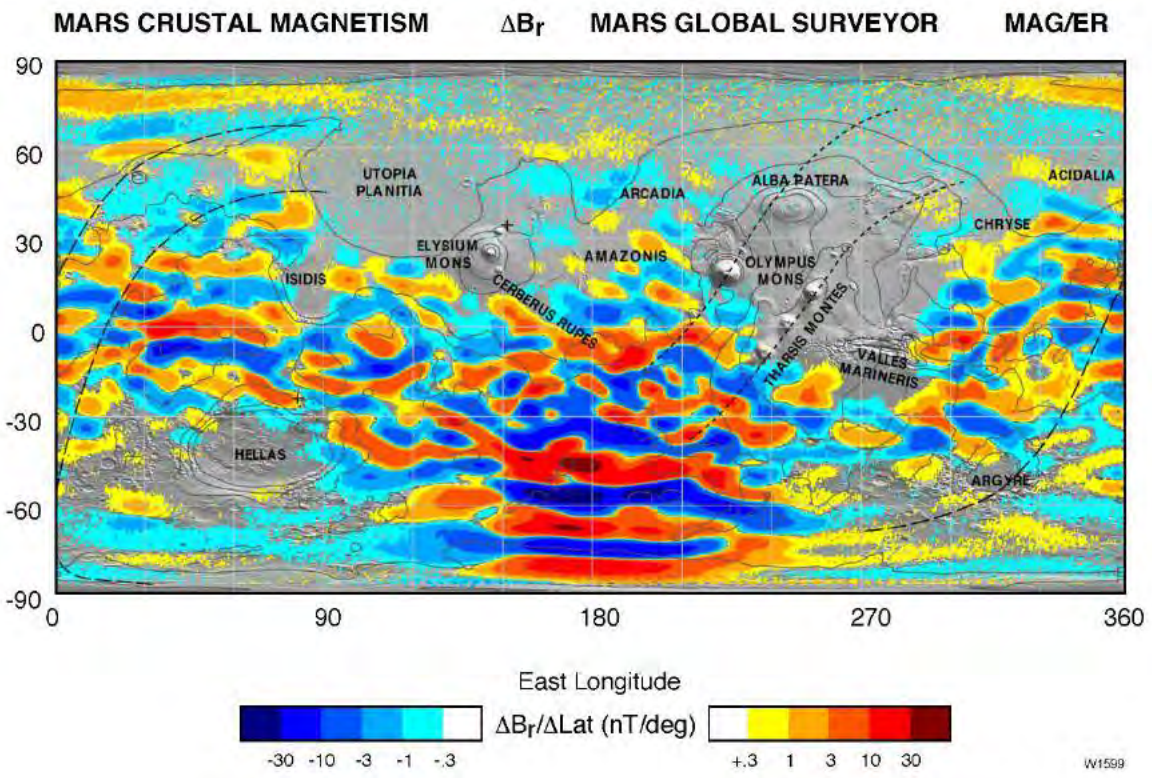

Figure 11. Map of the remnant magnetic field of Mars observed by MGS at its nominal altitude of 400 km. Each pixel is colored according to the median value of the filtered radial magnetic field component observed within the ½° by ½° latitude/longitude range represented by the pixel. Contours of constant elevation (-4, -2, 0, 2, 4 km elevation) are superimposed (after Connerney et al., 2005).

The Martian obstacle to the Sun is then composed of the **ionosphere**, together with the **crustal magnetic sources**. Both form magnetic fields that divert the incoming plasma around the planet. Crustal magnetic fields contribute to the deflection in some regions of Mars (mainly in the Southern hemisphere), creating 'mini-magnetospheres'. In other regions, the IMF carried by the solar wind induces currents (via Faraday's Law) in the conducting ionosphere that generate magnetic fields (via Ampere's Law). The shielding magnetic fields then deflect solar wind particles around the obstacle (via the Lorentz's law).

The interaction of Mars with the Sun will be extensively discussed in section 1.3, after a brief incursion into the Martian history.

1.2.2. Back to the history of Mars

Mars is currently an arid planet, with a thin atmosphere, having an atmospheric pressure of 636 Pa (0.006 bar), compared to the 10^5 Pa (1 bar) atmospheric pressure we currently have on the Earth. However, several missions (see section 2.1) revealed the occurrence on the Martian surface of geological features that are typically related to surface fluid flow on Earth, which tends to indicate the ancient flowing of liquid water on Mars. Hence, water would have been stable at the surface of Mars several billion years ago (see the timeline in Figure 12). Current temperature and pressure conditions at the surface of Mars prevent the presence of 'permanent' liquid water, even if transient liquid water has already been observed (e.g. *Martin-Torres et al.*, [2015]). The leading idea for explaining the observation of surface flow markers is the occurrence of a different climate during these early periods, with a **denser atmosphere** and **warmer temperatures** to sustain the flowing of liquid water at the surface of Mars. Warmer temperatures could be explained by a higher concentration of greenhouse gases in the Martian atmosphere, such as CO_2, as compared to current days. As for the higher atmospheric pressure in the past, it could be explained by a denser atmosphere, which could have been possible thanks to an intrinsic magnetic field strong enough to shield the atmosphere from the solar wind.

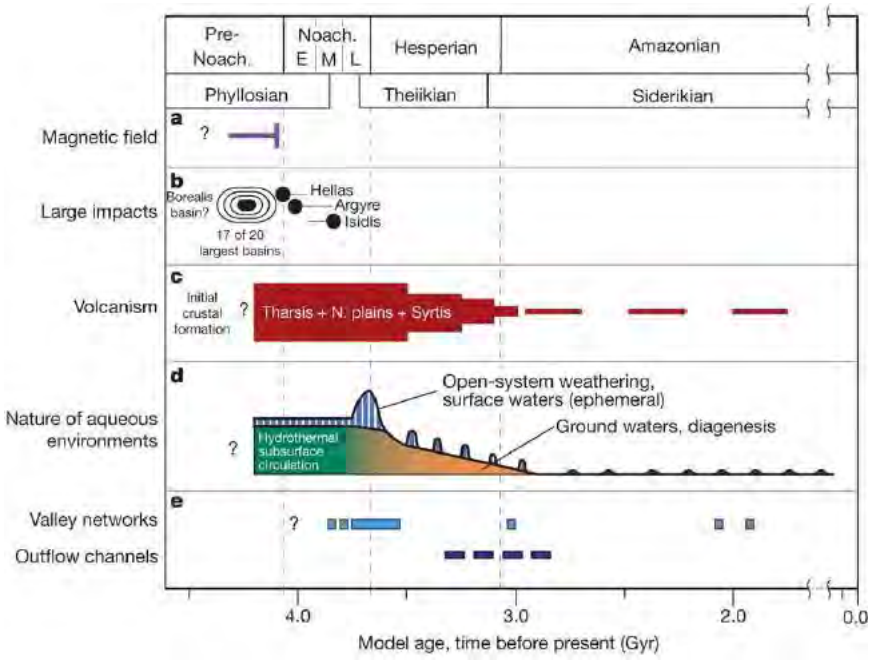

Figure 12. Timeline of major processes in Mars history (adapted from Ehlmann et al., [2011]). Panel a: Presence of an intrinsic magnetic field. Panel b: Impact cratering. Panel c: Volcanism. Panel d: Schematic depicting the changing nature of environments hosting liquid water. Panel e: Timing of valley network and outflow channel activity.

Liquid water on Mars is currently a hot topic, and consequently its disappearance too. As its disappearance seems to be strongly linked to the disappearance of the atmosphere and to an alteration of the climate and of the inventory of volatiles through time, the National Aeronautics and Space Administration (NASA) sent in 2013 a mission dedicated to the study of such phenomena: the MAVEN mission (see section 2.1.3 for more details about the mission).

1.2.2.1. A magnetic field history

The results obtained with the MGS spacecraft [*Acuña et al.*, 1998] showed that Mars does not possess any global magnetic field at the present time, and therefore no dynamo at present. However, the presence of crustal magnetic sources strongly suggest that Mars had a dynamo in the past, when the crust acquired intense **remnant magnetization**.

Geological interlude

On Earth, when igneous rocks cool down, they can acquire a thermoremanent magnetization from the Earth's magnetic field thanks to some of their components, such as iron-titanium oxide minerals in basalt. When the temperature decreases below the Curie temperature of the rock, the orientation and magnitude of the ambient magnetic field is recorded in the cristalline structure of the rock. This record can last for billion years, unless the rock is heated to temperatures higher than its Curie temperature.

The study of the remnant magnetic field on Earth gives a better understanding of the continental drift and the way oceanic ridges work. For example, alternate bands of opposite magnetization on each side of oceanic ridges show how the oceanic crust moves as the Earth dipole polarity reverses in time.

It is likely that a molten iron core formed early in the Martian history, after or during hot accretion, 4.5 or 4.6 billion years ago. A substantial global magnetic field may then have been generated for at least a few hundred million years by dynamo action in the core. During this time period, the planetary magnetic field must have been recorded in certain kind of rocks, as it can observed on Earth (Figure 13).

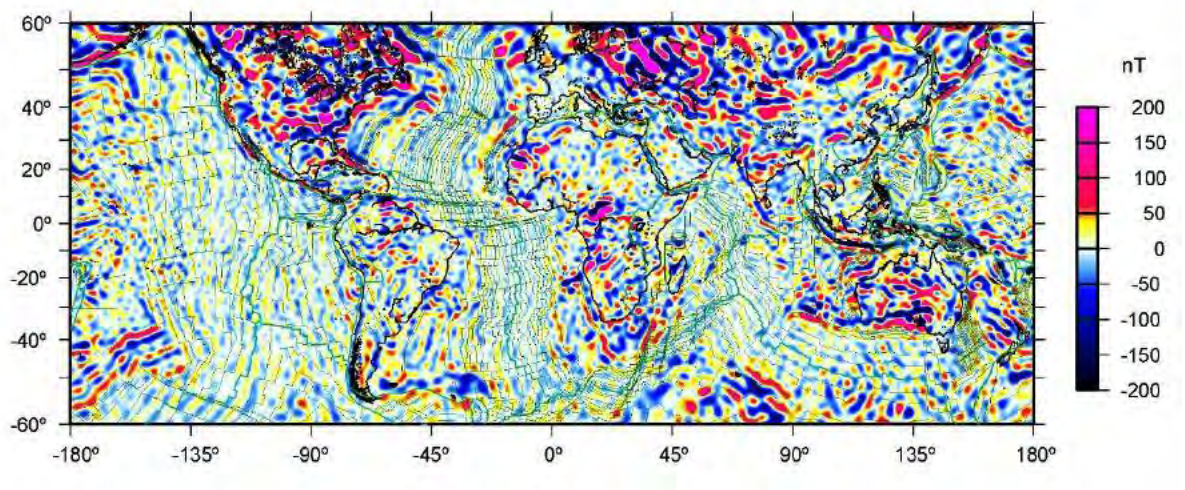

Figure 13. Modeled imprint of the intrinsic magnetic field in the Earth's crust.
Vertical component of the MF6 model crustal magnetic field at the Earth surface, overlain with the isochrones of an ocean-age model and plate boundaries, http://geomag.org/models/MF6.html

Based on the distribution of the Martian crustal magnetic fields (Figure 11), which are mainly coincident with the oldest terrains, *Acuña et al.*, [1998; 1999] proposed that the dynamo stopped early in the Martian history, prior to the last great impact (~4 billion years ago, see the timeline in Figure 12). When the dynamo was active, the entire crust acquired a magnetic imprint via crustal heating — implying the presence of an iron-rich magma (intrusive, impact or thermal event) — and cooling in the presence of a reversing dynamo [*Connerney et al.*, 2005]. This mechanism allowed the crust to acquire a permanent remnant magnetic field that records the orientation of the global Mars magnetic field at that epoch.

Large erasures of this imprint occurred when the crust was melted above its Curie temperature (thermal demagnetization) while no more ambient magnetic field was present, as during the last great impact for example. This left the large unmagnetized basins in the crust we can observe in Figure 11, as Utopia Planitia in the northern hemisphere. The extinction of the dynamo would then produce crustal magnetic sources as permanent record of the paleofield and crustal evolution, unless they get obliterated by subsequent thermal events.

This view has been supported by more complete analysis on the large impact basins [*Lillis et al.*, 2008a; 2013]. It appears through these studies that dynamo generation of the global magnetic field was extinguished before the formation of Hellas and Utopia basins approximately 4.0-4.1 Ga ago. A more complete review of the different mechanisms suspected to be implicated in the creation of the current Martian crustal magnetic field is reported in *Connerney et al.*, [2015].

1.2.2.2. A Mars' volatile and climate history

Knowing that Mars had a substantial global magnetic field billions of years ago, the atmosphere may have been protected against the solar wind for a geologically significant period. In the dynamo era, Mars may have retained a warm and dense atmosphere. When the dynamo stopped, there was no more protection against the solar wind and the planet was permanently subjected to atmospheric erosion.

Atmospheric loss may have contributed significantly to the evolution of the Martian climate over time. At the first times of the Martian history, the main mechanisms of atmospheric erosion were [*Brain and Jakosky*, 1998]:

- **Catastrophic degassing** by meteoritic bombing: impact erosion.
- **Hydrodynamic escaping**: it occurs when a light species escapes in abundance to space (usually enabled by high solar EUV flux or another form of heating) and drags heavier species along with it through collisions.
- **Absorption and storage in the regolith** of the surface and sub-surface.
- **Escape into space**: it is the result of a set of physical processes that provide particles of the thermosphere, ionosphere and exosphere with sufficient energy to escape the planet.

Hydrodynamic escape should have been significant for Mars during the first few hundred million years after its formation [*Zahnle and Kasting*, 1986]. When it ceased, impact erosion was a dominant loss mechanism, then decreasing as the impact flux declined over time [*Melosh and Vickery*, 1989]. The impact of these two escape processes on the atmosphere and climate of Mars are reviewed by *Jakosky and Phillips*, [2001]. The two remaining loss processes were then exchange with the surface (as polar caps) and sub-surface (as carbonate deposits within the crust) and escape to space. As the exchange with the regolith is largely reversible, escape to space permanently removes particles from the atmosphere. Escape to space is likely to have been the dominant permanent loss process over the last 3.8 billion years, and therefore a main contributor in the change of climate inferred to have occurred between present and 3.5-4.0 billion years ago.

Escape to space removes both neutral and ionized species from three atmospheric reservoirs: the thermosphere, the exosphere and the ionosphere (previously described in section 1.2.1.1). Most of the escape occurs between the homopause and the exobase, typically between 190 and 210 km [*Krasnopolsky et al.*, 1993]. A neutral or an ion escapes from Mars when it

acquired the required escape velocity. The **escape velocity** v_L is a ratio between the gravitational and electric potential energy of a given particle and the kinetic energy required to overcome it: G is the universal gravitational constant, M the mass of the planet, e the elementary charge, Z the number of electrical charges, δV the electrostatic potential difference in the case of charged particles, m the mass of the particle and r the radial distance of the particle from the center of the planet.

$$v_L = \sqrt{\frac{2GM}{r} - \frac{2Ze\delta V}{m}}$$

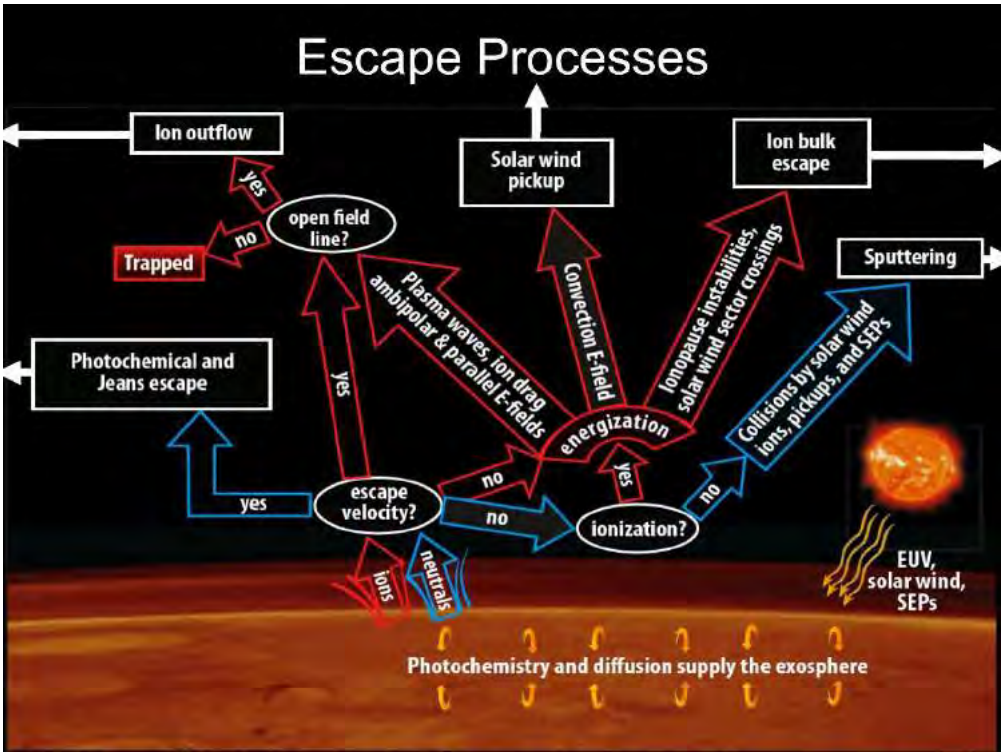

Figure 14. Schematic of contemporary escape processes relevant for atmospheric neutrals and ions. The escape processes are in the rectangular boxes and presented in a 'decision tree'. Solar inputs shown at the lower right contribute to the energization of atmospheric particles [Brain et al., 2017].

The different escape processes for atmospheric neutrals and ions are gathered in Figure 14. Three main escape processes have been identified for neutrals:

- **Jeans (or thermal) escape**: a portion of the thermal distribution for an atmospheric species exceeds the energy necessary for escape. Only species with small mass (H, D and He) can escape significantly via this mechanism. Photodissociation of water combined to Jeans

escape of H could explain the disappearance of water from the Martian atmosphere [*Pierrard*, 2003].

- **Photochemical escape**: exospheric chemical reactions (such as dissociative recombination of an ionized molecule with a nearby electron, resulting in two fast neutral atoms) provide atmospheric species with sufficient velocity to escape. Photochemical loss can be significant for O, N and C.
- **Atmospheric sputtering**: energetic incident particles (including ionospheric particles accelerated by the solar wind) can collide with particles of the thermosphere and ionosphere near the exobase. The momentum and energy exchange between particles carried out during the collision can lead to the ejection to space of the target particle. The incident particles can be solar wind protons or pickup ions.

When an atmospheric particle is ionized above the exobase, it can be accelerated, usually antisunward, by ambient electric fields. Some of the ions return to the atmosphere by precipitation while a certain amount is expected to escape. The main ion escape processes are:

- **Ion pickup**: an ionized neutral particle is accelerated away from the planet by a motional electric field **E** induced by the solar wind plasma (having a mean velocity of **v**) and its IMF **B** [Luhmann et al., 1991]: $\mathbf{E} = -\mathbf{v} \times \mathbf{B}$. It occurs primarily for ionized exospheric neutrals.
- **Ion outflow**: acceleration of low energy particles out of the ionosphere via plasma heating and outward directing charge separation electric field.
- **Bulk escape**: any process for which coherent portions of the ionosphere are detached via magnetic and/or velocity shear processes and accelerated away from the planet.

MAVEN data enable the identification of three escaping planetary ion populations [*Dong et al.*, 2015a]: strong **plume fluxes** over the MSE (Mars-Sun-Electric field) North Polar Region, strong antisunward ion fluxes in the tail region, and weak but energetic upstream pickup ion fluxes observed mostly on the dayside. The presence of such plumes has been conjectured before MAVEN, but previous measurements did not enable to set the permanent nature of this feature. The study of *Dong et al.* [2015a] illustrates the permanent presence of a substantial plume with strong ion fluxes widely distributed in the MSE northern hemisphere above the Magnetic Pile-up Boundary (see section 1.3.1.3), which gradually turn into tailward fluxes on the nightside without any significant boundary, as observed in Figure 15. In this figure are plotted the O^+ fluxes and velocities for energies greater than 25 eV, projected in the MSE X-Z

plane. At the time of this paper, the plume escape for O^+ was estimated at 30% of the tailward escape, a number later revised at 50% when more data were available. This escape varies with the solar wind density, dynamic pressure and EUV fluxes. It is highest for low EUV flux and high solar wind pressure.

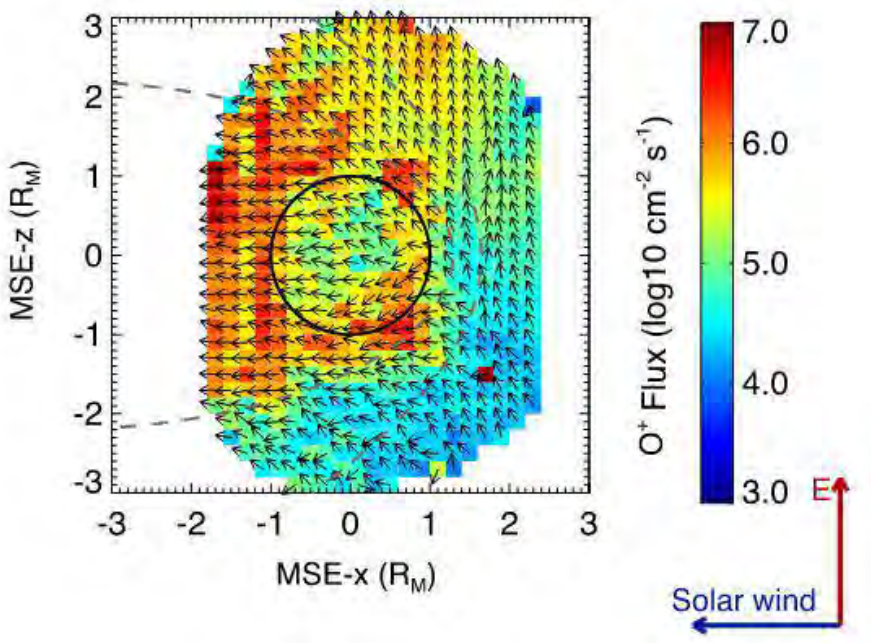

Figure 15. Observation of the plume fluxes over the MSE North Polar region [adapted from Dong et al., 2015a]. O^+ fluxes and velocities for energies greater than 25 eV are projected on the MSE X-Z plane. The arrows show flux and velocity directions, while the colors label the magnitudes. The two grey dotted lines set the approximate position of the bow shock and of the Magnetic Pile-up Boundary.

Data recorded by the numerous spacecraft orbiting around Mars enable us to better understand the physical processes that drive escape today. This knowledge then allows us to extrapolate to earlier conditions, when the drivers were enhanced and escape was more rapid.

Venus, in the same manner of Mars, presents no internal magnetic field. The atmospheres of the two planets are nevertheless strongly different: the atmospheric pressure at the surface of Venus is ~90 bar while it is ~0.006 bar at the surface of Mars. As Mars, Venus is permanently subjected to atmospheric erosion. However, due to the mass of the planet, the escape velocity on Venus is about twice the one of Mars, making it more difficult for particles to escape [*Pierrard*, 2003]. Moreover, Venus has developed through its history a greenhouse effect far more import than those on Earth and on Mars. These different specificities are part of the explanation why the planet has managed to keep its dense atmosphere despite the erosion by the solar wind.

1.3. The interaction of the solar wind with Mars

The exact nature of the interaction of the solar wind with Mars has only been elucidated around twenty years ago when MGS revealed the absence of intrinsic magnetic field at Mars but also highlighted the presence of crustal magnetic field sources on its surface. Before MGS, the bow shock and the magnetosheath had already been explored by Mariner 4, Mars 2, 3 and 5 in the 70s while Phobos 2 observed the magnetotail in the 80s (see Figure 26 and Table 2).

Two models for the Martian interaction with the solar wind were opposed at that time. On one hand, a model of magnetospheric interaction, proposed by *Dolginov et al.*, [1973] and *Gringauz et al.*, [1976], which claimed that the magnetic field of Mars controls the interaction of the solar wind with the planet. Their arguments were that they found more similitudes in the interaction of the solar wind with the Earth and Mars than between Mars and Venus, which was already known for not having any intrinsic magnetic field. Those conclusions were opposed to those of *Vaisberg et al.*, [1973] and *Russell et al.*, [1984] who proposed that the interaction of the solar wind with Mars is controlled by the Martian atmosphere, like the unmagnetized planet Venus. The different arguments of both camps are summarized by *Vaisberg* [1992].

The MGS magnetic measurements finally supported the proposition that the solar wind interacts with the extended atmosphere and ionosphere of Mars, creating a magnetospheric cavity, but also with the small-scale crustal magnetic fields. This interaction hence contrasts with the plasma interactions at any other solar system bodies. The obstacle that faces the solar wind is a combination of a **global atmospheric obstacle** (like for Venus or comets), punctuated by many smaller-scale obstacles formed by **strong crustal magnetic fields** (somehow similar to the Earth or the Moon to a lesser extend).

The main features of the Martian global plasma interaction with the solar wind are summarized in Figure 16 [*Brain et al.*, 2017]. Solar wind particles, coming from the left side, and the associated IMF, represented in yellow, induce magnetic fields in the conducting Martian ionosphere. This induced magnetosphere-like interaction forms a variety of plasma regimes and boundaries that can be distinguished using particle and field measurements obtained by the spacecraft orbiting around the planet.

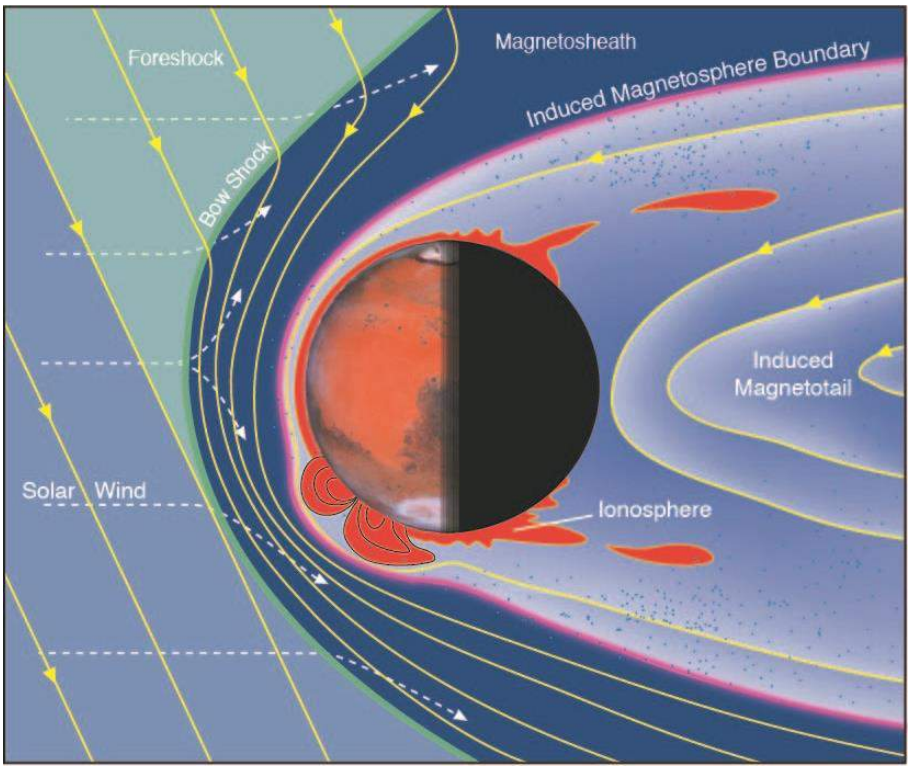

Figure 16. Schematic of the Martian plasma interaction regions [Brain et al., 2017].
The solar wind carries with it the IMF (yellow) as it streams (dashed lines) toward the bow shock (green) upstream of Mars. The ionosphere (orange) is delimited by the ionopause (outer limit of the orange area).

In order to identify the different regions and boundaries of the Martian environment from plasma instruments observations, the data recorded by several instruments of the particle and field package of the MAVEN spacecraft during one orbit in October 2016 are plotted in Figure 17 (see section 2.2.3 for more details about MAVEN instruments). During this orbit, the spacecraft entered in the Martian induced magnetosphere on the dayside southern hemisphere, then traveled toward the northern hemisphere and the nightside it reached at ~17:15 UT. On the first panel is plotted the energy-time spectrogram of omnidirectional electron energy flux (JE) measured by SWEA. On the second and third panel are plotted the energy-time and mass-time spectrogram of omnidirectional ion energy flux (JE), respectively, measured by STATIC. On the fourth panel are the electron (**red**) and ion (**black**) density measured by SWEA and SWIA, respectively. Note that the density calculated by SWIA is not trustworthy below the magnetosheath as it does not record ions with energy below a dozen of eV. On the fifth panel is plotted the in-situ magnitude of magnetic field (**black**) measured by MAG, superimposed with the calculated magnitude of the crustal magnetic field (**red**), from the model of *Morschhauser et al.* [2014] (see section 2.6 for more details). Finally, the altitude and the position of the spacecraft regarding Mars are plotted on panel 6 and 7 (see section 2.5 for more

details about the frames). The approximate location of the different boundaries discussed in next subsections are represented by the brown vertical lines.

In the subsequent sections we first describe the solar wind interaction with Mars as a steady-state interaction (section 1.3.1), using together Figure 16 and Figure 17. We then discuss time-dependent effects modifying the location of the different regions of the Martian environment (section 1.3.2). We finish on a focus on the nightside ionosphere (section 1.3.3), which is the main region that has been studied throughout my PhD.

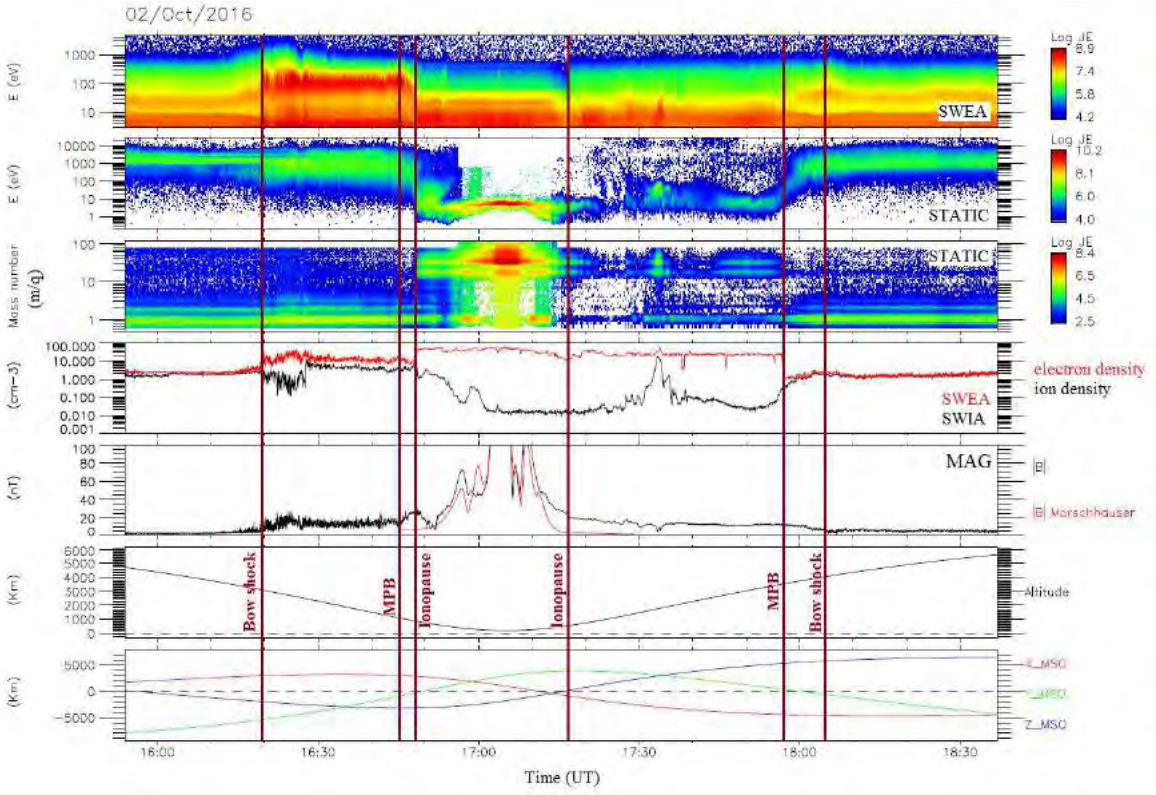

*Figure 17. Example of a MAVEN passage in the plasma environment of Mars, with a periapsis on the dayside. Panel 1: SWEA energy-time spectrogram of omnidirectional electron energy flux. Panel 2: STATIC energy-time spectrogram of omnidirectional ion energy flux (C0 mode). Panel 3: STATIC mass-time spectrogram of omnidirectional ion energy flux (C6 mode). Panel 4: Electron density measured by SWEA (**red**) and ion density measured by SWIA (**black**). Panel 5: Magnetic field intensity (measured by MAG in **black** and calculated from the model of Morschhauser et al. [2014] in **red**) versus time. Panel 6: Altitude versus time. Panel 7: Coordinates of the spacecraft in the MSO frame (see section 2.5). The vertical lines highlight the main boundaries of the Martian environment described in section 1.3.1.*

Models are also important tools for placing spacecraft measurements in context, and for probing causes and effects in the physics underlying the plasma interaction. Most of the models employ either magneto-hydrodynamic (**MHD**) or **hybrid** assumptions. MHD models implement equations for the motion of electrically conducting fluids subject to electromagnetic forces, while hybrid models strive to include ion kinetic effects by considering the numerical particle motion (still treating the electrons as a neutralizing massless fluid), where each macro-particle represents a cloud of physical ions. The MHD models are particularly well suited for reproducing characteristics of the interaction with the solar wind, while the hybrid models may better describe kinetic effects. Comparison of several models have been made by *Brain et al.,* [2010], *Kallio et al.,* [2011], and *Ledvina et al.,* [2008]. Some individual model results are discussed throughout this section, where appropriate.

1.3.1. The steady-state interaction

The characteristics of the solar wind interactions with weakly magnetized, or unmagnetized bodies, are in some regards similar to the flow around a magnetized planet [*Luhmann et al.,* 1992, *Brain,* 2006], but for the lack of a global scale magnetosphere within which the motion of charged particles is governed by an intrinsic planetary magnetic field. At Mars, the disturbance caused by the presence of the planet is much smaller compared to the size of the planet than at the Earth (see Figure 3). The distance of the obstacle "nose" at the Earth is ~10 Earth radii upstream while the nose of the obstacle at Mars is only a few hundred kilometers above the surface.

Due to the absence of magnetic obstacle at Mars, the solar wind interacts directly with the upper atmosphere and ionosphere and induces a magnetosphere by the pile up of the IMF. The solar wind decelerates to become subsonic as it crosses the bow shock (section 1.3.1.1) and enters the magnetosheath (section 1.3.1.2). Few solar wind protons are observed downstream a boundary sometimes called the Magnetic Pile-up Boundary (MPB) (section 1.3.1.3). Below the MPB is the Magnetic Pileup Region (MPR). The ionopause/Photoelectron Boundary (section 1.3.1.4) separates the planetary ionosphere (section 1.3.1.5) from the MPR. A two-lobed induced magnetotail (section 1.3.1.6) forms on the nightside, with a current sheet carrying planetary ions between the two lobes (see *Nagy et al.,* 2004 for a more complete review on the distinct plasma boundaries and regions resulting from the interaction of Mars with the solar wind).

1.3.1.1. The bow shock and the upstream region

When the solar wind, which is supersonic, encounters on its way a conductive obstacle such as Mars, a bow shock forms upstream of the planet (**green line** in Figure 16). The solar wind is then heated, deflected, and slowed down when it passes the shock so that it becomes subsonic. In Figure 17 the bow shock can be observed at ~16:20 UT on the inbound part of the orbit. This first boundary separates two regions:

- The upstream one which is characterized by **solar wind plasma** (mainly protons with a drift energy greater than 1000 eV and a temperature (width of the beam) of the order of 10 eV), a **low plasma density** and **temperature** (the ion beam is rather narrow on panel 2), a **low magnetic field** (at Mars < 5nT), and a **supersonic flow** (not shown). The typical shape of the electron flux spectrogram in the solar wind is plotted in **red** in Figure 18. The left part for energies below 10 eV should not be taken into account as it is due to the potential of the spacecraft (see section 2.2.4).

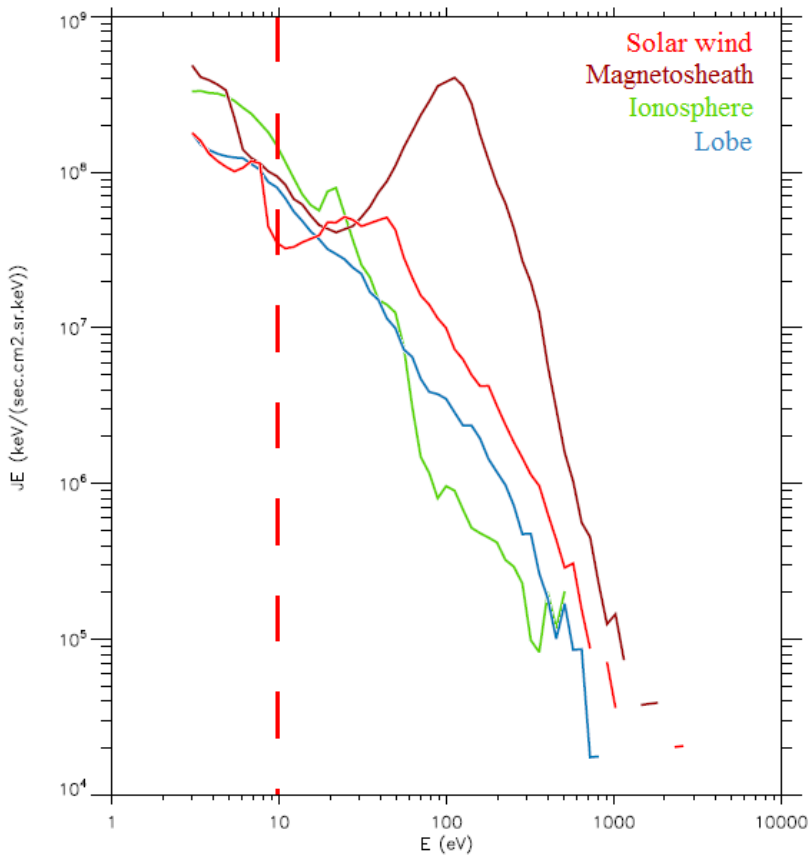

*Figure 18. Electron energy spectra measured by SWEA in different regions observed in Figure 17. (**the solar wind**, **the magnetosheath**, **the ionosphere** and **the lobes**). The vertical red line corresponds to the value of the spacecraft potential in the solar wind.*

- The downstream one, called magnetosheath, which is characterized by a more **intense magnetic field** and **density**, a **subsonic flow** (not shown) and a **higher temperature** (the ion beam is larger on panel 2). The typical shape of the electron flux spectrogram in the magnetosheath is plotted in **dark red** in Figure 18 and will be discussed in the next section.

Due to the low gravity of Mars and the absence of intrinsic magnetic field, the bow shock is close to the surface of the planet (~2000 km at the subsolar point, ~5500 km at the terminator), so that an important part of the exosphere is located well out of the shock and can interact directly with the incident solar wind. The interaction of Mars with the solar wind hence starts several planetary radii away from the planet, where the exospheric neutrals are ionized, mostly by photoionization and charge exchange. The resulting ions keep the same temperature as their neutral parents (a few eVs), but gain a small amount of energy during the process of photoionization. The new born ions, heavier but colder than the native ions of the solar wind, are accelerated by the electrical fields associated to the incoming flow, which tend to restore the thermodynamic equilibrium. These ions are called '**pickup ions**'. As the solar flow approaches Mars, an increasing number of cold exospheric newborn ions are created and lead to a significant **massloading** of the solar wind [*Bertucci et al., 2011*], which decelerates the flow by ~5% [Kotova et al., 1997]. The term 'mass-loading' refers to a situation where slow-moving mass is added to a flowing plasma, decelerating it via conservation of momentum.

Thanks to the several shock crossings observed by MGS, the altitude of the shock has been observed to increase from the subsolar point away to the tail, roughly forming a hyperboloid of revolution. Calculations of the bow shock shape have been made by *Vignes et al.* [2000, 2002] based on MGS crossings, by *Trotignon et al.* [2006], based on MGS and Phobos data, and by *Edberg et al.* [2008], based on MEX data. Comparison of the results of these three models are presented in Figure 19 [*Edberg et al.*, 2008]. The bow shock corresponds to the outer boundary plotted and the three fits can be observed to be globally in good agreement, slightly less at the subsolar point.

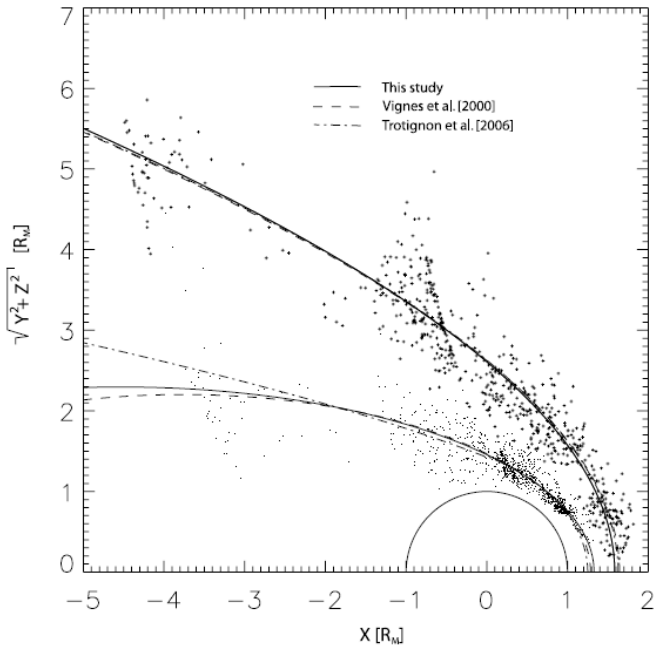

Figure 19. Comparison of the location of the bow shock and of the MPB calculated by three models: Edberg et al., [2008] (plain line), Vignes et al., [2000] (dashed line) and Trotignon et al. [2006] (dashed-dotted). All MPB and bow shock crossings found from the pre-mapping phase of MGS are plotted as dots and plus signs, respectively, in aberrated cylindrical MSO coordinates (taking into account the aberration of the solar wind flow direction by the planetary orbital motion, see section 2.5.1) [Edberg et al., 2008].

1.3.1.2. The magnetosheath

After the crossing of the bow shock, we can see in Figure 17 that the spacecraft enters into a region with the same ion population as in the solar wind (mainly protons and He^{++} ions), at approximately the same energy, but with a much higher temperature. The electron and ion densities are larger than in the solar wind, so as the amplitude of the magnetic field which however shows much more fluctuations. Moreover, if we observe the electron energy spectra recorded in this region in Figure 18 (**dark red** one), we can see that the electron population is at higher energy than in the solar wind, and is warmer. These characteristics are typical of the magnetosheath.

The magnetosheath is the region standing between the solar wind and the effective obstacle (**dark blue** region in Figure 16). It acts like a buffer between a region dominated by the solar wind dynamic pressure and the planetary induced magnetosphere dominated by the planetary plasma pressure. It is populated by shock-heated, dense and turbulent solar wind plasma. Indeed, the solar wind plasma is slowed to velocities lower than $100\ \mathrm{km.s^{-1}}$, compressed by up to several times its original density, and heated to temperature up to ~4 times

higher than upstream. The flow is also deflected from its original antisunward motion. As it travels deeper into the magnetosheath, the incoming flow continues to slow down.

As the plasma slows, the magnetic field increases, by up to ~4 times the upstream value. The magnetic field is compressed, distorted and "**draped**" as the plasma in which it is embedded is compressed and diverted around the obstacle. The understanding of the draping of magnetic field lines around a planet is based on the work of *Alfvèn et al.*, [1957] who first talked about this phenomenon. Indeed, as Mars is a conductive obstacle, the IMF cannot penetrate inside the planet. As the IMF is frozen in the solar wind plasma, when the plasma is slowed down upstream the planet, the magnetic field lines pile-up upstream the planet. However, as the IMF continues to be convected by the unperturbed solar wind flow around the planet, the magnetic field lines bend around the planet to form the magnetotail downstream. The IMF is wrapping around Mars.

The magnetosheath can be observed in two places in Figure 17: on the outbound part of the orbit in between ~16:30 UT and ~16:45 UT and on the outbound bound from ~18:05 UT to the end of the plot. The different characteristics of this region can be observed in both cases, but they are more visible on the inbound part, which is located on the dayside, than on the outbound part, which is located in the tail.

1.3.1.3. The Magnetic Pile-up Boundary and the Magnetic Pile-up Region

The region which separates the magnetosheath from the ionosphere is still controversial. It has proven difficult to determine whether there is a single outer boundary of the induced magnetosphere or several that are physically distinct. In the two following subsections we discuss several of the boundaries commonly used to describe this transition region.

As the spacecraft plunges deeper in the magnetosheath in Figure 17, we can see around 16:45 UT that the energy of the electrons and of the ions begins to decrease, at the same time as the magnetic field begins to strongly increase. These lower boundary of the magnetosheath is usually called the Magnetic Pile-up Boundary (**MPB**) [*Bertucci et al.*, 2004] and is represented as the **purple line** in Figure 16.

The MPB is a controversial boundary, which has also been called the induced magnetosphere boundary [Brain et al., 2017], the induced magnetopause, the planetopause [*Riedler et al.*, 1989], the magnetopause [*Rosenbauer et al.*, 1989; *Lundin et al.*, 1989], the

protonopause [*Sauer et al., 1994*], or the ion composition boundary [*Breus et al., 1991*], depending on the observed parameters. I chose in this manuscript to use the name MPB, arbitrarily emphasizing the behavior of the magnetic field. The other names emphasizing other plasma components, or an instrument- neutral designation, would also have been correct.

Despite the different names and plasma signatures associated with this boundary, it seems clear that it results from the interaction of the shocked solar wind with planetary heavy ions. The MPB distinctly separates two very different regions:

- The magnetosheath with low amplitude and turbulent magnetic fields.
- A region of high piled-up magnetic fields, the Magnetic Pile-up Region (**MPR**), where the solar wind magnetic field is piled up and draped around the ionosphere. The MPR marks the transition between plasma dominated by ions of solar wind origin (mainly protons) and plasma dominated by ions of planetary origin (mainly O^+ and O_2^+). The two types of ions are usually distinguished regarding the ion mass spectrogram (third panel of Figure 17).

Several sharp changes of the plasma and field parameters can be observed at the crossing of the MPB, like: the rotation of the magnetic field direction, a strong and sharp jump observed on the magnetic field amplitude (the draped IMF at Mars typically reaches strengths of 30-60 nT), a reduction of the field's directional variability, an increase in the field draping, and a strong drop of the suprathermal electron fluxes (energies > 10eV) by often more than one order of magnitude [*Acuña et al., 1998*; *Bertucci et al., 2003*]. There is also a drastic change in the ion composition: the proton density decreases, commensurate with an increase of planetary ions density. A sharp increase in electron density, and a decrease in the electron temperature can also be observed. Several of these features can be observed in Figure 17. However, all these characteristics are not always observed at each MPB crossing so that it is not yet understood which signatures help to form or maintain the MPB and which ones result from its existence.

As for the bow shock, the MPB is usually approximated by a paraboloid of revolution about the planet-Sun line. Its shape has been fitted using Phobos data [*Trotignon et al., 1996*], MGS data, [*Vignes et al., 2000*], a combination of Phobos and MGS data [*Trotignon et al., 2006*], and MEX data [*Edberg et al., 2008*]. The last three models are superimposed to MGS crossings in Figure 19. They all are in rough agreement except for the far nightside. From the model fit, the MPB is situated on average at ~850 km altitude near the subsolar point, and at ~1500 km altitude near the terminator.

1.3.1.4. The ionopause and the PhotoElectron Boundary

Between the MPR and the ionosphere is a boundary, sometimes called **ionopause**, sometimes called PhotoElectron Boundary (**PEB**), and which delimits the magnetospheric cavity that is almost void of solar wind plasma (outer limit of the orange region in Figure 16). The ionopause name is inherited from Venus, where it corresponds to the upper boundary of the ionosphere. It is defined as the location where ionospheric electron density increases rapidly or as the location where ionospheric thermal pressure is balanced by the magnetic pressure in the induced magnetosphere [*Phillips et al.*, 1988]. At Mars, the ionospheric thermal pressure is typically insufficient to balance magnetic pressure so that the magnetic field penetrates into the ionosphere, where the magnetic pressure is finally dominated by the thermal pressure [*Dubinin et al.*, 2008a] (pressure balance will be discussed in more details in section 1.3.2.2).

The PEB is considered as the boundary above which magnetosheath-like solar wind electrons are located and below which ionospheric photoelectrons are located [*Mitchell et al.*, 2001]. The PEB can be observed as the location between regions where photoelectrons are present and where they are not, in particular the **photoelectrons at 20-30 eV** induced by the strong 30.4 nm line of the solar spectrum [*Nagy et al.*, 2001].

In Figure 17 the ionopause/PEB can mainly be observed on the electron spectrogram, where the electron flux at energies greater than 100 eV decreases dramatically and the line at 20-30 eV begins to be observed. On the ion spectrogram, the ion energy drops from ~1000 eV to less than 10 eV, and planetary ions begin to be observed. The decrease in the magnetic field value that can be observed just below the ionopause/PEB at ~16:52 UT is also a typical feature of this boundary.

The ionopause and the PEB are quasi-circular boundaries on the dayside [*Han et al.*, 2014; *Garnier et al.*, submitted]. Their study on the nightside is more challenging as the nightside ionosphere is patchy. Thus, studies led on the PEB and on the ionopause are usually restricted to the dayside. In some cases, the PEB and the ionopause coincide but it is still not clear if the ionopause and the PEB are collocated or not [*Han et al.*, 2014]. The ionopause can usually be found at an altitude of ~450 km on the dayside [*Brain et al.*, 2017], and the PEB at an altitude of ~530km [*Garnier et al.*, submitted].

1.3.1.5. The ionosphere

The lowest region that can be observed in Figure 17 (at the periapsis), is the ionosphere. It is represented in **orange** in Figure 16. The ionosphere is a region of low energy planetary plasma, with relatively cold, heavy ions. It can be easily detected thanks to the spectral lines of photoelectrons on the electron spectrogram. The photoionization of atmospheric CO_2 and atomic O produces electrons with specific energies (two peaks at 21-24 eV and 27 eV) [*Mitchell et al., 2000*]. However, the individual peaks cannot be resolved by SWEA and only **one peak at ~20 eV** can be observed on the electron spectra corresponding to the ionosphere in Figure 18 (**green** one). The presence of photoelectrons is then used as a tracer of the ionosphere [*Mitchell et al., 2000*, *2001*; *Dubinin et al., 2006*; *Frahm et al., 2006*]. The ionosphere is also characterized by a sharp drop of the flux of electrons having an energy greater than ~30 eV. This decrease can reach one order of magnitude for ~100 eV electrons [Mitchell et al., 2001].

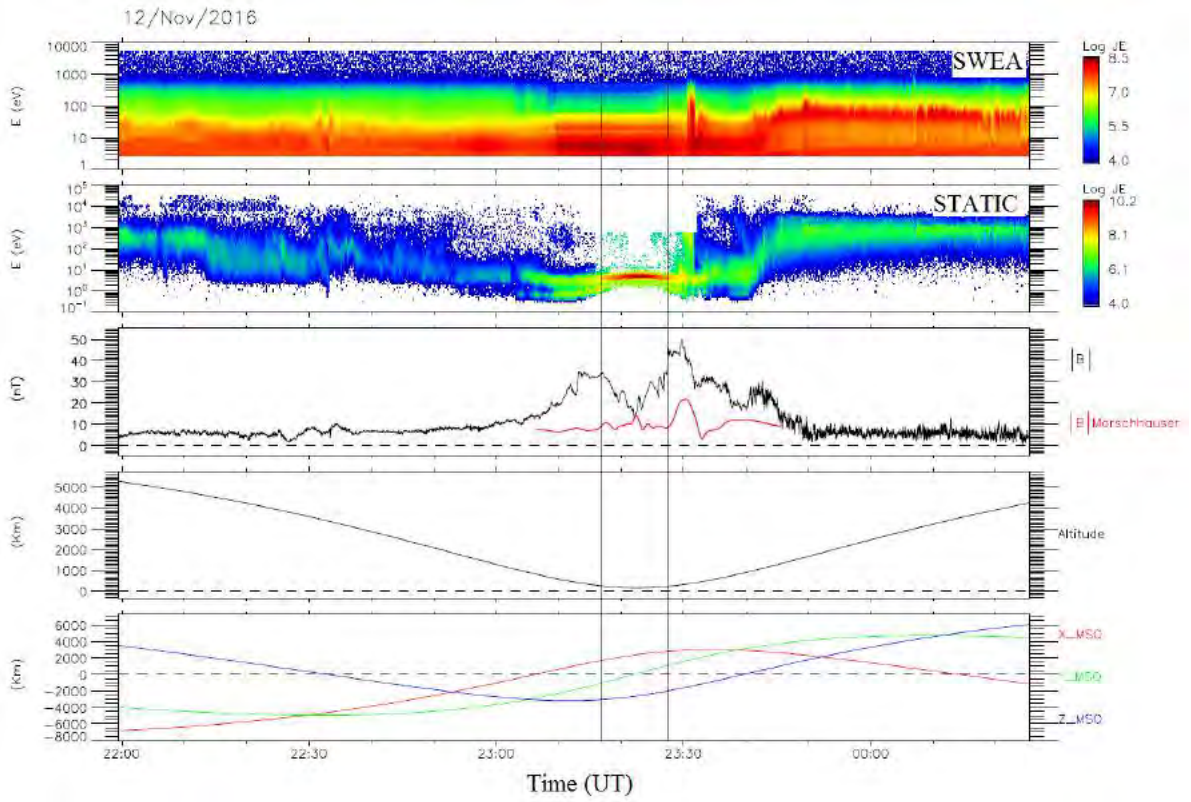

Figure 20. Example of an ionospheric cavity observed by MAVEN.

*Panel 1: SWEA energy-time spectrogram of omnidirectional electron energy flux. Panel 2: STATIC energy-time spectrogram of omnidirectional ion energy flux (C0 mode). Panel 3: Magnetic field intensity (measured by MAG in **black** and calculated from the model of Morschhauser et al.* [2014] *in **red**) versus time. Panel 4: Altitude versus time. Panel 5: Coordinates of the spacecraft in the MSO frame (see section 2.5). The two vertical black lines roughly delineate the ionospheric cavity.*

If no crustal magnetic field is present, the magnetic field measured in the ionosphere should reach a minimum, presenting the shape of an **ionospheric cavity**. The ionospheric plasma pressure indeed balances the magnetic pressure of the MPR (see section 1.3.2.2) at the ionopause. Such a cavity is presented in Figure 20. In this example, the spacecraft traveled in the ionosphere from ~23:10 UT to ~23:40 UT. We can observe on the modeled crustal magnetic field that no significant crustal magnetic sources are present during this time interval and a minimum of the in-situ magnetic field is visible at the periapsis, at ~23:25 UT. However, browsing plasma data, ionospheric cavity appears to be quite a rare structure.

1.3.1.6. The wake and the magnetotail

If we follow the MAVEN spacecraft going away from its periapsis in Figure 17, it exits the ionosphere at ~17:15 UT and enters a new region on the nightside of Mars. It corresponds to the lobes of the induced magnetotail (Figure 16). The magnetic field lines draped around Mars extend well downstream in the anti-sunward direction, and form the **induced magnetotail** by analogy with the magnetotail that forms downstream a magnetized planet. A magnetized planet imposes a geometry and a polarity on the magnetic field in its magnetotail, whereas the magnetotail formed downstream an unmagnetized body changes direction in response to changes in the direction of the IMF. *Yeroshenko et al.* [1990] found that the magnetic field in the Martian magnetotail can be organized into two tail lobes with two opposite magnetic field polarities: 'to' and 'away' from the Sun directions, separated by a thin magnetic neutral sheet. The **plasma sheet** consists primarily of planetary ions which are accelerated up to keV energies by the magnetic field tensions [*Dubinin et al.*, 1993]. Well-defined current sheets are sometimes evident as low as ~400 km. The magnetic field in the tail is weak (~10 nT), though it is still stronger than the unperturbed IMF. The boundaries separating the wake from the magnetosheath could be called the wake boundary, as an extension of the MPB to the nightside.

The two lobes of the magnetotail can be observed in Figure 17 from ~17:15 UT to ~17:55 UT with the current sheet at ~17:35 UT. The magnetic field is quite steady in the lobes, apart from the current sheet passage, where there is a drop in the amplitude of the magnetic field and an inversion of the three components of the magnetic field (not shown). The presence of planetary ions can also be observed at the crossing of the current sheet, as well as a little enhancement in the electron energy. A typical electron spectra that can be observed in the lobes is plotted in **blue** in Figure 18.

All the boundaries and regions described in the previous subsections can be observed in Figure 21, on which the Martian environment is plotted after the simulations realized by Ma et al., [2004]. The upper panels correspond to the calculated magnetic field (left) and plasma velocity (right) in the equatorial plane while the lower panels corresponds to the same parameters in the meridional plane. The bow shock is clearly visible in both velocity and magnetic field results, and its position corresponds quite well to the model of Vignes et al. [2000], plotted in black dashed line. The draping of the IMF is also clearly observed, especially in the equatorial plane, as well as the pile-up region. The presence of mini-magnetospheres in the southern hemisphere is clearly observed on the meridional plane, and we can notice that their presence has a significant impact on the draping of the IMF. We can also observe that in the ionosphere, the flow pattern is toward the terminator on the dayside, while on the nightside the flow is partially outward through the tail, contributing to the escape flux. The inward part of this flow contribute to maintaining the nightside ionosphere (section 1.3.3).

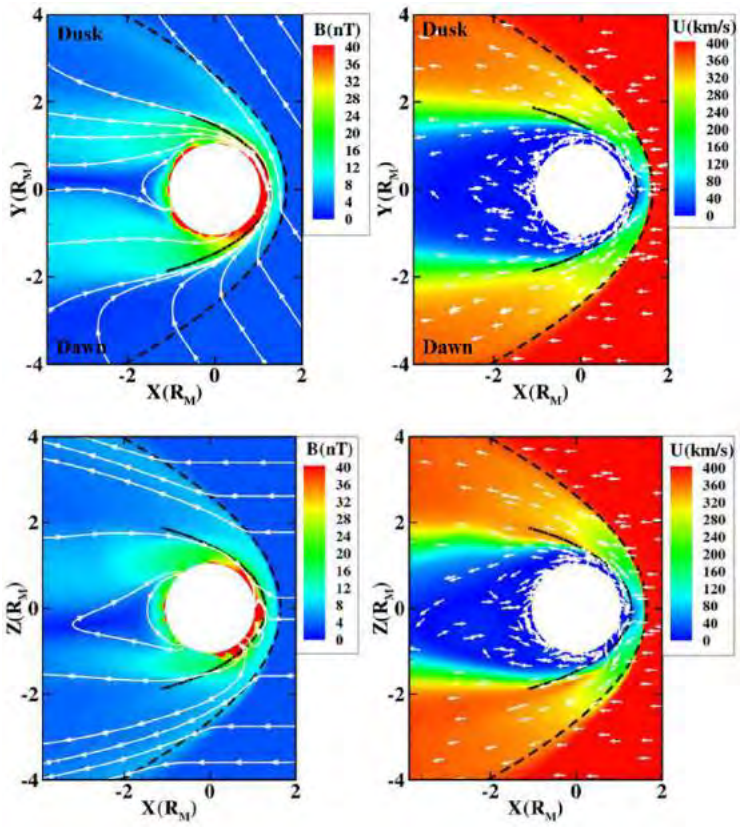

Figure 21. Martian environment simulated by Ma et al., [2004].

Calculated magnetic field (left) and velocity (right) in the equatorial plane (up) and in the meridional pane (bottom) of Mars. The color plots show the magnitudes, the white lines marked with arrows indicate the vector direction of the magnetic field and the arrows show the direction (not the magnitude) of the velocity. The dashed lines represents the mean bow shock and the dash-dot line is the mean MPB locations from Vignes et al. [2000].

1.3.2. Dynamics of the Martian interaction with the Sun

The description of the Martian magnetosphere proposed in section 1.3.1 is a steady-state description, which does not take into account neither the presence of crustal magnetic field (which visibly has an impact on the location of the MPB as observed on Figure 21) nor the variation of the external drivers (such as the direction of the IMF or the EUV flux).

1.3.2.1. Martian magnetic topology

Due to the presence of crustal magnetic sources, the magnetic field lines in the vicinity of Mars can be of three kinds [*Nagy et al., 2004*; *Bertucci et al., 2003*; *Brain et al., 2007*], summarized on the left side of Figure 22:

- **Closed**: magnetic field lines are connected at both ends to the crust ('a' configuration).
- **Open**: one end of the magnetic field line is connected to the crust and the other end to the IMF ('b' configuration).
- **Draped/Unconnected**: both ends of the magnetic field lines are unconnected to the crust and connected to the IMF ('c' and 'd' configuration).

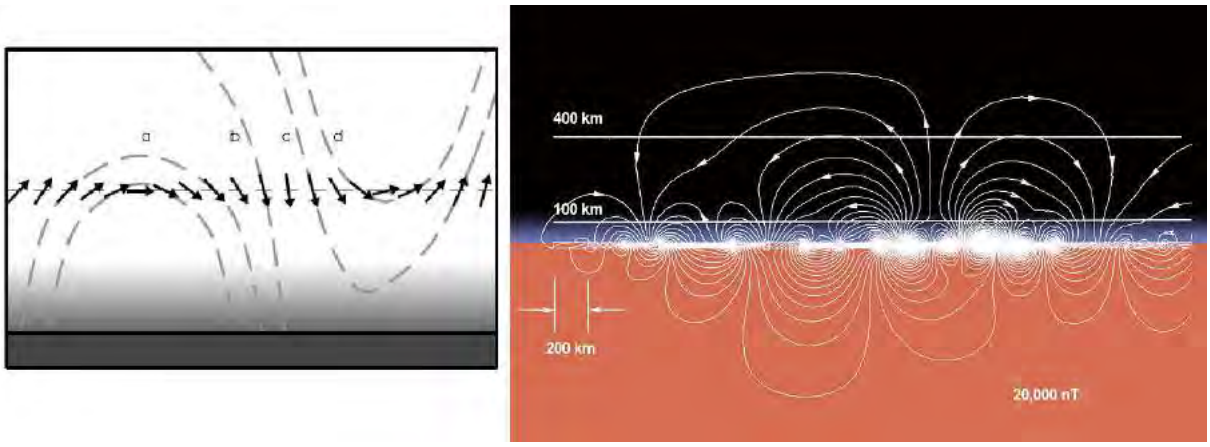

Figure 22. Possible magnetic topology in the vicinity of Mars.

Left. Four possible magnetic field topologies [Brain et al., 2007]: closed (curve a), open (curve b) or draped (curve c) in the ionosphere/atmosphere, or draped above the ionosphere/atmosphere (curve d). Right. Plane projection of the magnetic field geometry above the intensely magnetized southern highlands [Connerney et al., 2015] based on the crustal magnetic field model of Connerney et al. [1999]. This figure illustrates the field geometry that would be encountered during periapsis passes along a line of constant longitude (near 150° East) and centered at 50°S. Similar 'mini-magnetosphere' may be encountered above much of the magnetized crust, depending on spacecraft altitude and solar wind conditions.

Closed magnetic field lines are due to the presence of crustal magnetic sources in the Martian crust. If the magnetic field is strong enough, as in the southern hemisphere, closed magnetic field lines should shield the upper atmosphere from magnetized charged particles and from intrusion of magnetosheath plasma. There is hence formation of regions that act in many respects like **small-scale version of the terrestrial dayside magnetosphere** [*Fränz et al.*, 2006], as plotted on the right side of Figure 22. Crustal fields can be strong enough to dramatically alter the nature of the interaction with the solar wind, as it can be seen in the multi-fluid MHD simulation of *Ma et al.* [2004] presented in Figure 21.

Open field lines can be found at the edge of closed crustal magnetic field lines, and form **cusp-like regions**, analogous to terrestrial magnetospheric cusp regions. Such regions can provide a conduit for energy and particle exchange between the solar wind and the ionosphere [*Krymskii et al.*, 2002]. Open field lines at the edge of closed field lines can be confused with the signature of current sheets. Indeed, *Halekas et al.*, [2006] showed that the non-uniform geographic distribution of the current sheet at 400 km in the nightside suggests that crustal fields may play some role in their presence at low altitude. This interpretation has been supported by simulations of *Ma et al.*, [2002].

These three topologies have already been encountered at Mars and can be discriminated thanks to **electron pitch angle distributions** (PADs). The electron pitch angle corresponds to the angle between the electron velocity and the magnetic field vector. These distributions have been mapped geographically at 400 km by *Brain et al.*, [2007] and on a wider range of altitudes by *Xu et al.*, [2017]. The results of these studies are discussed in more details in section 3.1.2 and 4.3.1, respectively.

1.3.2.2. Pressure balance

Each boundary in the interaction of Mars with the Solar wind is the result of an equilibrium of pressure. Upstream from the planet, the solar wind is dominated by the **dynamic pressure** ($\sim \rho v^2$, where ρ is the density in kg. m^{-3} and v the velocity of the solar wind). The **thermal plasma pressure** ($\sim nk_BT$, where n is the density in m^{-3} and T the temperature of the medium) then becomes dominant in the magnetosheath. The dominant pressure term in the MPR is the **magnetic pressure** ($\sim B^2/2\mu_0$, where B is the ambient magnetic field and μ_0 the vacuum permability) from induced magnetic field. In the ionosphere the **plasma pressure** ($\sim nk_BT$) finally becomes dominant. In a steady-state situation, the force of the solar wind

against the magnetosphere and the force of the magnetosphere against the solar wind are in balance, and an equilibrium is reached so that the total pressure at any location in the Martian system is conserved.

For example, at the MPB the magnetospheric magnetic field and the ionospheric plasma exert an inward pressure: $nk_BT + B^2/2\mu_0$ (Figure 23). On the other side, the magnetosheath plasma and the draped magnetic field exert an inward pressure: $nk_BT + \rho v^2 + B^2/2\mu_0$. These two forces reach an equilibrium at the MPB [Luhmann et al., 1991].

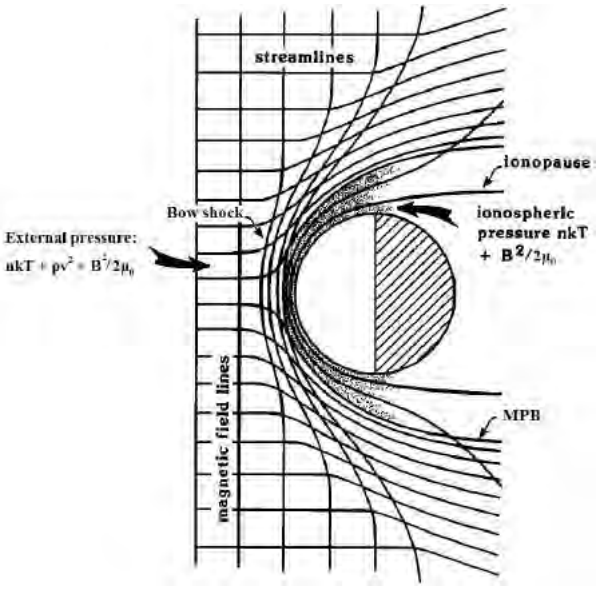

Figure 23. Illustration (not to scale) of the pressures involved in the interaction of Mars with the Solar wind. It shows how the interplanetary magnetic field may penetrate into the Martian ionosphere (stippled). The stream lines of plasma flow are those that are diverted around the planetary obstacle, while the cross-flow lines are magnetic field lines. Adapted from [Luhmann et al., 1991].

However, the Martian environment is embedded in the solar wind, whose properties are highly variable. Hence, these boundaries are moving, adjusting their location depending upon external and internal drivers. When the solar wind blows harder, the magnetosphere shrinks, and when the solar wind blows weaker, the magnetosphere expands.

1.3.2.3. Variability of the boundaries

The location of the different boundaries, and hence the extension of the different regions, depends on the intensity of the **external drivers** (solar wind plasma, solar UV photon flux, and IMF direction), but also of the **internal drivers** in the case of Mars (crustal magnetic sources and their orientation with respect to the Sun).

Influence of the crustal magnetic sources

The orientation of Mars with respect to the Sun would not be a major factor in controlling the variability of its plasma environment if it lacked crustal magnetic fields. However, the crustal fields rotate with the planet every ~24.6h. They are strong enough to influence the altitude of all the major plasma boundaries on timescales associated with Mars' rotation [*Brain et al.*, 2003, 2006].

Crustal magnetic fields add magnetic pressure to the Martian system at ionospheric altitudes, which helps opposing the pressure of the solar wind. This pressure addition alters the shape of the obstacle to the solar wind, locally perturbing various plasma boundaries upward locally [*Crider*, 2004; *Fränz et al.*, 2006], as illustrated in Figure 16 and in Figure 21 for the MPB, though the influence on the bow shock is relatively weak [Mitchell et al., 2001; Crider et al., 2002; Edberg et al., 2009; Duru et al., 2010].

Influence of the solar EUV photon flux

The solar EUV flux determines the ionospheric thermal pressure, which ultimately balances the incident pressure of the solar wind. The altitude of the MPB and of the bow shock have been successfully correlated with EUV flux [*Edberg et al.*, 2009], though attempts to correlate the ionopause/PEB with EUV flux have been unsuccessful [*Mitchell et al.*, 2001] so far.

Influence of the solar cycle

As the EUV flux is more important during solar maximum, one can think that the solar cycle has an impact on the position of the different boundaries of the Martian environment. However, *Modolo et al.*, [2005] simulations showed that the position of the bow shock and of the MPB hardly depend on the solar cycle, in agreement with the observations made by *Vignes et al.* [2000].

Influence of the IMF direction

Variations in the direction of the IMF change considerably the position and the shape of the shock and the MPB. Indeed, the shape of the bow shock and of the MPB is asymmetric with respect to the IMF direction [Acuña et al., 1998, Dubinin et al., 1998, Vignes et al., 2002]. This effect can be observed in Figure 21 on which the shock position on the dawn side is closer to the planet than at the dusk side. Hybrid simulations by *Modolo et al.*, [2012], using time-dependent input conditions, demonstrated that a rotation of the IMF causes the entire interaction

region to rotate in response, with a 'lag' of as much as two minutes in some regions. In addition, the orientation of the IMF directly influences the organization of the wake.

Influence of the parameters of the solar wind flow

The solar wind density and velocity determine the incident dynamic pressure at Mars. Since there is a pressure balance throughout the dayside interaction region, the density and the velocity play a large role in determining the size and position of the different plasma boundaries, the plasma temperature in the magnetosheath, and the strength of the magnetic field in the induced magnetosphere [Brain et al., 2017].

The speed and the temperature of the solar wind flow modify the sound speed and consequently the Mach number. This influence the shape of the shock. The position and the shape of the MPB is partially affected by the speed of the solar wind [Modolo et al., 2005].

Simulations are especially well-suited to study the effects and relative importance of the individual drivers. See for example: *Brecht and Ledvina* [2006]; *Harnett and Winglee* [2006]; *Modolo et al.*, [2006]; *Ma and Nagy* [2007]; *Kallio et al.*, [2008]; *Fang et al.*, [2010]; *Najib et al.*, 2011].

1.3.3. Focus on the nightside ionosphere

The Martian ionosphere is mainly due to photoionization of atmospheric oxygen and carbon dioxide (see section 1.2.1.1). As the recombination of the electrons and ions resulting from this interaction back into neutrals is rapid and that there is no nightside photoproduction, the ionosphere is generally a daytime phenomenon.

The presence of a nightside Martian ionosphere is made possible by **local production** processes and **transport** processes from the dayside. Impact ionization by precipitating particles, such as electrons from solar wind origin [*Verigin et al.*, 1991b; *Fox et al.*, 1993; *Haider*, 1997], solar wind protons, energetic neutral atoms or dayside photoelectrons [*Kallio and Janhunen*, 2001; *Haider et al.*, 2013; *Diéval et al.*, 2013; *Xu et al.*, 2016b], is one of the main process in nightside ionospheric production [Fillingim et al., 2010; Lillis et al., 2011; Lillis and Brain, 2013]. Transport of the dayside ionosphere to the nightside can be achieved by crossterminators winds [*Chaufray et al.*, 2014; *Cui et al.*, 2015], by the co-rotation of the ionosphere with the planet itself [*Cui et al.*, 2009; *Gonzalez-Galindo et al.*, 2013; *Cui et al.*,

2015] or by horizontal transport of plasma from dayside to nightside along draped magnetic field lines [*Ulusen and Linscott*, 2008; *Fränz et al.*, 2010]. More recently, *Fowler et al.*, [2015] showed that precipitation of energetic electrons are needed to sustain the nightside ionosphere and *Xu et al.*, [2016b] showed that dayside photoelectrons can be transported across the terminator along closed crustal magnetic field loops and then precipitate into the nightside atmosphere.

Despite the several spacecraft which have already visited Mars, its nightside ionosphere still remains an unfamiliar and mysterious place. Several studies have shown that the nightside ionosphere is irregular, spotty, faint and complex [*Zhang et al.*, 1990; *Němec et al.*, 2010; *Duru et al.*, 2011; *Withers et al.*, 2012]. In Figure 24 is plotted an orbit of MAVEN in February 2015, during which the periapsis is on the nightside. The panels are the same as in Figure 17. The different boundaries described in section 1.3.1 are highlighted by the brown vertical lines.

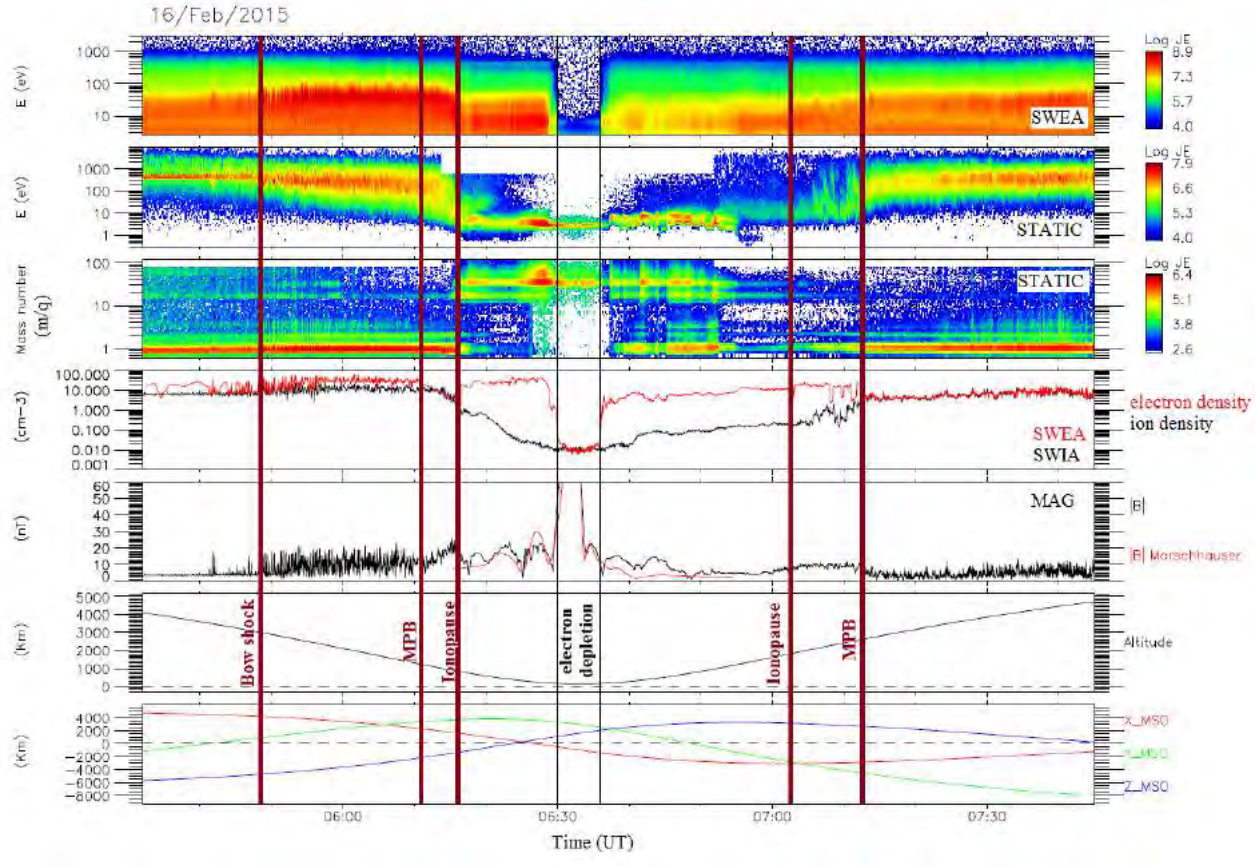

Figure 24. Example of a MAVEN passage in the plasma environment of Mars with a periapsis on the nightside. Same panels as in Figure 17. The vertical lines highlight the main boundaries of the Martian environment described in section 1.3.1.

During this orbit, the spacecraft enters the bow shock at ~06:50 UT, on the dayside southern hemisphere. It then travels in the magnetosheath until ~06:10 UT where it crosses the MPB and then the ionopause/PEB at ~06:15 UT. Then, the spacecraft stays in the ionosphere until ~07:00 UT. However, at ~06:25 UT, the spacecraft passes the terminator and carries on in the nightside. On this time interval, the spacecraft observes the dayside ionosphere as well as the nightside ionosphere.

We can observe between ~06:30 UT and ~06:35 UT a typical structure of the nightside ionosphere: a **suprathermal electron depletion** (which may be equally called electron depletion hereinafter). We can observe it on the first and on the fourth panel. During this event, the electron flux at all energies above 3 eV (the lower energy limit of the SWEA instrument), decreases by more than three orders of magnitude. At the same time, a sharp drop in the electron density is measured.

Why the nightside ionosphere?

The nightside ionosphere is an important feature of the plasma environment of Mars as it participates in the global-scale plasma circulation around the planet and it is a conduit through which particles from the neutral atmosphere can escape. However, the data provided so far by the different spacecraft orbiting around Mars only permit a restricted study of its structure and its dynamics.

Suprathermal electron depletions are recurrent and specific features of the nightside ionosphere. These characteristics make them an interesting tracer of this region. Their observation by MGS and MEX has already enabled the determination of the topology of the magnetic field in the nightside of Mars using electron spectrometers [*Mitchell et al.*, 2007; *Brain et al.*, 2007], and of possible conduits for atmospheric escape in cusp-like regions.

However, for suprathermal electron depletions as for the whole environment of Mars, the new measurements obtained with the MAVEN spacecraft enable a new vision of the phenomenon. A better understanding of the mechanisms involved in the creation of suprathermal electron depletions has proven necessary to efficiently use these features to characterize the structure and dynamics of the nightside ionosphere. For this purpose, the MAVEN multi-instrument capacity as well as its unprecedented spatial coverage has been used extensively, jointly with the dataset provided by MGS and MEX, so that it was possible to carry out a survey on eighteen years.

The following manuscript is organized as follows:

- As the present study is a multi-spacecraft and multi-instruments analysis, I first present in **section 2** the different spacecraft (section 2.1), instruments (section 2.2), datasets (section 2.3), analysis tools (section 2.4), frames (section 2.5) and models (section 2.6) which are used in the subsequent sections.
- In **section 3** the suprathermal electron depletions are presented in more details. First, I present how they were observed by MGS and MEX (section 3.1), and then how they are now observed by MAVEN (section 3.2). The three criteria I implemented to automatically detect suprathermal electron depletions in MGS, MEX and MAVEN data are developed in section 3.3, and their application to the three datasets to derive catalogs of events is detailed in section 3.4.
- The three catalogs of electron depletions thus obtained are used in **section 4** to understand the mechanisms at the origin of suprathermal electron depletions. The altitude distribution of these structures is presented in section 4.1.1, followed by their geographical distribution in section 4.1.2. So as to understand these observations, a closer look in the plasma composition and a pressure balance analysis are presented in section 4.2. In section 4.3 are discussed the different processes at the origin of electron depletions and the updated scenario of their creation.
- In **section 5** I present features of the dynamics of the nightside ionosphere that can be observed through electron depletions. First, I focus in section 5.1 on flux spikes which regularly punctuate electron depletions and which are privileged structures to study the dynamics of the nightside ionosphere. Some unexpected observations, or non-observations, of electron depletions are then investigated in section 5.2. Finally, the observation of the UV terminator and its dynamics thanks to suprathermal electron depletions is proposed in section 5.3.

2. Instrumentation, data and analysis tools used

The study of suprathermal electron depletions presented here has been possible by combining data from three spacecraft, sampled by their onboard instruments. Before entering the heart of the subject, we need to present the different spacecraft (section 2.1), their instruments (section 2.2), the datasets (section 2.3), the analysis tools (section 2.4), the frames (section 2.5) and the models (section 2.6) that have been used throughout my PhD.

2.1. Exploration of Mars

The launch of space vehicles to explore Mars started in 1960 with the launch of **Marsnik 1** by the Soviet Union. Unfortunately, the exploration of Mars only began four years later, on July 14-15, 1965, with the first Martian flyby made by the NASA spacecraft **Mariner 4**. Indeed, the Martian exploration has experienced a high failure rate, especially at its beginnings, from 1960 to 1971. Only five missions on the nineteen sent succeeded. This eagerness to explore Mars was motivated by its spatial proximity and by its past, when the planet may have looked like the Earth. Hence, the main objectives of the missions to Mars, past or future, are to determine if it has ever sheltered life, understand the evolution of the Martian weather, understand the origins and the evolution of the Martian geology and finally to prepare the human exploration of Mars.

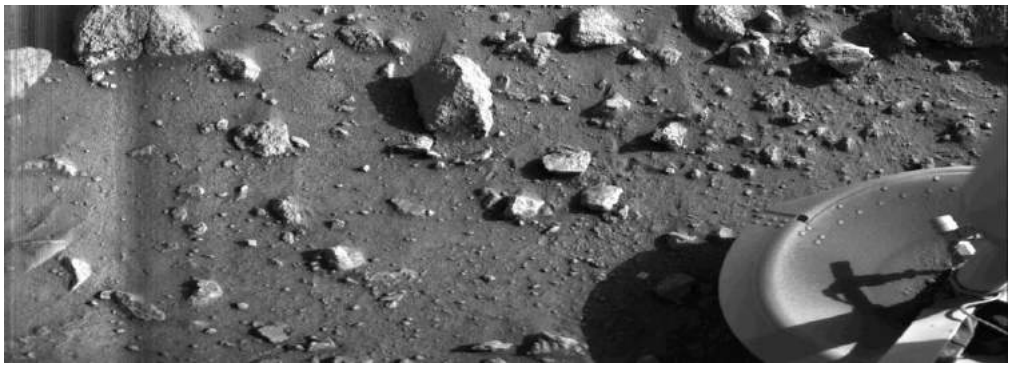

Figure 25. First photograph made by the lander Viking 1 of the Martian surface

On November 14, 1971, the NASA spacecraft **Mariner 9** became the first spacecraft to orbit another planet when it achieved its orbit insertion around Mars. The Soviets finally reached the Martian surface in 1971. **Mars 2** crashed on the surface on November 27, and **Mars**

3 landed successfully on the surface on December 2 but ceased transmission within 15 seconds. In July 1976, The NASA lander **Viking 1** offered us the first photograph ever taken from the surface of Mars (Figure 25). The two landers Viking 1 and Viking 2 also took the first in-situ measurement of the atmosphere during their descent toward the surface.

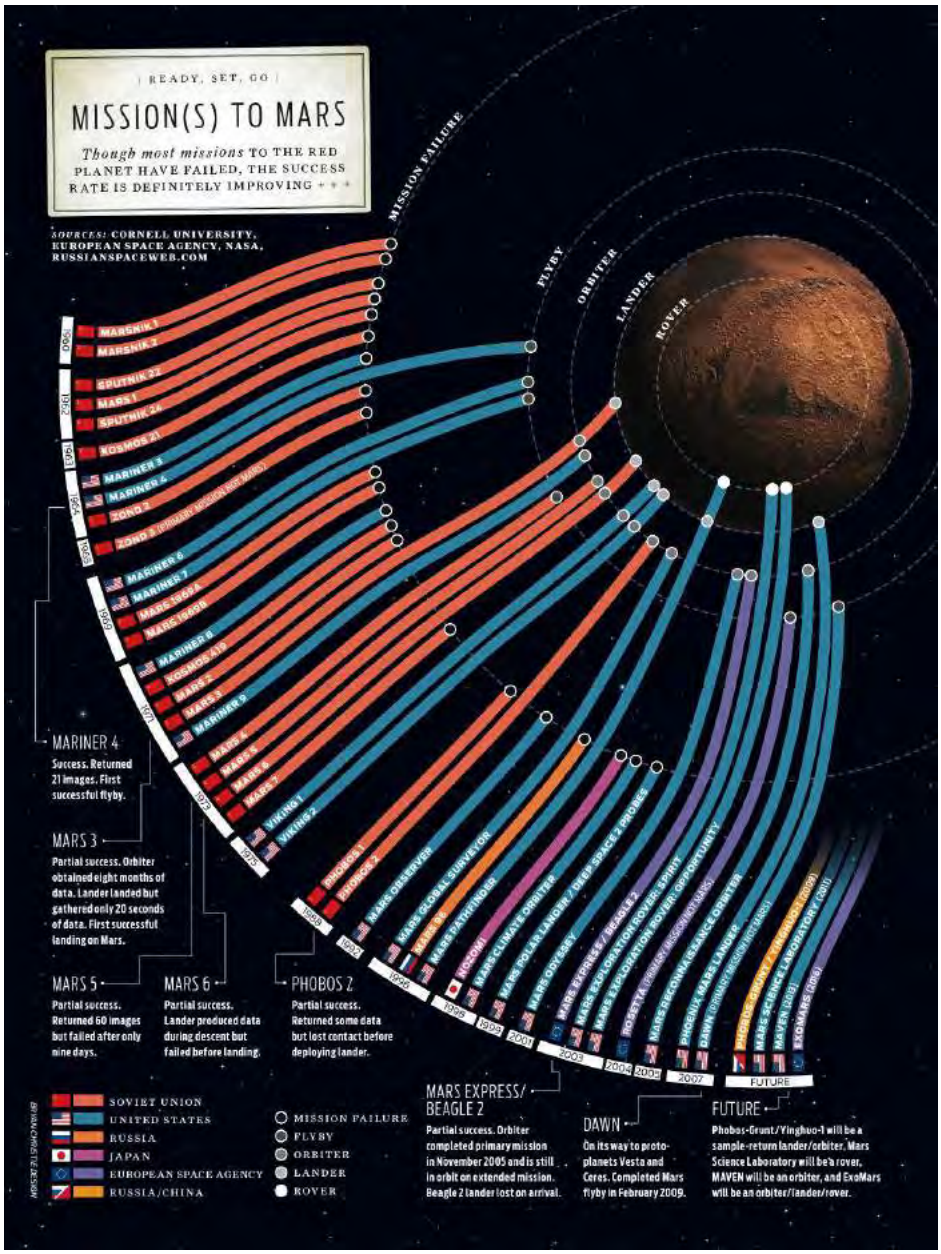

Figure 26. Summary of all the missions ever sent toward Mars [Bryan Christie, IEEE Spectrum, 2007]

*The Russian mission **Phobos-Grunt** failed its launch and stayed in a low Earth orbit. The NASA **Mars Science Laboratory** successfully landed on Mars and is still rolling on its surface. The NASA **MAVEN** spacecraft successfully orbits around Mars since 2014. The European **ExoMars-Trace Gas Orbiter** mission partially succeeded. The orbiter achieved its insertion around Mars but the **Schiaparelli** lander failed its landing. Next missions are: NASA lander **InSight**, ESA rover **ExoMars** and NASA rover **Mars2020**.*

Since then about twenty orbiters, landers and rovers have reached the red planet (Figure 26), even if error of units sometimes made them crash (R.I.P. to Mars Climate Orbiter). In 2017, the operational Martian fleet is composed of two scientific rovers rolling on its surface: **Curiosity** of the Mars Science Laboratory mission (NASA) and **Opportunity** of the Mars Exploration Rover mission (NASA) along with six orbiters surveying the planet: **Mars Odyssey** (NASA), **Mars Express** (ESA), **Mars Reconnaissance Orbiter** (NASA), **Mars Orbiter Mission** (Indian Space Research Organization), **MAVEN** (NASA) and the **ExoMars Trace Gas Orbiter** (ESA).

2.1.1. Mars Global Surveyor

After the success of the Viking program, about twenty years passed with no successful American mission to Mars but many questions about the origin and history of Mars remained unanswered. The **Mars Global Surveyor** (MGS) spacecraft was launched on November 7, 1996 from Cape Canaveral Air Force Station (Florida, USA), four years after the loss of contact with the previous mission spacecraft: Mars Observer (several days before its insertion around Mars).

2.1.1.1. Scientific objectives

MGS was the first mission of the NASA Mars Surveyor Program. The objectives of this program were to understand the current and past climates of Mars, the geological and geophysical evolution of the planet and whether life could have started and evolved on Mars [*Albee et al.*, 2001]. The primary objectives specific to the MGS mission were the following:

- Characterize the surface morphology at high spatial resolution to quantify surface features and geological processes.
- Determine the composition, distribution and thermophysical properties of surface minerals, rocks and ices.
- Determine the global topography, geodetic figure, and gravitational field.
- Establish the nature of the magnetic field and map the crustal remnant field.
- Monitor global weather and thermal structure of the atmosphere.
- Study surface-atmosphere interaction by monitoring surface features, polar caps, polar thermal balance, atmospheric dust, and condensate clouds over a seasonal cycle.

Several secondary objectives had been set during the extensions of the mission:

- Provide multiple years of on-orbit relay communications capability for Mars lander and atmospheric vehicles.
- Long-term weather and surface monitoring.
- Support landing site selection through acquisition of high-resolution imaging for the 2007 Phoenix lander and the 2011 Curiosity rover.

2.1.1.2. Orbitography

The MGS mission had been designed to be a global mapping mission which investigated the entire planet, from its interior to its surface, through its atmosphere, up to its ionosphere. These constraints lead to the definition of a low-altitude, near-circular, near polar, Sun-synchronous mapping orbit with a short repeat cycle. The selected characteristics were then: a "**frozen orbit**" with a period of 117.65 min, an inclination of 92.96°, an average altitude of 378 km varying from 368 to 438 km above the surface and a local time set at 1400/0200 LT.

The amount of propellants needed to reach this mapping orbit was too large to be launched. Hence, after Mars orbital insertion, an **aerobreaking phase** — during which the spacecraft would reach very low altitudes at its periapsis — had been planned to use the atmospheric drag on the spacecraft to slow it so as to reach its low-altitude mapping orbit. Such a technique was challenging as it had never been done before and few was known about the structure and dynamics of the Martian atmosphere.

After its launch on November 1996, the MGS spacecraft travelled 11 months before reaching Mars on September 11, 1997 and being inserted in a highly elliptical orbit of 45 hours period. On its third orbit, MGS initiated the aerobreaking phase, operating repeated dips into the upper atmosphere (down to 105 km altitude). According to the initial planning, the spacecraft would have reached its mapping orbit in the spring of 1998. However, due to a problem on one of its solar panel, MGS finally reached its mapping orbit on February 19, 1999 (Figure 27).

The MGS mapping mission was initiated on **March 9, 1999**. In the nominal mapping mode the spacecraft was continuously nadir-pointed, enabling the instruments to acquire and record data on a continuous basis. The nominal mapping mission end on February 1, 2001. It

was extended several times until the end of 2006. MGS then became silent, due to a battery failure. The MGS mission officially ended in January 2007.

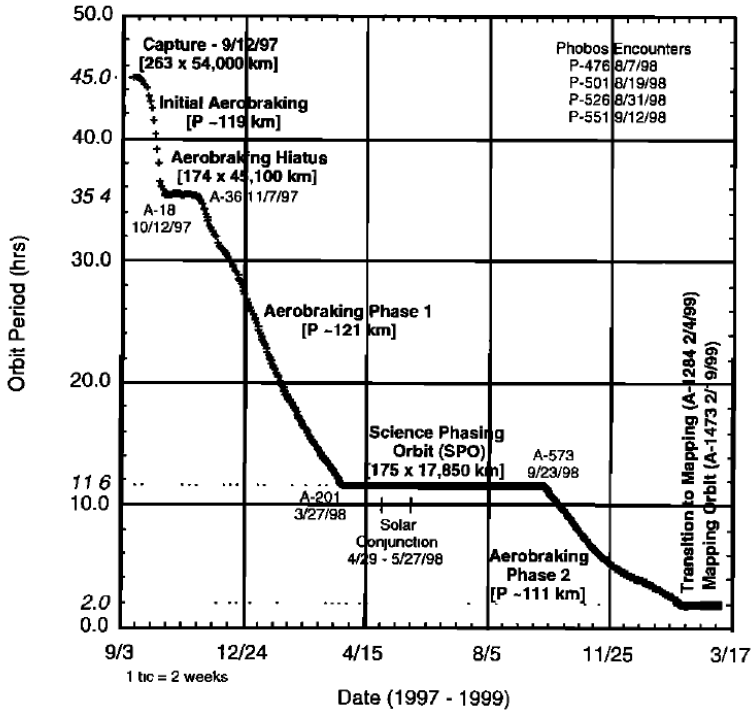

Figure 27. MGS orbit period during its aerobreaking phase. [Albee et al., 2001]

2.1.1.3. Instruments

After the failure of the Mars Observer mission, four of its science instruments were retooled for the MGS spacecraft. The aim of the instrument suite was to study Mars in its entirety, meaning at the same time its surface, interior and atmosphere. To meet the scientific objectives of the mission, the instruments had to both acquire high-quality data and maximize the data returned within the constraints of the mission. Four instruments and a radio science investigation have been operated onboard MGS, the configuration of which is shown in Figure 28:

- **MOC** (Mars Orbiter Camera): MOC is a high resolution camera which aim was to map the whole Martian surface [*Malin et al.*, 1992].

- **MOLA** (Mars Orbiter Laser Altimeter): MOLA is a laser altimeter which aim was to characterize the topology and the gravitational field of Mars [*Zuber et al.*, 1992].

- **TES** (Thermal Emission Spectrometer): TES is a thermal emission spectrometer which aim was to study the atmosphere and map the mineral composition of the surface thanks to infrared spectroscopy [*Christensen et al.*, 1992].

- **MAG/ER** (Magnetometer/ Electron Reflectometer): the MAG/ER experiment was composed of two magnetometers (MAG), and an electron spectrometer (ER) [*Acuña et al.*, 1992]. This experiment is described in more details in section 2.2.1.

- **Radio Science** (Gravity Field Experiment): the radio science investigation used data provided by the spacecraft telecommunications system, high-gain antenna and onboard ultra-stable oscillator to map variations in the gravity field and to determine the atmospheric pressure at specific locations.

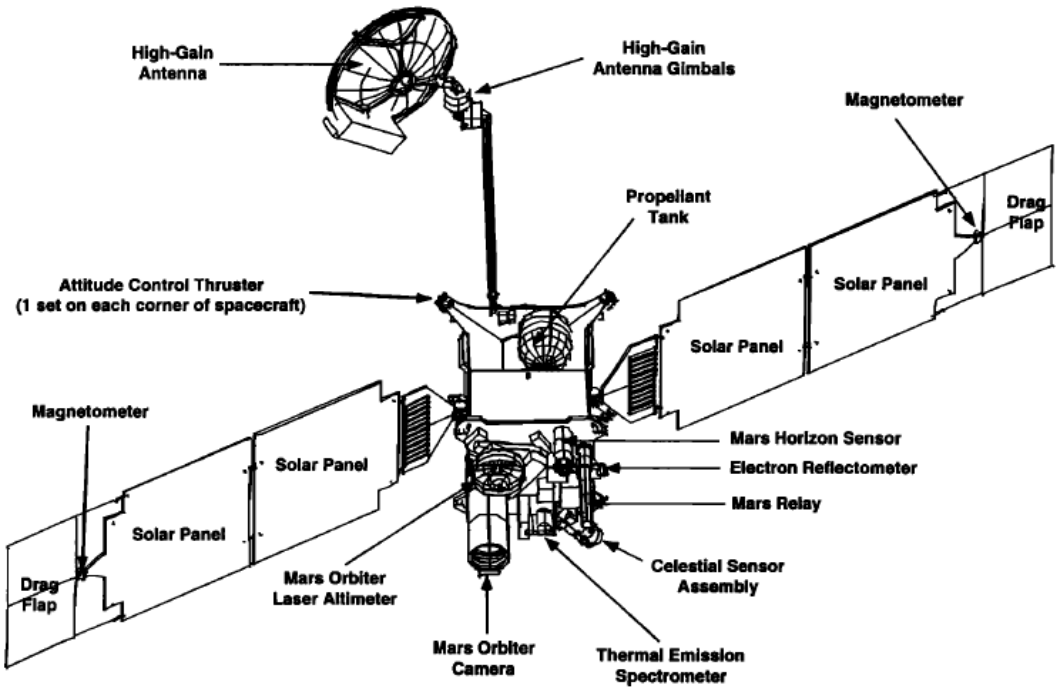

Figure 28. Global view of the MGS spacecraft with its main components and instruments [Albee et al., 2001].

2.1.1.4. Main discoveries

The use of MOLA data enables the production of a **high resolution map** (Figure 29) of the shape and topography of Mars [*Smith et al.*, 2001]. It showed that a difference of 30 km exists between the lowest point in Hellas and the top of Olympus Mons. It also revealed that Mars is flattened by ~20 km at the poles due to the rotation of the planet and that the North Pole is ~6 km lower than the South Pole. Pictures taken by MOLA also allowed the identification of

pathways for the **flow of past water** [*Kerr, 2003*], the height of clouds, and the first direct global measurement of the amount and distribution of condensed carbon dioxide.

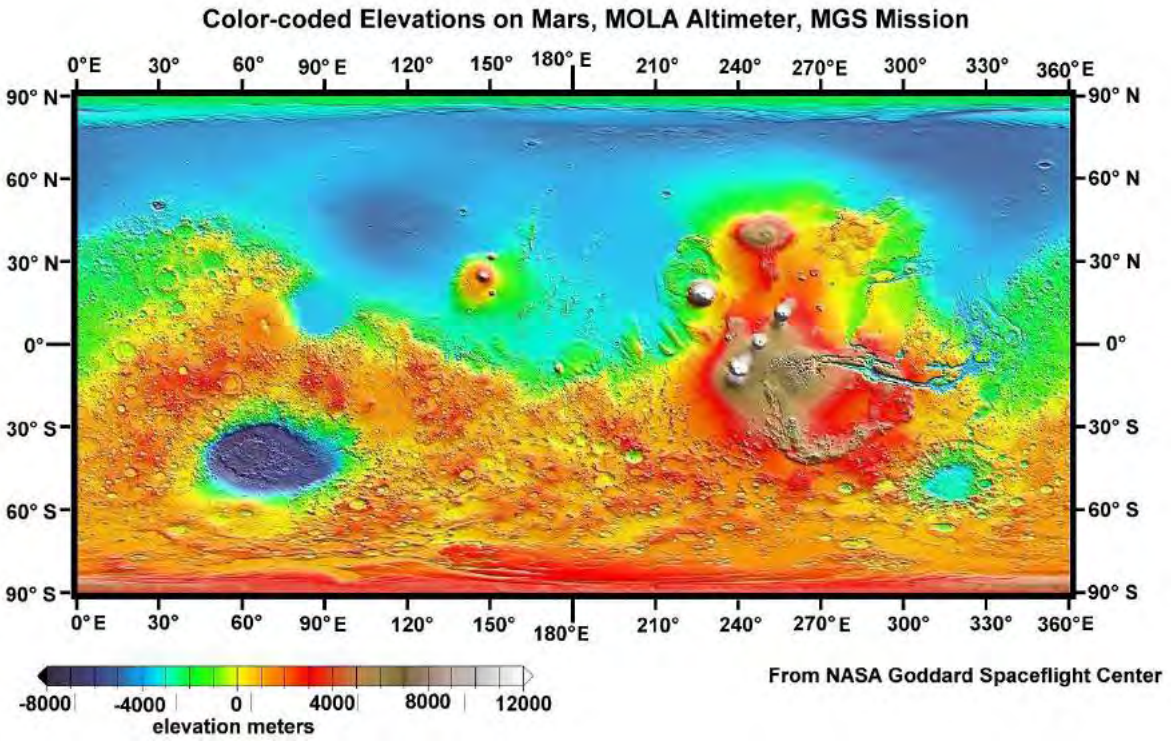

Figure 29. High resolution topographic map of Mars obtained thanks to the MOLA altimeter onboard MGS.

Visible imaging (MOC) and infrared spectral mapping (TES) provided information about the nature of the surface and processes operating on the surface. Thus, the TES data allowed the discovery of new mineralogical and topographic evidence suggesting Mars had abundant water and thermal activity in its early history. They also indicated evidence of an ancient **hydrothermal system**, implying stable liquid water at or near the surface, and hence implying that a thicker atmosphere existed in Mars' early history. MOC meanwhile had been used to characterize the properties of the currently active fluids involved in the gullies identified on Mars. It suggested the presence of a current source of liquid water, similar to an aquifer near the planet surface.

During the circularization phase, MAG/ER observations showed that the Martian magnetic field is not globally generated in the planet's core [*Acuña et al., 1998*], but is localized in specific areas of the ancient crust [*Acuña et al., 1999*]. These anomalies demonstrate that Mars had once an internal dynamo which ceased operation early in geologic time (see section 1.2.2.1). This discovery formed the basis of a new model of interaction between the solar wind and Mars, discussed in section 1.3.

2.1.2. Mars Express

Mars Express (MEX) is the first mission launched by the European Space Agency (ESA) to explore another planet of the solar system. It has been so called due to the short duration of its design and construction compared to similar missions. The MEX probe is composed of an orbiter and a lander called **Beagle 2**, named after Charles Darwin's ship. It was launched on June 2, 2003 from the Baikonur Cosmodrome (Kazakhstan).

2.1.2.1. Scientific objectives

As MGS, MEX is dedicated to the study of the planet's interior, subsurface, surface and atmosphere. However, the combination of the MEX orbiter and of the Beagle 2 lander would have allowed unprecedented orbital and in-situ measurements. The scientific objectives of MEX try to fulfill in part the scientific goals of the lost Russian **Mars 96** mission, and added two related new issues [*Chicarro et al.*, 2004]: the current inventory of ice or liquid water in the Martian crust, and possible traces of past or present biological activity on the planet.
The main scientific objectives of the orbiter are:

- Imaging the entire surface with a high-resolution of ~10m/pixel and selecting areas at super resolution (2m/pixel).
- Global infrared mineralogical mapping of the surface at 100m resolution.
- Radar sounding of the sub-surface structure down to the permafrost (depth of a few kilometers).
- Determining the global atmospheric circulation and mapping the atmospheric composition.
- Determining the interaction of the atmosphere with the surface and the solar wind.
- Collecting information about the atmosphere, ionosphere, surface and interior through radio science.

The Beagle 2 lander was designed to perform exobiology and geochemistry research on its landing site [*Pullan et al.*, 2004]. Its ultimate goal was to detect extinct or extant life on Mars. However, a more reachable objective was to establish the conditions that were suitable for the emergence and evolution of life. It was designed to perform in situ geological, mineralogical and geochemical analysis of rocks and soils, to study the Martian environment

(weather and climate) through chemical analysis of the atmosphere, to perform in situ isotopic dating, etc.

2.1.2.2. Orbitography

The year 2003 has not been chosen at random to launch MEX. This specific year enabled the maximum launch mass, a situation that only happen once every sixteen years. This enabled the launcher to bring Beagle 2, which would not have been possible otherwise. The design of the orbit of the MEX orbiter was set by the objectives of the mission (among others covering the poles) and at the beginning of the mission, by the landing site of Beagle 2. Indeed, for the first 6 months the orbiter needed to fly over the lander site in the Isidis Planitia area. The working orbit chosen initially was a **highly-elliptical quasi-polar** orbit, with a periapsis at 250 km and an apoapsis at 10 142 km, an inclination of 86.35° and a 6.75 h period.

After its launch in June 2003, the interplanetary journey only lasted 6 months (which also explain the denomination of Mars Express) and the spacecraft was captured into Mars orbit on December 25, 2003. Five days before insertion, the Beagle 2 descent capsule was ejected while the orbiter was still on a Mars collision course. From its hyperbolic trajectory, Beagle 2 was supposed to enter and descend through the atmosphere in about five minutes. However, nobody ever knew what happened to Beagle 2, no signal was ever received from the Martian surface. It has finally been found on the surface of Mars in 2015 thanks to pictures taken by Mars Reconnaissance Orbiter. The orbiter has continued its mission alone, moving to its operational near polar orbit in **January 2004**. Since then, it performs successfully measurements and is still operational at the present time. Its periapsis has varied from 245 to 365 km over the years and it is slowly precessing.

In Figure 30 is plotted the orbit of MGS and MEX on March 10, 2005 in the (X_{MSO};Y_{MSO}) plane (see section 2.5.1 for the definition of the MSO frame). The Sun is on the right side of the scene. The orbit of Phobos (circular at ~9300 km) has been superimposed to give a scale.

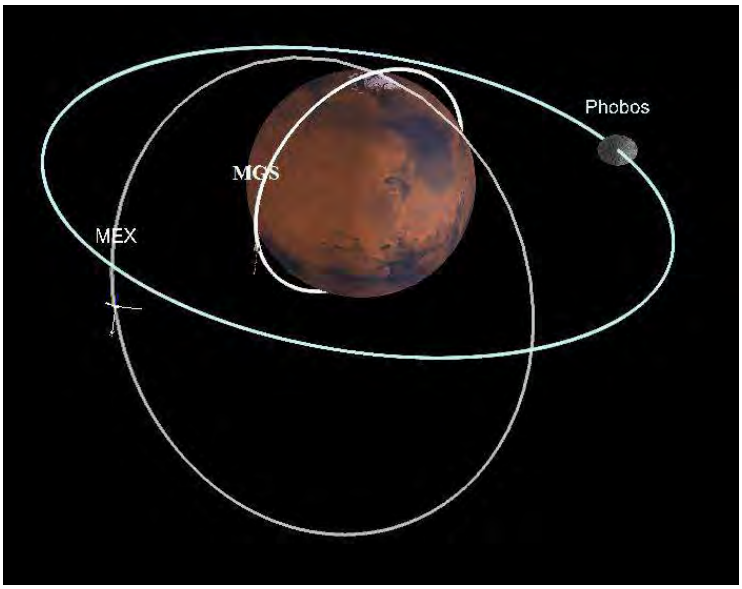

Figure 30. Orbit of MGS, MEX and Phobos on March 10, 2005 in the (X_{MSO};Y_{MSO}) plane. Created with 3D view.

2.1.2.3. Instruments

The Mars Express orbiter payload is composed of 6 instruments, some of them reusing directly the designs used for the failed Russian mission **Mars 96**, and a radio-science experiment that requires no additional hardware. These instruments can be sorted in two categories: HRSC, OMEGA and MARSIS are observing the solid planet (surface and subsurface) whereas PFS, SPICAM and ASPERA are studying the atmosphere and the Martian environment. Their location on the spacecraft are showed in Figure 31.

- **HRSC** (High Resolution Stereo Camera): the main goal of the HRSC camera is to image the entire planet in full color with a high spatial resolution [*Neukum et al.*, 2004].

- **OMEGA** (Observatoire pour la Minéralogie, l'Eau, les Glaces et l'Activité): OMEGA is a visible and near-IR mapping spectrometer [*Bibring et al.*, 2004] which can cover the planet at medium resolution (1-5 km) at altitudes between 1000 km and 4000 km.

- **MARSIS** (Mars Advanced Radar for Subsurface and Ionosphere Sounding): MARSIS is a subsurface radar sounder and altimeter [*Picardi et al.*, 2004] which maps the sub-surface structures to depth of a few kilometers.

- **PFS** (Planetary Fourier Spectrometer): The PFS instrument is a double-pendulum infrared spectrometer [*Formisano et al.*, 2005] which covers the wavelength range of 1.2-5µm and 5-45µm with a spatial resolution of 10-20 km.

- **SPICAM** (Studying the Global Structure and Composition of the Martian Atmosphere): SPICAM is a UV and IR spectrometer complementary to the PFS instrument [*Bertaux et al.*, 2004].

- **ASPERA** (Analyser of Space Plasmas and Energetic Ions for Mars Express): The ASPERA instrument measures ions, electrons and energetic neutral atoms at different locations along the spacecraft's orbit [*Barabash et al.*, 2004]. ASPERA is described in more details in section 2.2.2.

- **MaRS** (Mars Radio Science): the MaRS experiment [*Pätzold et al.*, 2004] is performing radio sounding experiment of the neutral atmosphere and of the ionosphere to provide vertical density, pressure and temperature profiles but also insights into the internal gravity anomalies and the surface roughness.

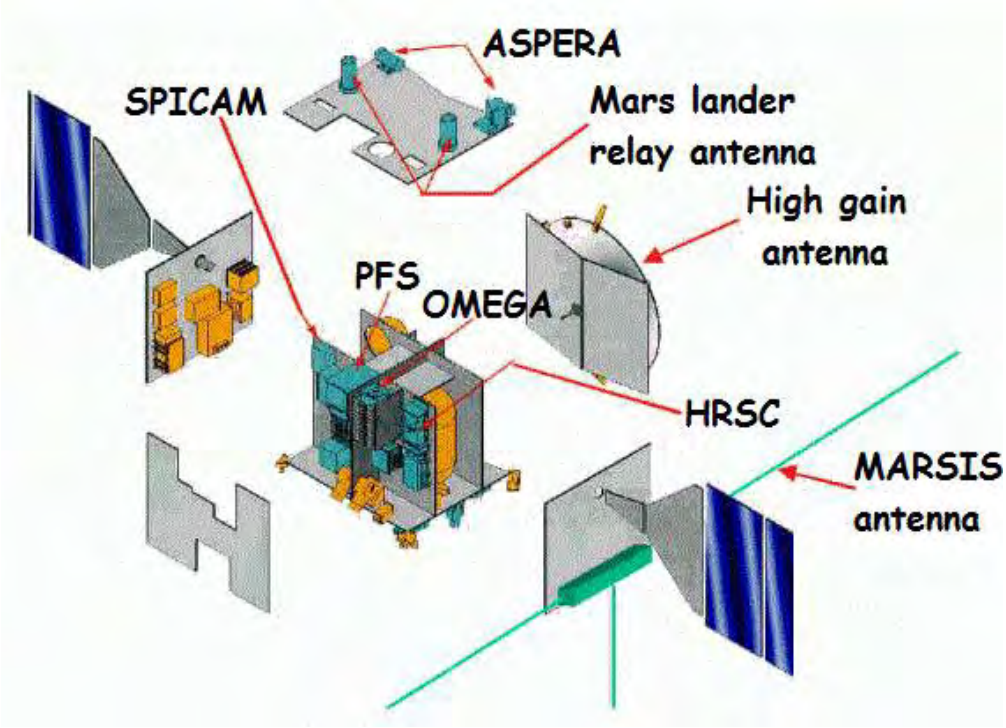

Figure 31. Exploded view of the MEX orbiter, revealing the arrangement of the scientific instruments.

2.1.2.4. Main discoveries

The MEX orbiter has provided us, for now more than twelve years, with **spectacular 3D pictures** of the canyons, polar caps or impact craters like the one of the Gale crater in which Curiosity is currently working (Figure 32). The orbiter also carried out the mapping of **Phobos**

with a high resolution, which enabled the determination of its mass and of its low density ($1.86\ \mathrm{g.cm^{-3}}$).

The OMEGA spectrometer detected for the first time **hydrated minerals** (phyllosilicate or hydrated sulfate) which proved that water was present on Mars' surface for a period long enough for these minerals to be formed. OMEGA data also revealed the composition of the Southern polar cap: 85% of CO_2 ice and 15% of H_2O ice. The HRCS camera showed that there is still **volcanism** on Mars and that the Olympus Mons and the Tharsis' volcano were still in activity several million years ago.

In 2004, the FPS spectrometer may have detected the presence of **methane** in the atmosphere. As its lifetime is short (440 years), it would implies the presence of mechanisms creating methane on Mars. The SPICAM data allowed the discovery of **localized polar aurorae**, which are located over regions with strong crustal magnetic fields. MEX also made the first direct observation of the formation of **carbon dioxide clouds**, and determined that they are observed on average at an altitude of 80 km.

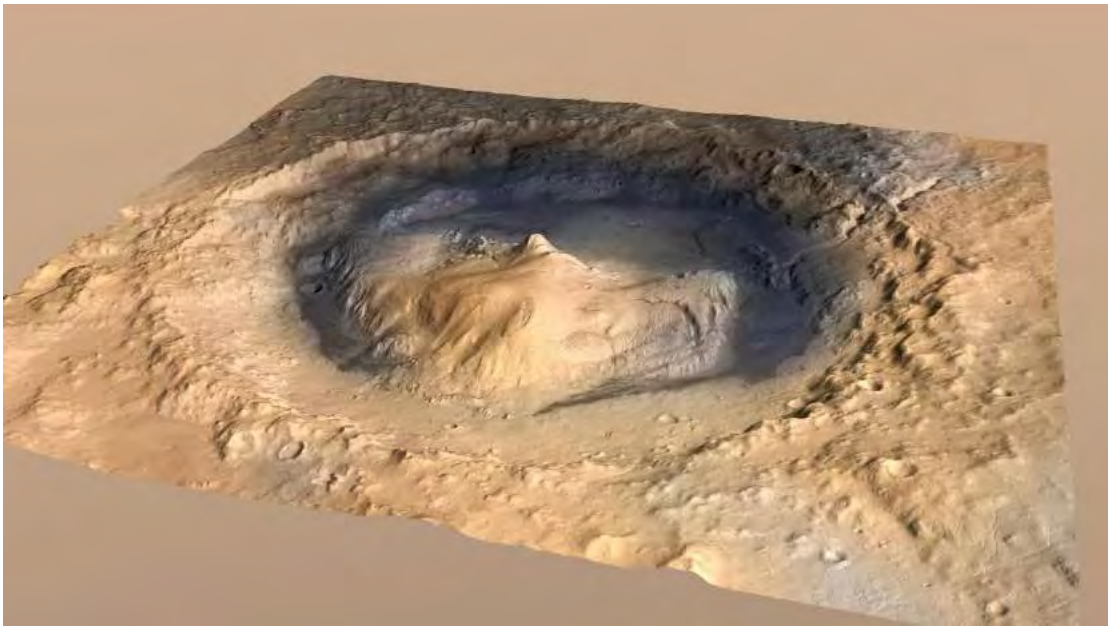

Figure 32. 3D picture of the Gale crater obtained with the HRSC instrument onboard MEX.

Closer to the problematic of my PhD, the different spacecraft and landers which reached Mars before MAVEN made significant discoveries on the Martian plasma environment which lead to the understanding we have today (section 1). Selected key results on the plasma environment obtained over nearly five decades are gathered in Table 2 [*Brain et al.*, 2017].

Mission	Dates	Selected Key Results
Mariner 4, 6, 7, 9	1965-1972	• Detected bow shock and magnetosheath • First ionospheric density profiles
Mars 2, 3, 5	1971-1974	• Measured bow shock, sheath, and inner magnetosphere
Viking 1, 2	1976	• *In situ* ionospheric profiles (density, composition, temperature)
Phobos 2	1989	• First sampling of central wake • Measured escaping ions
Mars Global Surveyor	1997-2006	• Discovered crustal fields • Sampled ionosphere down to / below main peak
Mars Odyssey & Mars Reconnaissance Orbiter	2001-present	• Ionospheric density profiles
Mars Express	2004-present	• Discovered localized aurora • Detected ionopause • Confirmed pressure balance near Mars
Rosetta	2007	• Distant bow shock crossing

Table 2. Spacecraft missions to Mars and their measurements relevant for describing the plasma environment of Mars before MAVEN [Brain et al., 2017].

2.1.3. MAVEN

The Mars Atmosphere and Volatile Evolution (MAVEN) mission is the latest mission sent by the NASA to study the red planet. Contrary to the MGS and MEX missions, MAVEN took the bias to focus its study on the Martian upper atmosphere. It has been sent from Cape Canaveral Air Force Station (Florida, USA) on November 18, 2013.

2.1.3.1. Scientific objectives

Thanks to previous Martian missions such as MGS or MEX, strong observational evidence support the idea that significant escape of gas from the Martian atmosphere to space has occurred, nowadays and since the early history of the planet (section 1.2.2.2). The MAVEN spacecraft is designed to measure the structure, the composition and the variability of the Martian upper atmosphere and its interaction with the Sun and the solar wind, so as the resulting

loss of gas from the top of the atmosphere to space [*Jakosky et al., 2015a*]. Its main objectives are:

- Measuring the composition and the structure of the upper atmosphere and of the ionosphere today, and determine the processes responsible for controlling them (dependence on geographical location, remnant magnetic field and external conditions). Extrapolating back in time to understand what the upper atmosphere would have looked like under the conditions encountered in the early solar system history.
- Measuring the loss rate of gas from the top of the atmosphere to space, and determine the processes responsible for controlling them.
- Determining properties and characteristics that will enable us to extrapolate backwards in time to calculate the integrated loss to space over the four-billion-year history recorded in the geological record.

2.1.3.2. Orbitography

After its launch in November 2013, the MAVEN spacecraft spent ten months in its interplanetary journey and finally reached Mars on September 21, 2014 (Figure 33). It was successfully inserted into a 35 hours elliptical orbit. The MOI was followed by a five weeks transition phase during which propulsive manoeuvers to get into the science mapping orbit have been operated, the science booms have been deployed and the instruments have been tested and calibrated. Once the science mapping orbit has been reached, the Science phase began on **November 16, 2014**.

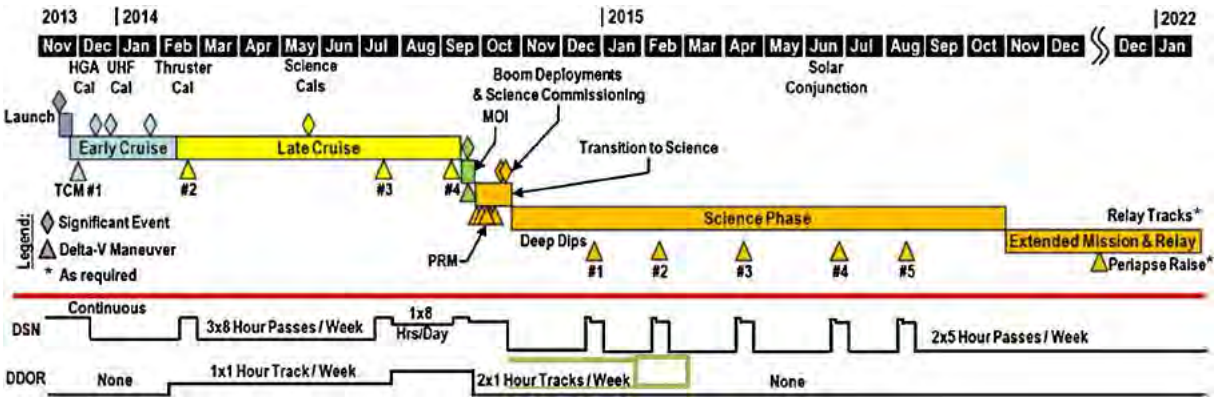

Figure 33. Overall timeline of the MAVEN mission, from launch through the end of the primary mission and into a possible extended mission [Jakosky et al., 2015a].

In order to fulfill the objectives of the mission, the spacecraft has been placed on a highly elliptical orbit, with a nominal periapsis at 150 km, and an apoapsis of ~6220 km, which means a period of ~4.5 hours. The periapsis is chosen on each orbit to be within the atmospheric density range of 0.05 - 0.15 kg. km^{-3}. Its altitude then varies around 150 km depending on the season, the location and the surface elevation. The periapsis is periodically lowered down to 125 km (density corridor 1.5-3.0 kg/km3) for five-day periods known as "**deep-dips**" [*Bougher et al., 2015*]. This altitude, though higher than the one reached by MGS during its first aerobreaking phase, is in the vicinity of the **homopause**, which separates the upper atmosphere from the well-mixed lower atmosphere. "Deep-dips" are only operated on selected times to limit the drag on the spacecraft that could alter the orbit (as in the aerobreaking technique) and to minimize the risk of high-voltage arcing that could alter some of the instruments.

The orbital inclination of 75° has been chosen together with the apoapsis altitude and the orbital period to provide an appropriate **precession rate** of the orbit in both local time and latitude (Figure 34).

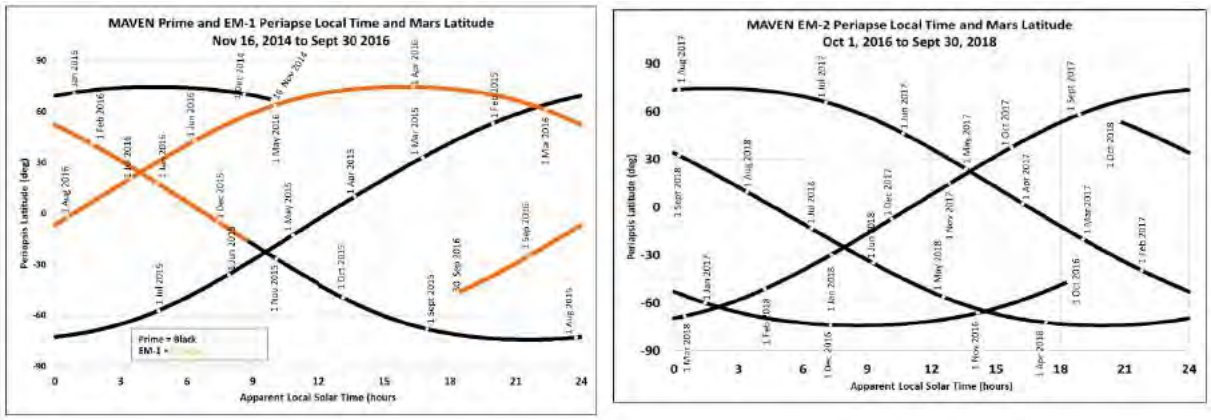

Figure 34. Precession of the MAVEN periapsis along its nominal mission and its two extensions. Left panel: Precession of the MAVEN periapsis during the primary mission and the first extension. Right panel: Precession of MAVEN periapsis during the second extension. Location of the spacecraft at its periapsis is plotted as a function of the apparent local time (see section 2.5.4) and latitude. [Jakosky et al., in preparation].

The primary mission of MAVEN lasted one Earth-year and the mission is now extended a second time through September 2018. At the end of its science phase, the MAVEN spacecraft will be able to act as a **data relay** for rovers or landers like Opportunity, Curiosity, and the upcoming Mars 2020, in the wake of Mars Reconnaissance Orbiter and Mars Odyssey.

In Figure 35 is plotted the orbit of MAVEN and MEX on March 10, 2016 in the (X_{MSO};Y_{MSO}) plane (see section 2.5.1 for the definition of the MSO frame). The Sun is on the right side of the scene. The orbit of Phobos (circular at ~9300 km) has been superimposed to give a scale.

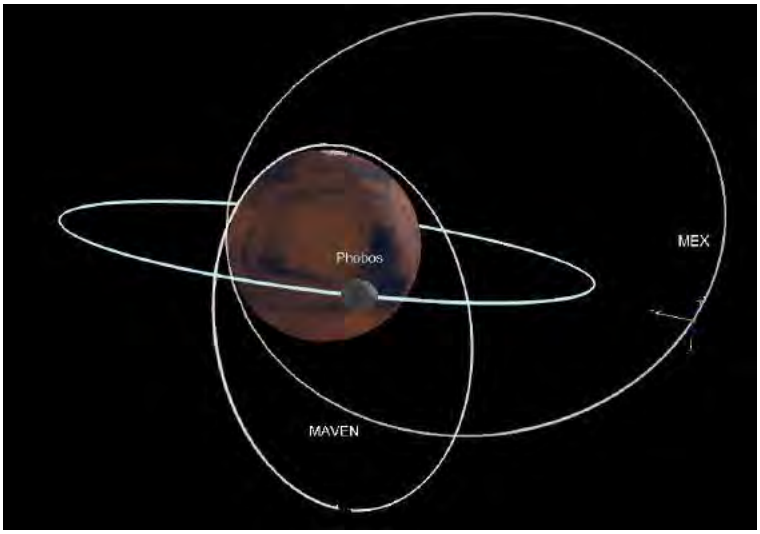

Figure 35. Orbit of MAVEN, MEX and Phobos on March 10, 2016 in the (X_{MSO};Y_{MSO}) plane. Created with 3D view.

2.1.3.3. Instruments

The MAVEN spacecraft carries onboard a complete suite of plasma and field instruments, plus an ultraviolet spectrometer and a neutral spectrometer. Three instruments (NGIMS, IUVS and STATIC) are located on an Articulated Payload Platform (APP) which allows them to be oriented in space independently of the spacecraft orientation (Figure 36).

- **SEP** (Solar Energetic Particle): the SEP instrument [*Larson et al.*, 2015] measures the energy spectrum and angular distribution of solar energetic electrons (30 keV-1 MeV) and ions (30 keV-12 MeV).

- **SWIA** (Solar Wind Ion Analyzer): the SWIA experiment [*Halekas et al.*, 2013] measures the energy and angular distributions of solar wind and magnetosheath ions.

- **STATIC** (Supra-Thermal And Thermal Ion Composition analyzer): The STATIC instrument [*McFadden et al.*, 2015] measures the velocity distributions, the temperature and the mass composition of suprathermal and thermal ions. It is described in more details in section 2.2.3.1.

- **MAG** (Magnetometer): MAG is a dual vector fluxgate magnetometer [*Connerney et al.*, 2015] which measures the intensity and direction of the magnetic field along the spacecraft orbit. It is described in more details in section 2.2.3.2.

- **SWEA** (Solar Wind Electron Analyzer): the SWEA experiment [Mitchell et al., 2016] measured the energy and angular distributions of solar wind and magnetosheath electrons and ionospheric photoelectrons. It is described in more details in section 2.2.3.3.

-**LPW** (Langmuir Probe and Waves): the LPW instrument [*Andersson et al.*, 2015] measures the electron density and temperature, and electric field waves in the Martian environment. It is described in more details in section 2.2.3.4.

- **EUV** (Extreme Ultraviolet monitor): the EUV monitor [*Eparvier et al.*, 2015] provides additional measurements for determining the solar EUV input to the Martian atmosphere.

- **IUVS** (Imaging Ultraviolet Spectrometer): the IUVS experiment [*McClintock et al.*, 2014] is a remote-sensing instrument that measures UV spectra with four modes: limb scans near periapsis, planetary mapping, coronal mapping and stellar occultation.

- **NGIMS** (Neutral Gas and Ion Mass Spectrometer): the NGIMS experiment [*Mahaffy et al.*, 2015] makes in-situ measurements of the neutral composition, isotopic ratios and scale height temperature of the major gas species and thermal ions in the Martian upper atmosphere.

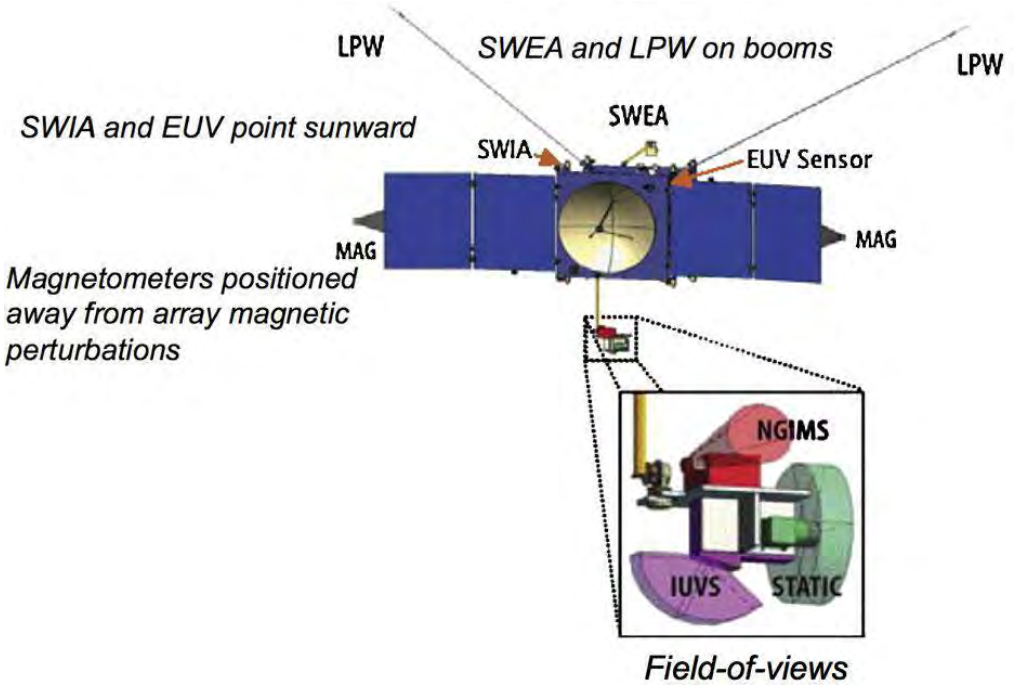

Figure 36. Instrument accommodation on the MAVEN spacecraft [Jakosky et al., 2015a].
It shows the locations of the science instruments on the body of the spacecraft and on the APP.

2.1.3.4. Main discoveries

On December 18-23, 2014 the IUVS instrument detected the "**Christmas light aurora**". It corresponds to nightside emissions at the same wavelengths as dayglow. Contrary to discrete aurora, which are observed near closed crustal magnetic field lines, this phenomenon, called diffusive aurora [*Schneider et al.*, 2015], are observed at low altitudes, over much of the Martian northern hemisphere. They hence seem to have no connection with crustal magnetic sources. These aurora were coincident with a solar energetic particles outburst, during which solar energetic particles with energies up to 200 keV have been observed. The nightside emission observed is consistent with the precipitation of high-energy electrons into the atmosphere, like polar rains on Earth.

Thanks to its Deep-Dip campaigns, the MAVEN mission made comprehensive measurements of the **Martian thermosphere** and **ionosphere** composition (Figure 8 and Figure 9), structure and variability at altitudes down to ~130 km. In-situ measurements of the upper atmosphere reveal previously unmeasured populations of neutral and charged particles, the altitude of homopause located at approximately 130 km, and an unexpected level of variability both on an orbit-to-orbit basis and within individual orbits [*Bougher et al.*, 2015].

In March 2015, observation of the response of Mars to an **Interplanetary Coronal Mass Ejection** impact enabled the observational correlation of these events with a significant enhancement in the escape rate of ions to space [*Jakosky et al.*, 2015*b*]. In addition, the total escaping rate for heavy ions has been calculating at 3×10^{24} s^{-1}, but this number is not expected to be constant through time [*Brain et al.*, 2015].

The different **Martian coronae** produced from H, C and O atoms have been observed by MAVEN, especially during the insertion phase [*Chaffin et al.*, 2015]. In Figure 37 is plotted the coronae made of atomic C, O and H [*Jakosky et al.*, 2015c]. The hydrogen flux proved to be more variable than expected, varying by one order of magnitude over one year. Imaging H, C and O coronae enables observation and quantification of carbon dioxide and water escape at the planet scale.

A **recurrent metal ions layer** has also been discovered in the ionosphere [*Grebowsky et al.*, 2017]. A metal ions layer had already been observed in late 2014-early 2015, following the passage of the Siding Spring comet and the associated impacts of cometary dust containing metals. This layer has been observed up to several months after the passage of the comet. However, *Grebowsky et al.*, [2017] found a recurrent metal ion layer, unbound to the passage

of the comet. MAVEN enabled the first in-situ detection of continuous presence of Na^+, Mg^+ and Fe^+ in the neutral atmosphere. The presence of such permanent ionospheric metal layer was expected at Mars, due to the vaporization and ionization of interplanetary dust particles, but it shows non-Earthlike features and processes due to the Martian environment specificities. Such discovery suggests that all the planets with an atmosphere also contains such metallic layer.

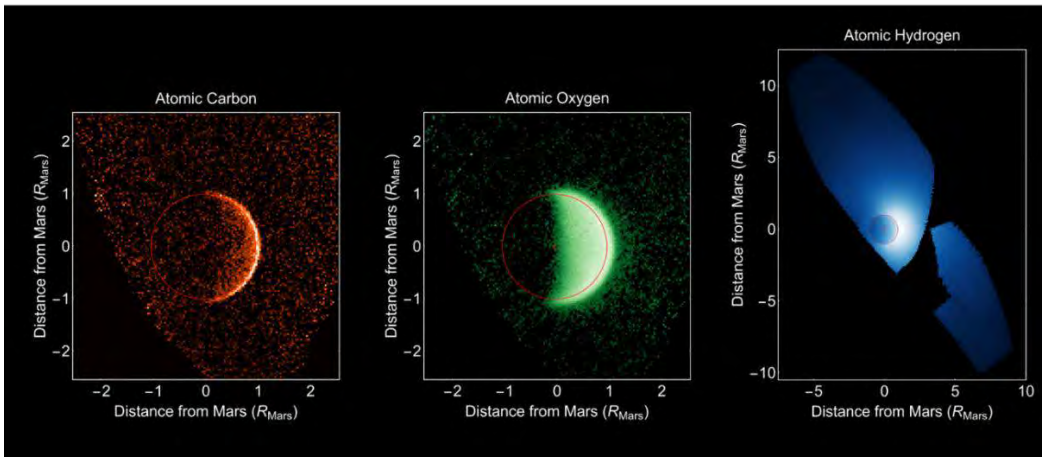

Figure 37.Coronae comprised of atomic C, O and H. [Jakosky et al., 2015c].

2.2. Instrumentation

Data from three spacecraft have been analyzed during my PhD: MGS, MEX and MAVEN. Each of the three spacecraft carried onboard its own specific suite of instruments. We here focus on several of their plasma and magnetic field instruments and detail their characteristics.

2.2.1. Mars Global Surveyor

The MGS magnetic field experiment was composed of a dual system of triaxial fluxgate magnetometers (MAG) which measured the "in situ" ambient field, and of an electron reflectometer (ER) sensor [*Acuña et al.*, 1992] which determine the parameters of the local electron distribution function. MGS did not carry an ion spectrometer.

2.2.1.1. The magnetometer: MAG

MAG was able to detect ambient magnetic fields from $\pm$ 4 nT to $\pm$ 65 536 nT. The use of two magnetometers allowed a real-time estimation of the spacecraft-generated magnetic field and provided redundancy for the measurements of the in-situ magnetic field. The sensors were mounted remote from the spacecraft body at the end of the solar panels (~5m away from the spacecraft body). Magnetometer sensors are best accommodated far away from the body of the spacecraft, to minimize the relative contribution of spacecraft generated magnetic fields, taking much advantage of the $1/r^3$ diminution of the magnetic amplitude with distance from the source.

An example of MAG measurements has been shown in Figure 10 and a comparison between MAG and ER measurements is proposed in Figure 39.

2.2.1.2. The Electron Reflectometer: ER

ER is a non-redundant hemispherical imaging electrostatic analyzer followed by a microchannel plate (MCP) and a resistive imaging anode. It has been developed by the Space Science Laboratory (Berkeley, USA) in collaboration with the Centre d'Etude Spatiale des

Rayonnements (Toulouse, France). The analyzer is composed of two concentric hemispheres (Figure 38): the outer hemisphere is connected to the spacecraft ground, and the inner hemisphere potential is adjustable to deflect incoming electrons within a specified energy range onto the MCP. Each electron hitting the MCP produces a cloud of electrons, which hit the anode. The relative signal level at each end of the anode is measured to determine where the electronic cloud landed on the anode. As the analyzer focuses on a disk called the plane of the **field of view** (FOV), this information enables to trace back the position of the initial incoming electron (the operation of an electron spectrometer is explained in more details in section 2.2.3.3).

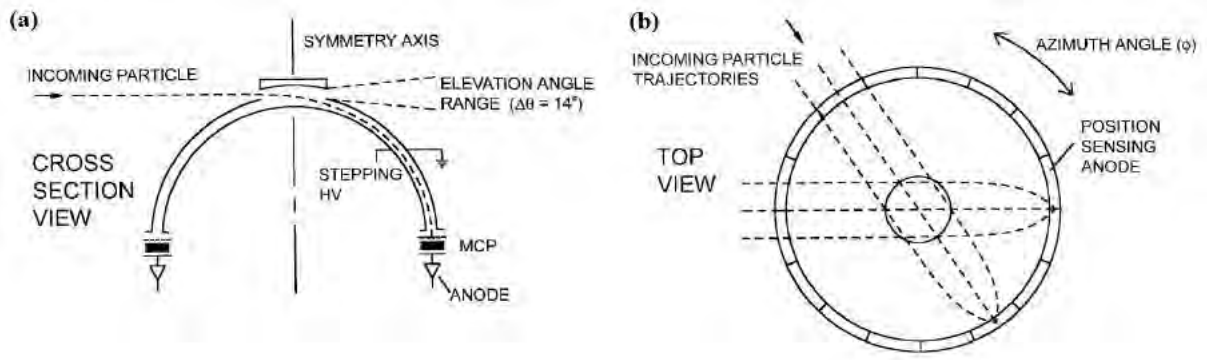

Figure 38. Schematic of the ER instrument showing the concentric hemispherical deflection plates, the MCP and the position-sensing resistive anode. Adapted from Mitchell et al. [2001].

The ER field of view is of 360° × 14° and is divided into sixteen 22.5° × 14° sectors. During a 2 to 48 seconds integration time, the analyzer images a slice of the electron distribution function that falls within the analyzer's energy acceptance and FOV. The energy acceptance, divided into 30 logarithmically spaced energy channels ranging from 10 eV to 20 keV with an energy resolution of $\frac{\delta E}{E} = 25\%$ (full width at half maximum), is selected by applying a deflection voltage to the inner hemisphere of the analyzer. All these characteristics are recorded in Table 3 so that they can be compared with those of MEX and MAVEN instruments. Among all the energy channels available, the three channels which collected the majority of the flux were 90-148 eV, 148-245 eV and 245-400 eV.

In Figure 39 are plotted the electron spectrogram measured by ER (first panel) and the magnitude of the magnetic field recorded by MAG (second panel) during a specific MGS orbit [adapted from *Acuña et al., 1998*]. The different boundaries detailed in section 1.3.1 are highlighted by vertical lines. Contrary to what can be observed in Figure 17 with MAVEN, we

can see that the absence of data for electrons with energies below 10 eV make it more difficult to identify the different boundaries.

Instrument Type	Quantity	MGS	MEX	MAVEN
Magnetometer	Magnitude range	4 – 65536 nT	none	0.06 - 65536 nT
Electron spectrometer	Energy range	10 – 20000 eV	1 – 20000 eV	3 – 4600 eV
	Energy resolution	25%	8%	17%
Ion spectrometer	Energy range	none	10-30000 eV/q	0.1-30000 eV/q
	Energy resolution		7%	16%
	Mass range		1, 2, 4, 8, 16 and >20 m/q	$H^+, He^{++}, He^+, O^+, O_2^+$ and CO_2^+
Langmuir probe	Temperature	none	none	0.05 to 5 eV

Table 3. Summary of the characteristics of the magnetometer, electron spectrometer, ion spectrometer and Langmuir probe onboard MGS, MEX and MAVEN.

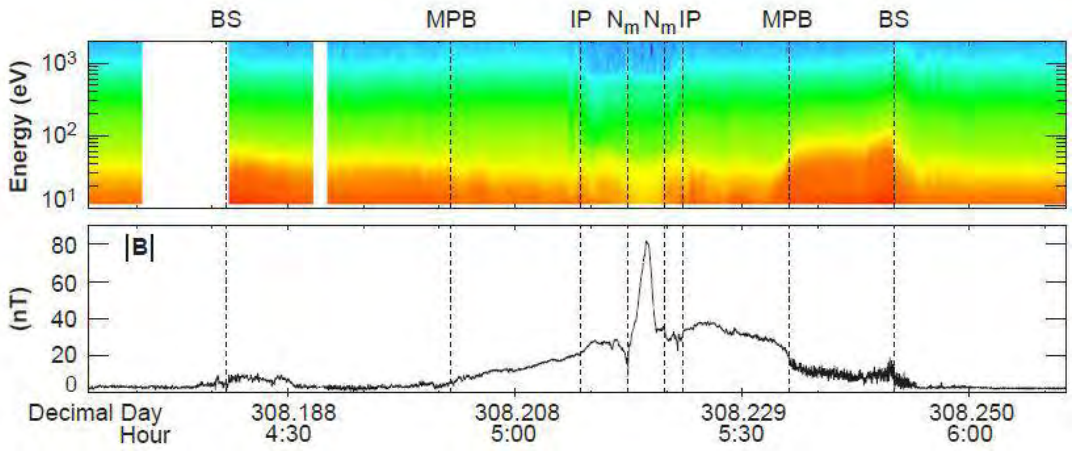

Figure 39. Example of electron spectrogram and magnetic field observed by MGS.

Panel 1: Electron fluxes ($cm^{-2}s^{-1}sr^{-1}eV^{-1}$) measured by ER are shown as a color spectrogram. Panel 2: Magnetic field amplitude measured by MAG. Vertical lines indicate the position of the bow shock (BS), of the MPB, of the ionopause (IP), and of the ionospheric main peak (N_m). Adapted from [Acuña et al., 1998].

2.2.2. Mars Express

The ASPERA-3 experiment is composed of four instruments including the Electron Spectrometer (ELS) and the Ion Mass Analyzer (IMA) [*Barabash et al., 2004*]. Three instruments, among which ELS, are mounted on a scanning platform, providing a full 4π coverage. IMA is technically a separated unit, connected by a cable to the ASPERA-3 main unit (Figure 40). Mars Express does not carry a magnetometer.

2.2.2.1. Electron Spectrometer: ELS

The ELS instrument is an electron sensor of a very compact design (only 300g compared to 2.2 kg for IMA). It is composed of a standard spherical top-hat electrostatic analyzer and a collimator system. It uses the same mechanisms as ER to image the electron distribution. During a 4 second integration time (maximum time resolution), the instrument can measure the electron fluxes in the energy range 0.001 – 20 keV/q in 128 logarithmically-spaced energy channels with an energy resolution of $\frac{\delta E}{E} = 8\%$ (which is the best energy resolution among the electron spectrometers of the three spacecraft). ELS has a field of view of 360° × 10° divided into sixteen sectors of 22.5° × 10°, corresponding to the sixteen anodes placed behind the MCP. As ELS is mounted on the scanning platform, the full 4π angular distribution of electrons is measured during each platform scan with a selectable scan time of 32, 64 or 128s. The characteristics of ELS are gathered in Table 3.

In general, ELS has been operated in four different modes (*Frahm et al., [2006]* and *Hall et al., [2016]*):

- **Default/Survey mode**: Full energy range across 128 log-spaced energy steps with a four second cadence.
- **Linear mode**: Reduced energy range of 1 - 127 eV across 128 linearly spaced energy steps, also with a four second cadence.
- **1s mode**: Reduced energy range of 10 - 160 eV across 32 log-spaced energy steps with a one second cadence.
- **32 Hz mode**: single energy channel (variable energy), with a cadence of 32 Hz.

The default mode is the most commonly used, operating more than 96% of the time from 2004 to 2014. The linear mode is utilized about once a month and the 32 Hz mode is rarely used. The 1s mode is sporadically used, but when operated, it lasts for several orbits. Over the course of the spacecraft in the induced magnetosphere, there is no change of mode within the same orbit. Regarding the use of the different modes, I only use in the following analysis data recorded in the **Default/Survey mode**.

Another specificity of ELS, compared to the other two missions, is that it only records data during **one portion of the orbit**, this portion varying all along the mission. It is usually centered on the periapsis.

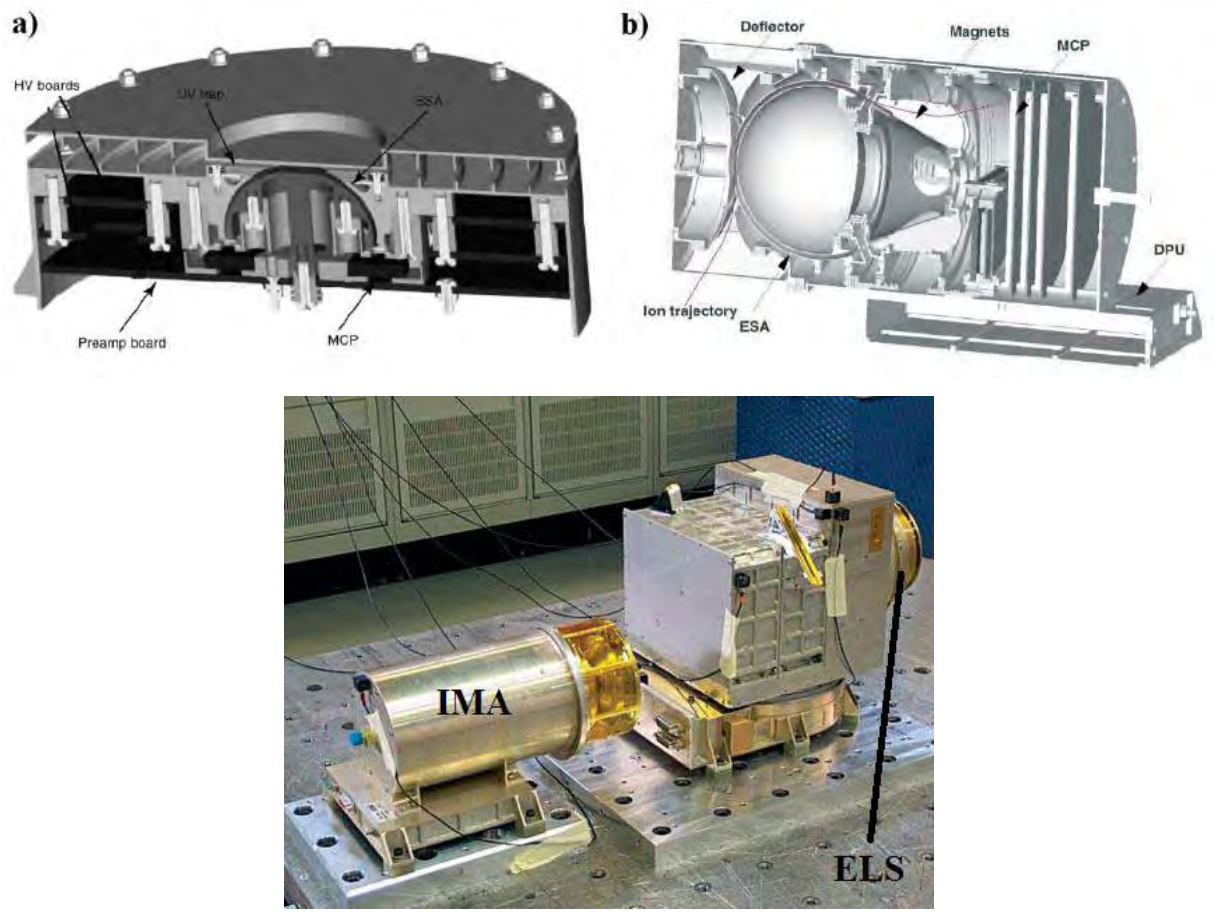

Figure 40. Schematic and pictures of the ELS and IMA instruments.
a) The MEX/ELS sensor b) Cross section of the IMA sensor c) The ASPERA-3 mechanical model during vibration testing [adapted from Barabash et al., 2004].

2.2.2.2. The ion spectrometer: IMA

IMA is an ion mass composition sensor. Particles enter the instrument through the outer grid. A deflection system is located behind the grid to divert particles coming from between 45° and 135° with respect to the symmetry axis into the electrostatic analyzer (ESA). Ions which are within a swept energy pass band pass the ESA. They are then deflected in a cylindrical magnetic field set up by permanent magnets. The field deflects lighter ions more than heavy ions away from the center of the analyzer. The ions finally hit an MCP and are detected by an anode system. Ions are simultaneously analyzed for direction and mass per charge (m/q). The mass range and mass resolution can be chosen by modifying the magnet assembly. A system of 32 concentric rings behind the MCP measures the radial impact position (representing the ion mass) and 16 sector anodes measure the azimuthal impact position (representing ion entrance angle).

IMA has a field of view of $360° \times 90°$. Electrostatic sweeping performs elevation coverage ($\pm 45°$). It can provide 3D ion fluxes in the energy range 0.01-30 keV/q, with an energy resolution of $\frac{\delta E}{E} = 7\%$, for the main ion components: H^+, He^{++}, He^+, O^+, and for the group of molecular ions: 20-80 amu/q. Its time resolution for full 3D is 32s. The characteristics of IMA are gathered in Table 3.

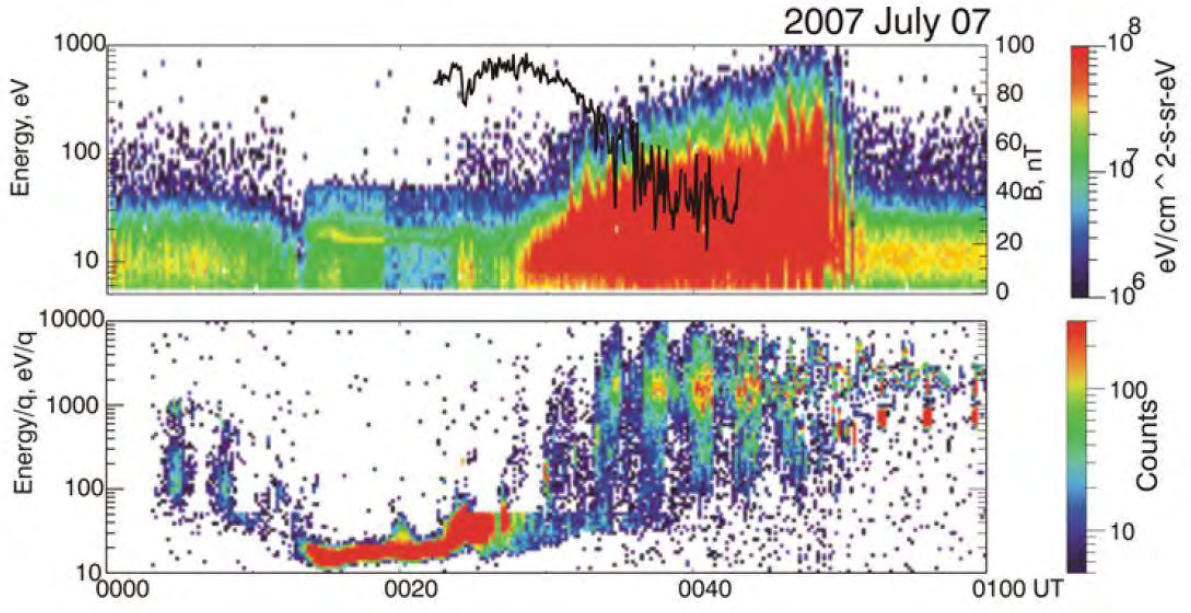

Figure 41. Example of electron and ion spectrogram observed by MEX. Adapted from Dubinin et al. [2008b]. Panel 1: Energy-time spectrogram of the electron fluxes with the superimposed curve of the magnetic field value determined by MARSIS. Panel 2: Energy-time spectrogram of the ion fluxes.

In Figure 41 is plotted data recorded by ELS (first panel) and IMA (second panel) at a MEX periapsis on July 7, 2007. Superimposed with the electron spectrogram is the amplitude of the magnetic field determined by the MARSIS instrument (not used in my PhD). Among MGS, MEX and MAVEN, ELS is the electron spectrometer which have the best energy resolution and hence we clearly see the photoelectron lines at ~20 eV between ~00:15 UT and ~00:22UT. The measurement of IMA allow to distinguish the two different ion populations present in the Martian environment: the planetary one, close to the planet, with low energy (~20 eV); and the solar wind ion population, farther from the planet and with higher energies. At the MPB, around 00:30 UT, the two populations are mixed.

2.2.3. MAVEN

The MAVEN particles and fields package is composed of seven instruments, including an ion spectrometer (STATIC), an electron spectrometer (SWEA), a Langmuir probe (LPW) and two magnetometers (MAG), presented in Figure 42.

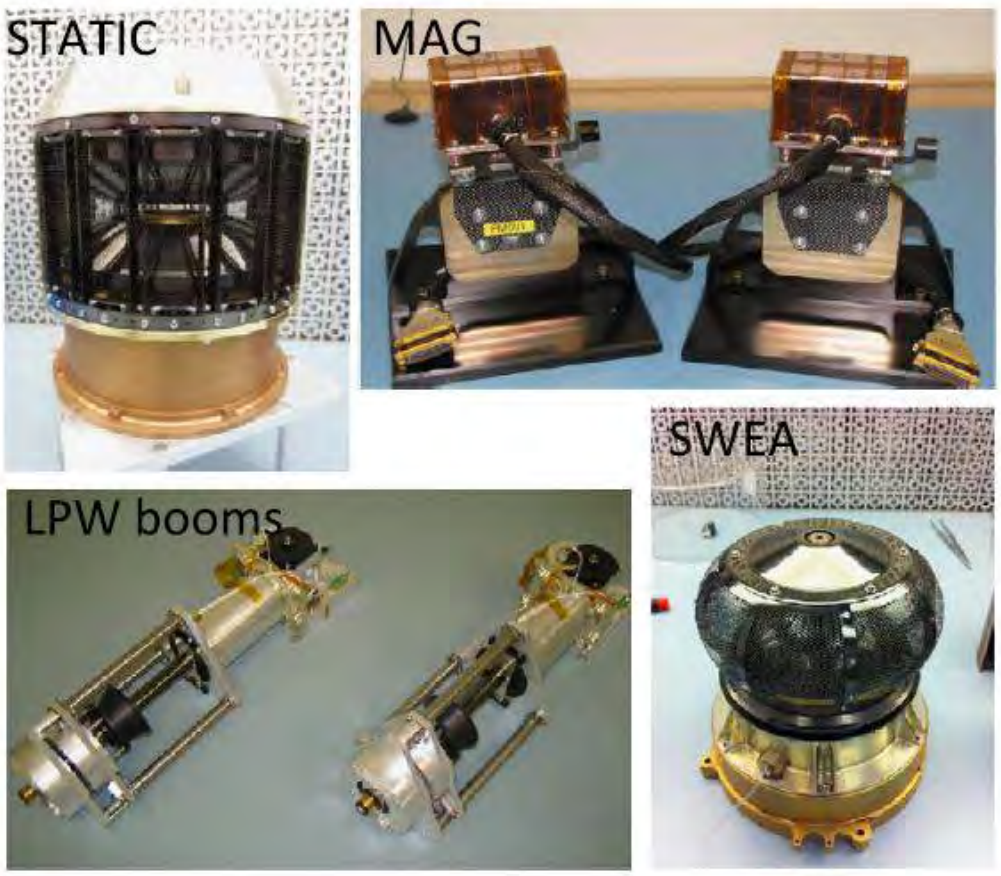

Figure 42. MAVEN science instruments used in this PhD. Adapted from Jakosky et al. [2015a].

2.2.3.1. The ion spectrometer: STATIC

The STATIC instrument consists of a toroidal "top hat" electrostatic analyzer with a nominal 360° × 6° field of view, followed by a time-of-flight velocity analyzer with 22.5° resolution in the detection plane. The energy analyzer also includes electrostatic deflectors at the entrance which expand the nominal FOV to 360° × 90°. The instrument is designed to resolve ion energy per charge (E/q), direction and velocity per charge. Knowing the charge state of the ions (nearly all ions at Mars are singly charged except solar wind alphas), these measurements lead to the velocity distributions and mass composition of suprathermal and thermal ions over an energy range of 0.1 eV to 30 keV with an energy resolution of $\frac{\delta E}{E} = 16\%$ and a base time resolution of 4 seconds [*McFadden et al.*, 2015]. STATIC is able to resolve major ions: $H^+, He^{++}, He^+, O^+, O_2^+$ and CO_2^+. It is mounted on the APP to orient differently its FOV according to the position of the spacecraft on its orbit. The characteristics of STATIC are gathered in Table 3.

STATIC is operated in several different modes, depending on the region or phenomenon of interest. These modes mainly differ on the time resolution, the number of energy and mass channels used, the integration on the deflectors and/or anodes sectors. I here only use two of them: **C0** (time resolution of 4s, omnidirectional, 64 energy channels, 2 mass channels) for the time-energy spectrograms and **C6** (time resolution of 4s, omnidirectional, 32 energy channels, 64 mass channels) for the time-mass spectrograms.

In Figure 43 is plotted an example of energy-mass spectrogram of the omnidirectional ion energy flux, measured with STATIC at a specific time in the nightside. We can observe four ion species: H^+(1 amu/q), He^{++}(2 amu/q), O^+(16 amu/q), and O_2^+(32 amu/q), with their main energy peak at ~10 eV. The H^+ energy spreads here toward thousands of eV.

The SWIA instrument is less relevant for my study as its measurements are restricted to higher energies (initial energy range of 5 eV to 25 keV, *Halekas et al.*, [2013]. Since November 27, 2014 its energy range has been restricted to 24 eV to 25 keV), which typically correspond to the magnetosheath and the solar wind. Moreover, SWIA cannot separated the different ion species.

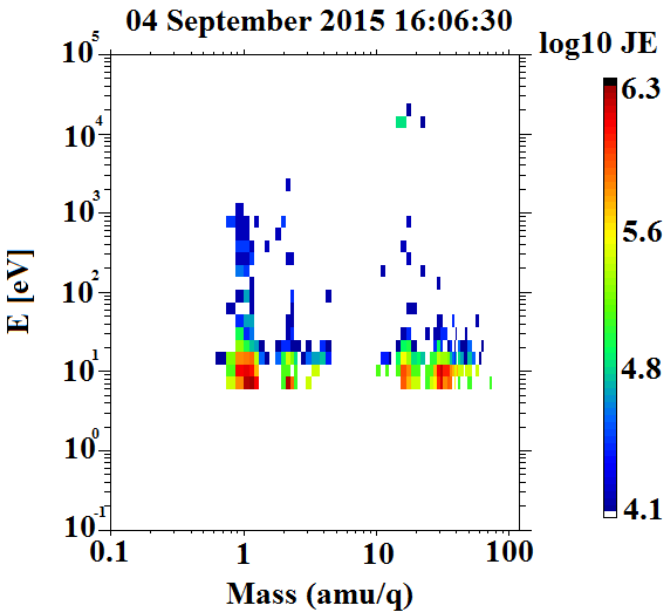

Figure 43. Example of STATIC energy-mass spectrogram of omnidirectional ion energy flux (C6 mode).

2.2.3.2. The Magnetometer: MAG

MAG consists of two identical independent triaxial fluxgate magnetometer sensors which can measure the magnitude and direction of the ambient magnetic field from ±0.06 to ±65 536 nT [*Connerney et al.*, 2015] with a resolution of 0.008 nT in the most sensitive dynamic range and an accuracy of better than 0.05%. Both magnetometers sample the ambient magnetic field at an intrinsic sample rate of 32 samples/sec. The two sensors are mounted at the ends of the solar arrays on small extensions (0.66m in length), placing them approximately at 5.6m from the center of the spacecraft body. The characteristics of MAG are gathered in Table 3.

A spacecraft magnetic control program has been implemented to provide a magnetically clean environment for the magnetic sensors and occasional spacecraft manoeuvers have been planned to characterize spacecraft fields and/or instrument offsets in flight.

In Figure 44 is plotted the projection of the magnetic field as measured by MAG along the MAVEN orbit onto two periapsis pass in the Southern hemisphere. We can clearly observe the enhancement of the magnitude and the rotation of the magnetic field as the spacecraft travels above crustal magnetic field sources.

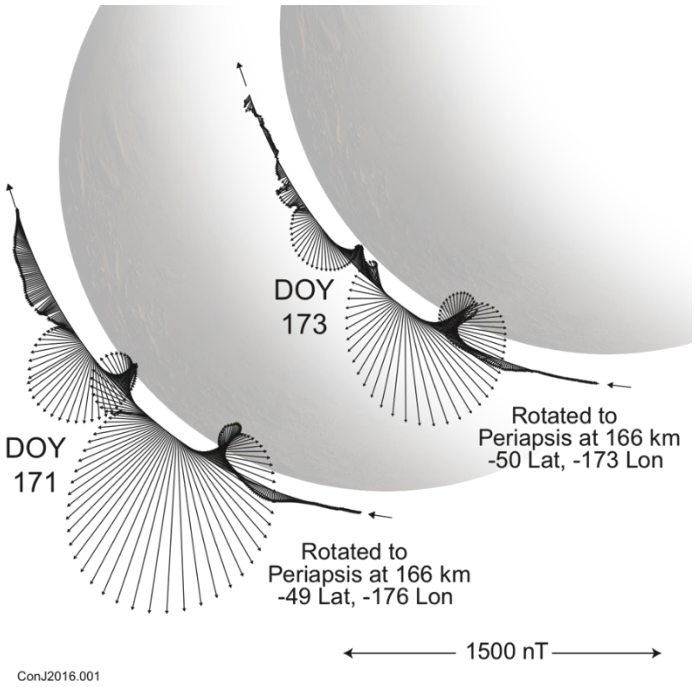

Figure 44. Example of the magnetic field measured by the MAG instrument onboard MAVEN. A projection of the MAVEN spacecraft trajectory and observed magnetic field onto a plane perpendicular to the Mars orbit plane and the Mars-Sun line for two specific periapsis (presented by J. E. P. Connerney at a MAVEN meeting).

2.2.3.3. The Electron spectrometer: SWEA

As ER on MGS and ELS on MEX, SWEA is a symmetric, hemispheric electrostatic analyzer with deflectors [*Mitchell et al.*, 2016]. It is designed to measure the energy and angular distributions of both solar wind electrons (core and halo populations) and ionospheric photoelectrons in the Martian environment, but also magnetosheath shock-energized electrons, tail lobe and auroral electrons. The instrument is a collaboration between the Space Sciences Laboratory at the University of California, Berkeley (UCB-SSL) and the Institut de Recherche en Astrophysique et Planétologie (IRAP) in Toulouse, France. The SWEA design is closely based on an instrument sharing the same name currently operating on the STEREO spacecraft [*Sauvaud et al.*, 2008]. For MAVEN, IRAP provided the electrostatic optics and front-end electronics (MCP, anode, preamplifiers and high voltage power supply), while UCB-SSL provided the low voltage power supply and digital electronics.

To fulfil its objectives and measure the energy and angular distributions of solar wind electrons, auroral electrons and ionospheric primary photoelectrons (Figure 18), the energy range chosen for SWEA is 3 to 4600 eV. The instrument works by measuring the electron flux

in consecutive given energy ranges. The pooling of all these measurements gives the distribution function of the electrons.

SWEA is roughly composed of two deflectors, followed by two concentric hemispheres leading to the electron detectors (MCPs + anodes), as shown in Figure 45. SWEA selects electrons within a specified energy range by placing a potential difference, ΔV_A, between the two concentric hemispheres. Electrons within this energy range are transmitted through the hemispheres to the exit grid to be counted, while those outside the range impact the walls, are scattered and absorbed. The center energy of transmitted electrons is proportional to ΔV_A through the following expression:

$$\mathrm{E_0} = \frac{\mathrm{R_0}}{2\mathrm{d}}\mathrm{q}\Delta\mathrm{V_A}$$

Where R_0 is the average radius of the two concentric hemispheres, q the elementary charge and d the distance between these two hemispheres. An energy spectrum is obtained by sweeping ΔV_A from 750 to 0.5 eV, which correspond – given the geometry of the instrument – to an energy range of 4600 to 3 eV. The energy resolution of SWEA is $\frac{\delta E}{E} = 17\%$. The different characteristics of SWEA are gathered in Table 3.

As only a small fraction of scattered electrons reaches the exit grid, they are accelerated by a 300-V potential onto a pair of MCPs mounted head to tail so as to maximize the amplification. The signal is amplified through this process by a factor of $\sim 10^6$. The resulting electron cloud lands on a charge collecting anode that is segmented into 16 equal sized sectors. An incident parallel electron beam is focused by the hemispheres to a point on the anode providing a 22.5° azimuth resolution.

The field of view of the concentric hemispheres is 360° × 7°. As MAVEN is not a spinning spacecraft but a three-axis stabilized spacecraft, it uses the deflectors to sweep the field of view above and below the aperture center plane. Electrons with a trajectory forming an angle up to θ with X_{SWEA} can then be selected (Figure 45). Deflection is achieved by placing a potential on either the upper or lower deflector, which bends the electron trajectories through an angle before reaching the aperture center plane and entering the hemispheres. The analyzer geometry limits the maximum deflection range to $\pm 60°$. This full deflection is achieved up to an energy of 2 keV, resulting in an overall FOV of 360° × 120°, which represents **87% of the sky**. At higher energies, the deflection range decreases with energy, reaching $\pm 26°$ at 4.6 keV.

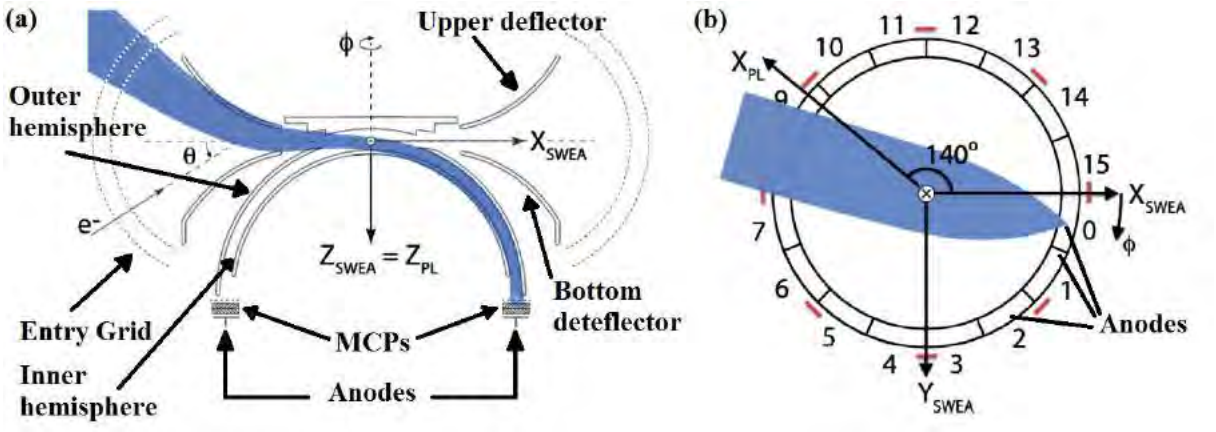

Figure 45. Schematic of the SWEA instrument onboard MAVEN. Adapted from [Mitchell et al., 2016]. Left: Cross-sectional view of SWEA, defining the instrument frame regarding the payload (PL) frame. Right: Top view of the anodes. Simulated electron trajectories (blue) are shown for a deflection of $\theta = -45°$.

The instrument is mounted at the end of a 1.5-meter boom, at which distance the spacecraft blocks **8%** of the instrument's FOV. Its final field of view is then 360° × 120°. It spans 80% of the sky with ~20° resolution. The position of SWEA regarding the spacecraft as well as the two different FOV depending on the energy are presented in Figure 46. SWEA has a 2-second measurements cadence. The instrument takes data over the first 1.95 seconds, as the analyzer and deflectors voltages are commanded to discrete values. This is followed by a 0.05 seconds "gap", during which the instrument does not take data as the voltages reset and settle in preparation for the next measurement. In parallel with these measurements, SWEA calculates three different data products (see *Mitchell et al.* [2016] for full description):

- **3D**: low cadence of 32, 16 or 8 seconds depending on the altitude, 64 energy channels, 16 azimuths/anode bins and 6 elevations/deflections bins.
- **PAD**: cadence of 2 or 4 seconds, average of the 3D products on the 6 elevation bins.
- **SPEC**: cadence of 2 or 4 seconds, average of the 3D products over the 96 azimuth-elevation bins.

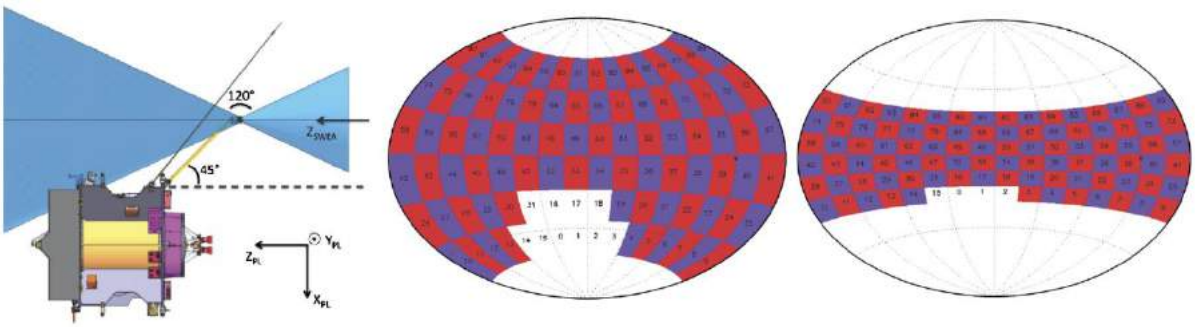

Figure 46. Illustration of the field of view of SWEA. Adapted from [Mitchell et al., 2016].
Left: SWEA is on the end of a 1.5-meter boom, with its symmetry axis (Z_{SWEA}) aligned with the spacecraft Z axis (Z_{PL}). SWEA has a 360° × 120° FOV (blue shading indicates the instruments blind spots). Middle: SWEA's field of view at all energies below 2 keV, mapped in SWEA coordinates over the full sky with an Aitoff projection. The FOV is subdivided into 96 angular bins (16 azimuths × 6 deflections). SWEA's blind spots are two oppositely directed cones. Ten of the angular bin, shown in white, are blocked by the spacecraft. Right: SWEA's field of view at an energy of 4.6 keV. At this energy, four angular bins are blocked by the spacecraft.

2.2.3.4. The Langmuir probe: LPW

LPW consists of two identical cylindrical sensors, 40 cm long, each located at the end of a 7-meter boom. It is designed to measure the temperature (T_e) and density (n_e) of thermal ionospheric electrons, and to measure spectral power density of waves in Mars' ionosphere [*Andersson et al.*, 2015]. The LPW instrument is optimized to measure n_e in a range covering $\sim 100\ cm^{-3}$ to $10^6 cm^{-3}$, T_e in the broad range of 500-50 000 K. The goal of the instrument is to have an altitude resolution better than 2 km, which is met with a time resolution of 4 seconds.

The technique used for LPW consists in measuring the current from the plasma to a voltage-biased probe over a range of probe voltages, creating a current-voltage (I-V) characteristic. The I-V characteristics are fitted so as to determine the electron density and temperature, the ion density, the spacecraft potential and properties of photoelectrons.

In Figure 47 is plotted the electron spectrogram measured by SWEA on the first panel, and the electron density measured by SWEA (in **black**) and by LPW (in **red**) on the second panel for a MAVEN pass in the ionosphere. The dayside ionosphere can be observed until ~23:43 UT, before the spacecraft enters the nightside ionosphere, where we can observe several electron depletions. Note that during this time interval the quality flag of the LPW density and of the spacecraft potential used for the calculation of the density from SWEA data is always

greater than 50, which means that these data are reliable (L. Andersson, *private communication*). The LPW quality flag is an automatic quality check calculated by the instrument team. It takes into account the quality of the fit of the IV curve, the thrusters, bad attitude, bad sunlight, etc. A quality flag of 50 have been identified by the LPW team as being the threshold above which data are good enough for science.

Due to instrumental limits the density calculated with SWEA data is restricted to electrons with energies greater than 3 eV (see Table 3), whereas the density calculated with LPW includes lower-energy electrons, which explains the difference observed between the two densities (especially here in the ionosphere where the plasma is essentially cold). The characteristic drop in the suprathermal electron flux is very clear in the SWEA density during the electron depletions, whereas there is no drop in LPW density, i.e., in thermal electron density.

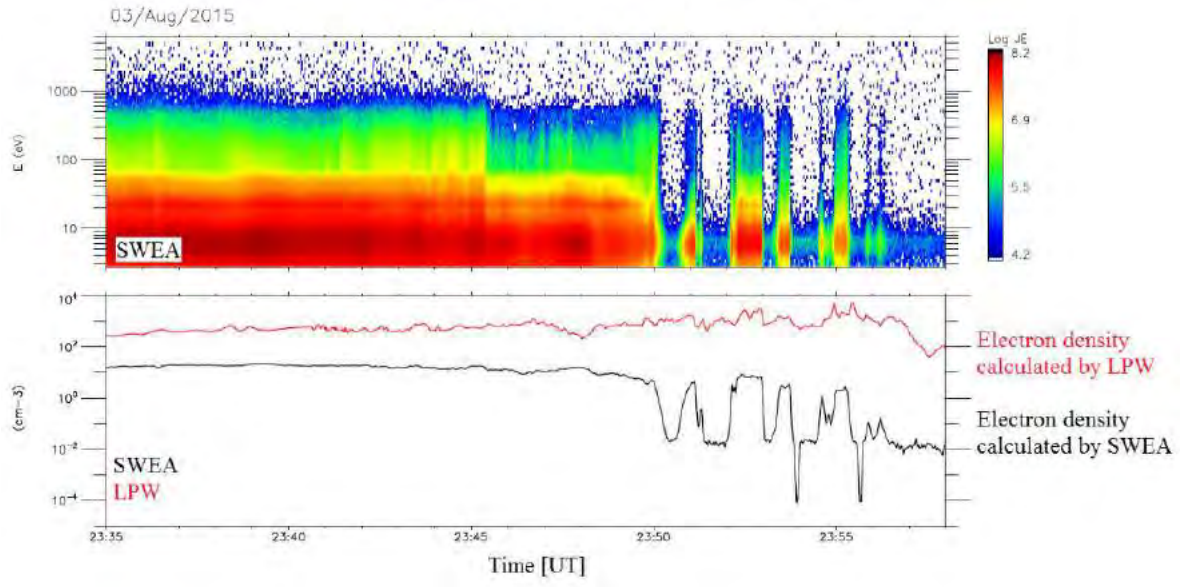

Figure 47. Comparison of LPW and SWEA densities.

*<u>Panel 1:</u> SWEA time-energy spectrogram of omnidirectional electron energy flux. <u>Panel 2:</u> Electron density calculated with SWEA (**black**) superimposed with the density calculated with LPW (**red**).*

In Table 3 are gathered the different characteristics of the MGS, MEX and MAVEN instruments that have been used during this PhD, so that they can be easily compared.

2.2.4. Contamination

The measurements made by the different instruments are subject to several sources of contamination, which degrade the data. For the study of electron depletions, the contamination on electron spectrometers is the most significant so that it will be the only kind of contamination discussed in this section.

Background

In Figure 48 is plotted the electron energy spectrum corresponding to the background of ER onboard MGS [*Mitchell et al.*, 2001]. This background can come from a variety of sources. First, outgassing of the different materials with which the detectors are made. After the cruising phase of the spacecraft, the outgassing background normally reached a negligible level. The radioactive decay of ^{40}K in the MCP glass is expected to produce a constant background of a few counts per second over the entire detector [*Mitchell et al.*, 2015].

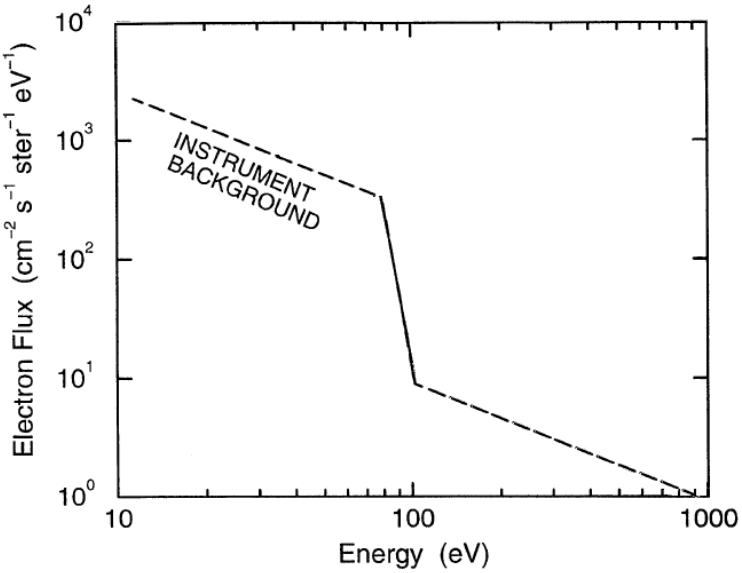

Figure 48. Electron energy spectra corresponding to the instrument background of ER. Adapted from Mitchell et al. [2001].

Another source of background are penetrating particles [*Delory et al.*, 2012]. They can come from **galactic cosmic rays** and **solar energetic particles** (SEP). Protons with energies greater than ~20-40 MeV can penetrate the instrument housing and internal walls and finally generate counts. Galactic cosmic rays are expected to generate several counts per second integrated over the entire detector. This value can be modified as a function of the solar cycle

or the position of the spacecraft regarding the planet. SEP fluxes are episodic and vary widely in intensity, but large events can increase the background by orders of magnitude for several days.

The instrument background is specific to each instrument. Hence, it is different for ER, ELS and SWEA.

Spacecraft potential

The plasma instrument energy scale is referenced to the spacecraft ground. All objects in a space plasma acquire a net electrical potential such that the total plasma current to the object sums to zero. This spacecraft potential can vary regarding the location of the spacecraft in the plasma environment and the illumination pattern of the spacecraft. The spacecraft potential affects plasma measurements by shifting the energies of incoming ions and electrons, bending the trajectories of low energy and low mass charged particles, and repelling charged particles with energies at or below the potential. The reliability of these instruments are thus relatively poor at low energies [*Mitchell et al.*, 2001].

In sunlight, the spacecraft potential typically floats a few volts positive relative to the plasma in which the spacecraft is immersed, due to the loss of photoelectrons from the spacecraft surface. Spacecraft photoelectrons with energies below the potential are attracted back to the spacecraft, while the other ones escape. Ambient electrons entering the electron spectrometer are accelerated by the spacecraft potential upstream the instrument: all energies are **shifted upward** by a few eV. Hence, electron spectrometers measure spacecraft photoelectrons at energies below the spacecraft potential and the ambient electrons for energies above the potential. The boundary between the two populations is often marked by a sharp change of slope in the energy spectrum at the spacecraft potential. This signature can be observed on the solar wind spectrum in Figure 18, as indicated by the red dotted vertical line. The spacecraft photoelectrons population corresponds to the peak observed near ~7 eV and the spacecraft potential in this case is ~8V. It can also be observed in the magnetosheath spectra at ~5V. In Figure 17, these photoelectrons coming from the spacecraft are clearly detected in the solar wind. They correspond to the dark orange color, below 10 eV.

When the spacecraft charge is negative, as in the nightside ionosphere, part of the electron distribution is repelled by the spacecraft or shifted to low energies not sampled by the electron spectrometers.

In the solar wind and the magnetosheath, the spacecraft potential can easily be determined with an **electron spectrometer**, thanks to spacecraft photoelectrons. At high plasma densities, and hence low altitudes, the spacecraft potential is well derived from a **Langmuir probe** like LPW. In the ionosphere, the potential can be derived from **ion spectrometers**, using the difference between the measured energy of the ions and the expected ram energy from the spacecraft motion (see section 3.2.2 for more details on the ram energy).

Secondary electrons

In some configurations of the spacecraft, sunlight can enter the aperture of the instrument and scatter inside it, creating secondary electrons. Some fraction of these electrons can scatter down to the anode and generate a pulse of spurious counts. This sunlight pulse appears at all energies but is most noticeable from 10 to 80 eV and above 1 keV [*Mitchell et al.*, 2001]. UV photons can also enter the aperture, scatter and produce photoelectrons from interior surfaces. The counts produced by such photoelectrons are usually few but can increase the total background by a factor of two under specific conditions.

Contamination by secondary electrons is usually suppressed by scalloping the inner and outer hemispheres.

2.3. Data coverage

In order to to obtain a global view of suprathermal electron depletions, I chose to take advantage of the different characteristics of the three missions described above. This enables an observation of these structures from different points of view.

MGS data are used from 1999 to 2006 in order to take advantage of the mapping **circular orbit** at a roughly constant altitude (~400 km) of the spacecraft, allowing observations of the phenomenon **every 2 hours** over the whole range of possible latitudes [-90°, 90°]. These seven years of data enables a coverage of the whole Martian surface on a restricted range of altitudes [368 km; 438 km] and at a local time fixed at 02:00 pm.

MEX data are used from 2004 to 2014, which gives us an unparalleled long-term view of the phenomenon at both relatively low (**down to ~250 km**) and high altitudes. This time period enables a coverage of the whole surface except the poles ([-86°; 86°]) at various altitudes and at all the local times in the nightside.

Finally, MAVEN data are used from October 2014 to March 2017. During this time period the spacecraft covered both hemispheres except the poles, but due to this short duration and MAVEN orbital parameters, all latitudes are not yet covered at all possible altitudes. Even though the coverage and duration of this data set are much lower than those of MGS and MEX, MAVEN reached during this time period altitudes **down to ~125 km**, which are unsampled by MGS nor MEX.

The different characteristics of the three datasets used are gathered in Table 4.

	MGS	**MEX**	**MAVEN**
Periapsis [km]	368	245-365	125-150
Apoapsis [km]	438	~10 000	6 200
Period [h]	2	6.75	4.5
Inclination [°]	93	86	75
Precession	Locked at 02am/02pm	yes	yes
Time coverage	1999-2006	2004-2014	2014-2017

Table 4. Characteristics of the three datasets used for the study of electron depletions.

In Figure 49 is plotted the spatial coverage of the three spacecraft. As MGS orbit was circular, we present in panel (a) its coverage in local time and solar zenith angle (SZA, see section 2.5.4), adapted from [*Brain*, 2006]. In color is plotted the density of measurements made between June 2, 1999 and March 31, 2004. In panel (b) is plotted the MEX orbital coverage used by *Hall et al.*, [2016] in the Mars-Centric Solar Orbital (MSO) coordinate frame (see section 2.5.1). In color is plotted the density of measurements made between February 9, 2004 and May 9, 2014. Superimposed is the *Edberg et al.*, [2008] model bow-shock (dash-dotted line) and MPB (dashed line). In panel (c) is plotted the typical MAVEN coverage on one year of measurements. In red is the solid body, in green the typical extend of the magnetosheath, in yellow the illuminated induced magnetosphere and in blue the wake of the planet. The orbits are plotted in white.

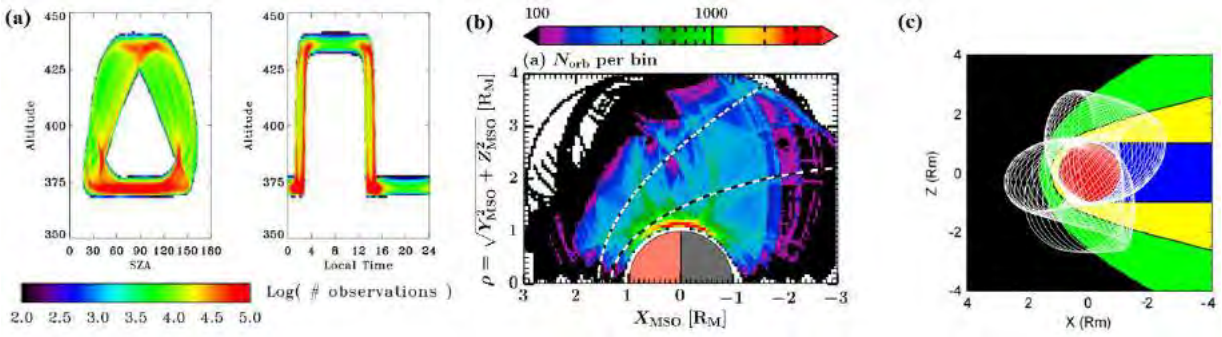

Figure 49. Spatial coverage of the three datasets under study

(a) Data coverage for MGS during its mapping orbits from 2 June 1999 to 31 March 2004. The two panels show data density as a function of altitude, Solar Zenith Angle (SZA) and Local Time [adapted from Brain, 2006*]. (b) MEX orbital coverage when ELS was in operation across the period of 9 February 2004 to 9 May 2014 in MSO coordinates (see section 2.5.1) [adapted from Hall et al.,* 2016*]. (c) MAVEN typical coverage on one year of measurement [presented at a MAVEN meeting].*

In Figure 50 is plotted the solar cycle as a function of the number of the sunspots counted at the surface of the Sun between 1995 and 2017. Superimposed are the duration of the MGS mission (**blue** dashed lines), the MEX mission (**green** dashed lines) and the MAVEN mission (**purple** dashed lines).

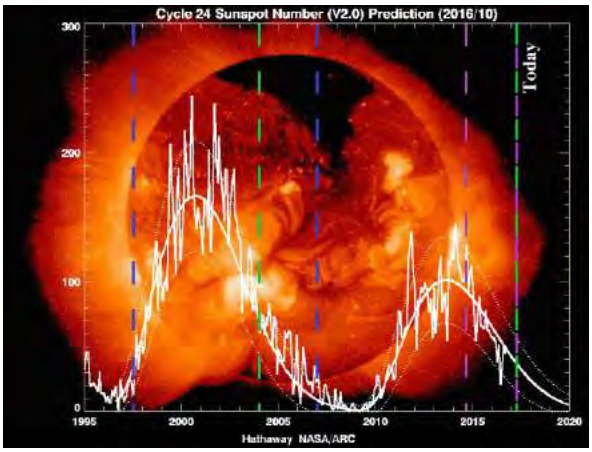

Figure 50. Solar cycle between 1995 and 2017 as observed by the number of sunspots observed on the Sun. The time periods of the MGS, MEX and MAVEN missions are delineated by the blue, green and purple dashed lines, respectively.

This huge data set gathering observations made over 18 years by different instruments reaching different altitude regimes enables us to compare events observed in similar conditions (several spacecraft in the same region) and enrich this joint vision with new observations closer to the surface (with MAVEN). Due to the large time interval under study for MGS and MEX, these two datasets are only used to show the global properties of suprathermal electron depletions in the following studies. MAVEN data, on the other hand, which are only available for two years and a half until now, are used to study in details the structure of electron depletions, their characteristics and their distribution in the Martian environment.

2.4. Analysis tools

Throughout my PhD I worked daily with different tools provided by the Virtual Observatories in planetary sciences developed in Europe. I have used intensively three of them: AMDA, 3DView and CL, in close interaction with the developing teams, enabling me to contribute to their evolution [*Modolo et al.*, 2017].

2.4.1. AMDA and 3D view

AMDA (Automated Multi-Dataset Analysis) and **3DView** are currently developed by the CDPP (Centre de Données de la Physique des Plasmas, www.cdpp.eu) within IRAP. The CDPP is the French national center for space physics data. It was jointly created by CNES (Centre National D'Etudes Spatiales) and CNRS (Centre National de la Recherche Scientifique) in 1998.

AMDA (http://amda.cdpp.eu/) is a web-based facility for on-line analysis of space physics data coming from its own database or from the user one [*Jacquey et al.*, 2010; *Génot et al.*, 2010], developed since 2006. Online classical manipulations can be performed by the user, such as visualization, parameter computation or data extraction. The user only manipulates **parameters** (density, magnetic field…) on AMDA, no more data files. The different parameters are associated with properties (scalar, vector, tensor, units …) and with corresponding options (frame of references…). AMDA also offers innovative functionalities, such as **event search** on data, in either visual or automated way, and the generation, use and management of **time-tables** (which are basically a collection of time intervals). User-edited automatic research will be developed in more details in section 3.3.

During my PhD I have been involved in including MAVEN data and Martian crustal magnetic field models in the AMDA database, in the cleaning of MEX datasets and in the development of new functionalities for the upcoming version of AMDA which is currently implemented (I was involved in the AMDA user committee in 2016 to test this new version).

MGS, MEX and MAVEN data are all available on AMDA. MGS data are taken from the PDS (Planetary Data System, https://pds-ppi.igpp.ucla.edu/) and are available from 1997/09/14 to 2006/10/11. MAVEN data are also taken from the PDS, which means that they have been treated upstream by the instrument team and that they are available ~6 months after their

acquisition. MEX data are treated internally at IRAP and are available shortly after their acquisition.

The 3DView tool (http://3dview.cdpp.eu/) provides **immersive visualizations** and is further developed to include simulation and observational data [*Génot et al.*, submitted]. The user is able to manipulate scenes of 3D orbit visualization. All celestial objects from the Solar System are included together most of scientific spacecraft. In Figure 30 and Figure 35 are two examples of the use of 3D view.

See [*Génot et al.*, 2014] for more information about the different tools developed by the CDPP.

2.4.2. CL

The CL software is currently developed by E. Penou at IRAP: http://clweb.irap.omp.eu/. It has been originally created for the Cluster project in 2000. The CL software can plot orbit data, as well as spectrograms as in Figure 17, Figure 18 or Figure 43. Durig my PhD I have been involved in including MAVEN data in the CL database, in the calculation of SWEA moments, and in adding some new functionalities to the software, such as the possibility to plot superimposed energy-flux spectrograms on a specific time period, as it is shown in section 3.2.2.

MAVEN raw data are directly treated by CL, so that they are available a few days after their acquisition by the spacecraft. The SWEA moments (density, velocity, heat flux, pressure...) and the electron pitch angle distributions are directly calculated through CL, independently from the American team.

2.5. Frames

Two dynamic reference frames are used in this manuscript: the **Mars-centric Solar Orbital** (MSO) and the **IAU_{Mars}**. After setting their definitions in section 2.5.1 and 2.5.2, we discuss the definition of the altitude (section 2.5.3) and of the nightside (section 2.5.4) I use throughout my PhD.

2.5.1. The Mars-centric Solar Orbital (MSO) frame

The MSO coordinates are defined as follows: the origin is the center of Mars, the X axis points from the center of Mars to the Sun, Y points opposite to Mars' orbital angular velocity and Z completes the right-handed set so that the frame rotates slowly as Mars orbits the Sun. All the ephemerides used in this manuscript are expressed in MSO coordinates.

This coordinate system can be rotated by ~4° around the Z-axis to take into account the aberration of the solar wind flow direction by the planetary orbital motion. It is in this case called the aberrated MSO frame. This coordinate system is not used in this study but can be found in some of the cited works, such as in Figure 19.

2.5.2. The IAU_{Mars} frame

The IAU_{Mars} frame is defined with respect to the Martian latitude and longitude. The zero longitude is defined by a small crater of 0.5 km diameter called "**Airy-0**". The setting of the (longitude; latitude) coordinate system regarding the relief can be observed in Figure 11 and Figure 29. However, this two figures do not use the same longitude convention. Only the positive East longitude convention is used in the studies I conducted.

The IAU_{Mars} coordinates are defined as follows: the origin is the center of Mars, the X axis points from the center of Mars to 0° East longitude, 0° Latitude, Y points from the center of Mars to +90° East Longitude, 0° Latitude and Z completes the right-handed set (+90° Latitude = rotation axis = north pole). The frame therefore rotates with the solid body.

From the IAU_{Mars} coordinates can be defined a planetocentric spherical coordinate system: the radial component r which points outward the planet, the azimuthal component θ and the zenithal component φ which are parallel to the surface of the planet. This system is mainly used for the components of the magnetic field.

2.5.3. Definition of the altitude

The altitude is the distance from a point to a reference surface. As there are different reference surfaces, there are different definitions of altitude.

The simplest reference surface is a sphere with Mars' volumetric mean radius of 3389.51 km. This leads to **areocentric** coordinates. This definition is the default altitude I use in my manuscript, when no precision is given.

However, another definition, more precise, is used in section 5.3. In this approach, the reference frame is the IAU 2000 Mars ellipsoid (oblate spheroid), which leads to **areodetic** coordinates. In this case the radius at the equator is $R_{equator} = 3396.19$ km and the radius at the poles is $R_{pole} = 3376.20$ km.

2.5.4. Definition of the nightside

Local Time

The local time (LT) corresponds to the angle (in hours) between the line linking the orthogonal projection of the spacecraft on the Martian equatorial plane to the center of Mars, and the line linking the center of Mars to the center of the Sun. The local time is defined between 00h00 and 24h00. **Dawn** corresponds to 06h00, noon to 12h00, **dusk** to 18h00 and midnight to 00h00. The local time is computed as follows:

$$LT[h] = \arctan\left(\frac{Y_{MSO}}{X_{MSO}}\right) * \frac{12}{\pi} + 12$$

Solar Zenith Angle

The solar zenith angle (SZA) corresponds to the angle between the line linking the spacecraft to the center of Mars, and the line between the center of Mars and the center of the

Sun. The SZA is between 0° and 180° and defined as follow (where r is the radial distance of the spacecraft from the center of Mars):

$$\mathrm{SZA}[°] = \mathrm{acos}\left(\frac{\mathrm{X_{MSO}}}{\mathrm{r}}\right) * \frac{180}{\pi}$$

These two parameters are complementary as the local time does not take into account the altitude of the spacecraft and the SZA does not make any difference between the dusk and the dawn side.

The nightside

The nightside can be defined different ways. The more coarsely, it can be defined as:

$$\mathrm{X_{MSO}} < 0$$

This definition also corresponds to $LT \in [00{:}00; 06{:}00] \cup [18{:}00; 24{:}00]$.

This simplistic definition is the one I chose to use during most of my studies. However, the real border between sunlit and dark sides (called **terminator**) occurs at different SZA for different altitudes. A more precise definition is discussed in section 5.3.1.2.

2.6. Model of crustal magnetic field: the model of *Morschhauser et al.* [2014]

Several models of crustal magnetic fields have been implemented following the measurements made by the MGS magnetometer around Mars, such as the model of Cain et al., [2003], which is still widely used by the Martian community. However, in this study I use the model developed by *Morschhauser et al.*, [2014] (hereinafter referred to as model of Morschhauser), which is more recent and more relevant when used at several different altitudes.

The Morschhauser model is based on the entire measurements of the MGS magnetometer (the three components of the magnetic field) during its aerobreaking phase, science phase and mapping phase (Figure 27). It uses the technique of the spherical harmonic functions to describe the potential associated with the magnetic field. The resulting model produces all known characteristics of the Martian crustal field and shows a richer level of details than previous models. It is characterized by a high resolution, a low level of noise and it is robust when downward continued to the surface. The Morschhauser model is hence relevant for altitudes **from 400 km down to the surface**.

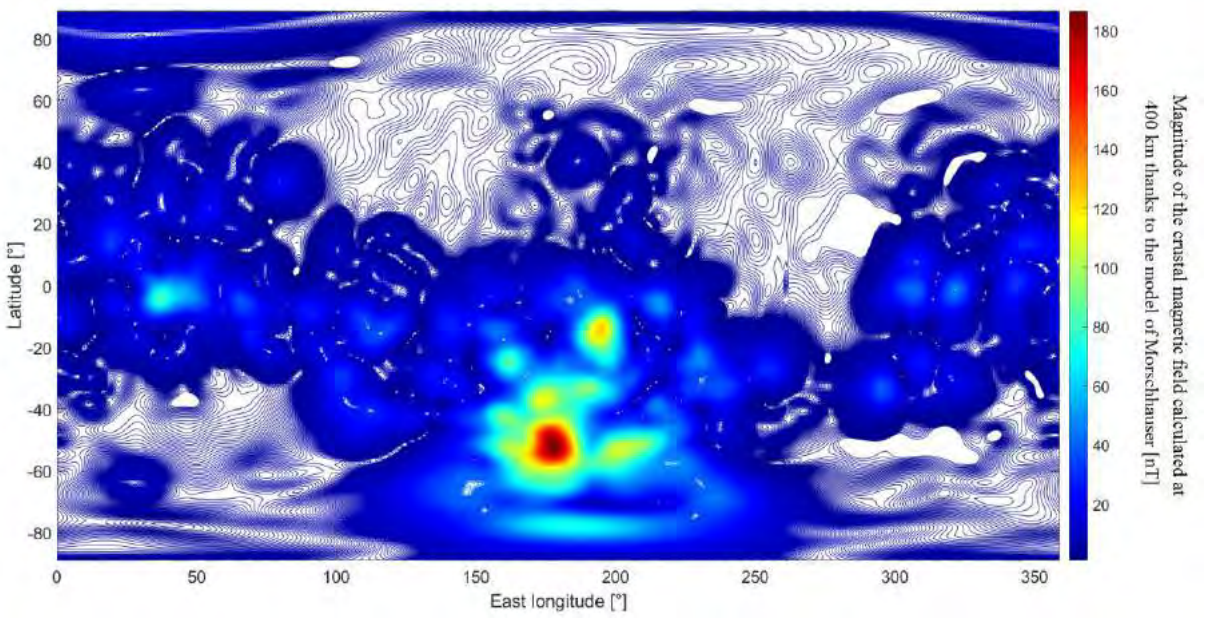

Figure 51. Amplitude of the crustal magnetic field calculated thanks to the Morschhauser model at 400 km altitude.

Two example maps of the magnitude of the crustal magnetic field calculated thanks to the Morschhauser model are plotted in Figure 51 and Figure 52. The first one is plotted at an altitude of 400 km, and the second one at 170 km, where a lot more details can be observed. These maps have been realized with the help of Arnaud Beth.

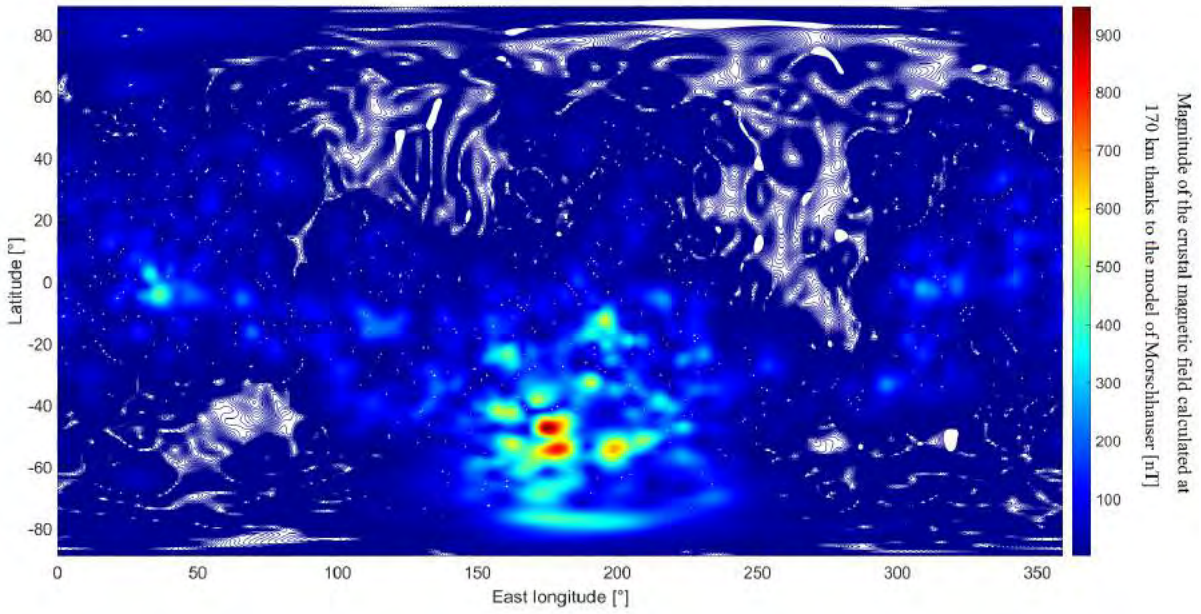

Figure 52. Amplitude of the crustal magnetic field calculated thanks to the Morschhauser model at 170 km altitude.

The use of models of crustal magnetic fields has proven necessary for the studies carried out during this PhD for several reasons:

- The raw data generally contain field contributions of non-crustal origin [Acuña et al., 1999; Ferguson et al., 2005]. This phenomenon can be observed on the fifth panel of Figure 17 and Figure 24, in which the in situ measurements present features (such as current sheets) which are not observed in the crustal magnetic field model.
- Each measurement is associated with a relatively large area of magnetized rock, as the footprint of the data points approximately corresponds to the satellite altitude.
- Data obtained over a same region are usually obtained at varying altitudes.

The Morschhauser model is a valuable tool to deal with the above issues, since it enables a consistent projection and downward continuation to any altitudes below 400 km. It also allows the distinction of the crustal and external parts of the magnetic field relative to the altitude of the spacecraft.

The three missions MGS, MEX and MAVEN offer three different ways of studying the nightside ionosphere, covering a time period of nearly eighteen years. The circular orbit of MGS, the longevity of MEX, and the low-altitude periapsis added to the instrumentation of MAVEN are used jointly in the next sections to better understand the structures called ‘plasma voids’ and the processes involved in their observation. The capabilities of AMDA and CL are exploited together in order to study the characteristics of plasma voids, automatically detect them, analyze their statistical properties and finally find the consistency between the observations made by the three spacecraft.

3. Identification of suprathermal electron depletions in the nightside ionosphere

Martian suprathermal electron depletions have been observed by three spacecraft to date: MGS, MEX, and MAVEN. First called 'plasma voids', the improved performances of the plasma instrument suites over the different missions allow now for a more accurate understanding of these structures and to rename them more adequately as 'suprathermal electron depletions'. After a review of the discoveries on electron depletions by MGS and MEX (section 3.1), I present how they are observed by MAVEN through several case studies (section 3.2). I then detail my automatic criteria to detect electron depletions in MGS, MEX and MAVEN data (section 3.3) and how they have been applied to the different datasets (section 3.4).

3.1. A story of depletions

3.1.1. Discovery of electron depletions

Using ER measurements, *Mitchell et al.* [2001] first observed that the nightside ionosphere was punctuated by abrupt drops of the instrumental count rate, by up to three orders of magnitude to near background levels across all energies, hence calling these structures "**plasma voids**".

An example of such structures observed by MGS is presented in Figure 53 [adapted from *Mitchell et al.*, 2001]. On the first panel is plotted the electron spectrogram measured by ER, and on the second panel are plotted the amplitude of the in situ magnetic field measured by MAG (**black**) and of the crustal magnetic field calculated thanks to the model of Morschhauser (**blue**). Different energy environments are separated by black vertical lines. Typical spectra for each region are plotted in Figure 54 [*Mitchell et al.*, 2001].

We can observe that plasma voids are located in the Martian nightside, and are punctuated by electron "**flux spikes**" at ~09:55, ~09:58, ~10:03 and ~10:05 UT (red arrows). Plasma voids are generally observed to occur in association with strong crustal magnetic fields, as in the case presented in Figure 53. Moreover, the flux spikes are usually observed to be coincident with a

maximum of the radial crustal magnetic field component (inward or outward). Finally, as the electron spectrum inside a plasma voids is more or less the same as the instrument background, in the flux spikes, the electron spectrum looks like a magnetosheath distribution, but with a reduction in flux level at all energy channels (Figure 54).

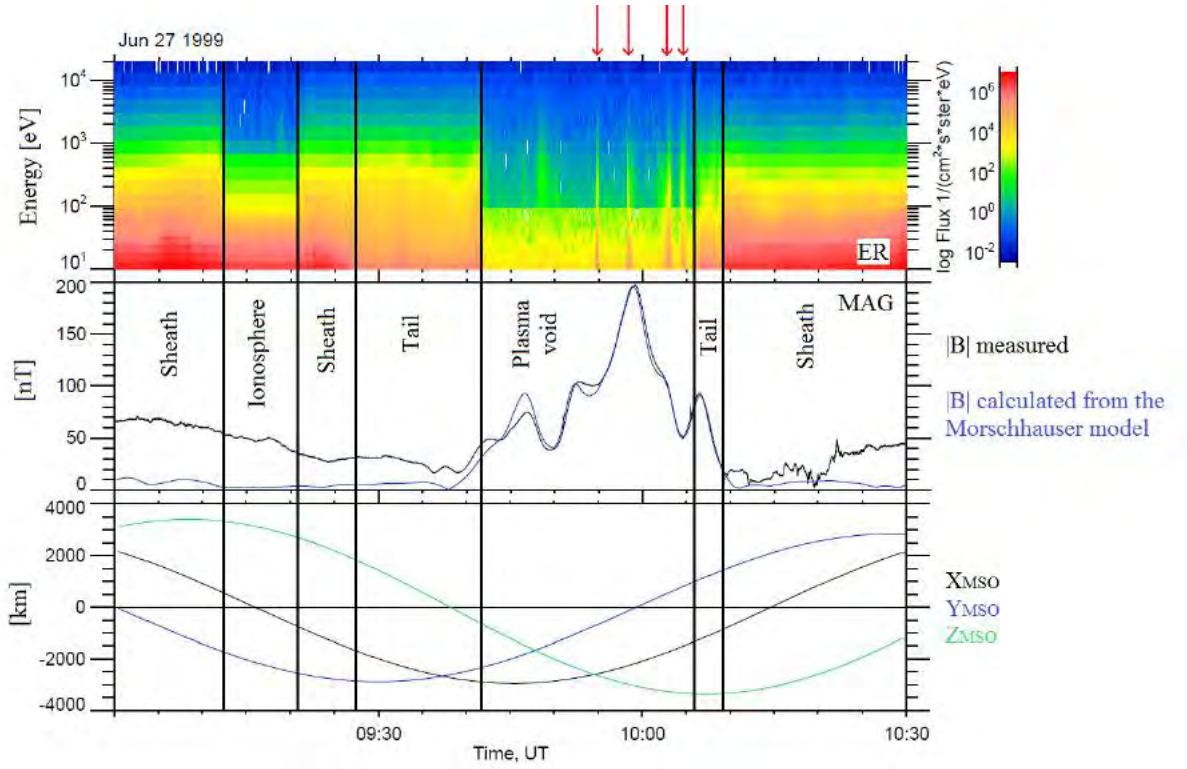

Figure 53. Example of a plasma void observed by MGS on June 27, 1999.

*Panel 1: ER energy-time spectrogram of omnidirectional electron flux. Panel 2: Amplitude of the magnetic field measured by MAG (**black**) and calculated thanks to the Morschhauser model (**blue**). Panel 3: MGS coordinates in the MSO frame. The black vertical lines delineate the main region of the Martian environment encountered by the spacecraft and the red arrows highlights the flux spikes.*

From all these observations, *Mitchell et al.*, [2001] concluded that, in the southern hemisphere, intense crustal magnetic fields are strong enough to form localized "magnetocylinders', or **closed crustal magnetic field loops**, that can stand off the solar wind at altitudes well above 400 km. On the nightside, these closed loops are marked by series of plasma voids, separated by flux spikes that can be observed on Earth-like cusps configuration. When the spacecraft travels through these closed crustal magnetic field loops, it is effectively cut off from the solar wind plasma traveling up the magnetotail and from ionospheric plasma from the sunlit hemisphere, so that plasma voids are recorded. When theses loops rotate in sunlight, they should become populated with newly created photoelectrons produced from the neutral atmosphere, so that no plasma void are observed on the dayside.

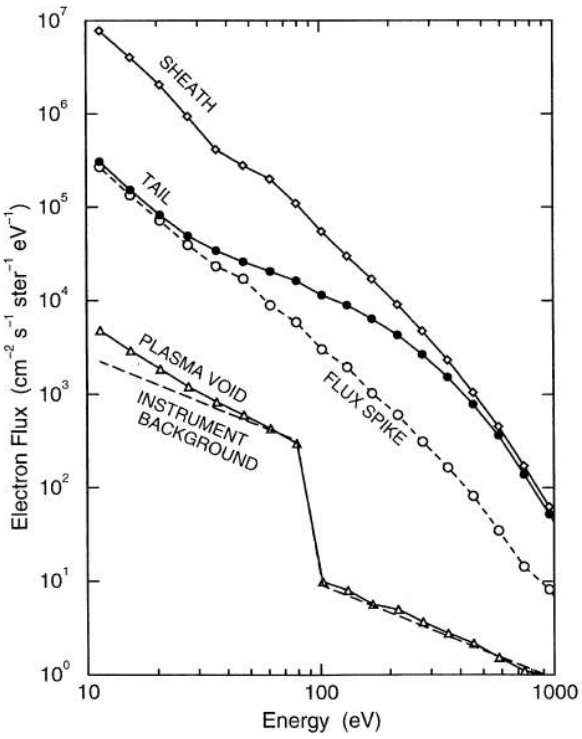

Figure 54. Electron energy spectra observed in different regions crossed by MGS in Figure 53.

Plasma voids should not be associated with "density depressions", which are reductions in the electron number density [*Brace et al.*, 1982], usually observed at Venus (see the Venusian interlude in the next subsection). Although both classifications should, a priori, be similar, it is important to mention the difference existing between the instruments used to derive electron fluxes and those used to derive electron densities. Electron spectrometers that typically make electron flux measurements sample suprathermal electron populations (> 10 eV), while instruments that measure electron number densities sample across thermal (<10 eV) and suprathermal electron populations. As these two parameters are not calculated for the same electron population, a density depression does not necessarily correspond to a reduction in the electron flux, and vice-versa. I here only focus on **decrease in the electron fluxes**.

A few years after the observations of *Mitchell et al.*, [2001], *Soobiah et al.*, [2006] observed thanks to 144 passages of MEX at low altitudes that the electrons flux underwent significant changes close to crustal magnetic fields. Intensified flux signatures were observed mainly on the dayside whereas flux depletions were features of the nightside hemisphere. They suggested that these phenomena were related to regions in which strong crustal magnetic fields reconnect with the IMF, leading to possible atmospheric loss channels. Hence, the topology of

the crustal magnetic fields can significantly influence the structure of the ionosphere, both on the dayside and on the nightside.

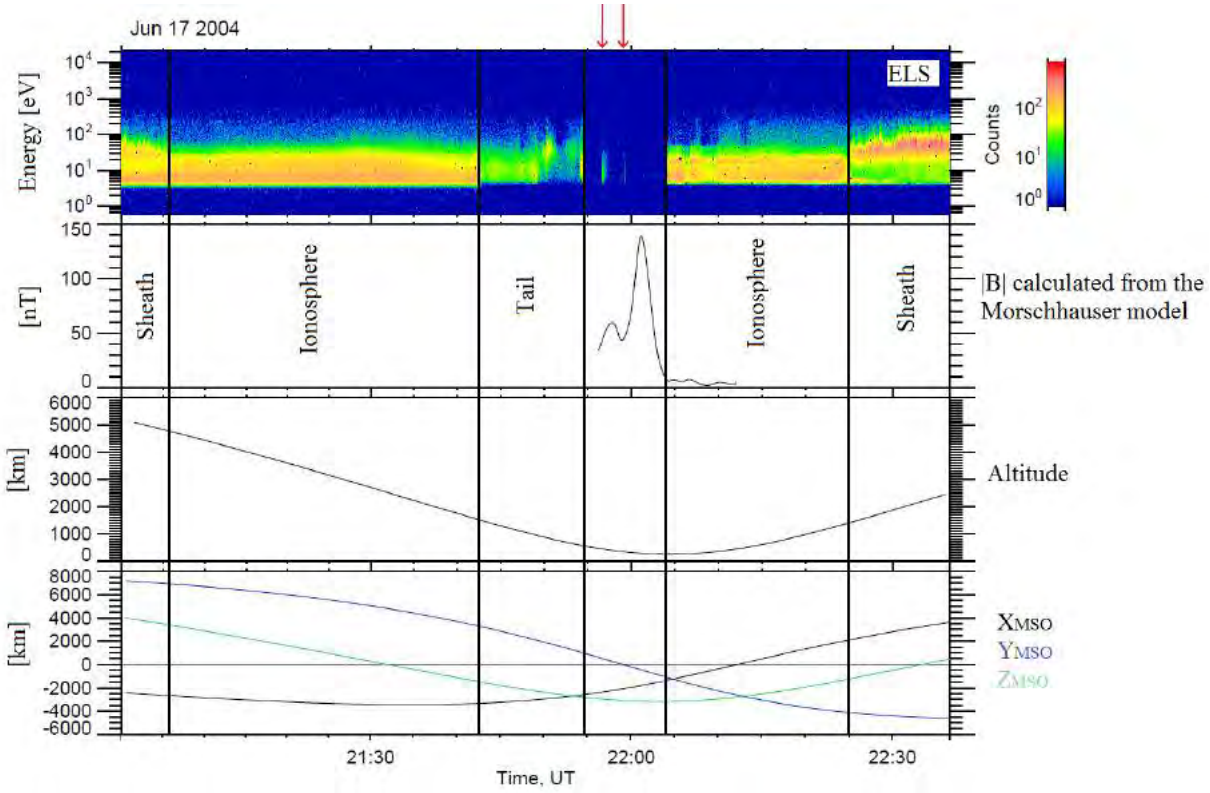

Figure 55. Example of a plasma void observed by MEX on June 17, 2004.

Panel 1: ELS energy-time spectrogram of omnidirectional electron counts. Panel 2: Amplitude of the magnetic field and calculated thanks to the Morschhauser model. Panel 3: Radial distance of MEX from Mars. Panel 4: MEX coordinates in the MSO frame. The black vertical lines delineate the main region of the Martian environment encountered by the spacecraft and the red arrows highlights the flux spikes.

An example of plasma void observed by ELS is plotted in Figure 55 (adapted from Soobiah et al., 2006]. On the first panel is plotted the electron energy-time spectrogram measured by ELS, and on the second panel is plotted the magnitude of the crustal magnetic field calculated thanks to the model of Morschhauser at the altitude of the spacecraft. Different plasma environments are separated by black vertical lines. As with the MGS example, we can observe that plasma voids are punctuated by flux spikes, at ~21:54 UT and ~21:59 UT. Looking at the Morschhauser model, we can observe that electron depletions are also located above strong crustal magnetic field sources, in the nightside.

3.1.2. On the origin of plasma voids

An indirect study of plasma voids by *Brain et al.*, [2007] looked statistically at seven and an half years of magnetic field and electron flux (at energies of 115 eV) measurements by the MAG and ER instruments onboard MGS. They used these data to determine the pitch angle distributions of the electrons across the surface of Mars. Different PADs were associated to the different magnetic topologies observed in Figure 22. The motion of electrons along such field lines can adiabatically change their pitch angle in regions of converging or diverging magnetic field. They can also be absorbed by the collisionally thick atmosphere and new electrons can be added to the distribution via source processes. If we restrict ourselves to the nightside at low altitudes, where production of electrons by photoionization is negligible, some of the different PADs that can be observed are plotted in Figure 56 [adapted from *Brain et al.*, 2007].

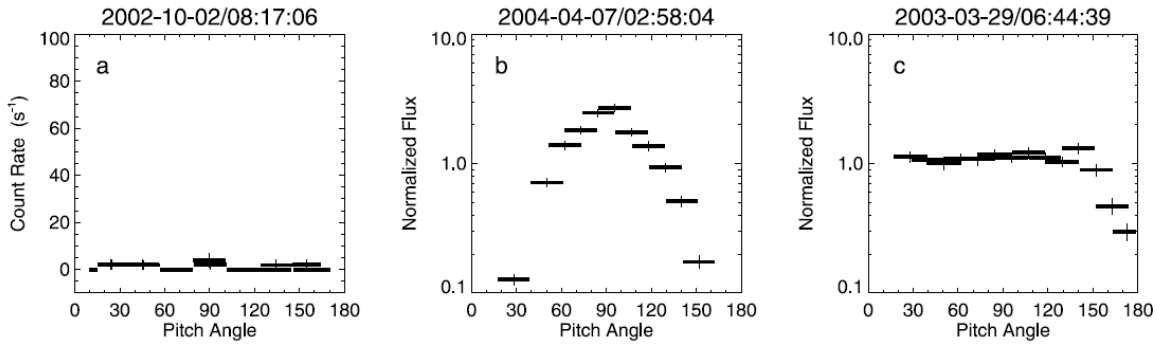

Figure 56. Three example of representative pitch angle distributions from MGS MAG/ER: (a) plasma void, (b) two-sided loss scone, (c) one-sided loss scone, [adapted from Brain et al., 2007].

When electrons travel on closed magnetic field lines ('a' configuration in Figure 22), they encounter with decreasing altitudes regions of increasing magnetic field strength, and should adiabatically mirror (reverse the direction of their velocity along the field line). They hence bounce back and force between the two mirror points along the magnetic field lines. The altitude of these mirror point is controlled by the electron pitch angle. Electrons with pitch angles close to 0° or 180° (**field aligned electrons**) mirror at lower altitudes than those with pitch angle near 90°. If the mirror point is low enough, the electron is absorbed by the atmosphere before bouncing, and lost from the distribution. If no electron source is present, the electron population is 'trapped' and the corresponding PADs is the 'b' configuration in Figure 56: **two-sided loss cone**.

If one end of the magnetic field line is no more connected to the crust, i.e. if the electrons are travelling on an open magnetic field line ('b' configuration in Figure 22), only a depletion in the field aligned flux returning from the atmosphere will form. The corresponding PADs is the 'c' configuration in Figure 56: **one-sided loss cone**.

Plasma voids, meanwhile, are characterized by PADs in which the electron flux is at background levels across all pitch angles ('a' configuration in Figure 56). Some other PADs exist, especially to characterize the draped field lines, but we won't describe them here. See *Brain et al.*, [2007] for more details about the different pitch angle distributions.

In the *Brain et al.*, [2007] study, the dayside was defined as SZA<90° while the nightside is defined as SZA >120° at 400 km. With these definitions, the plasma voids were found to be observed approximately 31.5% of the time when the spacecraft was in the nightside, while they were virtually never observed in the dayside (<7000 cases out of 31 million PADs).

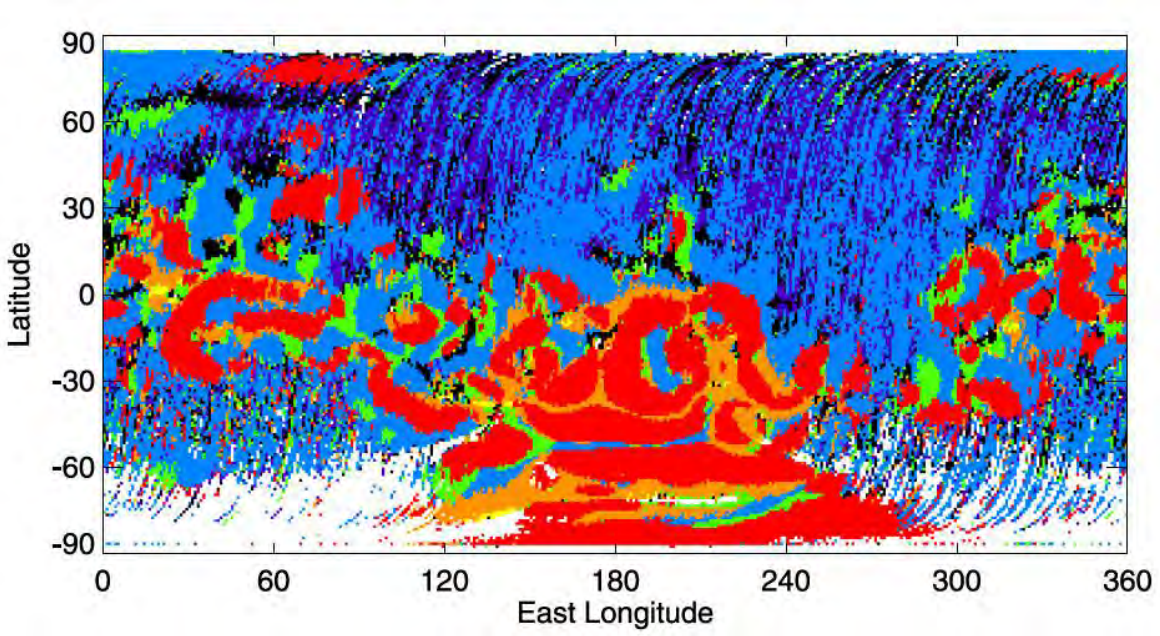

*Figure 57. Geographic map of dominant PAD types recorded by MGS ER at 400 km on the nightside: plasma voids (**red**); trapped (**orange**); fully isotropic (**green**); incident isotropic, return loss cone (**blue**); incident field-aligned beam, return loss cone (**purple**); conic (**yellow**); and others (**black**). [Brain et al., 2007].*

This statistical study also showed that plasma voids are concentrated near strong crustal magnetic fields and that very few events are observed at large distances from crustal magnetic sources, as shown in Figure 57, where plasma voids are plotted in **red**. A plasma void occurrence of 100% (across the full seven and an half years data set) had even been observed over the strongest crustal field regions in the southern hemisphere. They hence suggested than

these regions are closed crustal magnetic field regions that would remain closed irrespective of external conditions.

This study also revealed that plasma voids are surrounded by areas with trapped electron PADs (in **orange** in Figure 57), consistent with the idea of closed magnetic field lines and indicating that the outer layers of closed magnetic field regions are populated thanks to source processes such as reconnection with the draped IMF.

From the observation that nightside closed field lines regions are filled with isotropic electron PADs when they rotate in the dayside, *Brain et al.* [2007] suggested that plasma voids are the result of **a balance between electron source and loss processes**. On the dayside, closed crustal magnetic field loops can trap ionospheric plasma, including suprathermal photoelectrons. When they travel to the nightside, the electrons are removed through a combination of outward diffusion, scattering, and interactions with the collisional thick atmosphere at lower altitudes. Meanwhile, the external sources of plasma (solar wind plasma traveling up the magnetotail and ionospheric plasma) are excluded from the inner layers of the closed field regions, so that sinks overpass sources thus creating plasma voids. When the crustal magnetic loops rotate back to the dayside, they trap newly created ionospheric plasma and the source processes would dominate loss processes. As the ionospheric plasma is homogeneously created in the dayside, voids are essentially never seen on this side of Mars.

Venusian Interlude

The description of the Martian plasma voids may remind us the Venusian "ionospheric density holes" identified by *Brace et al.* [1982]. These structures, only observed in the nightside, are characterized by a strong sunward or antisunward enhancement in magnetic field compared to adjacent regions, a concurrent diminution in electron and ion density, and occur in pairs with oppositely polarized field enhancement, one sunward and the other tailward. *Collison et al.*, [2014] proposed that the plasma depletion associated with ionospheric holes are only a manifestation of tubes of enhanced draped IMF, emerging in pairs from low altitudes and stretching far down the tail.

However, one major difference with the Martian plasma voids is that the Venusian density holes occur in two main latitude-local time zones, whereas *Duru et al.*, [2011] found no convincing evidence of the same distribution at Mars.

3.1.3. Global properties of the plasma voids observed by MGS and MEX

Based on 27 MEX-observations of electron density depressions, *Duru et al.*, [2011] showed that electron flux reductions were coincident with density depression on 19 cases, and in 4 cases, no change has been observed in the electron flux. They suggested that density depressions joined by a flux reduction might correspond to plasma voids. Cases in which the electron flux has no change across a density depression may occur in closed magnetic field regions that have sudden access to external plasma, or where atmospheric degradation occurs.

Brain et al., [2007] statistically showed that plasma voids are restricted to the nightside. In addition, studies made with MEX data by *Soobiah et al.* [2006] and *Duru et al.* [2011] showed no dissymmetry between the dawn and the dusk side. Plasma voids are globally distributed regardless of nightside local time (18h00-24h00; 00h00-06h00), within the limits of their studies.

Crustal magnetic field loops do not necessarily stay closed as the planet rotates [*Ma et al.*, 2014] and crustal fields can connect and reconnect with the piled-up, draped and dynamic IMF. Hence, when they travel to the nightside, regions with strong enough horizontal crustal fields are able to stand off the IMF effects. The crustal magnetic loops in these regions thus stay closed all the way across the nightside and are populated by **permanent plasma voids**, which means we can observe this phenomenon during each passage above such regions on the nightside. On the other hand, regions with weaker horizontal fields are essentially **intermittently populated with plasma voids**, depending on the external drivers. For low and moderate solar wind pressure crustal magnetic loops are closed and devoid of plasma. However, for high solar wind pressure the crustal field lines open up and get connected to the IMF. These weak crustal magnetic field regions are then filled with solar wind plasma travelling through the tail [*Lillis and Brain*, 2013].

More recently, *Hall et al.*, [2016] used the rapid reductions of a proxy measurement of the electron flux derived from the MEX/ELS electron flux measurements integrated across the 20-200 eV energy range to automatically identify plasma voids. The study covers approximately ten years of the MEX mission from 2004 to 2014 and is restricted to the **illuminated induced magnetosphere** (region of space inside the magnetic pileup boundary and outside the optical shadow of the planet, see section 5.3.1.2). Using this method, plasma

voids were detected amongst 56% of the orbits under study, from 266 km (MEX lowest periapsis) to 10 117 km. A statistical study of the distribution of these events showed that approximately 80% of them occurred below 1 300 km, predominantly at SZA between 90° and 120°. The study of the spatial and altitudinal distributions of the detected plasma voids confirmed the strong link existing between the plasma voids occurrence and the magnitude of the crustal magnetic field. The bigger the source is, the higher plasma voids could be observed. However, some regions appear to be in contradiction with this global behavior which suggests that other processes are involved in plasma void creation such as the interaction between the solar wind and the Martian plasma. Comparisons of my methods and results with those of *Hall et al.*, 2016 will be made throughout the next sections (section 3.4.3 and 4.1.2.2.1 for example).

3.2. General properties of electron depletions observed with MAVEN

All the results presented in section 3.1 have been obtained using MGS or MEX data which have several constraints either in instrumentation or in orbitography. Neither of them reached altitudes below 250 km, MGS was locked in local time and did not carry an ion spectrometer while MEX does not carry a magnetometer. The MAVEN instrument payload dedicated to plasma study and its periapsis reaching ~125 km allows unprecedented measurements of the plasma phenomenon under study at previously unsampled altitudes.

Through several case studies, I present in the next subsections some properties of electron depletions observed thanks to MAVEN. I start explaining why I choose to rename plasma voids as suprathermal electron depletions (section 3.2.1). I then describe the characteristics of the ions and of the electrons observed in the electron depletions (section 3.2.2). In section 3.2.3 I give a quick overview of the variety of the flux spikes which punctuate the observation of electron depletions. We finally take a quick look on the location of different electron depletions regarding the distribution of crustal magnetic sources (section 3.2.4).

3.2.1. Plasma voids or suprathermal electron depletions?

The structures called plasma voids by *Mitchell et al.*, [2001] have been named after observations made with MGS, which did not carry any ion spectrometer but an electron spectrometer whose measurements were limited to electrons with energies greater than 10 eV. Plasma voids are then structures void of electrons having energies greater than 10 eV.

Thanks to a new multi-instruments vision of plasma voids, enabled by MAVEN, I choose to rename these structures as '**suprathermal electron depletions**'. This has been made possible thanks to SWEA, which detects electrons with energies down to 3 eV, STATIC, which separates ions species until low energies (i.e. in the ionosphere), and LPW which measures the thermal electron population (with energies below 5 eV).

Figure 58 shows an example of plasma voids observed with MAVEN on July 11, 2015. The first panel is the SWEA energy-time spectrogram of omnidirectional electron energy flux (also referred to as JE hereinafter). The plasma voids observed during this time interval are

roughly delimited by the two black vertical lines. However, we can see that they are not void of electrons: there is a remaining electron population at approximately **6-7 eV**, which could not be observed by MGS due to its energy range, and by MEX, probably due to higher negative spacecraft potential. Note that suprathermal electron depletions can be observed on each anode of SWEA and each deflection sector.

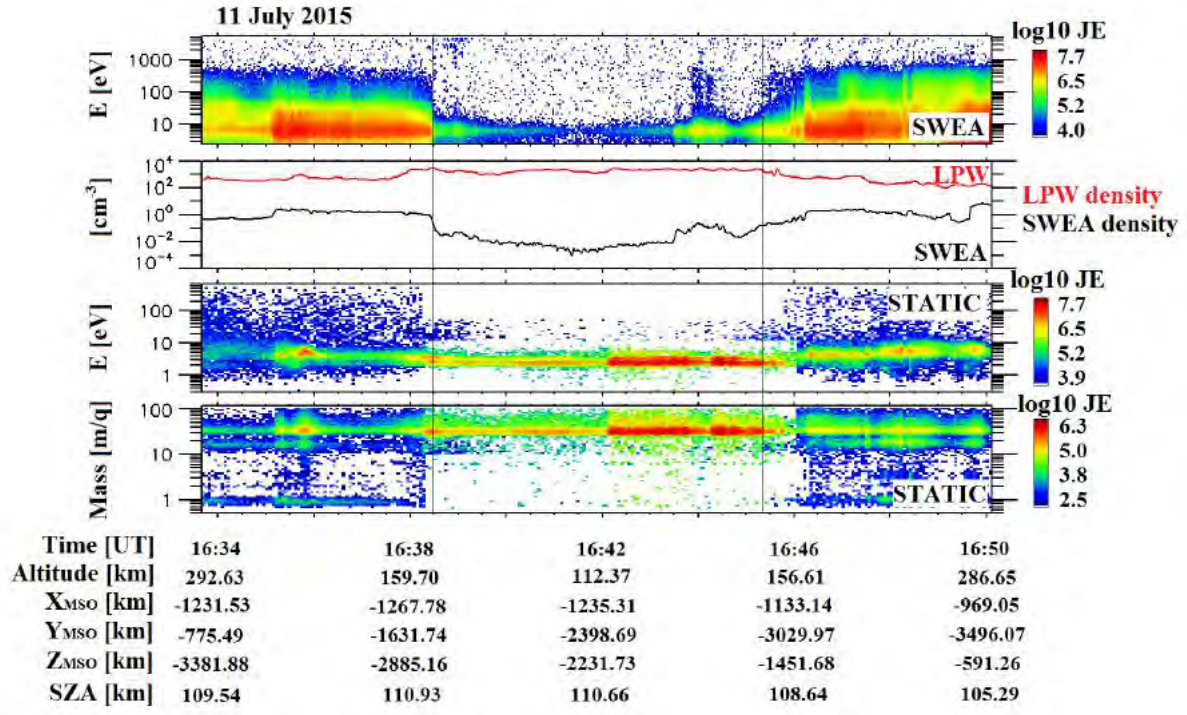

*Figure 58. Example of electron depletion observed with MAVEN on July 11, 2015. First panel: SWEA energy-time spectrogram of omnidirectional electron energy flux (ENGY mode) corrected for the potential measured with LPW. Second panel: Electron density calculated with SWEA (**black**) and with LPW (**red**). Third panel: STATIC energy-time spectrogram of omnidirectional ion energy flux (C0 mode). Fourth panel: STATIC mass-time spectrogram of omnidirectional ion energy flux (C6 mode).*

Moreover, the second panel shows the density calculated from SWEA data in **black** and the density from LPW in **red**. Note that during this time interval the quality flag of the LPW density and of the spacecraft potential used for the calculation of the density from SWEA data is always greater than 50 except for 16:37:55 (in the ionosphere) and 16:45:20 (at the end of the depletion) which means that these data are reliable [*L. Andersson*, private communication]. Due to instrumental limits the density calculated with SWEA data is restricted to electrons with energies greater than 3 eV (see Table 3), whereas the density calculated with LPW includes lower-energy electrons, which explains the difference observed between the two densities (in particular in the ionosphere where the plasma is essentially cold, typically $kT_e < 0.4\ eV$). The

non-thermal population measured by SWEA represents a small fraction of the total electron density. The characteristic drop in the suprathermal electron flux is very clear in the SWEA density during the electron depletion, whereas there is **no drop in LPW density**, i.e. in thermal electron density, which even increases slightly.

On panels 3 and 4 are plotted the STATIC energy-time and mass-time spectrogram of omnidirectional ion energy flux. In the electron depletions as in the surrounding ionosphere, the main ion beam is peaked at ~3eV in energy and 32 m/q in mass, which corresponds to O_2^+. Electron depletions are thus mainly filled with **O_2^+ at 3 eV**. The presence of ions inside plasma voids can also be observed with MEX/IMA measurements as plotted on Figure 59, an observation which seems to have been neglected so far. I here plotted an example of electron depletions observed by MEX on June 23, 2012. The first panel is the ELS energy-time spectrogram of omnidirectional electron counts per second. Note that ELS's geometric factor is approximately fixed, so that counts are proportional to electron flux. Two plasma voids can be observed between the two vertical black lines. The second panel is the energy-time spectrogram of the omnidirectional heavy ions counts per second (m/q >20) measured by IMA. There are few light ions detected (not shown) but we can see that electron depletions are filled with heavy ions (mainly O_2^+ at these altitudes in the nightside, see Figure 61), having an energy E/q of a dozen of eV. This difference of energy measured by IMA and STATIC could be explained by a difference of spacecraft potential between the two orbiters, which would be in agreement with the non-observation of the 6-7 eV remaining electron population inside electron depletions by ELS.

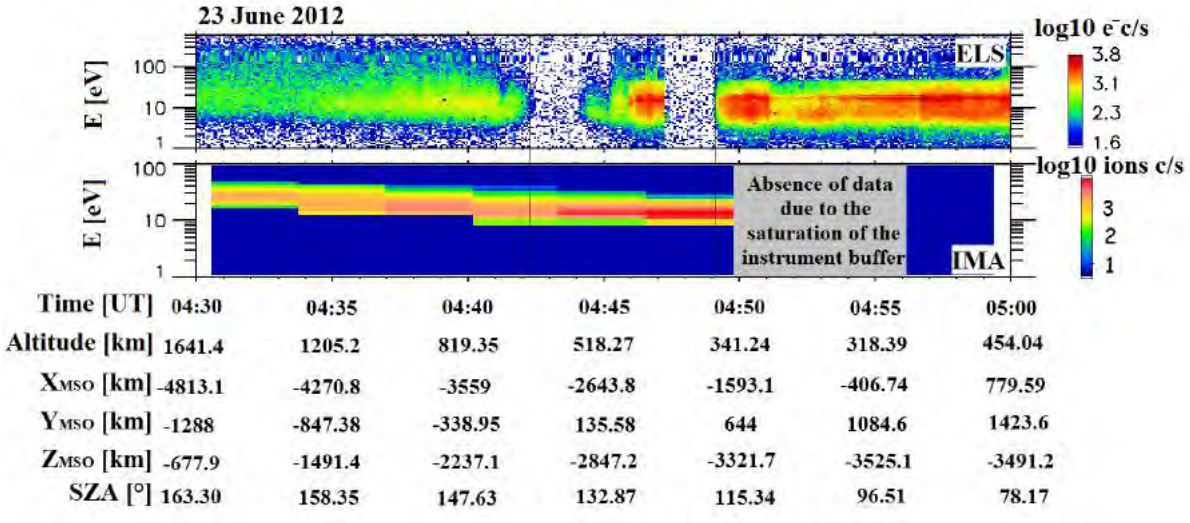

Figure 59. Example of electron depletion observed by MEX on June 23, 2012.

First panel: ELS energy-time spectrogram of omnidirectional electron counts per second. Second panel: IMA energy-time spectrogram of omnidirectional heavy ions counts per second (m/q>20).

Hence, plasma voids are not entirely void of plasma. Only suprathermal electrons with energies greater than ~10 eV are depleted, which justifies the name "**suprathermal electron depletions**" given by *Steckiewicz et al.* [2015].

3.2.2. Plasma composition

In Figure 60 are plotted the concatenated spectra of STATIC and SWEA inside the electron depletions plotted in Figure 58, between 16:38:28 UT and 16:45:20 UT. On the left is the energy-JE spectrogram obtained with the C0 mode of STATIC, on the middle is the mass-JE spectrogram obtained with the C6 mode of STATIC and on the right is the energy-JE spectrogram obtained with SWEA. All these data are corrected from the spacecraft potential measured by LPW when needed.

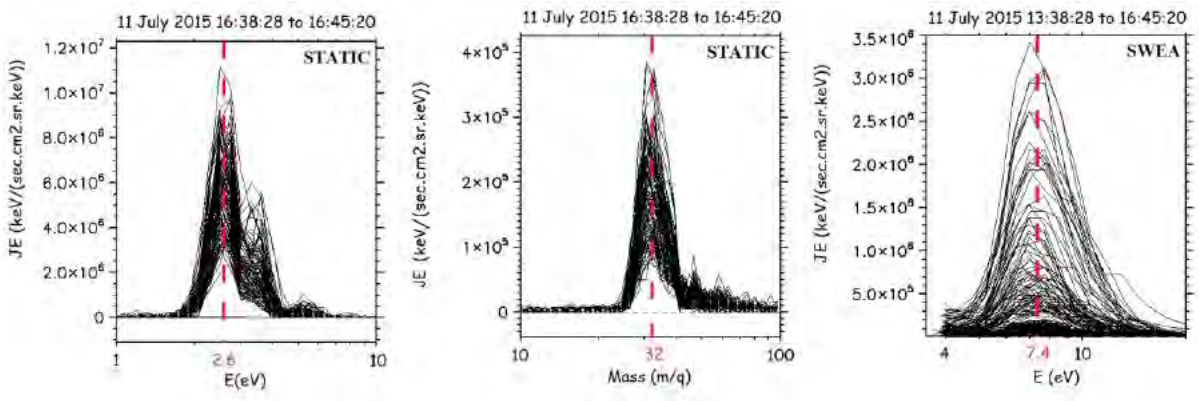

Figure 60. Concatenated spectrum of STATIC and SWEA during electron depletions on July 11, 2015. All data are corrected from the spacecraft potential measured by LPW.
Left: Ion energy-JE concatenated spectrogram (STATIC/C0 mode); Middle: Ion mass-JE concatenated spectrogram (STATIC/C6 mode); Right: Electron energy-JE concatenated spectrum (SWEA/ENGY mode).

3.2.2.1. Ions characteristics

We can clearly observe on the left panel of Figure 60 that the ion population is strongly peaked around a mean value of **~2.6 eV** with a full width at half maximum of about 1 eV. Looking in detail at the mass-time spectrogram (middle panel) enables us to derive the ion composition within electron depletions, dominated by $\mathbf{O_2^+/NO^+}$ at 32 m/q (note that STATIC cannot resolve between these species). A smaller peak can be observed at ~44 m/q, which may correspond to $\mathbf{CO_2^+}$. This observation is consistent with the median neutral density profiles

derived by *Girazian et al., [2017]* from NGIMS data in the nightside ionosphere (Figure 61). They indeed show that O_2^+ is the most abundant ion down to ~130 km at all nightside SZA, with significant amount of O^+, HCO^+, NO^+ and CO_2^+. However, below 130 km NO^+ is the most abundant ion and NO^+ densitites increase with decreasing altitude, at least down to 120 km altitude.

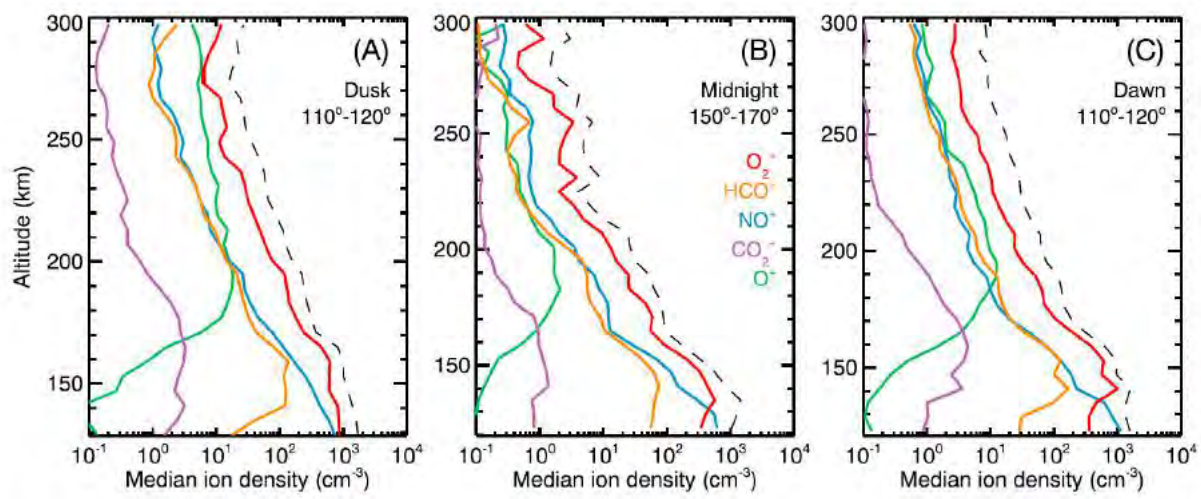

Figure 61. Nightside median density profiles from dawn, dusk and near midnight. The different colors represent the different ion species and the dashed line is the total ion density. (a) Dusk SZAs between +110° and +120°. (b) Near midnight SZAs between -150° and -170°. (c) Dawn SZAs between -110° and -120°, [Girazian et al., 2017].

Combining this two information, the energy of the ions measured by STATIC suggests that we observe cold ions with the **ram velocity**. If we consider ionospheric ions with no significant initial speed, the measured energy of the ions will be the energy given by the movement of the spacecraft, called the ram energy (m is the mass of the particle and v the speead of the spacecraft):

$$E = \frac{1}{2} * m * v^2$$

For O_2^+, this energy varies between 2.2 eV at 1000 km altitude and 3 eV at the periapsis of MAVEN. For CO_2^+, it varies between 3.0 eV at 1000 km altitude and 4.0 eV at the periapsis. The values calculated for O_2^+ well correspond to the main peak and its dispersion. Meanwhile, the secondary peak between 3 and 4 eV well corresponds to the ram velocity calculated for CO_2^+. Other ion species may also be present but their signature may be embedded in the O_2^+ peak.

3.2.2.2. Electrons characteristics

Looking at the right panel of Figure 60, we can observe that all the electron spectra inside the observed electron depletions are peaked at ~7 eV, after correction from the spacecraft potential. This electron population corresponds to the remaining electron population after **absorption by the atmospheric neutrals,** as we shall see in the following (section 4.2.1).

In Figure 62 is superimposed on the electron time-energy spectrogram the total scattering cross section corresponding to electron collision with CO_2. We can observe that the remaining electron population corresponds rather well to the CO_2 cross section dip and that hardly any electrons are observed at the location of the two CO_2 cross sections peaks. Since a peak in the cross section is related to an electron loss process, **electron absorption by the atmospheric CO_2** seems to be a good candidate to explain the large electron disappearance above 10 eV as well as the remaining thermal electron population observed between 4 and 12 eV and the electron disappearance observed at the lowest energies sampled by SWEA. Moreover, the observation of thermal electrons inside electron depletions (see Figure 58) is consistent with the dip observed in the CO_2 cross section at ~2 eV.

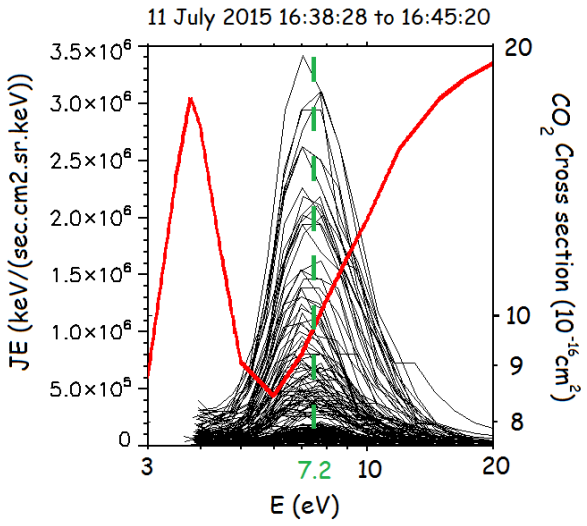

*Figure 62. Concatenated electron energy-JE spectrum of SWEA during electron depletions on July 11, 2015. All data are corrected from the spacecraft potential measured by LPW. Superimposed in **red** is the total scattering electron collision cross section for CO_2 taken from Itikawa et al.* [2002].

3.2.3. An overview of the variety of the flux spikes

Mitchell et al., [2001] observed that electron depletions were frequently punctuated by 'flux spikes', coincident with radial magnetic fields and showing an electron spectrum similar to a magnetosheath one, with reduced flux at all energies. In Figure 63 is plotted a MAVEN passage in the nightside ionosphere during which several electron depletions and flux spikes can be observed. I delineate the different flux spikes with black vertical lines, though their delimitation is not always obvious, especially at the beginning of the time interval.

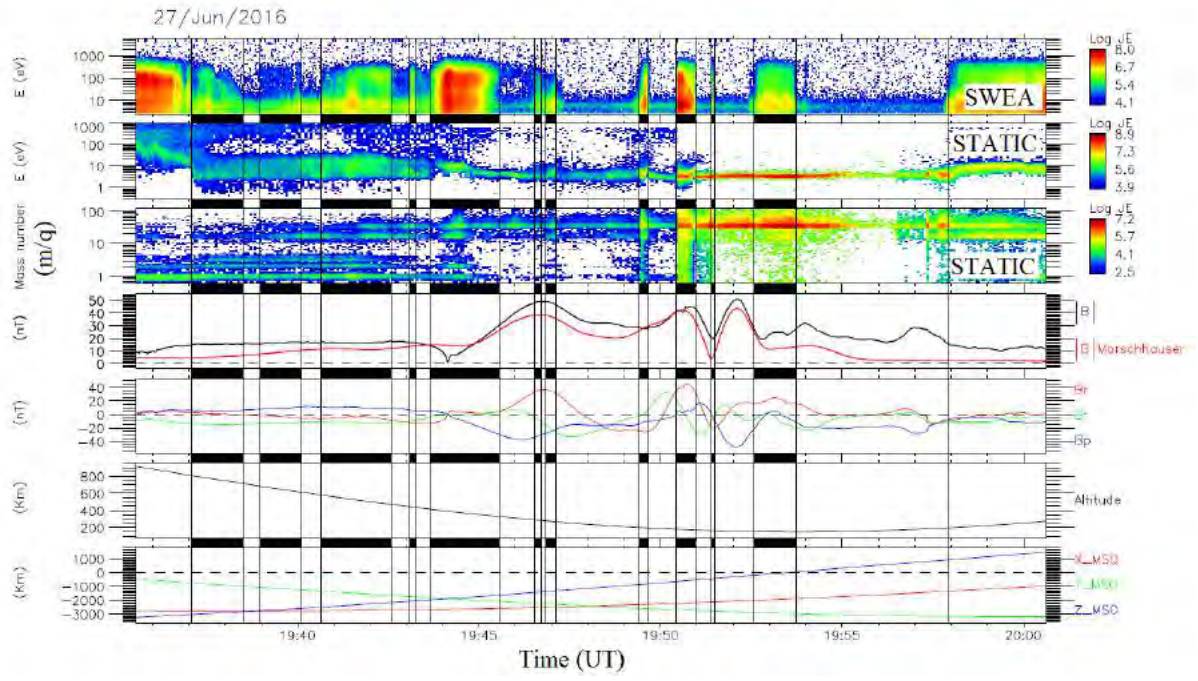

Figure 63. Example of flux spikes observed by MAVEN on June 27, 2016

*Panel 1: SWEA energy-time spectrogram of omnidirectional electron energy flux (ENGY mode). Panel 2: STATIC energy-time spectrogram of omnidirectional ion energy flux (C0 mode). Panel 3: STATIC mass-time spectrogram of omnidirectional ion energy flux (C6 mode). Panel 4: Magnitude of the magnetic field measured by MAG (**black**) superimposed with the amplitude of the crustal magnetic field calculated thanks to the model of Morschhauser (**red**). Panel 5: The three components of the magnetic field in the IAU frame measured by MAG. Panel 6: Altitude of the spacecraft. Panel 7: Position of the spacecraft in the MSO coordinates. The black boxes and the corresponding black vertical lines highlight the flux spikes observed during this time interval.*

We can observe that flux spikes are highly different from one another. Some can be long-lasting events, like the one at ~19:44 UT while others are punctual, as the one at ~19:51:30. Regarding the electron spectrogram, electrons with energies up to 1 keV are back during flux spikes, though some events are composed of two electron populations (like those at ~19:41 UT and ~19:44 UT) and others show few electrons above 100 eV (like the two at ~19:47 UT).

Regarding the ion spectrogram, some flux spikes are coincident with the observation of H^+ (like the one at ~19:49:30 UT), while others do not show any modification compared to electron depletions (like the one at ~19:53 UT).

Concerning the magnetic field, we can observe that some flux spikes are indeed coincident with a local extremum of the radial magnetic field, like the four events between 19:49 UT and 19:55 UT. However, other events are coincident with low radial magnetic field, like the one at ~19:44 UT, during which the magnetic field is first radial before being along B_φ.

The variety of flux spikes existing within a single orbit shows the variety of processes involved in the structure and the dynamics of the nightside ionosphere. This aspect will be investigated in more details in section 5.1.

3.2.4. Are electron depletions really related to crustal fields?

MGS and MEX mainly observed electron depletions above strong crustal magnetic sources, with few events reported out of these regions. Concerning MAVEN, electron depletions can be observed at all periapsis passes in the nightside except several specific cases which are presented in section 5.2.2. This implies that we still observe electron depletions above strong crustal magnetic sources, but that their observation is **not restricted to these regions**. In Figure 64 and Figure 65 I present two orbits of MAVEN during which electron depletions have been observed.

In Figure 64 is a pass over a relatively strong crustal magnetic source in the northern hemisphere (the periapsis is above the geographic location (40°N, 74°E), see Figure 52). The periapsis is in this case at 125 km altitude (it was made during the first "deep dip" campaign). During this orbit, SWEA recorded between 06:29 and 06:36 UTC a large electron depletion (delineated by brown vertical dashed lines). During this electron depletion, the spacecraft was in the nightside ionosphere below 160 km altitude and passed over a strong crustal magnetic source between 06:29 and 06:33 UTC as indicated by the pronounced increase observed in the magnetic field intensity (up to ~120 nT) which is in agreement with the model of Morschhauser. We can note that between 06:33 and 06:36 UTC the electron depletion is still present, whereas no significant magnetic field can be observed.

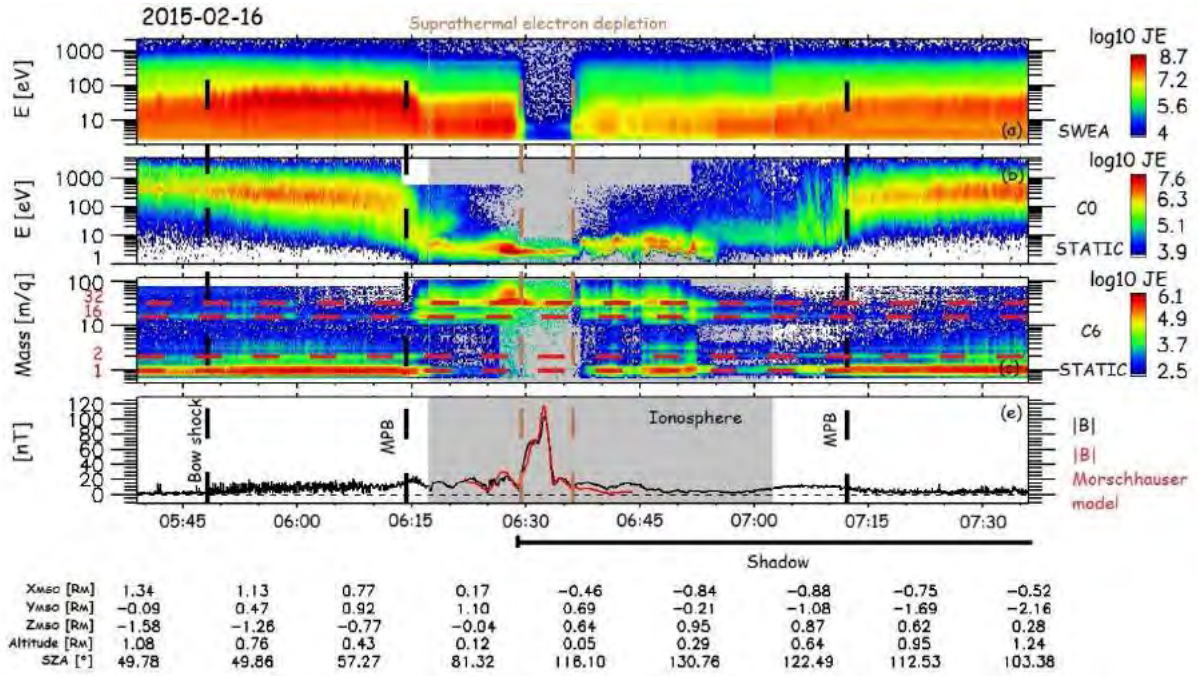

Xmso [Rm]	1.34	1.13	0.77	0.17	−0.46	−0.84	−0.88	−0.75	−0.52
Ymso [Rm]	−0.09	0.47	0.92	1.10	0.69	−0.21	−1.08	−1.69	−2.16
Zmso [Rm]	−1.58	−1.26	−0.77	−0.04	0.64	0.95	0.87	0.62	0.28
Altitude [Rm]	1.08	0.76	0.43	0.12	0.05	0.29	0.64	0.95	1.24
SZA [°]	49.78	49.86	57.27	81.32	116.10	130.76	122.49	112.53	103.38

*Figure 64. Example of electron depletion observed with MAVEN on February 16, 2015. First panel: SWEA energy-time spectrogram of omnidirectional electron energy flux (ENGY mode). Second panel: STATIC energy-time spectrogram of omnidirectional ion energy flux (C0 mode). Third panel: STATIC mass-time spectrogram of omnidirectional ion energy flux (C6 mode). Fourth panel: Magnitude of the magnetic field measured by MAG (**black**) superimposed with the amplitude of the crustal magnetic field calculated thanks to the model of Morschhauser (**red**). The bow shock and the MPB are roughly represented by the black dashed vertical lines.*

In Figure 65 is plotted a similar pass over a quiet crustal magnetic field area (the amplitude calculated by the Morschhauser model do not exceed 9 nT). In this case the spacecraft passed its periapsis at 150 km altitude, above the geographic location (50°N, 150°E). Several electron depletions can be observed between 18:12 and 18:21 UT (between the brown dashed vertical lines), below an altitude of 250 km.

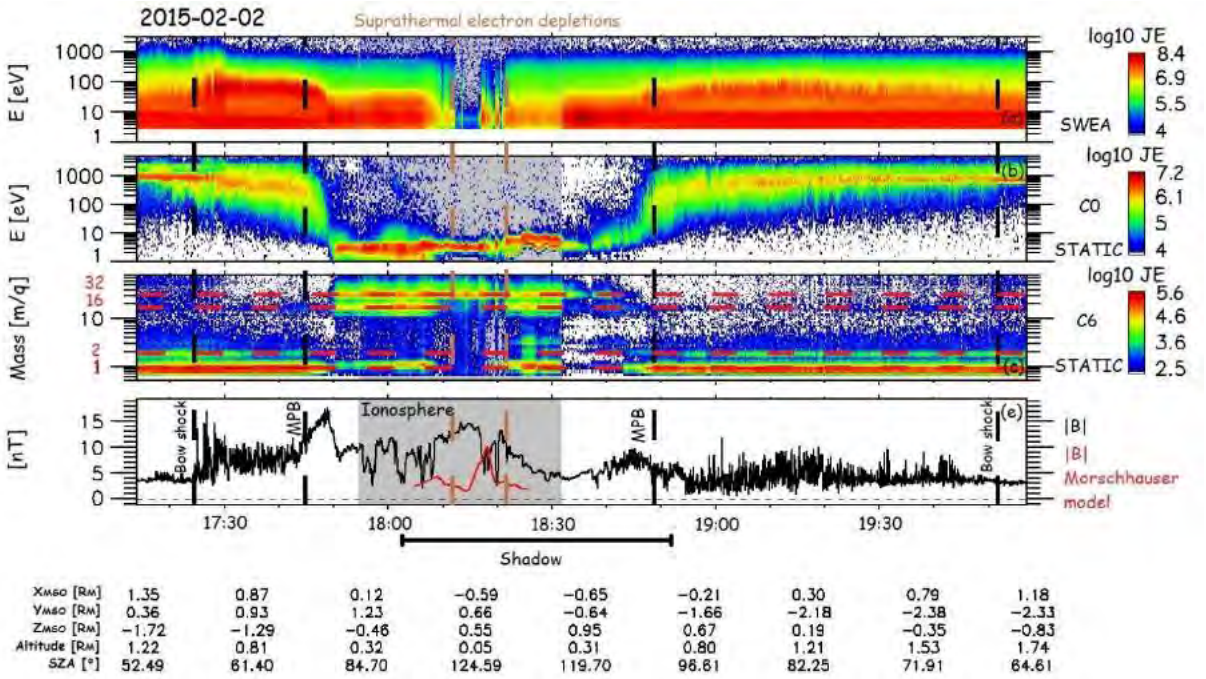

Figure 65. Example of electron depletion observed with MAVEN on February 02, 2015. The panels are the same as in Figure 64.

Electron depletions detected in both cases have the same properties, i.e. no electron above 10 eV, a remaining electron population peaked at ~6 eV and O_2^+ at ~3eV. The main difference between these two examples is the presence of crustal magnetic fields. In Figure 65, no significant crustal magnetic field is recorded. The model however predicts a small enhancement of the crustal field at 18:18 UT but this value seems too small to be significant as it is embedded in the ambient magnetic field.

These two case studies have been chosen as representative of a large number of electron depletions observed by MAVEN. The first one above a crustal magnetic field source corresponds to the typical case previously reported from MGS and MEX observations. The second one above a quiet magnetic area was occasionally reported from past observations (see *Hall et al.*, [2016] for example) but is now commonly observed by MAVEN, as it will be illustrated by the statistical analysis presented in sections 4.1.2 and 4.1.3.

3.3. Automatic detection of suprathermal electron depletions: definition of the criteria

The different characteristics of electron depletions highlighted by MAVEN data (section 3.2) enable me to implement a criterion able to automatically detect electron depletions in SWEA spectrogram [*Steckiewicz et al., 2015*]. I then adapt this criterion to the ER and ELS data sets [*Steckiewicz et al., 2016*]. I here first explain how this criterion has been defined for MAVEN (section 3.3.1) before being adapted to MEX (section 3.3.2) and MGS (section 3.3.3) and their own specificities.

3.3.1. MAVEN

Taking into account the electron depletions properties observed by MAVEN (section 3.2), both for the electron population inside the electron depletions and inside the flux spikes, I have created for SWEA data the criterion given in equation (1):

$$\frac{1}{3}\sum_{i=1}^{3}\frac{CR(E_i)}{< CR(E_i), 1h >} < 0.01 \quad (1)$$

It is based on electron count rates (CR) from SWEA observations and relies on three energy channels ($E_1 = 4.26$ eV, $E_2 = 98.93$ eV and $E_3 = 111.16$ eV). The numerator gives the count rate at an energy of E_i (per time step), whereas the denominator gives the mean count rate at the same energy over a one hour period centered on the current time step. This simple criterion thus gives an idea of how the electron flux is at the current time step compared to average conditions. An average time of one hour has been chosen so as to prevent any influence from SEP events (or any other events which occasionally would increase the electron flux in the Martian environment). An electron depletion is detected if a ratio of two orders of magnitude is identified.

These three channels have been chosen after looking at the electron spectrum inside electron depletions. As seen in section 3.2.2, inside electron depletions is a remaining electron population peaked at 6-7 eV and hardly any electrons above 10 eV. Hence I chose an energy channel below 6 eV (necessary in practice to properly distinguish electron depletions from flux

spikes), and two above, to give more weight to depletions of high energies electrons and to avoid a significant influence by the 6-7 eV electrons due to spacecraft charging. Usually, the spacecraft potential in the nightside ionosphere is approximately of -2 V. This implies a little modification in the energies detected which are reduced by the same amount (see section 2.2.4). These small potentials have no significant impact on the criterion results.

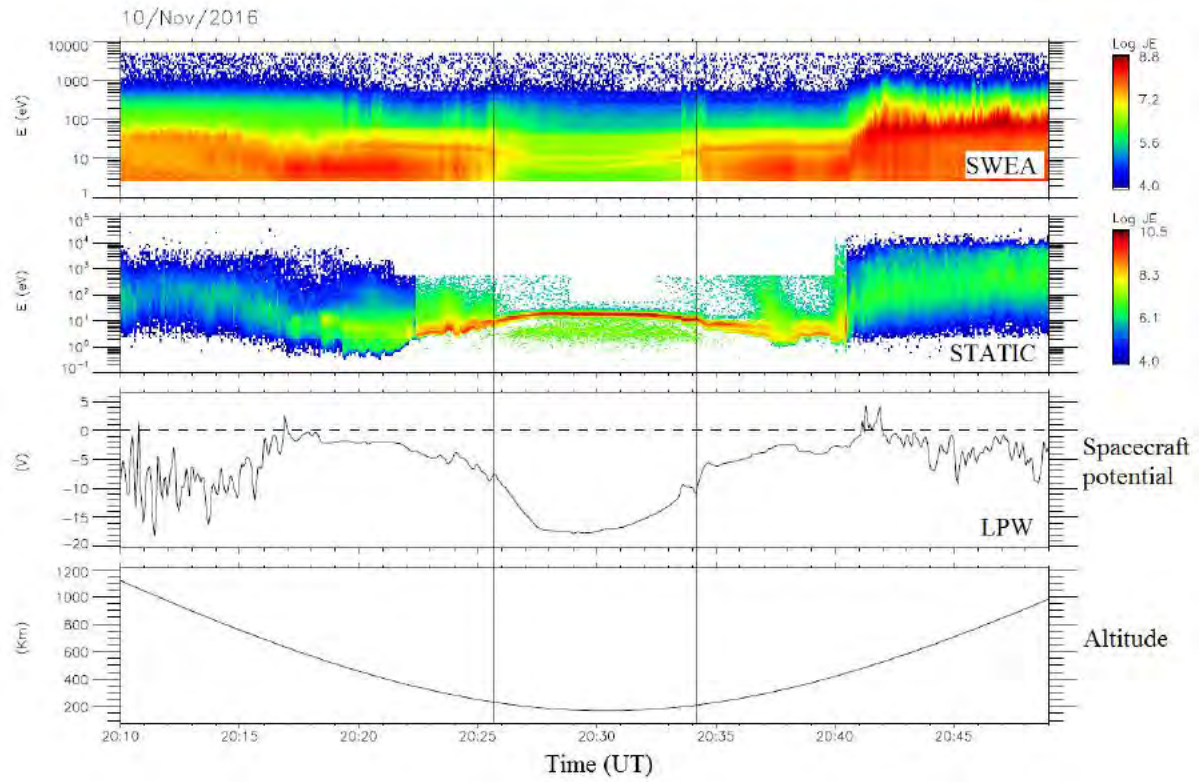

Figure 66. Example of a strong spacecraft charging observed on November 10, 2016. First panel: SWEA energy-time spectrogram of omnidirectional electron energy flux (ENGY mode). Second panel: STATIC energy-time spectrogram of omnidirectional ion energy flux (C0 mode). Third panel: Spacecraft potential measured by LPW Fourth panel: Altitude of the spacecraft.

However, some **strong spacecraft charging events** can bring the spacecraft potential to a dozen of volts. An example of such event is presented in Figure 66. The charging event can be observed between ~20:26 and ~20:34 UT, when the spacecraft potential decreases down to -18 V. A typical enhancement in the ion energy is observed at the same time, together with a modification of the electron spectrum and the occurrence of two distinct lines, here around 10 eV, corresponding to the two photoelectron lines (section 1.3.1.4) which are normally unresolved by MAVEN and merged into a single line (initially at 21-27 eV). The electron flux detected at 6 eV during these kind of events is then much lower than the mean electron flux calculated over one hour and an electron depletion can be detected, whereas no electron

depletions is effectively observed. A few cases have been found during the time period under study and have been removed by hand, as much as possible. Indeed, some of these cases are located on the dayside so that they do not have any incidence on the detection of electron depletions. However, in December 2016/January 2017 a lot of spacecraft charging events have been observed near the terminator, impacting the detection of electron depletions. This issue is discussed in more details in section 5.2.1.2.

The sampling time step used for criterion (1) is the same as the measurement cadence of the SWEA instrument: 4s. Consequently the electron depletions detected last at least 4s which corresponds to a minimum of 14 km traveled by the spacecraft.

3.3.2. MEX

Based on my experience with MAVEN data, I adapted criterion (1) to MEX/ELS data to obtain criterion (2):

$$\frac{1}{3}\sum_{i=1}^{3}\frac{CR(E_i)}{< CR(E_i), 1h >} < 0.02 \quad (2)$$

In this case I use the three following energy channels: $E_1 = 21.20$ eV (for low energies), $E_2 = 95.04$ eV and $E_3 = 103.25$ eV (for high energies). Thus, by taking a minimum energy above 20 eV we prevent most of the spacecraft charging effects that could impact results of criterion (2). Indeed, the charged particles of lower energies are in general most sensitive to spacecraft charging and the 20 eV energy has been found to be a good compromise (*Fränz et al.* [2006]; *Hall et al.* [2016]).

I also modify the threshold ratio from 1% to 2% based on the observations of ELS data. The sampling time step used for criterion (2) is the same as the measurements cadence of the ELS instrument when operated in its default survey mode: 4s. Consequently, the electron depletions detected last at least 4s which corresponds to a minimum of 15 km in the spacecraft orbital direction.

3.3.3. MGS

In the case of MGS, a criterion based on three energy channels (one low, two high) does not work well, probably due to the energy resolution of 25%. Hence, I decided to compare every two seconds the omnidirectional flux summed over all the available energies [11 eV; 16 127 eV] with the same product averaged over two orbits (4 hours). An electron depletion is detected if this ratio is less than 1%, which corresponds to a drop of two orders of magnitude in the electron flux. The MGS criterion is described in equation (3) with a similar form to equations (1) and (2).

$$\frac{\text{Flux}(\,[11\text{ eV}; 16\,127\text{ eV}]\,)}{<(\text{Flux}(\,[11\text{ eV}; 16\,127\text{ eV}]\,), 4\text{h})>} < 0.01 \quad (3)$$

Among the energy range [11 eV; 16 127 eV], the three channels which collected the majority of the flux were 90-148 eV, 148-245 eV and 245-400 eV. Electron depletions thus show up in those three most reliable energy channels which are far too high in energy to be affected by any spacecraft charging which would almost always be less than $\sim$20 eV. Hence, the criterion (3) is not really sensitive to spacecraft charging.

The sampling time step used for criterion (3) is the same as the measurements cadence of the ER instrument: 2s. Consequently, the electron depletions detected size is at least 7 km in the orbital direction.

3.4. Application of the criteria

Once the criteria were set, I applied them to the three datasets described in section 2.3. Application to MGS and MAVEN data has been relatively easy, while the specificities of the MEX mission makes it more complicated and implied the use of results from the other two. I thus first present the application of the MGS criterion in section 3.4.1, then the application of the MAVEN criterion in section 3.4.2 and I finish by the application of the MEX criterion in section 3.4.3. This leads to the creation of three catalogs of electron depletions used in the next sections to study the different processes leading to the observation of electron depletions (section 4) and the dynamics of the nightside ionosphere (section 5).

3.4.1. Application to MGS

For the study of the electron depletions observed with MGS, I only focus on the data obtained during the circular mapping phase at an altitude of ~400 km. The dataset covers the time period from March 10, 1999 to October 11, 2006 which represents more than 42 000 orbits. As the MGS orbit was circular during the time period under study, electron depletions can potentially be observed during each orbit. Such statistics average all the effects of external drivers on electron depletions so that only stands out the general behavior of these structures. However, due to this huge dataset, all the electron depletions detected have not been checked, as it has been done for MAVEN. Hence, some artifacts can be contained in the resulting catalog.

The example proposed in Figure 67 illustrates how the criterion detects electron depletions in agreement with the ER spectrogram. Five electron depletions are detected during this time interval, in good agreement with the electron spectrogram. However, we can notice that all the decreases that can be observed on panel 1 and 2 are not detected as electron depletions. This is due to the threshold of 1% chosen.

The application of criterion (3) on MGS data with no additional restriction resulted in a time table of **116 278 electron depletions** which means that several electron depletions have been detected during a single orbit as in the example shown in Figure 67. A median value of **four electron depletions observed per orbit** has been obtained (Table 5). Almost all these electron depletions have been detected in the nightside, except few (less than 100) isolated cases.

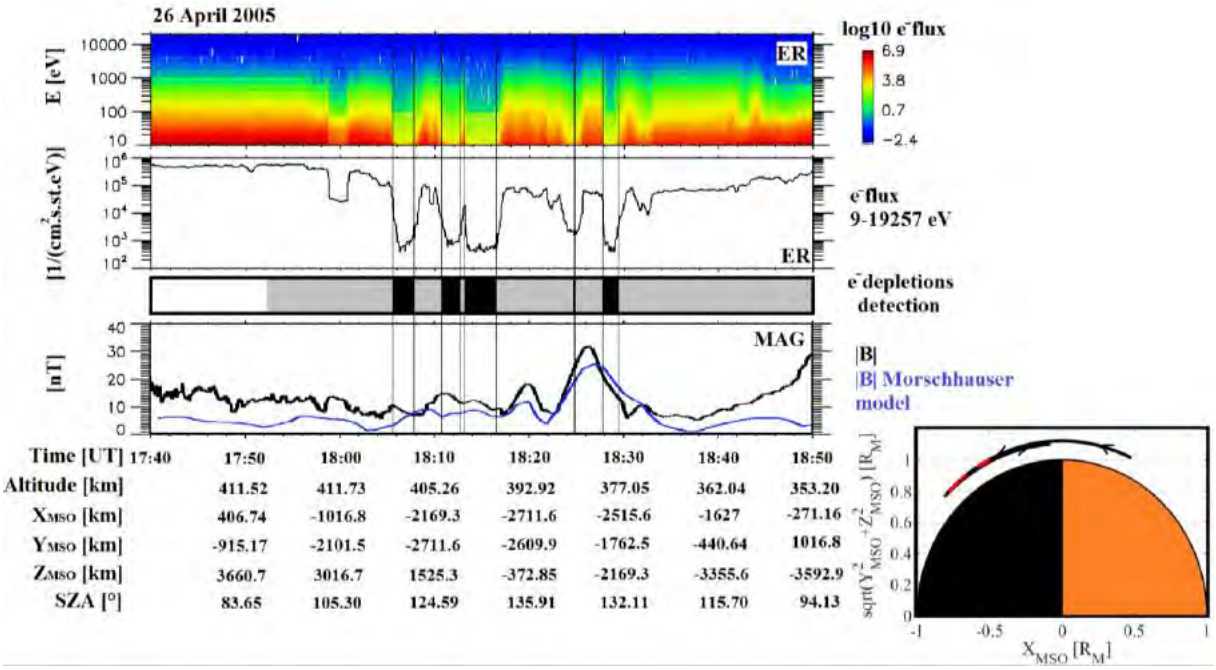

Figure 67. Example of electron depletions observed by MGS on April 26, 2005.

*First panel: ER energy-time spectrogram of omnidirectional electron flux. Second panel: ER omnidirectional electron flux summed over all energies available [11-16127 eV]. Third panel: Detection of electron depletions by criterion (3) (black boxes). The shadow corresponds to the nightside. Fourth panel: Magnetic field intensity (measured by MAG in **black** and calculated from the model of Morschhauser in **blue**). Fifth panel (bottom right): MGS orbital trajectory in a cylindrically symmetric MSO coordinates frame. The location of the electron depletions detected is highlighted in red.*

3.4.2. Application to MAVEN

3.4.2.1. Application of criterion (1)

The criterion specified in equation (1) has been applied to SWEA data from October 7, 2014 to March 13, 2017 with no restriction on the nightside nor on the altitude, which corresponds to more than 4 600 orbits.

The example proposed in Figure 68 illustrates how the criterion detects electron depletions in agreement with the SWEA spectrogram. Three electron depletions can be observed on this example, in good agreement with the SWEA spectrogram. The delimitation of the electron depletion is clear at ~16:39 UT, while on the three other cases, they are set by the threshold chosen. All the three electron depletions are located in the nightside.

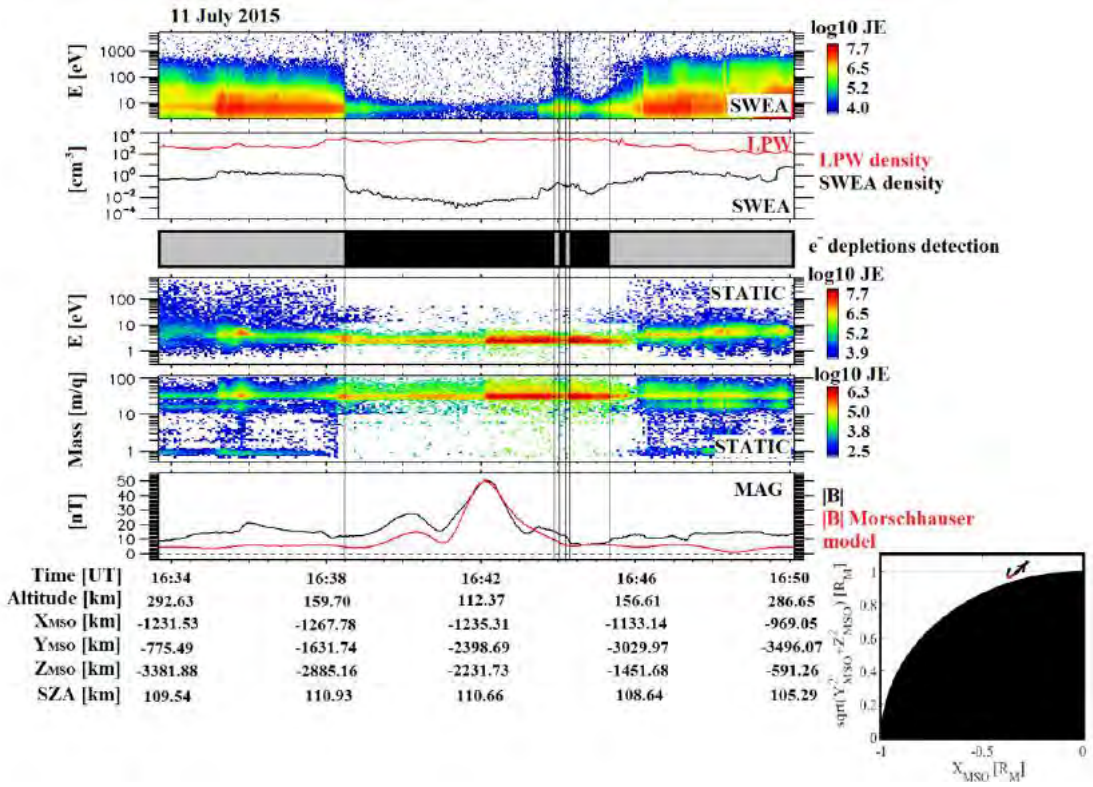

Figure 68. Example of electron depletions observed with MAVEN.

*First panel: SWEA energy-time spectrogram of omnidirectional electron energy flux (ENGY mode) corrected for the potential measured with LPW. Second panel: Electron density calculated with SWEA (black) superimposed with the density calculated with LPW (red). Third panel: Detection of electron depletions by criterion (1) (black boxes). The shadow corresponds to the nightside. Fourth panel: STATIC energy-time spectrogram of omnidirectional ion energy flux (C0 mode). Fifth panel: STATIC mass-time spectrogram of omnidirectional ion energy flux (C6 mode). Sixth panel: Magnetic field intensity (measured by MAG in **black** and calculated from the model of Morschhauser in **red**). Seventh panel (bottom right): MAVEN orbital trajectory in a cylindrically symmetric MSO coordinates frame. The location of the electron depletions detected has been highlighted in red.*

The application of criterion (1) to the time interval under study resulted in a dataset of **9802 electron depletions** identified. We thus detected several electron depletions per orbit, as for MGS. A median value of **four electron depletions observed per orbit** have been found, as it was found for MGS events (Table 5).

3.4.2.2. MAVEN coverage

During the time interval under study, electron depletions have only been detected during **five specific periods**, as it can be observed in Figure 69. In this figure is plotted in red the location of the electron depletions detected by criterion (1) in terms of altitude, latitude, local time and SZA. Superimposed in blue is the global coverage of MAVEN of the nightside low

altitudes ($X_{MSO} < 0$ and altitude < 900 km). The white stripes that can be observed at some times (like in March 2016) are data gaps which are due to safe mode of the spacecraft.

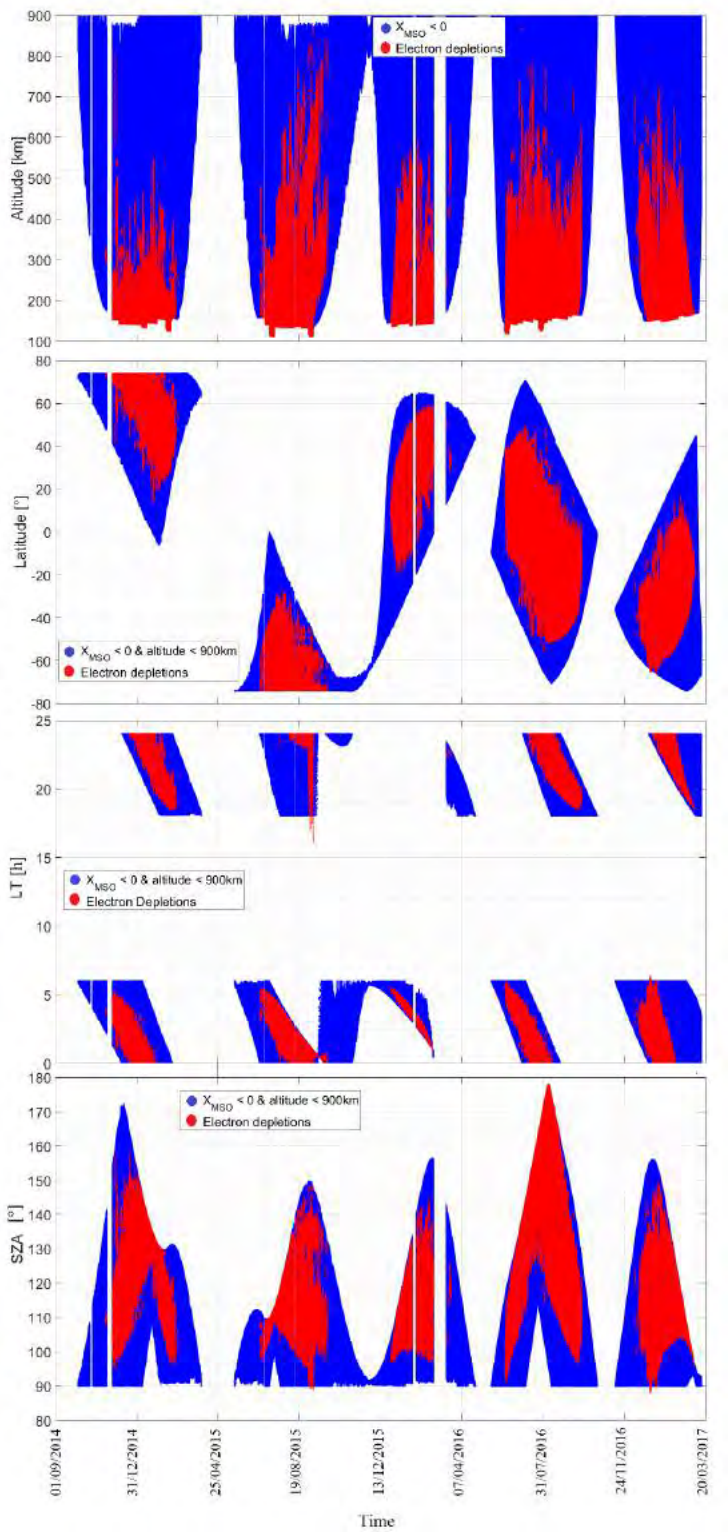

*Figure 69. The five time periods during which electron depletions have been detected by MAVEN. MAVEN coverage of the nightside region at low altitudes (<900km) (**blue**) superimposed with the location of the detected electron depletions (**red**). Panel 1: Altitude vs time; Panel 2: Latitude vs time; Panel 3: Local time vs time; Panel 4: SZA vs time.*

MAVEN observes electron depletions from **~110 km** (during a deep dip) up to **~900 km** (during the second period). Although MAVEN reached higher altitudes in the induced magnetosphere, criterion (1) detected no electron depletion above 900 km. Looking at panel 3 and 4 of Figure 69 we can see that all but seven electron depletions are located on the **nightside** defined as $X_{MSO} < 0$. These seven cases are investigated in section 5.2.1.1. At first glance, electron depletions seem to be more detected on the dawn side than on the dusk side, but it is only a coverage issue. Depending on the period, the dawn and the dusk sides are not equally covered, and the deep nightside (SZA close to 180°) is rarely reached. At the end of these five periods, approximately all the possible latitudes reachable by MAVEN have been sampled, but all the altitudes are not yet equally covered.

In summary, electron depletions are detected during specific periods when the spacecraft reaches low altitudes (<900 km) in the nightside. They can last from 4s (~14 km in the spacecraft orbital direction) up to 15 minutes (~3000 km in the spacecraft orbital direction).

3.4.3. Application to MEX

The time period under study for MEX data is from March 1, 2004 to December 31, 2014, which is similar to the one studied by *Hall et al.* [2016]. This corresponds to approximately 14072 orbits. However, I only applied criterion (2) on time intervals longer than one hour when ELS was working in the Survey mode, which corresponds to 9 983 time intervals. The time period under study is long enough to allow the periapsis to cover the whole surface of Mars between latitudes of -86° and +86° and all the local times in the nightside thanks to the precessing orbit of MEX.

3.4.3.1. Unrestricted application

The application of criterion (2) with no restriction on the altitude nor on the nightside resulted in a time table of 17 592 electron depletions. The example proposed in Figure 70 illustrates how the criterion detects electron depletions in ELS data. Three electron depletions are detected in this example, in good agreement with the electron spectrogram.

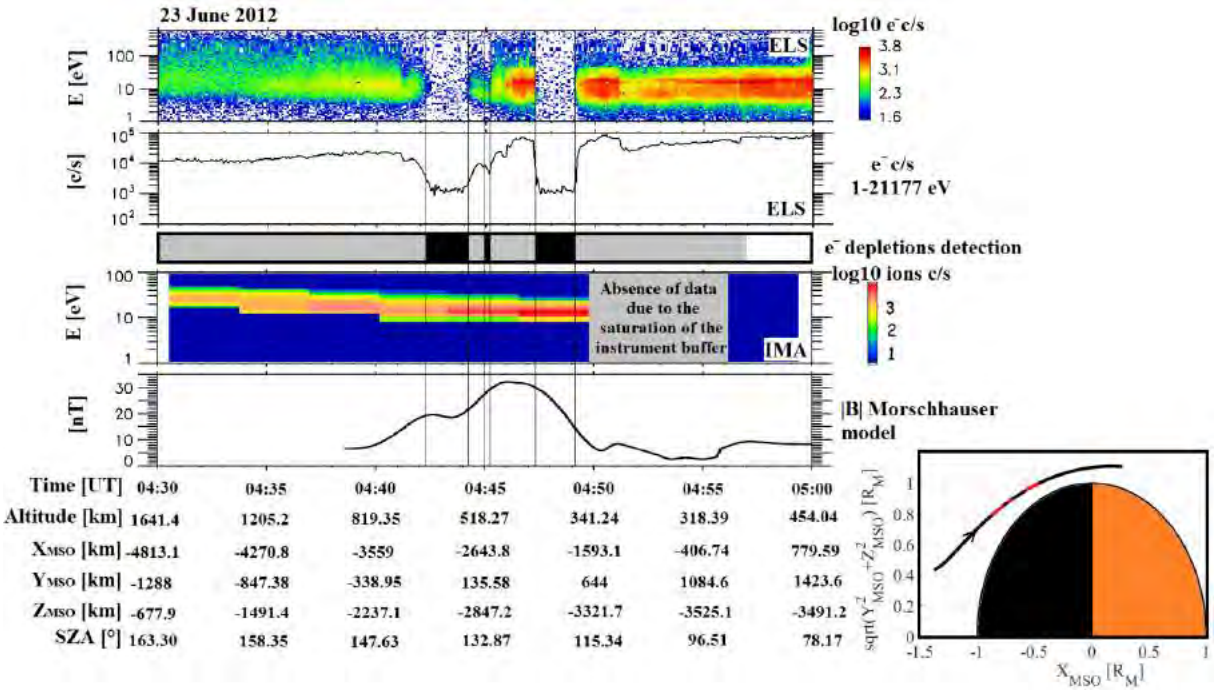

Figure 70. Example of electron depletion observed by MEX on June 23, 2012.

First panel: ELS energy-time spectrogram of omnidirectional electron counts per second. Second panel: ELS electron counts per second summed over all the energies available (1-21177 eV). Third panel: Detection of electron depletions by criterion (2) (black boxes). The shadow corresponds to the nightside. Fourth panel: IMA energy-time spectrogram of omnidirectional heavy ions counts per second (m/q>20). Fifth panel: Magnetic field intensity calculated from the Morschhauser model. Sixth panel (bottom right): MEX orbital trajectory in a cylindrically symmetric MSO coordinates frame. The location of the electron depletions detected is highlighted in red.

The electron depletions detected by criterion (2) are located from 245 km to ~ 10 000 km altitudes both on the nightside and on the dayside (for a small amount of cases), as in the study made by *Hall et al.*, [2016]. Globally, electron depletions have been detected as in the MAVEN case during specific time periods when the periapsis went across the nightside at low enough altitudes. However, most of the electron depletions observed on the dayside and at altitudes above 1 000 km have to be considered with caution (since they include very short **data gaps** and the **lobes** — the region located on either side of the plasma sheet with reduced particle fluxes — that cannot be easily excluded). An example of observation of the lobes is provided in Figure 71. The two electron count rates decreases observed between ~11:31 UT and ~11:38 UT, and between ~11:40 UT and ~11:48 UT are quite similar to two electron depletions separated by a spike. However, looking at the entire orbit, these structures are more likely to be two lobes, separated by a current sheet. Usually, criterion (2) cannot make this difference and

detects electron depletions as well as tail lobes. However, one main difference is that the tail lobes are usually observed at large distances from the planet.

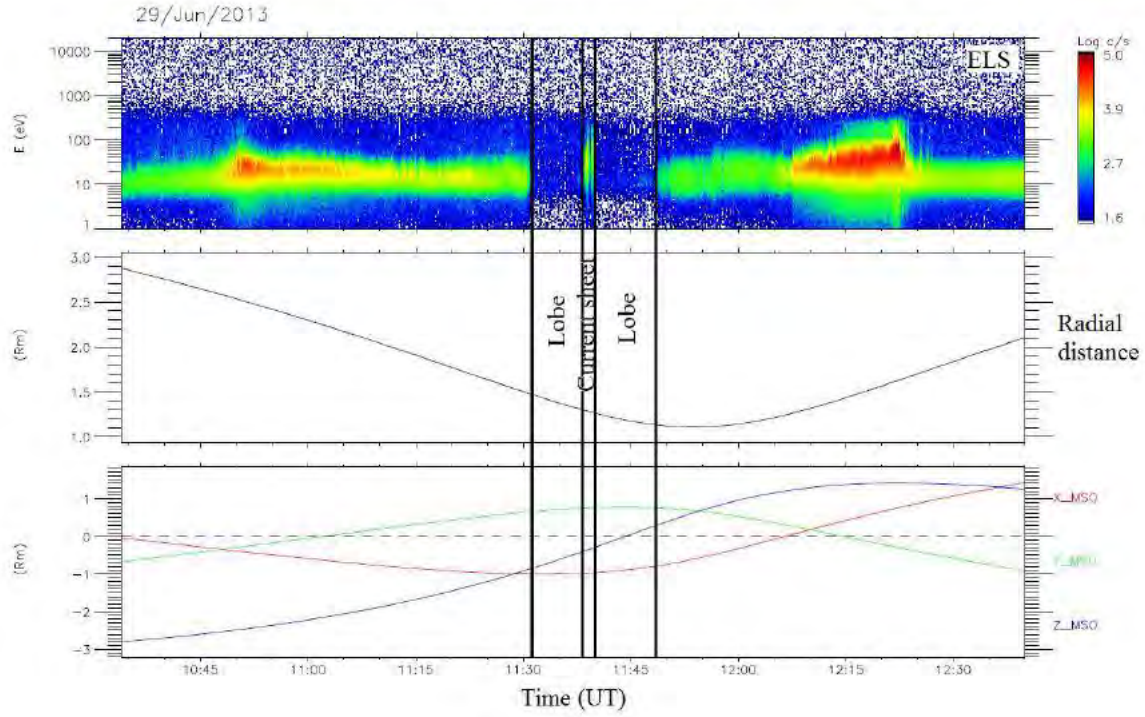

Figure 71. Example of a tail crossing by MEX on June 29, 2013.
Panel 1: ELS energy-time spectrogram of omnidirectional electron counts per second. Panel 2: Radial distance of the MEX spacecraft. Panel 3: Position of the MEX spacecraft in MSO coordinates.

Surprisingly, the MAVEN criterion succeeds in making the difference between electron depletions and lobes. This issue is not yet fully understood but may be due to the energy range of the instrument. Regarding MGS, its restriction to altitudes close to 400 km prevented it from detecting lobes.

Hence, the events found both by the unrestricted application of criterion (2) and by *Hall et al.*, [2016] above ~1000 km should be taken very cautiously. As MAVEN does not detect any electron depletion above 900 km, the majority of these events should be considered as false positives, either as a detection of tail lobes or short data gaps. As the lobes are not localized above specific regions of the Martian surface, including them induces a **background noise** in the geographical distribution of suprathermal electron depletions, as can be observed on the map proposed by *Hall et al.*, [2016] and plotted in Figure 78.

3.4.3.2. Restricted application

I therefore chose to only consider for the next studies electron depletions observed in the nightside below 900 km, which is consistent with my MAVEN results and enables the two studies to be compared. With these restrictions, 14 517 electron depletions have been found on 2 197 orbits, which implies a strong presence of spikes in MEX data as in the example in Figure 55 and Figure 70. A median value of **five electron depletions observed per orbit** have been found (Table 5).

The median number of electron depletions per MEX orbit is a slightly higher but remains similar to both MAVEN and MGS data, which confirms that the occurrence of the electron depletions is stable during the three periods and consistent among the three spacecraft.

Application of criterion (1), (2) and (3) results in three catalogs of electron depletions, corresponding to different coverages of the Martian environment. The complementarity of these three catalogs is used in the following section to better understand the processes at the origin of the observation of electron depletions in the nightside ionosphere of Mars.

	MGS	**MEX**	**MAVEN**
Number of orbits under study	42 048	9 983	4661
Number of electron depletions detected	116 278	14 517	9802
Number of orbits containing electron depletions	29 460	2 197	2 157
Median number of electron depletions per orbit	4	5	4

Table 5. For each mission are reported here the number of orbits under study (for MEX it corresponds to the number of time intervals longer than one hour when ELS was in the survey mode. It corresponds approximately to the number of orbits studied), the number of electron depletions detected by criterion (3) for MGS, criterion (2) for MEX and criterion (1) for MAVEN, the number of orbits containing electron depletions and the median number of electron depletions per orbit.

MGS and MEX used to observe sharp decreases of the electron flux above strong crustal magnetic field sources: the plasma voids. These structures were considered as being the result of the spacecraft crossing of closed crustal magnetic field loops, preventing the plasma coming from the dayside or from the sheath from populating the inner part of the loops. However, MAVEN data revealed that, (1) plasma voids are not void of plasma, leading us to rename them as suprathermal electron depletions, (2) electron depletions can be observed above the whole surface, whether there is crustal magnetic fields or not. In order to find some consistency between these observations, three automatic criterion have been implemented to detect electron depletions in the three datasets. Application of the criterion leads to the creation of three catalogs of electron depletions, used in the next section to better understand the new observations made by MAVEN and include them in a new scenario of creation of electron depletions.

4. On the processes at the origin of suprathermal electron depletions

We observed in section 3.2.3 and 3.2.4 that MAVEN can detect electron depletions above both strong and weak crustal magnetic field regions, and that flux spikes do not always correspond to radial magnetic fields. In order to include these new observations to the picture already set by MGS and MEX measurements (section 3.1.2) and make it evolve, we here investigate the different processes which lead to the creation of electron depletions in the nightside ionosphere of Mars. We first observe the altitude dependence of the electron depletion distribution, revealed by the MAVEN coverage (section 4.1). We then study the two main processes at the origin of electron depletions and how they influence the distribution of electron depletions (section 4.2). We finish with a discussion on the altitude of the exobase (section 4.3).

4.1. Altitude dependence of the distribution of suprathermal electron depletions

Three catalogs of electron depletions are available: one at a mean altitude of 400 km (MGS data), one at altitudes between 250 and 900 km (MEX data) and the last one at altitudes between 110 and 900 km (MAVEN data). As new characteristics of electron depletions showed up in this last one, we first investigate the altitude distribution of the electron depletions observed by MAVEN (section 4.1.1). We then compare the geographical distribution of electron depletions obtained by the three missions down to 250 km (section 4.1.2). We finally reveal the geographical distribution observed by MAVEN at altitudes below 250 km (section 4.1.3).

4.1.1. Altitude distribution of the electron depletions observed by MAVEN

MAVEN observed electron depletions from 110 km up to 900 km (section 3.4.2.2). In order to investigate the percentage of electron depletions observed depending upon the altitude,

I binned my data with constant bins of 2 km altitude. For each bin I first determined the number of time steps during which electron depletions have been detected therein, and then the number of time steps during which the MAVEN spacecraft was in this bin in the nightside for the whole time period under study (excluding data gaps during safe modes). The percentage of electron depletions per MAVEN passage is then the ratio of these two numbers. The percentage of electron depletions per MAVEN passage is used rather than the number of events in order to remove any orbital bias.

I treated separately the five periods during which electron depletions have been detected (section 3.4.2.2) to observe the evolution of the distribution regarding the mapping of the spacecraft. The result of my statistical binning is provided in Figure 72. Superimposed to the results obtained for each period is the global altitude distribution obtained over the whole time period under study (**red** line).

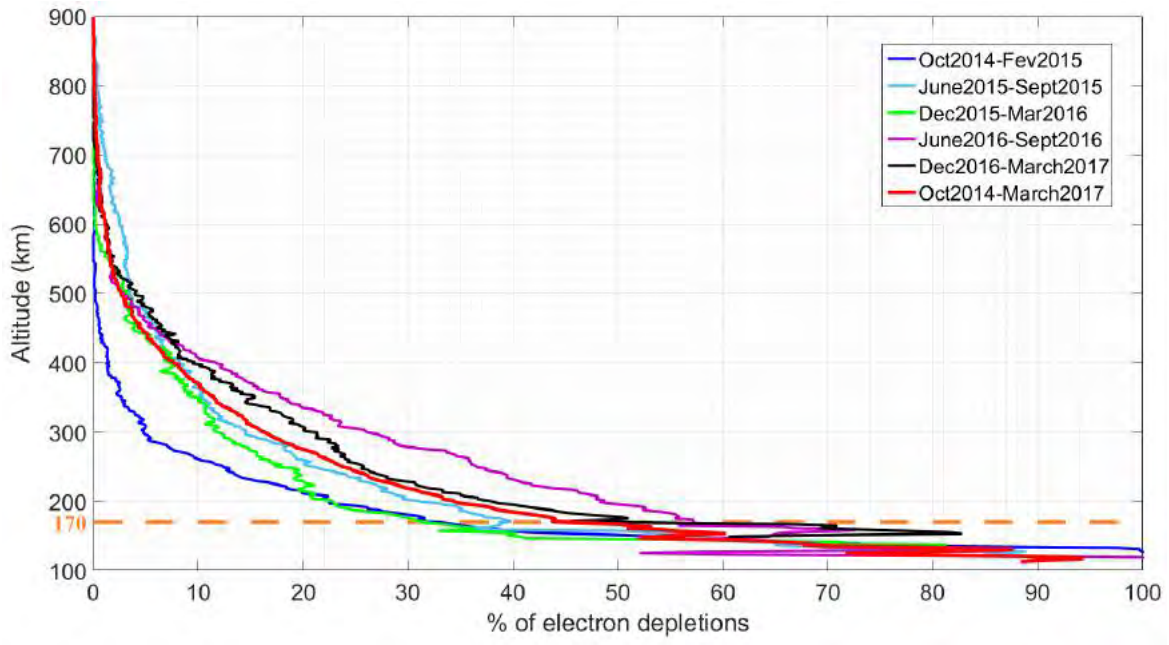

Figure 72. Altitude distribution of the electron depletions observed by MAVEN from 2014 to 2017. Percentage of electron depletions detected by criterion (1) per MAVEN passage calculated in bins of 2 km altitude for the five different periods during which electron depletions have been detected. In red is superimposed the altitude distribution obtained over the whole time period under study. The horizontal dashed orange line highlights the abrupt slope change observed at ~170 km.

First, the global shape of the distribution is the same for each period: the percentage of electron depletions detected increases with decreasing altitude. Second, on each distribution can be observed a particularly noticeable **slope change** around 170 km altitude (orange

horizontal dashed line). Below this altitude, the increase accelerates. For example, for the global distribution, there are 11.7% of electron depletions per MAVEN passage above 170 km, whereas below this altitude there are 57.6% of events per MAVEN passage. This percentage can even reach 100% at ~125 km altitude during the Deep-Dip campaigns (first and fourth period).

We can also notice that the different distributions are quite **dispersed at high altitudes**, varying from 5% to 26% at 300 km altitude, while they get closer to each other at low altitudes. The lowest percentages are found for the first period, when MAVEN sampled the high latitudes of the northern hemisphere and the largest percentages are found during the fourth period, during which MAVEN sampled the largest range of latitudes so far, from ~50°N to ~50°S.

The quick variations of the distribution at low altitudes could be due to the low number of points available at those altitudes, compared to the altitude resolution chosen.

4.1.2. Geographical distribution of suprathermal electron depletions: a common vision from above 250 km

In order to understand the altitude-dependence of the distribution of electron depletions which shows up in Figure 72, we first investigate in this section the geographical distribution of electron depletions, using the capabilities offered by the three catalogs available. We start with MGS, which enables an observation of the geographical distribution of electron depletions at a nearly constant altitude of 400 km (section 4.1.2.1). Then, we compare the results obtained by MEX and MAVEN for altitudes between 250 and 900 km (section 4.1.2.2).

4.1.2.1. Geographical distribution at 400 km

In Figure 73 is plotted the number of electron depletions detected by criterion (3) on a geographical map. The latitude-longitude map of Mars is detailed in spatial bins of 1° by 1°. We can observe the presence of streaks all over the map. This effect is only due to the spacecraft coverage which was not uniform, its traces did not overlap totally. Another effect of the spacecraft coverage is a distortion in latitudes, the high latitudes being more often observed than the equatorial ones.

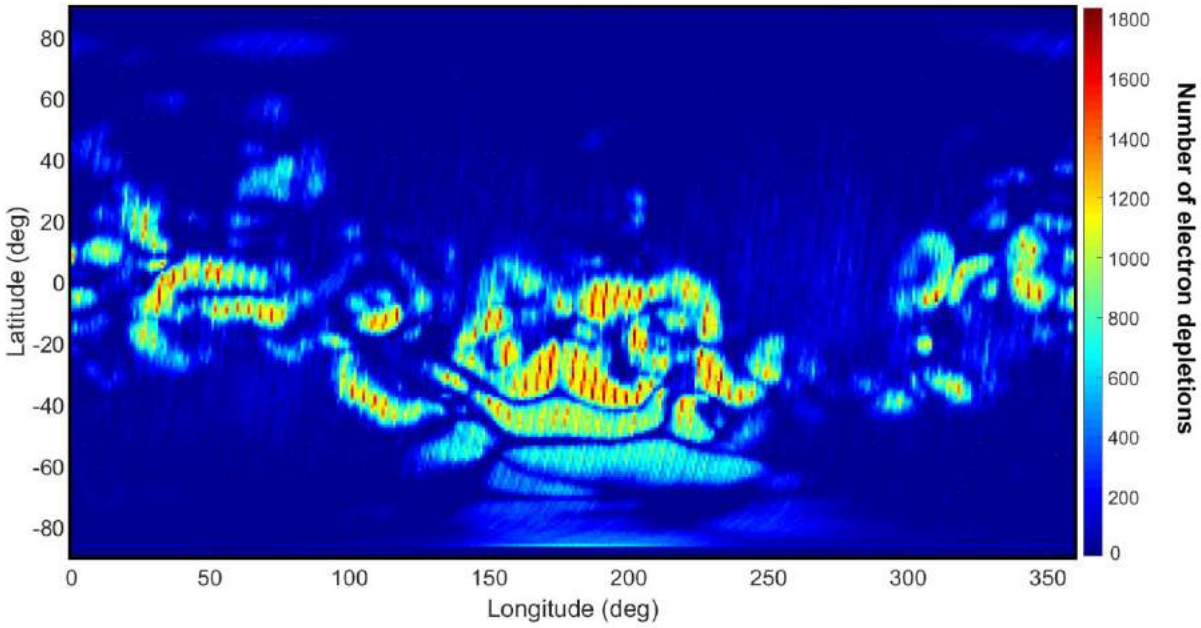

Figure 73. Geographical distribution of the electron depletions observed with MGS.
In color, the number of electron depletions detected by criterion (3) from MGS data on a geographic map of the Martian surface with a constant bin size of 1° per 1°.

So as to prevent these effects, I calculated the percentage of electron depletions detected per spacecraft passage. For each bin I scored the number of time steps when electron depletions are detected and divided it by the total number of time steps when MGS was in this bin on the nightside. There is on average more than 1 000 time steps per bin when MGS is in the nightside. The corresponding 'density map' of electron depletions is plotted in Figure 74. The color code corresponds to the percentage of electron depletions detected per MGS passage on the nightside. In Figure 75 is plotted on a geographical map the horizontal crustal magnetic field calculated at 400 km altitude thanks to the Morschhauser model. The horizontal magnetic field is the most relevant component of the crustal magnetic field here as it is an indicator of the presence of **closed crustal magnetic field loops**. In Figure 76 is plotted the same density map as in Figure 74, superimposed with logarithmically spaced (between 10 to 100 nT) contour lines of the horizontal crustal magnetic field calculated at 400 km altitude from the Morschhauser model and some area of interest (circled in white).

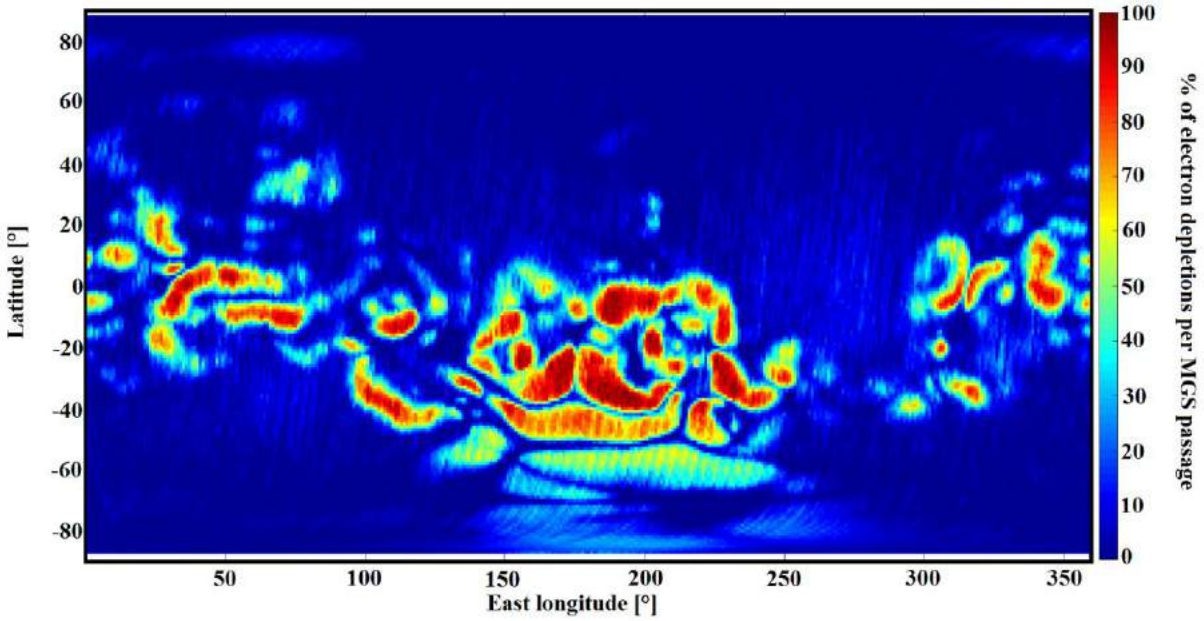

Figure 74. Density map of the geographical distribution of the electron depletions observed with MGS. In color, the percentages of electron depletions detected with criterion (3) per MGS passage on the nightside on a geographic map of the Martian surface with constant bin size of 1° by 1°.

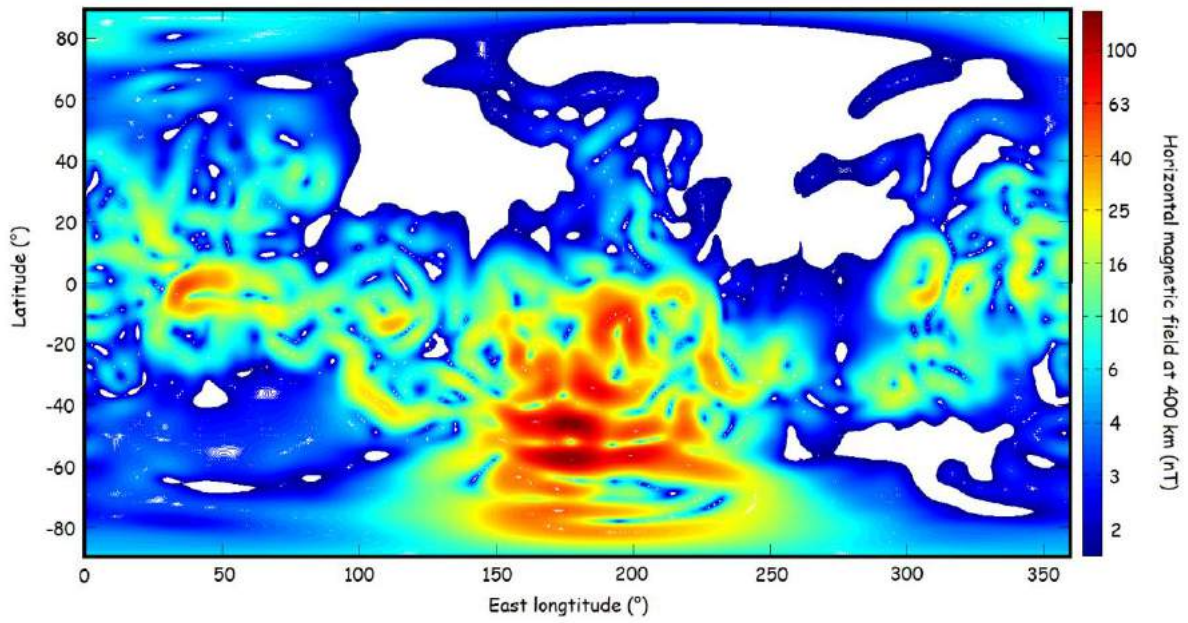

Figure 75. Geographical map of the horizontal component of the crustal magnetic field calculated at 400 km altitude thanks to the Morschhauser model.

We can see that, globally, electron depletions are gathered over some well-delimited spots, separated by regions where hardly any electron depletion has been recorded during more than seven years (Figure 74). The contours of the majority of these regions with enhanced electron depletions occurrence are in good agreement with the extension of strong horizontal

crustal magnetic fields (Figure 76). Regions where no electron depletion has been detected correspond either to weak crustal magnetic field area (like in the northern hemisphere, see Figure 75) or to cusp-like regions — where the crustal magnetic field is mainly radial — which are particularly well-delimited in the southern hemisphere. Hence, this first map confirms the strong link existing between the observation of electron depletions and the presence of horizontal crustal magnetic fields, and therefore closed crustal magnetic field loops, at 400 km, as it was first observed by *Mitchell et al.*, [2001].

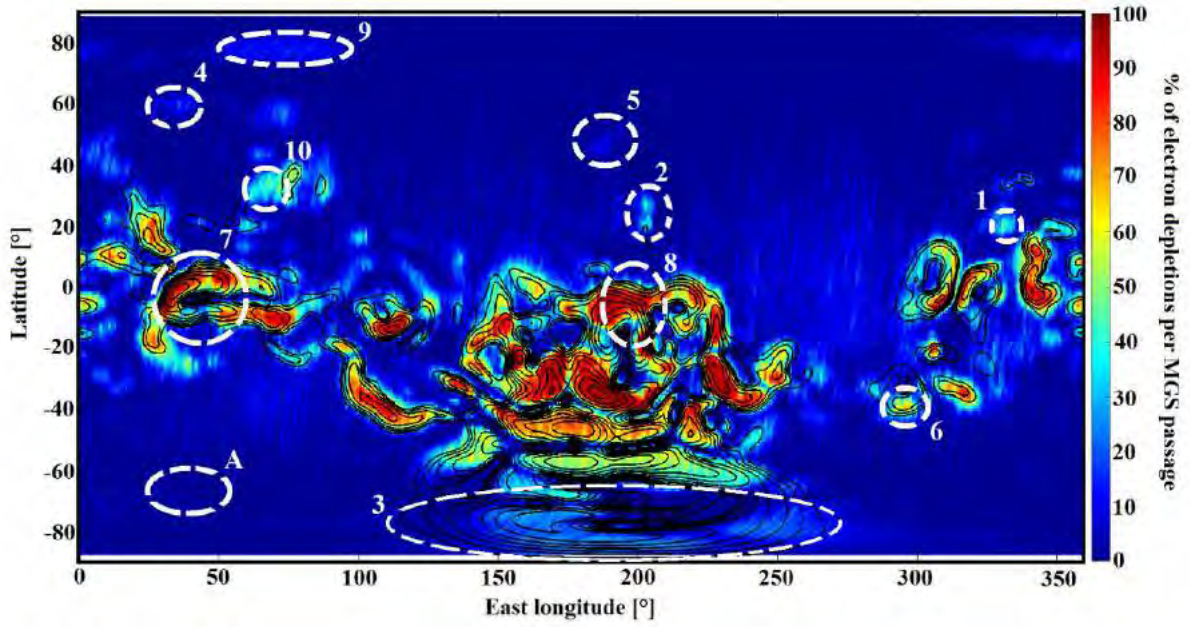

Figure 76. Density map of the electron depletions observed with MGS superimposed with horizontal crustal magnetic fields. The density map is the same as in Figure 74. In black are the horizontal magnetic field contour lines calculated from the model of Morschhauser at an altitude of 400 km. The contour lines have been plotted for horizontal crustal fields of 10, 13, 16, 20, 25, 32, 40, 50, 63, 79, and 100 nT. Circled in white are areas of interests, see description in the text.

The presence of permanent (100% of electron depletions detected per MGS passage in the nightside) and intermittent electron depletions can also be observed, as first reported by *Lillis and Brain*, [2013]. Permanent electron depletions seem to be coincident with the strongest horizontal crustal magnetic fields whereas intermittent ones are located over weaker crustal magnetic field sources or on the border of the strongest ones. This is consistent with the explanation proposed by *Lillis and Brain*, [2013]: closed crustal magnetic field loops of low intensity or the border of strong ones are most likely to be the first to open up to get connected to the IMF when the solar wind pressure increases. MGS data are particularly useful to study the permanent or intermittent nature of electron depletions as data have been sampled in a narrow range of altitudes.

Despite the global good consistency of Figure 76 with previous studies, several ugly duckling can be observed. Some depletions are located over weak horizontal crustal magnetic field areas, such as the first area circled in Figure 76: [340°E, 20°N], or are slightly shifted from the nearest crustal magnetic field source location, such as the second area circled in Figure 76: [200°E, 20°N]. Such depletions away from crustal magnetic sources may indicate the presence of loops of closed magnetic field lines connecting together crustal magnetic field sources in widely separated locations [*Brain et al.*, 2007], a distortion of the crustal magnetic field lines or more local, unmapped sources.

We can also notice that the large area with high horizontal crustal magnetic fields at high negative latitudes (circled area **#3**) does not fit well with high electron depletions density areas. This effect may be due to the **inclination of Mars** on its orbit which is about 25°. This implies seasons during which part of the polar regions are always in sunlight whereas they are considered as being in the nightside half of the time in this study due to the use of MSO coordinates. Thus, no electron depletion is detected during these periods which are however taken into account as MGS passage in the nightside. This effect is compared with MEX results in the next section (MAVEN does not cover this region).

4.1.2.2. Geographical distributions from 250 km to 900 km

In order to compare MAVEN and MEX observations, I chose to make a first map restricting MAVEN data to altitudes greater than 250 km. The MEX map is presented in section 4.1.2.2.1 and the MAVEN restricted map is presented in 4.1.2.2.2.

4.1.2.2.1. MEX observations

Figure 77 shows the density map of the electron depletions evaluated with criterion (2) for the MEX data. I chose to divide the surface of Mars into spatial bins of 2° by 2°, as there are less data points than for MGS (see Table 5). The color code corresponds to the percentage of electron depletions per MEX passage. For each bin I calculated the ratio between the number of time steps when an electron depletion is detected and the total number of time steps when MEX is in the nightside with an altitude below 900 km. There are on average 500 MEX observation time steps per bin. I have also superimposed logarithmically spaced (between 10

and 100 nT) contour lines of the horizontal crustal magnetic field calculated at 400 km altitude from the Morschhauser model, so that the map of MEX and MGS can be compared.

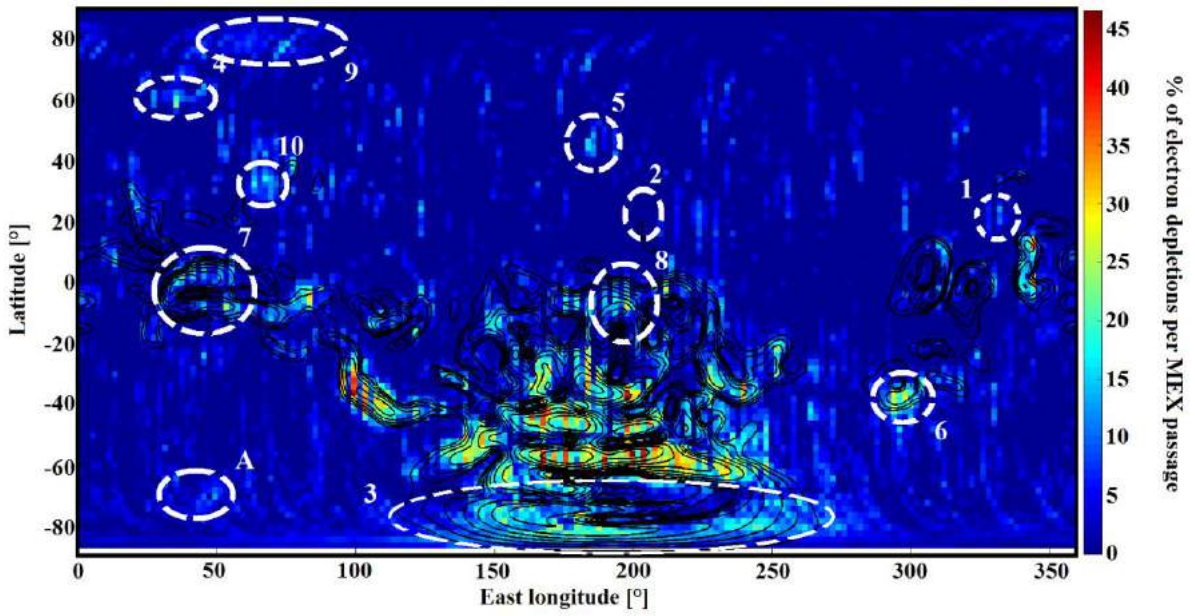

Figure 77. Density map of the geographical distribution of the electron depletions observed with MEX. In color, the percentages of electron depletions detected with criterion (2) from MEX data per MEX passage on the nightside on a geographic map of the Martian surface with constant bin size of 2° by 2°. In black, the horizontal magnetic field contour lines calculated from the model of Morschhauser at an altitude of 400 km. The contour lines have been plotted for horizontal crustal fields of 10, 13, 16, 20, 25, 32, 40, 50, 63, 79, and 100 nT. Circled in white are areas of interests, see description in the text.

As for the MGS map, we can see that the electron depletions are gathered over specific regions, a little less well-defined than in the MGS case, but globally localized over regions of strong horizontal crustal magnetic field, even if the correlation is less clear for small crustal magnetic field sources. Regions with strong concentration of electron depletions seems also to be surrounded by regions having moderate occurrence rate. However, this map is more difficult to read and to interpret than the one of MGS, which was really clear, for two main reasons. First, there is a **high level of noise**, though it has been drastically reduced thanks to the restriction in altitude (see section 3.4.3). Second, the percentage of electron depletions observed with MEX is globally much lower than with MGS. This effect is only due to the altitude range studied. MGS was at a roughly constant altitude for seven years, while for MEX we consider altitudes from 250 to 900 km. Some concentration of electron depletions (15-20%) can nonetheless be observed over areas without strong crustal magnetic fields such as the fourth [40°E, 60°N] or the fifth [180°E, 40°N] circled area. These two regions can also be found in

Figure 76, with very low percentages (circled area **#4** and **#5**). Circled region **#1** is hardly visible on Figure 77 while no enhancement can be observed at the location of the circled region **#2**.

The areas with strong crustal magnetic fields located at high southern latitudes are in a better agreement with the distribution of electron depletions in Figure 77 than in Figure 76. This difference with MGS may be due to the different ways MGS and MEX covered the Martian surface. MGS covered each latitude on the nightside on each orbit whereas MEX periapsis only covers the southern pole in the nightside during specific periods (due to its precessing orbit). Thus, depending on the seasons when these periods occurred, the percentages obtained in the southern polar region are shifted.

As previously mentioned, the percentages found in Figure 77 are much lower than those found in Figure 74 with MGS and do not enable us to analyze the presence of permanent and intermittent electron depletions. However, these percentages seem quite similar to those found by *Hall et al.* [2016]. Using the electron depletions automatically detected thanks to their criterion, *Hall et al.* [2016] produced an occurrence map (Figure 78) of the electron depletions observed with MEX during a similar time period as ours with a resolution of 15° by 15°, in order to emphasize large scale occurrences. This map highlights several areas where electron depletions are concentrated which are consistent with the ones observed on Figure 77, like the regions centered on [300°E, -40°N] (circled region **#6**) or [60°E, 0°N] (circled region **#7**). The two maps are comparable except for the regions centered on [200°E; -10°N] (circled region **#8**) where *Hall et al.* [2016] found their maximum occurrence of electron depletions. We here found for this region a percentage of $\sim 15-20\,\%$ with no real extension toward the Northern hemisphere but rather toward the Southern hemisphere where the maximum percentages are located, coincidentally with the strongest horizontal crustal magnetic fields.

Figure 76 and Figure 77 also revealed the presence of electron depletions in the region centered on [70°E, 80°N] (circled region **#9**) where a small crustal magnetic source exists but this is not observed by *Hall et al.* [2016], maybe due to the resolution chosen. Finally, the noise observed on Figure 77 has also been detected by *Hall et al.* [2016] who found a background level around 10% present all over their map. I here limit this noise by selecting events on the nightside and at altitudes below 900 km.

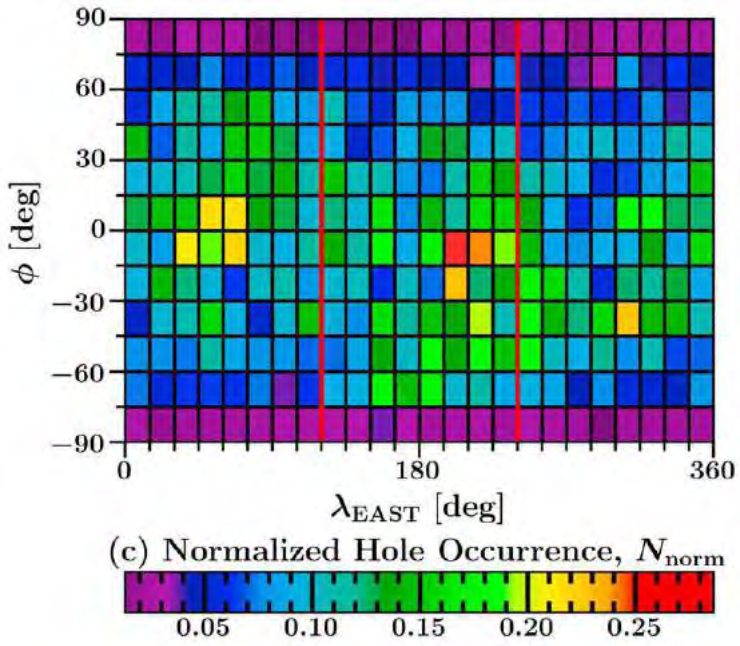

Figure 78. Density map of electron depletions occurrence obtained by Hall et al., [2016]. Electron hole occurrence normalized by orbital coverage (N_{norm}) at altitudes less than 1300 km above the surface of Mars. The map has a spatial resolution of 15°×15° latitude (φ) and east longitude (λ_E).

4.1.2.2.2. MAVEN: restricted to altitudes above 250 km

In Figure 79 is plotted the density map of the electron depletions evaluated with criterion (1) at altitudes greater than 250 km. I chose to divide the surface of Mars into spatial bins of 2° by 2°, as for the MEX map. As for Figure 74 and Figure 77 the color code corresponds to the percentage of electron depletions per MAVEN passage. For each bin I calculated the ratio between the number of time steps when an electron depletion is detected above 250 km and the total number of time steps when MAVEN is in the nightside with an altitude below 900 km and above 250 km. There are on average 227 MAVEN observation time steps per bin. I have also superimposed logarithmically spaced (between 10 and 100 nT) contour lines of the horizontal crustal magnetic field calculated at 400 km altitude from the Morschhauser model so that this map of MAVEN at high altitudes can be compared with the ones of MGS and MEX.

The map obtained with MAVEN data at high altitudes is quite similar to the MEX map, though the percentages are higher, certainly due to the recurrent passage of MAVEN at 250 km while MEX reached these altitudes only a few times. Electron depletions are in this case too gathered over regions of strong horizontal crustal magnetic field. However, as for MEX, it is difficult to judge of the permanent nature of electron depletions thanks to this map as it covers a large range of altitudes.

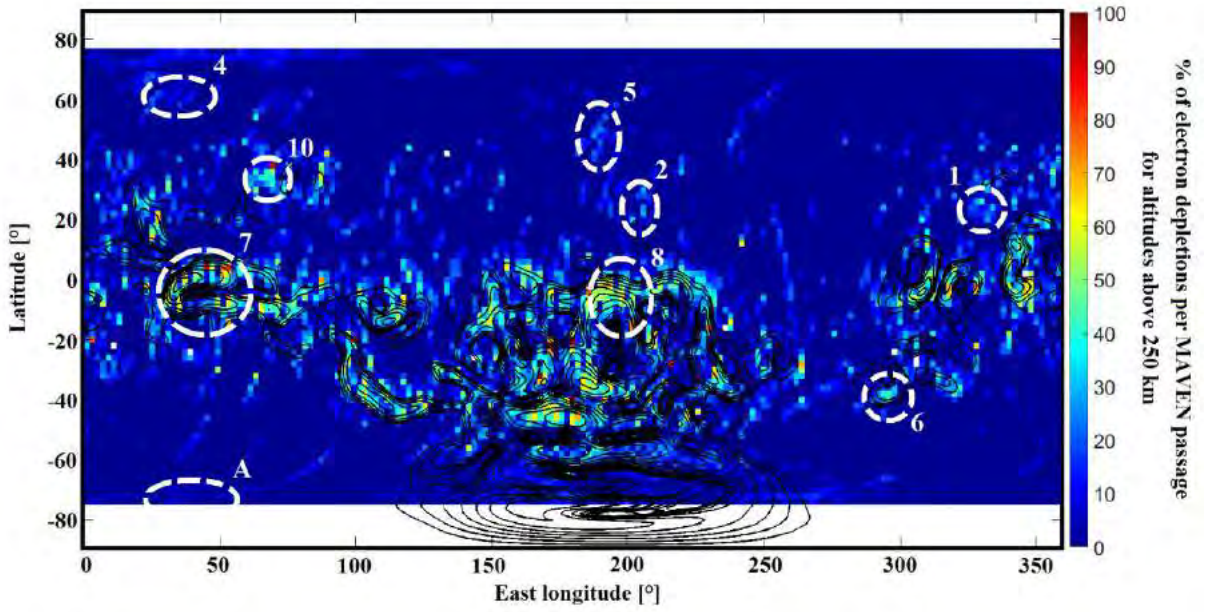

Figure 79. Density map of the geographical distribution of the electron depletions observed with MAVEN above 250 km. In color, the percentages of electron depletions detected above 250 km with criterion (1) from MAVEN data per MAVEN passage on the nightside on a geographic map of the Martian surface with constant bin size of 2° by 2°. In black, the horizontal magnetic field contour lines calculated from the model of Morschhauser at an altitude of 400 km. The contour lines have been plotted for horizontal crustal fields of 10, 13, 16, 20, 25, 32, 40, 50, 63, 79, and 100 nT. Circled in white are areas of interests, see description in the text.

Electron depletions which appear away from crustal magnetic sources in Figure 76 and Figure 77 (circled regions **#1**; **#2**; **#4**; **#5**) are still observed with MAVEN, though they less stand out. One region we clearly find on the three maps is the one at [70°E; 30°N] (circled region **#10**), in the middle of two weak crustal magnetic field sources. Regarding the distribution of crustal magnetic sources, this case is likely to correspond to loops of closed magnetic field connecting together crustal magnetic field sources in 'widely' separated locations.

The comparison of the geographical distribution of electron depletions obtained with the three datasets confirms the strong link existing between suprathermal electron depletions and closed crustal magnetic field lines, at least down to 250 km. Electron depletions are mainly observed above crustal magnetic sources, and few events are observed away from them. Thanks to MAVEN, we can now dive down to ~125 km to observe if this link still exists at low altitudes.

4.1.3. Going down to 125 km altitudes with MAVEN

In Figure 72 we observed that the altitude distribution of electron depletions presents a sharp acceleration downward ~170 km. We then first propose a map of the distribution of electron depletions for altitudes between 170 and 250 km (section 4.1.3.1) and then for altitudes below 170 km (section 4.1.3.2). This will enable us to understand the link between the crustal magnetic sources and the different altitude regimes of the electron depletions.

4.1.3.1. From 250 to 170 km

In Figure 80 is plotted the density map of electron depletions detected by MAVEN at altitudes between 170 and 250 km. As for Figure 79 I calculated the number of time steps when electron depletions are detected in spatial bins of 3° longitude by 3° latitude and divided it by the number of time steps when MAVEN is in the nightside at altitudes between 250 and 170 km in each bin. I chose for this map a lower spatial resolution as the MAVEN coverage of the Martian surface decreases with altitude. There are for this map an average of 147 MAVEN passages per bin. The density map is superimposed with a map of the horizontal crustal field calculated at 170 km with the Morschhauser model. The contour lines are logarithmically spaced between 10 and 1000 nT.

We can observe that the electron depletions are far more spread on the Martian surface than on the maps obtained for altitudes above 250 km. As the altitude decreases, the crustal magnetic field sources get more numerous and more resolved (see Figure 51 and Figure 52), and the amplitude of the magnetic field increases. The extension of the sources compared to the bin size makes it difficult to observe a clear correlation between the distribution of the electron depletions and the extension of the different sources. However, the general contours of both area with high electron depletions percentages and high horizontal crustal magnetic fields are in good agreement.

The variability of the percentage of electron depletions per MAVEN passage seems to support the idea of permanent and intermittent electron depletions. Hence, percentages close to 100% are preferentially observed near the local maxima of horizontal crustal magnetic fields whereas lower percentages are observed far from crustal magnetic field sources, which means that electron depletions are not always present when MAVEN observes these regions. However, as the MAVEN coverage is still not as fine as the one of MGS, we cannot state that permanent

electron depletions are surrounded by intermittent ones as it was observed on MGS distribution, but we can see a trend emerge.

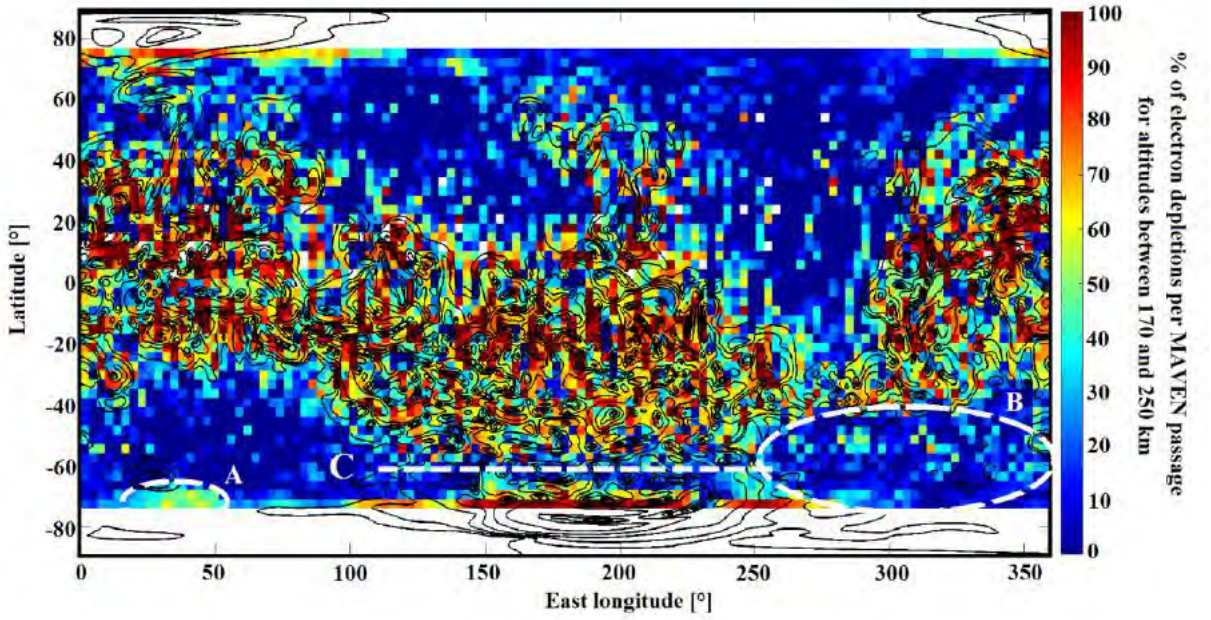

Figure 80. Density map of the electron depletions observed with MAVEN between 170 and 250 km altitude. In color, the percentages of electron depletions detected above 250 km with criterion (1) from MAVEN data per MAVEN passage on the nightside on a geographic map of the Martian surface with constant bin size of 3° by 3°. In black, the horizontal magnetic field contour lines calculated from the model of Morschhauser at an altitude of 170 km. The contour lines have been plotted for horizontal crustal fields of 10, 18, 32, 56, 100, 178, 316, 562 and 1000 nT. Circled in white are areas of interests, see description in the text.

As most of electron depletions are observed above strong horizontal crustal magnetic field, we still can observe aggregates of electron depletions far from crustal sources, such as the clear and well delimited structure at [40°E; 70°S] (circled region **A** in Figure 80). This structure slightly appears in the MEX map but not on the MGS one. Observing the neighboring magnetic topology, a small crustal magnetic source can be observed northward, slightly shifted westward. This shift has already been observed on MGS and could be attributed to a distortion of the magnetic field lines with altitude. The percentage of events far from crustal sources is globally higher than in Figure 79, especially in the circled region **B**. Hence, a **transition** in the distribution of electron depletions is being observed.

4.1.3.2. Below 170 km

In Figure 81 is plotted the density maps of electron depletions detected with MAVEN for altitudes below 170 km. In the same way as for Figure 80, I calculated the number of time steps when electron depletions are detected in spatial bins of 3° longitude by 3° latitude and divided it by the number of time steps when MAVEN is in the nightside below 170 km in each bin. There are on average 138 time steps per bin. The density map is superimposed with a map of the horizontal crustal field calculated at 170 km with the Morschhauser model. The contour lines are logarithmically spaced between 10 and 1000 nT.

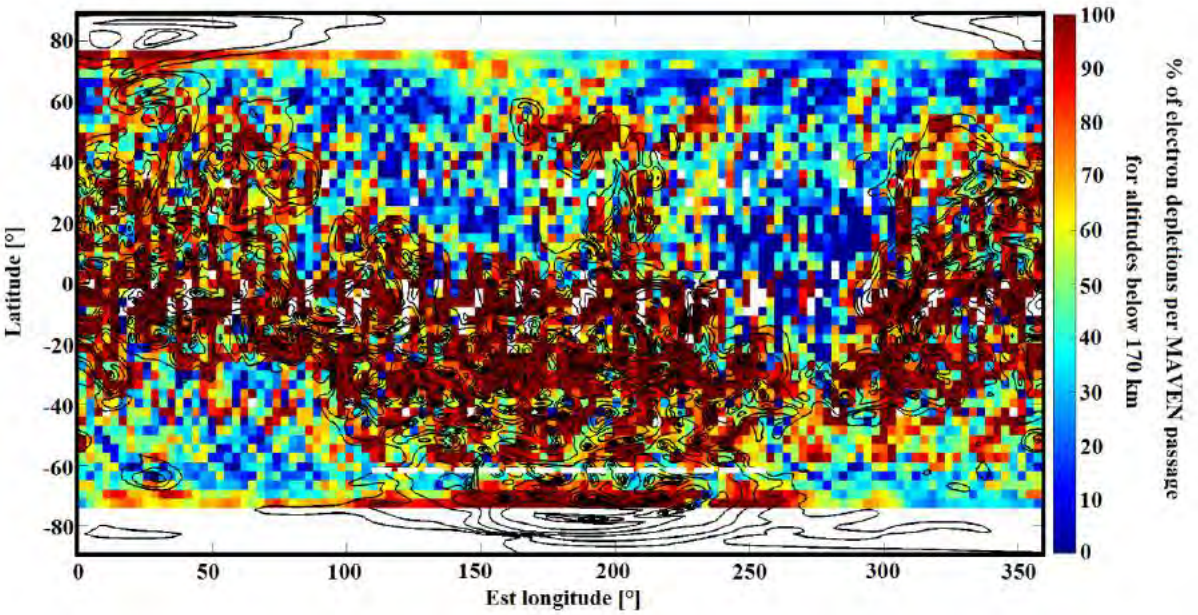

Figure 81. Density map of electron depletions observed with MAVEN at altitudes below 170 km. In color, the percentages of electron depletions detected below 170 km with criterion (1) from MAVEN data per MAVEN passage on the nightside on a geographic map of the Martian surface with constant bin size of 3° by 3°. In black, the horizontal magnetic field contour lines calculated from the model of Morschhauser at an altitude of 170 km. The contour lines have been plotted for horizontal crustal fields of 10, 18, 32, 56, 100, 178, 316, 562 and 1000 nT.

We can see that the highest percentages of electron depletions are still localized above strong crustal magnetic field sources but we can also notice that the global distribution is far **more homogeneous** than for the distribution above 170 km, regardless the horizontal magnetic field. A mean percentage of 61% can be observed above the whole surface. Above the whole surface? No! A small region populated by irreducible volcanoes resists again and again to the invader. The region of the **Tharsis Mons** (delimited in black in Figure 82. Be careful, a different

longitude reference is used in this figure compared to the maps presented through sections 4.1.2 and 4.1.3), shows the lowest percentages of electron depletions observations. This region corresponds to the region with the lowest crustal magnetization. This observation is investigated in more details in section 5.2.2.3.

An interesting common feature to Figure 80 and Figure 81 is the line at ~-65°N (white horizontal dashed line), at which we can observe a drop in the percentage of electron depletions while strong crustal magnetic sources are present. This behavior, highly unexpected, is not yet understood. This region has only been covered during the second period (see Figure 69), which may have induced an orbital bias.

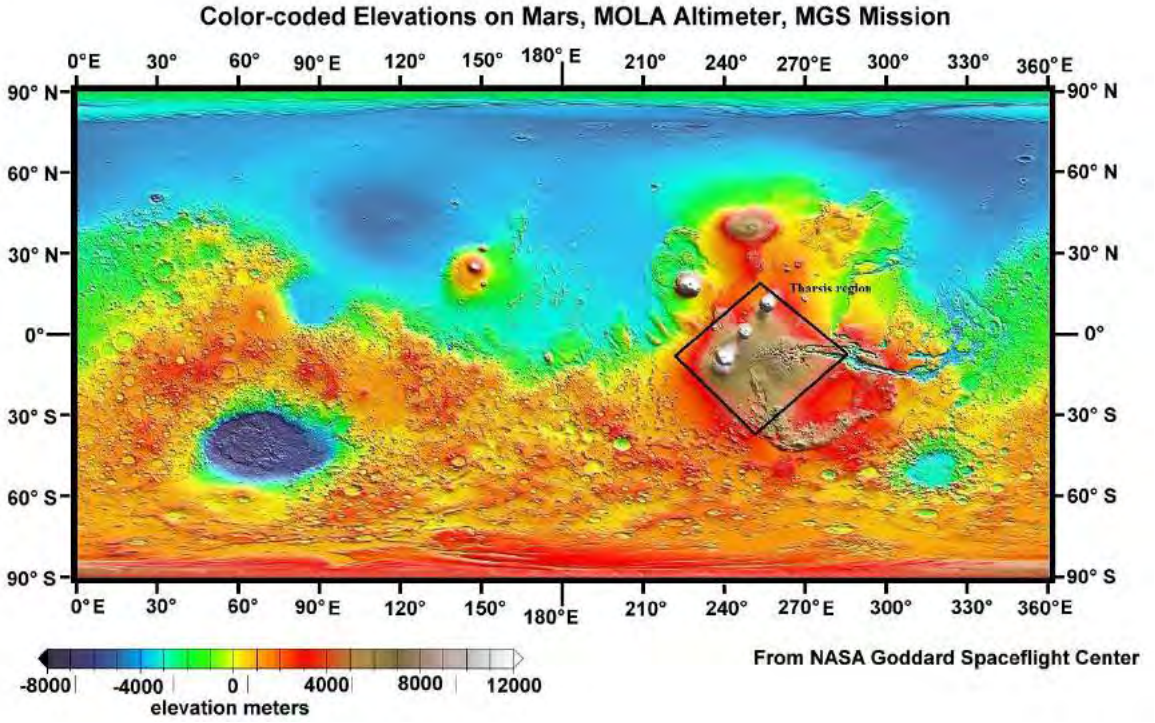

Figure 82. High resolution topographic map of Mars obtained thanks to the MOLA altimeter onboard MGS.

This evolution of the distribution of electron depletions with altitude has also been highlighted by *Xu et al.*, [2017]. The basic idea of this study is to examine if ionospheric photoelectrons or solar wind electrons are detected in the magnetic field parallel and anti-parallel directions, in order to infer the magnetic topology. This leads to the creation of a pitch angle-resolved shape parameter, leading to the determination of the magnetic configuration (Figure 22) observed. As in *Brain et al.* [2007], electron depletions are detected in this method as low omnidirectional electron fluxes. However, this study is restricted to altitudes above 160 km, which is the mean altitude of the electron exobase calculated by *Xu et al.*, [2016a].

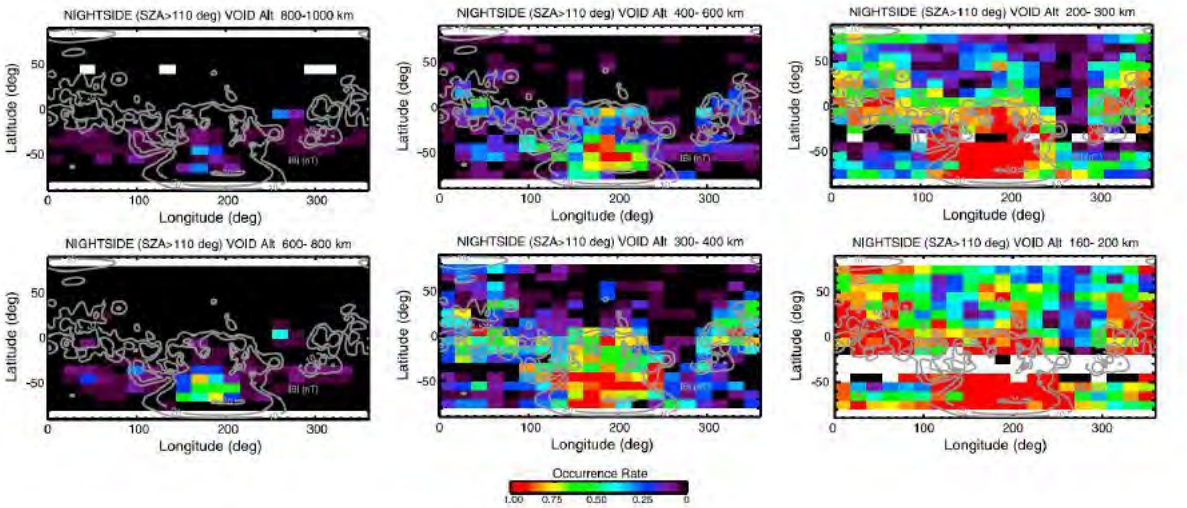

Figure 83. Maps of electron depletions on the nightside (SZA>110°), from Xu et al., [2017]. The color stands for the occurrence rate. The color scale is from 0 (black) to 1 (red). The data are divided into 18° × 10° *geographic longitude-latitude bins. Each plot is for the altitude range of 800-1000 km, 600-800 km, 400-600 km, 300-400 km, 200-300 km and 160-200 km, respectively. The gray contours are the modeled crustal magnetic field magnitude at 400 km, from the Morschhauser model.*

The distributions of electron depletions calculated by *Xu et al.*, [2017] for six different range of altitudes are plotted in Figure 83. We clearly observe that electron depletions are first populating the highest crustal magnetic field regions and spread toward lowest crustal magnetic field regions. Below 200 km, electron depletions occurrence is greater than 50% over most of the nightside and nearly 100% over the strongest crustal magnetic field sources, which is consistent with Figure 81. We can notice that the Tharsis Mons region is also in this study the region with the fewest occurrence of electron depletions.

4.2. A competition between two main loss processes

A clear altitude dependence exists in the distribution of electron depletions. At high altitudes, they are mainly coincident with strong horizontal crustal magnetic fields, while at low altitudes, their distribution becomes more and more homogeneous, with observations of electron depletions over the whole surface. Hence, we can wonder if the electron depletions observed above crustal magnetic sources are the same structures and are resulting from the same processes as electron depletions observed above weak crustal magnetic field area. In order to answer these questions, we propose in section 4.2.1 to look at the plasma composition of all (but not each) electron depletions detected by MAVEN. We then observe the influence of the crustal magnetic fields on the distribution of electron depletions in section 4.2.2.

4.2.1. Plasma composition of suprathermal electron depletions

In Figure 84 are plotted data recorded by SWEA, STATIC and MAG, only during time intervals when an electron depletion has been detected by criterion (1). In orange are highlighted the five time periods during which electron depletions have been recorded and in brown are highlighted time periods during which STATIC did not record data at low energy due to a change of instrument mode. We added in the bottom panel the altitude where electron depletions have been detected.

The different coverages of the Martian surface corresponding to the different time periods stand out in the two bottom panels. Keeping in mind Figure 69, the events of the first and third periods are detected at low altitudes, above weak crustal magnetic sources, corresponding to the sampling of the northern hemisphere. In contrast, events recorded during the other three time periods reached higher altitudes and are located over stronger crustal magnetic sources. These three periods correspond to the sampling of the southern hemisphere.

This plot gathers all the different types of electron depletions, both located over strong crustal magnetic sources and over regions with no significant presence of crustal magnetic fields. However, we can see that the characteristics of the main electron and ion populations are surprisingly **stable over time and space**. The energy of the ions is peaked at 3 eV, varying from ~2 eV to ~4 eV, which is consistent with the ram energy of the main ion species that can

be observed at these altitudes: O^+ and O_2^+ (see section 3.2.2). Several other lines can be observed on the STATIC mass-time spectrogram. The one at ~44 eV coincides with CO_2^+, while the others are much likely to be **ghost peaks** (anomalous mass peaks). Ghost peaks are spurious time-of-flight signals with peaked m/q values other than those expected for the ideal analyzer. They result from internal scattering of ions, variations in ion charge state or from molecular breakup (see *McFadden et al.*, [2015] for more details).

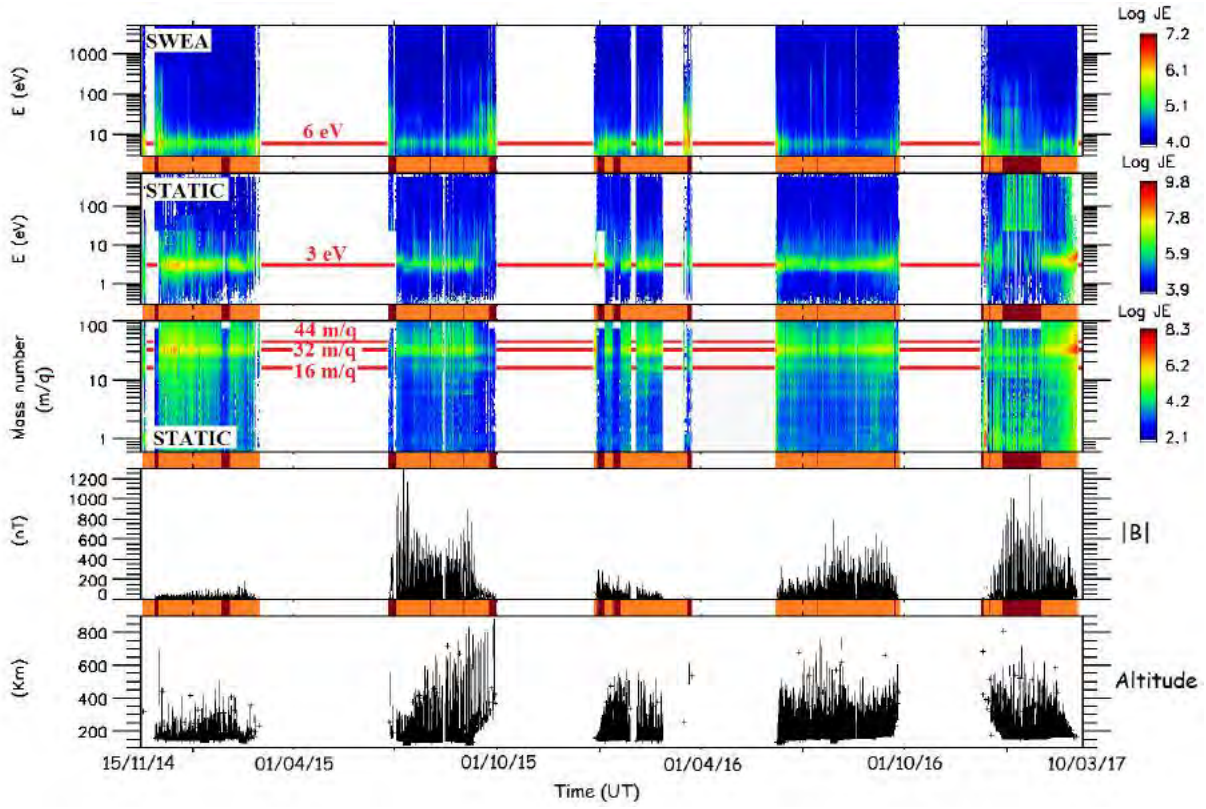

Figure 84. Concatenation of all time intervals when electron depletions have been detected by criterion (1). Panel 1: SWEA energy-time spectrogram of omnidirectional electron energy flux. Panel 2: STATIC energy-time spectrogram of omnidirectional ion energy flux. Panel 3: STATIC mass-time spectrogram of omnidirectional ion energy flux. Panel 4: Amplitude of the magnetic field measured by MAG. Panel 5: Altitude of the spacecraft.

Concerning the electron population, it is peaked at a constant energy of ~6-7 eV, regardless the altitude or the magnitude of the magnetic field. The several spikes that can be observed at higher energies, up to a hundred eV, correspond to the border of electron depletions, which sometimes overflow on flux spikes. The case of the fifth period is quite singular. As mentioned in section 3.3.1, December 2016 and January 2017 have been two months during which strong spacecraft charging events have been recorded. As they were in this specific case located near the terminator, their presence affected the detection of electron depletions so that large portions of other plasma regions are plotted in Figure 84 for this time period (this issue is

discussed in more details in section 5.2.1.2). Moreover, as during these charging events the spacecraft potential was highly negative (~-20 V), the peak of the remaining electron distribution has been shifted toward lower energies so that it is not visible on SWEA data.

I chose for this plot not to correct the data for the spacecraft potential. The spacecraft potential is indeed difficult to determine in this region and the quality flag associated with the potential measured by LPW is usually lower than 50, which means that it is not reliable. Instead of having a figure with both corrected and uncorrected data, I chose to only keep uncorrected data. However, as the spacecraft potential is usually at ~-2V, except for the fifth period, we can see that the peak at ~6-7 eV is relatively stable.

We saw in section 3.2.2.2 that the typical electron spectrum recorded inside electron depletions — no suprathermal electron observed above ~12 eV and below ~4 eV and a remaining electron population observed between 4 and 12 eV — is consistent with the total scattering cross section for electron collisions with CO_2, which is the most abundant neutral at altitudes below ~200 km (Figure 8). In Figure 85 are plotted the different cross sections for electron collisions with atomic oxygen (a), carbon dioxide (b), nitrogen molecules (c), and oxygen molecules (d) [*Itikawa et al.*, 1986, 1989; *Itikawa and Ichimura*, 1990; *Itikawa*, 2002], which are the dominant neutrals in the Martian atmosphere at the altitudes of interest (Figure 8). On each panel are plotted the corresponding cross sections for several specific mechanisms, such as ionization, elastic-scattering, momentum transfer, vibrational excitation, etc. We here only focus on the portion of the cross sections corresponding to energies greater than ~2eV.

At first, the total scattering cross section (and the elastic cross section for O) can be compared among the different species. The CO_2 and N_2 cross sections are clearly larger than the two other ones. The CO_2 total cross section presents a specific shape, with two strong dips at ~2 and ~6 eV and two strong peaks at 4 and 30 eV. We saw in Figure 62 that this specific shape well corresponds to the observed electron populations inside electron depletions, each peak corresponding to a depleted electron population and each dip to a remaining electron population.

The interaction between electrons and CO_2 is actually diverse. When electrons collide with atomic or molecular targets, a large variety of reactions can take place, such as elastic scattering, momentum transfer, excitation of vibrational and electronic states, ionization, and electron attachment:

- **Elastic-scattering**: the total kinetic energy of the system is conserved, only the direction of propagation of the projectile is modified by its interaction with the target. Elastic scattering

implies no breaking up of the particles or energy loss through vibrations. This process is the most important for high energy electron collisions with CO_2.

- **Momentum transfer**: during the scattering of two colliding particles, the total momentum of the system is conserved. If the neutral target is initially at rest, the momentum of the incident electron is distributed between the two scattered particles. This process is the most important for low energy electrons colliding with CO_2.

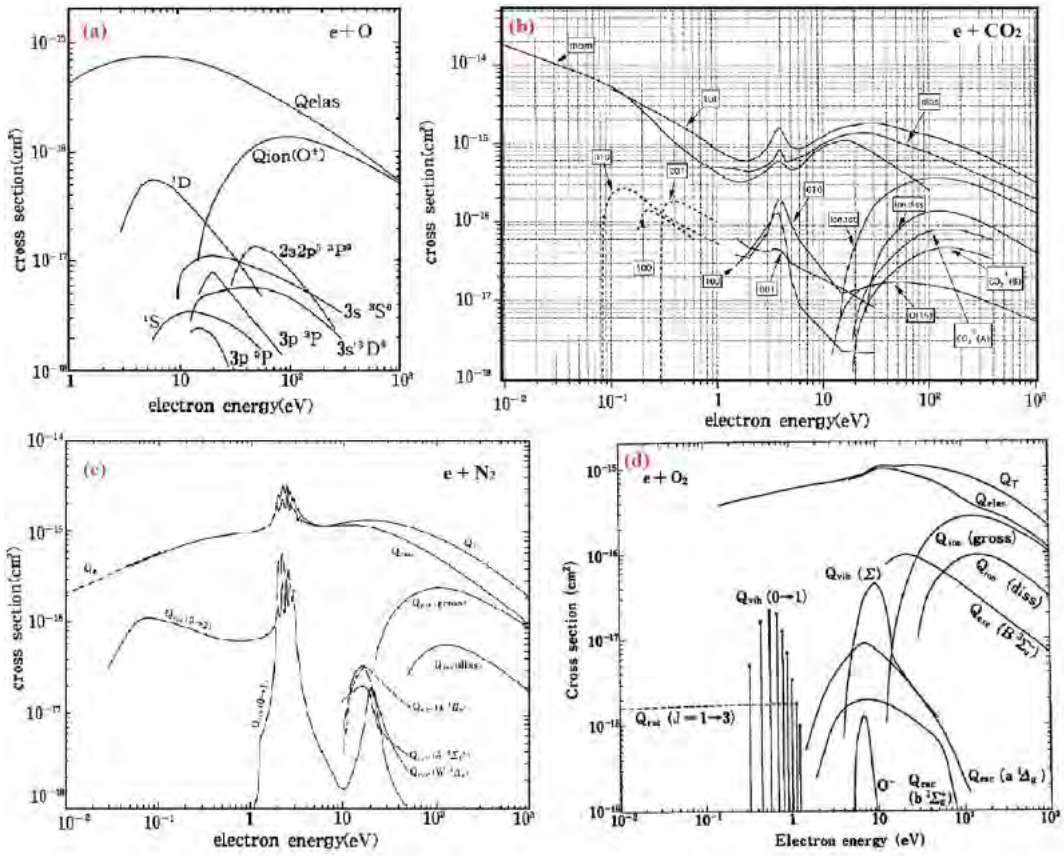

Figure 85. Summary of the cross sections for the electron collision with the main neutrals of the atmosphere: (a) Electron collision with atomic oxygen [Itikawa and Ichimura, 1989*]; (b) Electron collision with carbon dioxide [Itikawa,* 2002*]. The labels (100), (010) and (001) refers to excitation of the different vibrational state ; (c) Electron collision with nitrogen molecules [Itikawa et al.,* 1986*]; (d) Electron collision with oxygen molecules [Itikawa,* 1988].

- **Excitation of vibrational and electronic states**: a molecular vibration occurs when atoms in a molecule are in periodic motion at the vibration frequency. CO_2 has three normal modes of vibration ((001), (010), and (100)). A molecular vibration is excited when the molecule absorbs a quantum of energy corresponding to the vibration frequency. Vibrational excitation can occur in conjunction with electronic excitation: electrons of the molecule receive additional

energy from an incident energetic electron so that they can change to a more energetic bound state. These processes are important for low energy electrons, but also for the peak observed at ~4 eV in the total cross section.

- **Ionization**: when an electron collides with a CO_2 molecule, many different kinds of positive ions can be produced by ionization by electronic impact (see section 1.2.1.1), such as: $CO_2^+, CO^+, O^+, C^+, CO_2^{++}, C^{++}$ or O^{++}.

- **Electron attachment**: ionization of a gas phase atom or molecule A by attachment of an electron to create a negative ion:

$$A + e^- \rightarrow A^-$$

Ions such as O^- and C^- can be produced by dissociation following electron attachement with CO_2.

The evolution of the flux of particles Φ (in our case electrons) travelling through a layer of material (in our case the atmosphere) is given by:

$$\Phi = \Phi_0 e^{-n\sigma z}$$

Where Φ_0 is the initial flux, z the thickness of the layer of material, n the density of the target particles and σ the cross section corresponding to the process under study. The larger the cross section, the larger the decrease of the flux of particles. We can see in Figure 85 that the main processes involved in the peak observed at ~4 eV on the total cross section for the electron collision with CO_2 are: momentum transfer, elastic scattering and several excitation modes of CO_2. The elastic scattering is not involved in electron absorption by CO_2 as only their direction is modified following the collision. The two other processes are not directly electron loss processes: they gradually **thermalize** electrons. Electrons give part of their energy to target neutrals so that they are eventually removed from the suprathermal electron population observed by SWEA, and join the ranks of the thermal population. Concerning the peak at higher energies (~30 eV), the main processes involved are momentum transfer, elastic scattering, ionization and electron attachment. The two last processes induce a **direct loss** of electrons. **Momentum** transfer seems to be the main process involved in the electron absorption observed inside suprathermal electron depletions.

The other neutral cross sections presented in Figure 85 do not present such structures that can explain the presence of the peaked remaining electron population inside the electron depletions. **Electron absorption by the atmospheric CO_2** seems to be the best candidate to explain the specific electron populations observed inside electron depletions. However, absorption by other neutrals can also be involved in the global depletion of electrons.

All electron depletions have then the same plasma composition, wherever they are located. They are all filled with cold heavy ions with the ram energy and with the electron populations remaining after absorption by atmospheric CO_2.

4.2.2. The role of crustal magnetic sources

As the altitude decreases, strong crustal magnetic sources are the first places where electron depletions are observed. However, at low enough altitudes they do not seem to be anymore necessary for electron depletions to be observed. We here investigate the influence of crustal magnetic sources on the observation of suprathermal electron depletions. In section 4.2.2.1 is proposed a comparison of the distribution of electron depletions between the northern and the southern hemisphere. In section 4.2.2.2 we then investigate the influence of the amplitude of the crustal magnetic fields on the altitude distribution of electron depletions. Finally, in section 4.2.2.3 we implement an analysis of the pressure balance within electron depletions.

4.2.2.1. Comparison between the northern and southern hemispheres with both MAVEN and MEX

In order to study the influence of the magnitude of the crustal magnetic field on the distribution of suprathermal electron depletions, I chose to first compare the distributions obtained during the two first periods when MAVEN detected electron depletions (see Figure 69). During these two periods the spacecraft only recorded data above the northern hemisphere (latitudes > 20°N), where few crustal magnetic field sources are located, and above the southern hemisphere (latitudes < -20°N), where the strongest crustal magnetic field sources are located, respectively.

I also include MEX observations of the electron depletions detected in the same range of latitudes. For both spacecraft I took an altitude resolution of 2 km, which represents ~10 000 MEX passages per bin and ~2 600 MAVEN passages per bin, on average. For each bin I calculated the number of time steps when electron depletions are detected and the number of time steps when the spacecraft is in the nightside. The ratio gives the percentage of electron depletions among the spacecraft passages in each altitude bin. The MGS observations previously discussed are not applicable to this analysis, since the spacecraft had a circular orbit with an almost constant altitude.

Figure 86 shows the percentage of electron depletions detected along the MAVEN and MEX passages as a function of altitude. The red and green profiles correspond to observations made above the southern hemisphere, whilst the blue and black profiles correspond to observations made above the northern hemisphere. We can notice that MEX data are only available down to 307 km in the northern hemisphere whereas they are available down to 245 km in the southern hemisphere. This difference is only due to MEX orbital geometry.

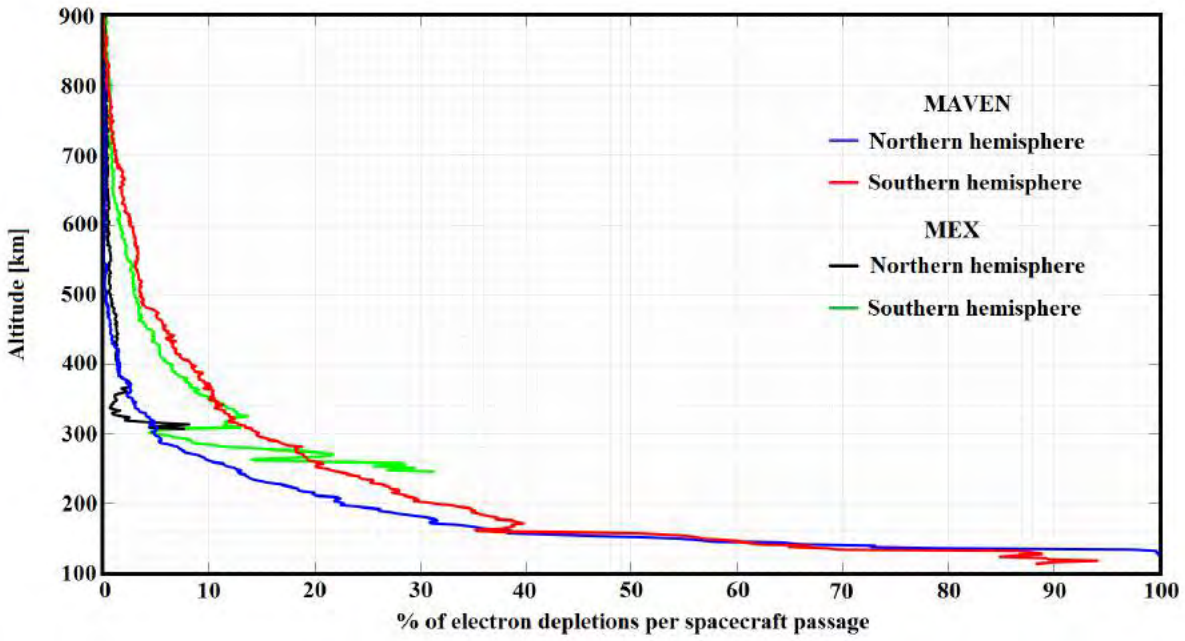

Figure 86. Comparison of the altitude distribution of electron depletions between both hemispheres. Percentages of electron depletions detected by criterion (1) among MAVEN passages (in blue and red) and by criterion (2) among MEX passages (in black and green) calculated in bins of 2 km altitude. The red and green lines correspond to the depletions observed in the Southern Hemisphere, and the red and black lines correspond to the depletions detected in the Northern Hemisphere.

We can see that the MEX and MAVEN data match well between 900 and 300 km. In this range of altitudes, both datasets show that there is far more chance to detect an electron

depletion in the southern hemisphere than in the northern hemisphere. Between 300 and 245 km, as data are no more recorded by MEX in the northern hemisphere, there are still some in the southern hemisphere. Although strong variations can be observed on MEX data, we can see that the profile follows the trend set by MAVEN data. These variations may be due to the range of altitudes which is beneath the MEX nominal periapsis and hence sparsely covered by the spacecraft.

For altitudes greater than 500 km, *Hall et al.* [2016] found that the normalized occurrence of electron depletions was less than 5% across the majority of latitudes and altitudes, except for the strongest crustal magnetic field regions around which the majority of the events are distributed and where enhanced occurrence are then detected up to 1 000 km. This is consistent with the results obtained in Figure 86 even if the percentages are lower than those found by *Hall et al.* [2016] (maybe due to not taking into account the equatorial region): 1% in the Northern hemisphere and 3% in the Southern hemisphere at 500 km. Below 500 km, the occurrence of electron depletions increases rapidly in both studies. The main difference is that *Hall et al.* [2016] found that below 500 km the distribution of electron depletions becomes more homogeneous, even if the higher occurrence are still located above the strongest crustal magnetic fields area. In Figure 86 we clearly see that there are more electron depletions detected by MEX in the southern hemisphere than in the northern hemisphere, at least until 300 km. The difference between the two hemispheres even increases between 500 km and 300 km. Such difference between the two studies is not yet understood.

Where MEX ceases to record data, MAVEN continues to observe electron depletions at lower altitudes. We can see that the difference in percentage between the southern and the northern hemispheres persists until a transition region near 160-170 km altitude, where the two curves join and stay close until 125 km. Hence, while at high altitudes more electron depletions are observed in the hemisphere with the strongest crustal magnetic sources, at low altitudes the electron depletion distribution seems not to depend on the hemisphere.

4.2.2.2. Evolution of the altitude distribution of electron depletions with crustal magnetic field amplitude

As more electron depletions are detected at high altitudes in the hemisphere where the strongest crustal magnetic sources are located, we here investigate the influence of the

amplitude of the crustal magnetic field on the observation of electron depletions. In order to be able to compare the different electron depletions observed at different altitudes, I calculated for each event the corresponding value of the magnitude of the crustal magnetic field, at a common altitude of 170 km. In Figure 87 is plotted the altitude distribution of the electron depletions detected by MAVEN, as a function of the magnitude of the crustal magnetic field at 170 km calculated from the Morschhauser model. I chose six ranges of magnetic field amplitude, containing enough observations to be relevant.

The trend observed with the comparison of the two hemispheres turns out to be a more global trend. We clearly can see that the percentage of electron depletions observed at a given altitude increases with the strength of the underlying crustal magnetic sources. At 300 km altitude, the percentage of observations made above the weakest crustal magnetic field sources is 2% while above the greatest ones it is 40%. This gap between weak and strong crustal magnetic fields widens with decreasing altitude, until about 200 km where the gap between the profiles starts to decrease toward the lowest altitudes.

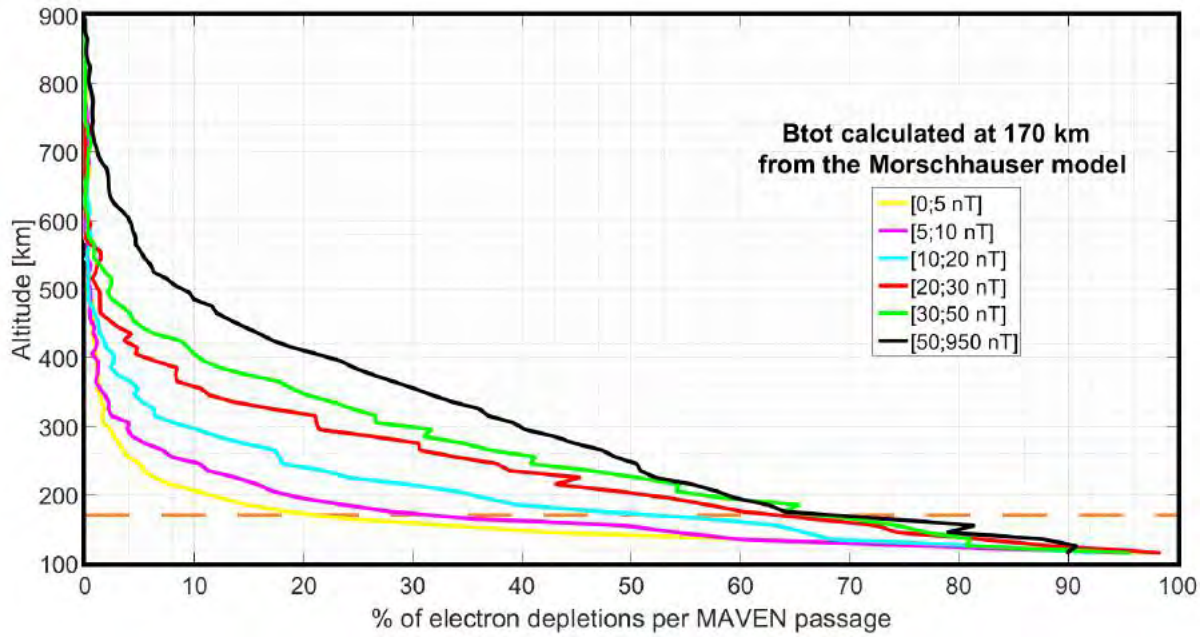

Figure 87. Influence of the strength of crustal magnetic sources on the distribution of electron depletions. Percentages of electron depletions detected by criterion (1) among MAVEN passages calculated in bins of 2 km altitude. Data are binned regarding the amplitude of the crustal magnetic field calculated from the Morschhauser model at 170 km altitude. The orange dashed line corresponds to 170 km altitude.

4.2.2.3. Pressure balance

We saw in section 1.3.2.2 that the different boundaries in the Martian environment are usually due to a pressure balance between the inner and the outer regions. In our case, closed crustal magnetic field loops, in which the magnetic pressure $B^2/2\mu_0$ is dominant, are embedded in the nightside ionosphere, in which the thermal pressure of low energy particles nk_BT is dominant. In order to confirm the relative importance of these two pressures for the observation of electron depletions, I calculate them in the following way:

- **Magnetic pressure:** I use both the in-situ amplitude of the magnetic field measured by MAG and the amplitude of the magnetic field calculated at the position of the spacecraft thanks to the Morschhauser model. The crustal magnetic pressure is restricted to altitudes below 400 km (see section 2.6).
- **Thermal pressure:** I consider for this study that the electron density is the same as the ion density. I use a typical altitude profile of electron temperature in the nightside [*Hanson and Mantas, 1988*] and the electron density profile calculated by *Lillis et al.* [2009] (Figure 88). In-situ data from LPW are not used for the calculation of thermal pressure as they are not always available and the associated quality flag is usually not good enough for the data to be used.

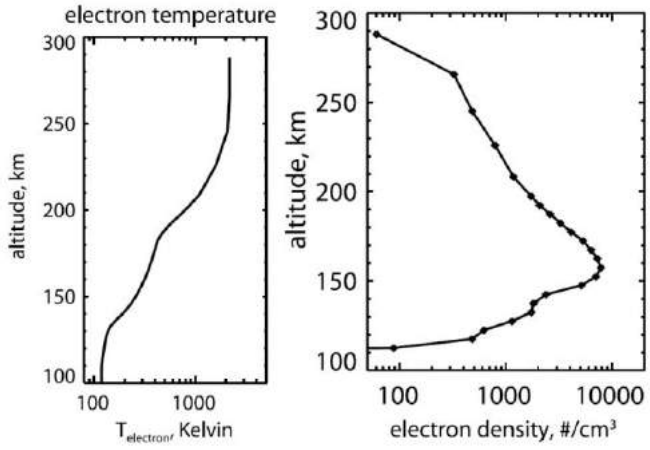

Figure 88. Altitude profile of the electron temperature and density used to calculate the thermal pressure. Left panel: Typical electron temperature in the nightside as a function of altitude, from Hanson and Mantas [1988]. *Right panel: Typical electron density profile calculated by Lillis et al.* [2009].

For each time step during which an electron depletion has been observed, I calculated the ratio between the magnetic pressure and the thermal pressure at that point (corresponding to $1/\beta$). I then binned our data into 60 logarithmically spaced bins. As we saw in section 4.1

that the distribution of electron depletions is different above and below a mean altitude of 170 km, I treat this two ranges of altitudes separately. In Figure 89 is plotted the percentage of electron depletions detected per MAVEN passage, above 200 km altitude on the left side and below 170 km on the right side, as a function of the ratio magnetic pressure/thermal pressure. Shaded areas correspond to less than 50 time steps during which electron depletions have been recorded. The two distributions corresponding to in-situ (**blue**) and crustal magnetic fields (**red**) are plotted separately.

First looking at high altitudes (left panel), we can see that few electron depletions are observed when the thermal pressure is greater than the magnetic pressure. A plateau at ~5% can be observed when the thermal pressure exceeds the crustal magnetic pressure whereas almost none electron depletions can be observed for the calculation made with the in-situ magnetic pressure. These electron depletions are thus coincident with thermal pressure exceeding crustal magnetic pressure but not in-situ magnetic pressure, which implies the presence of induced magnetic field. The percentage of electron depletions observed then takes off from a ratio of ~0.6 and reaches the pressure equilibrium at 5-10%. These electron depletions observed at high altitudes where the thermal pressure dominates both the crustal and in-situ magnetic pressure are likely to correspond to those observed far or shifted from crustal magnetic sources, as previously observed in Figure 76, Figure 77, and Figure 79.

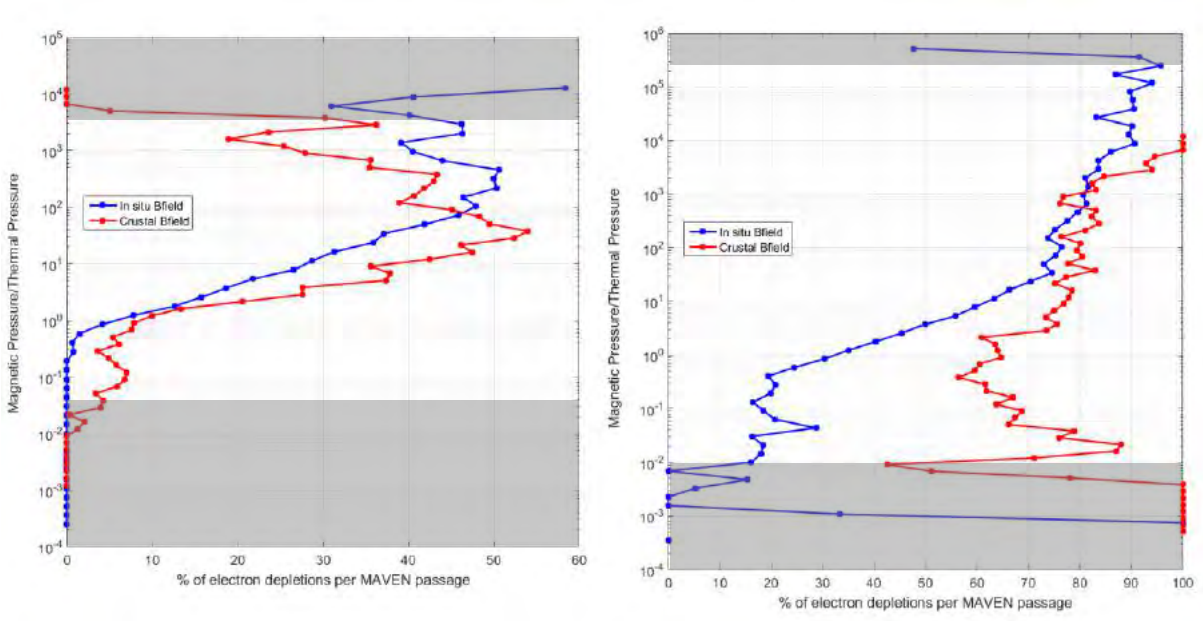

Figure 89. Pressure balance analysis inside suprathermal electron depletions.
*Percentage of electron depletions per MAVEN passage as a function of the ratio magnetic pressure over thermal pressure. In situ (**blue**) and calculated from the Morschhauser model (**red**) magnetic fields are taken into account. Left panel: Electron depletions detected above 200 km. Right panel: Electron depletions detected below 170 km.*

As the in-situ magnetic pressure becomes dominant versus the thermal pressure, the percentage of electron depletions observed increases until reaching a maximum value of ~50% for a ratio of several hundreds. The percentage of electron depletions observed then reaches a plateau at 40-50%. Therefore, the stronger the in-situ magnetic field is, the more electron depletions can be observed, until some threshold when increasing the magnetic field does not increase the percentage of electron depletions observed. The ratio calculated for the crustal magnetic pressure globally follows the same trend, except that the percentage of electron depletions observed seems to decrease with increasing ratio after it reaches its maximum for a ratio of ~40. The difference between the two distributions mainly comes from induced magnetic fields which may exist in the nightside ionosphere, influencing the pressure ratio.

Regarding the low altitudes (right panel), we first observe that high percentages of electron depletions are observed when the thermal pressure is dominant: ~20% for in-situ magnetic pressure and ~60-70% for crustal magnetic pressure. Concerning the ratio calculated with the crustal magnetic pressure, the percentage of electron depletions observed is relatively stable, with a minimum at the pressure equilibrium, followed by a slow increase (compared to low altitudes) at higher pressure ratio. This implies the involvement of a process more efficient than closed crustal magnetic loops to deplete the suprathermal electrons population at low altitudes, no matter the pressure ratio.

The distribution obtained with the in-situ magnetic pressure is quite different. The percentage of electron depletions increases rapidly from a pressure ration of 0.3 to 30. There is then a sharp slope change and the two distributions increase the same way with increasing pressure ratio. The differences observed between the two profiles highlight the importance of induced magnetic fields at low altitudes, which may induce a strong reconfiguration of the magnetic field at low altitudes regarding the Morschhauser model (unless the model is too inaccurate at low altitudes due to the way it has been implemented).

The influence of the magnetic fields can be observed both at low and high altitudes: the percentage of electron depletions per MAVEN orbit increases with increasing ratio magnetic pressure over thermal pressure. However, this tendency is less pronounced at low altitudes, with significant percentages of electron depletions when the thermal pressure is dominant. This simple pressure balance analysis enable us to confirm that the role of closed magnetic field loops is dominant at high altitudes, whereas at low altitudes other processes depleting suprathermal electrons homogeneously over the whole surface are dominant.

A more in-depth analysis will require the use of in-situ measurements from LPW, STATIC and NGIMS, instead of average vertical profiles dating from before MAVEN. Looking at case studies with in-situ measurements from LPW, the thermal pressure calculation just taking into account the thermal electron population seems to be too simplistic. Other components of the plasma pressure should be taken into account, such as thermal ions, but also suprathermal ions and electrons, which could have a significant influence on the pressure balance. High energies electrons that precipitate between electron depletions may also be an important population that should be taken into account for a more accurate pressure balance analysis.

4.3. Discussion on the altitude of the electron exobase

We observed through sections 4.1 and 4.2 that the distribution of electron depletions is highly dependent on the altitude. This observation can be explained by the crossing of the **electron exobase**. In section 4.3.1 we piece together the different observations made through sections 4.1 and 4.2 to update the scenario of creation of suprathermal electron depletions. This enables us to highlight the location of the electron exobase. In section 4.3.2 we then discuss on the variation of the altitude of the electron exobase with SZA.

4.3.1. Updated scenario of creation of suprathermal electron depletions

The different elements that have been observed through sections 4.1 and 4.2 can be summarized as follows:

- All electron depletions are filled with a suprathermal electron population issued from absorption by atmospheric CO_2.
- The distribution of electron depletions is altitude-dependent.
- At high altitudes, electron depletions are observed when the magnetic pressure is greater than the thermal pressure, and the percentage of electron depletions observed increases with the strength of the crustal magnetic sources.
- At low altitudes, electron depletions are observed above almost the whole Martian surface.

In the Martian environment, suprathermal electrons are typically magnetized (with the gyrocenters of their helical motion constrained to follow the magnetic field lines). Closed magnetic field lines with both ends intersecting the **dayside ionosphere** fill with photoelectrons which are simultaneously isolated from solar wind electrons. The trapped electrons bounce back and forth between the two mirror points and the whole electron population undergoes absorption by the collisional neutral atmosphere (among which CO_2 is the major species) if the mirror points are low enough (due to the convergence of the magnetic field lines as in the cusps). However, as photoelectrons are continuously created in the dayside ionosphere, no depletions in the suprathermal electron population is observed.

When closed crustal magnetic field loops rotate toward the nightside with the planet rotation, there is a **transition period** when one foot of the closed magnetic field loop is on the dayside and the other is on the nightside. This configuration can induce precipitations of photoelectrons in the nightside as it will be observed in section 5.1.

When these closed field lines continue their rotation and found their both ends in the **nightside**, absorption by the collisional atmosphere continues whereas fewer electrons are locally produced (mostly by electron impact ionization). The electron population inside closed crustal magnetic field loops is then thermalized via collisions with the neutral atmosphere, leaving only the thermal population and a remaining suprathermal electron population peaked at 6-7 eV, due to the shape of the collisional cross section with CO_2. Electrons coming from other sources, such as horizontal transport of photoelectrons from dayside to nightside or solar wind plasma traveling up the magnetotail, are routed along the external magnetic field lines of the closed magnetic field loops toward the neutral atmosphere (creating flux spikes). They hence are not able to penetrate inside these loops to repopulate them: the inside of closed magnetic field loops forms suprathermal electron depletions. Hence, the stronger the crustal magnetic source is, the higher closed crustal magnetic loops can extend and the higher electron depletions can be observed.

However, the electrons motion is governed by electric and magnetic fields only above the electron exobase. Below it, electron motion is dominated by collisions rather than by the magnetic field. All electrons in this region are then subjected to collisions, not only those travelling along closed magnetic field lines. The thermalization of the suprathermal electron population no longer depends directly on the geographical distribution of the crustal magnetic sources. The distribution of electron depletions in this regions should then be more homogeneous than at higher altitudes. We indeed observed in Figure 72, Figure 86, Figure 87 and Figure 90 that the distribution of electron depletions becomes more homogeneous below a transition region around 150-170 km. The study of electron depletions hence enables me to set an approximate altitude for the electron exobase: **~170 km** [*Steckiewicz et al.*, 2015]. This boundary is generally found at an altitude from 130 to 170 km [*Mantas and Hanson*, 1979; *Lillis et al.*, 2008b; *Xu et al.*, 2016a], which is consistent with our result.

Electron depletions are then the result of two main processes, **absorption by atmospheric CO_2** and **exclusion by closed magnetic field loops**. At high altitudes, the closed magnetic field loops lead electrons toward the lower atmosphere, where they are absorbed. At low altitudes, no need for closed magnetic field lines, electrons are locally absorbed.

4.3.2. Evolution of the altitude of the exobase with the Solar Zenith Angle

The electron exobase is not a sharp boundary, but rather a gradual transition that has a finite thickness [*Lillis and Fang*, 2015]. Its altitude varies with electron energy (because of the collision cross section) and also depends on the atmospheric density profile and the orientation of the magnetic field with respect to vertical. When electron field lines are not vertical, the electron exobase occurs at a higher altitude [*Xu et al.*, 2017].

The electron exobase altitude varies with solar zenith angle due to the decrease of the density of the atmosphere with SZA. The Chapman theory [*Chapman*, 1931a; 1931b] predicts that the peak electron density is proportional to $\cos(SZA)^{1/2}$. The electron exobase should then occur at a lower altitude at midnight than at the terminator.

In Figure 90 is plotted the altitude distribution of electron depletions as a function of the solar zenith angle. I chose five SZA ranges corresponding to $\cos(\mathrm{SZA}) \in [0, 0.2]; [0.2, 0.3]; [0.3, 0.4]; [0.4, 0.8]$ and $[0.8, 1]$, each containing enough events to be relevant. For this study, only electron depletions detected during the first four periods are taken into account. As observed in Figure 69, low altitudes have indeed been sparsely sampled during the fifth period and the corresponding records stopped around the altitude we are interested in here (160-170 km).

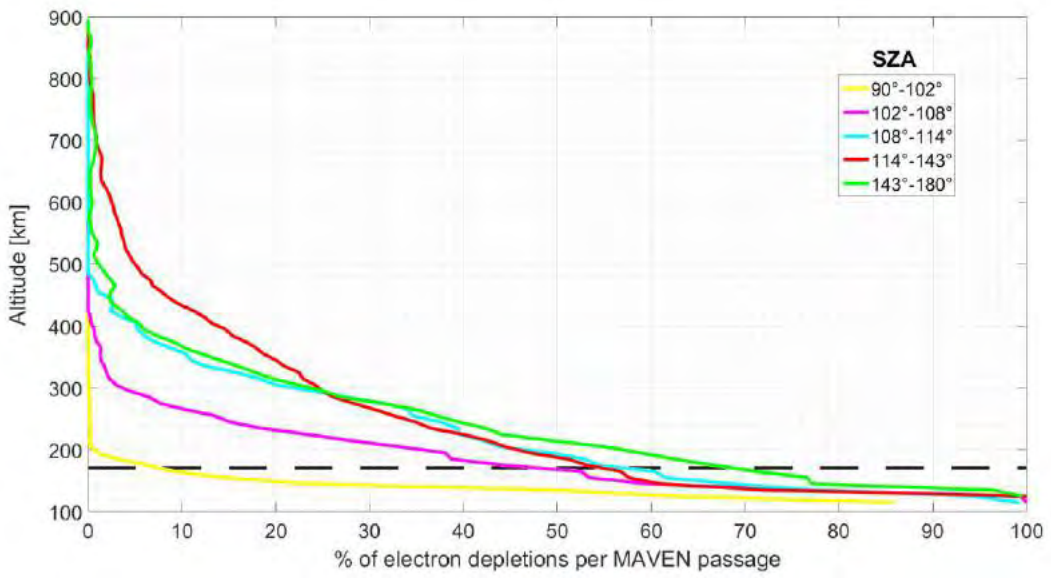

Figure 90. Altitude distribution of electron depletions as a function of their Solar Zenith Angle. I divided my data into five range of solar zenith angle, corresponding to the different colors: [90°-102°], [102°-108°], [108°-114°], [114°-143°], [143°-180°].

We can observe in Figure 90 that the different distributions merge effectively at lower altitudes as the SZA increases. This is particularly visible for the highest SZA. The slope change occurs at 200 km for SZA between 90° and 102°, while it is around 170 km for SZA between 102° and 143°, and 150 km for SZA between 143° and 180°. With the study of electron depletions we hence find that the electron exobase varies from **~200 km at the terminator** to **~150 km in the deep nightside**.

A more precise study of this variation with SZA is made difficult using electron depletions due to the superposition of other effects, such as the presence of crustal magnetic fields of different strengths. However, the values found are in the same range of altitudes than previous studies, such as *Xu et al.*, [2016a]. Overall, few studies have been led so far to determine the altitude of the electron exobase in the nightside, due to the low densities in this region and the lack of measurements realized in the nightside ionosphere. It would be worth to perform a comparison with an ionospheric model to complete this study.

The observations made by MAVEN revealed that the electron depletions distribution evolves with altitude: at high altitudes they are coincident with strong horizontal crustal magnetic field areas whereas at low altitudes their distribution tends to homogenize. Electron depletions are the result of electron absorption by the collisional atmosphere, which is not balance by an electron supply (creation/transport of photoelectrons or injection of plasma from the sheath for example). At high altitudes this absorption is restricted to closed crustal magnetic field loops which lead electrons down to the collisional atmosphere. At low enough altitudes, electrons are locally absorbed by the collisional atmosphere, enabling the creation of electron depletions above the whole surface of the planet. The modification of the electron depletions distribution reveals in fact the location of the electron exobase, separating the collisional and collisionless atmosphere. A mean altitude of ~170 km has been found.

5. Around the holes: the dynamics of the nightside ionosphere

A first analysis of suprathermal electron depletions enabled me to update the general scenario of creation of these structures and to observe the location of the electron exobase. Observation of electron depletions in the nightside ionosphere depends both on the magnetic topology and on the structure and dynamics of the neutral atmosphere. The study of electron depletions, and of the spikes which punctuate them, thus enables me to study some aspects of the dynamics of the nightside ionosphere. I start in section 5.1 by a presentation of several case studies of flux spikes. These structures, observed in section 3.2.3 to be miscellaneous, are the expression of more global processes. We then investigate in section 5.2 unexpected observations, or non-observations, of electron depletions regarding the scenario set in section 4.3.1. A study on the UV terminator and its variations between the dusk and dawn sides in section 5.3 terminate my manuscript.

5.1. Where the electron depletions stop: the flux spikes

The scenario set in section 4.3.1 to explain the observation of electron depletions at both high and low altitudes is the result of a statistical analysis, and express the global trend observed. However, looking at each periapsis separately, the scenario leading to a specific electron depletions and to its stop, is more complicated. On a single periapsis, electron depletions are indeed often observed by groups of three or four (see section 3.4), separated by structures called ‘flux spikes’ by *Mitchell et al.* [2001]. These structures can be the expression of various processes, three of which are investigated in the next subsections.

In Figure 91 is plotted a MAVEN orbit of August 2015 during which five electron depletions have been recorded, separated by four flux spikes. The portion of the orbit which is plotted is located on the nightside above a region with significant crustal magnetic fields in the southern hemisphere. At the beginning of the time interval the spacecraft is located in the ionosphere (until ~03:58 UT), and it enters the induced magnetotail at the end of the fifth electron depletion (from 04:13 UT).

At first glance, the four observed flux spikes can be divided into two categories. The first spike is localized, and mainly composed of low energy electrons, while the three others are

dispersed structures: the external parts of the spikes are composed of two electron populations which are separated by what looks like an injection of plasma.

The case of the first flux spike is investigated in section 5.1.1, and the case of the last three flux spikes is then investigated in section 5.1.2. Another case study is presented in section 5.1.3 to observe the presence of current sheets at relatively low altitudes.

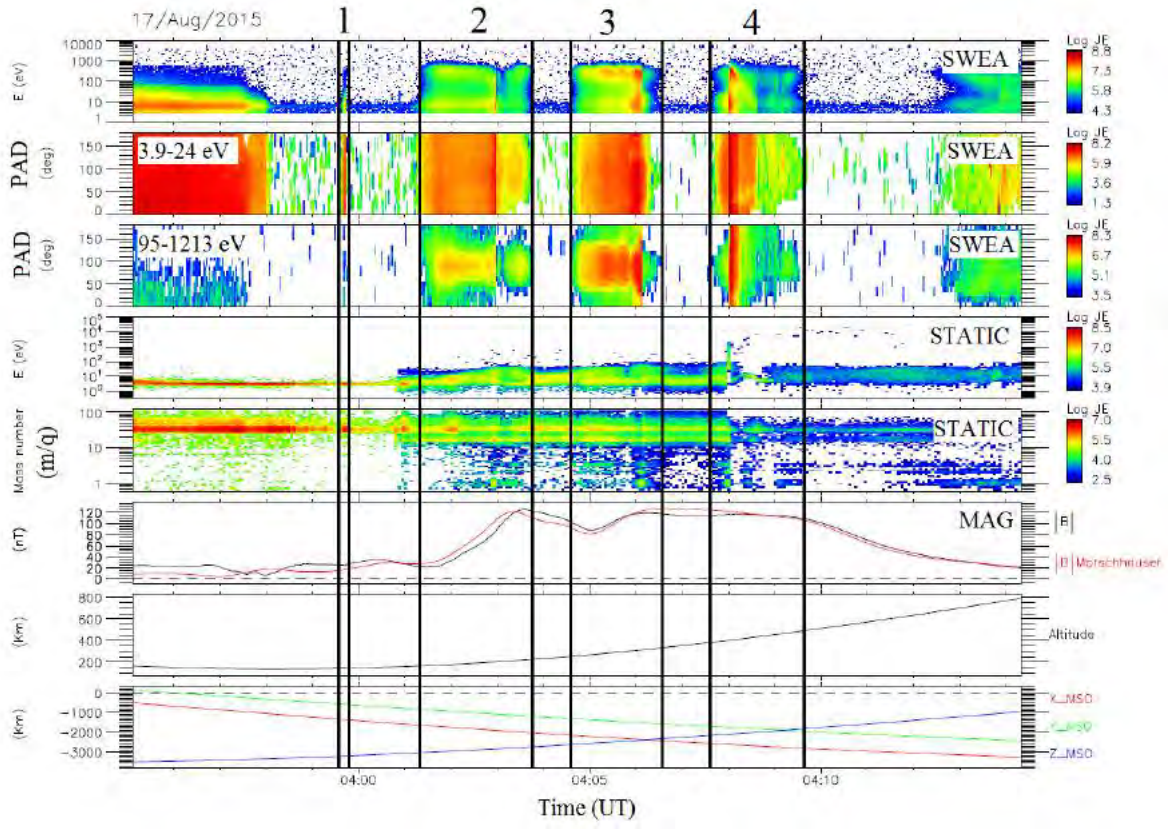

*Figure 91. Example of four flux spikes observed during a MAVEN orbit in August 2015. Panel 1: SWEA energy-time spectrogram of omnidirectional electron energy flux (ENGY mode). Panel 2: Electron PAD calculated by SWEA for electrons with energies between 3.9 and 24 eV. Panel 3: Electron PAD calculated by SWEA for electrons with energies between 95 and 1213 eV. Panel 4: STATIC energy-time spectrogram of omnidirectional ion energy flux (C0 mode). Panel 5: STATIC mass-time spectrogram of omnidirectional ion energy flux (C6 mode). Panel 6: Magnitude of the magnetic field measured by MAG (**black**) superimposed with the amplitude of the crustal magnetic field calculated thanks to the model of Morschhauser (**red**). Panel 7: Altitude of the spacecraft. Panel 8: Position of the spacecraft in the MSO coordinates.*

5.1.1. Injection of ionospheric plasma

In the left panel of Figure 92 is plotted the electron spectra measured by SWEA around the location of the first flux spike: from 03:59:30 UT to 03:59:55 UT. In red are highlighted the

electron spectra corresponding to the flux spike. The two electron depletions surrounding the flux spike are clearly identifiable with the electron flux peaked at ~6-7 eV which is one or two orders of magnitude lower than what is observed inside the flux spike. The electron spectra corresponding to the flux spike look like those that can be observed in the dayside ionosphere (see Figure 18), the peak corresponding to the photoelectrons at 20-30 eV is even observable in one of the spectra.

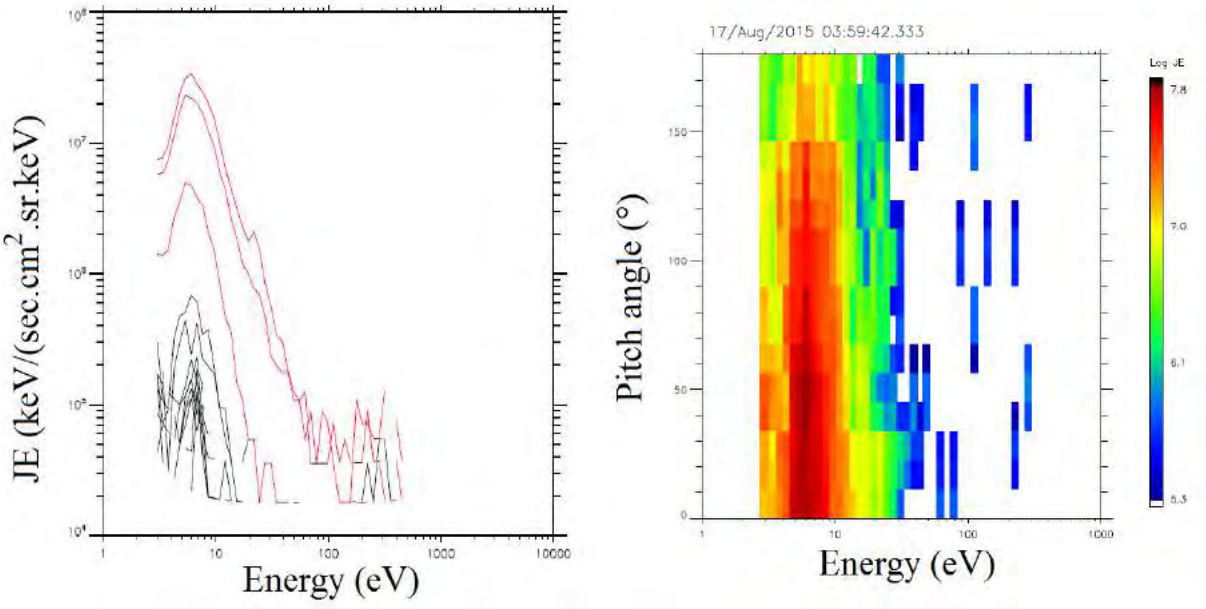

*Figure 92. Characteristics of the electron population recorded inside the first flux spike of Figure 91. Left panel: Concatenation of the electron spectra measured by SWEA between 03:59:30 UT and 03:59:55 UT on August 17, 2015. In **red** are the electron spectrum inside the first flux spike. Right panel: Electron pitch angle distributions inside the first flux spike. The PADs are calculated by CL from SWEA and MAG data.*

The right panel of Figure 92 corresponds to the pitch angle distributions of the electrons observed inside the flux spike. We can see that they correspond to one-sided loss cones (Figure 56). As B_r is positive, these PADs indicate that electrons are travelling toward the planet and are absorbed before being able to bounce back. This configuration is typical of open field lines. However, as the electron population observed in the flux spike seems to be of ionospheric origin, this configuration is more likely to be a **trans-terminator closed magnetic field loop**, with one foot anchored on the dayside on the other one on the nightside. *Dong et al.*, [2015b] showed that closed magnetic field loops can extend on thousands of kilometers, connecting together crustal magnetic field sources on either side of the terminator. An illustration of such configuration is proposed in Figure 93.

Xu et al., [2017] proposed that the photoelectron spectral features that can be observed in the nightside are photoelectrons precipitating into the nightside on closed field lines that straddle the terminator. Photoelectrons are produced on the dayside ionosphere, travel across the terminator along those closed field lines (above the electron exobase), and precipitate into the nightside ionosphere in a cusp-like region. Part of the returning flux is magnetically reflected, while the most field aligned flux suffers collisions with the neutral atmosphere, forming the one-sided loss cones observed in Figure 92. This day-night magnetic connectivity hence provides a source of plasma and energy to the nightside. From a preliminary examination of hundreds of orbits, *Xu et al.*, [2017] found that such nightside **precipitations of photoelectrons** are quite common.

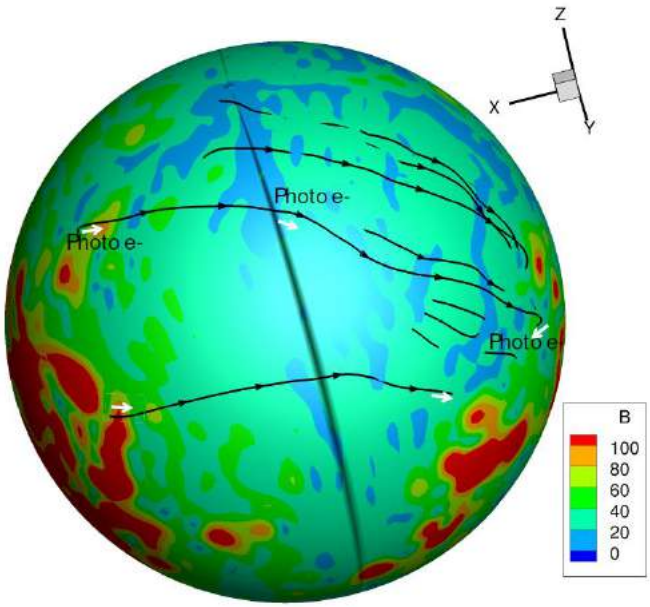

Figure 93.Illustration of trans-terminator closed magnetic field loops [Xu et al., 2016b].
Magnetic strength and several magnetic field lines from a Mars multi-fluid MHD simulation with solar maximum and perihelion conditions. The magnetic field strength (nT) at 170 km altitude is shown in color. The white arrows indicate photoelectrons flowing along magnetic field from sunlit region to deep nightside. The black arrows show the direction of the magnetic fields.

In the second panel of Figure 94 is plotted the amplitude of the in-situ magnetic field together with the absolute value of the radial and horizontal components of the in-situ magnetic field recorded during the orbit under study. Concerning the first flux spike, we can see that, as during the two electron depletions which surround it, the magnetic field is mainly **horizontal**, though the radial component is increasing at the passage of the flux spike. The magnetic topology of the first flux spike hence does not correspond to a cusp of crustal magnetic field. This however does not contradict the proposition of *Xu et al.*, [2017] of travelling

photoelectrons on trans-terminator closed magnetic field lines. Looking at the altitude of the event (~145 km), its SZA (~113°) and the amplitude of the magnetic field measured (~25 nT), we can infer that this portion of the orbit is located below the electron exobase, which explains the presence of electron depletions despite the low crustal magnetic field amplitude. If the trans-terminator closed magnetic field lines only extend slightly above the electron exobase (which is consistent with the low magnetic field amplitude recorded), near horizontal magnetic field lines can cross the electron exobase in the nightside before the magnetic field becomes mainly radial (which is consistent with the increasing radial magnetic field). The photoelectrons travelling from the dayside along these field lines can thus precipitate in the collisional neutral atmosphere while the in-situ magnetic field is mainly horizontal. The second panel of Figure 94 is discussed in section 5.1.2.

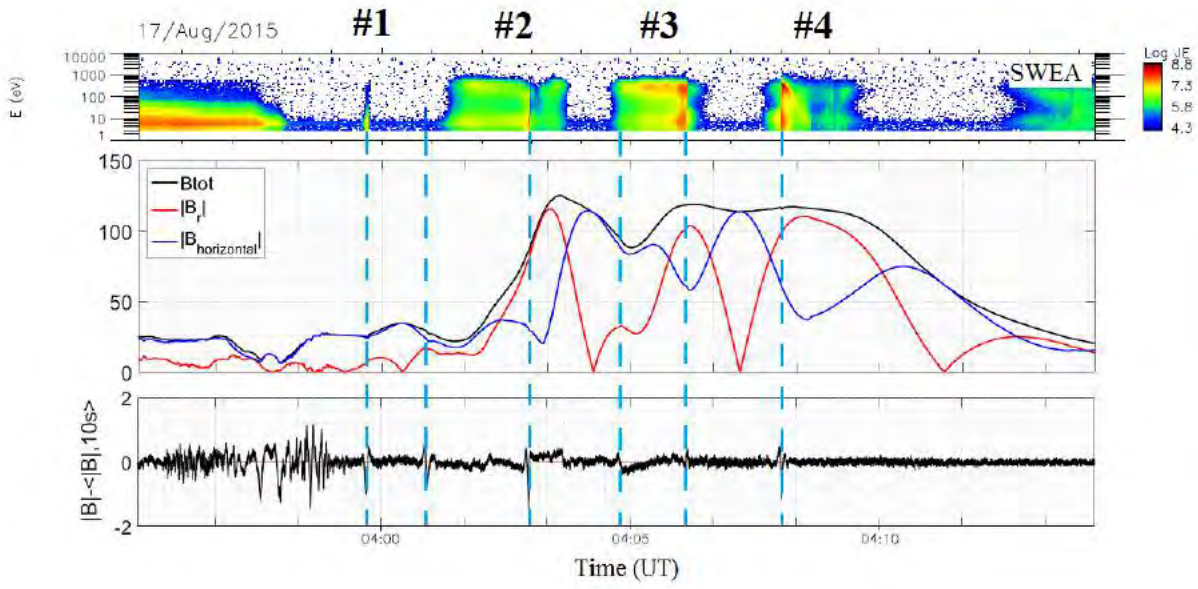

*Figure 94. Magnetic field configuration during the four flux spikes presented in Figure 91. Panel 1: SWEA energy-time spectrogram of omnidirectional electron energy flux. Panel 2: Amplitude of the in-situ magnetic field (**black**) superimposed with the absolute value of the radial (**red**) and horizontal (**blue**) component of the in-situ magnetic field. Panel 3: Residual amplitude of the in-situ magnetic field.*

5.1.2. Energy-time dispersed electron signature

The three last spikes that can be observed in Figure 91 are located in a different plasma environment than what was observed in section 5.1.1. The three events are observed at increasing altitudes from ~170 km to ~480 km, and increasing SZA from ~120° to ~135°, so that they are likely to be above the electron exobase. In addition, the three events are located in

a strong crustal magnetic field region. The amplitude of the in-situ magnetic field reaches ~120 nT and is very consistent with the predicted crustal magnetic field, which indicates that the crustal fields dominate over the external fields at the MAVEN position. Regarding the scenario set in section 4.3.1, we should observe electron depletions where the magnetic field is mainly horizontal (presence of closed magnetic field lines) and flux spikes where the magnetic field is mainly vertical (cusp-like regions).

Looking at the second panel of Figure 94, we can see that the four electron depletions surrounding the three flux spikes under study are indeed centered on an inversion of the radial component of the magnetic field. The flux spikes are meanwhile centered on maxima of the radial magnetic field and on a minima of the horizontal magnetic field, which are likely to be the location of cusp-like configurations.

On the last panel of Figure 94 is plotted the residual amplitude of the magnetic field. At each time step, this parameter corresponds to the amplitude of the local in-situ magnetic field subtracted from the mean value of the amplitude of the in-situ magnetic field calculated over 10 seconds centered on the current time step. We can observe quick and strong variations of this parameter at each crossing of the short burst observed during each flux spike under study, but also coincidently with the first flux spike. This is consistent with the pressure balance conducted in section 4.2.2.3: at high altitudes, electron depletions are observed when the **magnetic pressure dominates the thermal pressure**. We here observe at the passage of the flux spikes a decrease in the residual magnetic field (vertical dashed lines) surrounded by two increases of this parameter (except for the flux spike #3 for which the variations are less clear). A decrease in the residual magnetic field implies a sudden depletion in the magnetic pressure: the thermal pressure is then predominant, allowing the presence of suprathermal electrons at these locations. The two surrounding increases correspond to the magnetic pressure taking over the thermal pressure enabling the presence of electron depletions. Such analysis revealed a fifth flux spikes at ~04:01 UT, which is barely observable on SWEA spectrogram. The three flux spikes under study are then coincident with **magnetic cusp-like regions**.

Looking in more details at the electron and ion populations observed inside the flux spikes, they all three seem to present the same three-parts structure. In Figure 95 are plotted the concatenated electron spectra corresponding to the three events. The **red** spectra correspond to the first part of the flux spike, the **black** spectra correspond to the second part and the **blue** spectra correspond to the third part described thereafter:

- The first part is composed of two electron populations: a 6-7 eV **ionospheric-like** population with isotropic PADs distributions (panel 2 of Figure 91); a second electron population peaked at 150-200 eV, more dispersed, **magnetotail** (flux spike #4) or **magnetosheath-like** (flux spikes #2 and #3) and trapped (panel 3 of Figure 91). The peak energy of this second electron population decreases with time from ~200 eV to ~50 eV, forming a **"falling tone" dispersion**.

- A **short burst** of peaked electron spectra is then observed followed by a brutal modification of the electron spectrogram (which is not due to a SWEA mode change). In the fourth flux spike, the corresponding spectra look very similar to magnetosheath spectra (Figure 18), while the other two cases are more complicated. The strong enhancement of the electron flux is observed simultaneously to the observation of H^+ ions dispersed between 1 and 40 eV (04:03 UT, 04:06 UT and 04:08 UT);

- On the last part, the two electron populations are again observable, with lower electron flux values. The higher energies electron population seems to form a "rising tone" dispersion, at least on the flux spike #2 and #3, and the very end of the last flux spike. The electron population at high energy is in this part magnetosheath-like in the second flux spike and more magnetotail-like in the third and fourth flux spikes.

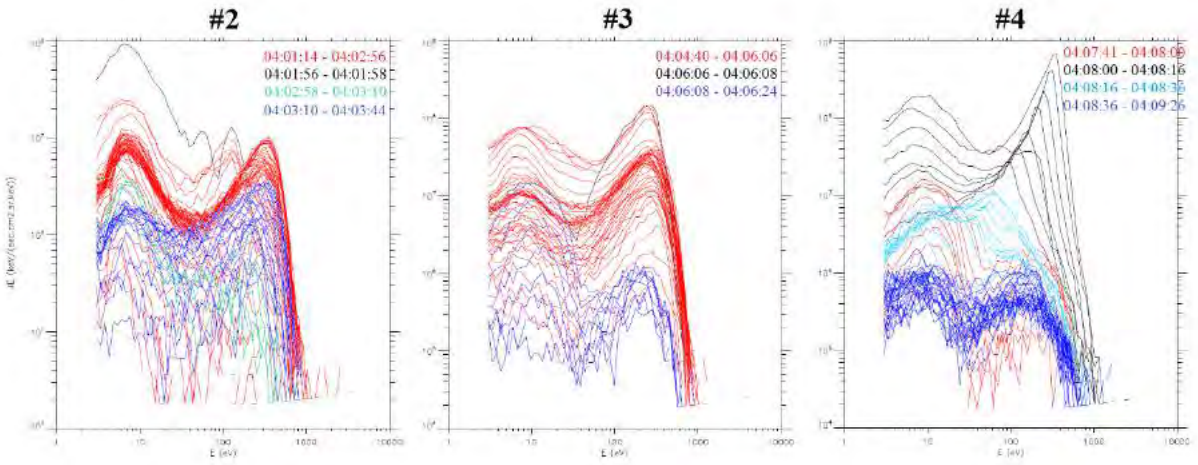

*Figure 95. Concatenation of the SWEA electron spectra measured during the last three flux spikes of Figure 91. In **red** are the electron spectrum in the first part of the spike, in **black** those in the second part and in **blue** those in the third part.*

Regarding the ions, during the first and the second events under study, the energies of O^+ and O_2^+ seem to be more spread between 3 and 40 eV than during the surrounding electron depletions. The third event presents specific features on its ion spectrogram: a sharp and localized increase of the ion energy at ~04:08 UT followed by a plume at high energies and a

current-like feature at low energies. These observations may indicate the presence of strong field aligned currents. However, they should be taken with caution as a change of mode of STATIC occurs at ~04:08 UT.

We can notice that the 'boundaries' separating regions of suprathermal electron precipitation and suprathermal electron depletions are more sharply defined than the corresponding patches of O^+ and O_2^+ ions. This is partly due to the ion-neutral collision frequency which is much higher than the electron-neutral collision frequency, so that ions are more diffusive than electrons.

The fourth event of Figure 91 has been classified by *Harada et al.*, [2016] as an **energy-time dispersed electron signature**. *Harada et al.*, [2016] indeed conducted a statistical survey of dispersed electron events in the Martian magnetosphere, selecting events visually in MAVEN data from November 2014 to September 2015. Fifty discrete dispersion signatures have been identified, mainly on the nightside at altitudes below 1500 km. Most of their events are characterized by trapped PADs for electrons between 40 and 400 eV, falling tone dispersions and are distributed near strong crustal magnetization. *Harada et al.*, [2016] proposed that this type of events are due to impulsive and local injection of hot electrons with broad energies into closed crustal magnetic field lines. The hot electrons can come from the magnetosheath, as we observed it in the middle part of the fourth flux spike, or from other sources. The electrons get trapped in the closed crustal loops and are dispersed by magnetic drift. As high energy electrons drift faster than lower energy electrons, a spacecraft at a distant place on the particles' drift paths will observe a discrete dispersion signature in which higher-energy particles arrive first, followed by lower-energy particles.

In Figure 96 is plotted the electron motion inferred by *Harada et al.*, [2016] on the dispersed signature plotted in the right corner of each plot. The injection field lines are colored in yellow, and the trajectories of 200 eV and 70 eV electrons at the injection time are plotted in red and blue, respectively. The position of MAVEN is represented by a black star. Both electrons at 200 eV and 70 eV are injected on nearly the same field lines (panel a) and travel back and forth between the mirror points, dispersed at different magnetic drift velocities as shown in panels b, c and d. The 200 eV electrons drift faster in the azimuthal direction of the closed loops and arrive at MAVEN earlier (just after the time of panel c) compared to the arrival of the more slowly drifting of 70 eV electrons (just after the time of panel d).

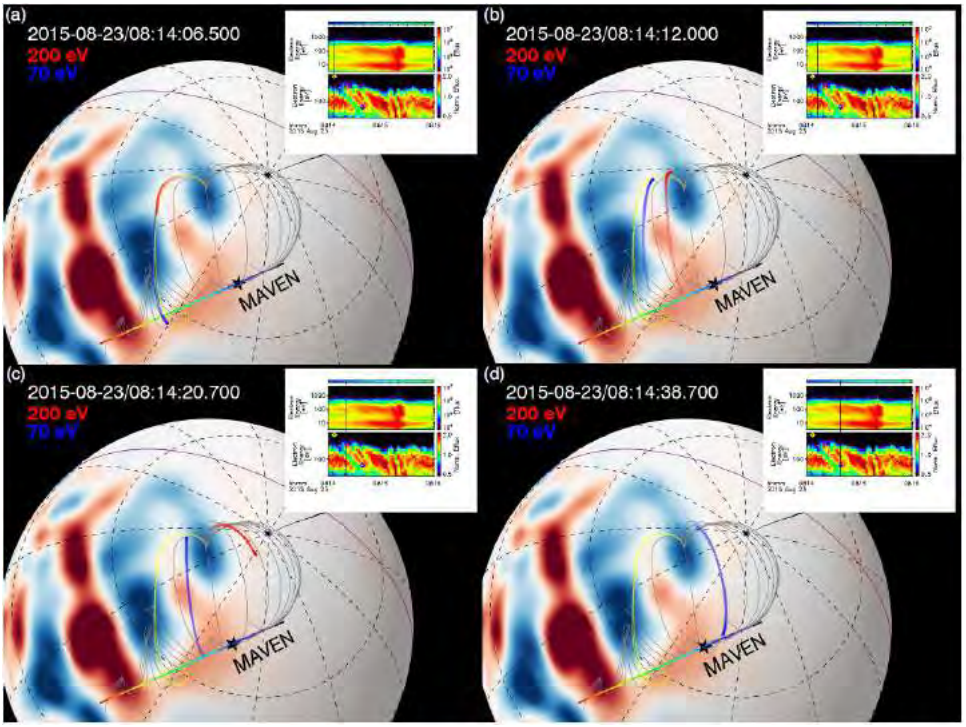

Figure 96. Energy-time dispersed electron signatures observed by Harada et al. [2016]. Snapshot of 200 eV (red) and 70 eV (blue) electron trajectories based on backtracking of the dispersed electrons with an initial pitch angle of 80° in the Morschhauser model. The vertical black bars in the spectrograms indicate the time of each snapshot. The yellow diamonds in the spectrograms denote the estimated injection time, and the yellow traces in the 3D plot show the estimated injection lines. The red and blue diamonds in the spectrogram show the arrival times of the 200 eV and 70 eV electrons.

The events listed by *Harada et al.*, [2016] correspond to the more eye-catching and representative events they found, while ambiguous and complicated events, such as flux spikes #2 and #3, have been set aside from their study. However, looking at the characteristics of flux spikes #2 and #3 compared to those of the #4, these two events may also be considered as possible cases of energy-time dispersed electron signatures. However, the origin of the hot injected electrons is still not clear in these two cases. For the flux spike #3, magnetosheath plasma may be involved while no magnetosheath plasma is observed during the middle part of the flux spike #2, a priori. The presence of H^+ also remains to be studied. These signatures seems real (not an instrument artefact) as they are not correlated with the heavy ions flux and they have slightly different energies from heavy ions. The study of their directional distributions (upward/downward, parallel/perpendicular to B, same directions as heavy ions or not, etc.) may be useful to identify their source. These dispersion signatures are also studied by some members of the MAVEN team as they could be the expression of the presence of strong-negative field-aligned potential below the spacecraft.

5.1.3. Current sheet crossing at low altitudes

In Figure 97 is plotted a series of electron depletions, separated by nature-different flux spikes, which have already been presented in Figure 63. Coincidently with three of these flux spikes (highlighted by the black vertical lines at ~19:44 UT, ~19:50:30 UT and ~19:51:30 UT), we can observe a diminution of the amplitude of the magnetic field, as well as an inversion of some of its components, and an enhancement of the particles flux (ions and/or electrons). These are typical features of current sheet crossings. However, as during this passage the spacecraft is very close to the planet (lower than 600 km), a closer look at the crustal magnetic field is necessary before setting the current sheet nature of these flux spikes.

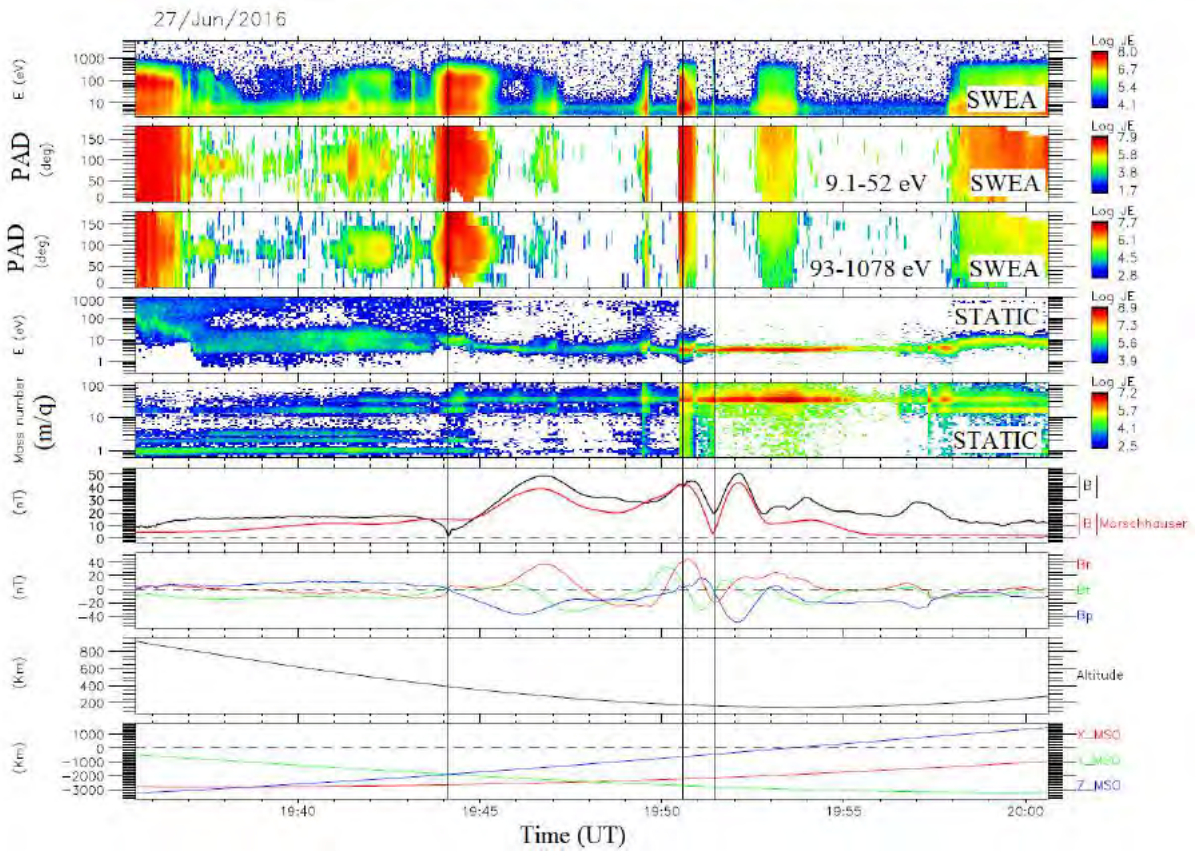

*Figure 97. Example of current sheet crossing observed by MAVEN during an electron depletion. Panel 1: SWEA energy-time spectrogram of omnidirectional electron energy flux (ENGY mode). Panel 2: Electron PAD calculated by SWEA for electrons with energies between 9.1 and 52 eV. Panel 3: Electron PAD calculated by SWEA for electrons with energies between 93 and 1078 eV. Panel 4: STATIC energy-time spectrogram of omnidirectional ion energy flux (C0 mode). Panel 5: STATIC mass-time spectrogram of omnidirectional ion energy flux (C6 mode). Panel 6: Magnitude of the magnetic field measured by MAG (**black**) superimposed with the amplitude of the crustal magnetic field calculated thanks to the model of Morschhauser (**red**). Panel 7: The three components of the magnetic field in the IAU frame measured by MAG. Panel 8: Altitude of the spacecraft. Panel 9: Position of the spacecraft in the MSO coordinates.*

In Figure 98 are plotted the three components of the magnetic field measured by MAG, superimposed with the three components of the magnetic field calculated thanks to the model of Morschhauser at the position of the spacecraft. We can see that, for the second and the third events, the in-situ magnetic field is very consistent with the predicted crustal magnetic field, which indicates that the crustal fields dominate over the external fields at the MAVEN position. Thus, the observed reversal of the magnetic field components are due in both cases to the crustal magnetic topology of Mars. The sharp variations that can be observed in the B_r and B_φ components coincidentally with a sharp decrease in the amplitude of the in-situ magnetic field during the second event is due to the presence of a flux spike, as already observed in the previous section (Figure 94).

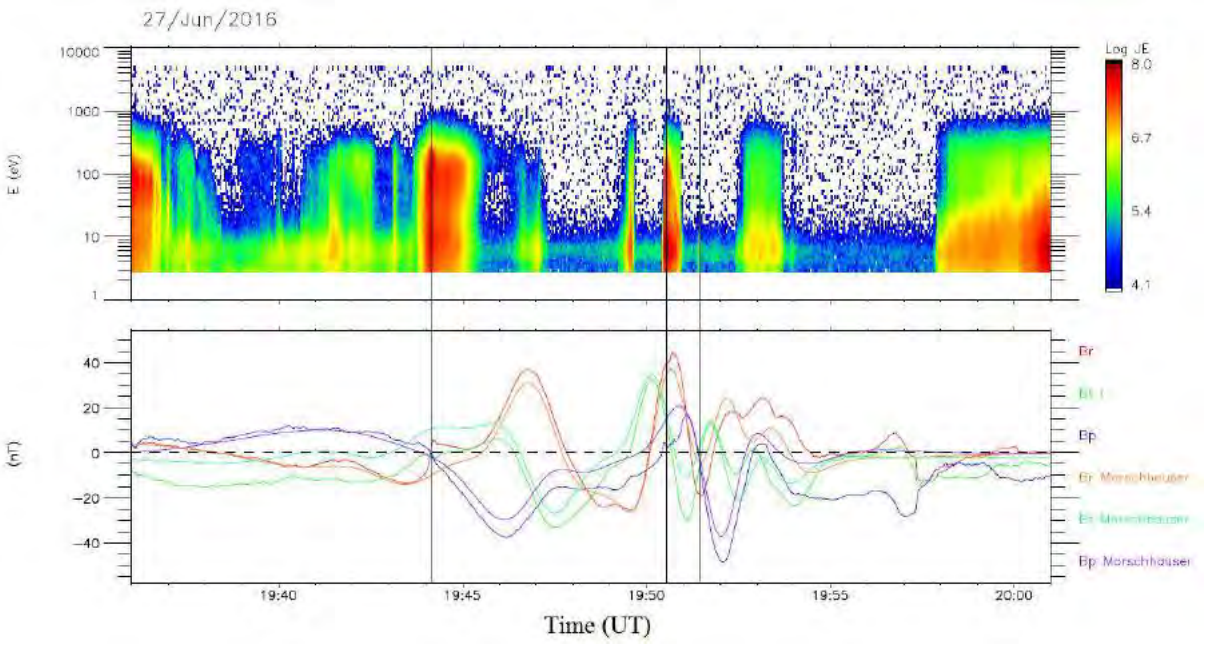

Figure 98. Example of current sheet crossing observed by MAVEN during an electron depletion. Panel 1: SWEA energy-time spectrogram of omnidirectional electron energy flux (ENGY mode). Panel 2: The three components of the magnetic field in the IAU frame measured by MAG superimposed with the three components of the magnetic field in the IAU frame calculated thanks to the Morschhauser model.

We can observe that these two last events are coincident with an extremum of B_r and an inversion of the horizontal components of the magnetic field. Meanwhile, the magnetic field in the surrounding electron depletions is mainly horizontal, centered on a reversal of the radial magnetic field. The observed enhancement in the particle flux can then be due to precipitation of particles along radial magnetic field lines in cusp-like regions. This is supported by the PADs of high energies electrons (not shown) which corresponds to one-sided loss cones. These

distributions are characteristic of open field lines, or trans-terminator closed field lines as previously observed in section 5.1.1. An in-depth analysis of the characteristics of the electron population might help determining their origin.

Concerning the first flux spike, we can observe that the three components of the in-situ magnetic field change of sign approximately at the same time. Looking at the crustal magnetic field components, we can see that the B_θ and B_φ components also revearse at the same time or a little bit earlier for B_θ. The measurements are consistent with crustal magnetic fields for these two components. However, the reversal of the B_r component is clearly not due to the crustal magnetic topology of Mars. This event is a good candidate for being a current sheet crossing.

Applying the **Minimum Variance Analysis** (MVA) to this event — a method whose main purpose is to find, from a single-spacecraft data, an estimator for the direction normal to an approximately one-dimensional current layer [*Sonnerup and Scheible*, 1998] — we found the result presented in Figure 99. In **yellow**, **orange** and **blue** are plotted the maximum, intermediate and minimum variance components of the magnetic field, respectively, and in **purple** is plotted the magnitude of the magnetic field. We clearly observe a change of polarity of the maximum component, along with the minimum of the magnitude of the magnetic field. The Eigen values associated with the maximum, intermediate and minimum variance are respectively:

$$\lambda_1 = 32.0439; \quad \lambda_2 = 0.7594 \quad \text{and} \quad \lambda_3 = 0.0318$$

This gives a ratio λ_2/λ_3 of 23.8867, which is large enough for the current sheet to be well-defined. Its normal vector corresponds to the Eigen vector associated with the minimum variance which is in this case [0.0025, 0.6962, -0.7179] in MSO coordinates. The current sheet is then tilted from the $(X_{MSO}; Y_{MSO})$ plane in this case.

The single or multiple nature of the Martian current sheet is challenged by MAVEN data. The frequent observation at high altitudes of multiple current sheet crossings through a single tail traversal reveals steady flapping, due to a global motion of the current sheet, and kink-like flapping, resulting from localized waves propagation along the tail current sheet [*DiBraccio et al.*, 2017]. Such multiple crossings are also observed at low altitudes, which may suggest the presence of multiple current sheets, induced by the Martian magnetic topology. It is

nevertheless quite difficult to set the precise nature of any structure in the presence of high crustal magnetic fields, which highly complicate the data interpretation and the research for low altitude current sheet crossings. However, highlighting the presence of magnetosheath induced by the magnetic topology of Mars would be really interesting, as it would be specific to the Martian case.

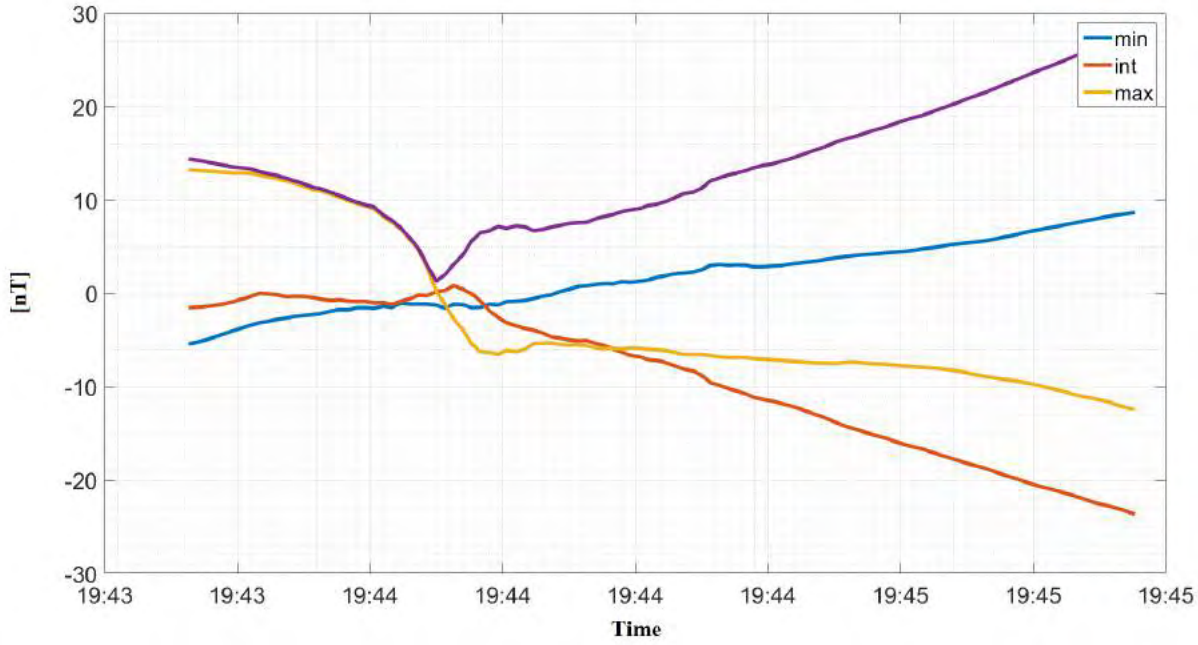

Figure 99. Results of the application of the MVA to the first event of Figure 97.
In yellow, red and blue are the maximum, intermediate and minimum variance components of the magnetic field, respectively. In purple is the magnitude of the magnetic field.

Injection of ionospheric plasma, current sheet crossing or injection and dispersion of hot electrons are ones among others highly dynamic processes operating in the Martian nightside ionosphere and which are observed as flux spikes punctuating suprathermal electron depletions. Another interesting point would have been to study the possible link existing between the observation of flux spikes and aurora.

5.2. Unexpected (non-)observations of suprathermal electron depletions

We noticed in Figure 69 that several electron depletions were observed on the dayside, which is counter-intuitive as the production of photoelectrons in the dayside should be sufficient to balance the absorption of suprathermal electrons by the neutral atmosphere. These seven cases are investigated in section 5.2.1. We then propose in section 5.2.2 to examine several periapsis in the nightside during which electron depletions are not observed while the periapsis is located below the mean altitude of the electron exobase.

5.2.1. Observation of electron depletions on the dayside

Among the five periods during which MAVEN detected electron depletions (section 3.4.2.2), we found seven cases during which part of the electron depletion is located on the dayside ($X_{MSO} > 0$). Four were recorded during the second period hosting electron depletions, in September 2015, and the three others were recorded during the fifth period, in December 2016/January 2017. The detection of such structures in the dayside is not due to the same process in both cases.

5.2.1.1. An altitude issue

The four portions of electron depletion detected by MAVEN in the dayside in September 2015 correspond to the boundaries of real electron depletions, which are observed shortly before entering the nightside. These four cases occurred during a MAVEN deep dip campaign, during which the spacecraft reached **~110 km altitude**. Such low altitudes have never been reached again since then in the nightside.

The boundaries of suprathermal electron depletions can be discussed, as they are fixed by the threshold chosen for criterion (1). However, as the same criterion has been applied to the whole MAVEN data, we can consider these boundaries as legitimate as the others and that at very low altitudes, electron depletions can slightly extend to the dayside. Another process is then necessary to be taken into account in the creation of electron depletions: the **UV terminator**. This issue is discussed in more details in section 5.3.

5.2.1.2. A spacecraft charging issue

The three portions of electron depletion detected by MAVEN on the dayside in December 2016/January 2017 are artefacts due to spacecraft charging. As mentioned in section 3.4.2, a lot of spacecraft charging events occurred in late 2016, early 2017. Before December 2016, the periapsis occurred on the dayside so that spacecraft charging events were easily observable and removable. However, from December 09, 2016, the periapsis got close enough to the nightside for electron depletions to be observed on SWEA data. As criterion (1) detects the same way electron depletions and spacecraft charging events (see section 3.3.1), if an electron depletion is present close to the terminator, and a spacecraft charging event occurs when the spacecraft reaches the dayside, it will be considered as the extension of the electron depletion by criterion (1). The presence of such spacecraft charging events close to an electron depletion results in the detection of a bigger electron depletion than it truly is. An example of such "overflow" is proposed in Figure 100.

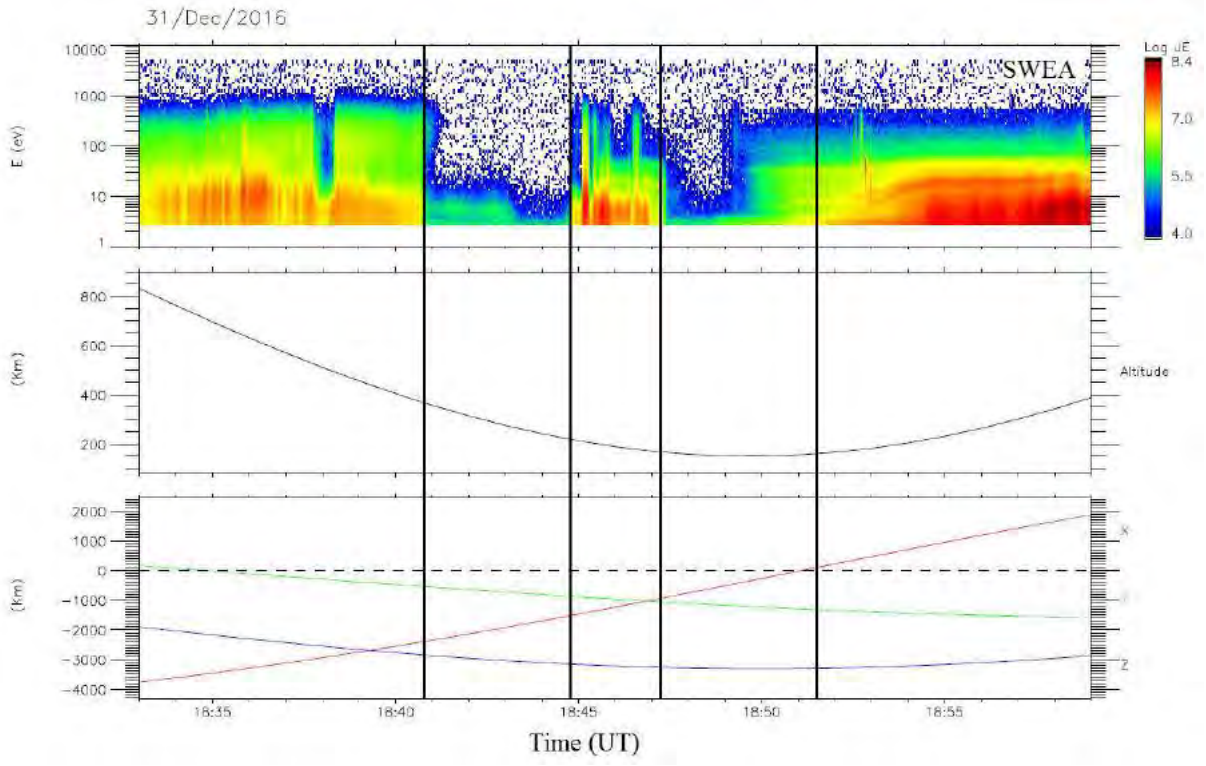

Figure 100. Example of overflow of an electron depletion detected by criterion (1) due to spacecraft charging. Panel 1: SWEA energy-time spectrogram of omnidirectional electron energy flux (ENGY mode). Panel 2: Altitude of the MAVEN spacecraft. Panel 3: Position of the MAVEN spacecraft in the MSO coordinates. The black vertical lines highlight the boundaries of the electron depletions detected with criterion (1).

On the first panel of Figure 100 is plotted SWEA electron spectrogram and the boundaries of the electron depletions detected by criterion (1) are represented by the black vertical lines. Two electron depletions have been detected in the nightside and close to the terminator (X_{MSO} reverses at ~18:51 UT). We can observe the presence of a spacecraft charging event between ~18:50 UT and ~18:53 UT. As the first electron depletion is roughly well delimited, the second one extends until 18:51:32 UT while it should stop at ~18:50 UT. The spacecraft charging event is detected in this case as an electron depletion. As there is no boundary between both structures, from the point of view of the criterion, it results in a huge electron depletion, which spread toward the dayside.

Due to this specific configuration, a lot of electron depletions detected in December 2016/January 2017 are bigger than they truly are, even if they do not extend until the dayside. This issue does not have a great impact on the geographical maps presented in section 4.1.2 nor on the altitude distribution presented in section 4.1.1, 4.2.2.1 and 4.2.2.2, due to the volume of data. I hence chose to include this period in those studies. However, the impact of such overflow has already been observed in Figure 84 and will be an issue for the study of the UV terminator (section 5.3).

5.2.2. Non-observation of electron depletions at low altitudes

As observed in Figure 81, some regions of the Martian surface exhibit very low percentages of electron depletions detected, even below the mean altitude of the electron exobase (~170 km). This observation is in fact representative of a more global trend. Several MAVEN orbits gathering all the necessary conditions for electron depletions to be observed (the periapsis located in the nightside below the mean altitude of the electron exobase) do not present any electron depletion. I gathered visually sixty one such orbits, distributed over the five periods of detection of electron depletions. We first propose in section 5.2.2.1 an overview of different orbits during which no electron depletion has been observed. In section 5.2.2.2 we then investigate the location of these sixty one orbits in the Martian environment. We finish in section 5.2.2.3 by a comparison of several periapsis located over the Tharsis region, presenting or not electron depletions.

5.2.2.1. Different types of orbits with no electron depletion

Looking at the scenario of creation of electron depletions (section 4.3.1), and at the MAVEN orbitography (section 2.1.3.2), electron depletions are expected to be observed, at least, on each periapsis located in the nightside. We here propose to investigate three different periapsis, located in three different regions of the Martian environment, during which no electron depletion has been recorded.

The Martian deep nightside

In Figure 101 is plotted a MAVEN orbit performed on July 7, 2016. The approximate locations of the boundary between the MPR and the induced magnetotail are represented by the black vertical lines. The periapsis is in this case located at ~146 km altitude in the deep nightside (SZA~140°), above a region with no significant crustal magnetic field sources, near the Tharsis Mons (see Figure 82). Two possible current sheet crossings surround the MAVEN pass in the induced magnetotail at ~13:33 UT and 14:05 UT. The modification of the electron spectrogram that can be observed at ~14:05 UT corresponds to the crossing of the UV terminator (see section 5.3.1.3).

Despite the low altitudes reached by the spacecraft at its periapsis, no electron depletion can be observed during this periapsis passage and no electron depletion have been detected by criterion (1). The electron flux is indeed rather constant all along the spacecraft passage in the nightside magnetotail. A slight decrease of the electron flux can be observed at energies greater than 20 eV between 13:44 UT and 13:55 UT (orange vertical dashed lines). However, this decrease is not significant enough to be considered as an electron depletion. We can furthermore notice that this decrease is not centered on the periapsis, but rather on the maximum of the solar zenith angle, reached ~6mn before the periapsis.

The non-observation of electron depletions during this kind of orbit could be explained by the variation of the altitude of the electron exobase with SZA. We saw in section 4.3.1 that the mean altitude of the electron exobase is ~170 km but that this altitude can vary from ~200 km in the terminator region to ~150 km in the deep nightside region (section 4.3.2). Hence, in the case of Figure 101, the electron exobase is likely to be at roughly the same altitude as the periapsis (~150 km). As no crustal magnetic source is present in this region, neither of the two processes discussed in section 4.3.1 can deplete the suprathermal electron distribution to form an electron depletion.

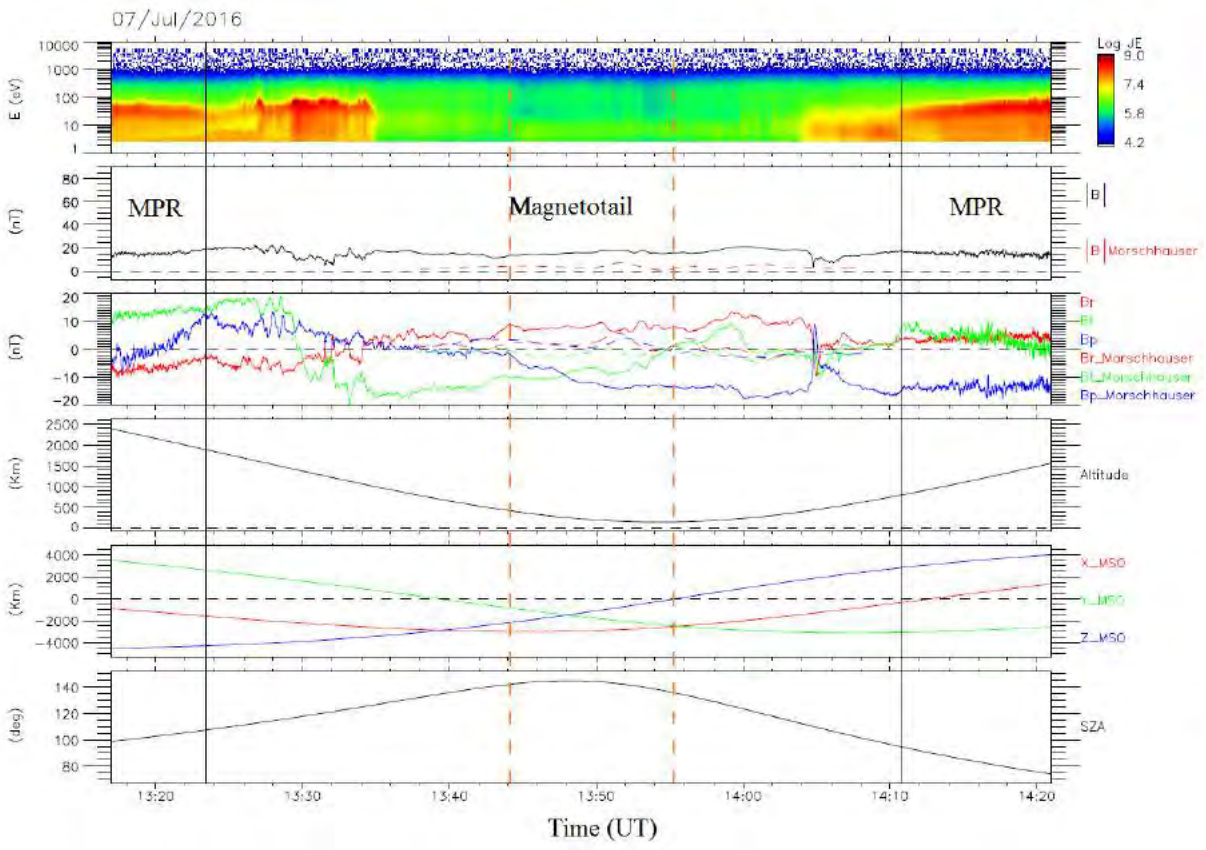

*Figure 101. Example of MAVEN periapsis in the deep nightside when no electron depletion has been detected. First panel: SWEA energy-time spectrogram of omnidirectional electron energy flux (ENGY mode). Second panel: Magnetic field intensity (measured by MAG in **black** and calculated from the model of Morschhauser in **red**). Third panel: Magnetic field components (measured by MAG in solid lines and calculated from the Morschhauser model in dashed lines). Fourth panel: Altitude of the spacecraft. Fifth panel: Position of the spacecraft in the MSO coordinates. Sixth panel: Solar zenith angle at the position of the spacecraft.*

The terminator region with significant induced magnetic fields

In Figure 102 is plotted a MAVEN orbit performed on September 24, 2016. The approximate delimitations of the magnetosheath, MPR, ionosphere and induced magnetotail are represented by the black vertical lines. The periapsis is in this case at ~166 km, slightly before the terminator, at a solar zenith angle of 88°. It is however located in the vicinity (eastward) of a medium crustal magnetic source centered at [330°E; -40°N] (see Figure 52).

As no crustal magnetic field are observed during this event, the observation of electron depletions can only be expected below the electron exobase. As the periapsis is close to the terminator, the electron exobase should be located between 170 and 200 km. However, no electron depletion can be observed, even if several decrease in the electron flux can be noticed between ~05:40 UT and 05:44 UT. These decreases do not look like electron depletions, even

in formation (see next case study). They seem to be restricted to electrons with energies between ~4 and ~30 eV.

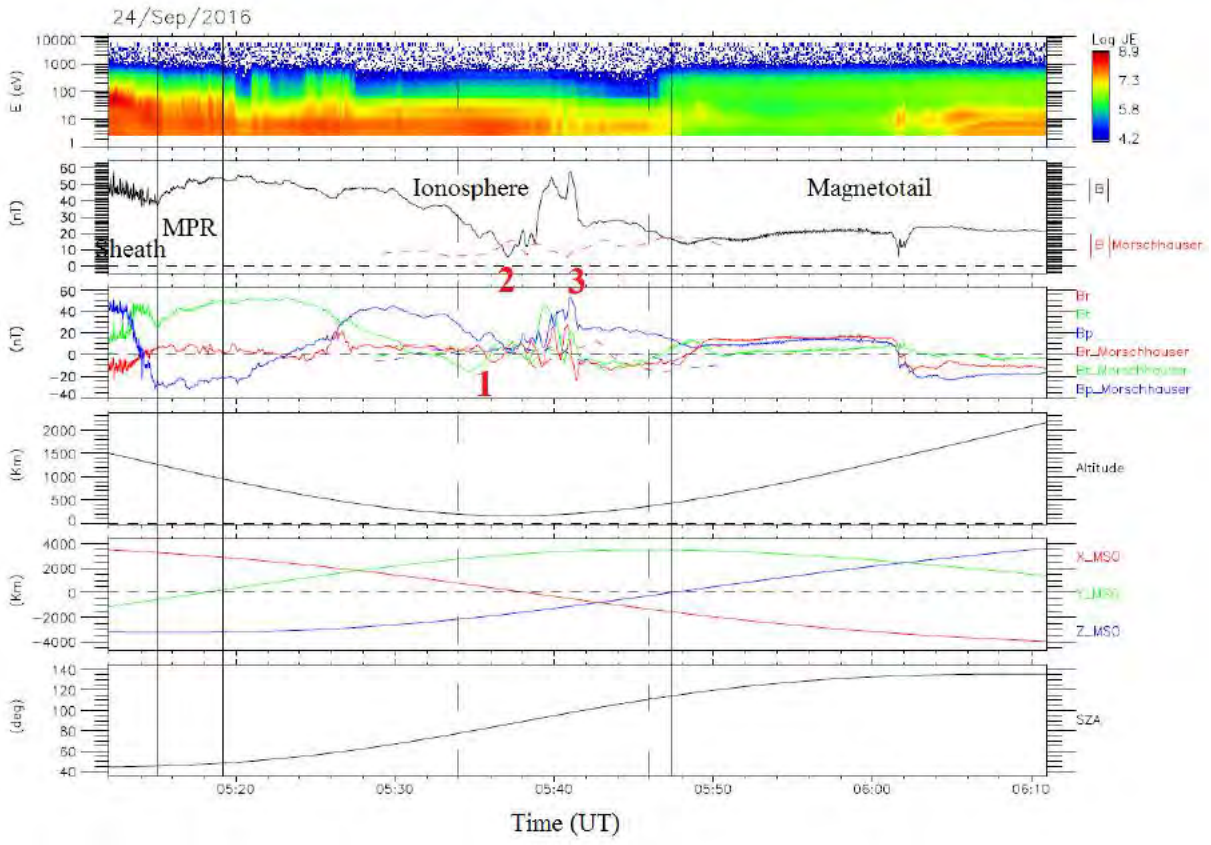

Figure 102. Example of a MAVEN periapsis located near the terminator during which no electron depletion has been detected. The panels are the same as in Figure 101.

We can observe at 05:37 UT an ionospheric cavity, followed by a sharp enhancement in the magnitude of the in-situ magnetic field between 05:39 UT and 05:42 UT, which is not coincident with an enhancement in the magnitude of the crustal magnetic field calculated thanks to the Morschhauser model (dashed red line). Looking at the three components of the in-situ magnetic field during this time period, the magnetic field is mainly horizontal and present variations that are highly different from what can be observed in the remaining ionosphere. These kind of variations are usually observed in the presence of **crustal magnetic sources**. As the Morschhauser model is based mostly on high-altitudes data, crustal magnetic fields located below 200 km could indeed be underestimated by the model. Another possibility would be that the closed crustal magnetic field lines from the nearby crustal magnetic field source are distorted nightward due to currents in the terminator region. The feet of the crustal magnetic field lines would be in the dayside, away from the spacecraft, while the top of the loops would

reach the location of the spacecraft in the nightside, so that crustal magnetic fields are recorded but not expected.

However, looking in more details at the structure of the magnetic field between the two vertical black dashed lines (Figure 103), its variations do not seem smooth enough and at the right scale to correspond to crustal magnetic fields. In the inbound segment, the magnetic field is mostly horizontal. There is a small rotation in the field direction (event **#1**) around 200 km, maybe due to the presence of a low altitudes current sheet. At periapsis (event **#2**), the in-situ magnitude of the magnetic field is lower than what is predicted by the Morschhauser model. If we consider that the model is reliable at such altitudes, this may imply the presence of low altitudes ionospheric currents which partially cancel the crustal field.

The outbound segment is much more complicated, though the magnetic field is still mostly horizontal. Application of the MVA to some portions of the orbit (like the event **#3**) reveals several rotation of the magnetic field, suggesting the crossing of a pair (or more) of **magnetic flux ropes** below 200 km. Magnetic flux ropes are bundles of magnetic field lines that helically wrap around a magnetic axis, under the action of electric current densities.

The magnetic topology observed at the periapsis of this orbit is more complicated than first expected. An in-depth study is needed to isolate the different structures at the origin of the variations observed on the magnetic field.

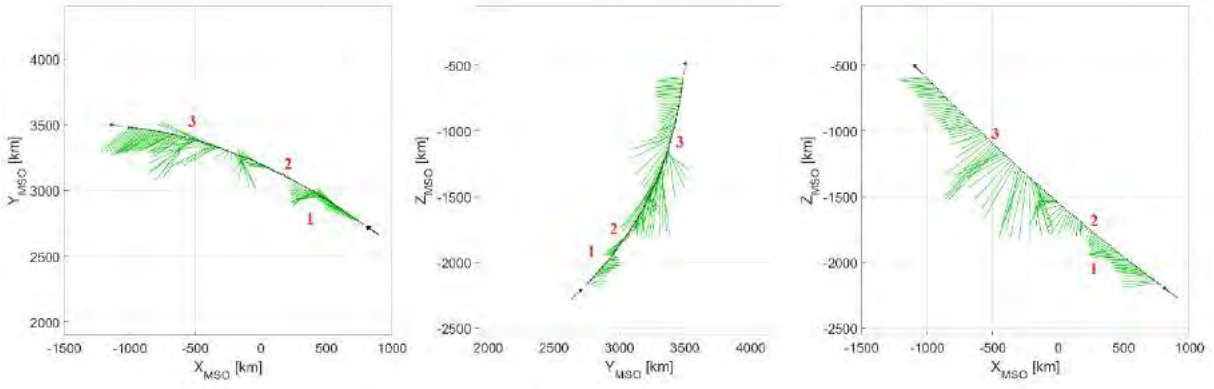

Figure 103. Orientation of the in-situ magnetic field along the MAVEN orbit in MSO coordinates on September 2016, 24 between 05:34 UT and 05:46 UT.

Whatever the process leading to the magnetic configuration observed between 05:39 UT and 05:42 UT (crustal magnetic fields, current systems, flux ropes, or something else), it provides a favorable configuration for the observation of electron depletions: the nightside, at

low altitudes, and the presence of significant horizontal magnetic fields (the B_φ component is dominant). However, still no electron depletions can be observed.

Photoelectrons can be observed in the nightside until ~05:47 UT, where the spacecraft reaches 450 km altitude and enters the induced magnetotail. The electron pitch angle distributions during the enhancement of the magnetic field until the entry in the magnetotail correspond to one-sided loss cones. Gathering all these different elements, we can infer that the same process as that described in section 5.1.1 is involved. The horizontal magnetic field lines that can be observed must have one of their feet anchored in the dayside ionosphere, where the photoelectrons are created. They then cross the terminator and dive below the electron exobase in the nightside for the photoelectrons to be absorbed by the collisional atmosphere. This precipitation of dayside photoelectrons prevent the observation of electron depletions.

The terminator region without crustal or induced magnetic field

In Figure 104 is plotted a MAVEN orbit performed on August 20, 2015. The approximate delimitations of the magnetosheath, the MPR, the ionosphere and the induced magnetotail are represented by the black vertical lines. The periapsis is in this case at ~148 km, slightly after the terminator, at a solar zenith angle of 105°. It is located in a region with low crustal magnetic field sources (around [300°E; -75°N], see Figure 52). Contrary to the previous example, no unexpected induced magnetic field can be observed near the periapsis in the nightside.

As no crustal magnetic field is observed during this event, the observation of electron depletions can only be expected below the electron exobase. As the periapsis is close to the terminator, the electron exobase should be located between 170 and 200 km. We can indeed observe between 15:17 UT and 15:23 UT a strong decrease of the electron flux, but the depletion is completed only at energies greater than 50 eV. It looks as if the absorption of the suprathermal electrons by the neutral atmosphere began, but did not manage to entirely deplete the electron population. This event is hence not considered as an electron depletion. This kind of event may be due to a **local diminution of the CO_2 density** but is not yet fully understood though it is the case the most often encountered. A global comparative study with NGIMS data would be worth being conducted to compare the dynamics of electron depletions with the dynamics of the neutral atmosphere.

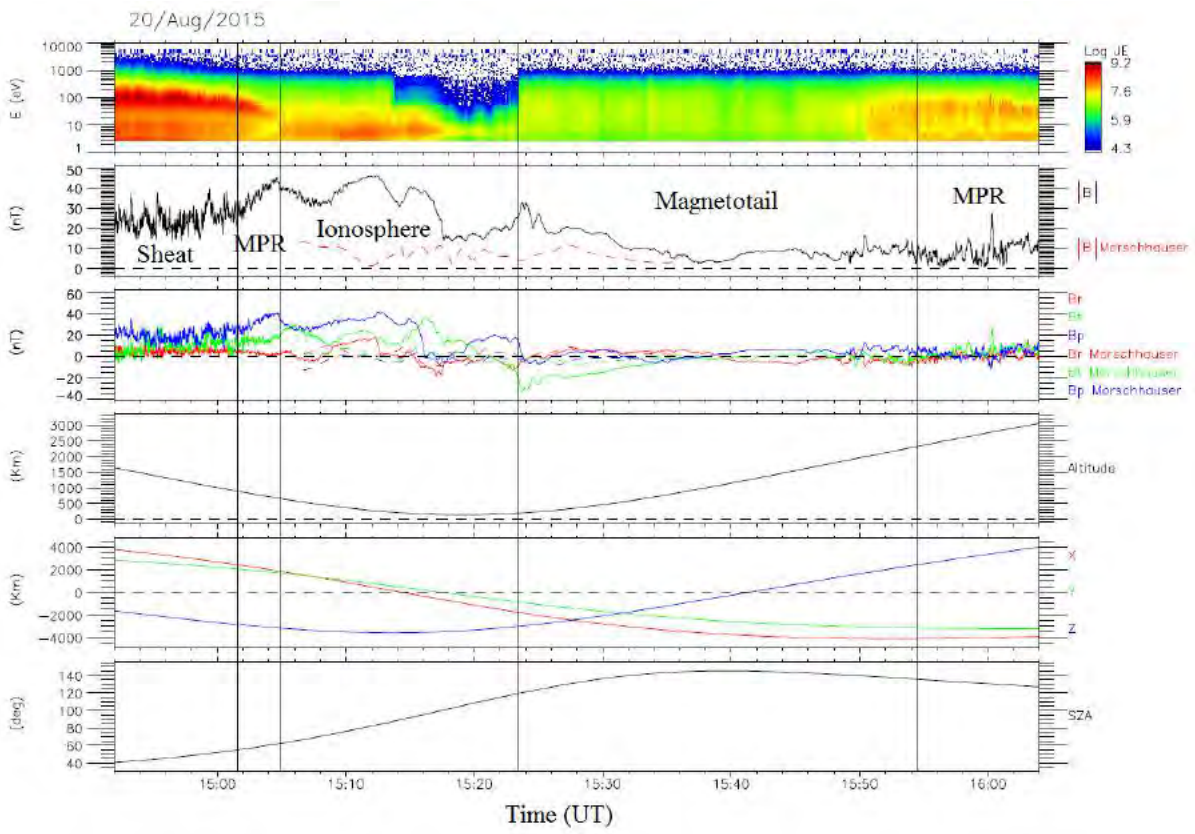

Figure 104. Example of a MAVEN periapsis located near the terminator during which no electron depletion have been detected. The panels are the same as in Figure 101.

5.2.2.2. Distribution of the 61 events in the Martian environment

In order to better understand the processes leading to the non-observation of electron depletions, I plotted in Figure 105 the horizontal crustal magnetic field calculated at 170 km thanks to the Morschhauser model. It represents the expected closed crustal magnetic field loops at this altitude. Superimposed in black are the traces of the 61 orbits during which no electron depletion has been recorded. I only plot the passage of the spacecraft below 200 km in the nightside. Indeed, as the exobase can vary from 200 to 150 km, the absence of electron depletion above 200 km is expected if no crustal magnetic field are present. The red crosses correspond to the periapsis of the different orbits. We can notice that on several events, as the second case study presented in section 5.2.2.1, the periapsis is located shortly before the terminator.

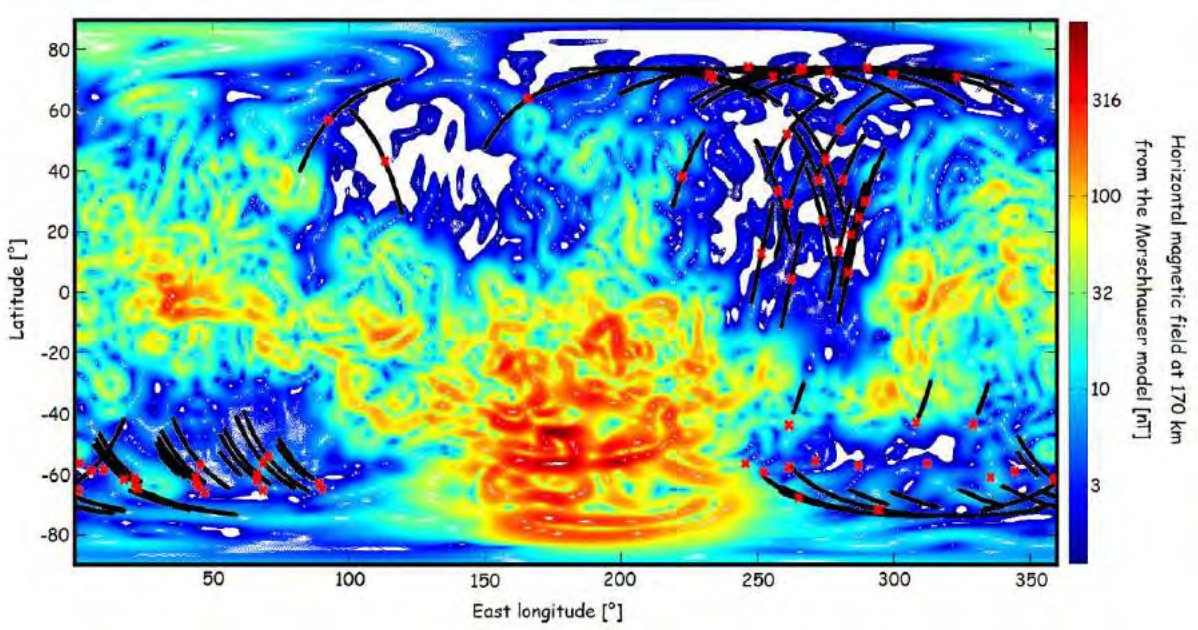

Figure 105. Location of the 61 orbits during which no electron depletion has been recorded. I only plotted in black the traces corresponding to altitudes lower than 200km in the nightside. The red crosses correspond to the periapsis of the different orbits.

The orbits during which no electron depletion can be observed are gathered over two main areas:

- A triangle between [240°E; 76°N], [320°E; 76°N] and [270°E; -10°N] (the upper limit being set by the orbitography of MAVEN). The orbits localized in this region can be divided in two categories: the ones which are aligned at 60°-76°N and the others, located in the Tharsis region (see Figure 82);
- An elongated region centered at -60°N from 250°E to 100°E.

At first glance, these regions seem to coincide with regions where the weakest crustal magnetic fields are recorded. However, we can notice that the region of Utopia Planitia, ([120°E; 40°N], see Figure 11), only gathers two cases, compared to the region of the Tharsis Mons where 15 cases have been recorded.

The longitudinal extension of some regions where electron depletions are not observed indicates that the corresponding orbits are consecutive in time. It is especially the case for high northern and southern latitudes. On the other hand, the Tharsis region gathers orbits from the second, the third and the fourth periods, which are most of the time non-consecutive orbits. This observation should nevertheless be taken with caution, as the different latitudes have not yet been covered the same way by MAVEN (see Figure 69). The Tharsis and Utopia regions are

however at approximately the same latitudes and hence have been covered the same way by MAVEN. We can then infer that the low amplitude of the magnetic field in these regions is not the main, or the unique, process leading to the non-observation of electron depletions.

Another important number to keep in mind is the total number of orbits under study: **4661** (Table 5). The number of events with no observation of electron depletions can seem paltry but it shows that the non-observation of electron depletions is not due to a systematic process.

In Figure 106 is plotted the distribution in terms of altitude, latitude, local time and solar zenith angle of the portions of orbits plotted in Figure 105. In color is plotted the corresponding value (in logarithmic scale) of criterion (1) in order to observe to which extent the orbits are depleted in electrons. The more the color is blue, the more the orbit is depleted in electrons. Due to the issue of the charging events reported during the fifth period of observation, the corresponding orbits can present values of criterion (1) below 0.01 while no electron depletion is actually observed. I then chose not to take into account this period in Figure 106. The corresponding orbits are those located in the southern hemisphere between 0°E and 100°E in Figure 105.

We first can observe that more orbits are located on the dawn side than on the dusk side (the non-plotted orbits of the fifth period are also located in the dawn side). This may be a coverage issue as during the second and third period (see Figure 69), few observations have been recorded on the dusk side due to the orbitography. However, we need more observations to validate or not this dissymmetry. Regarding the SZA, we find several cases, such as the first case presented in section 5.2.2.1, located in the deep nightside, but most of them are located between 90° and 140° SZA. The quick increase in criterion (1) that can be observed at ~150km altitude and ~150° SZA is the crossing of a current sheet at very low altitudes.

A large number of orbits present a significant depletion in their electron population, most of them being located at low altitudes in the dawn side, which indicate that these orbits present electron depletions in formation, nearly reaching the threshold of criterion (1). However, no such low value of criterion (1) can be observed near the terminator. The other way around would have been expected as the exobase is higher near the terminator than in the deep nightside. This effect is due to another process which needs to be taken into account in the terminator region and that will be investigated in section 5.3: the **UV terminator**. The most interesting cases are then those showing high values of criterion (1) away from the terminator, such as the orbits labeled 1, 2 and 3 in the upper right panel, which should be the subject of a specific study.

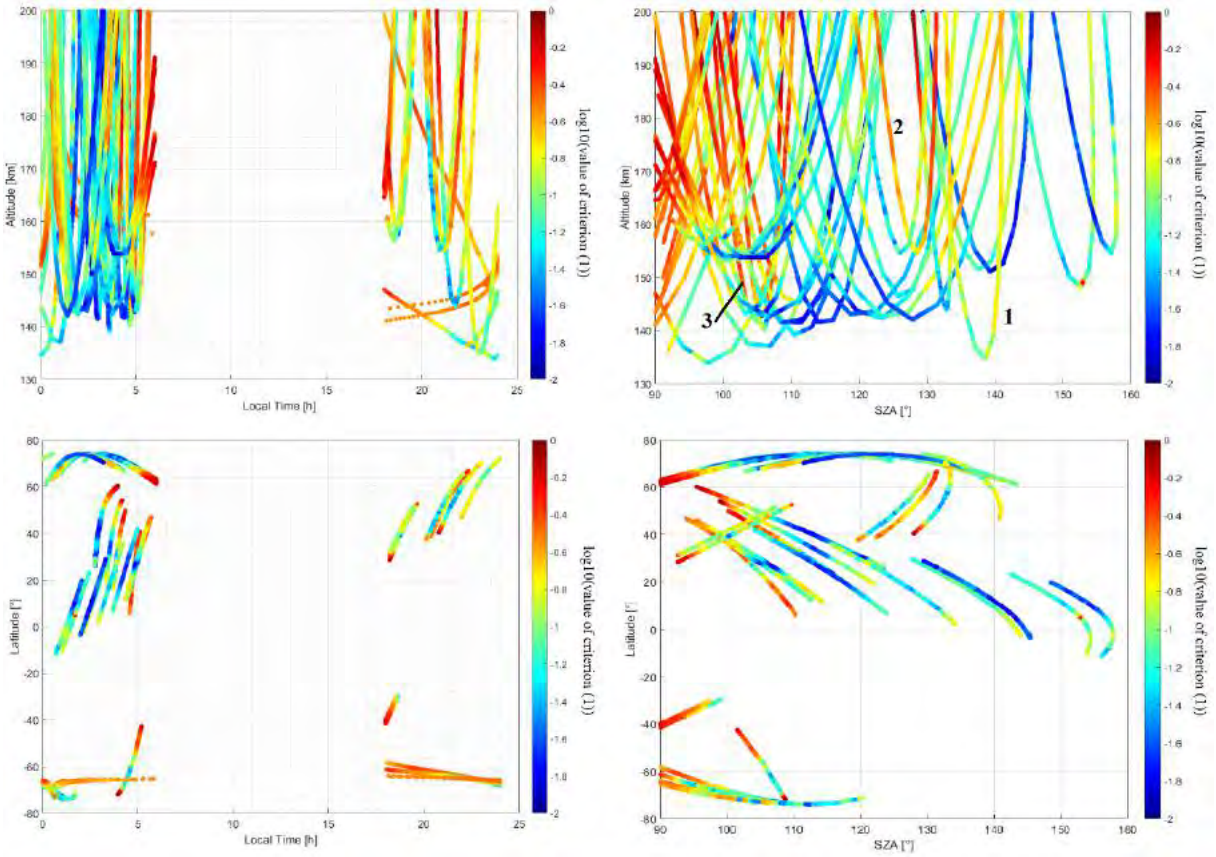

Figure 106. Location of the periapsis with no detection of electron depletion in the Martian environment. The altitude (first line) and latitude (second line) of each periapsis are plotted as a function of SZA (right column) and Local Time (left column). Only the portion of the orbit in the nightside at altitude below 200 km are plotted. The value of criterion (1) is given in color. The fifth period of detection of electron depletions has not been taken into account.

As most of the orbits during which no electron depletions has been detected are however depleted, to some extent, of electrons, we want to observe the influence of the variations of the atmospheric density on the variations of the electron flux in these specific cases. I plotted in Figure 107 the corresponding theoretical attenuation of an electron flux as a function of the value of criterion (1), which corresponds to the effective attenuation of the electron flux measured by SWEA. As for Figure 106, I restricted this study to the orbits of the first four periods of detection of electron depletions. In red is plotted the median distribution.

The theoretical attenuation A is calculated for an electron coming from the infinite and moving along the path ds until the altitude z_0:

$$A(z_0) = e^{-\int_{z_0}^{+\infty} n\sigma ds}$$

Where n is the neutral density crossed by the electron and σ the cross section for the electron collision with the encountered neutrals. Considering for a simple analysis that the temperature and the cross section are constant, that the electron moves radially toward the planet, and that the density evolves according to the following relation:

$$n(z_0) = n_0 e^{-\frac{z-z_0}{H}}$$

We obtain after integration on the altitude:

$$A(z_0) = e^{-n(z_0)\sigma H}$$

For each time step of each orbit under consideration I calculated the corresponding attenuation, taking an average neutral temperature of 140 K, a mean cross section for electron collision with CO_2 of $\sigma = 2 \times 10^{-15} cm^{-2}$ (according to Figure 85), and the CO_2 density from NGIMS measurements.

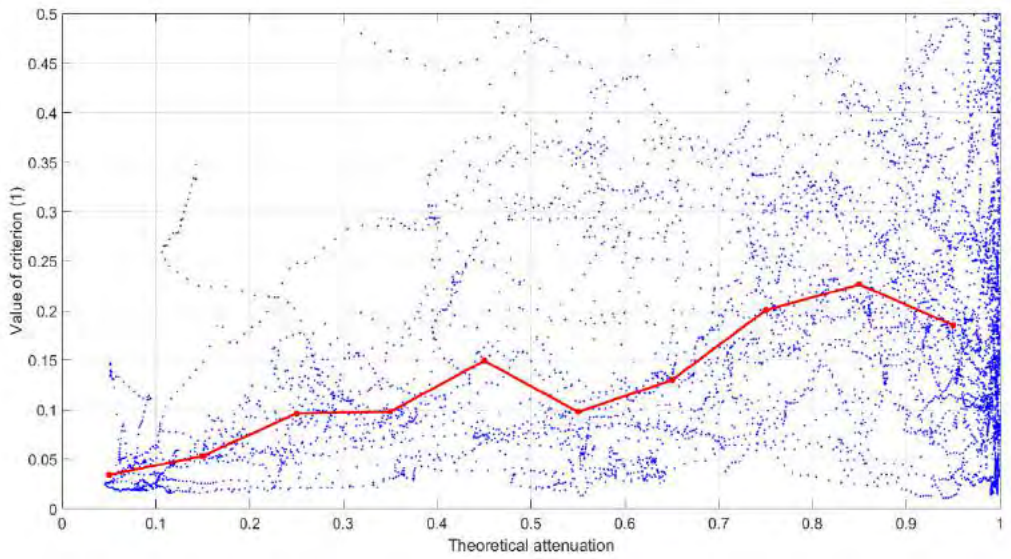

Figure 107. Theoretical versus effective attenuation of an electron flux through the neutral atmosphere. Only the orbits during which no electron depletions has been observed during the first four periods are taken into account. See the text for the details of the calculation of the theoretical attenuation. The red line corresponds to the median distribution.

A linear trend emerge from Figure 107, which means that the attenuation of the electron flux is actually dependent on the attenuation due to atmospheric neutrals. The lowest values of

criterion (1) well corresponds to the lowest values of the theoretical attenuation and no measurement has been made for low theoretical attenuation and high value of criterion (1). However, at high theoretical attenuation, the dispersion in criterion (1) is higher, which may be explained by the several other processes involved (such as induced magnetic field or the evolution of the altitude of the electron exobase). A better analysis would need to take into account the MAVEN trajectory, which is not radial, the energy-dependent cross section, the evolution of the temperature with altitude and a better model of the evolution of the density with altitude.

This analysis, although simplistic, enable us to show that on orbits during which no electron depletion has been detected, the variations observed in the electron flux are dependent on the variations in the atmospheric neutral densities. As previously mentioned, such study would be worth be extended to the MAVEN catalog of electron depletions.

5.2.2.3. Focus on the Tharsis region

We can observe in Figure 106 that the events located in the Tharsis region are highly spread in local time and SZA. They almost all present a depletion in their electron population, more or less pronounced, except for the deep nightside due to the decrease of the altitude of the electron exobase. As for this region orbits with no electron depletions are observed during each period covering it, with various orbital parameters, we can infer that this region possesses specific characteristics preventing the formation of electron depletions.

The Tharsis region is characterized by **very low crustal magnetic fields**, but also by the presence of the **Tharsis Mons**. These volcanoes are parts of the Tharsis dome (see Figure 82), a large volcanic uplift of 5600 km diameter and rising between 4 and 8 km above the reference Martian level. As a low level of crustal magnetic field seems not to be sufficient for preventing the formation of electron depletions, we then focus on the possible effects of the presence of such an uplift of the Martian surface.

I selected four orbits in January 2016, two of them presenting electron depletions and the two others not. I chose events close in time so that we have globally the same conditions in terms of orbitography (~110° SZA and 140 km altitude at the periapsis) but also in terms of Martian season (Northern Summer). The different characteristics of these four orbits are gathered in Table 6.

Orbit #	Day of periapsis	Position of the periapsis	Altitude of the periapsis	Number of electron depletions
2504	12/01/2016	258°E; 26°N	139 km	2
2553	22/01/2016	257°E; 33°N	144 km	0
2569	25/01/2016	279°E;35°N	138 km	1 + several short ones
2580	27/01/2016	272°E; 37°N	139 km	0

Table 6. Characteristics of four orbits of January 2016 whose periapsis are located on the Tharsis region in the nightside.

In Figure 108 is plotted the SWEA and MAG observations made during the four orbits under study. The four of them show very low crustal magnetic field which is consistent with the passage over the Tharsis region. However, the electron spectrogram and the evolution of the magnetic field along the orbit is specific to each case:

- **Case #2504:** the magnetic field is rather stable, the horizontal component being predominant. We hence can only observe electron depletions at the lowest altitudes, when the spacecraft is below the electron exobase.
- **Case #2569:** the magnetic field is more variable. The B_r and B_φ components reverse twice, and are in phase opposition. A first depletion in the electron population can be observed at the periapsis, when the spacecraft is below the exobase. Some electron depletions are detected locally during this depletion, but it is globally not enough depleted to satisfy criterion (1). There is then a minimum of the magnetic field together with a reversal of the B_r and B_φ components (~04:26 UT). This may be a current sheet crossing or field aligned currents. A second electron depletion can be then observed at higher altitudes coincidently with the reversal of B_φ and an increase of the radial component. This configuration may be a magnetic cusp. This orbit is hence easternmost, grazing some weak crustal magnetic sources (see Figure 105).
- **Case #2553:** a reversal of the three components of the magnetic field can be observed just before the passage at the periapsis, coincidently with a minimum of the magnitude of the magnetic field. The magnetic field is then rather stable, as in the case of orbit #2504. However, no electron depletions can be observed, even at the periapsis. A slight decrease of high energies electron can be observed at ~04:17 UT.

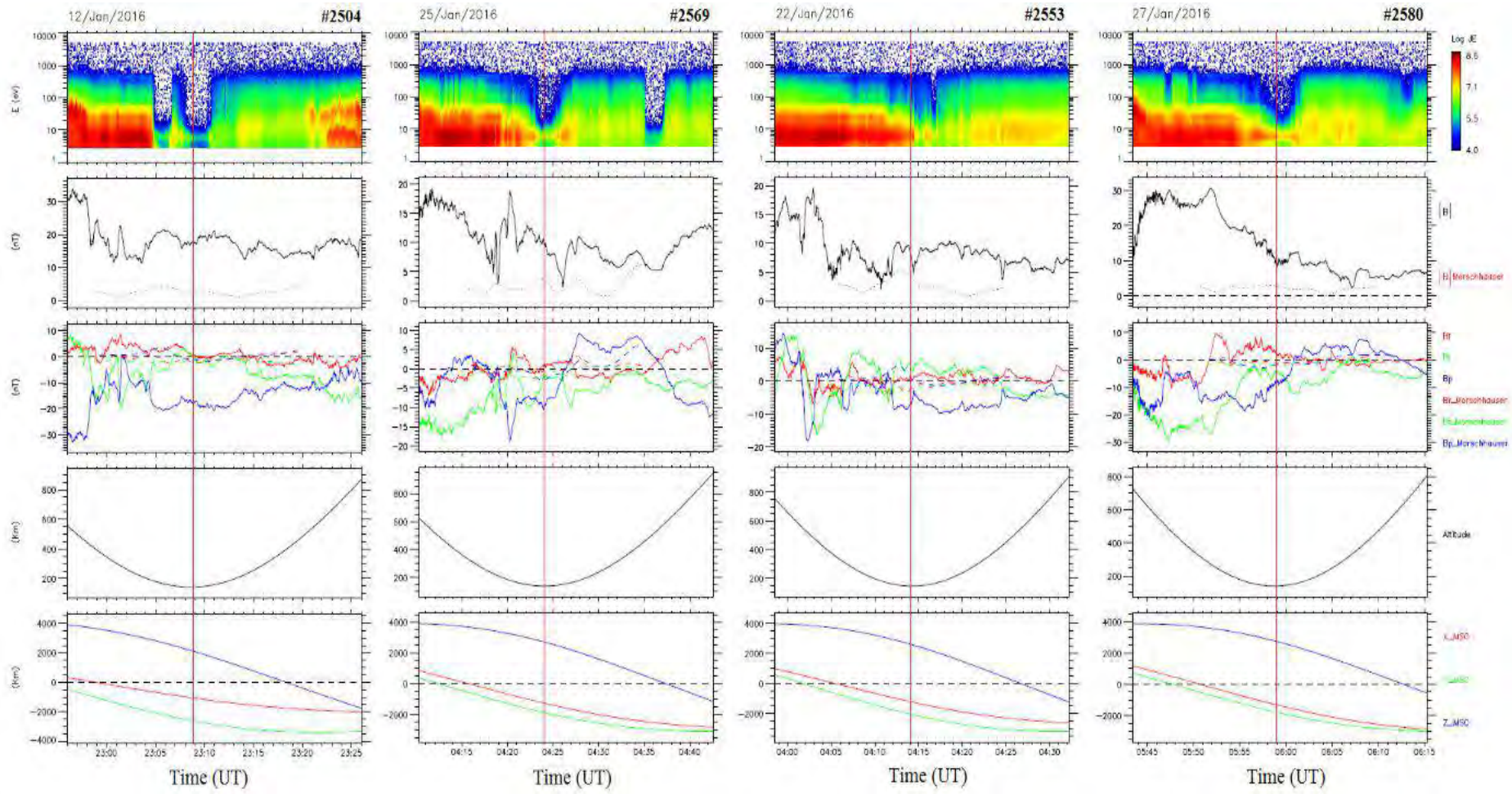

Figure 108. Four MAVEN periapsis located above the Tharsis region.

First panel: SWEA energy-time spectrogram of omnidirectional electron energy flux (ENGY mode). Second panel: Magnetic field intensity (measured by MAG in **black** and calculated from the model of Morschhauser in **red**). Third panel: Magnetic field components (measured by MAG in solid lines and calculated from the Morschhauser model in dashed lines). Fourth panel: Altitude of the spacecraft. Fifth panel: Position of the spacecraft in the MSO coordinates. The red vertical lines correspond to the periapsis.

- **Case #2580:** the magnetic field is globally decreasing along the orbit. An inversion of the B_φ component can be observed just after the passage at the periapsis. A strong decrease of high energies electrons can be observed at the periapsis, but not enough to form an electron depletion, as the third case study of section 5.2.2.1. We can notice that at the same time as this depletion the magnetic field presents high frequency oscillations, a phenomenon not observed in the three other cases nor on the case presented in section 5.2.2.1.

In order to understand such differences at altitudes below the mean altitude of the electron exobase, the NGIMS team (in the person of Meredith Elrod) provided me the CO_2 neutral density profiles obtained by NGIMS during the four orbits under study (Figure 109). The four orbits have approximately the same density at their periapsis. The profiles then spread upward 145-150 km, with orbit #2504 having the lowest density and orbit #2580 having the highest one until 160 km, where the #2569 reaches the same values. This observation is counter-intuitive regarding the electron spectrogram of Figure 108. As orbit #2504 is the only one presenting a clear electron depletion at low altitudes, we could have expected that the CO_2 density would have been higher for this case than for the other three.

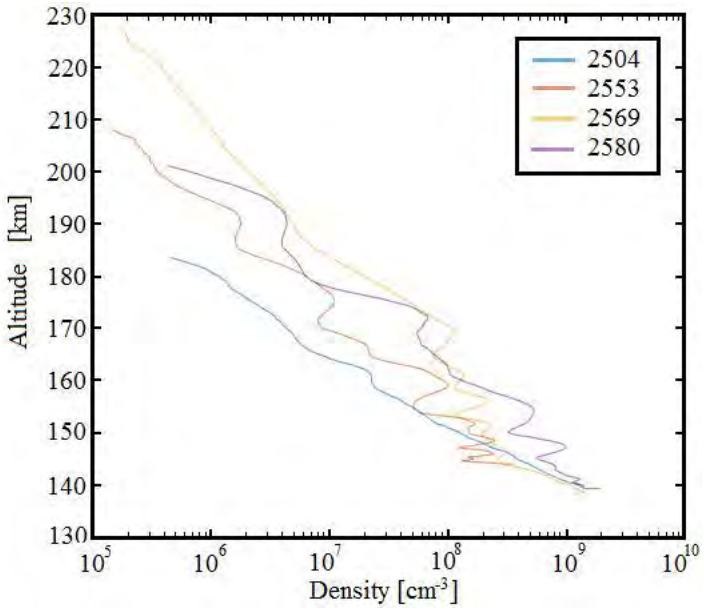

Figure 109. Density profiles recorded by NGIMS for the four orbits under study.

Another interesting parameter observed in Figure 109 is the presence of waves in the density profiles. The obvious point is the orbit #2504 that presents relatively no fluctuation compared to the three others. The density profiles of orbits #2553, #2569, and #2580 present

strong oscillations, downward 170 km for orbit #2569, 160 km for orbit #2553 and 155 km for orbit #2580. However, the waves seem to stop a ~145 km altitude. We hence notice that the three orbits presenting oscillations in their density profiles are the three orbits where the depletion of the suprathermal electron population is not total at the periapsis.

Early in situ observations of the upper atmosphere made by MGS, Mars Odyssey or Mars Reconnaissance Orbiter revealed that the density in this region is highly variable and spatially periodic. Several kind of internal atmospheric waves have been observed, among which **gravity waves** (GWs). Gravity waves are generated in a fluid when the force of gravity tries to restore the equilibrium. The restoration of the fluid to equilibrium produce a back and forth movement of the fluid, creating gravity waves.

Radio occultation measurements made by MGS reported significant GW activity over the tropics and the Tharsis region in the Martian lower atmosphere at 10-30 km [*Creasey et al.*, 2006]. Although GW amplitudes are relatively small in the lower atmosphere, they are known for having a significant impact on both the dynamics and energy budget of the Martian thermosphere: GWs have appreciable effects on large-scale winds, thermal balance, and density in the lower thermosphere [*Terada et al.*, 2017]. The model of *Yiğit et al.*, [2015a] even shows that GWs facilitate carbon dioxide ice cloud formation in the low thermosphere of Mars by locally cooling the atmosphere. Gravity waves can also be observed in the upper atmosphere, up to 250 km altitude [*Yiğit et al.*, 2015b].

The NGIMS instrument onboard MAVEN also detected gravity waves in the Martian upper atmosphere [*England et al.*, 2017]. The amplitude of gravity waves has been observed to be anti-correlated with the background temperature (or equally with the scale height) [*England et al.*, 2017]. Hence, the higher the amplitude of the GW, the lower the ambient temperature and the scale height. GWs can then produce thermal effects in the upper atmosphere, which manifest as heating in the lower thermosphere and cooling at higher altitudes.

Possible sources of this GWs can be upward propagation of harmonics from the lower and middle atmosphere (e.g. due to **topography**) and **in situ excitation** of GWs in the thermosphere by precipitating particles. The uplift of the Martian surface in the Tharsis region could hence be at the origin of gravity waves in this region, which may disrupt the neutral density profiles and explain the absence of electron depletions. However, several studies such as *Terada et al.*, [2017] showed that no clear connection can be set between the thermospheric wave activity and the topography of Mars. This study nevertheless observe a latitudinal variability, slightly weaker activity being observed at low latitudes.

5.3. Where suprathermal electron depletions reveal the UV terminator

Suprathermal electron depletions not only enable us to infer the magnetic topology in the nightside, or to observe processes of injection of plasma in the nightside ionosphere. These structures also enable us to study the neutral atmosphere and its dynamics. We started examining this facet of electron depletions with gravity waves in section 5.2.2.3 and we here investigate the dawn/dusk asymmetry of the neutral atmosphere through the study of the UV terminator. We first propose in section 5.3.1 to describe how electron depletions enable the observation of the UV terminator. We then use these structures to determine the mean altitude of the UV terminator over one Martian year (section 5.3.2) and to highlight its seasonal variations between the dawn and the dusk side (section 5.3.3).

5.3.1. Observation of the UV terminator

The nightside, the dayside, and the terminator separating them are notions which depend on the phenomenon, or on the process that is studied. The terminator is indeed the boundary between where photons are received and where they are not. However, the neutral atmosphere of Mars interacts with the incoming photons, absorbing them more or less depending on their wavelengths, and hence modifying the location of the corresponding terminator. The UV terminator is especially interesting in the Martian case as the main ionization process of the neutral atmosphere is the photoionization of O_2 and CO_2 by UV and EUV photons (section 1.2.1.1).

We first propose in section 5.3.1.1 to observe the distribution of suprathermal electron depletions as a function of SZA, which presents a specific shape. In order to explain it, a more precise definition of the nightside and of the terminator is discussed in section 5.3.1.2. This enables us to identify the UV terminator through SWEA and LPW measurements (section 5.3.1.3). These methods are however restricted to high altitudes and models are usually used instead to infer the location of the UV terminator. Electron depletions meanwhile enable the observation of the UV terminator down to ~110 km (section 5.3.1.4).

5.3.1.1. Distribution of electron depletions as a function of SZA

We observed in Figure 106 that the value of criterion (1) was very high near the terminator for the events during which no electron depletion was observed. This behavior reveals in fact a more general trend. In Figure 110 I binned electron depletions observations per MAVEN passage in altitude and SZA to obtain a statistical picture of their nightside distribution. All suprathermal electron depletions have been used in this plot (except the few cases detected on the dayside). The non-homogeneity of the distribution in the nightside defined as $X_{MSO} < 0$ (beyond 90° SZA) catches the eyes. No electron depletion can be observed near the terminator, except at very low altitudes. Globally, the lower the altitude, the closer to the terminator electron depletions can be observed.

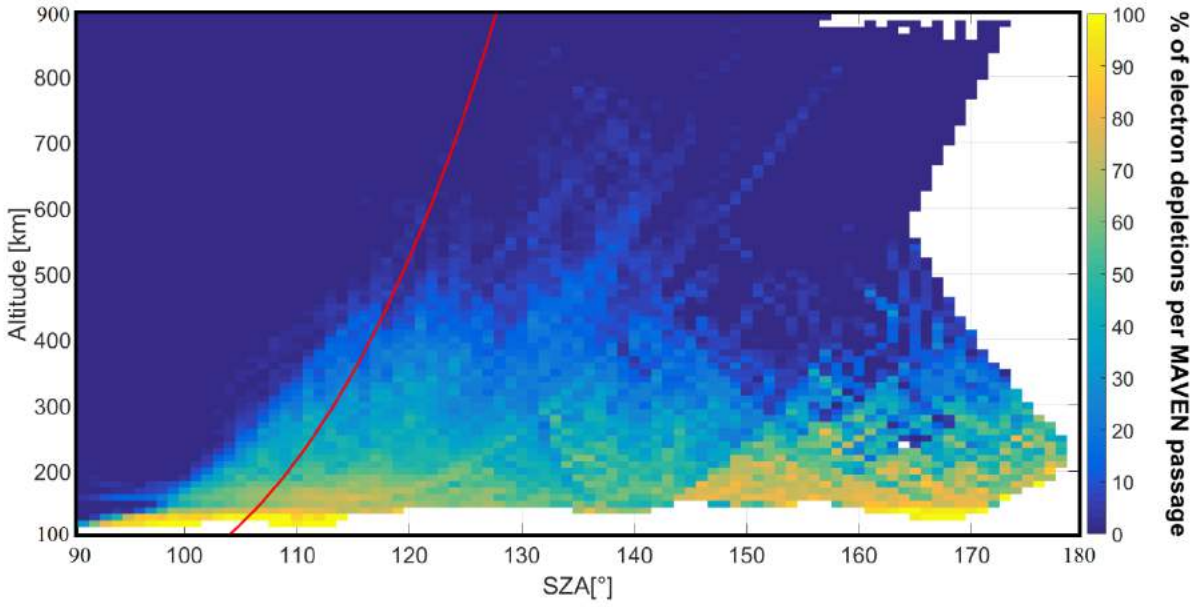

Figure 110. Distribution of the percentage of electron depletions per MAVEN orbit in SZA versus altitude. All data from November 2014 to March 2017 have been taken into account. The areodetic altitude have been used. In red is plotted the optical terminator as defined in section 5.3.1.2.

A clear boundary is in fact observed at SZA from 90° to 120°, between where electron depletions are observed and where they are not. The four cases of electron depletions observed in the dayside and discussed in section 5.2.1.1 are not plotted in Figure 110 but would be in the continuity of the distribution: ~110 km at SZA < 90°. Electron depletions are then not only restricted to the nightside as defined by $X_{MSO} < 0$.

5.3.1.2. Review of the nightside definition

In the previous sections of this manuscript I defined the nightside as $X_{MSO} < 0$, which was good enough for the studies led. This definition is however simplistic. The terminator, which is the boundary between where sunlight is received and where it is not, is not located at the same altitude for all SZA.

The nightside defined as the **optical shadow** of the planet can be represented by a cylinder whose radius is the planet radius R_{Mars} (left part of Figure 111). The nightside is in this case defined as:

$$SZA > 90 + \text{acos}\left(\frac{R_{Mars}}{r}\right)$$

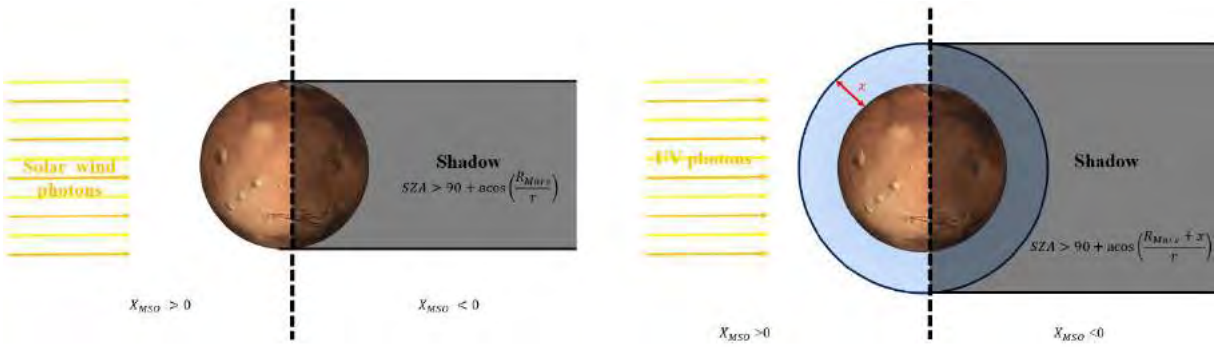

Figure 111. Definition of the nightside.

On the left side is the optical shadow. On the right side is the UV shadow.

A **conic shadow**, taking into account the distance of Mars from the Sun, could also have been considered. However, this would result in a cone which angle is $\sim 8.5 \times 10^{-4}$ °. The difference between the cylindrical and the conic shadow at an altitude of 1000 km would be of ~65 m, which is far below the resolution of our data. The cylindrical shadow is sufficiently accurate for our purpose.

All the sunlight wavelengths however do not reach the Martian surface. Photons interact with the atmosphere and some of them are no more present below a certain altitude due to the thickness of the atmosphere. One specific wavelength range interests us in this study on the ionosphere: the **EUV-UV wavelength** range. We saw in section 1.2.1.1 that EUV and UV photons were the main particles involved in the photoionization of the atmosphere and the creation of the ionosphere. Hence, below some altitudes, EUV-UV photons are no more

observed and we can define a EUV-UV shadow and EUV-UV terminator (called hereinafter UV shadow and UV terminator for convenience). The **UV shadow** corresponds to the cylindrical shadow obtained with Mars surrounded by an atmospheric layer of x km (right side of Figure 111), where all the EUV-UV photons are considered as absorbed. In this case, the nightside is defined as:

$$\mathrm{SZA} > 90 + \mathrm{acos}\left(\frac{\mathrm{R_{Mars}} + \mathrm{x}}{\mathrm{r}}\right)$$

The UV shadow is illustrated in Figure 112 [*Andersson et al.*, to be submitted]. Assuming that total absorption occurs at 150 km altitude (which is the usual value used), the blue rays indicate the UV photons beams coming from the Sun (on the left). The black line is the surface of the planet and the green lines represent SZA from 85° to 115° in 5° increments. The red cross indicates 150 km altitude and the green crosses indicate the last light observable for each green line. From 95° to 115° SZA, the green crosses are at approximate altitudes of 160, 195, 270, 370 and 500 km. Hence, no photoionization occurs at low altitudes (below 150 km) for SZA between 90° and 115°, but can still occur at higher altitudes, resulting in an increase in electron density at high altitudes compared to low altitudes.

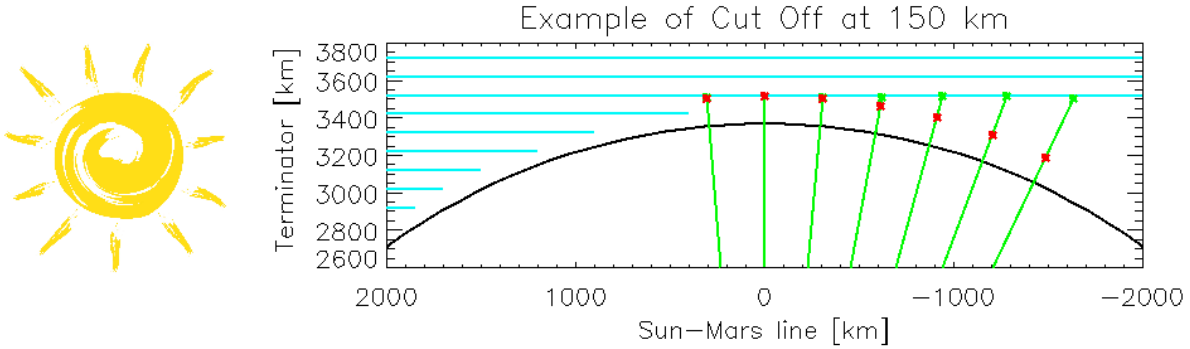

Figure 112. Illustration of how much of the ionosphere is in shadow past the terminator assuming total absorption at 150 km [Andersson et al., to be submitted].

5.3.1.3. Observation of the UV terminator with LPW and SWEA

The UV terminator can be observed thanks to both an electron spectrometer (SWEA) and a Langmuir probe (LPW). In Figure 113 is plotted a MAVEN periapsis observed by the SWEA and LPW instruments. On the first panel is plotted the electron energy-time spectrogram

recorded by SWEA, on the second panel is plotted the floating potential, and on the third panel is the Current/Voltage spectrogram recorded by LPW. Depending on the plasma in which it is embedded, the Langmuir probe measures essentially two currents in the negative potential regime: the **photoelectrons current** (induced by the removal of electrons at the surface of the probe by photoionization) and the **ion current** (induced by the impact of the ambient ions on the probe). At low plasma density, such as at high altitudes, the photoelectrons current dominates whereas at high plasma densities, such as in the ionosphere, the ion current dominates.

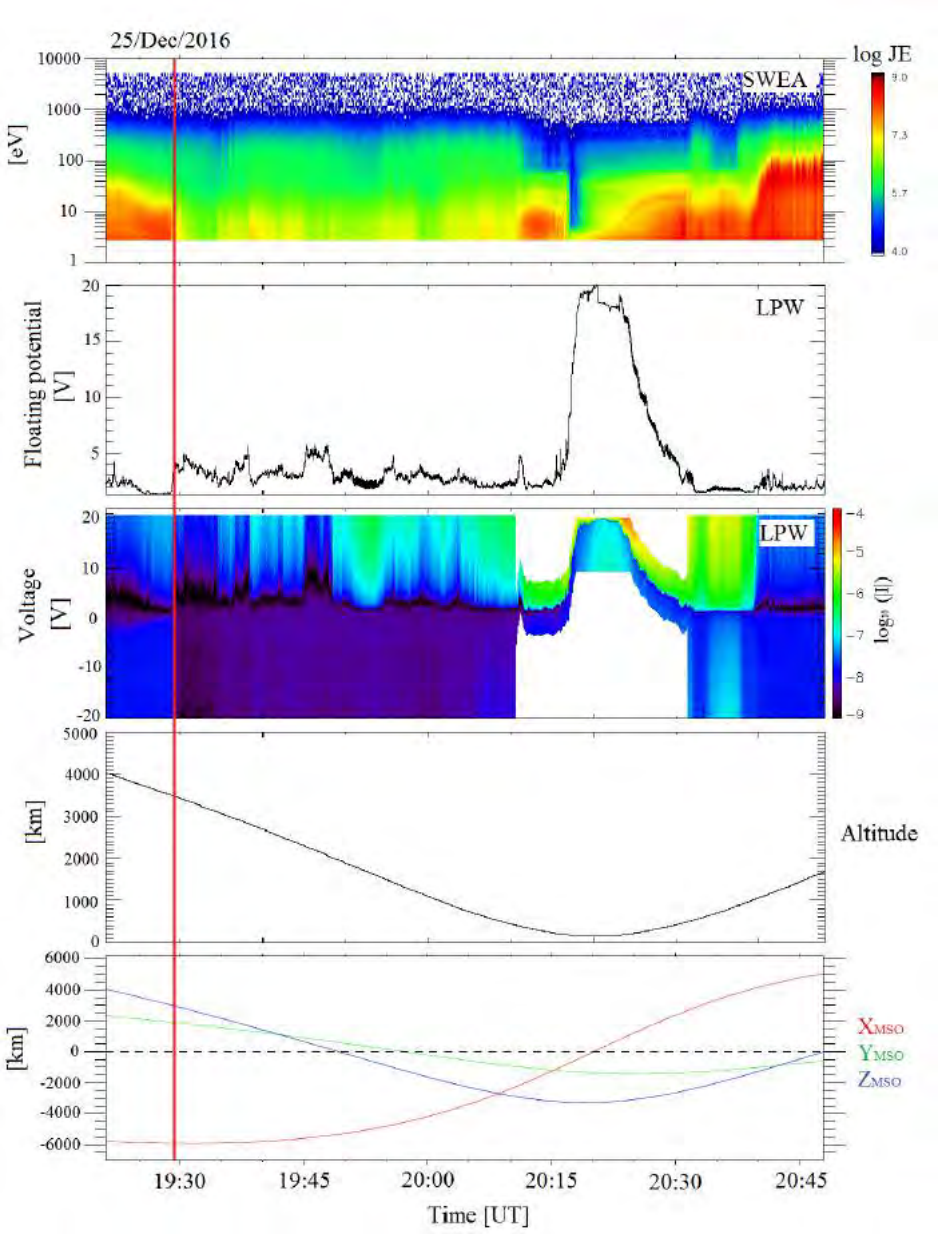

Figure 113. Observation of the UV terminator with the LPW and SWEA instruments. Panel 1: SWEA energy-time spectrogram of omnidirectional electron energy flux (ENGY mode). Panel 2: Floating potential derived by LPW. Panel 3: Current-Voltage spectrogram by LPW. Panel 4: Altitude of the MAVEN spacecraft. Panel 5: Position of the MAVEN spacecraft in the MSO coordinates.

Two crossing of the UV terminator are present in Figure 113. The first one is located at ~19:30 UT and can be observed both on SWEA spectrogram and on LPW I-V spectrogram (red vertical line). It is located at high enough altitudes so that the dominant current measured by LPW is the photoelectron current. As the spacecraft crosses the UV terminator from dayside to nightside, no more photoelectrons are produced. The electron flux measured by SWEA and the current measured by LPW (at negative potentials, i.e. below the floating potential) decrease suddenly, showing a clear boundary. As the spacecraft passes its periapsis, X_{MSO} reverses at ~20:20 UT, so that the UV terminator should be crossed close to that point. However, as the spacecraft is at low altitudes, the ion current dominates so that the identification of the UV terminator is more difficult. The identification in the SWEA data seems not easier at first glance.

A precise identification of the UV terminator is then only possible at high altitudes with the measurements available on MAVEN. So as to obviate this issue, models (such as the one of Robert Lillis presented in section 5.3.2.3) may be used to determine the altitude of the UV terminator.

5.3.1.4. Back to suprathermal electron depletions

In Figure 110 we observed a clear boundary between the regions where electron depletions are observed and where they are not. The shape of this boundary looks like a terminator, however it does not correspond to the optical terminator (plotted in red). In Figure 114 is plotted the same distribution of electron depletions as in Figure 110 but in this case we superimposed a terminator calculated with an atmospheric layer of 120 kilometers. We can see that this terminator fits rather well the global shape of the distribution: it corresponds to the **UV terminator**.

Indeed, electron depletions are the result of a balance between electron loss and production processes. In first approximation (neglecting transport and local production of electrons), electron depletions can be observed when no more photoelectrons are created in the ionosphere. As photoelectrons are mainly produced by photoionization of the neutral atmosphere by EUV and UV photons, the limit of detection of electron depletions corresponds roughly to the UV terminator. Electron depletions could then be observed in the dayside at low enough altitudes, as shown in section 5.2.1.1.

A faint line at ~160 km altitude can be observed between 90° and 100° SZA, which seems in disagreement with the rest of the distribution. This feature is the result of the spacecraft charging events discussed in section 5.2.1.2. The concerned electron depletions detection does not stop at the UV terminator, it extends too far in the UV dayside, polluting the data.

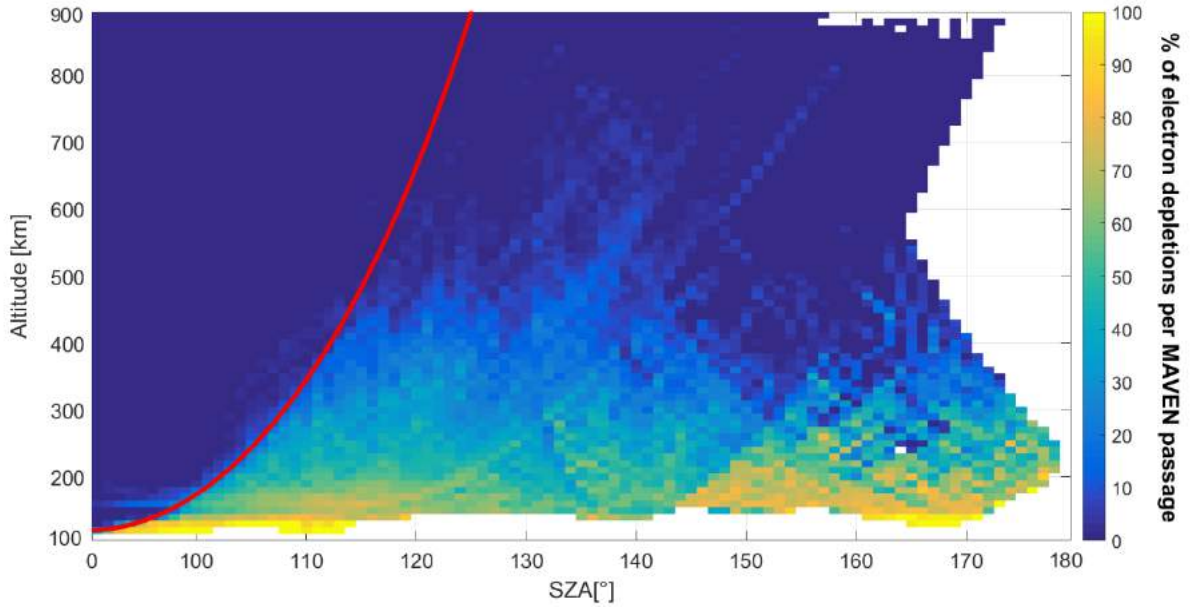

Figure 114. Distribution of the percentage of electron depletions per MAVEN orbit in SZA versus altitude. All data from November 2014 to March 2017 have been taken into account. The areodetic altitude have been used. In red is plotted the UV terminator as defined in section 5.3.1.2, with an atmosphere thickness of 120 km.

The average altitude of the UV terminator can then be derived from SWEA data thanks to the distribution of electron depletions. Besides, the detection of the UV terminator using electron depletions is more accurate at low altitudes, where crustal magnetic sources have less influence on the distribution.

5.3.2. Determination of the average altitude of the UV terminator

The MAVEN data have been recorded for more than one Martian year so far. Such a data set enables us to set an average altitude of the UV terminator. We first present in section 5.3.2.1 the electron depletions distribution over one Martian year, then the methodology used to determine the altitude of the UV terminator (section 5.3.2.2) and finally the results obtained compared to the model of absorption implemented by Robert Lillis (section 5.3.2.3).

5.3.2.1. Distribution of electron depletions over one Martian year

Each period of detection of electron depletions (Figure 69) can be related to a Martian season:

- **First period:** Winter of the Northern hemisphere (Mars perihelion)
- **Second period:** Spring of the Northern hemisphere (equinox)
- **Third period:** Summer of the Northern hemisphere (Mars aphelion)
- **Fourth period:** Autumn of the Northern hemisphere (equinox)
- **Fifth period:** Winter of the Northern hemisphere (Mars perihelion)

So as not to be biased by any seasonal effects (see section 5.3.3), I chose to only use data obtained during the first four periods, which cover the four seasons. In addition, not taking into account the fifth period allows to remove to pollution generated by the spacecraft charging events. The distribution of electron depletions over the first four periods altogether is plotted in Figure 115.

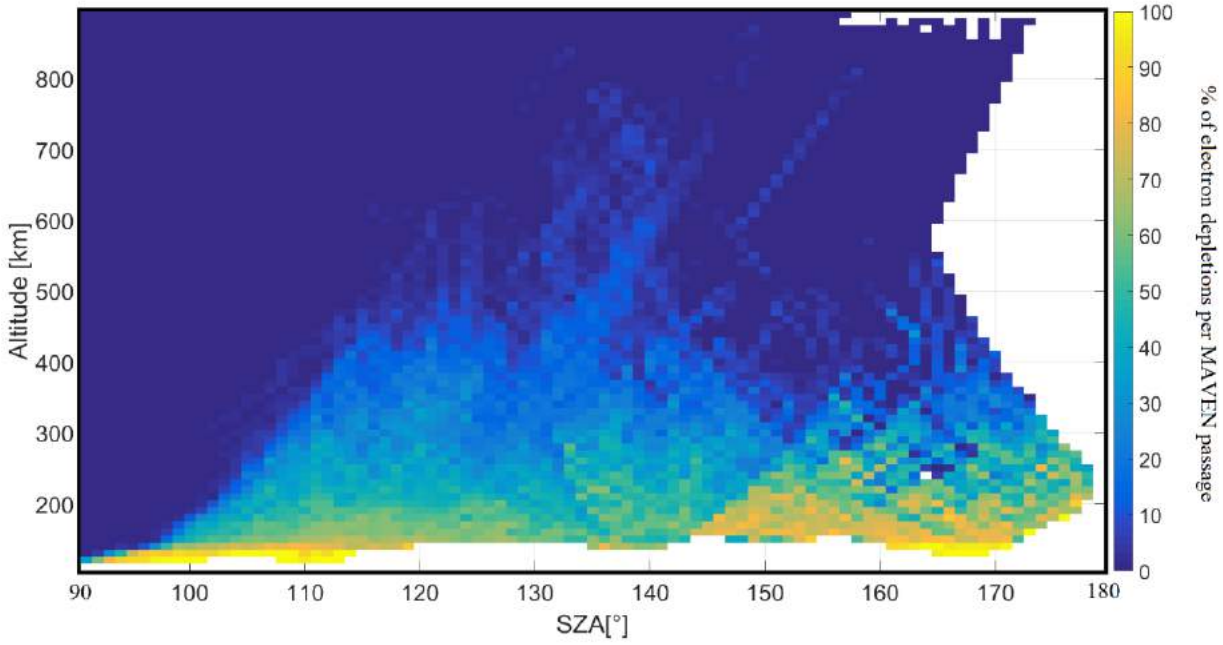

Figure 115. Distribution of the percentage of electron depletions per MAVEN orbit in SZA versus altitude. Data from November 2014 to September 2016 has been taken into account. The areodetic altitude has been used.

As this study needs more precision than previous ones regarding the altitude, I use the **areodetic altitude** (varying with latitude, see section 2.5.3), instead of the areocentric altitude

with which the previous analysis have been made. This altitude is used all along the study on the UV terminator.

5.3.2.2. Methodology

The boundary delimiting the region where electron depletions are observed is easily visually identifiable in Figure 115. However, it corresponds in fact to a gradient of percentage of electron depletions. In order to set a clear criteria to define the position of the UV terminator, I chose to find the best fit of the electron depletions distribution restricted at percentages greater than 10%. This threshold is arbitrary but enable a clear observation of the boundary under study.

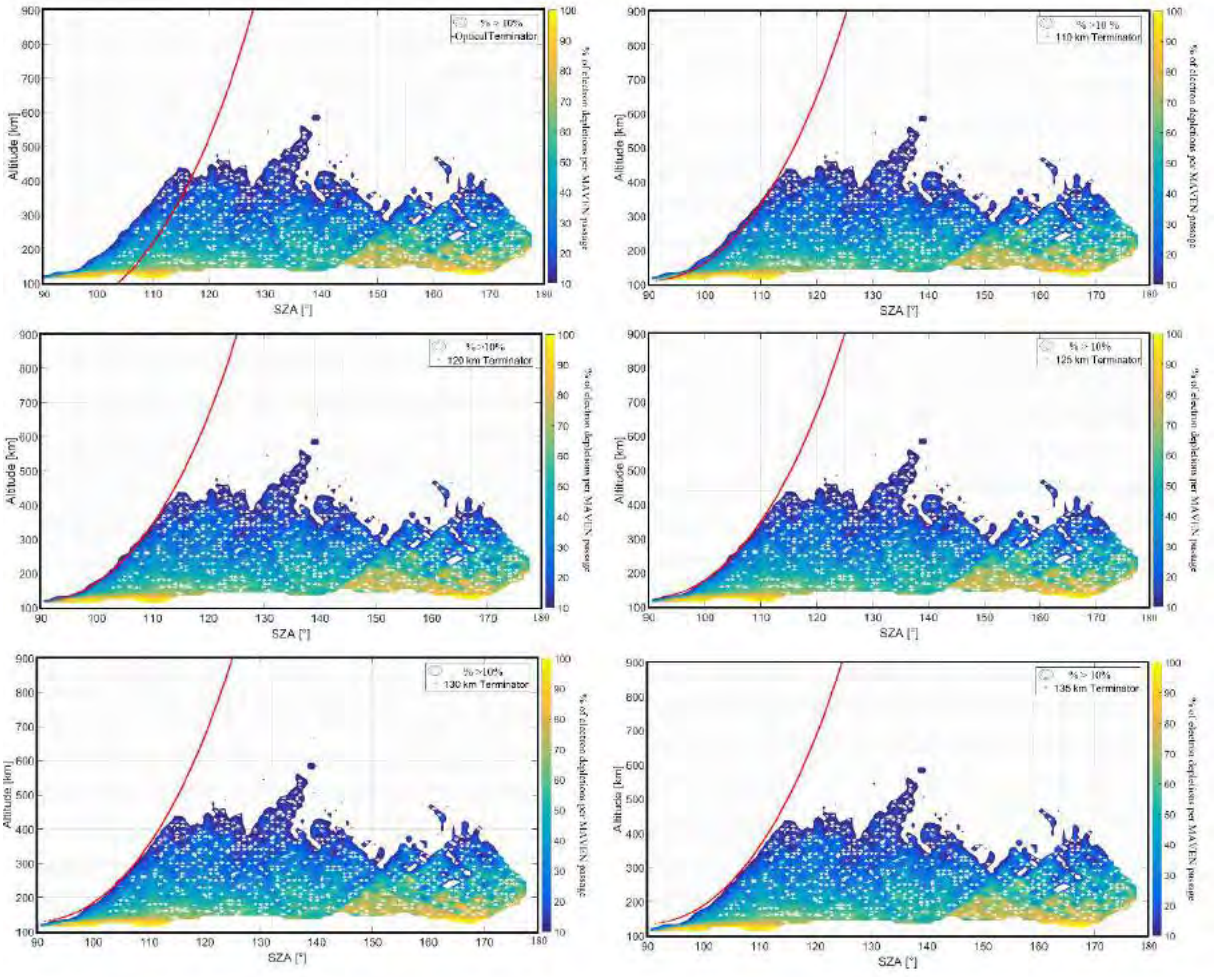

Figure 116. Contour plot of the percentage of electron depletions per MAVEN passage as a function of SZA and altitude, restricted to percentage greater than 10%.

On each plot is plotted a terminator calculated with a variable thickness of the absorbing atmosphere (from left to right, top to bottom) : 0 (optical terminator), 110, 120, 125, 130, 135 km.

In Figure 116 is plotted the contour lines of the percentages of electron depletions per MAVEN passage greater than 10%. I chose five possible thicknesses for the atmospheric layer (110, 120, 125, 130 and 135 km) and superimposed the corresponding UV terminator on each plot. The optical terminator has also been plotted as a reference.

I then chose visually which terminator fits best the data. As previously mentioned, the observation of the UV terminator is more relevant at low altitudes than at high altitudes due to the presence of crustal magnetic fields. If a different terminator fits low and high altitudes distributions, the one for the low altitudes is preferred.

5.3.2.3. Results and comparison with model

Looking at Figure 116, several terminators clearly do not fit the boundary: the optical one, and the three ones corresponding to 110, 130 and 135 km thickness for the atmospheric layer. The UV terminator lays in this case between **120 and 125 km** altitude above the optical terminator. These altitudes correspond to the lower and higher limits framing the effective boundary.

In Figure 117 is plotted the transmission rate of photons at the 30.4 nm wavelength, calculated thanks to the atmospheric model of Robert Lillis at the terminator. This wavelength indeed corresponds to the main wavelength involved in the ionization of atmospheric CO_2, creating photoelectrons. The entries of this model have been taken from the **Mars Climate Database** (MCD, http://www-mars.lmd.jussieu.fr/mcd_python/). The MCD is a database of atmospheric statistics compiled from the **Mars Global Climate Model** (MGCM) simulations of the Martian atmosphere. This model computes in 3D the atmospheric circulation and climate of Mars taking into account the radiative transfer and the CO_2 ice condensation and sublimation, among others. The different colors and the dashed and solid lines correspond to different entry conditions (season, solar cycle, amount of dust) that will be discussed in the next section. If we consider that the UV terminator corresponds to 10% of transmission, the UV terminator varies from 3540 to 3580 km from the center of Mars which corresponds to an altitude of 144 to 184 km taking a radius of 3396 km (value at the equator, the average latitude of the electron depletions detected being -2°N).

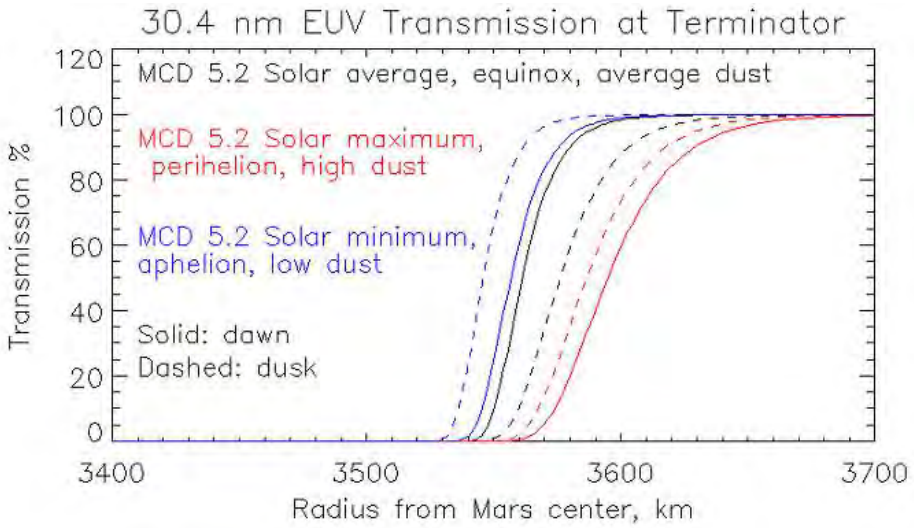

Figure 117. Transmission of the 30.4 nm photons calculated thanks to the atmospheric model of Robert Lillis. The different colors correspond to different input conditions taken from the MCD. The solid and dashed lines correspond respectively to the dawn and dusk sides.

These values are higher from what we obtained with electron depletions. Several issues have to be kept in mind when determining the UV terminator using electron depletions. First, we only use percentage greater than 10%. Using a lower percentage may increase slightly the altitude of the UV terminator of few kilometers, but not of forty. Then, we consider that electron depletions are observed when no more photoelectrons are created, without considering the other processes that may bring electrons in the nightside. The boundary delimiting the observation of electron depletions may then be at lower altitude than the effective UV terminator. Another main difference between the two studies is that we use in-situ measurements while the entry of the model are taken from a model of the Martian atmosphere. Despite these differences, the two results are of the same order of magnitude.

5.3.3. Evolution of the UV terminator with seasons: the dawn- dusk asymmetry

The UV terminator location is not fixed and homogeneous in time and space. As the other plasma boundaries of the Martian environment (section 1.3.2.3), its location depends on several parameters, among which the temperature and density of the neutral atmosphere which have an impact on the absorption of photoelectrons by neutrals. These two parameters, as for them, both vary with SZA (see section 4.3.2) and with seasons. In order to investigate the evolution of the

location of the UV terminator regarding seasons and SZA, we first analyze the results obtained for different atmospheric conditions with the model of Robert Lillis (section 5.3.3.1). We then disclose the results obtained thanks to electron depletions (section 5.3.3.2). The equinox proved to be the only season during which a comparative study between the observation and the model could be done. Section 5.3.3.3 hence focus on this specific season. We finish by an overview of the mystery surrounding the localization of the UV terminator at the aphelion and perihelion of Mars (section 5.3.3.4).

5.3.3.1. Predictions from the model of Robert Lillis

Figure 117 provides the transmission rate of 30.4 nm photons for three different atmospheric conditions:

- Solar maximum, perihelion, high dust
- Solar minimum, aphelion, low dust
- Solar average, equinox, average dust

We can observe that the UV terminator is the lowest at the aphelion, and the highest at the perihelion, with a variation of ~30 km. One main difference between these two conditions is the UV flux which should be higher at the perihelion than at the aphelion. However, this has little impact on the electron absorption. The parameter that really impact the electron absorption by the neutral atmosphere is the inclination of planet on the ecliptic and the corresponding season. On the hemisphere which is in summer, the temperature is higher, so as the neutral scale height. The neutral density at high altitudes is then higher in the summer hemisphere than in the winter hemisphere, implying an absorption of UV photons at higher altitudes and consequently a higher UV terminator in the summer hemisphere. As the calculations have been made at the equator, this effect was not expected to be so pronounced but the variations observed between the perihelion and the aphelion in Figure 117 have been confirmed by another model (model of Dominique Toublanc, see section 5.3.3.4).

The dusk (local time between 18:00 and 00:00) and the dawn sides (local time between 00:00 and 06:00) have also been separated. We can observe a dozen of kilometers of difference between the two sides. At the equinox, the UV terminator is higher on the dusk side than on the dawn side whereas at the aphelion and perihelion, the UV terminator is higher on the dawn side

than on the dusk side. The variation observed at the equinox is expected as the temperature of the atmosphere is usually higher on the dusk side compared to the dawn side. This induces a higher scale height on the dusk side, which means higher neutral densities at high altitudes than on the dawn side. Photoelectrons are then absorbed at higher altitudes and the UV terminator location is at higher altitudes. However, the reversal observed at the aphelion and perihelion is quite unexpected and is investigated in more details in section 5.3.3.4.

In order to take into account the different wavelengths involved in the ionization of the atmosphere, a convolution of an average EUV spectrum with the transmission rate at the various wavelengths between 10 and 89 nm has been made by Robert Lillis, 89 nm being the longest wavelength which can still ionize CO_2. The resulting transmission rate as a function of the radial distance and SZA is plotted in Figure 118. The same conditions as in Figure 117 have been taken, separating for each case the dawn from the dusk side. We can clearly see the decrease of the altitude of the UV terminator from perihelion to aphelion. The difference from the dawn and dusk side is more difficult to observe on this kind of plot, except at the perihelion where the UV terminator is clearly higher on the dawn side.

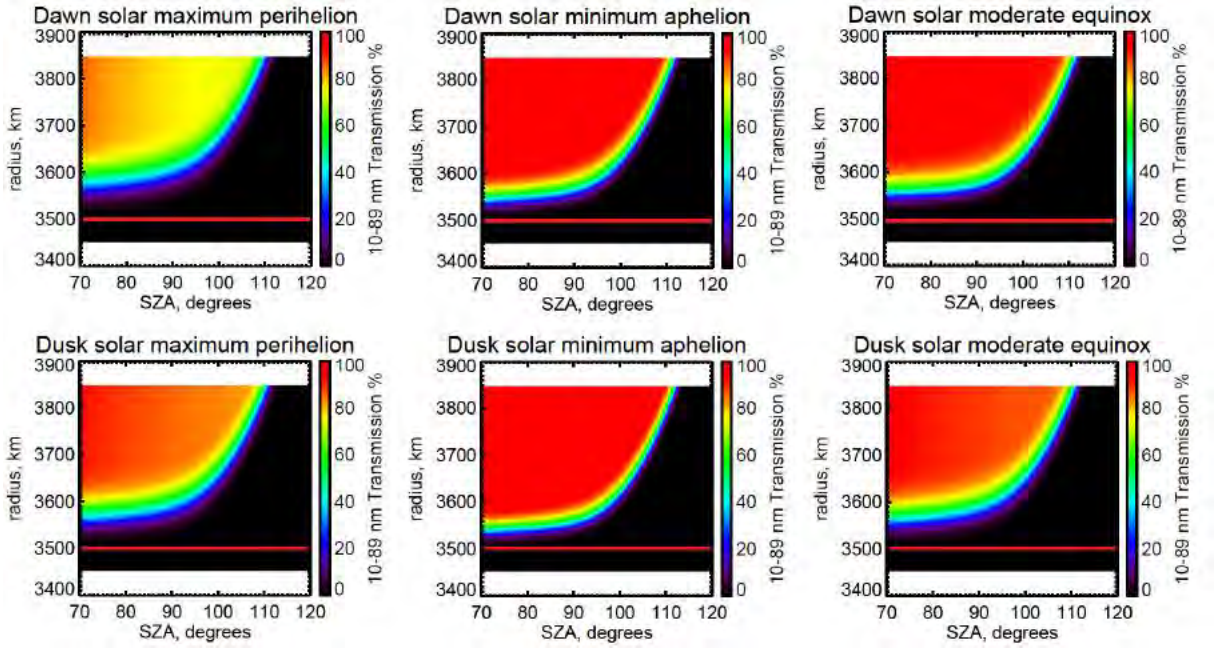

Figure 118. Transmission rate as a function of the radial distance and the SZA for wavelength from 10 to 89 nm. This figure has been made thanks to the model of Rob Lillis. The horizontal red lines highlight the radial distance of 3500 km.

The three conditions chosen by Robert Lillis correspond to the two extreme cases and to a medium case. The MAVEN measurements have been obtained during the declining phase of solar cycle 24 (see Figure 50), corresponding to moderate and minimum solar conditions. Throughout this period the EUV irradiance at Mars changed by a factor of 2, mainly due to the varying Mars-Sun distance rather than solar cycle variability. The EUV irradiance was highest at the beginning of the mission, when Mars was near its perihelion [*Girazian et al.*, 2017].

5.3.3.2. Results obtained with electron depletions

As each period of detection of electron depletions corresponds to a different season, I applied to each of them the same methodology as in section 5.3.2.2 to determine the corresponding altitude of the UV terminator, separating the dusk from the dawn side. I am however not yet able to apply this method to the fifth period, due to the presence of the spacecraft charging events polluting data at low altitudes, which are the more relevant altitudes to determine the location of the UV terminator. The corresponding data should be cleaned from these events before being used and compared with the other periods. The characteristics of the first four periods along with the corresponding results are gathered in Table 7.

Period	**Solar longitude**	**Season**	**Median Latitude**	**Distance to the Sun**	**Altitude of the EUV terminator [km]**		
					Global	**Dawn**	**Dusk**
10/14 → 10/16	all	all	-2°	all	120-125	120	130
10/14 → 04/15	240°→300°	Northern winter	63°	Perihelion	130	?	130
04/15 → 10/15	0°→50°	Southern Autumn	-70°	Equinox	120	120	(120)
10/15 → 04/16	90° →130°	Northern Summer	26°	Aphelion	120	120	×
04/16 → 10/16	170°→230°	Southern Spring	-21°	Equinox	125	125	135

Table 7. Altitude of the UV terminator above the optical terminator for the different periods during which electron depletions have been observed.

During a Martian year, the UV terminator is observed from 120 to 135 km above the optical terminator. Looking at the first line, gathering all electron depletions observed during one Martian year, we can see that the UV dawn terminator is located at ~120 km above the optical terminator whereas the UV dusk terminator is located at ~130 km above the optical terminator. The UV terminator is hence on average 10 km higher on the dusk side than on the dawn side, which is what was expected. This result should however be taken with caution. If we detail it per period:

- **First period:** electron depletions have equally been observed on the dusk and the dawn side. However, few observations have been made at low altitudes in the dawn side so that setting a clear value for the altitude of the UV terminator has not been possible. The largest nightside densities have been observed at high northern altitudes during this time period coincidently with a major solar energetic particle event [*Lee et al.*, 2017]. The presence of such events is likely to have increased the altitude of the UV terminator compared to its nominal value.
- **Second period:** very few events have been observed on the dusk side due to the orbitography of the spacecraft. However, the few events obtained were at low altitudes and their distribution show a clear boundary at 120 km. This value is in brackets as it has been obtained with few data.
- **Third period:** very few events have been observed on the dusk side due to the orbitography of the spacecraft. Contrary to the second period, these events were located at high altitudes so that no fitting was possible.
- **Fourth period:** this period has a perfect coverage in both dawn and dusk sides. It is the only period permitting to set a clear altitude for the UV terminator on both sides.

Hence, the results for the dawn-dusk variations obtained over one Martian year are biased by the coverage obtained during the different seasons. Concerning the seasonal variations, an interesting point is that the southern hemisphere has been covered both at perihelion and at aphelion whereas the northern hemisphere has been covered during the two equinoxes. However, as at the perihelion (the aphelion, respectively), only a value for the dusk side (dawn side, respectively) is available, both seasonal and SZA effects are mixed so that no conclusion can be set. At the equinox, a reliable value of the altitude of the UV terminator on the dusk side is lacking in 2015 to observe or not a difference between the autumn and spring equinoxes.

5.3.3.3. Focus on the equinox of 2016

The fourth period turned out to be the only period during which the UV terminator is clearly identifiable both on the dusk and on the dawn side. The results of my study set the UV terminator at 125 km above the optical terminator in the dawn side, whereas it is at 135 km in the dusk side. The dusk terminator is then above the dawn terminator. This conclusion is in agreement with the model of Robert Lillis at the equinox (section 5.3.3.1): a dozen of kilometers separate the dawn from the dusk terminator in both studies.

This asymmetry is predicted by the MGCM. It is attributed to a dawn-dusk asymmetry in the composition of the neutral atmosphere (e.g. atomic oxygen) driven by cooler temperatures at dawn than at dusk [*Gonzalez-Galindo et al.*, 2013; *Chaufray et al.*, 2014]. Neutrals have then a higher scale height and consequently a greater density at high altitudes on the dusk side than on the dawn side. Photons are absorbed at higher altitudes in the dusk side and the corresponding UV terminator is located at higher altitudes than in the dawn side.

This prediction can be checked through NGIMS measurements. In Figure 119 is plotted the density profiles of three main neutral species of the neutral atmosphere: O, N_2 and CO_2, obtained during the fourth period on the dawn (**black** lines) and dusk (**red** lines) sides. The solid lines correspond to the average NGIMS profiles while the stars correspond to the set of models HELIOSARES [*Leblanc et al.*, submitted]. This project aims to couple three independent models of the Martian environment: the MGCM, the Mars LATmos Hybrid Simulation (LatHyS) magnetospheric model and the Mars Exospheric Global Model (EGM), in order to describe the Martian environment from its surface to the exosphere for any given conditions.

We can see that HELIOSARES is globally in good consistency with the in-situ data, at least for altitudes downward 250 km. For the three species under study, the density on the dusk side is actually observed to be higher than on the dawn side, at least for altitudes downward 250 km.

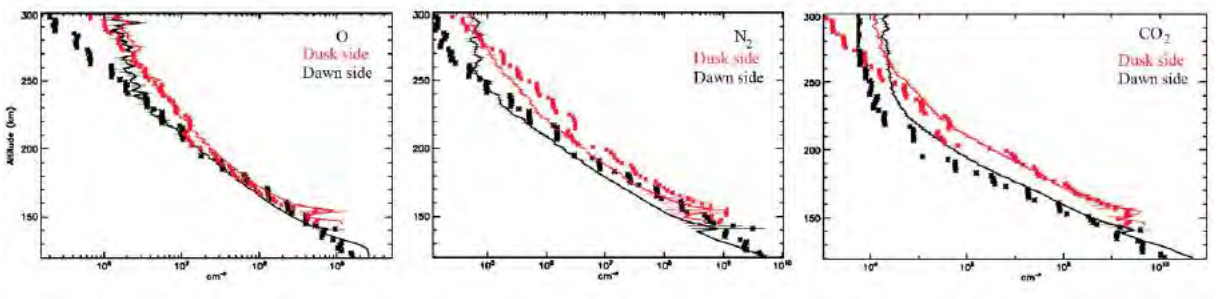

Figure 119. Density profiles of O, N_2 and CO_2 obtained by NGIMS during the fourth period. The red lines and stars correspond to the dusk side and the black lines and stars correspond to the dawn side. The solid lines are the average NGIMS profiles and the stars correspond to the model set HELIOSARES.

The dawn-dusk asymmetry of the neutral atmosphere has been observed to be coincident with a dawn-dusk asymmetry of the ionosphere. Regarding the electrons, this asymmetry has been noticed on the electron temperature and density derived from LPW [*Andersson et al.*, in preparation]. The altitude profiles of the densities and temperatures measured for dawn and dusk from October 2014 through August 2016 at altitudes below 500 km are shown in Figure 120. Color coding for each SZA range is detailed in the figure caption. The reference profiles for noon, terminator, and midnight are plotted in dashed lines.

A clear dawn-dusk asymmetry can be observed in the electron density on the nightside. The densities observed on the dusk side are clearly higher than on the dawn side. This observation can be explained by the rotation of the planet. As the planet rotates, the sunlit ionosphere rotates past the dusk terminator leading to a high-density dusk terminator ionosphere. There is then a rapid loss of ions in the nightside ionosphere and as the ionosphere rotates past midnight the density is low. At dawn, the sunlight reaches first the highest altitudes so that the high altitude ionosphere recovers faster than the lower one. As the full ionosphere rotates into sunlight the photoionization increases ion production. As this global behavior was expected, what turns out to be unexpected is the delay for the ionosphere to replenish: the dawn density profiles only become close to dusk ones (reaching a quasi-stationary situation) around noon, which means that it takes ~6 hours for the Martian ionosphere to recover, to compare with the 1-2 hours in the case of the Earth. This delay is another indicator of the underlying neutral atmosphere dawn-dusk asymmetry as the ionosphere is closely coupled to the neutral atmosphere.

Concerning the electron temperature, the dawn-dusk asymmetry is less clear than for the density. At high altitudes, the dusk ionosphere is warmer than the dawn ionosphere while at low altitudes the dawn ionosphere is warmer than the dusk ionosphere.

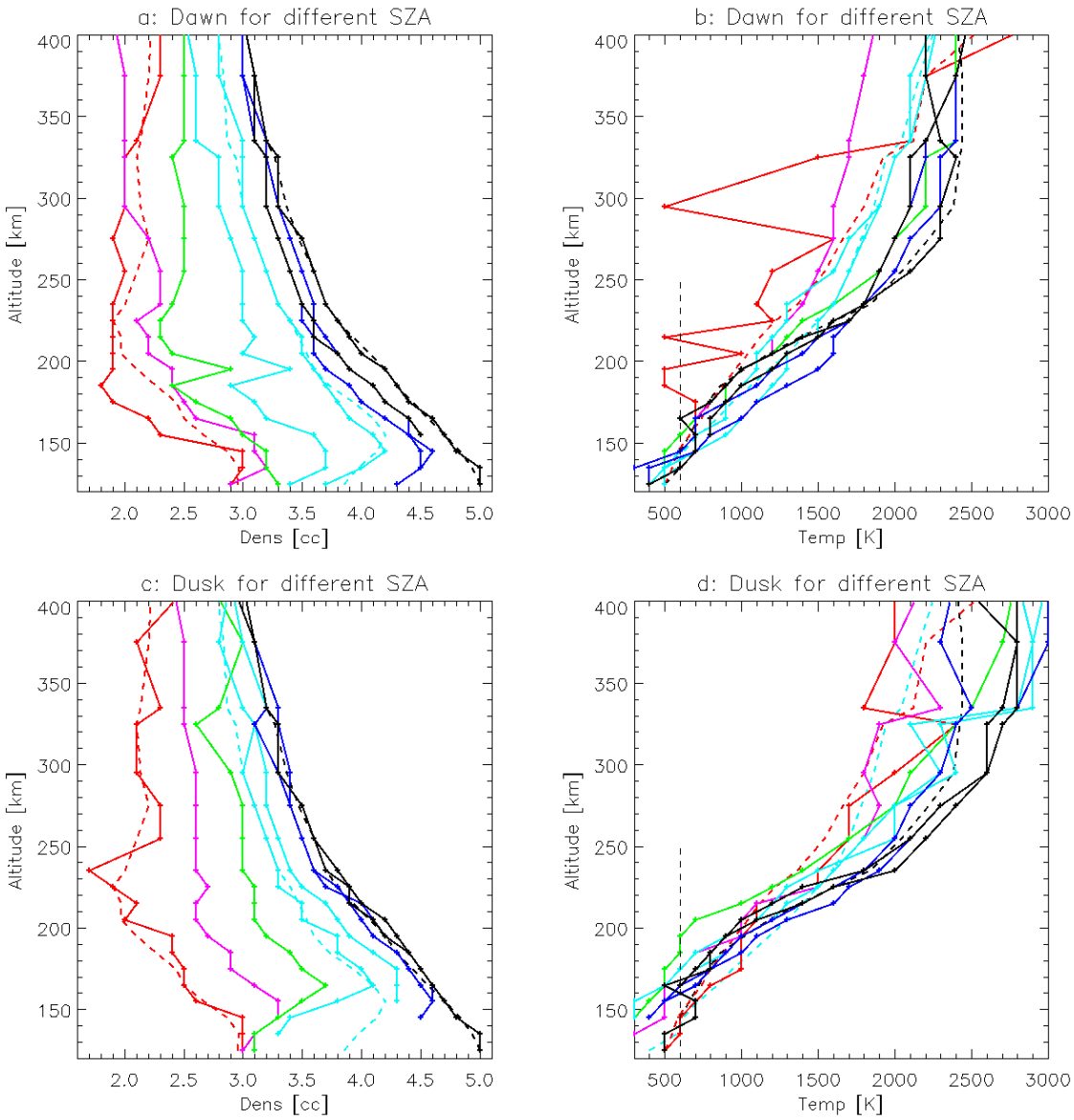

Figure 120. The most likely density and temperature measured by LPW as a function of altitude for dawn (top row) and dusk (bottom row) measurements [Andersson et al., in preparation].

*The dashed lines are most likely density/temperature in each altitude range. Each line represents a different SZA range: 0-30 (**black**),30-50 (**black**), 50-70 (**blue**), 70-90 (**blue**), 90-95 (**light blue**), 95-100 (**light blue**), 100-110 (**green**), 110-150 (**pink**),732 and 150-180°(**red**). Colors are duplicated for the lower SZA ranges so that distinct colors can be used to emphasize the SZA ranges where the largest changes occur.*

5.3.3.4. The mystery of the reversal at the aphelion and perihelion

We saw in the previous section that, at the equinox, the dusk terminator is higher than the dawn terminator, which is consistent with models as well as neutrals and electrons observations. However, looking back at Figure 117, we can see that the atmospheric model of Robert Lillis

predicts that this configuration is specific to the equinox: the two terminators reverse position at the perihelion and aphelion of Mars. In order to check if this inversion is a model issue, I used the atmospheric model of Dominique Toublanc which is a Monte Carlo radiation transfer model that follows photons in absorption and diffusion in the atmosphere [*Toublanc et al., 1995*, adapted to Mars]. In order to observe the inversion between seasons, we used two sets of input conditions from the MGCM (pressure, temperature) corresponding to the fourth and fifth period of detection of electron depletions:

- August 1st, 2016 at 12:00 UT (equinox), a mean latitude of -21° on the dusk side and 9° on the dawn side.
- January 22, 2017 at 12:00 UT (Northern winter), a mean latitude of -24° on the dusk side and -46° on the dawn side.

The transmission rates corresponding to these two conditions on the dusk and on the dawn side are plotted in Figure 121. We clearly see that the dusk terminator is higher than the dawn terminator at the equinox. However, as in the model of Robert Lillis, their position reversed at the perihelion of Mars.

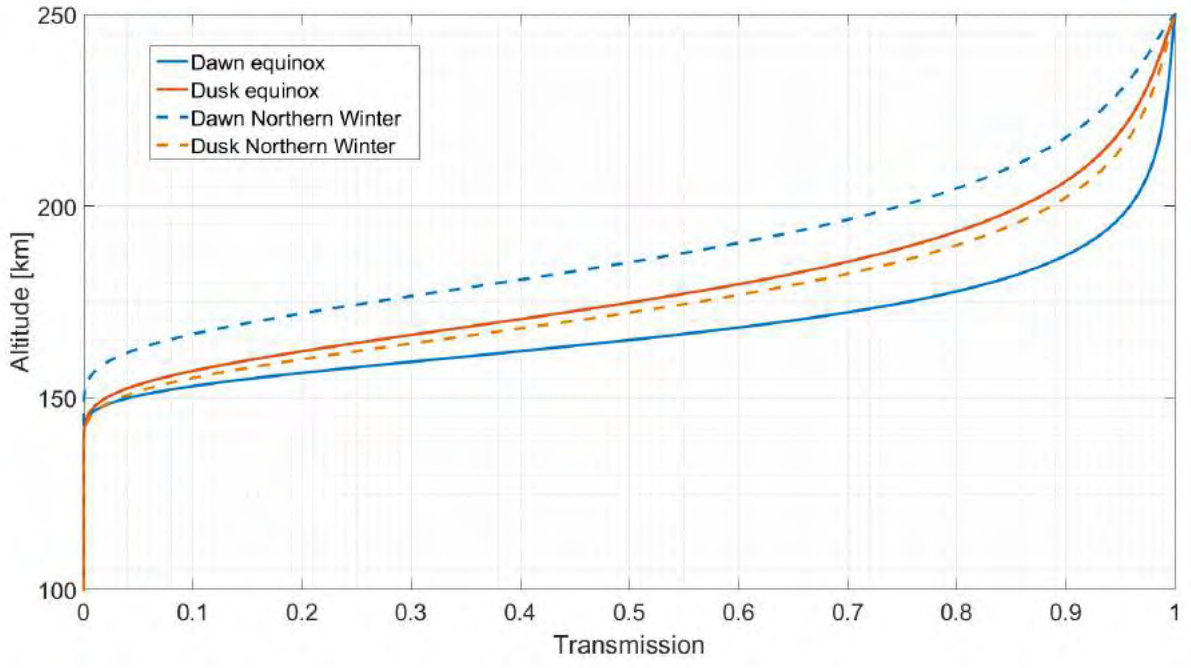

Figure 121. Transmission rate calculated thanks to the model of Dominique Toublanc for the fourth (equinox) and fifth (northern summer) period.

As the two models show the same inversion between the location of the dawn and dusk terminator, this phenomenon does not come from the model used, a priori. Another possibility is that it comes directly from the inputs of the models, which both come from the MGCM. We then plot in Figure 122 the corresponding temperature and pressure profiles used to calculate the transmission profiles in Figure 121. We can see that there is indeed an inversion of the density and temperature profiles between the two periods. At the equinox the temperature and the density are higher on the dusk side than on the dawn side, while at the Northern winter the density is slightly higher in the dawn side and the temperature profile in the dawn side is more complicated, as observed in Figure 120. What catches the eyes is the dawn density at the equinox which falls at high altitudes compared to what is observed at the northern winter. This phenomenon is not yet understood and may be due to some condensation in the dawn side.

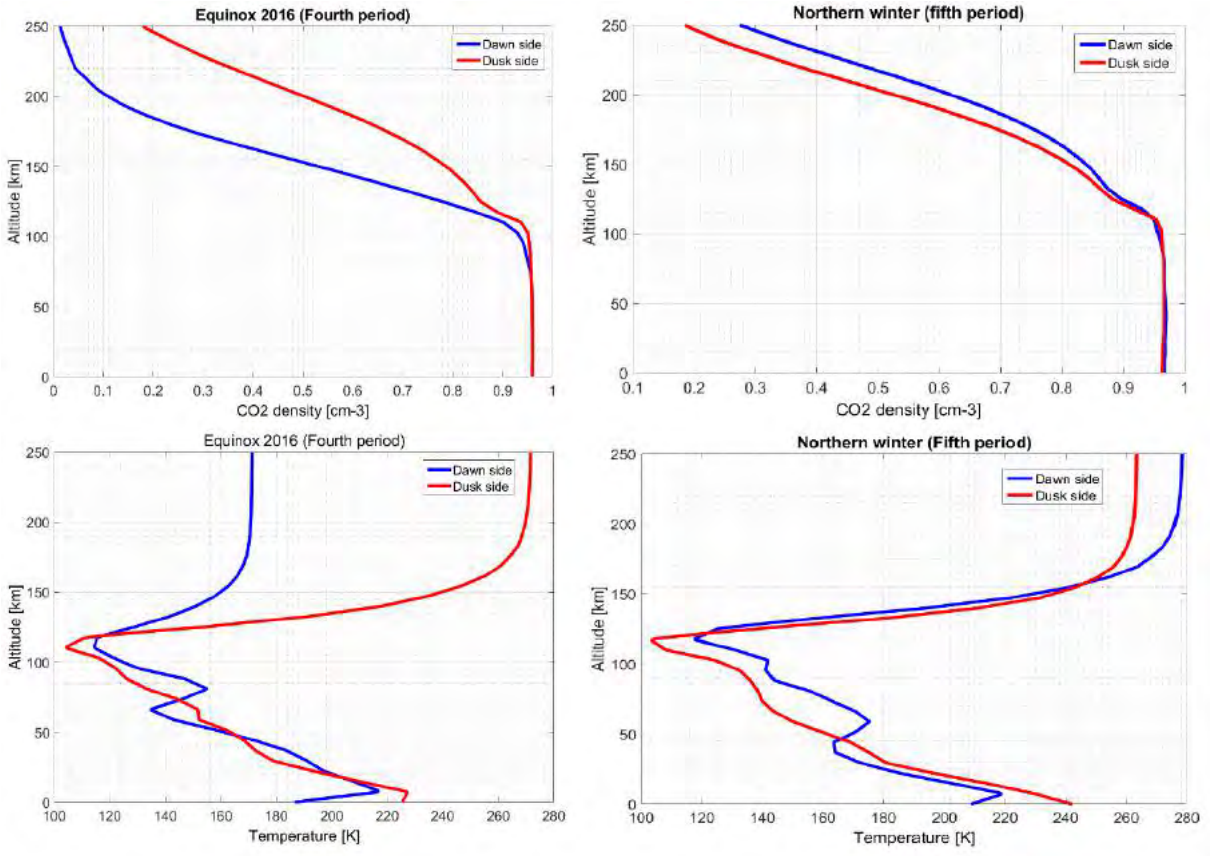

Figure 122. Density (first line) and temperature (second line) profiles on the dusk and dawn side from the GCM model on August 1st, 2016 for the first column and on January 22, 2017 for the second column.

The use of the fifth period of detection of electron depletions, which equally covers the dusk and dawn sides, could have enabled me to support the models and to observe the inversion of the location of the dawn and dusk UV terminator, or on the contrary to set that there is no

inversion in the in-situ data. Both observations would have raised various questions. However, the presence of spacecraft charging events prevents me from setting a clear conclusion concerning this period. Removing the effects due to these events in order to observe the location of the UV terminator during this time period would be a necessary step to improve this study. Unfortunately, NGIMS data are also partially available during this period so that they cannot be used for the moment.

A study on the impact of external drivers such as the solar wind pressure or the incoming EUV flux would be interesting to be led in order to disentangle the effects of the different parameters. The differences observed between the five periods could indeed be due to variations in the nightside plasma sources or to diurnal and seasonal variations in the composition of the neutral atmosphere. The present state of this study makes it difficult to distinguish between the different sources of variability.

The basic element for creating electron depletions is a mechanism that absorbs electrons. Above the electron exobase, closed crustal magnetic field loops are necessary to lead electrons toward the collisional atmosphere whereas below it electrons are locally absorbed. If no mechanism supply enough electrons to balance this absorption, electron depletions are observed. On the dayside, the in-situ creation of photoelectrons balances the electron absorption by the collisional atmosphere so that no electron depletion is observed. Photoelectrons are produced until the UV terminator, behind which very few electrons are produced through other processes. It hence corresponds to a boundary behind which electron depletions are usually observed. An average altitude of ~120 km above the optic terminator have been found for the UV terminator. Transport processes can bring electrons behind the UV terminator, creating flux spikes or totally preventing the creation of electron depletions, filling closed crustal magnetic field loops with transported electrons.

Conclusions and Perspectives

The nightside ionosphere of Mars, though faint, irregular and spotty, is a central region of the Martian plasma environment as it spans from the lower altitudes, where collision processes dominate, to the higher altitudes, where plasma transport dominates. It participates in the global plasma circulation around Mars and is a conduit through which particles from the neutral atmosphere can escape.

Despite its importance, this region had little opportunity to be studied before the arrival of the MAVEN spacecraft in September 2014. The MGS spacecraft was indeed restricted to ~400 km altitude at a fixed local time and MEX lowest altitude is currently around 300 km. Moreover, MGS did not carry any ion spectrometer and MEX does not carry any magnetometer. These two missions nevertheless discovered the presence of recurrent structures, specific to the nightside ionosphere: the plasma voids. Plasma voids are characterized by a sharp drop of the electron flux at all energies observed by the electron spectrometers (down to a dozen of eV). These structures, only observed on the nightside above strong crustal magnetic field sources, have mostly been used so far to infer the magnetic topology in the nightside hemisphere. However, they have a greater potential.

The MAVEN spacecraft entered into orbit around Mars on September 21, 2014, with a complete suite of plasma and field instruments onboard. Its elliptical precessing orbit, with a nominal periapsis located at ~150 km altitude which can be sporadically lowered down to ~125 km, enables a more accurate vision and understanding of the nightside ionosphere at various altitudes, local times and solar zenith angles. Thanks to these unprecedented capabilities, plasma voids have been observed over the whole Martian surface, not only above strong crustal magnetic field sources. Moreover, plasma voids do not seem to be void of plasma anymore.

In this manuscript I decided to investigate plasma voids in order to better understand the structure and dynamics of the nightside ionosphere. The first step has been to characterize the detailed properties of plasma voids on a statistical basis and to understand the different processes leading to their creation. To this end I have analyzed observations of electron depletions from three different Martian missions (MGS, MEX, and MAVEN). These three datasets are complementary, the new MAVEN observations nicely extending toward the low altitude neutral atmosphere observations obtained at higher altitudes with MGS and MEX. I thus provide the first multispacecraft analysis of plasma voids covering 17 years of Martian exploration, offering a comprehensive view of the phenomenon. While previous studies used

different approaches to identify plasma voids in MGS and MEX data, I here used the same method to automatically detect these events in the three Martian orbiter data sets. In addition, I did not impose any geometric restrictions in my conditional research — contrary to previous studies like the one of *Hall et al.*, [2016], which was restricted to the illuminated induced magnetosphere.

My first results show that plasma voids are in fact filled with low energy planetary ions, thermal electrons and a remaining electron population peaked at 6-7 eV. This leads me to rename these structures as suprathermal electron depletions [*Steckiewicz et al.*, 2015, 2016].

I then show that electron depletions are spread on the nightside of the Martian environment at altitudes between 110 and 900 km (110 km being the lowest altitude reached by MAVEN in the nightside). For comparable altitude ranges (i.e., above about 250 km), the geographic distributions of electron depletions for each mission produced results in agreement with each other and with previous studies: electron depletions are strongly linked with the presence of closed crustal magnetic field loops. However, the MAVEN observations show that this link mostly occurs above a transition region near 160-170 km altitude, under which the distribution of electron depletions is more homogeneous, regardless the presence of crustal magnetic fields. This altitude corresponds to the electron exobase, which was not observable with MGS and MEX due to their orbitography. These observations lead me to review the pre-established scenario of creation of electron depletions as follows. Electron depletions are the result of a balance between electron source and loss processes. In the nightside, electrons locally created or transported from the dayside are trapped in the outer magnetic field lines of closed crustal magnetic field loops. They are then routed toward the neutral atmosphere where they are absorbed, mainly by CO_2. Only the remaining electrons (thermal and 6-7 eV populations due to the collision cross section energy dependence) can be observed inside closed crustal magnetic loops. However, below the electron exobase, we enter the collisional region and radial magnetic fields are no more necessary for electrons to be absorbed by the neutral atmosphere. The observation of electron depletions hence depends both on the magnetic topology and on the state of the neutral atmosphere at the observational point.

Once the general processes at the origin of electron depletions have been understood, this enabled me to study various structures of the nightside ionosphere. Specific features of the Martian magnetic topology, such as trans-terminator closed crustal magnetic field lines or low altitudes current sheets have been identified. However, the coupling with the neutral atmosphere

should always be taken into account. Electron depletions are indeed only observed below the UV terminator, providing us an indirect method to set its localization. On average over one Martian year, the UV terminator has been found to be located 120-125 km above the optical terminator. The UV terminator has been observed to lay at higher altitudes on the dusk side than on the dawn side at the equinox, in agreement with atmospheric models and recent results from LPW and NGIMS. However, atmospheric models predict that the situation reverses at the perihelion and the aphelion, and data did not enable us to confirm or invalidate this inversion yet. More work on this issue is needed, in collaboration with Robert Lillis, Dominique Toublanc, François Leblanc and the MGCM model team to better understand the seasonal dynamics of the atmosphere.

Another interesting deepening in my study is the absence of observation of electron depletions in specific regions of the Martian environment, such as above the Tharsis region. The analysis of the influence of gravity waves on the observation of electron depletions is in progress, and should be carried on in collaboration with Scott England and Meredith Elrod. Further analysis are required to understand the link existing between gravity waves, the neutral temperature and the density profiles observed. The use of models may be necessary to confirm or infirm the influence of gravity waves on the creation of electron depletions.

Many issues that have remained unresolved at the end of my PhD may find answers as MAVEN continues to monitor the nightside ionosphere under different conditions. Continued monitoring will also be useful for exploring the drivers of the nightside variability which may be linked to crustal magnetic field conditions, ion circulation patterns, thermospheric conditions, and changes in the energetic particle environment.

Electron depletions are tremendous structures worth being deeper studied. Their observation due to the coupling between the magnetic topology, the ionosphere, and the neutral atmosphere is a significant asset to study these three features in the nightside of Mars.

Conclusions et Perspectives

L'ionosphère du côté nuit de Mars, bien que faible, irrégulière et intermittente, est une région centrale de l'environnement plasma de la planète, s'étendant des basses altitudes où les processus de collision dominent, jusqu'aux hautes altitudes où les processus de transport dominent. Elle participe à la circulation globale du plasma autour de Mars et représente un canal permettant aux neutres sous-jacents de s'échapper de l'atmosphère martienne.

Bien que l'intérêt pour cette région soit significatif, elle a finalement eu peu l'occasion d'être étudiée avant l'arrivée de la mission MAVEN en Septembre 2014. En effet, MGS était sur une orbite circulaire à ~ 400 km, bloquée en temps local et n'était pas équipé pas de spectromètre à ions. Le satellite MEX quant à lui a actuellement un périapse à ~300 km et ne possède toujours pas de magnétomètre à son bord. Ces deux missions ont cependant découvert, entre autres, la présence dans l'ionosphère du côté nuit de structures récurrentes et spécifiques à cette région : les 'trous de plasma'. Les trous de plasma sont caractérisés par une diminution brutale du flux d'électrons à toutes les énergies observées par les spectromètres à électrons (jusqu'à une dizaine d'eV). Ces structures sont alors interprétées comme le passage du satellite au sein de boucles fermées de champ magnétique d'origine crustale, dont l'intensité est suffisante pour empêcher la pénétration de plasma. Elles ont donc jusqu'ici principalement été utilisées pour déterminer la topologie magnétique de Mars du côté nuit. Elles ont cependant beaucoup plus de potentiel.

Le satellite MAVEN est entré en orbite autour de Mars en Septembre 2014, avec à son bord un ensemble cohérent d'instruments plasma et champ magnétique. Son orbite elliptique précessant naturellement, dont le périapse peut atteindre ~125 km d'altitude, nous permet d'avoir une vision plus globale et une compréhension plus fine de l'ionosphère du côté nuit. Grâce à ces capacités sans précédent, les trous de plasma ont été observés au-dessus de toute la surface martienne, contrairement aux observations précédentes. De plus, ils se sont révélés moins vide de plasma que nous le pensions.

Dans ce manuscrit j'ai décidé d'étudier les trous de plasma afin de mieux comprendre la structure et la dynamique de l'ionosphère du côté nuit de Mars. Dans ce but, j'ai analysé les observations de trous de plasma effectuées par trois missions martiennes (MGS, MEX, et MAVEN). Ces trois jeux de données sont complémentaires, les nouvelles observations de MAVEN étendant vers l'atmosphère neutre les mesures effectuées à plus hautes altitudes par

MGS et MEX. J'ai ainsi effectué la première analyse multi-satellites de trous de plasma couvrant une période de 17 ans, offrant ainsi une vision plus complète du phénomène. Alors que les études précédentes utilisaient différentes approches pour identifier les trous de plasma dans les données de MGS et MEX, j'ai ici utilisé la même méthode pour automatiquement détecter ces événements dans les données des trois orbiteurs. Je n'ai par ailleurs imposé aucune restriction géométrique à ma recherche conditionnelle, contrairement à d'autres études comme celle de *Hall et al.*, [2016], qui était restreinte à la partie illuminée de la magnétosphère induite.

Mon premier résultat a été de montrer que les trous de plasma n'étaient pas vides mais étaient remplis d'ions planétaires de basses énergies, d'électrons thermiques et d'une population d'électrons piquée à 6-7 eV. Cela m'a amenée à renommer ces structures les déplétions d'électrons suprathermiques [*Steckiewicz et al.*, 2015, 2016].

J'ai ensuite montré que les déplétions d'électrons était réparties du côté nuit entre 110 et 900 km d'altitude (110 km étant la plus basse altitude atteinte par MAVEN du côté nuit). A des altitudes comparables (i.e., au-dessus de ~250 km), les distributions géographiques des déplétions d'électrons détectées par chaque mission offrent des résultats cohérents entre eux et avec les études précédentes : l'observation de déplétions d'électrons est fortement liée à la présence de boucles fermées de champ magnétique d'origine crustale. Cependant, les observations réalisées par MAVEN nous ont dévoilé que ce lien n'était prédominant qu'au-dessus d'une région de transition autour de 160-170 km d'altitude. En-deçà de cette altitude, la distribution de déplétions d'électrons est plus homogène, indépendamment de la présence de champs magnétiques d'origine crustale. Cette altitude correspond à l'exobase des électrons, qui n'était observable ni avec MGS ni avec MEX de par leur orbitographie. Ces observations m'ont amené à revoir le scénario précédemment établi de la création des déplétions d'électrons comme suit. Les déplétions d'électrons sont le résultat d'un équilibre entre les mécanismes sources et les mécanismes de perte d'électrons. Du côté nuit, les électrons créés localement ou transportés depuis le côté jour sont piégés dans les lignes de champ externes des boucles fermées de champ magnétique. Ils sont ensuite acheminés vers l'atmosphère neutre où ils sont absorbés, principalement par le CO_2. Les électrons n'ayant pas été absorbés dans l'atmosphère (thermiques et la population à 6-7 eV, dû à la variation en énergie de la section efficace de collision) sont les seuls qui peuvent être observés à l'intérieur des boucles fermées de champ magnétique. Cependant, sous l'exobase des électrons se trouve la région collisionnelle. Les champs magnétiques radiaux ne sont alors plus nécessaires à l'absorption des électrons par l'atmosphère neutre. Les déplétions d'électrons sont donc potentiellement

observables au-dessus de toute la surface. L'observation de déplétions d'électrons dépend donc à la fois de la topologie magnétique et de l'état de l'atmosphère neutre au point d'observation.

Une fois que le processus général à l'origine de la création des déplétions d'électrons a été compris, j'ai pu étudier un certain nombre de phénomènes de l'ionosphère du côté nuit : des structures spécifiques à la topologie magnétique martienne, telles que des boucles fermées de champ magnétique enjambant le terminateur, ou des couches de courant à très basses altitudes, ont pu être identifiées. Le couplage entre l'ionosphère et l'atmosphère nous a aussi permis d'observer le terminateur UV. Les déplétions d'électrons sont en effet uniquement observées sous le terminateur UV, nous fournissant une méthode indirecte pour déterminer sa localisation. En moyenne sur une année martienne, le terminateur UV se trouve 120-125 km au-dessus du terminateur optique. A l'équinoxe, il a été observé à plus haute altitude du côté soir que du côté matin, en accord avec les modèles atmosphériques et les résultats récents de LPW et NGIMS. Cependant, les modèles atmosphériques prédisent que la situation s'inverse au périhélie et à l'aphélie de Mars, mais les données ne nous ont pas permis de confirmer ou d'infirmer cette inversion jusqu'à maintenant. Une analyse complémentaire sera nécessaire afin de mieux comprendre la dynamique saisonnière de l'atmosphère, en collaboration avec Robert Lillis, Dominique Toublanc, François Leblanc et l'équipe du modèle MGCM.

Un autre point approfondi dans mon étude est l'absence d'observation de déplétions d'électrons dans certaines parties de l'environnement martien, comme au-dessus de la région du dôme de Tharsis. Une analyse de l'influence des ondes de gravité sur l'observation des déplétions d'électrons est en cours, et devrait être poursuivie en collaboration avec Scott England et Meredith Elrod. Une étude du lien existant entre les ondes de gravité, la température des neutres et les profils de densité observés est nécessaire. L'utilisation de modèles pourra s'avérer nécessaire pour confirmer ou infirmer l'influence des ondes de gravité sur la création des déplétions d'électrons.

Un certain nombre de questions qui sont restées sans réponses au terme de mon doctorat devraient trouver une réponse grâce aux données qui continuent d'être mesurées par MAVEN dans l'ionosphère du côté nuit. Une surveillance continue sera nécessaire pour étudier les différents paramètres influençant la variabilité de l'ionosphère du côté nuit. Ceux-ci peuvent être liés à la topologie du champ magnétique crustal, aux modèles de circulation des ions et des électrons, aux conditions thermosphériques, ou encore aux injections de particules énergétiques. Les déplétions d'électrons sont des structures dignes d'intérêt, qui méritent d'être

étudiées plus en détail. Leur observation due au couplage entre la topologie magnétique, l'ionosphère et l'atmosphère neutre est un atout significatif pour étudier ces trois structures du côté nuit de Mars.

Acronyms

AMDA: Automated Multi-Dataset Analysis

APP: Articulated Payload Platform (on MAVEN)

ASPERA: Analyser of Space Plasmas and Energetic Ions for Mars Express (on MEX)

AU: Astronomical Unity

BS: Bow Shock

CDPP: Centre de Données de la Physique des Plasmas

CNES: Centre National D'Etudes Spatiales

CNRS: Centre National de Recherche Scientifique

CR: Count Rate

ELS: Electron Spectrometer (on MEX)

EUV: depending on the context, it can be either Extrem Ultra Violet or the instrument Extreme Ultraviolet monitor (on MAVEN)

ER: Electron Reflectometer (on MGS)

ESA: European Space Agency

FOV: Field Of View

GW: Gravity Wave

HRSC: High Resolution Stereo Camera (on MEX)

IMA: Ion Mass Analyzer (on MEX)

IMB: Induced Magnetosphere Boundary

IMF: Interplanetary Magnetic Field

IP: Ionopause

IRAP: Institut de Recherche en Astrophysique

IUVS: Imaging Ultraviolet Spectrometer (on MAVEN)

I-V: Current - voltage

JE: omnidirectional particle energy flux

LPW: Langmuir Probe and Waves (on MAVEN)

LT: Local Time

MAG: Magnetometer (on MGS, MEX and MAVEN)

MaRS: Mars Radio Science (on MEX)

MARSIS: Mars Advanced Radar for Subsurface and Ionosphere Sounding (on MEX)

MAVEN: Mars Atmosphere and Volatile EvolutioN

MCP: MicroChannel Plate

MEX: Mars EXpress

MGS: Mars Global Surveyor

MHD: Magneto-HydroDynamic

MOC: Mars Orbiter Camera (on MGS)

MOLA: Mars Orbiter Laser Altimeter (on MGS)

MPB: Magnetic Pile-up Boundary

MPR: Magnetic Pile-up Region

MSE: Mars-Sun-Electric field

MSO: Mars-Centric Solar Orbital

MVA: Minimum Variance Analysis

NASA: National Aeronautics and Space Administration

NGIMS: Neutral Gas and Ion Mass Spectrometer (on MAVEN)

OMEGA: Observatoire pour la Minéralogie, l'Eau, les Glaces et l'Activité (on MEX)

PAD: Pitch Angle Distribution

PEB: PhotoElectron Boundary

PL: PayLoad

PDS: Planetary Data System

PFS: Planetary Fourier Spectrometer (on MEX)

SEP: Solar Energetic Particle (depending on the context it refers to the particles or to the instrument on MAVEN)

SPICAM: Studying the Global Structure and Composition of the Martian Atmosphere (on MEX)

STATIC: Supra-Thermal And Thermal Ion Composition analyzer (on MAVEN)

SWEA: Solar Wind Electron Analyzer (on MAVEN)

SWIA: Solar Wind Ion Analyzer (on MAVEN)

SZA: Solar Zenith Angle

TES: Thermal Emission Spectrometer (on MGS)

UV: Ultra Violet

Table of figures

Table of tables

Bibliography

Acuña, M. H., J. E. P. Connerney, P. Walilewski, R. P. Lin, K. A. Anderson, C. W. Carlson, J. McFadden, D. W. Curtis, H. Rème, A. Cros, J. L. Médale, J. A. Sauvaud, C. d'Uston, S. J. Bauer, P. Cloutier, M. Mayhew, and N. F. Ness (1992), Mars Observer Magnetic Fields Investigation, *Journal of Geophysical Research, 97*(E5), 7799-7814, doi: 10.1029/92JE00344

Acuña, M. H., et al. (1998), Magnetic field and plasma observations at Mars: Initial results of the Mars Global Surveyor mission, *Science, 279*(5357), 1676-1680, doi: 10.1126/science.279.5357.1676

Acuña, M. H., et al. (1999), Global distribution of crustal magnetization discovered by the Mars Global Surveyor MAG/ER Experiment, *Science*, 284: 790-793, doi: 10.1126/science.284.5415.790

Acuña, M. H., et al. (2001), Magnetic field of Mars: Summary of results from the aerobreaking and mapping orbits, *Journal of Geophysical Research, 106*(E10), 23403-23417, doi: 10.1029/2000JE001404

Albee, A. L., R. E. Arvidson, F. Palluconi and T. Thorpe (2001), Overview of the Mars Global Surveyor mission, *Journal of Geophysical Research, 106*(E10), 23291-23316, doi: 10.1029/2000JE001306

Alfvèn, H. (1957), On the theory of comet tails, *Tellus*, IX, pp. 92-96

Anderson, D. E. Jr, and C. W. Hord (1971), Mariner 6 and 7 ultraviolet spectrometer experiment: Analysis of hydrogen Lyman-alpha data, *Journal of Geophysical Research, 76*(28), doi: 10.1029/JA076i028p06666

Andersson, L., R. E. Ergun, G. T. Delory, A. I. Eriksson, J. Westfall, H. Reed, J. McCauly, D. Summers, and D. Meyers (2015), The Langmuir Probe and Waves instrument for MAVEN, *Space Sci. Rev., 195*: 173-198, doi: 10.1007/s11214-015-0194-3

Andersson, L., C. M. Fowler, T. M. Chamandy, R. E. Ergun, A. Eriksson, G. Delory, D. Andrews, A. K. Woodson, J. E. P. Connerney, B. M. Jakosky (to be submitted), Electron temperature and density profiles from the Martian ionosphere: A statistical analysis.

Barabash, S., Lundin, R., & Andersson, H. et al. (2004), ASPERA-3: Analyser of Space Plasmas and Energetic Ions for Mars Express, Mars Express: the Scientific Payload (ESA SP-1240), ed. A. Wilson & A. Chicarro (Noordwijk: ESA), 121

Barabash, S. (2012), Classes of the solar wind interactions in the solar system, *Earth Planets Space*, 64, 57-59, doi: 10.5047/eps.2012.01.005

Benna, M., P. R.Mahaffy, J. M. Grebowsky, J. L. Fox, R. V. Yelle, and B. M. Jakosky (2015), First measurements of composition and dynamics of the Martian ionosphere by MAVEN's Neutral Gas and Ion Mass Spectrometer, *Geophys. Res. Lett., 42*, 8958–8965, doi: 10.1002/2015GL066146

Bertaux, J.-L., et al. (2004), SPICAM: Studying the Global Structure and Composition of the Martian Atmosphere, *Planetary Missions Division, Research & Scientific Support Department, ESA/ESTEC, PO box 299, 2200 AG Noordwijk, The Netherlands*

Bertucci, C., et al. (2003), Magnetic field draping enhancement at the Martian magnetic pileup boundary from Mars Global Surveyor observations, *Geophysical Research Letters, 30*(2), doi: 10.1029/2002GL015713

Bertucci, C., et al. (2004), MGS MAG/ER observations at the magnetic pileup boundary of Mars: draping enhancement and low frequency waves, *Advances in Space Research, 33*(11), 1938-1944, doi: 10.1016/j.asr.2003.04.054

Bertucci, C., F. Duru, N. Edberg, M. Fraenz, C. Martinecz, K. Szego, and O. Vaisberg (2011), The induced magnetospheres of Mars, Venus, and Titan, *Space Sci. Rev.*, 162:113-171, doi: 10.1007/s1124-011-9845-1

Bibring, J-P., et al. (2004), OMEGA: Observatoire pour la Minéralogie, l'Eau, les Glaces et l'Activité, *Planetary Missions Division, Research & Scientific Support Department, ESA/ESTEC, PO box 299, 2200 AG Noordwijk, The Netherlands*

Bougher, S. W. (1995), Comparative thermospheres: Venus and Mars, *Adv. Space Res.*, *15* (4), 21–25, doi: 10.1016/0273-1177(94)00062-6

Bougher, S. W., Engel, S., Roble, R. G., and Foster, B. (2000), Comparative terrestrial planet thermospheres 3. Solar cycle variation of global structure and winds at solstices, *J. Geophys. Res.*, *105*, 17669–17692, doi: 10.1029/1999JE001232

Bougher, S. W., McDunn, T. M., Zoldak, K. A., and Forbes, J. M. (2009), Solar cycle variability of Mars dayside exospheric temperatures: Model evaluation of underlying thermal balances, *Geophys. Res. Lett.*, *36*, L05201, doi: 10.1029/2008GL036376

Bougher, S. W., Brain, D. A., Fox, J. L., Gonzalez-Galindo, F., Simon-Wedlund, C., and Withers, P. G. (2014), Upper Neutral Atmosphere and Ionosphere, *in Mars Book II* (Cambridge University Press, Cambridge, 2014), Chap. 14

Bougher, S., B. Jakosky, J. Halekas, J. Grebowsky, J. Luhmann, P. Mahaffy, J. Connerney, F. Eparvier, R. Ergun, D. Larson, J. McFadden, D. Mitchell, N. Schneider, R. Zurek, C. Mazelle, L. Andersson, D. Andrews, D. Baird, D. N. Baker, J. M. Bell, M. Benna, D. Brain, M. Chaffin, P. Chamberlin, J.-Y. Chaufray, J. Clarke, G. Collinson, M. Combi, F. Crary, T. Cravens, M. Crismani, S. Curry, D. Curtis, J. Deighan, G. Delory, R. Dewey, G. DiBraccio, C. Dong, Y. Dong, P. Dunn, M. Elrod, S. England, A. Eriksson, J. Espley, S. Evans, X. Fang, M. Fillingim, K. Fortier, C. M. Fowler, J. Fox, H. Gröller, S. Guzewich, T. Hara, Y. Harada, G. Holsclaw, S. K. Jain, R. Jolitz, F. Leblanc, C. O. Lee, Y. Lee, F. Lefevre, R. Lillis, R. Livi, D. Lo, Y. Ma, M. Mayyasi, W. McClintock, T. McEnulty, R. Modolo, F. Montmessin, M. Morooka, A. Nagy, K. Olsen, W. Peterson, A. Rahmati, S. Ruhunusiri, C. T. Russell, S. Sakai, J.-A. Sauvaud, K. Seki, M. Steckiewicz, M. Stevens, A. I. F. Stewart, A. Stiepen, S. Stone, V. Tenishev, E. Thiemann, R. Tolson, D. Toublanc, M. Vogt, T. Weber, P. Withers, T. Woods, R. Yelle (2015), Early MAVEN Deep Dip Campaigns: First Results and Implications, *Sciences*, *350*(6261), doi: 10.1126/science.aad0459

Brace, L. H., R. F. Theis, H. G. Mayr, S. A. Curtis, and J. G. Luhmann (1982), Holes in the nightside ionosphere of Venus, J. Geophys. Res., *87*, 199–211, doi: 10.1029/JA087iA01p00199

Brain, D. A., and B. M. Jakosky (1998), Atmospheric loss since the onset of the Martian geologic record: Combined role of impact erosion and sputtering, *Journal of Geophysical Research*, *103*(E10), 22689-22694, doi: 10.1029/98JE02074

Brain, D. A., F. Bagenal, M. H. Acuña, and J. E. P. Connerney (2003), Martian magnetic morphology: Contributions from the solar wind and crust, *Journal of Geophysical Research*, *108*(A12), 1424, doi: 10.1029/2002JA009482

Brain, D. A. (2006), Mars Global Surveyor measurements of the Martian Solar wind interaction, *Space Science Review*, 126: 77-112, doi: 10.1007/s11214-006-9122-x

Brain, D. A., R. J. Lillis, D. L. Mitchell, J. S. Halekas, and R. P. Lin (2007), Electron pitch angle distributions as indicators of magnetic field topology near Mars, *Journal of Geophysical Research*, 112(A09201), doi: 10.1029/2007JA012435

Brain, D. A., et al. (2010), A comparison of global models for the solar wind interaction with Mars, *Icarus*, *206*, 139-151, doi: 10.1016/j.icarus.2009.06.030

Brain, D. A., et al. (2015), The spatial distribution of planetary ion fluxes near Mars observed by MAVEN, *Geophysical Research Letters*, *42*(21), 9142-9148, doi: 10.1002/2015GL065293

Brain, D. A., S. Barabash, S. W. bougher, F. Duru, B. M. Jakosky and R. Modolo (2017), Solar wind interaction and atmospheric escape. Robert M. Haberla, R. Todd Clancy, François

Forget, Michael D. Smith, Richard W. Zurek (eds.). The Atmosphere and Climate of Mars, Cambridge University Press, ISBN: 978-1-107-01618-7. <insu-01536193>

Brecht, S. H., and S. A. Ledvina (2006), The Solar Wind Interaction With the Martian Ionosphere/Atmosphere, *Space Sci. Rev.*, *126*(1), 15–38, doi:10.1007/s11214-006-9084-z

Breus, T. K., A. M. Krymskii, R. Lundin, E. M. Dubinin, J. G. Luhmann, Ye G. Yeroshenko, S. V. Barabash, V. Ya Mitnitskii, N. F. Pissarenko, and V. A. Styashkin (1991), The solar wind interaction with Mars: Consideration of Phobos 2 mission observations of an ion composition boundary on the dayside, *Journal of Geophysical Research, 96*(A7), 11165-11174, doi: 10.1029/91JA01131

Cain, J. C., B. B. Ferguson, and D. Mozzoni (2003), An n=90 internal potential function of the Martian crustal magnetic field, *Journal of Geophysical Research, 108*(E2), 5008, doi: 10.1029/2000JE001487

Chaffin, M. S., et al. (2015), Three-dimensional structure in the Mars H corona revealed by IUVS on MAVEN, *Geophys. Res. Lett., 42*, 9001–9008, doi: 10.1002/2015GL065287

Chapman, S. (1931a), The absorption and dissociative or ionizing effect of monochromatic radiation in an atmosphere on a rotating Earth, *Proc. Phys. Soc., 43*, 26–45, doi: 10.1088/0959-5309/43/1/305

Chapman, S. (1931b), The absorption and dissociative or ionizing effect of monochromatic radiation in an atmosphere on a rotating Earth part II. Grazing incidence, *Proc. Phys. Soc., 43*, 483–501, doi: 10.1088/0959-5309/43/5/302

Chaufray, J.-Y., F. Gonzalez-Galindo, F. Forget, M. Lopez-Valverde, F. Leblanc, R. Modolo, S. Hess, M. Yagi, P.-L. Blelly, and O. Witasse (2014), Three-dimensional Martian ionosphere model: II. Effect of transport processes due to pressure gradients, *J. Geophys. Res. Planets, 119*, 1614–1636, doi:10.1002/2013JE004551.

Chicarro, A., P. Martin, and R. Trautner (2004), The Mars Express Mission: An overview, *Planetary Missions Division, Research & Scientific Support Department, ESA/ESTEC, PO box 299, 2200 AG Noordwijk, The Netherlands*

Christensen, P. R., et al., Thermal EmissionS pectrometer experiment: The Mars Observer mission, *Journal of Geophysical Research, 97*, 7719-7734, doi: 10.1029/92JE00453

Collison, G. A., et al. (2014), The extension of ionospheric holes into the tail of Venus, *J. Geophys. Res. Space Physics*, *119*, 6940-6953, doi: 10.1002/2014JA019851

Connerney, J. E. P., et al. (1999), Magnetic lineations in the Ancient crust of Mars, *Nature, 284*(5415), 794-798, doi: 10.1126/sience.284.5415.794

Connerney, J. E. P., M. H. Acuña, N. F. Ness, G. Kletetschka, D.L. Mitchell, R. P. Lin, and H. Rème (2005), Tectonic implications of Mars crustal magnetism, *PNAS, 102*, 42, doi: 10.1073/pnas.0507469102

Connerney, J. E. P., J. Espley, P. Lawton, S. Murphy, J. Odom, R. Oliverson, and D. Sheppard (2015), The MAVEN magnetic field investigation, *Space Sci. Rev.*, 195:257, doi: 10.1007/s11214-015-0169-4

Creasey, J. E., J. M. Forbes, and D. P. Hinson (2006), Global and seasonal distribution of gravity wave activity in Mars' lower atmosphere derived from MGS radio occultation data, *Geophys. Res. Lett., 33*, L01803, doi: 10.1029/2005GL024037.

Crider, D. H. et al. (2002), Observations of the latitude dependence of the location of the Martian magnetic pileup boundary, *Geophys. Res. Lett.*, *29*(8), 11–1, doi: 10.1029/2001GL013860.

Crider, D. H., et al. (2004), Mars Global Surveyor Observations of Solar Wind Magnetic Field Draping Around Mars, *Space Sci. Rev.*, *111*(1), 203–221, doi: 10.1023/B:SPAC.0000032714.66124.4e

Cui, J., M. Galand, R. V. Yelle, V. Vuitton, J.-E. Wahlund, P. P. Lavvas, I. C. F. Müller-Wodarg, T. E. Cravens, W. T. Kasprzak, and J. H. Waite (2009), Diurnal variations of Titan's ionosphere, *J. Geophys. Res.*, *114*, A06310, doi: 10.1029/2009JA014228

Cui, J., M. Galand, R. V. Yelle, Y. Wei, and S.-J. Zhang (2015), Day-to-night transport in the Martian ionosphere: Implications from total electron content measurements, *J. Geophys. Res. Space Physics*, *120*, 2333–2346, doi: 10.1002/2014JA020788

Delory G. T., J. G. Luhmann, D. Brain, R. J. Lillis, D. L. Mitchell, R. A. Mewaldt, and T. Vilstrup Falkenberg (2012), Energetic particles detected by the Electron Reflectometer instrument on the Mars Global Surveyor, 1999-2006, *Space Weather, 10*(6), S06003, doi: 10.1029/2012SW000781

DiBraccio, G. A., et al. (2017), MAVEN observations of tail current sheet flapping at Mars, *J. Geophys. Res. Space Physics*, *122*, 4308–4324, doi: 10.1002/2016JA023488.

Diéval, C., G. Stenberg, H. Nilsson, and S. Barabash (2013), A statistical study of proton precipitation onto the Martian upper atmosphere: Mars Express observations, *J. Geophys. Res. Space Physics*, *118*, 1972–1983, doi: 10.1002/jgra.50229

Dolginov, Sh. Sh., Ye. G. Yeroshenko, and L. N. Zhuzgov (1973), Magnetic field in the very close neighborhood of Mars according to data from the Mars 2 and Mars 3 spacecraft, *Journal of Geophysical Research, 78(*22), doi: 10.1029/JA078i022p04779

Dolginov, Sh. Sh., and L. N. Zhuzgov (1991), The magnetic field and the magnetosphere of the planet Mars, *Planet. Space Sci.*, *39*(11), 1493-1510, doi: 10.1016/0032-0633(91)90077-N

Dong, Y., X. Fang, D. A. Brain, J. P. McFadden, J. S. Halekas, J. E. P. Connerney, S. M. Curry, Y. Harada, J. G. Luhmann, and B. M. Jakosky (2015a), Strong plume fluxes at Mars observed by MAVEN: An important planetary ion escape channel, *Geoph. Res. Lett.*, *42*, 8942-8950, doi: 10.1002/2015GL065346

Dong, C., S. W. Bougher, Y. Ma, G. Toth, Y. Lee, A. F. Nagy, V. Tenishev, D. J. Pawlowski, M. R. Combi, and D. Najib (2015b), Solar wind interaction with the martian upper atmosphere: Crustal field orientation, solar cycle, and seasonal variations, *Journal of Geophysical Research: Space Physics*, *120* (9), 7857–7872, doi: 10.1002/2015JA020990

Dubinin, E, R. Lundin, O. Norberg, and N. Pissarenko (1993), Ion acceleration in the Martian tail: Phobos observations, *Journal of Geophysical Research, 98*(A3), 3991-3997, doi: 10.1029/92JA02233

Dubinin, E., K. Sauer, M. Delva, and A. Skalsky (1998), The IMF bending upstream of the Martian bow shock, *Earth, Planets and Space*, doi: 10.1186/BF03352116

Dubinin, E., M. Fränz, J. Woch, E. Roussos, S. Barabash, R. Lundin, J. D. Winningham, R. A. Frahm, and M. Acuña (2006), Plasma morphology at Mars. ASPERA-3 observations, *Space Science Reviews*, 126: 209-238, doi: 10.1007/s11214-006-9039-4

Dubinin, E., et al. (2008a), Structure and dynamics of the solar wind/ionosphere interface on Mars: MEX-ASPERA-3 and MEX-MARSIS observations, *Geophys. Res. Lett., 35(1),* 11103, doi: 10.1029/2008GL033730

Dubinin, E., et al. (2008b), Plasma environment of Mars as observed by simultaneous MEX-ASPERA-3 and MEX-MARSIS observations, *Journal of Geophysical Research*, *113*(A10217), doi: 10.1029/2008JA013355

Duru, F., D. A. Gurnett, J. D. Winningham, R. Frahm, and R. Modolo (2010), A plasma flow velocity boundary at Mars from the disappearance of electron plasma oscillations, *Icarus*, *206*(1), 74–82, doi: 10.1016/j.icarus.2009.04.012

Duru, F., D. A. Gurnett, D. D. Morgan, J. D. Winningham, R. A. Frahm, and A. F. Nagy (2011), Nightside ionosphere of Mars studied with local electron densities: A general overview

and electron density depressions, *J. Geophys. Res., 116*(A10316), doi: 10.1029/2011JA016835

Edberg, N. J. T., M. Lester, S. W. H. Cowley, and A. I. Eriksson (2008), Statistical analysis of the location of the Martian magnetic pileup boundary and bow shock and the influence of crustal magnetic fields, *Journal of Geophysical Research, 113*, A08206, doi: 10.1029/2008JA013096

Edberg, N. J. T., D. A. Brain, M. Lester, S. W. H. Cowley, R. Modolo, M. Fränz, and S. Barabash (2009), Plasma boundary variability at Mars as observed by Mars Global Surveyor and Mars Express, *Ann Geophys-Germany*, *27*(9), 3537–3550, doi: 10.5194/angeo-27-3537-2009

Ehlmann, B. L., J. F. Mustard, S. L. Murchie, J. - P. Bibring, A. Meunier, A. A. Fraeman, and Y. Langevin (2011), Subsurface water and clay mineral formation during the early history of Mars, *Nature*, *479*, 53-60, doi: 10.1038/nature10582

England, S. L., G. Liu, E. Yiğit, P. R. Mahaffy, M. Elrod, M. Benna, H. Nakagawa, N. Terada, and B. Jakosky (2017), MAVEN NGIMS observations of atmospheric gravity waves in the Martian thermosphere, *J. Geophys. Res. Space Physics*, *122*, 2310–2335, doi: 10.1002/2016JA023475

Eparvier, F. G., P. C. Chamberlin, T. N. Woods, E. M. B. Thiemann (2015), The Solar Extreme Ultraviolet Monitor for MAVEN, *Space Science Reviews*, *195*(1), 293-301, doi: 10.1007/s11214-015-0195-2

Fang, X., M. W. Liemohn, A. F. Nagy, J. G. Luhmann, and Y. Ma (2010), Escape probability of Martian atmospheric ions: Controlling effects of the electromagnetic fields, *J. Geophys. Res.*, *115*(A), 04308, doi: 10.1029/2009JA014929

Ferguson, B. B., J. C. Cain, D. H. Crider, D. A. Brain, and E. M. Harnett (2005), External fields on the nightside of Mars at Mars Global Surveyor mapping altitudes, *Geophysical Research Letters*, *32*, L16105, doi: 10.1029/2004GL021964

Fillingim, M. O., L. M. PetiColas, R. J. Lillis, D. A. Brain, J. S. Halekas, D. Lummerzheim, and S. W. Bougher (2010), Localized ionization patches in the nighttime ionosphere of Mars and their electrodynamic consequences, *Icarus*, *206*, 112–119, doi: 10.1016/j.icarus.2009.03.005

Formissano, V., et al. (2004), The Planetary Fourier Spectrometer (PFS) onboard the European Mars Express mission, *Planetary Missions Division, Research & Scientific Support Department, ESA/ESTEC, PO box 299, 2200 AG Noordwijk, The Netherlands*

Fox, J. L. (1993), The production and escape of nitrogen atoms on Mars, *J. Geophys, Res.*, *98*, 3297–3310, doi: 10.1029/92JE02289

Fowler, C. M., et al. (2015), The first in situ electron temperature and density measurements of the Martian nightside ionosphere, *Geophys. Res. Lett.*, *42*, 8854–8861, doi: 10.1002/2015GL065267

Frahm, R. A., et al. (2006), Locations of atmospheric photoelectron energy peaks within the Mars environment, *Space Science Reviews*, 126 : 389-402, doi : 10.1007/s11214-006-9119-5

Fränz, M., E. Dubinin, E. Roussos, J. Woch, J. D. Winningham, R. Frahm, A. J. Coates, A. Fedorov, S. Barabash, and R. Lundin (2006), Plasma Moments in the Environment of Mars, *Space Sci Rev*, *126*(1-4), 165–207, doi:10.1007/s11214-006-9115-9.

Fränz, M., E. Dubinin, E. Nielsen, J. Woch, S. Barabash, R. Lundin, and A. Fedorov (2010), Transterminator ion flow in the Martian ionosphere, *Planet. Space Sci.*, *58*, 1442–1454, doi: 10.1016/j.pss.2010.06.009

Garnier, P., M. Steckiewicz, C. Mazelle, S. Xu, D. Mitchell, M. Holmberg, J. Halekas, L. Anderson, D. Brain, J. Connerney, J. Espley, R. Lillis, J. Luhmann, J.-A. Sauvaud, and B. Jakosky (submitted to Journal of Geophysical Research), The Martian photoelectron

boundary as seen by MAVEN
Genot, V., et al. (2010), Space Weather applications with CDPP/AMDA, *Advances in Space Research, 45*(9), 1145-1155, doi: 10.1016/j.asr.2009.11.010
Genot, V., et al. (2014), Joining the yellow hub: Uses of the simple application messaging protocol in space physics analysis tools, *Astronomy and Computing*, vol. 7, doi: 10.1016/j.ascom.2014.07.007
Genot, V., et al. (submitted in 2016), Science data visualization in planetary and heliospheric contexts with 3DViews, *PSS*
Girazian, Z., P. R. Mahaffy, R. J. Lillis, M. Benna, M. Elrod, and B. M. Jakosky (2017), Nightside ionosphere of Mars: Composition, vertical structure, and variability, *J. Geophys. Res. Space Physics, 122*, doi: 10.1002/2016JA023508
González-Galindo, F., J.-Y. Chaufray, M. A. López-Valverde, G. Gilli, F. Forget, F. Leblanc, R. Modolo, S. Hess, and M. Yagi (2013), Three-dimensional Martian ionosphere model: I. The photochemical ionosphere below 180 km, *J. Geophys. Res., 118*, 2105–2123, doi: 10.1002/jgre.20150.
Grebowsky, J. M., et al. (2017), Unique, non-Earthlike, meteoritic ion behavior in upper atmosphere of Mars, *Geophysical Research Letters, 44*(7), 3066-3072, doi: 10.1002/2017GL072635
Gringauz, K. I. (1976), Interaction of Solar wind with Mars as seen by charged particle traps on Mars 2, 3 and 5 satellites, *Reviews of geophysics and space physics, 14*(3), doi: 10.1029/RG014i003p00391
Gringauz, K. I., Verigin, M., Luhmann, J., Russell, C. T. and Mihalov, J. D. (1993), On the Compressibility of the Magnetic Tails of Mars and Venus, in *Plasma Environments of Non-magnetic Planets*, Pergammon, New York, pp. 265–270
Haider, S. A. (1997), Chemistry of the nightside ionosphere of Mars, *J. Geophys. Res., 102*, 407–416, doi: 10.1029/96JA02353
Haider, S. A., B. M. Pandya, and G. J. Molina-Cuberos (2013), Nighttime ionosphere caused by meteoroid ablation and solar wind electron-proton-hydrogen impact on Mars: MEX observation and modeling, *J. Geophys. Res. Space Physics, 118*, 6786–6794, doi: 10.1002/jgra.50590
Halekas, J. S., D. A. Brain, R. J. Lillis, M. O. Fillingim, D. L. Mitchell, and R. P. Lin (2006), Current sheets at low altitudes in the Martian magnetotail, *Geophysical Research Letter, 33*(L13101), doi: 10.1029/2006GL026229
Halekas, J. S., E. R. Taylor, G. Dalton, G. Johnson, D. W. Curtis, J. P. McFadden, D. L. Mitchell, R. P. Lin, and B. M. Jakosky (2013), The Solar Wind Ion Analyzer for MAVEN, Space Sci. Rev., 1-27, doi: 10.1007/s11214-013-0029-z
Hall, B. E. S., M. Lester, J. D. Nichols, B. Sànchez-Cano, D. J. Andrews, H. J. Opgenoorth, and M. Fränz (2016), A survey of suprathermal electron flux depressions, or 'electron holes', within the illuminated Martian induced magnetosphere, *Journal of Geophysical Research, 121*(5), 4835-4857, doi: 10.1002/2015JA021866
Han, X., et al. (2014), Discrepancy between ionopause and photoelectron boundary determined from Mars Express measurements, *Geophysical Research Letters, 41*, 8221-8227, doi: 10.1002/2014GL062287
Hanson, W. B., and G. P. Mantas (1988), Viking electron temperature measurements: Evidence for a magnetic field in the Martian atmosphere, *J. Geophys. Res., 93*, 7538–7544, doi:10.1029/JA093iA07p07538
Harada, Y., et al. (2016), MAVEN observations of energy-time dispersed electron signatures in Martian crustal magnetic fields, *Geophys. Res. Lett., 43*, 939-944, doi: 10.1002/2015GL067040

Harnett, E. M., and R. M. Winglee (2006), Three-dimensional multifluid simulations of ionospheric loss at Mars from nominal solar wind conditions to magnetic cloud events, *J. Geophys. Res.*, *111*(A), 09213, doi: 10.1029/2006JA011724

Itikawa, Y., M. Hayashi, A. Ichimura, K. Onda, K. Sakimoto, K. Takayanagi, M. Nakamura, H. Nishimura, and T. Takayanagi (1986), Cross sections for collisions of electrons and photons with nitrogen molecules, *J. Phys. Chem. Ref. Data*, *15*(3), 985–1010

Itikawa, Y., A. Ichimura, K. Onda, K. Sakimoto, T. Takayanagi, Y. Hatano, M. Hayashi, H. Nishimura, and S. Tsurubuchi (1989), Cross sections for collisions of electrons and photons with oxygen molecules, *J. Phys. Chem. Ref. Data*, *18*(1), 23–42

Itikawa, Y., and A. Ichimura (1990), Cross section for collisions of electrons and photons with atomic oxygen, *J. Phys. Chem. Ref. Data*, *19*(3), 637–651

Itikawa, Y. (2002), Cross sections for electron collisions with carbon dioxide, *J. Phys. Chem. Ref. Data*, *31*(3), doi:10.1063/1.1481879

Jacquey, C., et al. (2010), AMDA, Automated Multi-Dataset Analysis: A web-Based Service Provided by the CDPP, *In: Laasko H., Taylor M., Escoubet C. (eds) The Cluster Active Archive. Astrophysics and Space Science Proceedings, Springer, Dordrecht,* doi: 10.1007/978-90-481-3499-1_16

Jakosky, B. M., and R. J. Phillips (2001), Mars' volatile and climate history, *Nature*, *412*, 6843, pp. 237-244

Jakosky, B. M., et al. (2015a), The Mars Atmosphere and Volatile Evolution (MAVEN) mission, *Space Sci. Rev.*, 195:3-48, doi: 10.1007/s11214-015-0139-x

Jakosky, B. M., J. M. Grebowsky, J. G. Luhmann, J. Connerney, F. Eparvier, R. Ergun, J. Halekas, D. Larson, P. Mahaffy, J. McFadden, D. L. Mitchell, N. Schneider, R. Zurek, S. Bougher, D. Brain, Y. J. Ma, C. Mazelle, L. Andersson, D. Andrews, D. Baird, D. Baker, J. M. Bell, M. Benna, M. Chaffin, P. Chamberlin, J.-Y. Chaufray, J. Clarke, G. Collinson, M. Combi, F. Crary, T. Cravens, M. Crismani, S. Curry, D. Curtis, J. Deighan, G. Delory, R. Dewey, G. DiBraccio, C. Dong, Y. Dong, P. Dunn, M. Elrod, S. England, A. Eriksson, J. Espley, S. Evans, X. Fang, M. Fillingim, K. Fortier, C. M. Fowler, J. Fox, H. Gröller, S. Guzewich, T. Hara, Y. Harada, G. Holsclaw, S. K. Jain, R. Jolitz, F. Leblanc, C. O. Lee, Y. Lee, F. Lefevre, R. Lillis, R. Livi, D. Lo, M. Mayyasi, W. McClintock, T. McEnulty, R. Modolo, F. Montmessin, M. Morooka, A. Nagy, K. Olsen, W. Peterson, A. Rahmati, S. Ruhunusiri, C. T. Russell, S. Sakai, J.-A. Sauvaud, K. Seki, M. Steckiewicz, M. Stevens, A. I. F. Stewart, A. Stiepen, S. Stone, V. Tenishev, E. Thiemann, R. Tolson, D. Toublanc, M. Vogt, T. Weber, P. Withers, T. Woods, R. Yelle (2015b), MAVEN observations of the response of Mars to an interplanetary coronal mass ejection, *Science*, *350*(6261), doi: 10.1126/science.aad0210

Jakosky, B. M., J. M. Grebowsky, J. G. Luhmann, and D. A. Brain (2015c), Initial results from the MAVEN mission to Mars, *Geophys. Res. Lett.*, *42*, 8791-8802, doi: 10.1002/2015GL065271

Jakosky, B. M., J. M. Grebowsky, J. G. Luhmann, and D. A. Brain (in preparation), The MAVEN mission to Mars at the end of one Mars year of science observations, *J. Geophys. Res.*

Kallio, E., and P. Janhunen (2001), Atmospheric effects of proton precipitation in the Martian atmosphere and its connection to the Mars-solar wind interaction, *J. Geophys. Res.*, *106*, 5617–5634, doi: 10.1029/2000JA000239

Kallio, E., R. A. Frahm, Y. Futaana, A. Fedorov, and P. Janhunen (2008), Morphology of the magnetic field near Mars and the role of the magnetic crustal anomalies: Dayside region, *Planetary and Space Science*, *56*(6), 852–855, doi: 10.1016/j.pss.2007.12.002

Kallio, E., J.-Y. Chaufray, R. Modolo, D. Snowden, and R. Winglee (2011), Modeling of Venus, Mars, and Titan, *Space Sci Rev*, *162*(1), 267–307, doi:10.1007/s11214-011-

9814-8
Kerr, R. A. (2003), Running water eroded a frigid early Mars, *Science, 300*(5625), 1496-1497, doi: 10.1126/science.300.5625.1496
Kivelson, M. G., and C. T. Russel (1995), Introduction to space physics, *Cambridge University Press*
Kotova, G. et al. (1997), Study of the solar wind deceleration upstream of the Martian terminator bow shock, *J. Geophys. Res., 102*(A), 2165–2174, doi: 10.1029/96JA01533
Krasnopolsky, V. A. (1993), Solar cycle variations of the hydrogen escape rate and the CO mixing ratio on Mars, *Icarus (ISSN 0019-1035), 101*, 33–41, doi: 10.1006/icar.1993.1003
Krymskii, A. M., T. K. Breus, N. F. Ness, M. H. Acuña, J. E. P. Connerney, D. H. Crider, D. L. Mitchell, and S. Bauer (2002), Structure of the magnetic field fluxes connected with crustal magnetization and topside ionosphere at Mars, *Journal of Geophysical Research, 107(*A9), 1245, doi: 10.1029/2001JA000239
Larson, D. E., et al. (2015), The MAVEN Solar Energetic Particle Investigation, *Space Science Reviews, 195*(1), 153-172, doi: 10.1007/s11214-015-0218-z
Leblanc, F., et al. (submitted), On the origins of Mars' exospheric non-thermal oxygen components as observed by MAVEN and modeled by HELIOSARES, *Journal of Geophysical Research*
Ledvina, S. A., Y. J. Ma, and E. Kallio (2008), Modeling and Simulating Flowing Plasmas and Related Phenomena, *Space Sci Rev, 139*(1), 143–189, doi:10.1007/s11214-008-9384-6
Lee, C., et al. (2017), MAVEN observations of the solar cycle 24 space weather conditions at Mars, *J. Geophys. Res.*, 122, doi: 10.1002/2016JA023495, in press.
Lillis, R. J., H. V. Frey, and M. Manga (2008a), Rapid decrease in Martian crustal magnetization in the Noachian era: implications for the dynamo and climate of early Mars, *Geophysical Research Letter, 35*, L14203, doi: 10.1029/2008GL034338
Lillis, R. J., D. L. Mitchell, R. P. Lin, and M. H. Acuña (2008b), Electron reflectometry in the Martian atmosphere, *Icarus, 194*, 544–561, doi:10.1016/j.icarus.2007.09.030
Lillis, R. J., M. O. Fillingim, L. M. Peticolas, D. A. Brain, R. P. Lin, and S. W. Bougher (2009), Nightside ionosphere at Mars: Modeling the effects of crustal magnetic fields and electron pitch angle distributions on electron impact ionization, *Journal of Geophys. Research, Planets, 114*(E11), doi: 10.1029/2009JE003379
Lillis, R. J., M. O. Fillingim, and D. A. Brain (2011), Three-dimensional structure of the Martian nightside ionosphere: Predicted rates of impact ionization from Mars Global Surveyor magnetometer and Electron Reflectometer measurements of precipitating electrons, *J. Geophys. Res.*, *116*(A12317), doi: 10.1029/2011JA016982.
Lillis, R. J., S. Robbins, M. Manga, J. S. Halekas and H. V. Frey (2013), Time history of the Martian dynamo from crater magnetic field analysis, *Journal of Geophysical Research, 118*, 1488-1511, doi: 10.1002/jgre.20105
Lillis, R. J., and D. A. Brain (2013), Nightside electron precipitation at Mars: Geographic variability and dependence on solar wind conditions, *J. Geophys. Res. Space Physics*, *118*, 3546–3556, doi: 10.1002/jgra.50171
Lillis, R. J., and X. Fang (2015), Electron impact ionization in the Martian atmosphere: Interplay between scattering and crustal magnetic field effects, *J. Geophys. Res. Planets*, *120*, 1332–1345, doi: 10.1002/2015JE004841
Luhmann, J. G. and L. H. Brace (1991), Near-Mars space, *Review of Geophysics, 29*(2), 121-140, doi: 10.1029/91RG00066
Luhmann, J. G. (1992), Comparative studies of the solar wind interaction with weakly magnetized planets, *Adv. Space Res.*, *12*(9), pp. 191-203, doi: 10.1016/0273-1177(92)90331-Q

Luhmann, J. G. (1995), Plasma interactions with unmagnetized bodies, in Introduction to Space Physics, *Cambridge University Press*.

Luhmann, J. G., S. A. Ledvina, and C. T. Russell, (2004), Induced magnetosphere, *Advances in Space Reasearch*, doi: 10.1016/j.asr.1003.03.031

Lundin, R., A. Zakharov, R. Pellinen, H. Borg, B. Hultqvist, N. Pissarenko, E. M. Dubinin, S. W. Barabash, I. Liede, and H. Koskinen (1989), First measurements of the ionospheric plasma escape from Mars, *Nature, 341*, 609-612, doi: 10.1038/341609a0

Ma, Y., A. F. Nagy, K. C. Hansen, D. L. DeZeeuw, T. I. Gombosi, and K. G. Powell (2002), Three-dimensional multispecies MHD studies of the solar wind interaction with Mars in the presence of crustal fields, *Journal of Geophysical Research-Space*, *107*(A), 1282, doi:10.1029/2002JA009293

Ma, Y., A. F. Nagy, I. V. Sokolov, and K. C. Hansen (2004), Three-dimensional, multispecies, high spatial resolution MHD studies of the solar wind interaction with Mars, *Journal of Geophysical Research*, *109*, A07211, doi: 10.1029/2004JA010367

Ma, Y., and A. F. Nagy (2007), Ion escape fluxes from Mars, *Geophys. Res. Lett.*, *34*(8), 08201, doi: 10.1029/2006GL029208

Ma, Y., X. Fang, C. T. Russell, A. F. Nagy, G. Toth, J. G. Luhmann, D. A. Brain, and C. Dong (2014), Effects of crustal field rotation on the solar wind plasma interaction with Mars, *Geophys. Res. Lett.*, *41*, 6563–6569, doi: 10.1002/2014GL060785.

Mahaffy, P. R., et al. (2015a), The Neutral Gas and Ion Mass Spectrometer on the Mars Atmosphere and Volatile Evolution Mission, *Space Sci. Rev.*, 195:49-73, doi: 10.1007/s11214-014-0091-1

Mahaffy, P. R., M. Benna, M. Elrod, R. V. Yelle, S. W. Bougher, S. W. Stone, and B. M. Jakosky (2015b), Structure and composition of the neutral upper atmosphere of Mars from the MAVEN NGIMS investigation, *Geophysical Research Letter*, *42*, 8951-8957, doi: 10.1002/2015GL065329

Malin, M. C., G.E. Danielson, A. P. Ingersoll, H. Masursky, J. Veverka, M. A. Ravine, and T. A. Soulanille (1992), Mars Observer Camera, *Journal of Geophysical Research*, *97*(E5), 7699-7718, doi: 10.1029/92JE00340

Mantas, G. P., and W. B. Hanson (1979), Photoelectron fluxes in the Martian ionosphere, *J. Geophys. Res.*, *84*(A2), 369–385, doi:10.1029/JA084iA02p00369

Martin-Torres, F. J., et al. (2015), Transient liquid water and water activity at Gale crater on Mars, *Nature Geoscience*, *8*, 357-361, doi: 10.1038/ngeo2412

McClintock, W. E., et al. (2014), The Imaging Ultraviolet Spectrograph (IUVS) for the MAVEN mission, *Space Sci. Rev.*, *195*(1), 75-124, doi: 10.1007/s11214-014-0098-7

McFadden, J. P., et al. (2015), MAVEN SuparThermal and Thermal Ion Composition (STATIC) Instrument, *Space Sci. Rev., 195(1-4)* 199-256, doi: 10.1007/s11214-015-0175-6

Melosh, H. J., and A. M. Vickery (1989), Impact erosion of the primordial atmosphere of Mars, *Nature (ISSN 0028-0836)*, *338*, 487–489, doi: 10.1038/338487a0

Mitchell, D. L., R. P. Lin, H. Rème, D. H. Crider, P. A. Cloutier, J. E. P. Connerney, M. H. Acuña, and N. F. Ness (2000), Oxygen Auger electrons observed in Mars' ionosphere, *Geophysical Research Letter*, *27*(13), 1871-1874, doi: 10.1029/1999GL010754

Mitchell, D. L., et al. (2001), Probing Mars' crustal magnetic field and ionosphere with the MGS Electron Reflectometer, *Journal of Geophysical Research, 106(E10)*, 23419-23427, doi: 10.1029/2000JE001435

Mitchell, D. L., R. J. Lillis, R. P. Lin, J. E. P. Connerney, and M. H. Acuña (2007), A global map of Mars' crustal magnetic field based on electron reflectometry, *Journal of Geophysical Research*, *112*, E01002, doi: 10.1029/2005JE002564

Mitchell, D. L., et al. (2016), The MAVEN Solar Wind Electron Analyzer, *Space Sci. Rev.*,1-34 doi: 10.1007/s11214-015-0232-1

Modolo, R., G. M. Chanteur, E. Dubinin, and A. P. Matthews (2005), Influence of the solar EUV flux on the Martian plasma environment, *Ann Geophys-Germany*, *23*(2), 433–444, doi: 10.5194/angeo-23-433-2005

Modolo, R., G. M. Chanteur, E. Dubinin, and A. P. Matthews (2006), Simulated solar wind plasma interaction with the Martian exosphere: influence of the solar EUV flux on the bow shock and the magnetic pile-up boundary, *Ann Geophys-Germany*, *24*(12), 3403–3410

Modolo, R., G. M. Chanteur, and E. Dubinin (2012), Dynamic Martian magnetosphere: Transient twist induced by a rotation of the IMF, *Geophys. Res. Lett.*, *39*(1), 01106, doi: 10.1029/2011GL049895

Modolo, S. Hess, V. Génot, L. Leclercq, F. Leblanc, J.-Y. Chauffray, P. Weill, M. Gangloff, A. Fedorov, E. Budnik, M. Bouchemit, M. Steckiewicz, N. André, L. Beigbeder, D. Popescu, J.-P. Toniutti, T. Al-Ubaidi, M. Khodachenko, D. Brain, S. Curry, B. Jakosky, M. Holmström (2017), The LatHyS database for planetary plasma environment investigations: Overview and a case study of data/model comparisons. *Planetary and Space Science, Elsevier*, (in press), doi: 10.1016/j.pss.2017.02.015

Möhlmann, D., W. Riedler, J. Rustenbach, K. Schwingenschuh, J. Kurths, U. Motschmann, T. Roatsch, K. Sauer, and H. T. M. Lichtenegger (1991), The question of an internal Martian magnetic field, *Planetary and Space Science*, *39*(1-2), 83-88, doi: 10.1016/0032-0633(91)90130-3

Morschhauser, A., V. Lesur, and M. Grott (2014), A spherical harmonic model of the lithospheric magnetic field of Mars, *Journal of Geophysical Research: Planets*, *119*, 1162-1188, doi: 10.1002/2013JE004555

Nagy, A. F., M. W. Liemohn, J. L. Fox, and J. Kim (2001), Hot carbon densities in the exosphere of Mars, *J. Geophys. Res.*, *106*(A), 21565–21568, doi:10.1029/2001JA000007

Nagy, A. F., et al. (2004), The plasma environment of Mars, *Space Science Reviews*, 111: 33-114, doi: 10.1023/B:SPAC.0000032718.47512.92

Najib, D., A. F. Nagy, G. Tóth, and Y. Ma (2011), Three-dimensional, multifluid, high spatial resolution MHD model studies of the solar wind interaction with Mars, *J. Geophys. Res.-Space*, *116*(5), A05204, doi: 10.1029/2010JA016272

Němec, F., D. D. Morgan, D. A. Gurnett, and F. Duru (2010), Nightside ionosphere of Mars: Radar soundings by the Mars Express spacecraft, *J. of Geophys. Res.*, *115*, E12009, doi: 10.1029/2010JE003663

Neukum, G., et al. (2004), HRSC: the High Resolution Stereo Camera of Mars Express, *Planetary Missions Division, Research & Scientific Support Department, ESA/ESTEC, PO box 299, 2200 AG Noordwijk, The Netherlands*

Nier, A. O., and M. B. McElroy (1976), Structure of the Neutral upper atmosphere of Mars: results from Viking 1 and Viking 2, *Science*, *194*(4271), 1298-1300, doi: 10.1126/science.194.4271.1298

Nier, A. O., W. B. Hanson, A. Seiff, M. B. McElroy, N. W. Spencer, R. J. Duckett, T. C. D. Knight, and W. S. Cook (1976), Composition and Structure of the Martian atmosphere: Preliminary results from Viking 1, *Science*, *193*(4255), 786-788, doi: 10.1126/science.193.4255.786

Pätzold, M., et al. (2004), MaRS: Mars Express Orbiter Radio Science, *Planetary Missions Division, Research & Scientific Support Department, ESA/ESTEC, PO box 299, 2200 AG Noordwijk, The Netherlands*

Parker, E. N. (1958), Dynamics of the interplanetary gas and magnetic fields, *Astrophysical Journal*, vol. 128, p. 664, doi:10.1086/146579

Phillips, J. L., J. G. Luhmann, W. C. Knudsen, and L. H. Brace (1988), Asymmetries in the location of the Venus ionopause, *Journal of Geophysical Research (ISSN 0148-0227), 93*, 3927–3941, doi: 10.1029/JA093iA05p03927

Picardi, G., et al. (2004), MARSIS: Mars Advanced Radar for Subsurface and Ionosphere Sounding, *Planetary Missions Division, Research & Scientific Support Department, ESA/ESTEC, PO box 299, 2200 AG Noordwijk, The Netherlands*

Pierrard, V. (2003), Evaporation of hydrogen and helium atoms from the atmospheres of Earth and Mars, *Planet. Space. Sci., 51*, 319-327, doi: 10.1016/S0032-0633(03)00014-X

Pullan, D., M. R. Sims, I. P. Wright, C. T. Pillinger, and R. Trautner (2004), Beagle 2: the Exobiological Lander of Mars Express, *Planetary Missions Division, Research & Scientific Support Department, ESA/ESTEC, PO box 299, 2200 AG Noordwijk, The Netherlands*

Riedler, W., et al. (1989), Magnetic fields near Mars: first results, *Nature, 341*, 604-607, doi: 10.1038/341604a0

Rosenbauer, H., et al. (1989), Ions of Martian origin and plasma sheet in the Martian magnetosphere: initial results of the TAUS experiment, *Nature, 341*, 612-614, doi: 10.1038/341612a0

Russell, C. T., J. G. Luhmann, J. R. Spreiter, and S. S. Stahara (1984), The magnetic field of Mars: Implications from gas dynamic modeling, *Journal of geophysical research, 89*(A5), pp. 2997-3003, doi: 10.1029/JA089iA05p02997

Russell, C. T., T. Mulligan, M. Delva, T. L. Zhang, and K. Schwingenschuh (1995), A simple test of the induced nature of the Martian tail, *Advances in Space Research, 16*(6), 69-73, doi: 10.1016/0273-1177(95)00251-9

Sauer, K., A. Bogdanov, and K. Baumgärtel (1994), Evidence of an ion composition boundary (protonopause) in bi-ion fluid simulations of solar wind mass loading, *Geophysical Research Letter, 21*(20), 2255-2258, doi: 10.1029/94GL01691

Sauvaud, J.-A., D. Larson, C. Aoustin, J.-L. Médale, A. Fedorov, J. Rouzaud, J. G. Luhmann, T. Moreau, P. Schröder, P. Louarn, I. Dandouras, E. Penou (2008), The IMPACT Solar Wind Electron Analyzer (SWEA), *Space Science Reviews, 136*(1), 227-239, doi: 10.1007/s11214-007-9174-6

Schneider et al. (2015), Discovery of diffuse aurora on Mars, *Science, 350*(6261), doi: 10.1126/science.aad0313

Slavin, J. A., K. Schwingenschuh, W. Riedler, and Ye. Yeroshenko (1991), The solar wind interaction with Mars: Mariner 4, Mars 2, Mars 3, Mars 5, and Phobos 2 observations of bow shock position and shape, *Journal of Geophys. Research, 96*(A7), 11235-11241, doi: 10.1029/91JA00439

Smith, E. J., L. Davis Jr, P. J. Coleman Jr, and D. E. Jones (1965), Magnetic field measurements near Mars, *Science, 149*(3689), 1241-1242, doi: 10.1126/science.149.3689.1241

Smith, D. E., et al. (2001), Mars Orbiter Laser Altimeter: Experiment summary after the first year of global mapping of Mars, *Journal of Geophysical Research, 106*(E10), 23689-23722, doi: 10.1029/2000JE001364

Sonnerup, B. U. Ö., and M. Scheible (1998), Minimum and Maximum Variance Analysis, Analysis Methods for Multi-Spacecraft data, (SR-001) ed. G. Paschmann and P. W. Daly

Soobiah, Y., et al. (2006), Observations of magnetic anomaly signatures in Mars Express ASPERA-3 ELS data, *Icarus, 182(396-405)*, doi: 10.1016/j.icarus.2005.10.034

Soobiah, Y. I. J. (2009), The investigation of crustal magnetic field signatures at Mars by the Mars Express ASPERA-3 Electron Spectrometer (ELS), Doctoral thesis, Department of

Space and Climate Physics, Mullard Space Science Laboratory, UCL (Univ. College London), London, U. K.

Steckiewicz, M., C. Mazelle, P. Garnier, N. André, E. Penou, A. Beth, J.-A. Sauvaud, D. Toublanc, D. L. Mitchell, J. P. McFadden, J. G. Luhmann, R. J. Lillis, J. E. P. Connerney, J. R. Espley, L. Andersson, J. S. Halekas, D. E. Larson, and B. M. Jakosky (2015), Altitude dependence of nightside Martian suprathermal electron depletions as revealed by MAVEN observations, *Geophysical Research Letters, 42*, 8877-8884, doi: 10.1002/2015GL065257

Steckiewicz, M., P. Garnier, N. André, D. L. Mitchell, L. Andersson, E. Penou, A. Beth, A. Fedorov, J.-A. Sauvaud, C. Mazelle, D. A. Brain, J. R. Espley, J. McFadden, J. S. Halekas, D. E. Larson, R. J. Lillis, J. G. Luhmann, Y. Soobiah, and B. M. Jakosky (2016), Comparative study of the Martian suprathermal electron depletions based on Mars Global Surveyor, Mars Express and the Mars Atmosphere and Volatile Evolution mission observations, *Journal of Geophysical Research: Space Physics*, *121*, doi: 10.1002/2016JA023205

Stewart, A. I. F. (1987) Revised time dependent model of the martian atmosphere for use in orbit lifetime and sustenance studies, *LASP-JPL Internal Report*, NQ-802429, Jet Propulsion Lab, Pasadena, California

Terada, N., et al. (2107), Global distribution and parameter dependences of gravity wave activity in the Martian upper thermosphere derived from MAVEN/NGIMS observations, *Journal of Geophysical Research: Space Physics*, *122 (2)*, 2374-2397, doi: 10.1002/2016JA023476

Toublanc, D., J. P. Parisot, J. Brillet, D. Gautier, F. Raulin, and C. P. McKay (1995), Photochemical modeling of Titan's atmosphere, *Icarus, 113*, 2-26, doi: 10.1006/icar.1995.1002

Trotignon, J. G., E. Dubinin, R. Grard, S. Barabash, and R. Lundin (1996), Martian planetopause as seen by the plasma wave system onboard Phobos 2, *Journal of Geophysical Research, 101*(A11), 24965-24977, doi: 10.1029/96JA01898

Trotignon, J. G., et al. (2006), Martian shock and magnetic pile-up boundary positions and shapes determined from Phobos 2 and Mars Global Surveyor data sets, *Planetary and Space Science*, 54, 357-369, doi: 10.1016/j.pss.2006.01.003

Ulusen, D., and I. R. Linscott (2008), Low-energy electron current in the Martian tail due to reconnection of draped interplanetary magnetic field and crustal magnetic fields, *J. Geophys. Res., 113*, E06001, doi: 10.1029/2007JE002916

Vaisberg, O. L., A. V. Bogdanov, N. F. Borodin, A. A. Zertzalov, B. V. Polenov, and S. Romanov (1973), Solar Plasma Interaction with Mars: Preliminary results, *Icarus*, *18*, 59-63, doi: 10.1016/0019-1035(73)90172-3

Vaisberg, O. L. (1992), The solar wind interaction with Mars: a review of results from previous soviet missions to Mars, *Adv. Space Res.*, *12*(9), 137-161, doi: 10.1016/0273-1177(92)90328-U

Verigin, M. I., N. M. Shuttle, A. A. Galeev, K. I. Gringauz, G. A. Kotova, and A. P. Reminoz (1991a), Ions of planetary origin in the Martian magnetosphere (Phobos 2/TAUS experiment), *Planetary and Space Science, 39*(1-2), 131-137, doi: 10.1016/0032-0633(91)90135-W

Verigin, M. I., K. I. Gringauz, N. M. Shutte, S. A. Haider, K. Szego, P. Kiraly, A. F. Nagy, and T. I. Gombosi (1991b), On the possible source of the ionization in the nighttime Martian ionosphere: 1. Phobos 2 Harp Electron Spectrometer measurements, *J. Geophys. Res., 96*(19), 307–19,313, doi: 10.1029/91JA00924.

Vignes, D., et al. (2000), The solar wind interaction with Mars: locations and shapes of the bow shock and the magnetic pile-up boundary from the observations of the MAG/ER

experiment onboard Mars Global Surveyor, *Geophysical Research Letter*, *27*(1), 49-52, doi: 10.1029/1999GL010703

Vignes, D., et al. (2002), Factors controlling the location of the bow shock at Mars, *Geophysical Research Letters, 29*(9), 1328, doi: 10.1029/2001GL014513

Withers, P., M. O. Fillingim, R. J. Lillis, B. Häusler, D. P. Hinson, G. L. Tyler, M. Pätzold, K. Peter, S. Tellmann, and O. Witasse (2012), Observations of the nightside ionosphere of Mars by the Mars Express Radio Science Experiement (MaRS), *J. Geophys. Res., 117*(A12307), doi: 10.1029/2012JA018185

Xu, S., M. Liemohn, S. Bougher, and D. Mitchell (2016a), Martian high-altitude photoelectrons independent of solar zenith angle, *J. Geophys. Res. Space Physics, 121*, 3767–3780, doi: 10.1002/2015JA022149.

Xu, S., et al. (2016b), Deep nightside photoelectron observations by MAVEN SWEA: Implications for Mars northern hemispheric magnetic topology and nightside ionosphere source, *Geophysical Research Letters, 43*, 17, pp 8876-8884, doi: 10.1002/2016GL070527

Xu, S., D. Mitchell, M. Liemohn, X. Fang, Y. Ma, J. Luhmann, D. Brain, M. Steckiewicz, C. Mazelle, J. Connerney, and B. Jakosky (2017), Martian low-altitude magnetic topology deduced from MAVEN/SWEA observations, *Journal of Geophysical Research Space Physics, 122*, doi: 10.1002/2016JA023467

Yeroshenko, Y., W. Riedler, K. Schwingenschuh, J. G. Luhmann, and M. Ong (1990), The magnetotail of Mars - PHOBOS observations, *Geophysical Research Letters (ISSN 0094-8276), 17*, 885–888, doi: 10.1029/GL017i006p00885

Yiğit, E., A. S. Medvedev, and P. Hartogh (2015a), Gravity waves and high-altitude CO2 ice cloud formation in the Martian atmosphere, *Geophys. Res. Lett., 42*, doi: 10.1002/2015GL064275

Yiğit, E., S. L. England, G. Liu, A. S. Medvedev, P. R. Mahaffy, T. Kuroda, and B. M. Jakosky (2015b), High-altitude gravity waves in the Martian thermosphere observed by MAVEN/NGIMS and modeled by a gravity wave scheme, *Geophys. Res. Lett., 42*, 8993–9000, doi: 10.1002/2015GL065307.

Zahnle, K. J., and J. F. Kasting (1986), Mass fractionation during transonic escape and implications for loss of water from Mars and Venus, *Icarus (ISSN 0019-1035), 68*, 462–480, doi: 10.1016/0019-1035(86)90051-5

Zhang, M. H. G., J. G. Luhmann, A. J. Kliore (1990), An observational study of the nightside ionospheres of Mars and Venus with radio occultation methods, *J. Geophys. Res., 95*(A10), (17095-17102) doi: 10.1029/JA095iA10p17095

Zuber, M. T., D. E. Smith, S.C. Solomon, D. O. Muhleman, J. W. Head, J. B. Garvin, J. B. Abshire, and J. L. Bufton (1992), The Mars Observer Laser Altimeter investigation, *Journal of Geophysical Research, 97*, 7781-7798, doi: 10.1029/92JE00341

Appendices

In the next pages are gathered the two articles I am the first author of and the five articles I have co-authored during my PhD.

(1) Steckiewicz, M., C. Mazelle, P. Garnier, N. André, E. Penou, A. Beth, J.-A. Sauvaud, D. Toublanc, D. L. Mitchell, J. P. McFadden, J. G. Luhmann, R. J. Lillis, J. E. P. Connerney, J. R. Espley, L. Andersson, J. S. Halekas, D. E. Larson, and B. M. Jakosky (2015), Altitude dependence of nightside Martian suprathermal electron depletions as revealed by MAVEN observations, *Geophysical Research Letters, 42*, 8877-8884, doi: 10.1002/2015GL065257

(2) Steckiewicz, M., P. Garnier, N. André, D. L. Mitchell, L. Andersson, E. Penou, A. Beth, A. Fedorov, J.-A. Sauvaud, C. Mazelle, D. A. Brain, J. R. Espley, J. McFadden, J. S. Halekas, D. E. Larson, R. J. Lillis, J. G. Luhmann, Y. Soobiah, and B. M. Jakosky (2016), Comparative study of the Martian suprathermal electron depletions based on Mars Global Surveyor, Mars Express and the Mars Atmosphere and Volatile Evolution mission observations, *Journal of Geophysical Research: Space Physics*, *121*, doi: 10.1002/2016JA023205

(3) Bougher, S., B. Jakosky, J. Halekas, J. Grebowsky, J. Luhmann, P. Mahaffy, J. Connerney, F. Eparvier, R. Ergun, D. Larson, J. McFadden, D. Mitchell, N. Schneider, R. Zurek, C. Mazelle, L. Andersson, D. Andrews, D. Baird, D. N. Baker, J. M. Bell, M. Benna, D. Brain, M. Chaffin, P. Chamberlin, J.-Y. Chaufray, J. Clarke, G. Collinson, M. Combi, F. Crary, T. Cravens, M. Crismani, S. Curry, D. Curtis, J. Deighan, G. Delory, R. Dewey, G. DiBraccio, C. Dong, Y. Dong, P. Dunn, M. Elrod, S. England, A. Eriksson, J. Espley, S. Evans, X. Fang, M. Fillingim, K. Fortier, C. M. Fowler, J. Fox, H. Gröller, S. Guzewich, T. Hara, Y. Harada, G. Holsclaw, S. K. Jain, R. Jolitz, F. Leblanc, C. O. Lee, Y. Lee, F. Lefevre, R. Lillis, R. Livi, D. Lo, Y. Ma, M. Mayyasi, W. McClintock, T. McEnulty, R. Modolo, F. Montmessin, M. Morooka, A. Nagy, K. Olsen, W. Peterson, A. Rahmati, S. Ruhunusiri, C. T. Russell, S. Sakai, J.-A. Sauvaud, K. Seki, M. Steckiewicz, M. Stevens, A. I. F. Stewart, A. Stiepen, S. Stone, V. Tenishev, E. Thiemann, R. Tolson, D. Toublanc, M. Vogt, T. Weber, P. Withers, T. Woods, R. Yelle (2015), Early MAVEN Deep Dip Campaigns: First Results and Implications, *Sciences*, *350*(6261), doi: 10.1126/science.aad0459

(4) Jakosky, B. M., J. M. Grebowsky, J. G. Luhmann, J. Connerney, F. Eparvier, R. Ergun, J. Halekas, D. Larson, P. Mahaffy, J. McFadden, D. L. Mitchell, N. Schneider, R. Zurek, S. Bougher, D. Brain, Y. J. Ma, C. Mazelle, L. Andersson, D. Andrews, D. Baird, D. Baker, J. M. Bell, M. Benna, M. Chaffin, P. Chamberlin, J.-Y. Chaufray, J. Clarke, G. Collinson, M. Combi, F. Crary, T. Cravens, M. Crismani, S. Curry, D. Curtis, J. Deighan, G. Delory, R. Dewey, G. DiBraccio, C. Dong, Y. Dong, P. Dunn, M. Elrod, S. England, A. Eriksson, J. Espley, S. Evans, X. Fang, M. Fillingim, K. Fortier, C. M. Fowler, J. Fox, H. Gröller, S. Guzewich, T. Hara, Y. Harada, G. Holsclaw, S. K. Jain, R. Jolitz, F. Leblanc, C. O. Lee, Y. Lee, F. Lefevre, R. Lillis, R. Livi, D. Lo, M. Mayyasi, W. McClintock, T. McEnulty, R. Modolo, F. Montmessin, M. Morooka, A. Nagy, K. Olsen, W. Peterson, A. Rahmati, S. Ruhunusiri, C. T. Russell, S. Sakai, J.-A. Sauvaud, K. Seki, M. Steckiewicz, M. Stevens, A. I. F. Stewart, A. Stiepen, S. Stone, V. Tenishev, E. Thiemann, R. Tolson, D. Toublanc, M. Vogt, T. Weber, P. Withers, T. Woods, R. Yelle (2015b), MAVEN observations of the response of Mars to an interplanetary coronal mass ejection, *Science*, *350*(6261), doi: 10.1126/science.aad0210

(5) Modolo, S. Hess, V. Génot, L. Leclercq, F. Leblanc, J.-Y. Chauffray, P. Weill, M. Gangloff, A. Fedorov, E. Budnik, M. Bouchemit, M. Steckiewicz, N. André, L. Beigbeder, D. Popescu, J.-P. Toniutti, T. Al-Ubaidi, M. Khodachenko, D. Brain, S. Curry, B. Jakosky, M. Holmström (2017), The LatHyS database for planetary plasma environment investigations: Overview and a case study of data/model comparisons. *Planetary and Space Science, Elsevier*, (in press), doi: 10.1016/j.pss.2017.02.015

(6) Xu, S., D. Mitchell, M. Liemohn, X. Fang, Y. Ma, J. Luhmann, D. Brain, M. Steckiewicz, C. Mazelle, J. Connerney, and B. Jakosky (2017), Martian low-altitude magnetic topology deduced from MAVEN/SWEA observations, *Journal of Geophysical Research Space Physics*, *122*, doi: 10.1002/2016JA023467

(7) Garnier, P., M. Steckiewicz, C. Mazelle, S. Xu, D. Mitchell, M. K. G. Holmberg, J. S. Halekas, L. Andersson, D. A. Brain, J. E. P. Connerney, J. R. Espley, R. J. Lillis, J. G. Luhmann, J.-A. Sauvaud, and B. M. Jakosky (2017), The Martian photoelectron boundary as seen by MAVEN, *Journal of Geophysical Research Space Physics*, doi: 10.1002/2017JA024497

AGU PUBLICATIONS

Geophysical Research Letters

RESEARCH LETTER
10.1002/2015GL065257

Special Section:
First Results from the MAVEN Mission to Mars

Altitude dependence of nightside Martian suprathermal electron depletions as revealed by MAVEN observations

M. Steckiewicz[1,2], C. Mazelle[1,2], P. Garnier[1,2], N. André[1,2], E. Penou[1,2], A. Beth[1,2], J.-A. Sauvaud[1,2], D. Toublanc[1,2], D. L. Mitchell[3], J. P. McFadden[3], J. G. Luhmann[3], R. J. Lillis[3], J. E. P. Connerney[4], J. R. Espley[4], L. Andersson[5], J. S. Halekas[6], D. E. Larson[3], and B. M. Jakosky[5]

[1]Université de Toulouse, UPS-OMP, IRAP, Toulouse, France, [2]CNRS, IRAP, Toulouse, France, [3]Space Sciences Laboratory, University of California, Berkeley, California, USA, [4]NASA Goddard Space Flight Center, Greenbelt, Maryland, USA, [5]Laboratory for Atmospheric and Space Physics, University of Colorado Boulder, Boulder, Colorado, USA, [6]Department of Physics and Astronomy, University of Iowa, Iowa City, Iowa, USA

Key Points:
- MAVEN observes on almost each periapsis in the nightside ionosphere suprathermal electron depletions
- Observed depletions are populated by 6 eV electrons resulting from absorption by CO_2 and by 3 eV O_2^+
- The geographical distribution of nightside suprathermal electron depletions depends on altitude

Correspondence to:
M. Steckiewicz,
morgane.steckiewicz@irap.omp.eu

Citation:
Steckiewicz, M., et al. (2015), Altitude dependence of nightside Martian suprathermal electron depletions as revealed by MAVEN observations, *Geophys. Res. Lett.*, *42*, 8877–8884, doi:10.1002/2015GL065257.

Received 7 JUL 2015
Accepted 18 AUG 2015
Published online 5 NOV 2015

Abstract The MAVEN (Mars Atmosphere and Volatile EvolutioN) spacecraft is providing new detailed observations of the Martian ionosphere thanks to its unique orbital coverage and instrument suite. During most periapsis passages on the nightside ionosphere suprathermal electron depletions were detected. A simple criterion was implemented to identify the 1742 depletions observed from 16 November 2014 to 28 February 2015. A statistical analysis reveals that the main ion and electron populations within the depletions are surprisingly constant in time and altitude. Absorption by CO_2 is the main loss process for suprathermal electrons, and electrons that strongly peaked around 6 eV are resulting from this interaction. The observation of depletions appears however highly dependent on altitude. Depletions are mainly located above strong crustal magnetic sources above 170 km, whereas the depletions observed for the first time below 170 km are globally scattered onto the Martian surface with no particular dependence on crustal fields.

1. Introduction

The Mars Atmosphere and Volatile EvolutioN (MAVEN) mission is designed to study the structure, composition, and variability of the upper atmosphere and ionosphere of Mars, its interaction with the Sun/solar wind, and the atmospheric escape [*Jakosky et al.*, 2015]. Its insertion into orbit around Mars occurred on 21 September 2014. The spacecraft since then reached its mapping orbit which is a highly elliptical precessing orbit with a periapsis at 150 km, a period of 4.5 h and an inclination of 75°. This periapsis can also be lowered down to 125 km during deep-dip campaigns such as in mid-February 2015.

The nightside ionosphere of Mars is a poorly investigated area compared to the dayside one. One of the main observational properties of this region is the presence of recurrent structures characterized by significant depletions in electron fluxes and hence called "nightside suprathermal electron depletions" (hereinafter referred to as electron depletions). The first observations of these structures were obtained during the 400 km mapping orbit of Mars Global Surveyor (MGS) by the Electron Reflectometer instrument that detected on Mars' optical shadow pronounced decreases of the electron count rates up to 3 orders of magnitude at all energies [*Mitchell et al.*, 2001]. The same structures were then detected by the Mars Express (MEX) Electron Spectrometer [*Soobiah et al.*, 2006]. The statistical analysis of their geographical distribution suggested a strong correlation with crustal magnetic field in both hemispheres [*Mitchell et al.*, 2001; *Soobiah et al.*, 2006; *Soobiah*, 2009]. *Lillis and Brain* [2013] showed thanks to MGS data fixed at 02:00 A.M. local time that permanent electron depletions are located in regions of strong horizontal crustal fields whereas intermittent depletions are located in weaker horizontal field regions, only existing for low and moderate solar wind pressure. *Duru et al.* [2011] also reported these structures from measurements obtained down to 275 km altitude by the Mars Advanced Radar for Subsurface and Ionospheric Sounding on board MEX. These last measurements revealed the diversity of electron depletions which were sometimes correlated with ion flow features or ion density depletion regions. Martian electron depletions appeared different from the plasma holes reported at Venus [*Brace et al.*, 1982] since no local time, latitude, or altitude dependencies were detected [*Duru et al.*, 2011]. However, *Soobiah* [2009] demonstrated that they could not be distinguished from Venus-like electron

holes without the use of in situ magnetic field measurements and plasma density and temperature calculations. To date the origin of electron depletions stays mysterious, and a few processes have been proposed including plasma escape, recombination with ionized components above closed magnetic field lines, or a photochemical process [*Duru et al.*, 2011].

From late November 2014 to late February 2015 the periapsis of MAVEN occurred in the nightside of Mars. This time period therefore appears ideal to study electron depletions observed by MAVEN at low altitudes never reached before together with a unique complete suite of particles and fields instruments not flown on board MGS (no ion spectrometer) and MEX (no magnetometer). In this study we will combine for the first time (1) electron observations from the Solar Wind Electron Analyzer (SWEA) that measures the energy and angular distributions of 5 eV to 5 keV electrons with up to 2 s resolution (D. L. Mitchell et al., The MAVEN Solar Wind Electron Analyzer (SWEA), *Space Science Reviews*, in preparation 2015), (2) ion composition observations from the SupraThermal And Thermal Ion Composition (STATIC) analyzer that measures the velocity distributions and mass composition of suprathermal and thermal ions (J. P. McFadden et al., MAVEN SupraThermal And Thermal Ion Composition (STATIC) Instrument, submitted to *Space Science Reviews*, 2015), (3) magnetic field measurements from the Magnetometer (MAG) with a resolution of 8 pT [*Connerney et al.*, 2015], and (4) observations from the Solar Wind Ion Analyzer (SWIA) that measures the energy spectrum and angular distribution of solar wind and magnetosheath ions with energy from 5 eV to 25 keV [*Halekas et al.*, 2013].

This study will show how MAVEN sampled electron depletions above strong crustal magnetic sources and above places without any significant ones. Thanks to an exhaustive data set of electron depletions we will investigate the ion and electron populations' characteristics inside the electron depletions. We will also examine the altitude dependence of electron depletions and see if the known influence of crustal magnetic anomalies is dependent on altitude.

2. MAVEN Observations of Electron Depletions

2.1. Case Studies

The measurements of SWEA, STATIC, SWIA, and MAG on two particular orbits of MAVEN are presented in Figures 1 and 2. A nightside pass of MAVEN over a strong magnetic anomaly in the northern hemisphere is shown in Figure 1, whereas a similar pass over a quiet magnetic area is shown in Figure 2. During orbit 740 (Figure 1) the spacecraft came from the dayside, passed its periapsis at a local time of 19:15, 125 km above the geographic location (40°N, 74°E), and went out the induced magnetosphere on the nightside. During orbit 669 (Figure 2) it passed its periapsis at a local time of 20:45, 150 km above the geographic location (50°N, 150°E). In both cases we used multiinstrument observations to identify the different boundaries and key regions of the Martian-induced magnetosphere. The bow shock corresponds to the heating of the interplanetary plasma (H^+ and He^{++}) by the interaction between the supersonic solar wind and the Martian obstacle. The so-called magnetic pileup boundary (MPB) corresponds to the boundary where the solar wind proton and the suprathermal magnetosheath electron density decrease suddenly but not the core solar wind electron fluxes nor the solar wind magnetic field that piles up [*Acuña et al.*, 1998; *Bertucci et al.*, 2003; *Nagy et al.*, 2004]. The ionosphere is the region where the atmospheric photoelectrons dominate and the flux of electrons having an energy greater than ~30 eV decreases. This decrease can reach 1 order of magnitude for ~100 eV electrons [*Mitchell et al.*, 2001].

During orbit 740, SWEA recorded between 06:29 and 06:36 UTC a large electron depletion (delineated by brown dashed vertical lines) characterized by a decrease of the electron energy flux by more than 2 orders of magnitude at almost all energies. There is however a remaining electron population around 6 eV (Figure 1a). STATIC observations revealed a strong peak around 3 eV inside the depletion (Figure 1b) with mostly O_2^+, whereas the ionosphere was mainly composed of H^+, He^{++}, O^+, and O_2^+ (Figure 1c). Note that for O_2^+ 3 eV corresponds to the ram energy resulting from the satellite speed in the case of a thermalized background of ions. Just after the end of the electron depletion, at 06:36 UTC, the mean O_2^+ energy jumps from 3 to 6 eV which is due to a spacecraft potential effect a priori.

During the electron depletions the spacecraft was in the nightside ionosphere below 160 km altitude and passed over a strong magnetic anomaly between 06:29 and 06:33 UTC as indicated by the observed pronounced increase in magnetic field intensity and in agreement with the model of *Morschhauser et al.* [2014]

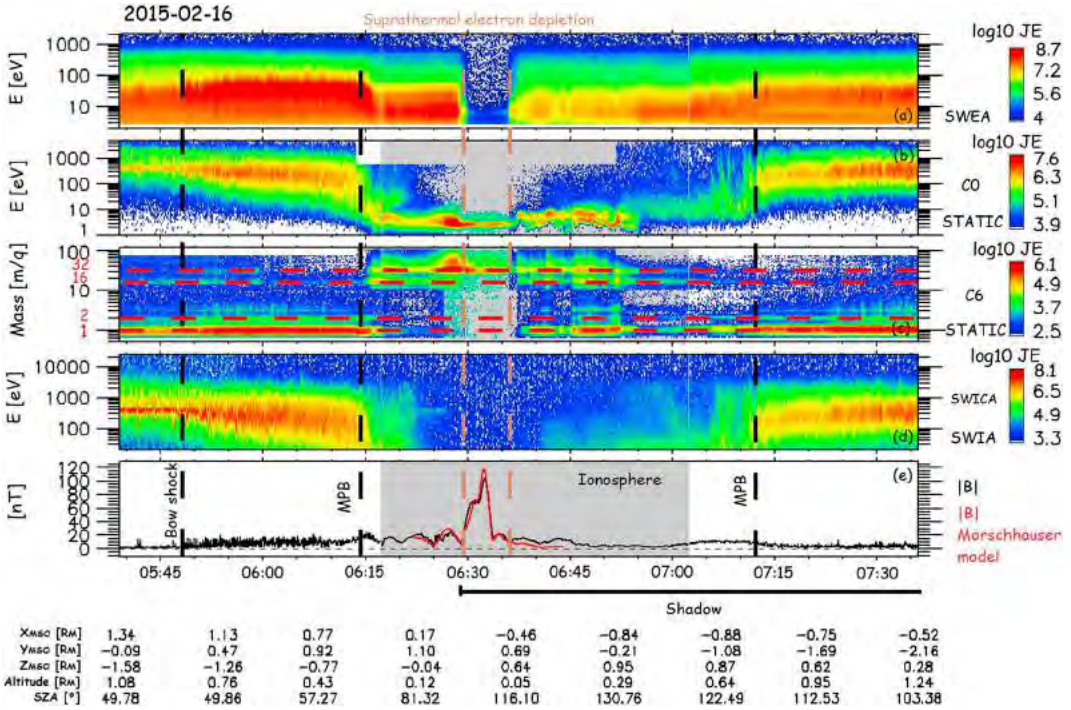

Xmso [Rm]	1.34	1.13	0.77	0.17	−0.46	−0.84	−0.88	−0.75	−0.52
Ymso [Rm]	−0.09	0.47	0.92	1.10	0.69	−0.21	−1.08	−1.69	−2.16
Zmso [Rm]	−1.58	−1.26	−0.77	−0.04	0.64	0.95	0.87	0.62	0.28
Altitude [Rm]	1.08	0.76	0.43	0.12	0.05	0.29	0.64	0.95	1.24
SZA [°]	49.78	49.86	57.27	81.32	116.10	130.76	122.49	112.53	103.38

Figure 1. Example of electron depletion in its plasma environment observed above a crustal magnetic field anomaly during orbit 740 on 16 February 2015. (a) SWEA energy-time spectrogram of omnidirectional electron energy flux, (b) STATIC energy-time spectrogram of omnidirectional ion energy flux (C0 mode), (c) STATIC mass-time spectrogram of omnidirectional ion energy flux (C6 mode), (d) SWIA energy-time spectrogram of omnidirectional ion energy flux (SWICA mode), and (e) magnetic field intensity (measured by MAG in black and calculated from the model of *Morschhauser et al.* [2014] in red) versus time. The grey shading highlights the ionosphere. The shadow corresponds to solar zenith angle (SZA) larger than 100°.

(Figure 1d). Electron depletions above magnetic anomalies appear to be a recurrent structure of the nightside ionosphere as reported from MGS and MEX data. Their observations were ascribed to spacecraft crossings of closed magnetic loops whose feet were anchored to crustal magnetic sources on the nightside. Inside those loops the spacecraft was then cut off from solar wind plasma traveling toward the magnetotail and ionospheric plasma coming from the sunlit side [*Mitchell et al.*, 2001]. It was also suggested that electron depletions are not seen on the dayside because when the loops travel on the dayside they are filled with ionospheric photoelectrons. Electron depletions are then the result of a balance between electron loss and creation processes. We can note that between 06:33 and 06:36 UTC the electron depletion is still present, whereas no significant magnetic field can be observed. This phenomenon will be observed in more details in Figure 2.

Figure 2 provides another observation of electron depletions (delineated by brown dashed vertical lines). The depletions are observed between 18:12 and 18:21 UTC below an altitude of 250 km and have similar properties to the depletion described previously. However, within this time interval electron energy flux decreases intermittently and electron depletions are observed alternately with "spikes" [*Mitchell et al.*, 2001]. The main difference with the Figure 1 example is the absence of significant crustal magnetic sources below the spacecraft at the time of the depletion, with very low values of the measured and predicted (by the Morschhauser model, in red in Figure 1e) magnetic fields. The model however predicts a small enhancement of the crustal field of 9 nT at 18:18. This value seems too small to be significant as it is embedded in the ambient magnetic field and coincident with electron spikes. This observation demonstrates that crustal magnetic anomalies cannot be the unique source of electron depletions.

These two case studies have been chosen as representative of a large number of electron depletions observed by MAVEN. The first one above a crustal magnetic anomaly corresponds to the typical case reported previously from MGS and MEX observations. The second one above a quiet magnetic area was occasionally reported from those past observations but is now commonly observed by MAVEN as illustrated by the statistical analysis presented in the next sections.

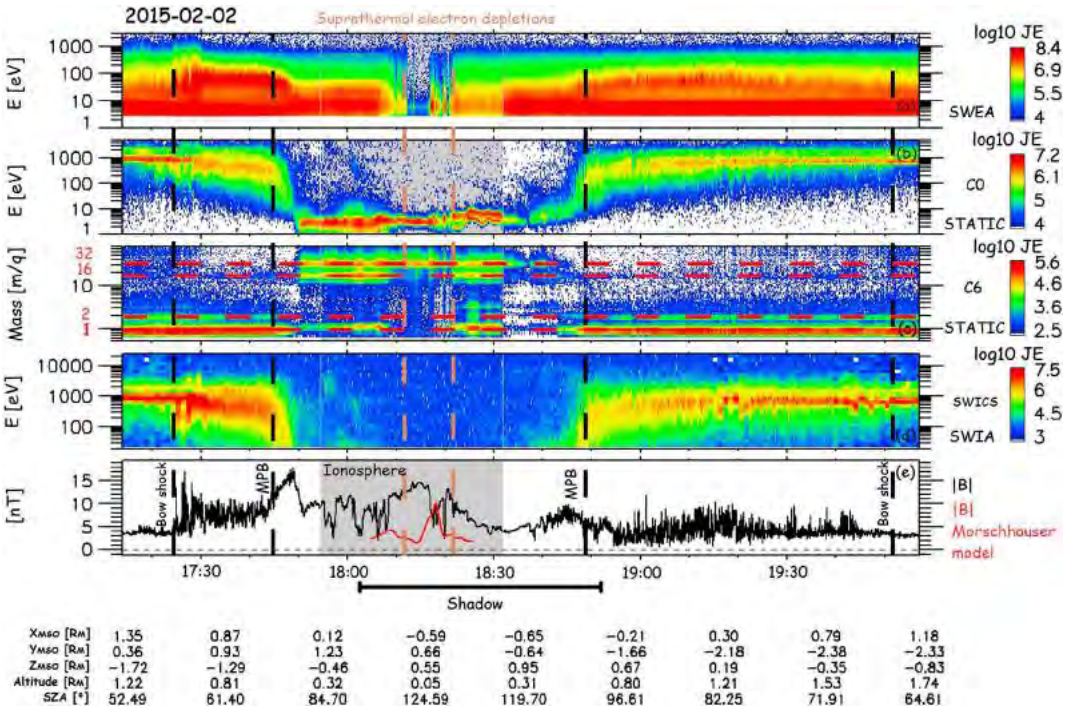

Figure 2. (a–e) Same as Figure 1. Example of electron depletions observed above a quiet magnetic area during orbit 669 on 2 February 2015.

3. Statistical Analysis

3.1. Methodology

A simple but robust criterion was implemented in order to detect electron depletions in MAVEN data. Our criterion is based on electron count rates (CRs) from SWEA observations and is described by equation (1). It relies on three energy channels ($E_1 = 4.26$ eV, $E_2 = 98.93$ eV, and $E_3 = 111.16$ eV) that enable us to distinguish electron depletions from spikes. The sampling time step used is the same as SWEA data: 4 s. Consequently, electron depletions detected last at least 4 s which corresponds to 16 km traveled by the spacecraft. Application of this criterion to data obtained between 16 November 2014 and 28 February 2015 resulted in a data set of 1742 electron depletions identified on 457 orbits among the 494 where data are available. During the 37 others no electron depletion satisfying our criteria was found.

$$\sum_{i=1}^{3} \frac{\mathrm{CR}(Ei)}{< \mathrm{CR}(Ei), 1\ \mathrm{h} >} < 0.03 \tag{1}$$

3.2. Properties of Electron Depletions

In order to derive the properties of electron depletions we concatenated all time intervals obtained with our criterion. The local time distribution of our data set covers the whole nightside sector, and the solar zenith angle (SZA) distribution varies from 95° to 155° so that some depletions can cross the terminator (SZA ∈ [90°, 100°]). There is therefore no particular local time or SZA dependence detected for the electron depletions considered in this study. However, any dependence with complete local time and solar zenith angle coverage is still undetermined but will be studied with future MAVEN data. Figure 3 provides the measurements of SWEA and STATIC obtained within the depletions. The data gap between 18 and 27 November 2014 corresponds to a safe mode. The different time intervals when low-energy ion populations are not measured by STATIC correspond to a change in instrument mode.

The electron population with energy above 10 eV has disappeared inside the depletions, and the remaining population is strongly peaked around a mean value remarkably constant of 6–7 eV with a full width at half maximum of 2 eV (Figure 3a). The neutral composition of the Martian nightside atmosphere is dominated by CO_2

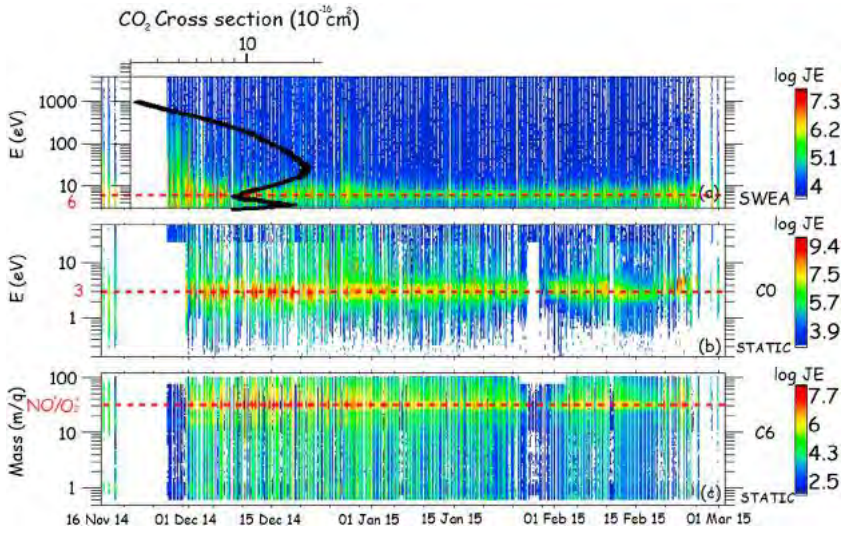

Figure 3. Concatenation of all the time intervals where electron depletions have been detected by our criterion. (a) SWEA energy-time spectrogram of omnidirectional electron energy flux, together with the total electron collision cross section for CO_2 (black line) taken from *Itikawa* [2002]. (b) STATIC energy-time spectrogram of omnidirectional ion energy flux (C0 mode). (c) STATIC mass-time spectrogram of omnidirectional ions energy flux (C6 mode).

below 200 km [*Haider et al*., 2013] but also includes O, N_2, CO, and O_2. Depending on the model considered the altitude where O becomes dominant is variable [*Haider et al*., 2013; *Krasnopolsky*, 2002], but all models describe the same composition. Inspection of the cross section for electron collisions with these five species [*Itikawa*, 2002; *Itikawa and Ichimura*, 1990; *Itikawa et al*., 1986, 1989; *Kanik et al*., 1993] reveals that only the CO_2 cross section (superimposed on top of the electron time-energy spectrogram in Figure 3a)—due to momentum transfer, excitation, and ionization processes—is in agreement with the inner electron population. It indeed presents a strong dip at 6 eV coincident with the remaining electron population and two strong peaks at 4 and 30 eV. Since a peak in the cross section is related to an electron loss process, electron absorption by the atmospheric CO_2 seems a good candidate to explain the large electron disappearance above 10 eV observed in all depletions as well as the remaining thermal electron population observed between 4 and 12 eV.

The energy of the ion population inside electron depletions (Figure 3b) is also strongly peaked around a mean value of 3 eV with a full width at half maximum of 1 eV on each mode, again suggesting that we observe cold ions with the ram velocity. Looking in detail at the mass-time spectrogram (Figure 3c) enable us to derive the ion composition within electron depletions dominated by O_2^+/NO^+(Note that STATIC cannot resolve between these species). This observation is consistent with the nightside ionosphere composition calculated by *Haider et al*. [2013] with O_2^+ as the main ion species below 200 km followed by NO^+ and CO_2^+. In summary the main ion and electron populations of all electron depletions identified in our study appear surprisingly constant independently of the altitude and the period they are observed. We will look into more details to their altitude distribution in the next section.

4. Interpretation

4.1. Altitude Distribution of Electron Depletions

In order to investigate the altitude distribution of all electron depletions we binned our data with constant bins of 2 km altitude. For each bin we first determined the number of electron depletions and then the number of MAVEN's passages contained therein during the time period under study (excluding data gaps during safe mode) in order to remove any orbital bias. The percentage of electron depletions per MAVEN passage is then the ratio of these two numbers, and the result of our statistical binning is provided in Figure 4.

First, the number of electron depletions increases with decreasing altitude. Second, there is a particularly noticeable slope change in our data distribution around 170 km: above 170 km there are 14% of depletions per passage, whereas below 170 km there are 46% of depletions per passage. The percentage even reaches

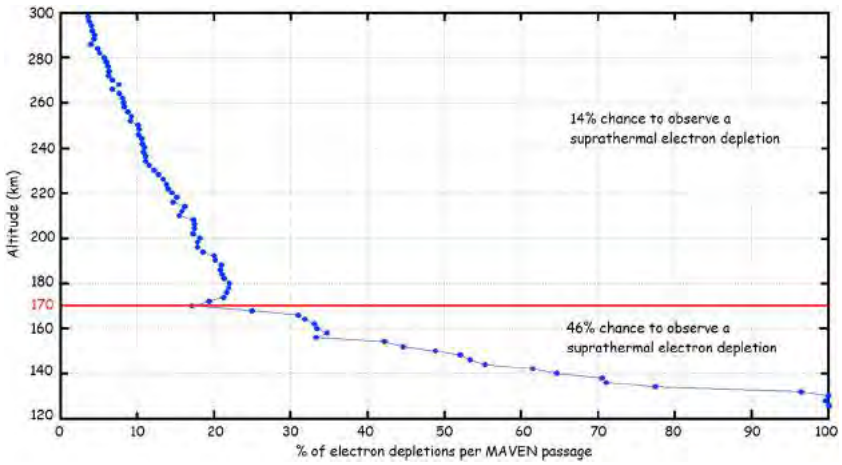

Figure 4. Percentage of electron depletions detected by our criterion per MAVEN passage calculated in bins of 2 km altitude. The horizontal red line highlights the abrupt slope change observed around 170 km.

100% at 125 km during the deep-dip campaign. In order to understand the differences between electron depletion occurrence above and below 170 km we will at first examine the geographic distribution of the electron depletions below this altitude and then above.

4.2. Geographical Distribution of Electron Depletions

We binned the Martian surface with a constant bin size of 5° longitude and 5° latitude and then estimated the percentage of electron depletions per MAVEN passage above each bin. Figure 5 displays the results of our binning for depletions observed below 170 km (Figure 5a) and above 170 km (Figure 5b) with the color-coded percentage of depletions per MAVEN passage projected onto a geographic map of the Martian surface. We superimposed on the resulting map contour lines for the intensity of the magnetic field calculated from the model of *Morschhauser et al*. [2014] at an altitude of 170 km. Only magnetic field intensities greater than 10 nT are indicated for clarity. We note that the number of time steps and of orbits is significant in all cells although weaker at the lowest latitudes ($<$40°) and altitudes ($<$150 km).

Figure 5a indicates that the geographic distribution of electron depletions below 170 km is homogeneous above the northern hemisphere between 30°N and 75°N with no significant latitude or longitude dependence. Whereas some of the high percentages bins are located above the two largest magnetic areas located around coordinates (180°E, 45°N) and (10°E, 50°N), many others are not related to them. Therefore, the presence of crustal magnetic sources below the location where electron depletions are observed probably influences their properties, but crustal fields cannot be invoked as the main mechanism to explain their origin in this altitude range. Hence, below a mean altitude of 170 km the predominant process at the origin of electron depletions is electron absorption by atmospheric CO_2.

Contrary to depletions observed below 170 km, Figure 5b indicates a strongly heterogeneous electron depletions distribution above 170 km, mostly observed above the large magnetic areas mentioned previously and very few depletions away from them. This explains why electron depletions previously observed by MEX and MGS were predominantly associated with crustal magnetic fields since their observations were restricted to altitudes above 275 km, which introduced a bias in their interpretation. Hence, the predominant source mechanism at the origin of electron depletions above 170 km seems to be linked with strong crustal magnetic sources. Note however that some depletions do not perfectly fit with the scenario, especially in the regions (230°E, 260°E) and (40°N, 70°N).

5. Conclusions

We have presented new in situ observations of nightside suprathermal electron depletions obtained by MAVEN in the Martian northern hemisphere. These observations are obtained for the first time at low altitudes down to 125 km and nicely extend previous observations of electron depletions by MGS and MEX that

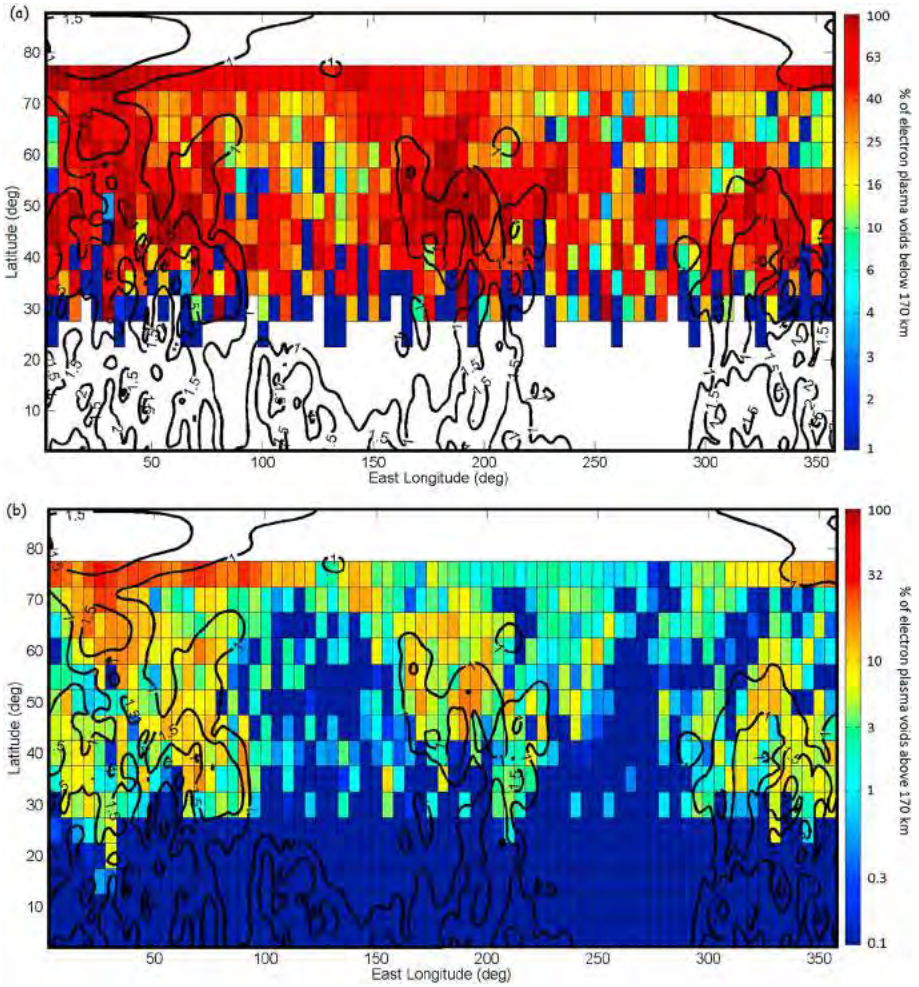

Figure 5. Percentage of electron depletions detected by our criterion per MAVEN passage superimposed on a geographic map of the Martian surface with constant bin size of 5 × 5°. The black lines correspond to magnetic field intensity contour lines (in logarithmic scale) calculated from the model of *Morschhauser et al.* [2014] at an altitude of 170 km. Distribution of depletions observed (a) below 170 km and (b) above 170 km.

were restricted to altitudes above 275 km. Taking advantage of the unique suite of particles and field instruments on board MAVEN we showed that the main ion and electron populations inside the electron depletions appear surprisingly constant with time and altitude. Inspection of the cross section for electron collision with the main constituents of the ionosphere suggests that electron absorption by CO_2 is the best candidate to explain the origin of electron depletions. Our statistical analysis however reveals that the presence of electron depletions in the nightside ionosphere is highly dependent on altitude, with the probability of observing an electron depletion above 170 km being 14% compared to 46% below 170 km. Our study indicates that the electron depletions above 170 km—as previously reported by MGS and MEX—are strongly favored by the presence of crustal magnetic fields, whereas electron depletions observed for the first time below 170 km are globally scattered onto the surface of the planet with no particular dependence on crustal fields. Hence, the two main sources of electron depletions highlighted here have different predominance area: low altitude for CO_2 absorption and geographical spots for the crustal magnetic field effect.

MAVEN will soon observe the Martian southern hemisphere where the strongest magnetic crustal sources are located. We naturally plan to extend our analysis in the near future to include these measurements and further test our proposed interpretation about these structures' origin.

Acknowledgments
This work was supported by the French space agency CNES for the part based on observations obtained with the SWEA instrument embarked on MAVEN. The MAVEN project is supported by NASA through the Mars Exploration Program. The authors acknowledge the support of the MAVEN project and particularly all the instrument and science teams for making the MAVEN mission such an outstanding success and providing us with high-quality data. We are also grateful to the CDPP/AMDA team (http://amda.cdpp.eu) and Emmanuel Penou for providing support with data analysis tools. MAVEN data are publicly available through the Planetary Data System. The authors thank Yasir Soobiah and an anonymous reviewer for their assistance in evaluating this paper.

The Editor thanks two anonymous reviewers for their assistance in evaluating this paper.

References

Acuña, M. H., et al. (1998), Magnetic field and plasma observations at Mars: Initial results of the Mars Global Surveyor mission, *Science*, *279*(5357), 1676–1680, doi:10.1126/science.279.5357.1676.

Bertucci, C., et al. (2003), Magnetic field draping enhancement at the Martian magnetic pileup boundary from Mars Global Surveyor observations, *Geophys. Res. Lett.*, *30*(2), 1099, doi:10.1029/2002GL015713.

Brace, L. H., R. F. Theis, H. G. Mayr, S. A. Curtis, and J. G. Luhmann (1982), Holes in the nightside ionosphere of Venus, *J. Geophys. Res.*, *87*(A1), 199–211, doi:10.1029/JA087iA01p00199.

Connerney, J. E. P., J. Espley, P. Lawton, S. Murphy, J. Odom, R. Oliverson, and D. Sheppard (2015), The MAVEN magnetic field investigation, *Space Sci. Rev.*, doi:10.1007/s11214-015-0169-4.

Duru, F., D. A. Gurnett, D. D. Morgan, J. D. Winningham, R. A. Frahm, and A. F. Nagy (2011), Nightside ionosphere of Mars studied with local electron densities: A general overview and electron density depressions, *J. Geophys. Res.*, *116*, A10316, doi:10.1029/2011JA016835.

Haider, S. A., B. M. Pandya, and G. J. Molina-Cuberos (2013), Nighttime ionosphere caused by meteoroid ablation and solar wind electron-proton-hydrogen impact on Mars: MEX observation and modeling, *J. Geophys. Res. Space Physics*, *118*, 6786–6794, doi:10.1002/jgra.50590.

Halekas, J. S., E. R. Taylor, G. Dalton, G. Johnson, D. W. Curtis, J. P. McFadden, D. L. Mitchell, R. P. Lin, and B. M. Jakosky (2013), The Solar Wind Ion Analyzer for MAVEN, *Space Sci. Rev.*, 1–27, doi:10.1007/s11214-013-0029-z.

Itikawa, Y. (2002), Cross sections for electron collisions with carbon dioxide, *J. Phys. Chem. Ref. Data*, *31*(3), doi:10.1063/1.1481879.

Itikawa, Y., and A. Ichimura (1990), Cross section for collisions of electrons and photons with atomic oxygen, *J. Phys. Chem. Ref. Data*, *19*(3), 637–651.

Itikawa, Y., M. Hayashi, A. Ichimura, K. Onda, K. Sakimoto, K. Takayanagi, M. Nakamura, H. Nishimura, and T. Takayanagi (1986), Cross sections for collisions of electrons and photons with nitrogen molecules, *J. Phys. Chem. Ref. Data*, *15*(3), 985–1010.

Itikawa, Y., A. Ichimura, K. Onda, K. Sakimoto, T. Takayanagi, Y. Hatano, M. Hayashi, H. Nishimura, and S. Tsurubuchi (1989), Cross sections for collisions of electrons and photons with oxygen molecules, *J. Phys. Chem. Ref. Data*, *18*(1), 23–42.

Jakosky, B. M., et al. (2015), The Mars Atmosphere and Volatile Evolution (MAVEN) mission, *Space Sci. Rev.*, doi:10.1007/s11214-015-0139-x.

Kanik, I., S. Trajmar, and J. C. Nickel (1993), Total electron scattering and electronic state excitations cross sections for O_2, CO and CH_4, *J. Geophys. Res.*, *98*(E4), 7447–7460, doi:10.1029/92JE02811.

Krasnopolsky, V. A. (2002), Mars' upper atmosphere and ionosphere at low, medium and high solar activities: Implications for evolution of water, *J. Geophys. Res.*, *107*(E12), 5128, doi:10.1029/2001JE001809.

Lillis, R. J., and D. A. Brain (2013), Nightside electron precipitation at Mars: Geographic variability and dependence on solar wind conditions, *J. Geophys. Res. Space Physics*, *118*, 3546–3556, doi:10.1002/jgra.50171.

Mitchell, D. L., R. P. Lin, C. Mazelle, H. Rème, P. A. Cloutier, J. E. P. Connerney, M. H. Acuña, and N. F. Ness (2001), Probing Mars' crustal magnetic field and ionosphere with the MGS Electron Reflectometer, *J. Geophys. Res.*, *106*(E10), 23,419–23,427, doi:10.1029/2000JE001435.

Morschhauser, A., V. Lesur, and M. Grott (2014), A spherical harmonic model of the lithospheric magnetic field of Mars, *J. Geophys. Res. Planets*, *119*, 1162–1188, doi:10.1002/2013JE004555.

Nagy, A. F., et al. (2004), The plasma environment of Mars, *Space Sci. Rev.*, *111*(1–2), 33–114, doi:10.1023/B:SPAC.0000032718.47512.92.

Soobiah, Y. I. J. (2009), The investigation of crustal magnetic field signatures at Mars by the Mars Express ASPERA-3 Electron Spectrometer (ELS), Doctoral thesis, Department of Space and Climate Physics, Mullard Space Science Laboratory, UCL (Univ. College London), London, U. K.

Soobiah, Y. I. J., et al. (2006), Observations of magnetic anomaly signatures in Mars Express ASPERA-3 ELS data, *Icarus*, *182*, 396–405, doi:10.1016/j.icarus.2005.10.034.

AGU PUBLICATIONS

JGR

Journal of Geophysical Research: Space Physics

RESEARCH ARTICLE
10.1002/2016JA023205

Special Section:
Major Results From the MAVEN Mission to Mars

Key Points:
- Automatic detection of suprathermal electron depletions observed by three spacecraft (MGS, MEX, and MAVEN) during 17 years
- At high altitudes electron depletions are clearly observed by the three spacecraft over crustal magnetic field sources
- At low altitudes interaction with crustal magnetic fields is no longer the dominant creation process for electron depletions

Correspondence to:
M. Steckiewicz,
morgane.steckiewicz@irap.omp.eu

Citation:
Steckiewicz, M., et al. (2016), Comparative study of the Martian suprathermal electron depletions based on Mars Global Surveyor, Mars Express, and Mars Atmosphere and Volatile EvolutioN mission observations, *J. Geophys. Res. Space Physics*, *121*, doi:10.1002/2016JA023205.

Received 19 JUL 2016
Accepted 18 NOV 2016
Accepted article online 20 NOV 2016

Comparative study of the Martian suprathermal electron depletions based on Mars Global Surveyor, Mars Express, and Mars Atmosphere and Volatile EvolutioN mission observations

M. Steckiewicz[1,2], P. Garnier[1,2], N. André[1,2], D. L. Mitchell[3], L. Andersson[4], E. Penou[1,2], A. Beth[5], A. Fedorov[1,2], J.-A. Sauvaud[1,2], C. Mazelle[1,2], D. A. Brain[4], J. R. Espley[6], J. McFadden[3], J. S. Halekas[7], D. E. Larson[3], R. J. Lillis[3], J. G. Luhmann[3], Y. Soobiah[6], and B. M. Jakosky[4]

[1]Université de Toulouse, UPS-OMP, IRAP, Toulouse, France, [2]CNRS, IRAP, Toulouse, France, [3]Space Sciences Laboratory, University of California, Berkeley, California, USA, [4]Laboratory for Atmospheric and Space Physics, University of Colorado Boulder, Boulder, Colorado, USA, [5]Department of Physics, Imperial College London, London, UK, [6]NASA Goddard Space Flight Center, Greenbelt, Maryland, USA, [7]Department of Physics and Astronomy, University of Iowa, Iowa City, Iowa, USA

Abstract Nightside suprathermal electron depletions have been observed at Mars by three spacecraft to date: Mars Global Surveyor, Mars Express, and the Mars Atmosphere and Volatile EvolutioN (MAVEN) mission. This spatial and temporal diversity of measurements allows us to propose here a comprehensive view of the Martian electron depletions through the first multispacecraft study of the phenomenon. We have analyzed data recorded by the three spacecraft from 1999 to 2015 in order to better understand the distribution of the electron depletions and their creation mechanisms. Three simple criteria adapted to each mission have been implemented to identify more than 134,500 electron depletions observed between 125 and 900 km altitude. The geographical distribution maps of the electron depletions detected by the three spacecraft confirm the strong link existing between electron depletions and crustal magnetic field at altitudes greater than ~170 km. At these altitudes, the distribution of electron depletions is strongly different in the two hemispheres, with a far greater chance to observe an electron depletion in the Southern Hemisphere, where the strongest crustal magnetic sources are located. However, the unique MAVEN observations reveal that below a transition region near 160–170 km altitude the distribution of electron depletions is the same in both hemispheres, with no particular dependence on crustal magnetic fields. This result supports the suggestion made by previous studies that these low-altitudes events are produced through electron absorption by atmospheric CO_2.

1. Introduction

At the present time, Mars does not possess any global dynamo magnetic field. However, localized magnetic fields of crustal origin provide evidence of an ancient dynamo which existed prior to ~4 Ga ago [*Lillis et al.*, 2008, 2013]. These crustal fields can reach intensities exceeding 200 nT at 400 km in the Southern Hemisphere [*Acuña et al.*, 2001]. Hence, Mars does not possess a global intrinsic magnetosphere, but rather several minimagnetospheres induced by closed loops of crustal magnetic field (where magnetic field lines are connected at both ends to the crust). These structures can extend to hundreds of kilometers above the surface with sufficient magnetic pressure to stand off the solar wind flow up to 1000 km [*Brain et al.*, 2003]. The inner magnetic field lines are then isolated from the interplanetary magnetic field (IMF). The magnetic topology near Mars is thus quite complex with closed loops of crustal magnetic field, open field lines connecting the crust to the IMF, and draped field lines unconnected to the crust [*Nagy et al.*, 2003; *Bertucci et al.*, 2003; *Brain et al.*, 2007].

Mars is surrounded by a thin CO_2-dominated atmosphere. The solar extreme ultraviolet radiations impinging the neutral part of this atmosphere lead to the creation of the dayside Martian ionosphere. However, the photoelectrons liberated in the dayside of Mars mainly from ionization of atmospheric CO_2 and O by solar photons are also observed in the nightside hemisphere [*Frahm et al.*, 2006]. The nightside Martian ionosphere is maintained by transport processes from the dayside (e.g., horizontal transport of photoelectrons from dayside to nightside along draped magnetic field lines [*Ulusen and Linscott*, 2008; *Fränz et al.*, 2010]), as well

as by production processes such as electron impact ionization of precipitating magnetosheath electrons [*Fillingim et al*., 2010; *Lillis et al*., 2011; *Lillis and Brain*, 2013].

The nightside ionosphere still remains an unfamiliar and mysterious place. Several studies have shown that the nightside ionosphere is irregular, spotty, faint, and complex [*Zhang et al*., 1990; *Němec et al*., 2010; *Duru et al*., 2011; *Withers et al*., 2012]. Using Mars Global Surveyor (MGS) Electron Reflectometer (ER) measurements, *Mitchell et al*. [2001] first observed that the nightside ionosphere was punctuated by abrupt drops of the instrumental count rate by up to 3 orders of magnitude to near-background levels across all energies, hence calling them "plasma voids." These structures seemed to be observed where closed crustal magnetic loops existed at 400 km on the nightside; i.e., they did not connect with the magnetotail, and hence, tail electrons could not access them. On the dayside, these loops can trap ionospheric plasma, including suprathermal photoelectrons. When they travel to the nightside, the electrons are removed through a combination of outward diffusion, scattering, and interactions with the collisional thick atmosphere at lower altitudes. Meanwhile, the external sources of plasma (solar wind plasma traveling up the magnetotail and ionospheric plasma) are excluded from the inner layers of the closed field regions, so that sinks overpass sources, thus creating plasma voids. The topology of the crustal magnetic fields can therefore significantly influence the structure of the nightside ionosphere.

Based on 144 passages of the Mars Express (MEX) spacecraft at low altitudes, *Soobiah et al*. [2006] observed thanks to the Analyser of Space Plasmas and Energetic Atoms that the electron flux underwent significant changes close to crustal magnetic fields. Intensified flux signatures were observed mainly on the dayside, whereas flux depletions were features of the nightside hemisphere. Through a study over 7.5 years of the MGS mission, *Brain et al*. [2007] showed statistically that plasma voids are indeed concentrated near strong crustal magnetic fields and that very few voids are seen at large distances from crustal magnetic sources. This study also revealed that plasma voids are surrounded by areas with trapped and conic electron pitch angle (angle between the electron velocity and the magnetic field vectors) distributions, consistent with the idea of closed magnetic field lines and indicating that the outer layers of closed magnetic field regions are populated thanks to source processes such as reconnection with the draped IMF.

Furthermore, the long-term statistical survey by *Brain et al*. [2007] highlighted that hardly any plasma voids are observed on the dayside (defined as solar zenith angle (SZA) greater than 90°). This means that when the crustal magnetic loops rotate to the dayside, they trap newly created ionospheric plasma. As the ionospheric plasma is homogeneously created in the dayside, voids are essentially never seen on this side of Mars. While plasma voids are restricted to the nightside, studies made with MEX data by *Soobiah et al*. [2006] and *Duru et al*. [2011] showed no dissymmetry between the dawnside and the duskside. Plasma voids are globally distributed regardless of nightside local time (1800 h–2400 h and 0000 h–0600 h), within the limits of their studies.

Crustal magnetic loops do not necessarily stay closed as the planet rotates [*Ma et al*., 2014], and crustal fields can connect and reconnect with the piled-up, draped, and dynamic IMF. Hence, when they travel to the nightside, regions with strong enough horizontal crustal fields are able to stand off the IMF effects. The crustal magnetic loops in these regions thus stay closed all the way across the nightside and are populated by permanent plasma voids, which means that we can observe this phenomena during each passage above such regions on the nightside. On the other hand, regions with weaker horizontal fields are essentially intermittently populated with plasma voids, depending on the external drivers. For low and moderate solar wind pressure crustal magnetic loops are closed and devoid of plasma. However, for high solar wind pressure the crustal field lines open up and get connected to the IMF. These weak crustal magnetic field regions are then filled with solar wind plasma travelling through the tail [*Lillis and Brain*, 2013].

More recently, *Hall et al*. [2016] used the rapid reductions of a proxy measurement of the electron flux derived from the MEX ASPERA-3 Electron Spectrometer (ELS) electron flux measurements integrated across the 20–200 eV energy range to automatically identify plasma voids. The study covers approximately 10 years of the MEX mission from 2004 to 2014 and is restricted to the illuminated induced magnetosphere (region of space inside the magnetic pileup boundary and outside the cylindrical shadow of the planet). Using this method, plasma voids were detected among 56% of the orbits under study, from 266 km (MEX lowest periapsis) to 10 117 km. A statistical study of the distribution of these events showed that approximately 80% of them occurred below 1300 km, predominantly at SZA between 90° and 120°. Study of the spatial

and altitudinal distributions of the detected plasma voids confirmed the strong link existing between the plasma void occurrence and the magnitude of the crustal magnetic field. The bigger the source was, the higher plasma voids could be observed. However, some regions appear to be in contradiction with this global behavior, which suggests that other processes are involved in plasma void creation such as the interaction between the solar wind and the Martian plasma.

All these results have been obtained from MGS and MEX data that have several constraints. MGS did not carry any ion spectrometer and was fixed in local time at 02:00 A.M./02:00 P.M. via a circular orbit (altitude between 370 and 430 km). MEX on the other hand does not carry any magnetometer and has a periapsis between 245 and 365 km. The Mars Atmosphere and Volatile EvolutioN (MAVEN) spacecraft entered into orbit around Mars in September 2014 with a complete suite of plasma and field instruments, including a magnetometer, two ion and one electron spectrometers. The altitude of the spacecraft reaches 150 km during nominal orbits and is periodically lowered down to 125 km for 5 days periods known as "deep dips" [*Bougher et al*., 2015], which allows measurements of these plasma phenomena at previously unsampled altitudes. Initial results on the plasma voids observed by MAVEN above the Northern Hemisphere was then investigated by *Steckiewicz et al*. [2015]. At the time of that initial study, the data available were restricted to latitudes between 20°N and 74°N. This multiinstrument study leads to rename the "electron plasma voids" into "nightside suprathermal electron depletions" (hereinafter referred as electron depletions). It suggested that the distribution of electron depletions is highly dependent on altitude. Above a transition region near 160–170 km altitude, electron depletions are strongly linked to horizontal crustal magnetic fields as previously shown by MEX and MGS observations. However, below that transition region the distribution was found to be more homogeneous, irrespective of crustal magnetic field sources. Thus, two main electron sinks leading to the creation of electron depletions have been identified: the exclusion by closed crustal magnetic loops and the absorption by atmospheric CO_2. These two processes seem to always play a role in electron depletions creation but have two different predominance areas: the exclusion by closed crustal magnetic sources is predominant at high altitudes, whereas absorption by atmospheric CO_2 is predominant at low altitudes.

The present paper takes advantage of the different characteristics of these three missions to study the geographical and altitudinal distributions of electron depletions from different points of view. MGS data are used from 1999 to 2006 in order to take advantage of the mapping circular orbit at a roughly constant altitude (~400 km) of the spacecraft, allowing observations of the phenomenon every 2 h over the whole range of possible latitudes [−90°, 90°]. MEX data are used from 2004 to 2014, which gives us an unparalleled long-term view of the phenomenon at both relatively low (down to ~300 km) and high altitudes. Finally, MAVEN data are used from October 2014 to November 2015. During this time period the spacecraft covered both hemispheres except the poles, but due to this short duration and MAVEN orbital parameters, all latitudes are not yet covered at all possible altitudes. Even though the coverage and duration of this data set are much lower than those of MGS and MEX, MAVEN reached during this time period altitudes down to 125 km, which are unsampled by MGS nor MEX.

This huge data set gathering observations made over 17 years by different instruments reaching different altitude regimes enables us to compare events observed in similar conditions (several spacecraft in the same region) and enrich this joint vision with new observations closer to the surface (with MAVEN). We first show examples of how electron depletions are observed by MGS, MEX, and MAVEN, then describe the three criteria used to automatically detect electron depletions in each mission electron spectrometer measurements. An exhaustive data set of electron depletions derived from these three criteria is then used to compare their geographical distribution with the location of crustal magnetic sources. We finally investigate and compare the altitude distributions obtained with MAVEN and MEX, before a conclusion ends the paper.

2. Three Spacecraft, Three Different Perspectives of Suprathermal Electron Depletions

Martian suprathermal electron depletions have been observed to date by three spacecraft: MGS, MEX, and MAVEN. The last two are still in good operating condition at the time of writing. Figures 1–3 display the plasma observations of these structures made chronologically by MGS, MEX, and MAVEN, respectively, and are described next in more details. The improved performances of the plasma instrument suite over the different missions allow now for a more accurate understanding of electron depletions.

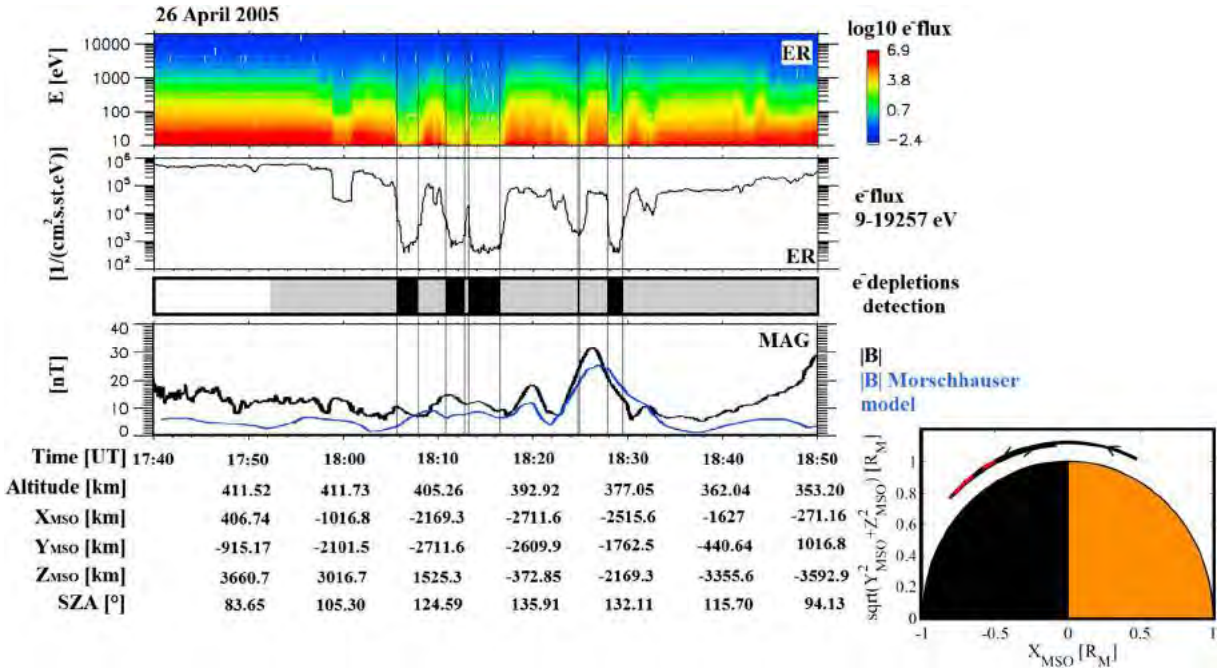

Figure 1. Example of electron depletion observed by MGS on 26 April 2005. (first panel) ER energy-time spectrogram of omnidirectional electron flux. (second panel) ER omnidirectional electron flux summed over all energies available (11–16127 eV). (third panel) Detection of electron depletions by criterion (3) (black boxes). See section 3 for more details. The shadow corresponds to the nightside. (fourth panel) Magnetic field intensity (measured by MAG in black and calculated from the model of Morschhauser in blue). (fifth panel, bottom right) MGS orbital trajectory in a cylindrically symmetric MSO coordinate frame. The locations of the electron depletions detected are highlighted in red. The altitude is defined with respect to a sphere with the Mars' volumetric mean radius of 3389.51 km.

All the ephemerides used in this paper are expressed in the Mars-centric Solar Orbital (MSO) coordinates defined as follows: the origin is the center of Mars, the x axis points from the center of Mars to the Sun, y points opposite to Mars' orbital angular velocity, and z completes the right-handed set so that the frame rotates slowly as Mars orbits the Sun. The nightside is here considered as $x < 0$. However, the real border between sunlit and dark sides occurs at different SZA for different altitudes. Hence, if an electron depletion is observed in the nightside, it can be to some extent in the illuminated terminator region.

2.1. MGS: First Observations

The Mars Global Surveyor spacecraft was placed in its mapping orbit around Mars on 9 March 1999 [*Albee et al.*, 2001]. This orbit was nearly circular, Sun-synchronous, near-polar, and at an altitude varying between 368 and 438 km, which corresponded to a period of approximately 2 h. The orbit was also fixed at a local time of 02:00 A.M./02:00 P.M. Contact with the spacecraft was lost in early November 2006. The MGS magnetic field experiment was composed of two redundant triaxial fluxgate magnetometers (MAG) and an Electron Reflectometer (ER) [*Acuña et al.*, 2001]. MAG was able to detect ambient magnetic fields from ± 4 nT to $\pm$ 65 ,536 nT, and ER measured electrons in 19 logarithmically spaced energy channels ranging from 10 eV to 20 keV with an energy resolution of $\frac{\delta E}{E} = 25\%$ (full width at half maximum). MGS did not carry an ion spectrometer.

Figure 1 shows an example of electron depletions observed by MGS on 26 April 2005. The first panel is the ER energy-time spectrogram of omnidirectional electron flux, and the second panel is the ER electron flux summed over all the observed energies. The blacked out regions in the third panel delineate the electron depletions automatically detected by criterion (3), when the electron flux drops by more than 2 orders of magnitude at all observed energies. This criterion is described in more details in section 3.3. The fourth panel is the magnitude of the magnetic field measured by MAG (black profile) superimposed with the magnitude of the crustal magnetic field calculated from the model of *Morschhauser et al.* [2014] (blue profile; hereinafter referred as the Morschhauser model). Thus, the first three depletions (between 18:05 and 18:15) are located over weak crustal field regions, whereas the two last (between 18:25 and 18:30) are located over a modest

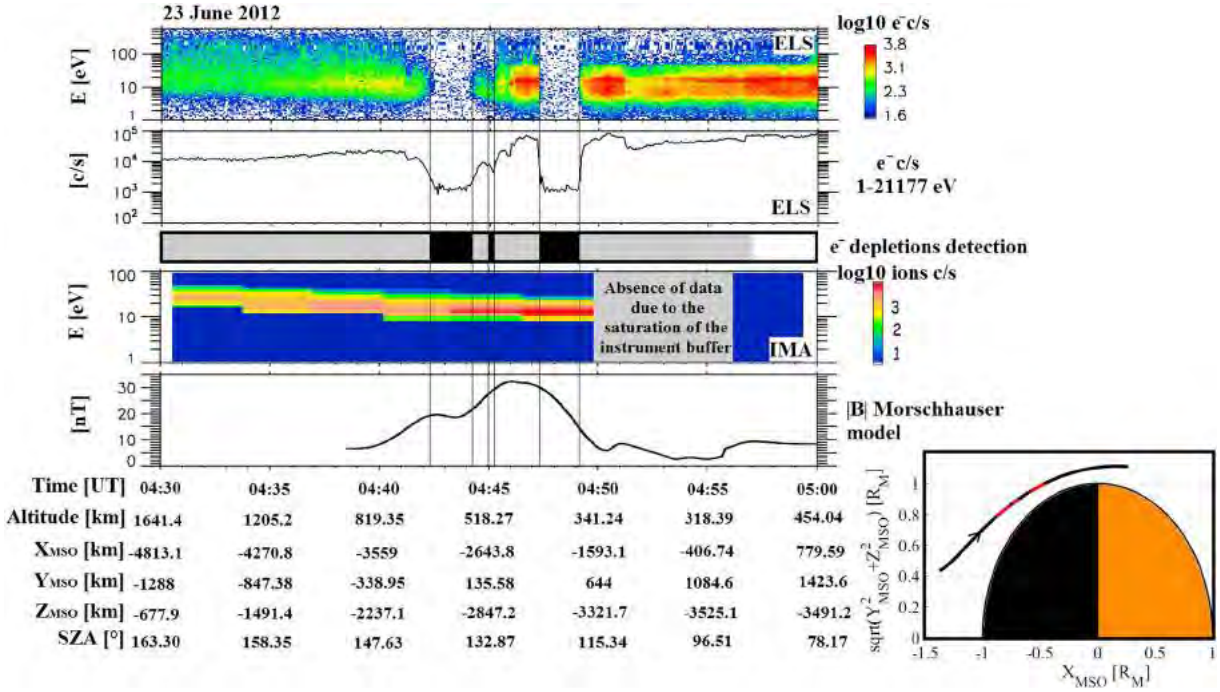

Figure 2. Example of electron depletion observed by MEX on 23 June 2012. (first panel) ELS energy-time spectrogram of omnidirectional electron counts per second. (second panel) ELS electron counts per second summed over all the energies available (1–21177 eV). (third panel) Detection of electron depletions by criterion (2) (black boxes). See section 3 for more details. The shadow corresponds to the nightside. (fourth panel) IMA energy-time spectrogram of omnidirectional heavy ions counts per second (m/q > 20). (fifth panel) Magnetic field intensity calculated from the Morschhauser model. (sixth panel, bottom right) MEX orbital trajectory in a cylindrically symmetric MSO coordinate frame. The locations of the electron depletions detected are highlighted in red.

crustal magnetic field source (~25 nT at 400 km altitude). On the last bottom right plot, the orbital trajectory of MGS in a cylindrically symmetric MSO coordinate frame is plotted. The depletions are highlighted in red and are all located on the nightside.

As shown in this example, the electron flux measured by ER inside the electron depletions is barely above the background level (see Figure 10 of *Mitchell et al*. [2001] for a detailed description of the background level) at all energies observed, which lead *Mitchell et al*. [2001] to designate them as plasma voids.

2.2. Mars Express

The Mars Express spacecraft was inserted into orbit around Mars in January 2004. Its orbit is highly elliptical, with a periapsis altitude between 245 and 365 km and an apoapsis altitude of ~10,000 km, which implies a period of ~6.75 h. The inclination of the orbit is 86°, and it precesses slowly [*Chicarro et al*., 2004]. The ASPERA-3 experiment is composed of four instruments including the Electron Spectrometer (ELS) and the Ion Mass Analyzer (IMA) [*Barabash et al*., 2004]. The IMA sensor measures 3-D fluxes of different ion species with a mass-to-charge ratio (m/q) resolution of 1, 2, 4, 8, 16, and >20 in the energy range of 0.01–30 keV/q, with an energy resolution of $\frac{\delta E}{E} = 7\%$. The ELS instrument measures the electron fluxes in the energy range of 0.001–20 keV/q in 128 logarithmically spaced energy channels with an energy resolution of $\frac{\delta E}{E} = 8\%$ (which is the best energy resolution among the electron spectrometers of the three spacecraft; see Table 1). In general, ELS has been operated in four different modes (default/survey mode, linear mode, 1 s mode, and 32 Hz mode), differing mainly in the energy ranges, the energy steps, and the measuring cadences used (see *Frahm et al*. [2006] and *Hall et al*. [2016] for more details about the different ELS modes). In this study, we only include measurements when ELS is operating in survey mode. Mars Express does not carry a magnetometer.

Figure 2 shows an example of electron depletions observed by MEX on 23 June 2012. The first panel is the ELS energy-time spectrogram of omnidirectional electron counts per second, and the second panel is the ELS

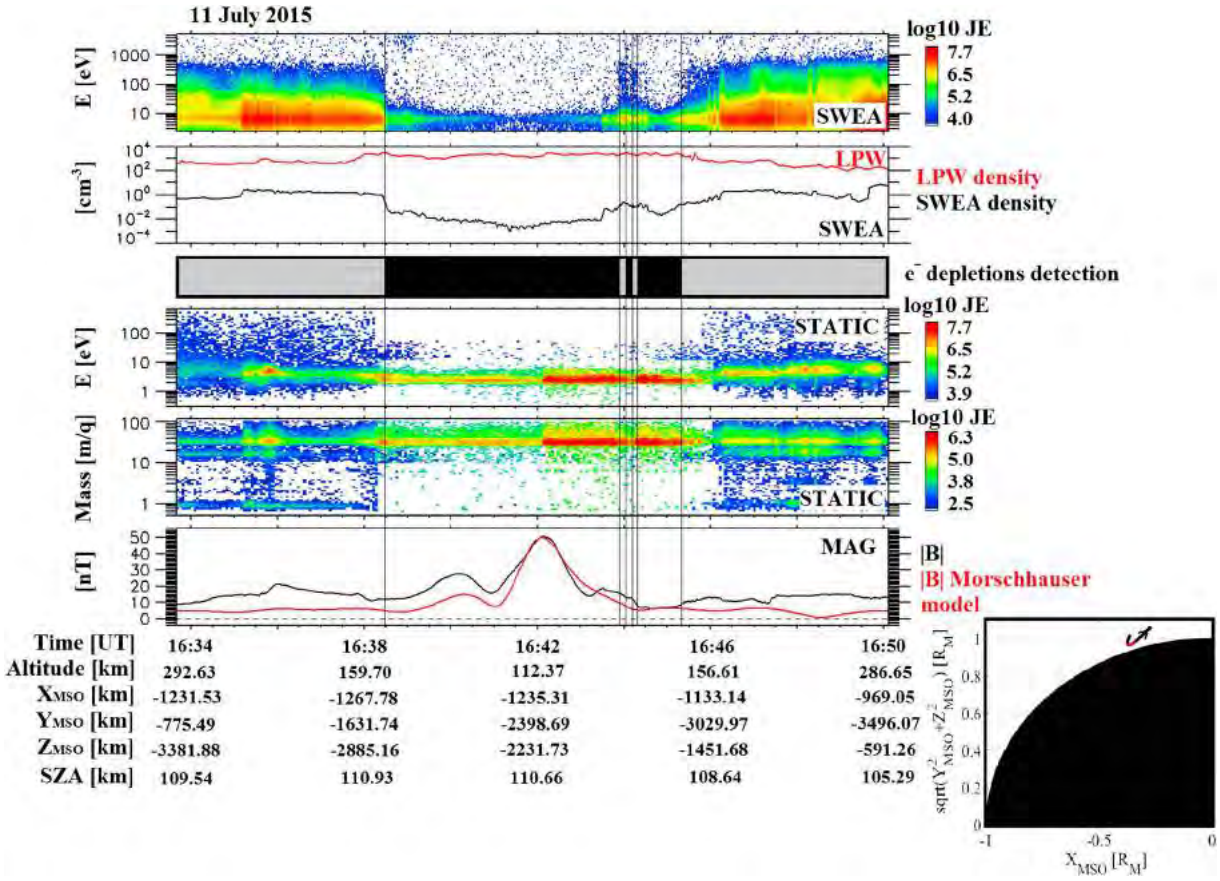

Figure 3. Example of electron depletion observed with MAVEN. (first panel) SWEA energy-time spectrogram of omnidirectional electron energy flux (ENGY mode) corrected for the potential measured with LPW. (second panel) Electron density calculated with SWEA (black) superimposed with the density calculated with LPW (red). (third panel) Detection of electron depletions by criterion (1) (black boxes). See section 3 for more details. The shadow corresponds to the nightside. (fourth panel) STATIC energy-time spectrogram of omnidirectional ion energy flux (C0 mode). (fifth panel) STATIC mass-time spectrogram of omnidirectional ion energy flux (C6 mode). (sixth panel) Magnetic field intensity (measured by MAG in black and calculated from the model of Morschhauser in red). (seventh panel, bottom right) MAVEN orbital trajectory in a cylindrically symmetric MSO coordinate frame. The locations of the electron depletions detected have been highlighted in red.

omnidirectional electron counts per second summed over all the available energies. Note that ELS's geometric factor is approximately fixed, so that counts are proportional to electron flux. The blacked out regions in the third panel delineate the electron depletions automatically detected by criterion (2), when the electron count drops abruptly by more than 2 orders of magnitude at all the considered energies and thus reaches the background noise level (~40 c/s). This criterion is described in more details in section 3.2. The fourth panel is the energy-time spectrogram of the omnidirectional heavy ions counts per second (m/q >20) measured by IMA. There are few light ions detected (not shown), but we can see that electron depletions are filled with heavy ions (mainly O_2^+ and CO_2^+ at this altitude in the nightside [*Krasnopolsky*, 2002]), having an energy E/q of a dozen of eV. Hence, we cannot name these structures plasma voids anymore but still "electron plasma voids." As there is no magnetometer on board MEX we plot on the fifth panel the magnitude of the crustal magnetic field calculated from the model of Morschhauser as a guide. As for the MGS case, the three electron depletions are located above a medium crustal magnetic area (35 nT at 500 km altitude). On the last bottom right plot, the orbital trajectory of MEX in a cylindrically symmetric MSO coordinate frame is plotted. The depletions are highlighted in red and are all located on the nightside.

2.3. MAVEN

The MAVEN spacecraft entered into orbit around Mars on 21 September 2014 [*Jakosky et al.*, 2015]. Its orbit is elliptical with an inclination of 74°, a periapsis altitude of 150 km (with four strategically located "deep-dip" campaigns during which the periapsis was lowered to 125 km), and an apoapsis altitude of 6200 km, which

Table 1. Summary of the Characteristics of the Magnetometer, Electron Spectrometer, Ion Spectrometer, and Langmuir Probe On Board MGS, MEX, and MAVEN

Instrument Type	Quantity	MGS	MEX	MAVEN
Magnetometer	Magnitude range	4–65,536 nT	None	0.06–65,536 nT
Electron spectrometer	Energy range	10–20,000 eV	1–20,000 eV	3–4,600 eV
	Energy resolution	25%	8%	17%
Ion spectrometer	Energy range	None	10–30,000 eV/q	0.1–30,000 eV/q
	Energy resolution		7%	16%
	Mass range		1, 2, 4, 8, 16, and >20 m/q	H^+, He^{++}, He^+, O^+, O_2^+, and CO_2^+
Langmuir probe	Temperature	None	None	0.05 to 5 eV

implies a period of 4.5 h. During the first year of the primary mission, the orbit precessed so that the periapsis and apoapsis points visited a wide range of longitudes, latitudes, SZAs, and local times.

The MAVEN particles and fields package is composed of seven instruments, including the Suprathermal and Thermal Ion Composition (STATIC) analyzer, the Solar Wind Electron Analyzer (SWEA), the Langmuir Probe and Waves (LPW), and the Magnetometer (MAG). STATIC operates over an energy range of 0.1 eV to 30 keV with an energy resolution of $\frac{\delta E}{E} = 16\%$ and a nominal time resolution of 4 s [*McFadden et al.*, 2015]. It is able to resolve H^+, He^{++}, He^+, O^+, O_2^+, and CO_2^+ ions. SWEA can measure the energy and angular distributions of 3–4600 eV electrons with an energy resolution of $\frac{\delta E}{E} = 17\%$ [*Mitchell et al.*, 2016]. LPW is designed to measure the temperature and density of thermal ionospheric electrons, which have temperatures (*Te*) ranging from 0.05 to 5 eV [*Andersson et al.*, 2015], as well as the spacecraft potential. MAG consists of two identical triaxial fluxgate sensors, which can measure the magnitude and direction of the ambient magnetic field from 0.06 to 65,536 nT [*Connerney et al.*, 2015]. All these characteristics are recorded in Table 1 so that they can be compared with those of MGS and MEX instruments.

Figure 3 shows an example of an electron depletion observed with MAVEN on 11 July 2015. The first panel is the SWEA energy-time spectrogram of omnidirectional electron energy flux (also referred to as JE in Figure 3). Similarly to the examples shown for MEX and MGS, the blacked out regions in the third panel delineate the electron depletions automatically detected by criterion (1), when the electron flux at all the considered energies drop abruptly by more than 2 orders of magnitude. This criterion is described in more details in section 3.1. However, we can see that there is a remaining electron population at approximately 6–7 eV, which could not be observed by MGS due to its energy range and by MEX probably due to higher negative spacecraft potential. Moreover, the third panel shows the density calculated from SWEA data in black and the density from LPW in red. Note that during this time interval the quality flag of the LPW density and of the spacecraft potential used for the calculation of the density from SWEA data is always greater than 50 except for 16:37:55 (in the ionosphere) and 16:45:20 (at the end of the depletion), which means that these data are reliable (L. Andersson, private communication). Due to instrumental limits the density calculated with SWEA data is restricted to electrons with energies greater than 3 eV (see Table 1), whereas the density calculated with LPW includes lower-energy electrons, which explains the difference observed between the two densities (in particular in the ionosphere where the plasma is essentially cold). The characteristic drop in the suprathermal electron flux is very clear in the SWEA density during the electron depletion, whereas there is no drop in LPW density, i.e., in thermal electron density, which even increases slightly.

On the fourth and fifth panels, the STATIC energy-time spectrogram of omnidirectional ion energy flux and the STATIC mass-time spectrogram of omnidirectional ion energy flux are plotted. Thus, the electron depletion is mainly filled with O_2^+ (32 m/q) at 3 eV. This is consistent with the expected ionosphere composition at this altitude and with the energy corresponding to the ram velocity given by the spacecraft to cold O_2^+. Hence, the depletions are not entirely void of plasma, as suggested in the MEX example. Only suprathermal electrons with energies greater than 10 eV are depleted, which justifies the name "suprathermal electron depletions" given by *Steckiewicz et al.* [2015].

The sixth panel shows the magnetic field intensity measured by MAG (black profile) superimposed with the intensity of the crustal magnetic field calculated from the model of Morschhauser (red profile). In this example, the depletions are observed above a moderate crustal magnetic source (50 nT at 125 km). As for MGS and

MEX, on the last bottom right plot, the orbital trajectory of MEX in a cylindrically symmetric MSO coordinate frame is plotted. The depletions are highlighted in red and are all located on the nightside.

3. Criteria Used to Automatically Detect Electron Depletions

Electron depletions can be observed by MGS, MEX, and MAVEN, respectively, on ER, ELS, and SWEA spectrograms. We present here the three criteria, adapted to each set of data, used to automatically detect electron depletions. The starting point of the definition of these criteria is the criterion developed in *Steckiewicz et al*. [2015] for the MAVEN/SWEA data. We thus first explain how this criterion is used for MAVEN before adapting it to MEX and MGS and their own specificities. The application of these three criteria leads to three catalogs of electron depletions used in the next sections to compare the electron depletion distributions as observed by the three spacecraft.

3.1. MAVEN

For MAVEN SWEA data we use the same criterion as in *Steckiewicz et al*. [2015] and given in equation (1). It is based on electron count rates (CR) from SWEA observations and relies on three energy channels ($E_1 = 4.26$ eV, $E_2 = 98.93$ eV, and $E_3 = 111.16$ eV). The numerator gives the count rate at an energy of E_i (per time step), whereas the denominator gives the mean count rate at the same energy over a 1 h period centered on the current time step. This simple criterion thus gives an idea of how the electron flux is at the current time step compared to average conditions. An electron depletion is detected if a ratio of 2 orders of magnitude is identified. These three channels have been chosen after looking at the electron spectrum inside the electron depletions. As seen in Figure 3, inside the electron depletions there is a remaining electron population peaked at 6 eV and hardly any electrons above 10 eV. Hence, we chose an energy channel below 6 eV, and two above to give more weight to depletions of high-energy electrons and to avoid a significant influence by the 6 eV electrons due to spacecraft charging. Usually, the spacecraft potential in the nightside ionosphere is approximately −2 V. This implies a little modification in the energies detected, which are reduced by the same amount. These small potentials have no significant impact on the criterion results. However, some strong spacecraft-charging events can bring the spacecraft potential to a dozen of volts. The electron flux detected at 6 eV during these events is then much lower than the mean electron flux calculated over 1 h, and an electron depletion can be detected. A few cases have been found during the time period under study and have been removed by hand. The sampling time step used for the criterion is the same as the measurement cadence of the SWEA instrument: 4 s. Consequently, the electron depletions detected last at least 4 s, which corresponds to a maximum of 16 km traveled by the spacecraft when at the periapsis.

$$\frac{1}{3}\sum_{i=1}^{3}\frac{\mathrm{CR}(E_i)}{<\mathrm{CR}(E_i), 1h>} < 0.01 \tag{1}$$

The criterion specified in equation (1) worked well for electron depletions in the Northern Hemisphere as shown in *Steckiewicz et al*. [2015]; it is thus also used here in the Southern Hemisphere. The example proposed in Figure 3 illustrates how the criterion detects the electron depletions in agreement with the SWEA spectrogram. Criterion (1) has been applied from 7 October 2014 to 25 November 2015 with no restriction on the nightside nor on the altitude, which corresponds to more than 2000 orbits.

During this time interval electron depletions have only been detected during two specific periods when the spacecraft reaches low altitudes (<900 km) in the nightside. Although MAVEN reached higher altitudes in the induced magnetosphere, criterion (1) detected no depletion above 900 km nor on the dayside. These two periods can be described in terms of aerographic coverage as the following:

1. from October 2014 to April 2015 during which the periapsis was above the Northern Hemisphere;
2. from May 2015 to November 2015 during which the periapsis was above the Southern Hemisphere.

Both of these time periods did not cover the equatorial region and not all local times due to orbital limitations. Over the next few years of the MAVEN mission, the spacecraft will have covered the entire surface of Mars, all local times, and solar zenith angles. The application of this criterion to the time interval under study

resulted in a data set of 1742 electron depletions identified above the Northern Hemisphere and 1956 ones identified above the Southern Hemisphere. We thus detected a lot of electron depletions per orbit. A median value of four depletions observed per orbit has been found. In terms of altitude distribution, the electron depletions detected are observed from 110 km up to 900 km altitude above the strongest crustal magnetic sources. The altitude distribution will be investigated in more details in section 5.

3.2. Mars Express

Based on our experience with MAVEN data, we adapted criterion (1) to MEX ELS data to obtain criterion (2). In this case we use the three following energy channels: $E_1 = 21.20$ eV (for low energies), $E_2 = 95.04$ eV, and $E_3 = 103.25$ eV (for high energies). Thus, by taking a minimum energy above 20 eV, we prevent most of the spacecraft-charging effects to impact results of criterion (2) (see *Fränz et al*. [2006] and *Hall et al*. [2016] for more details concerning spacecraft-charging impacts on ELS spectrograms). We also modify the threshold ratio from 1% to 2% based on the observations of ELS data. The time period under study for MEX data is from 1 March 2004 to 31 December 2014, which is similar to the one studied by *Hall et al*. [2016]. This corresponds to approximately 14,072 orbits. However, we only applied criterion (2) on time intervals longer than 1 h when ELS was working in the survey mode, which corresponds to 9983 time intervals. The time period under study is long enough to allow the periapsis to cover the whole surface of Mars between latitudes of −86° and +86° and all the local times in the nightside thanks to the precessing orbit of MEX. The sampling time step used for the criterion is the same as the measurement cadence of the ELS instrument when operated in its default survey mode: 4 s. Consequently, the electron depletions detected last at least 4 s, which corresponds to a maximum of 17 km in the spacecraft orbital direction when at periapsis.

$$\frac{1}{3}\sum_{i=1}^{3}\frac{\mathrm{CR}(E_i)}{<\mathrm{CR}(E_i), 1h>} < 0.02 \tag{2}$$

The application of this criterion with no restriction on the altitude nor on the nightside resulted in a time table of 17,592 electron depletions. The example proposed in Figure 2 illustrates how the criterion detects the electron depletions in agreement with the ELS spectrogram. Those depletions are detected from 245 km to ~10,000 km both on the nightside and on the dayside (for a small amount of cases). Globally, the depletions have been detected as in the MAVEN case during specific time periods when the periapsis went across the nightside at low enough altitudes. However, most of the depletions observed on the dayside and at altitudes above 1000 km have to be considered with caution (since they include very short data gaps and the lobes—the region located on either side of the plasma sheet with reduced particle fluxes—that cannot be easily excluded). We therefore chose to only consider for the next studies depletions observed in the nightside below 900 km, which is consistent with our MAVEN results and enables the two studies to be compared. With these restrictions, 14,517 depletions have been found on 2197 orbits, which implies a strong presence of spikes in MEX data as in the example in Figure 2. A median value of five depletions observed per orbit has been found.

3.3. Mars Global Surveyor

For the study of the electron depletions observed with MGS we only focus on the data obtained during the circular mapping orbit phase at an altitude of ~400 km. The data set covers the time period from 10 March 1999 to 11 October 2006, which represents more than 42,000 orbits. Such statistics average all the effects of external drivers on electron depletions so that we only see the general behavior of the electron depletions. As the MGS orbit was circular at 400 km, electron depletions can potentially be observed during each orbit. This data set covers the entire surface of Mars but only the 02:00 A.M. local time sector. ER data have a time resolution of 2 s, which corresponds to ~7 km traveled by the spacecraft.

In the case of MGS, a criterion based on three energy channels (one low and two high) does not work well, probably due to the energy resolution of 25%. Hence, we decided to compare the measured omnidirectional flux summed over all the available energies [11 eV; 16,127 eV] every 2 s with the same product averaged over two orbits (4 h). An electron depletion is detected if this ratio is less than 1%, which corresponds to a drop of 2

Table 2. Characteristics of the Electron Depletion Catalogs Derived From the Electron Spectrometer Data of MGS, MEX, and MAVEN

	MGS	MEX	MAVEN
Number of orbits under study[a]	42,048	9,983	2,138
Number of depletions detected[b]	116,278	14,517	3,698
Number of orbits containing depletions	29,460	2,197	899
Median number of depletions per orbit	4	5	4

[a]For MEX it corresponds to the number of time intervals longer than 1 h when ELS was in the survey mode. It corresponds approximately to the number or orbits studied.
[b]The number of depletions detected by criterion (3) for MGS, criterion (2) for MEX and criterion (1) for MAVEN.

orders of magnitude in the electron flux. The MGS criterion is described in equation (3) with a similar form to equations (1) and (2). Consequently, the electron depletion detected size is at least 7 km in the orbital direction.

Among the energy range [11 eV; 16,127 eV], the three channels which collected the majority of the flux were 90–148 eV, 148–245 eV, and 245–400 eV. Electron depletions thus show up in those three most reliable energy channels which are far too high energy to be affected by any spacecraft charging, which would almost always be less than ~20 eV. Hence, the way criterion (3) has been defined makes it insensitive to spacecraft charging.

$$\frac{\mathrm{Flux}(\,[11\ \mathrm{eV}; 16,127\ \mathrm{eV}]\,)}{<(\mathrm{Flux}(\,[11\ \mathrm{eV}; 16,127\ \mathrm{eV}])\,,\,4\ \ \mathrm{h})>} < 0.01 \tag{3}$$

The example proposed in Figure 1 illustrates how the criterion detects the electron depletions in agreement with the ER spectrogram. However, we can notice that all the decreases that can be observed in the second panel are not detected as electron depletions. This is due to the threshold of 1% chosen. The application of this criterion resulted in a time table of 116,278 electron depletions, which means that, as for MAVEN and MEX, several electron depletions can be detected during a single orbit as in the example shown in Figure 1. Almost all these electron depletions have been detected in the nightside, except few (less than 100) isolated cases. A median value of four depletions observed per orbit has been obtained, as it was found for MAVEN events (Table 2). The median number of depletions per orbit for MEX data is a slightly higher but remains similar to both MAVEN and MGS, which confirms that the occurrence of the electron depletions is stable during the three periods and consistent among the three spacecraft.

4. Geographical Distribution Maps of Electron Depletions

It was observed with MEX and MGS that the electron depletions mainly coincide with strong horizontal crustal fields. With MAVEN data *Steckiewicz et al.* [2015] showed that in the Northern Hemisphere the electron depletions are strongly linked with crustal magnetic field only above a transition region near 160–170 km altitude, whereas below this altitude, they are more homogeneously scattered irrespective of crustal source locations. Thanks to the three catalogs obtained after application of the three criteria described above, we created geographical distribution maps of electron depletions detected by MGS and MEX above all the Martian surface and by MAVEN, which now covers the Northern and Southern Hemispheres except the poles and the equatorial region. In the next three subsections we present the geographical distributions obtained with the three spacecraft whose periapsis decreased from MGS to MAVEN. We start with a mean altitude of 400 km with MGS, then go down to 300 km with MEX, and finally reach altitudes of 125 km with MAVEN.

4.1. MGS

Figure 4 shows the density map of the geographical location of the electron depletions detected with criterion (3). The latitude-longitude map of Mars is detailed in spatial bins of 1° by 1°. For each bin we scored the number of time steps when electron depletions are detected and divided it by the total number of time steps per bin with MGS on the nightside. There are on average more than 1000 time steps when MGS is in the nightside per bin. The color code corresponds to the percentage of electron depletions detected per MGS passage on the nightside. We have also superimposed logarithmically spaced (between 10 and 100 nT) contour lines of the horizontal crustal field calculated at 400 km altitude from the Morschhauser model.

We can see that, globally, the electron depletions are localized over some spots where the horizontal crustal field is at a local maximum. The contours of the majority of these regions with enhanced depletions occurrence are in good agreement with the extension of the strong crustal magnetic field sources. Hence, this

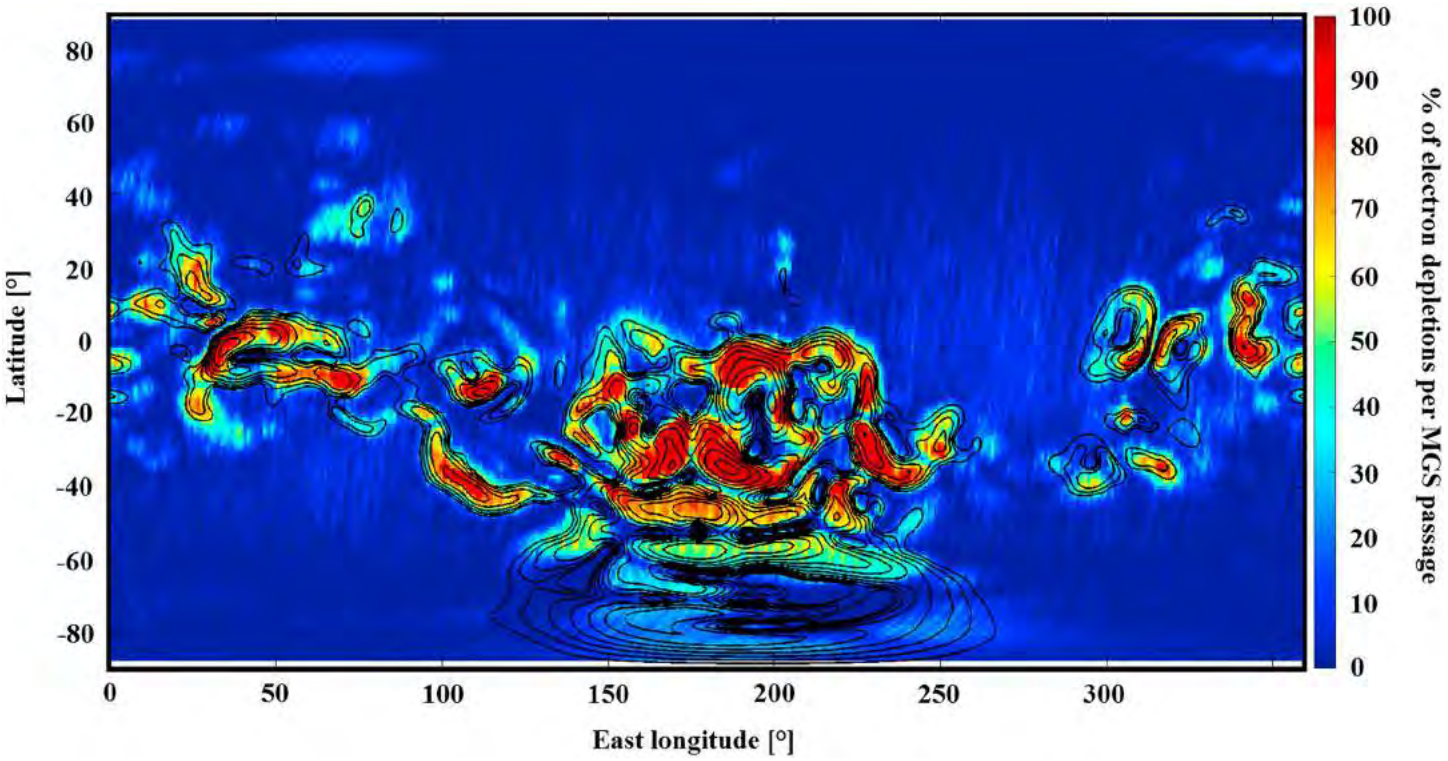

Figure 4. In color, the percentages of electron depletions detected with criterion (3) from MGS data per MGS passage on the nightside on a geographic map of the Martian surface with constant bin size of 1° by 1°. In black, the horizontal magnetic field contour lines calculated from the model of Morschhauser at an altitude of 400 km. The contour lines have been plotted for horizontal crustal fields of 10, 13, 16, 20, 25, 32, 40, 50, 63, 79, and 100 nT.

map confirms the strong link existing between electron depletions and horizontal crustal magnetic field at 400 km. However, we can see that some depletions are located over weak horizontal crustal magnetic field areas such as [340°E, 20°N] or are slightly shifted from the nearest crustal magnetic field source location such as [200°E, 20°N]. Such depletions away from crustal magnetic sources may indicate the presence of loops of closed magnetic field connecting together crustal magnetic field sources in widely separated locations [*Brain et al*., 2007]. We can also notice that the large area with high horizontal crustal magnetic field at high negative latitudes does not fit well with high electron depletion density area. This effect may be due to the inclination of Mars on its orbit, which is about 25°. This implies seasons during which part of the polar regions are always in sunlight, whereas they are considered as being in the nightside due to the use of the MSO coordinates. Thus, no depletions are detected, but these periods are taken into account as MGS passages in the nightside. We will be able to compare this effect with MEX results in the next section (MAVEN does not cover this region).

The presence of permanent (100% of electron depletions detected per MGS passage in the nightside) and intermittent electron depletions can also be observed, as first reported by *Lillis and Brain* [2013]. The permanent depletions seem to be coincident with the strongest horizontal crustal magnetic fields, whereas the intermittent ones are located over weaker crustal magnetic sources or on the border of the strongest ones.

4.2. Mars Express

Figure 5 shows the density map of the electron depletions evaluated with criterion (2). We chose to divide the surface of Mars into spatial bins of 2° by 2°, as there are less data points than for MGS (Table 2). The color code corresponds to the percentage of electron depletions per MEX passage. For each bin we calculated the ratio between the number of time steps when an electron depletion is detected and the total number of time steps when MEX is in the nightside with an altitude below 900 km. There are on average 500 MEX observation time steps per bin. We have also superimposed logarithmically spaced (between 10 and 100 nT) contour lines

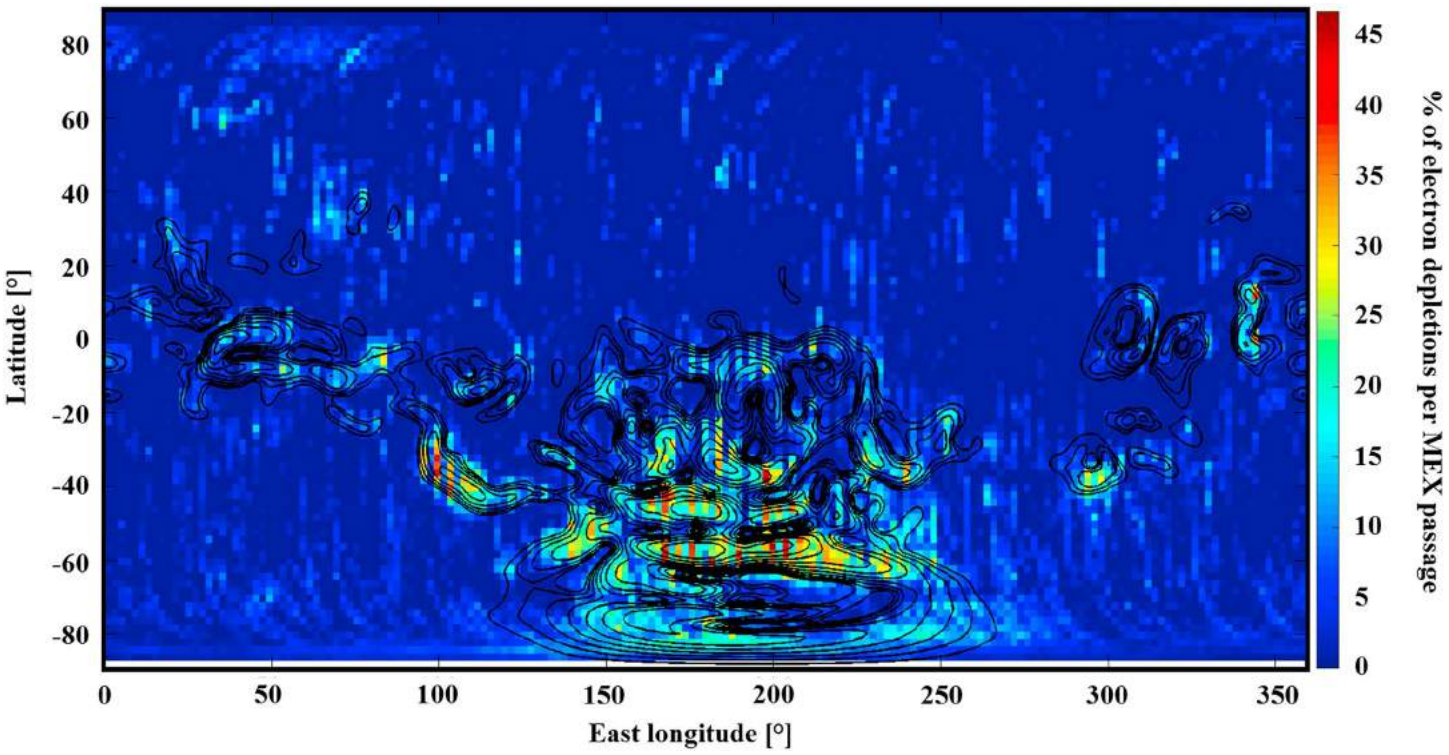

Figure 5. In color, the percentages of electron depletions detected with criterion (2) from MEX data per MEX passage on the nightside on a geographic map of the Martian surface with constant bin size of 2° by 2°. In black, the horizontal magnetic field contour lines calculated from the model of Morschhauser at an altitude of 400 km. The contour lines have been plotted for horizontal crustal fields of 10, 13, 16, 20, 25, 32, 40, 50, 63, 79, and 100 nT.

of the horizontal crustal magnetic field calculated at 400 km altitude from the Morschhauser model so that the maps of MEX and MGS can be compared.

As for MGS, we can see that the electron depletions are globally localized over regions of strong horizontal crustal magnetic field. This supports the idea that, above ~300 km, the main mechanism responsible for electron depletions is still the exclusion by closed crustal magnetic loops. Some electron depletions can still be found over areas without strong crustal magnetic field such as [40°E, 60°N]. However, we can see on this map that the areas with strong crustal fields located at high southern latitudes are now in a better agreement with the distribution of electron depletions. This difference with MGS may be due to the different ways MGS and MEX covered the Martian surface. MGS covered each latitude on the nightside on each orbit, whereas MEX periapsis only covers the southern pole during specific periods. Thus, depending on the seasons when these periods occurred, the percentages obtained in the southern pole region are modified.

The percentages found in Figure 5 are much lower than those found in Figure 4 with MGS and do not enable us to analyze the presence of permanent and intermittent depletions. However, these percentages seem quite similar to those found by *Hall et al.* [2016]. Using the depletions automatically detected thanks to their criterion, *Hall et al.* [2016] produced an occurrence map of the electron depletions observed with MEX during the same time period with a resolution of 15° by 15°, in order to emphasize large-scale occurrences. Their map highlights several areas where electron depletions are concentrated, which are consistent with the ones observed in Figure 5 like the regions centered on [300°E, −40°S] or [200°E, −60°S]. The two maps are comparable except for the regions centered on [200°E, −10°S], where *Hall et al.* [2016] found their maximum occurrence of depletions. We here found for this region a percentage of ~15 % with no real extension toward the Northern Hemisphere but rather toward the Southern Hemisphere where the maximum percentages are located, coincident with the strongest horizontal crustal magnetic fields. Figures 5 and 4 also reveal the presence of electron depletions in the region centered on [70°E, 80°N], where a small crustal magnetic source exists, but which is not observed by *Hall et al.* [2016], maybe due to the resolution chosen by the authors.

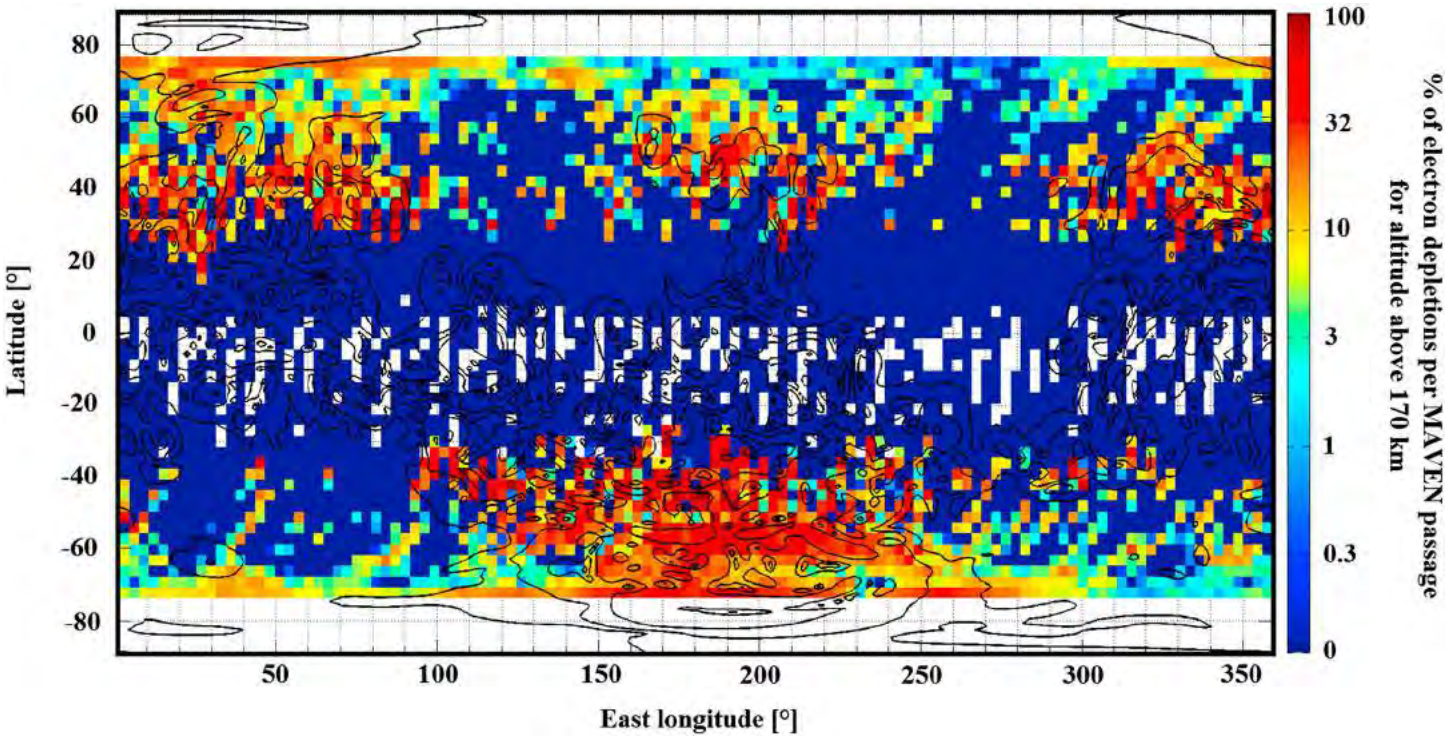

Figure 6. In color, the percentages of electron depletions detected above 170 km with criterion (1) from MAVEN data per MAVEN passage on the nightside on a geographic map of the Martian surface with constant bin size of 3° by 3°. In black, the horizontal magnetic field contour lines calculated from the model of Morschhauser at an altitude of 170 km. The contour lines have been plotted for horizontal crustal fields of 10, 32, 100, 316, and 1000 nT.

As was also mentioned by *Hall et al*. [2016], Figure 4 shows that the regions with strong concentration of electron depletions are surrounded by regions having moderate occurrence rate. Finally, the noise observed in Figure 5 has also been detected by *Hall et al*. [2016], who found a background level around 10% present all over their map. We here tend to limit this noise by selecting events on the nightside and at altitudes below 900 km.

4.3. MAVEN

While MGS was at an altitude of ~400 km and MEX has its lower periapsis at 245 km, MAVEN can reach altitudes down to 125 km during its deep-dip campaigns, which enables a more comprehensive view of the electron depletion phenomenon. Figures 6 and 7 show the density maps of electron depletions detected with MAVEN. In the same way as for the map of MGS and MEX, we calculated the number of time steps when electron depletions are detected in spatial bins of 3° longitude by 3° latitude and divided it by the number of time steps when MAVEN is in the nightside in each bin. Since *Steckiewicz et al*. [2015] showed that the electron depletion distribution was different for altitudes below and above 160–170 km in the Northern Hemisphere, we here provide two maps, the first for altitudes above 170 km and below 900 km (Figure 6) and the second for altitudes below 160 km (Figure 7). This choice enables us to emphasize the differences between the distributions of electron depletions at low and high altitudes. The density maps are superimposed with a map of the horizontal crustal field calculated at 170 km with the Morschhauser model. The contour lines are logarithmically spaced between 10 and 1000 nT. Larger bins of 3° by 3° have been chosen for MAVEN as there are less data than for MEX and MGS (Table 2). On average, there are 280 time steps per bin in Figure 6 and 90 in Figure 7.

In Figure 6, for events at altitudes greater than 170 km, we found the same behavior as for MEX and MGS: the depletions are aggregated on areas of strong horizontal crustal magnetic fields. The variability of the percentage of electron depletions per MAVEN passage seems to support the idea of permanent and intermittent electron depletions. Hence, percentages close to 100% are preferentially seen near the local maxima of

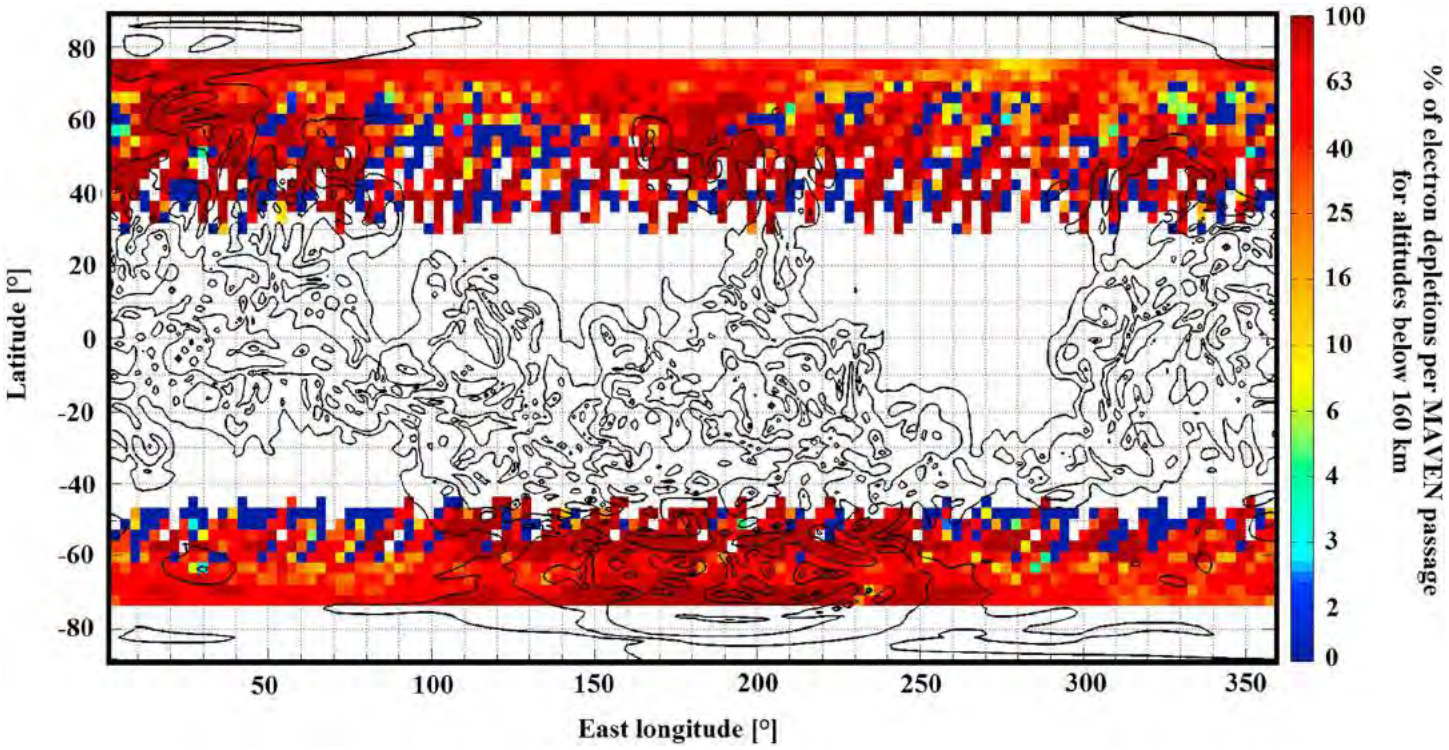

Figure 7. In color, the percentages of electron depletions detected below 160 km with criterion (1) from MAVEN data per MAVEN passage on the nightside on a geographic map of the Martian surface with constant bin size of 3° by 3°. In black, the horizontal magnetic field contour lines calculated from the model of Morschhauser at an altitude of 170 km. The contour lines have been plotted for horizontal crustal fields of 10, 32, 100, 316, and 1000 nT.

horizontal crustal fields, whereas lower percentages are observed far from crustal magnetic field sources, which means that electron depletions are not always present when MAVEN observes these regions. However, as the MAVEN coverage is still not complete, we cannot affirm that permanent depletions are surrounded by intermittent ones as it was observed on MGS distribution but we can see a trend emerge. In Figure 7, for events at altitudes lower than 160 km, we can see that the higher percentage of electron depletions are still localized above strong crustal magnetic field sources, but we can notice that the global distribution is far more homogeneous than for the distribution above 170 km, regardless of the horizontal magnetic field. Thus, closed crustal magnetic loops are still an important process responsible for electron depletions. However, there is also another important process which is involved and which does not depend a priori on crustal magnetic field, like electron absorption by atmospheric CO_2. The study of the Southern Hemisphere of Mars confirms the fact that the distribution of electron depletions is highly dependent on altitude.

5. Altitude Dependence of Electron Depletion Distribution

In *Steckiewicz et al*. [2015] we showed that the altitude distribution of electron depletions detected by MAVEN observations in the Northern Hemisphere was different above and below a transition region near 160–170 km altitude. There were far more chances to detect an electron depletion during a passage of MAVEN below this region than above. Here we complement this study with data from MAVEN above the Southern Hemisphere midlatitudes and data from MEX above both hemispheres. The time periods studied are, respectively, the same as for the previous section.

5.1. Description of the Method

Since the MAVEN data currently only cover latitudes northward of ~20° and southward of ~−20°, we only include MEX observations of the electron depletions detected in the same range of latitudes. We have also studied the Northern and the Southern Hemispheres separately. For both spacecraft we took an altitude

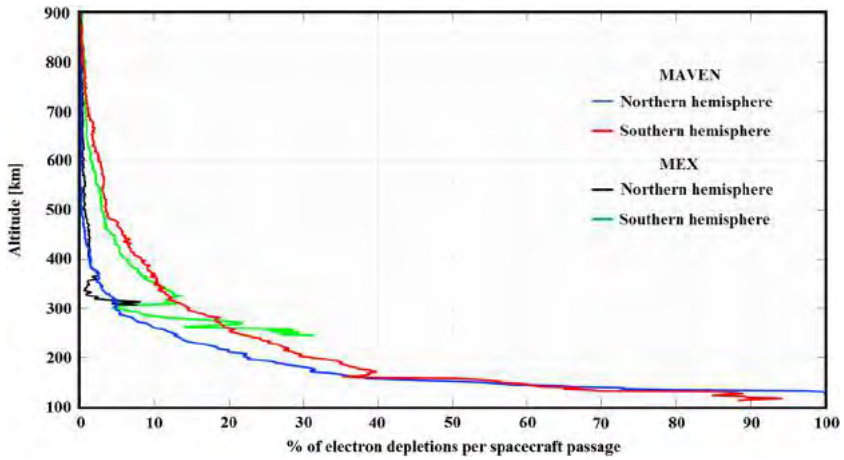

Figure 8. Percentages of electron depletions detected by criterion (1) among MAVEN passages (in blue and red) and by criterion (2) among MEX passages (in black and green) calculated in bins of 2 km altitude. The red and green lines correspond to the depletions observed in the Southern Hemisphere, and the red and black lines correspond to the depletions detected in the Northern Hemisphere.

resolution of 2 km, which represents ~10,000 MEX passages per bin and ~2600 MAVEN passages per bin on average. For each bin we calculated the number of time steps when electron depletions are detected and the number of time steps when the spacecraft is in the nightside. The ratio gives the percentage of electron depletions among the spacecraft passages in each altitude bin. The MGS observations previously discussed are not applicable to this analysis, since the spacecraft had a circular orbit with an almost constant altitude.

5.2. Results

Figure 8 shows the percentage of electron depletions detected along the MAVEN and MEX passages as a function of altitude. The red and green profiles correspond to the observations made by MAVEN and MEX, respectively, above the Southern Hemisphere, while the blue and black profiles correspond to the observations made by MAVEN and MEX, respectively, above the Northern Hemisphere. We can notice that MEX data are only available down to 307 km in the Northern Hemisphere, whereas they are available down to 245 km in the Southern Hemisphere. This difference is only due to MEX orbital geometry.

We can see that the MEX and MAVEN results match well between 900 and 300 km. In this range of altitude, both data sets show that there is far more chance to detect an electron depletion in the Southern Hemisphere than in the Northern Hemisphere. This phenomenon seems to be due to the presence in the Southern Hemisphere of stronger crustal magnetic sources than in the Northern Hemisphere. Hence, the closed crustal magnetic loops can extend higher in the Southern Hemisphere than in the Northern Hemisphere. Between 300 and 245 km, even though data are no more recorded by MEX in the Northern Hemisphere, there are still some in the Southern Hemisphere. Although strong variations can be observed on MEX data, we can see that the profile follows the trend set by MAVEN data. These variations may be due to the range of altitudes, which is beneath the nominal periapsis and hence sparsely covered by the spacecraft.

For altitudes greater than 500 km, *Hall et al*. [2016] found that the normalized occurrence of electron depletions was less than 5% across the majority of latitudes and altitudes, except for the strongest crustal magnetic field regions around which the majority of the events are distributed and where enhanced occurrence are then detected up to 1000 km. This is consistent with the results obtained in Figure 8 even if the percentages are lower than those found by *Hall et al*. [2016]: 1% in the Northern Hemisphere and 3% in the Southern Hemisphere at 500 km. Below 500 km, the occurrence of electron depletions increases rapidly in both studies. The main difference is that *Hall et al*. [2016] found that the distribution of electron depletions becomes more homogeneous below 500 km, even if the highest occurrences are still located above the strongest crustal magnetic field areas. In Figure 8 we clearly see that there are more electron depletions detected by MEX in the Southern Hemisphere than in the Northern Hemisphere, at least until 300 km. The difference between the two hemispheres even increases between 500 km and 300 km.

Where MEX ceases to record data, MAVEN continues to observe electron depletions at lower altitudes. We can see that the difference in percentage between the Southern and the Northern Hemispheres persists until a transition region near 160–170 km altitude, where the two curves join and stay close until 125 km. Hence, at low altitudes the electron depletion distribution does not depend on the hemisphere nor on the presence of crustal magnetic sources. This result reinforces the conclusions of *Steckiewicz et al*. [2015] about the presence of two processes responsible for electron depletions, each of them being predominant in a specific altitude regime. Depletion events above 160–170 km altitude are predominantly produced by the exclusion of suprathermal electrons by closed crustal magnetic fields, whereas events below 160–170 km are predominantly produced by absorption by atmospheric CO_2. The study of the Southern Hemisphere with MAVEN data also shows that the transition between the altitude regimes seems to be the same in both hemispheres, regardless the intensity of the crustal magnetic sources.

6. Conclusions

In this paper we have analyzed observations of electron depletions from three different Martian missions (MGS, MEX, and MAVEN) in order to better characterize their altitude and geographical distributions and understand their formation processes. We thus provide here the first multispacecraft analysis of electron depletions covering 17 years of Martian exploration, offering a comprehensive view of the phenomenon.

While previous studies used different approaches to identify electron depletions in MGS and MEX data, we here used the same method to automatically detect these events in the three Martian orbiter data sets. In addition, we did not impose any geometric restrictions in our conditional research—contrary to previous studies like the one of *Hall et al*. [2016], which was restricted to the illuminated induced magnetosphere.

Our results show that electron depletions are spread on the nightside of the Martian environment at altitudes between 110 and 900 km. For comparable altitude ranges (i.e., above about 250 km), the aerographic distributions of electron depletions for each mission produced result in agreement with each other and with previous studies: electron depletions are strongly linked with the horizontal crustal magnetic fields. The study of *Steckiewicz et al*. [2015] has been extended to the Southern Hemisphere of Mars at low altitudes and has confirmed this link with the crustal magnetic sources until a transition region near 160–170 km altitude regardless the hemisphere (and thus regardless of the intensity of the crustal magnetic sources). It was obviously not possible to identify this transition region with MGS and MEX due to their altitude limitations (~400 km for MGS and greater than 245 km for MEX). The comparison of the altitudinal distribution of the electron depletions detected in both hemispheres by MEX and MAVEN showed that above this transition region far more depletions are observed above the Southern Hemisphere, where the strongest crustal magnetic field sources are located. The crustal fields thus act as a barrier preventing the replenishing of the electron-depleted area (depleted due to the absence of solar EUV photoionization) by external incoming electrons. However, below the transition region at 160–170 km, the MAVEN data have revealed that the distribution is globally homogeneous in latitude-longitude and between both hemispheres. Thus, at low altitudes crustal magnetic fields are no longer predominant in the creation of electron depletions, further suggesting that the denser atmospheric CO_2 population is responsible for creating the depletions at those altitudes by absorption processes [*Steckiewicz et al*., 2015].

One original application of our study is using nightside suprathermal electron depletions as an indirect method of detecting crustal fields allowing the determination of the topology of the magnetic field using electron spectrometers [*Mitchell et al*., 2007; *Brain et al*., 2007]. Closed magnetic field lines are indeed associated with the Martian crustal magnetic fields and can be identified in the nightside by the presence of electron depletions notably at altitudes above approximately 170 km.

As studied by *Hall et al*. [2016], electron depletions can be observed to some extent in the terminator region. The processes creating electron depletions in regions illuminated or in shadow could be different. The electron depletion distributions obtained in the dawn and the dusk sector are also expected not to be the same since the photoelectrons—liberated on the dayside of Mars mainly from ionization of atmospheric CO_2 and O by solar photons—are travelling from the dayside to the nightside following the rotation of the planet. A delay is expected on the duskside for the electrons to be depleted. A study of the distribution of electron depletion with respect to local time and solar zenith angle will be made when the complete local time coverage will be achieved by MAVEN and reported in a future paper.

Acknowledgments
This work has been supported by the French Space Agency CNES for the part based on observations obtained with the SWEA instrument on MAVEN. The MAVEN project is supported by NASA through the Mars Exploration Program. The authors acknowledge the support of the MAVEN project and particularly of the instrument and science teams. Data analysis was performed with the AMDA science analysis system (http://amda.cdpp.eu) provided by the Centre de Données de la Physique des Plasmas CDPP supported by CNRS; CNES; Observatoire de Paris; and Université Paul Sabatier, Toulouse, France. The MGS, MEX, and MAVEN data used in this paper are publicly available through the Planetary Data System (http://ppi.pds.nasa.gov/). The authors sincerely thank the two anonymous reviewers for their constructive comments.

References

Acuña, M. H., et al. (2001), Magnetic field of Mars: Summary of results from the aerobraking and mapping orbits, *J. Geophys. Res.*, *106*, 23,403–23,417, doi:10.1029/2000JE001404.

Albee, A. L., R. E. Arvidson, F. Palluconi, and T. Thorpe (2001), Overview of the Mars Global Surveyor mission, *J. Geophys. Res.*, *106*, 23,291–23,316, doi:10.1029/2000JE001306.

Andersson, L., R. E. Ergun, G. T. Delory, A. I. Eriksson, J. Westfall, H. Reed, J. McCauly, D. Summers, and D. Meyers (2015), The Langmuir Probe and Waves instrument for MAVEN, *Space Sci. Rev.*, *195*, 173–198, doi:10.1007/s11214-015-0194-3.

Barabash, S., et al. (2004), ASPERA-3: Analyser of Space Plasmas and Energetic Ions for Mars Express, in *Mars Express: the Scientific Payload (ESA SP-1240)*, edited by A. Wilson and A. Chicarro, 121 pp., ESA, Noordwijk, Netherlands.

Bertucci, C., et al. (2003), Magnetic field draping enhancement at the Martian magnetic pileup boundary from Mars Global Surveyor observations, *Geophys. Res. Lett.*, *30*(2), 1099, doi:10.1029/2002GL015713.

Bougher, S., et al. (2015), Early MAVEN deep dip campaigns: First results and implications, *Sciences*, *350*(6261), doi:10.1126/science.aad0459.

Brain, D. A., F. Bagenal, M. H. Acuña, and J. E. P. Connerney (2003), Martian magnetic morphology: Contributions from the solar wind and crust, *J. Geophys. Res.*, *108*(A12), 1424, doi:10.1029/2002JA009482.

Brain, D. A., R. J. Lillis, D. L. Mitchell, J. S. Halekas, and R. P. Lin (2007), Electron pitch angle distributions as indicators of magnetic field topology near Mars, *J. Geophys. Res.*, *112*, A09201, doi:10.1029/2007JA012435.

Chicarro, A., P. Martin, and R. Trautner (2004), The Mars Express mission: An overview, Planetary Missions Division, Research & Scientific Support Department, ESA/ESTEC, PO box 299, 2200 AG Noordwijk, Netherlands.

Connerney, J. E. P., J. Espley, P. Lawton, S. Murphy, J. Odom, R. Oliverson, and D. Sheppard (2015), The MAVEN magnetic field investigation, *Space Sci. Rev.*, doi:10.1007/s11214-015-0169-4.

Duru, F., D. A. Gurnett, D. D. Morgan, J. D. Winningham, R. A. Frahm, and A. F. Nagy (2011), Nightside ionosphere of Mars studied with local electron densities: A general overview and electron density depressions, *J. Geophys. Res.*, *116*, A10316, doi:10.1029/2011JA016835.

Fillingim, M. O., L. M. PetiColas, R. J. Lillis, D. A. Brain, J. S. Halekas, D. Lummerzheim, and S. W. Bougher (2010), Localized ionization patches in the nighttime ionosphere of Mars and their electrodynamic consequences, *Icarus*, *206*, 112–119, doi:10.1016/j.icarus.2009.03.005.

Frahm, R. A., et al. (2006), Locations of atmospheric photoelectron energy peaks within the Mars environment, *Space Sci. Rev.*, *126*, 389–402, doi:10.1007/s11214-006-9119-5.

Fränz, M., E. Dubinin, E. Roussos, J. Woch, J. D. Winningham, R. Frahm, A. J. Coates, A. Fedorov, S. Barabash, and R. Lundin (2006), Plasma moments in the environment of Mars: Mars Express ASPERA-3 observations, *Space Sci. Rev.*, *126*, 165–207, doi:10.1007/s11214-006-9115-9.

Fränz, M., E. Dubinin, E. Nielsen, J. Woch, S. Barabash, R. Lundin, and A. Fedorov (2010), Transterminator ion flow in the Martian ionosphere, *Planet. Space Sci.*, *58*, 1442–1454, doi:10.1016/j.pss.2010.06.009.

Hall, B. E. S., M. Lester, J. D. Nichols, B. Sánchez-Cano, D. J. Andrews, H. J. Opgenoorth, and M. Fränz (2016), A survey of suprathermal electron flux depressions, or 'electron holes', within the illuminated Martian induced magnetosphere, *J. Geophys. Res. Space Physics*, *121*, 4835–4857, doi:10.1002/2015JA021866.

Jakosky, B. M., J. M. Grebowsky, J. G. Luhmann, and D. A. Brain (2015), Initial results from the MAVEN mission to Mars, *Geophys. Res. Lett.*, *42*, 8791–8802, doi:10.1002/2015GL065271.

Krasnopolsky, V. A. (2002), Mars' upper atmosphere and ionosphere at low, medium and high solar activities: Implications for evolution of water, *J. Geophys. Res.*, *107*(E12), 5128, doi:10.1029/2001JE001809.

Lillis, R. J., and D. A. Brain (2013), Nightside electron precipitation at Mars: Geographic variability and dependence on solar wind conditions, *J. Geophys. Res. Space Physics*, *118*, 3546–3556, doi:10.1002/jgra.50171.

Lillis, R. J., H. V. Frey, and M. Manga (2008), Rapid decrease in Martian crustal magnetization in the Noachian era: Implications for the dynamo and climate of early Mars, *Geophys. Res. Lett.*, *35*, L14203, doi:10.1029/2008GL034338.

Lillis, R. J., M. O. Fillingim, and D. A. Brain (2011), Three-dimensional structure of the Martian nightside ionosphere: Predicted rates of impact ionization from Mars Global Surveyor magnetometer and Electron Reflectometer measurements of precipitating electrons, *J. Geophys. Res.*, *116*, A12317, doi:10.1029/2011JA016982.

Lillis, R. J., S. Robbins, M. Manga, J. Halekas, and H. V. Frey (2013), Time history of the Martian dynamo from crater magnetic field analysis, *J. Geophys. Res. Planets*, *118*, 1488–1511, doi:10.1002/jgre.20105.

Ma, Y., X. Fang, C. T. Russell, A. F. Nagy, G. Toth, J. G. Luhmann, D. A. Brain, and C. Dong (2014), Effects of crustal field rotation on the solar wind plasma interaction with Mars, *Geophys. Res. Lett.*, *41*, 6563–6569, doi:10.1002/2014GL060785.

McFadden, J. P., et al. (2015), MAVEN Suprathermal and Thermal Ion Composition (STATIC) instrument, *Space Sci. Rev.*, *195*(1–4), 199–256, doi:10.1007/s11214-015-0175-6.

Mitchell, D. L., R. P. Lin, C. Mazelle, H. Rème, P. A. Cloutier, J. E. P. Connerney, M. H. Acuña, and N. F. Ness (2001), Probing Mars' crustal magnetic field and ionosphere with the MGS Electron Reflectometer, *J. Geophys. Res.*, *106*, 23,419–23,427, doi:10.1029/2000JE001435.

Mitchell, D. L., R. J. Lillis, R. P. Lin, J. E. P. Connerney, and M. H. Acuña (2007), A global map of Mars' crustal magnetic field based on elecron reflectometry, *J. Geophys. Res.*, *112*, E01002, doi:10.1029/2005JE002564.

Mitchell, D. L., et al. (2016), The MAVEN Solar Wind Electron Analyzer, *Space Sci. Rev.*, *200*, 495–528, doi:10.1007/s11214-015-0232-1.

Morschhauser, A., V. Lesur, and M. Grott (2014), A spherical harmonic model of the lithospheric magnetic field of Mars, *J. Geophys. Res. Planets*, *119*, 1162–1188, doi:10.1002/2013JE004555.

Nagy, A. F., et al. (2003), The plasma environment of Mars, *Space Sci. Rev.*, *111*, 33–114, doi:10.1023/B:SPAC.0000032718.47512.92.

Němec, F., D. D. Morgan, D. A. Gurnett, and F. Duru (2010), Nightside ionosphere of Mars: Radar soundings by the Mars Express spacecraft, *J. Geophys. Res.*, *115*, E12009, doi:10.1029/2010JE003663.

Soobiah, Y., et al. (2006), Observations of magnetic anomaly signatures in Mars Express ASPERA-3 ELS data, *Icarus*, *182*, 396–405, doi:10.1016/j.icarus.2005.10.034.

Steckiewicz, M., et al. (2015), Altitude dependence of nightside Martian suprathermal electron depletions as revealed by MAVEN observations, *Geophys. Res. Lett.*, *42*, 8877–8884, doi:10.1002/2015GL065257.

Ulusen, D., and I. R. Linscott (2008), Low-energy electron current in the Martian tail due to reconnection of draped interplanetary magnetic field and crustal magnetic fields, *J. Geophys. Res.*, *113*, E06001, doi:10.1029/2007JE002916.

Withers, P., M. O. Fillingim, R. J. Lillis, B. Häusler, D. P. Hinson, G. L. Tyler, M. Pätzold, K. Peter, S. Tellmann, and O. Witasse (2012), Observations of the nightside ionosphere of Mars by the Mars Express Radio Science Experiment (MaRS), *J. Geophys. Res.*, *117*, A12307, doi:10.1029/2012JA018185.

Zhang, M. H. G., J. G. Luhmann, and A. J. Kliore (1990), An observational study of the nightside ionospheres of Mars and Venus with radio occultation methods, *J. Geophys. Res.*, *95*, 17,095–17,17102, doi:10.1029/JA095iA10p17095.

PLANETARY SCIENCE

Early MAVEN Deep Dip campaign reveals thermosphere and ionosphere variability

S. Bougher,[1*] B. Jakosky,[2] J. Halekas,[3] J. Grebowsky,[4] J. Luhmann,[5] P. Mahaffy,[4] J. Connerney,[4] F. Eparvier,[2] R. Ergun,[2] D. Larson,[5] J. McFadden,[5] D. Mitchell,[5] N. Schneider,[2] R. Zurek,[6] C. Mazelle,[7,8] L. Andersson,[2] D. Andrews,[9] D. Baird,[10] D. N. Baker,[2] J. M. Bell,[11] M. Benna,[4] D. Brain,[2] M. Chaffin,[2] P. Chamberlin,[4] J.-Y. Chaufray,[12] J. Clarke,[13] G. Collinson,[4] M. Combi,[1] F. Crary,[2] T. Cravens,[14] M. Crismani,[2] S. Curry,[5] D. Curtis,[5] J. Deighan,[2] G. Delory,[5] R. Dewey,[2] G. DiBraccio,[4] C. Dong,[1] Y. Dong,[2] P. Dunn,[5] M. Elrod,[4] S. England,[5] A. Eriksson,[9] J. Espley,[4] S. Evans,[15] X. Fang,[2] M. Fillingim,[5] K. Fortier,[2] C. M. Fowler,[2] J. Fox,[16] H. Gröller,[17] S. Guzewich,[4] T. Hara,[5] Y. Harada,[5] G. Holsclaw,[2] S. K. Jain,[2] R. Jolitz,[5] F. Leblanc,[12] C. O. Lee,[5] Y. Lee,[1] F. Lefevre,[12] R. Lillis,[5] R. Livi,[5] D. Lo,[17] Y. Ma,[18] M. Mayyasi,[13] W. McClintock,[2] T. McEnulty,[2] R. Modolo,[12] F. Montmessin,[12] M. Morooka,[2] A. Nagy,[1] K. Olsen,[1] W. Peterson,[2] A. Rahmati,[14] S. Ruhunusiri,[3] C. T. Russell,[18] S. Sakai,[14] J.-A. Sauvaud,[7,8] K. Seki,[19] M. Steckiewicz,[7,8] M. Stevens,[20] A. I. F. Stewart,[2] A. Stiepen,[2] S. Stone,[17] V. Tenishev,[1] E. Thiemann,[2] R. Tolson,[11] D. Toublanc,[7,8] M. Vogt,[13] T. Weber,[2] P. Withers,[13] T. Woods,[2] R. Yelle[17]

The Mars Atmosphere and Volatile Evolution (MAVEN) mission, during the second of its Deep Dip campaigns, made comprehensive measurements of martian thermosphere and ionosphere composition, structure, and variability at altitudes down to ~130 kilometers in the subsolar region. This altitude range contains the diffusively separated upper atmosphere just above the well-mixed atmosphere, the layer of peak extreme ultraviolet heating and primary reservoir for atmospheric escape. In situ measurements of the upper atmosphere reveal previously unmeasured populations of neutral and charged particles, the homopause altitude at approximately 130 kilometers, and an unexpected level of variability both on an orbit-to-orbit basis and within individual orbits. These observations help constrain volatile escape processes controlled by thermosphere and ionosphere structure and variability.

The Mars upper atmosphere—the top ~100 to 500 km encompassing the thermosphere, ionosphere, and lower portion of the exosphere—constitutes the reservoir that regulates present-day escape processes from the planet. Understanding the coupling of the lower to upper atmosphere is essential to characterizing energy deposition and upward flow of material that can ultimately result in neutral and ion escape from the planet (*1*). In principle, it is possible to constrain the short-term (current) atmospheric escape rates making use of the Mars Atmosphere and Volatile Evolution (MAVEN) measurements over this reservoir region and at higher altitudes. However, without knowledge of the physics and chemistry operating in this reservoir region and driving its variations (such as solar cycle, seasonal, and diurnal), it is not possible to reliably extrapolate the results over evolutionary history. The characterization of this upper atmosphere reservoir is therefore one of the major science objectives of the MAVEN mission (*2*).

Here, we present measurements of subsolar neutral atmospheric composition and temperature, together with ionospheric charged-particle and magnetic-field structure, extending from near the homopause to above the exobase, as enabled by MAVEN's "Deep Dip" campaigns. During each week-long campaign, periapsis is lowered from a nominal altitude of ~150 to 170 km to ~120 to 135 km in order to reach a peak mass density of ~2 to 3.5 kg/km^3. This strategy allows direct in situ sampling of the entire reservoir region for atmospheric escape, from the exosphere downward to near the homopause (*3*). During each orbit, MAVEN makes in situ measurements along the elliptical orbit track of neutral and thermal ion species, thermal electrons, magnetic fields, and suprathermal electrons and ions, using a suite of science instruments (*4*). Periapsis migrates around the planet during the course of the mission, providing comprehensive coverage of latitude and local time, and deep dips are dispersed in time in order to sample different regions of interest (*5*). We focused on the second campaign (DD2), spanning 17 to 22 April 2015, which provided sampling near the subsolar region (local time = 12 to 13), late in the martian year (L_S ~ 327 to 330), and near the equator (*6*). Measurements of the subsolar region are important for constraining neutral-ion chemistry and dynamics in numerical simulations that estimate both neutral and ion escape rates. In addition, thermosphere-ionosphere structure and neutral temperatures are believed to be controlled in part by the changing solar extreme ultraviolet–ultraviolet (EUV-UV) fluxes; this forcing is greatest at low solar zenith angles (SZAs).

We present two sequential DD2 orbits (O1085 and O1086, on 22 April 2015), the first focusing on charged-particle and field measurements and the second on neutral composition and temperatures (Fig. 1). The thermal ion and neutral measurements were made with NGIMS on alternating orbits, necessitating the emphasis on two sequential orbit passes. Both of these orbits had periapses in a region with moderate crustal magnetic fields and occurred during nominal upstream solar wind conditions. We also examined the full suite of DD2 orbits for orbit-to-orbit neutral density and temperature variability.

Neutral composition and temperature observations

The martian upper atmosphere between the exosphere and the homopause encompasses the region of changing importance of heterogeneous (diffusive separation) and homogeneous (small-scale mixing) processes that control the density structure, the location of the peak solar EUV energy deposition, and the main reservoir for escaping particles (*1*). During nominal orbits, MAVEN does not reach the well-mixed atmosphere, but during the Deep Dip campaigns, MAVEN instruments can sample the column extending from near the homopause upward into the exosphere, where neutral and ion escape can occur.

During the DD2 campaign, MAVEN successfully made measurements of the structure and variability of this critical altitude range in the subsolar region. Previously, the thermospheric neutral composition had only been directly measured in situ with the Upper Atmosphere Mass Spectrometer (UAMS) instruments onboard the descending Viking Landers 1 and 2 (*7*). These two descent profiles provided measurements for

[1]CLaSP Department, University of Michigan, Ann Arbor, MI, USA. [2]Laboratory for Atmospheric and Space Physics, University. of Colorado, Boulder, CO, USA. [3]Department of Physics and Astronomy, University of Iowa, Iowa City, IA, USA. [4]NASA/Goddard Space Flight Center, Greenbelt, MD, USA. [5]Space Sciences Laboratory, University of California at Berkeley, Berkeley, CA, USA. [6]Jet Propulsion Laboratory, California Institute of Technology, Pasadena, CA, USA. [7]CNRS/Institut de Recherche en Astrophysique et Planétologie, Toulouse, France. [8]University Paul Sabatier, Toulouse, France. [9]Swedish Institute of Space Physics, Kiruna, Sweden. [10]NASA/Johnson Space Center, Houston, TX, USA. [11]National Institute of Aerospace, Hampton, VA, USA. [12]Laboratoire Atmosphères, Milieux, Observations Spatiales /CNRS, Verrieres-le-Buisson, France. [13]Department of Astronomy, Boston University, Boston, MA, USA. [14]Department of Physics and Astronomy, University of Kansas, Lawrence, KS, USA. [15]Computational Physics, Springfield, VA, USA. [16]Department of Physics, Wright State University, Fairborn, OH, USA. [17]Lunar and Planetary Laboratory, University of Arizona, Tucson, AZ, USA. [18]Institute of Geophysics and Planetary Physics, University of California, Los Angeles, Los Angeles, CA, USA. [19]Solar-Terrestrial Environment Laboratory, Nagoya University, Nagoya, Aichi, Japan. [20]Naval Research Laboratory, Washington, DC, USA.
*Corresponding author. E-mail: bougher@umich.edu

SZA near 44° at low-to-middle latitude for two afternoon locations during solar minimum and near aphelion conditions. The total mass density of the Mars thermosphere has also been measured by several spacecraft accelerometers (*5*, *8*, *9*).

The MAVEN NGIMS instrument measures the neutral composition of the major gas species (such as He, N, O, CO, N_2, O_2, NO, Ar, and CO_2) and their major isotopes, with a vertical resolution of ~5 km for targeted species and a target accuracy of <25% for most of these species (*10*). Corresponding temperatures can be derived from the neutral-scale heights. These multispecies measurements are obtained along an orbit trajectory that combines both vertical and horizontal variations of the upper atmosphere structure (*1*). These convolved variations cannot be separated without the use of numerical models.

Four key neutral species are presented (CO_2, Ar, N_2, and O) for the inbound leg (Fig. 2). The NGIMS and Mars Global Ionosphere-Thermosphere Model (M-GITM)–simulated CO_2, N_2, and Ar density profiles match reasonably well throughout the altitude range (supplementary text S1) (*9*). For example, in the range of 160 to 220 km, M-GITM diurnal variations of CO_2 encompass NGIMS densities quite well, whereas below 160 km, M-GITM underestimates NGIMS CO_2 densities (up to a factor of ~2 at 130 km). Both models and observations show an exponential variation of density with altitude. The scale heights of these species are different at higher altitudes, with most of them (CO_2, Ar, and N_2) showing a common scale height as 130 km is approached. This is consistent with a homopause near 130 km, but quantitative confirmation of the precise homopause altitude cannot be seen in this figure. Atomic O scale heights do not follow this pattern of transitioning scale heights because local chemical production and loss processes are important (*3*). These multispecies, subsolar, neutral-atmosphere measurements capture near-homopause (~130 km) to exosphere (above ~200 km) structure together on the same orbit.

The atomic O density profiles from NGIMS (Fig. 2) constrain the ion-neutral chemistry, thermal heat budget, and dynamics of the Mars dayside upper atmosphere (*1*). NGIMS-measured O densities have been corrected for (i) open-source neutral beaming (OSNB) retrieval, (ii) contributions from CO_2 at lower altitudes, and (iii) "pile up" RAM direction enhancement of densities when approaching periapsis altitudes, with largest corrections present for the higher densities during Deep Dip orbits. Atomic O densities are determined to be reliable (within the ~25% error) down to ~150 km. Comparison of measured and simulated DD2 atomic O profiles shows reasonable agreement at all altitudes, with densities at ~200 km close to ~5.0×10^7 to 6.0×10^7 cm^{-3}. These NGIMS-measured O densities are nearly a factor of ~5 larger than corresponding Mars Express (MEx)/Spectroscopy for Investigation of Characteristics of the Atmosphere of Mars (SPICAM) estimates derived via remote sensing (*11*). The differences in the seasonal (equinox versus aphelion) and solar cycle (solar moderate versus minimum)

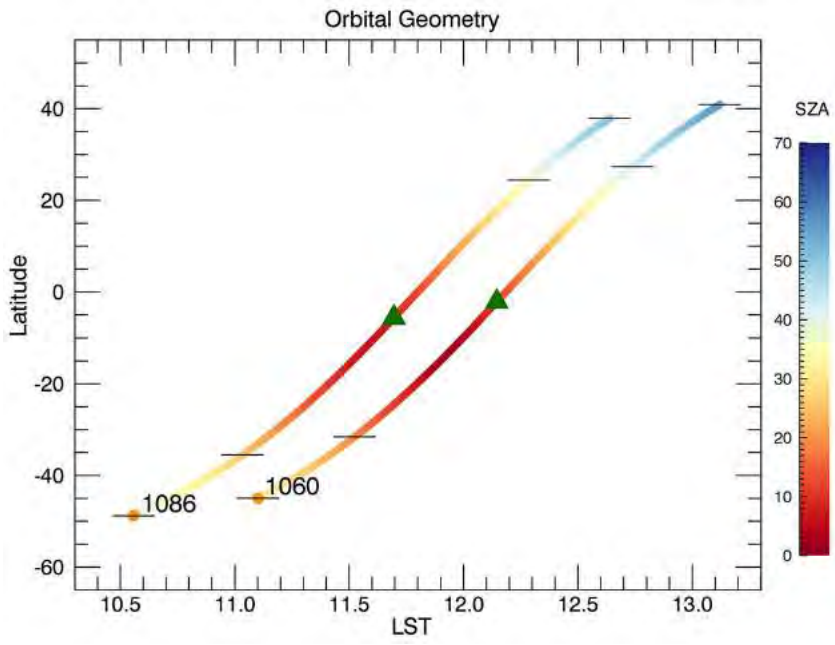

Fig. 1. MAVEN Deep Dip 2 orbital geometry. MAVEN spacecraft "along-track" latitude versus local time coverage of DD2 sampling below 500 km is illustrated (NGIMS measurements are limited to this altitude range). Beginning (O1060) and ending (O1086) orbit information is provided, capturing both inbound and outbound legs, plus the periapsis location (triangles). The 500 and 300 km points on each leg are also delineated by black tick marks. The start of each inbound leg is identified (yellow dots). Specific orbits selected for detailed investigation (O1085 and O1086) fall in between these bounding orbits. SZA is also indicated along these orbit trajectories.

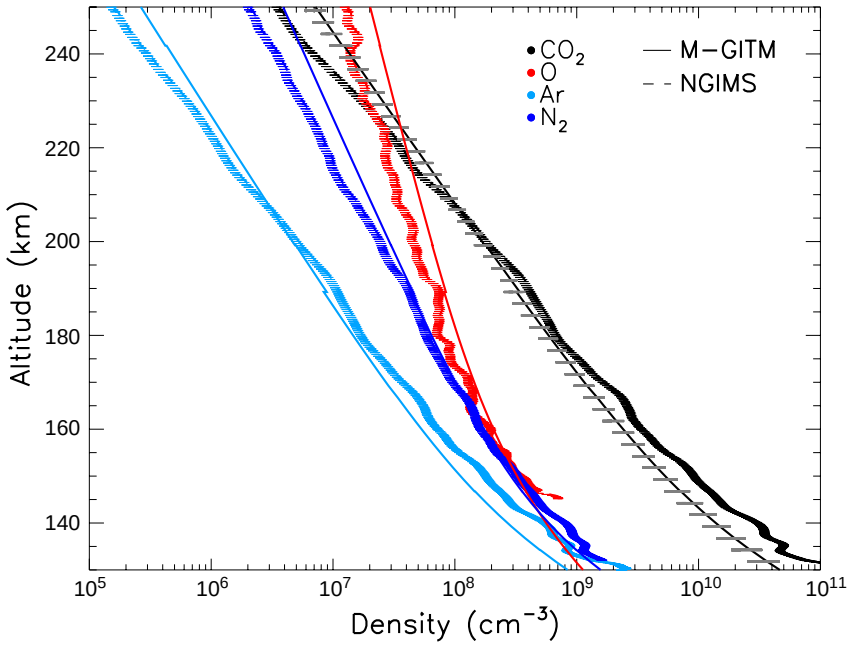

Fig. 2. Neutral density environment near periapsis during the subsolar DD2 campaign. These altitude profiles are provided over ~130 to 250 km specifically for a single orbit (O1086) from 22 April 2015 (supplementary text S2). Four key neutral species are plotted (CO_2, Ar, N_2, and O) for the inbound leg (hashed curves). Simulated subsolar density profiles from the M-GITM, calculated at the location of the spacecraft along its orbit for the solar moderate case (Equinox), are overplotted (solid curves) for comparison (supplementary text S1). The plotted NGIMS densities have been processed by using a 20-s polynomial time-averaging technique so as to remove high-frequency, small-scale variations (supplementary text S3). Calculated NGIMS error bars are included in each profile (supplementary text S4). In addition, 1-[σ] variance bars are added to the 1-SOL averaged M-GITM CO_2 densities in order to illustrate their expected diurnal variation.

sampling between these two data sets may be responsible for this factor of ~5 variation. This substantial variation in atomic O densities at 200 km may have important implications for mass loading of the solar wind because thermospheric and exospheric O densities are simulated to respond similarly to solar cycle and seasonal changes (*12*).

The O/CO_2 ratio is expected to vary with the changing solar EUV-UV fluxes reaching Mars (affecting CO_2 photolysis rates) and the ability of the thermospheric circulation to transport atomic O around the planet (*1*). A data-model comparison shows that the altitude at which this ratio is unity occurs around ~225 km for both NGIMS and M-GITM profiles near the subsolar region (Fig. 3A). This profile determines that the O abundance becomes important above 225 km in the Mars exosphere. This cold O constraint is important for making proper calculations of hot O escape (*1*). Similarly, this O/CO_2 ratio near 150 km (about ~20 km above the expected primary ion peak) is measured to be ~4.0% and is consistent with the NGIMS-measured O_2^+/CO_2^+ ratio of ~6.0 at the same altitude. This occurs because this ion ratio is directly controlled by the atomic O abundance (*13*).

As the measured N_2 and CO_2 profiles approach ~130 km, the N_2/CO_2 ratio converges on the bulk atmosphere value of ~2.0% (Fig. 3B), recently measured by the Mars Science Laboratory (MSL) Sample Analysis at Mars Suite (SAMS) instrument (*14*). The decrease of the ratio with decreasing height is expected because the N_2 scale height is larger than that for CO_2. The convergence of this NGIMS N_2/CO_2 ratio to the constant value of ~2.0% near 130 km indicates that the N_2 homopause altitude during this orbit is located at ~130 km. In fact, all species are subject to the same small-scale mixing, but each has a slightly different homopause altitude owing to small variations in molecular diffusion coefficients (*3*). By this same method, the simulated M-GITM N_2/CO_2 ratio places the N_2 homopause at ~120 km altitude. The difference between these two homopause altitudes implies that some refinement of the small-scale mixing (eddy diffusion) is needed in the M-GITM code (supplementary text S1) (*9*). This model adjustment is expected because the homopause altitude is very sensitive to small-scale mixing, which is itself poorly constrained other than by these new MAVEN measurements. In addition, M-GITM assumes the Viking mixed-atmosphere value of the N_2/CO_2 ratio (~2.7%) (*7*), which is larger than measured by SAMS (*14*). These NGIMS density profiles provide an important initial determination of the dayside homopause altitude, which was previously estimated from Viking modeling studies to be located between ~120 and 130 km (*7*).

Derived NGIMS and simulated M-GITM average temperature profiles (over the entire DD2 campaign) each include averaging over longitude and various wave features (Fig. 4). These averaged NGIMS temperature profiles are constructed by using the Snowden method with hydrostatic integration over the DD2 averaged Ar and N_2 density profiles (*15*). Such averaging serves to smooth out much of the wave structure and determines that the upper-boundary temperature gradients should be close to zero (isothermal).

For M-GITM, simulated temperatures are extracted along each orbit trajectory and subsequently averaged together over all DD2 orbits. The

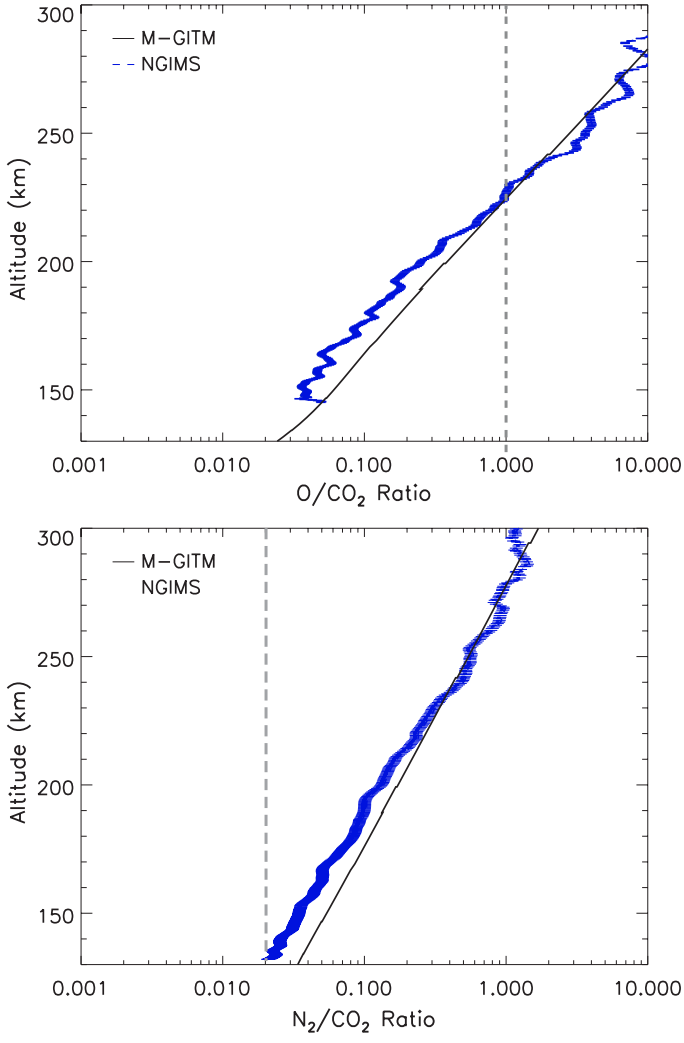

Fig. 3. Altitude plots illustrating key neutral density ratios below 300 km for DD2. These ratios (**Top**) O/CO_2 and (**Bottom**) N_2/CO_2 are composed of the same O1086 NGIMS and M-GITM density profiles illustrated in Fig. 2. The $O/CO_2 = 1$ crossover point near ~225 km (for both NGIMS and M-GITM) is indicated with a vertical dashed line. The measured N_2/CO_2 MSL mixed-atmosphere value of ~2.0% is also indicated with a vertical dashed line (*14*).

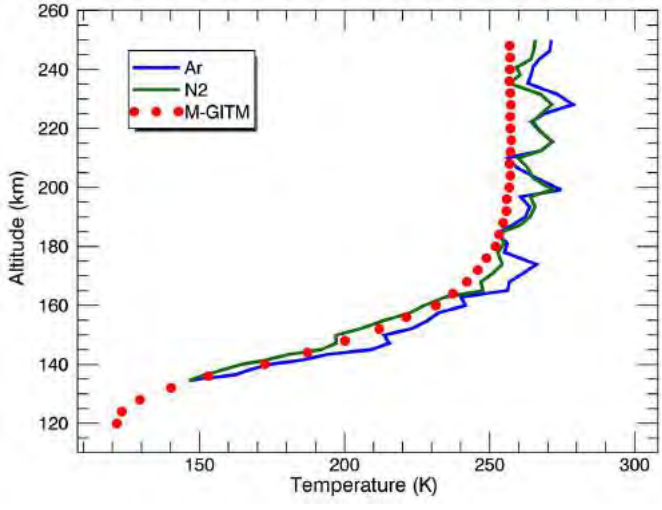

Fig. 4. Profiles of averaged temperature profiles from the entire DD2 campaign. Both NGIMS derived (N_2 and Ar) and M-GITM–simulated temperature profiles are plotted up to 250 km. Mean exospheric temperatures (200 to 250 km) approach ~268 K (NGIMS) and ~257 K (M-GITM).

observed large vertical temperature gradient over ~140 to 170 km coincides with the peak layer of EUV heating, whereas the topside temperatures approach isothermal values above ~200 km. In particular, exospheric temperatures (T_{exo}) are separately extracted from Ar densities by averaging temperatures over ~200 to 250 km for each orbit, then averaging all orbit values together. CO_2 and N_2 densities could also be used, yielding similar temperatures (*16*). The resulting NGIMS extracted mean T_{exo} value of ~268 K is compared with the simulated mean value of ~257 K from M-GITM.

This MAVEN dayside temperature profile is the result of averaging over several DD2 orbits and consequently masks the significant orbit-to-orbit (1σ) variability of NGIMS exospheric temperatures (268 ± 19 K) (*16*). This temporal behavior is similar to that observed from MEx dayside measurements (~270 ± 25 K) extracted from SPICAM dayglow scale heights over 2004–2009 (*17*, *18*). Furthermore, M-GITM simulations (primarily solar-driven) cannot capture this orbit-to-orbit variability, yet M-GITM simulations can reasonably match the DD2 orbit mean T_{exo} value. This large orbit-to-orbit variability implies that dayside thermospheric temperatures are not controlled exclusively by solar EUV forcing, as models might predict (*17*, *18*).

Repeated MAVEN sampling at the 200-km level provides another method for characterization of upper-atmosphere variability near the base of the exosphere. NGIMS neutral densities show a substantial orbit-to-orbit variability throughout the DD2 campaign. Altitude profiles of O and CO_2 densities spanning 14 orbits from O1060 to O1086 show substantial variability on ~4- to 5-hour time scales (Fig. 5). The altitude at which the O/CO_2 ratio crosses through unity varies from ~225 to 238 km for these orbits. The O and CO_2 variations at a constant altitude are also substantial, with measured O densities at 200 km ranging from ~5.0×10^7 to ~1.0×10^8 cm^{-3} (factor of 2), whereas CO_2 densities vary from ~1.3×10^8 to ~3.5×10^8 cm^{-3} (factor of 2.7). These density variations are notable, especially when combined with exospheric temperature variations described above. The implication is that upper-atmosphere structure near 200 km varies substantially from orbit to orbit (on at least ~5-hour time scales), and also as a function of season and solar cycle as illustrated by MEx versus MAVEN results. Orbit-to-orbit variability may be driven from below owing to gravity wave interactions with the global wind structure and small-scale mixing processes (*19*, *20*). This combined density and temperature variability at this exobase altitude (*21*) ultimately has a direct impact upon volatile escape rates (*1*).

Charged-particle and magnetic-field observations

Plasma measurements extending from the magnetosphere down to the main peak of the subsolar martian ionosphere have been collected by MAVEN. MGS and MEx previously explored the induced magnetosphere and the transition to the upper ionosphere (*22*, *23*), but neither mission carried a complete complement of plasma instrumentation. Meanwhile, characterization of the lower-altitude collisional ionosphere has primarily used remote sounding techniques (*24*, *25*), revealing variable structure (*26*) and only occasionally a Venus-like ionopause (*27*). Viking provided the only previous direct measurements of lower ionospheric structure and composition (*13*), but only in a narrow range of SZA.

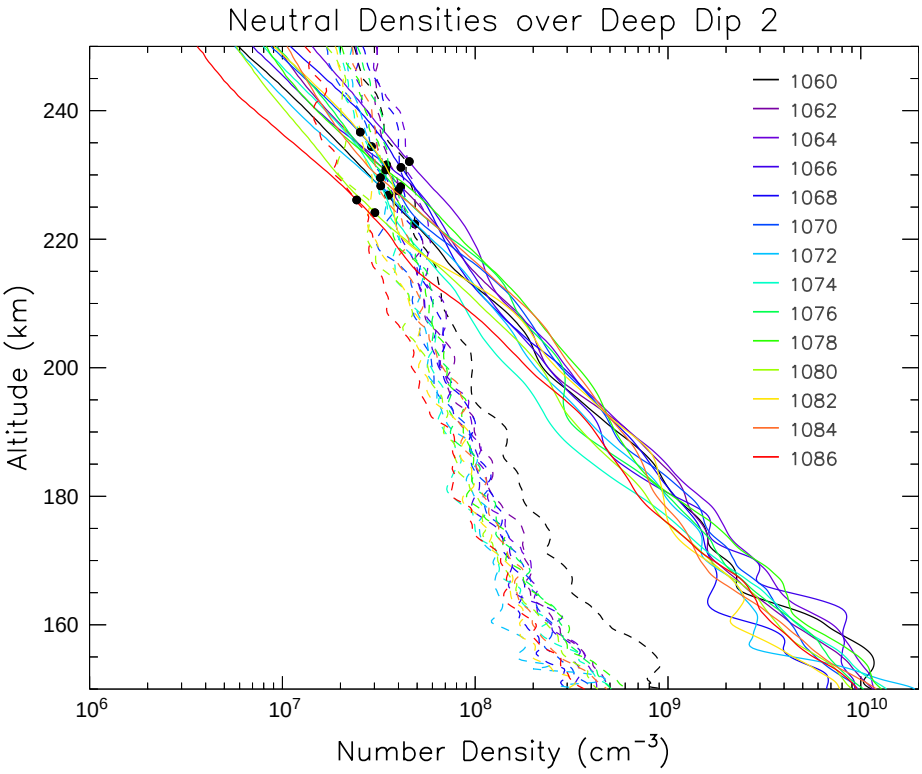

Fig. 5. Altitude plots of O and CO_2 densities over 150 to 250 km. NGIMS O (dashed lines) and CO_2 (solid lines) density profiles are plotted throughout the DD2 campaign, spanning 14 orbits from O1060 to O1086. Separate profiles are color-coded for orbit identification. The black dots for each orbit correspond to the crossing point at which the O/CO_2 ratio is unity. These altitudes range from ~225 to 238 km. The mean height is 230.5 ± 2.5 km.

Measurements from MAG (*28*), SWEA (*2*), SWIA (*29*), LPW (*30*), and NGIMS (*10*) reveal the complex morphology of the inner magnetosphere and ionosphere (Figs. 6 and 7). Periapsis for this orbit (O1085) occurred at 48°W, 6°S, in a region with moderate crustal magnetic fields, at an altitude of ~130 km and SZA of ~5°. During this period, the spacecraft remained below the induced magnetospheric boundary until 02:18 UTC, after which MAVEN observed suprathermal particles characteristic of the magnetosheath. Before 02:18 UTC, electron spectra displayed features characteristic of atmospheric photoelectrons throughout. Outside of the main peak of the ionosphere (before 02:02 and after 02:12 UTC), in the transport-dominated regime (above ~200 km, major ion lifetimes are >~600 s), charged-particle populations and magnetic fields show substantial structure, likely consisting of a mix of transient variations and horizontal and/or vertical structure. O^+ and O_2^+ dominate the thermal ion composition, with both varying over orders of magnitude, particularly on the outbound pass. The draped magnetic-field rotations, compositional changes, and electron temperature changes associated with the ion density layers at L3 and L4 and the intervening density depletions suggest that these represent primarily temporal variations, implying rapid ionospheric reconfigurations, indicative of substantial transport and/or strong compressional waves.

At times L1 and L2, the spacecraft passed sharp thermal ion density layers (more pronounced on the inbound segment). At the same locations, MAVEN observed the signatures of localized currents, visible as a discontinuity in the magnetic field [and a rotation toward a more horizontal field below the layers (Fig. 7)]. These features occurred just above a transition to a smoothly varying photoelectron population, which is consistent with the collisional photochemically controlled region of the ionosphere (*31*). This ion layer may represent the topside layer previously seen in radar (*32*) and radio sounding (*33*) by MEx [perhaps also in the Viking-2 descent (*13*)] but appears narrower (~5 to 10 km) than is apparent from remote measurements. The sharpness of the layer in comparison with expected variations in neutral density and EUV energy deposition implies vertical transport and suggests that it could represent a transition between a region dominated by draped and/or induced magnetic fields and one dominated by crustal fields (*33*, *34*). Localized electric fields could also play a role, as previously observed at Earth (*35*). The sharp drop in electron temperature

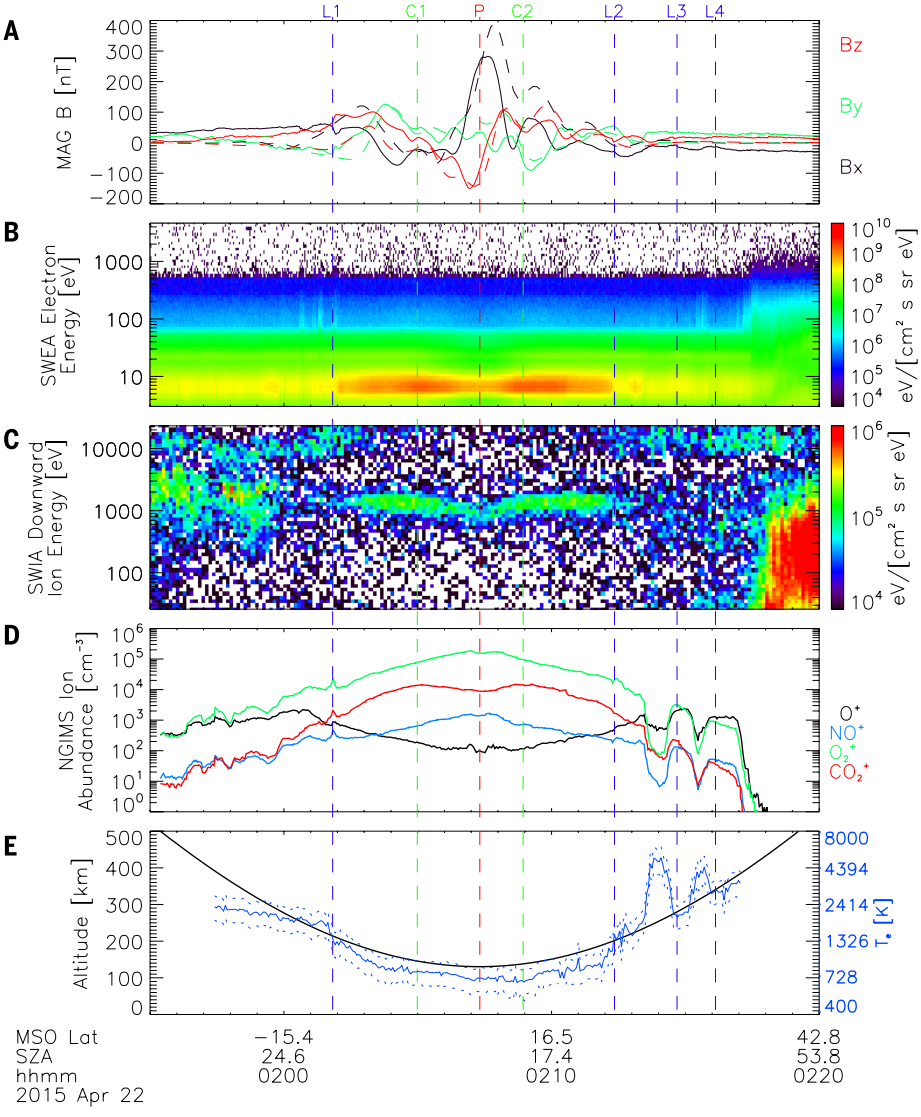

Fig. 6. Plasma environment near periapsis during the subsolar DD2 campaign. These time series plots are provided over 130 to 500 km in a region with moderate crustal fields, during a time period with quiet solar wind conditions, and specifically for 01085 (22 April 2015). (**A**) MAG-measured (solid) and spherical harmonic model (dashed) crustal magnetic-field vector components (Bx, By, and Bz) in Mars-Solar-Orbital coordinates. (**B**) SWEA energy spectra of suprathermal electrons. (**C**) SWIA energy spectra of downward-going suprathermal ions. (**D**) NGIMS abundances of major ion species (O^+, O_2^+, CO_2^+, and NO^+). (**E**) Spacecraft altitude plus LPW electron temperatures (dashed lines indicate upper and lower bounds, with the solid lines showing the best-fit value). Mars-Solar-Orbital latitude (MSO Lat), solar zenith angle (SZA), and universal time coordinated hour and minute (hhmm) are also provided along the time series below 500 km. Labeled vertical dashed lines are provided to highlight features discussed in the text, including localized ion layers (L1 to L4), peaks in CO_2^+ density (C1 and C2), and periapsis (P), which occurs at 02:07 UTC, at a SZA of ~5°.

below this layer also indicates a topological boundary that locally affects photoelectron transport and suggests that photochemical processes play a role (*36*).

At lower altitudes, O^+ densities drop rapidly owing to reactions with neutral molecules, but suprathermal photoelectrons and thermal CO_2^+ ions continue to increase in density (with very similar altitude dependence, commensurate with their production primarily from neutral CO_2). These populations peak at the times marked C1 and C2—at altitudes of ~140 km, below which they decrease—presumably because of recombination and reactions with neutral species. CO_2^+ densities peak at a higher altitude than that of O_2^+ densities, and higher than observed at higher SZA by Viking (*13*). Meanwhile, O_2^+ densities continue to increase until just above periapsis (time P). The slight decrease in density at periapsis may indicate that the spacecraft reached the main M2 peak of the ionosphere, which is consistent with the periapsis altitude.

The different altitude profiles for major ion species and photoelectrons reflect the variations in source and loss processes as a function of altitude, stemming from the varying deposition of EUV and other energy inputs (comprehensively measured by MAVEN), changes in neutral composition, and the steeply increasing neutral density. Multifluid magnetohydrodynamic (MHD) model results capture some, but not all, of the observed variations in ion abundance along the orbit track (supplementary text S5) (*37*, *38*). The model correctly reproduces the structure of the dominant O_2^+ ions at altitudes below ~220 km and also captures the structure of the CO_2^+ ions over most of this altitude range. Above ~220 km, in the transport-dominated region, the time-stationary model results cannot adequately capture the transient dynamics. The model also underestimates O^+ density everywhere except periapsis and does not capture the turnover in the CO_2^+ density at low altitudes.

All the major ion species show substantial wave structure on the outbound segment (but not on the inbound), extending almost down to periapsis. This wave structure correlates closely (although not one-to-one everywhere) with fluctuations seen in the neutral density at the same time, suggesting that many of the observed neutral and ion fluctuations might have a common origin, presumably gravity waves (*19*, *20*).

Suprathermal ion measurements provide another probe of collisional processes in the atmosphere. A downward-going population of ~1 keV ions appears between L1 and L2. These ions represent the products of hydrogen energetic neutral atoms (ENAs) produced through charge exchange between solar wind protons and exospheric atoms in the distant corona outside of the bow shock (*39*, *40*). In neutral form, these particles pass through the magnetosphere unaffected by electromagnetic form, maintaining the same velocity as that of the solar wind. Upon encountering the atmosphere, some of the ENAs undergo charge-stripping reactions and regain their charge, allowing MAVEN to measure them. As the neutral density rises, these particles lose energy through numerous collisions with atmospheric gases. The ratio of electron-stripping to charge-exchange cross sections decreases sharply at lower energies, leading to a decrease in the charged fraction of the precipitating hydrogen between C1 and C2. These penetrating solar wind particles represent an additional source of energy to the upper atmosphere, with a different deposition profile from that of EUV. They also provide a proxy measurement of the solar wind, allowing us to infer an upstream solar wind speed of ~500 km/s and density of ~1.1 cm^{-3} (*40*).

At higher energies of ~10 to 20 keV, SWIA observes an additional population of precipitating ions, which penetrate well into the photochemical region of the atmosphere (below the "exobase"). When this population extends to higher altitudes, at which suprathermal ion composition measurements in this energy range from STATIC (*2*) are available, they indicate predominantly O^+, which is consistent with pickup ions produced by photoionization and charge-transfer reactions in the upstream corona. These precipitating ions

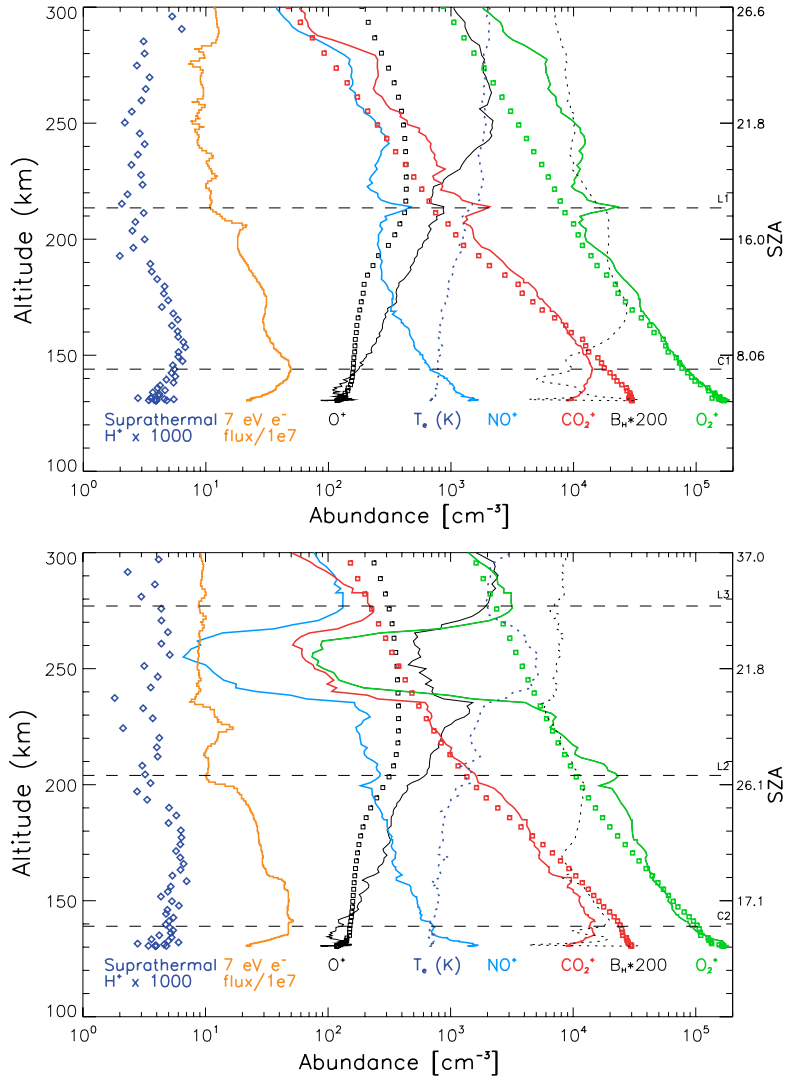

Fig. 7. Altitude plots of ion densities and other plasma fields over 130 to 300 km. NGIMS ion densities are plotted for DD2 orbit 01085, with the corresponding SZA indicated on the right. Four NGIMS key ion species are provided (O^+, O_2^+, CO_2^+, and NO^+) for the (**Top**) inbound and (**Bottom**) outbound legs (solid, color-coded curves). Corresponding simulated ion density profiles along the orbit from the multifluid MHD model are plotted (colored squares) for comparison (O^+, O_2^+, CO_2^+ only) (supplementary text S5) (*37*, *38*, *42*). The measured inbound ratio (O_2^+/CO_2^+) at 150 km is a factor of ~6, whereas that at 220 km is a factor of ~10. These ratios can be compared with corresponding values of 6 and 7 to 9 from Viking Landers 1 and 2, respectively (*13*). Also shown for context are scaled values corresponding to the electron temperature, the horizontal magnetic-field magnitude measured by MAG, the suprathermal electron flux measured at 7 eV (the peak of the suprathermal electron flux) by SWEA, and the suprathermal H^+ density measured by SWIA.

may drive sputtering escape of the neutral atmospheric particles (*41*).

Interpretations and implications

The thermospheric neutral densities and temperatures vary substantially from orbit to orbit, driven in part by tidal and gravity wave forcing. Solar EUV regulation of mean exospheric temperatures (averaged over several orbits) is confirmed for these DD2 measurements, in comparison with solar-driven numerical model simulations. However, this solar forcing does not appear to control interorbital variations of these temperatures. Like the neutral atmosphere to which it is coupled, the ionosphere revealed by MAVEN is highly dynamic, with substantial structure and temporal variations often observed within a single orbit. Crustal fields clearly affect the structure of the ionosphere, and their effects on transport may lead to the formation of the observed narrow current-carrying plasma layers.

REFERENCES AND NOTES

1. S. W. Bougher, T. E. Cravens, J. Grebowsky, J. Luhmann, The aeronomy of Mars: Characterization by MAVEN of the upper atmosphere reservoir that regulates volatile escape. *Space Sci. Rev.* (2014). doi: 10.1007/s11214-014-0053-7
2. B. M. Jakosky *et al.*, The Mars Atmosphere and Volatile Evolution (MAVEN) Mission to Mars. *Space Sci. Rev.* (2015). doi: 10.1007/s11214-015-0139-x
3. The homopause altitude of a given planetary upper atmosphere is commonly estimated as the altitude at which a given species diffusion coefficient matches the specified eddy diffusion coefficient. This altitude represents that level in the atmosphere below which this species is well mixed (homosphere) and above which molecular diffusion serves to separate species according to their individual scale heights (heterosphere). Each species has its particular homopause altitude, owing to the slight variation of molecular diffusion coefficients by species. In reality, the homopause is not a single altitude level, but a transition region across which these molecular and eddy diffusion processes gradually exchange their dominant roles. For Mars, a common mixed-atmosphere scale height is revealed by CO_2, Ar, and N_2 below their homopauses. However, photochemically active species (such as O) do not conform to this mixed-atmosphere scale height.
4. The MAVEN in situ instruments are the Accelerometer (ACC), Langmuir Probe and Waves (LPW), Magnetometer (MAG), Neutral Gas and Ion Mass Spectrometer (NGIMS), Solar Wind Electron Analyzer (SWEA), Solar Wind Ion Analyzer (SWIA), and Supra-thermal and Thermal Ion Composition (STATIC).
5. R. W. Zurek, R. H. Tolson, D. Baird, M. Z. Johnson, S. W. Bougher, M. Z. Johnson, and S. W. Bougher, Application of MAVEN accelerometer and attitude control data to Mars atmospheric characterization. *Space Sci. Rev.* (2014). doi: 10.1007/s11214-014-0095-x
6. Areocentric longitude of the Sun, Ls, is used as an angular measure of the Mars year: Ls = 0, 90, 180, and 270 correspond to the start of the northern spring, summer, fall, and winter, respectively.
7. A. O. Nier, M. B. McElroy, Composition and structure of Mars' upper atmosphere: Results from the neutral mass spectrometers on Viking 1 and 2. *J. Geophys. Res.* **82**, 4341–4349 (1977). doi: 10.1029/JS082i028p04341
8. G. M. Keating *et al.*, The structure of the upper atmosphere of mars: In situ accelerometer measurements from mars global surveyor. *Science* **279**, 1672–1676 (1998). doi: 10.1126/science.279.5357.1672; pmid: 9497278
9. S. W. Bougher *et al.*, Mars Global Ionosphere-Thermosphere Model: Solar cycle, seasonal and diurnal variations of the Mars upper atmosphere. *J. Geophys. Res.* **120**, 311–342 (2015). doi: 10.1002/2014JE004715
10. P. R. Mahaffy *et al.*, The Neutral Gas and Ion Mass Spectrometer on the Mars Atmosphere and Volatile Evolution Mission. *Space Sci. Rev.* **185**, 1–25 (2014). doi: 10.1007/s11214-014-0043-9
11. J.-Y. Chaufray, F. Leblanc, E. Quemerais, J.-L. Bertaux, Martian oxygen density at the exobase deduced from OI 1304.-nm observations by Spectroscopy for the Investigation of the Characteristics of the Atmosphere of Mars on Mars Express. *J. Geophys. Res.* **114** (E2), E02006 (2009). doi: 10.1029/2008JE003130
12. A. Valeille, M. R. Combi, S. W. Bougher, V. Tenishev, A. F. Nagy, Three-dimensional study of Mars upper thermosphere-ionosphere and hot oxygen corona: Solar cycle, seasonal variations and evolution over history. *J. Geophys. Res.* **114**, E11006 (2009). doi: 10.1029/2009JE003389
13. W. B. Hanson, S. Sanatani, D. R. Zuccaro, The Martian ionosphere as observed by the Viking retarding potential analyzers. *J. Geophys. Res.* **82**, 4351–4363 (1977). doi: 10.1029/JS082i028p04351
14. P. R. Mahaffy *et al.*, Abundance and isotopic composition of gases in the martian atmosphere from the Curiosity rover. *Science* **341**, 263–266 (2013). pmid: 23869014
15. D. Snowden *et al.*, The thermal structure of Titan's upper atmosphere, I. Temperature profiles from Cassini INMS observations. *Icarus* **226**, 552–582 (2013). doi: 10.1016/j.icarus.2013.06.006
16. P. R. Mahaffy *et al.*, Structure and composition of the neutral upper atmosphere of Mars from the MAVEN NGIMS investigation. *Geophys. Res. Lett.* **42**, (2015). doi: 10.1002/2015GL065329
17. F. LeBlanc, J. Y. Chaufray, J. Lilenstein, O. Witasse, J.-L. Bertaux, Martian dayglow as seen by the SPICAM UV spectrograph on Mars Express. *J. Geophys. Res.* **111** (E9), E09S11 (2006). doi: 10.1029/2005JE002664
18. A. Stiepen *et al.*, Mars thermospheric scale height: CO Cameron and CO_2^+ dayglow observations from Mars Express. *Icarus* **245**, 295–305 (2015). doi: 10.1016/j.icarus.2014.09.051
19. A. S. Medvedev, E. Yiğit, P. Hartogh, E. Becker, Influence of gravity waves on the Martian atmosphere: General circulation modeling. *J. Geophys. Res.* **116** (E10), E10004 (2011). doi: 10.1029/2011JE003848

20. A. Medvedev, E. Yigit, Thermal effects of internal gravity waves in the Martian upper atmosphere. *Geophys. Res. Lett.* **39**, L05201 (2012). doi: 10.1029/2012GL050852
21. The exobase of a given planetary upper atmosphere is traditionally estimated as the altitude at which, for a single constituent atmosphere, the collision mean free path equals the temperature scale height of this constituent. For Mars, atomic O is the dominant species considered, and calculated global averaged exobase heights vary from ~170 km (Equinox, solar minimum conditions) to ~185 km (Equinox, solar maximum conditions) (*43*). In reality, the exobase is not a fixed altitude that separates collisional (thermosphere) and collisionless (exosphere) regimes. Instead, a full transitional domain must be considered, which extends from the altitude at which a hot O particle produced in this region has a high probability to be thermalized to an altitude at which the collision frequency is very low. Modern hot O exosphere models confirm that this transitional domain extends from ~135 to 300 km altitude (*43*). The ~200 km altitude is commonly used as an approximation for the traditional exobase altitude.
22. A. F. Nagy *et al*., The plasma environment of Mars. *Space Sci. Rev.* **111**, 33–114 (2004). doi: 10.1023/B:SPAC.0000032718.47512.92
23. E. Dubinin *et al*., Plasma morphology at Mars. ASPERA-3 observations. *Space Sci. Rev.* **126**, 209–238 (2006). doi: 10.1007/s11214-006-9039-4
24. M. H. G. Zhang, J. G. Luhmann, A. J. Kliore, J. Kim, A post-Pioneer Venus reassessment of the Martian dayside ionosphere as observed by radio occultation methods. *J. Geophys. Res.* **95** (B9), 14,829–14,839 (1990). doi: 10.1029/JB095iB09p14829
25. D. A. Gurnett *et al*., Large density fluctuations in the Martian ionosphere as observed by the Mars Express radar sounder. *Icarus* **206**, 83–94 (2010). doi: 10.1016/j.icarus.2009.02.019
26. P. Withers, A review of observed variability in the dayside ionosphere of Mars. *Adv. Space Res.* **44**, 277–307 (2009). doi: 10.1016/j.asr.2009.04.027
27. F. Duru *et al*., Steep, transient density gradients in the Martian ionosphere similar to the ionopause at Venus. *J. Geophys. Res.* **114** (A12), A12310 (2009). doi: 10.1029/2009JA014711
28. J. E. P. Connerney *et al*., The MAVEN magnetic field investigation. *Space. Sci. Rev.* 10.1007s11214-015-0169-4 (2015).
29. J. S. Halekas *et al*., The Solar Wind Ion Analyzer for MAVEN. *Space Sci. Rev.* (2013). doi: 10.1007/s11214-013-0029-z
30. R. Ergun *et al*., Dayside electron temperature and density profiles at Mars: First results from the MAVEN Langmuir Probe and Waves instrument. *Geophys. Res. Lett.* **42**, (2015). doi: 10.1002/2015GL065280
31. J. L. Fox, A. Dalgarno, Ionization, luminosity, and heating of the upper atmosphere of Mars. *J. Geophys. Res.* **84** (A12), 7315 (1979). doi: 10.1029/JA084iA12p07315
32. A. J. Kopf, D. A. Gurnett, D. D. Morgan, D. L. Kirchner, Transient layers in the topside ionosphere of Mars. *Geophys. Res. Lett.* **35**, L17102 (2008). doi: 10.1029/2008GL034948
33. P. Withers *et al*., A clear view of the multifaceted dayside ionosphere of Mars. *Geophys. Res. Lett.* **39**, L18202 (2012). doi: 10.1029/2012GL053193
34. H. Shinagawa, T. E. Cravens, The ionospheric effects of a weak intrinsic magnetic field at Mars. *J. Geophys. Res.* **97** (E1), 1027–1035 (1992). doi: 10.1029/91JE02720
35. S. Kirkwood, H. Nilsson; Kirkwood and Nilsson, High-latitude sporadic-E and other thin layers - the role of magnetospheric electric fields. *Space Sci. Rev.* **91**, 579–613 (2000). doi: 10.1023/A:1005241931650
36. J. L. Fox, K. E. Yeager, Morphology of the near-terminator Martian ionosphere: A comparison of models and data. *J. Geophys. Res.* **111** (A10), A10309 (2006). doi: 10.1029/2006JA011697
37. C. Dong *et al*., Solar wind interaction with Mars upper atmosphere: Results from the one-way coupling between the multi-fluid MHD model and the MTGCM model. *Geophys. Res. Lett.* **41**, 2708–2715 (2014). doi: 10.1002/2014GL059515
38. C. Dong *et al*., Solar wind interaction with the Martian upper atmosphere: Crustal field orientation, solar cycle, and seasonal variations. *J. Geophys. Res.* **120**, (2015). doi: 10.1002/2015JA020990
39. E. Kallio, S. Barabash, Atmospheric effects of precipitating energetic hydrogen atoms on the Martian atmosphere. *J. Geophys. Res.* **106** (A1), 165–177 (2001). doi: 10.1029/2000JA002003
40. J. S. Halekas *et al*., MAVEN observations of solar wind hydrogen deposition in the atmosphere of Mars. *Geophys. Res. Lett.* **42**, (2015). doi: 10.1002/2015GL064693
41. J. Luhmann, J. U. Kozyra, Dayside Pickup Oxygen Ion Precipitation at Venus and Mars - Spatial Distributions, Energy Deposition and Consequences. *J. Geophys. Res.* **96** (A4), 5457–5467 (1991). doi: 10.1029/90JA01753
42. D. Najib, A. Nagy, G. Toth, Y. Ma, Three-dimensional, multi-fluid, high spatial resolution MHD model studies of the solar wind interaction with Mars. *J. Geophys. Res.* (2011). doi: 10.1029/2010JA016272
43. Y. Lee, M. Combi, V. Tenishev, S. Bougher, D. Pawlowski, N. Franklin, Impacts of the Martian crustal magnetic fields on the thermosphere, ionosphere, and hot oxygen corona. *Bulletin of the American Astronomical Society*, **46**, abstract 306.01, Div. for Planetary Sciences, 46th Annual Meeting, Tucson, AZ (2014).

ACKNOWLEDGMENTS

The MAVEN Deep Dip 2 data sets reported in the paper are archived on the public version of the MAVEN Science Data Center (SDC) website, at the LASP url (https://lasp.colorado.edu/maven/sdc/public/) and on the Planetary Data System (PDS). Datacubes from three-dimensional model simulations reported in this paper are also available on the public MAVEN SDC website at https://lasp.colorado.edu/maven/sdc/public/pages/models.html. This work was partially supported by the Centre National d'Études Spatiales for the part based on observations with the SWEA instrument embarked on Maven. Part of this research was also carried out at the Jet Propulsion Laboratory, California Institute of Technology, under a contract with the National Aeronautics and Space Administration (NASA). A. Stiepen was supported by the Belgian American Educational Foundation and the Rotary District 1630. G. DiBraccio was supported by a NASA Postdoctoral Program appointment at NASA Goddard Space Flight Center, administered by Oak Ridge Associated Universities through a contract with NASA. The MAVEN project is supported by NASA through the Mars Exploration Program.

SUPPLEMENTARY MATERIALS

www.sciencemag.org/content/350/6261/aad0459/suppl/DC1
Supplementary Text

17 July 2015; accepted 21 September 2015
10.1126/science.aad0459

Early MAVEN Deep Dip campaign reveals thermosphere and ionosphere variability

S. Bougher, B. Jakosky, J. Halekas, J. Grebowsky, J. Luhmann, P. Mahaffy, J. Connerney, F. Eparvier, R. Ergun, D. Larson, J. McFadden, D. Mitchell, N. Schneider, R. Zurek, C. Mazelle, L. Andersson, D. Andrews, D. Baird, D. N. Baker, J. M. Bell, M. Benna, D. Brain, M. Chaffin, P. Chamberlin, J.-Y. Chaufray, J. Clarke, G. Collinson, M. Combi, F. Crary, T. Cravens, M. Crismani, S. Curry, D. Curtis, J. Deighan, G. Delory, R. Dewey, G. DiBraccio, C. Dong, Y. Dong, P. Dunn, M. Elrod, S. England, A. Eriksson, J. Espley, S. Evans, X. Fang, M. Fillingim, K. Fortier, C. M. Fowler, J. Fox, H. Gröller, S. Guzewich, T. Hara, Y. Harada, G. Holsclaw, S. K. Jain, R. Jolitz, F. Leblanc, C. O. Lee, Y. Lee, F. Lefevre, R. Lillis, R. Livi, D. Lo, Y. Ma, M. Mayyasi, W. McClintock, T. McEnulty, R. Modolo, F. Montmessin, M. Morooka, A. Nagy, K. Olsen, W. Peterson, A. Rahmati, S. Ruhunusiri, C. T. Russell, S. Sakai, J.-A. Sauvaud, K. Seki, M. Steckiewicz, M. Stevens, A. I. F. Stewart, A. Stiepen, S. Stone, V. Tenishev, E. Thiemann, R. Tolson, D. Toublanc, M. Vogt, T. Weber, P. Withers, T. Woods and R. Yelle (November 5, 2015)

Science **350** (6261), . [doi: 10.1126/science.aad0459]

Editor's Summary

PLANETARY SCIENCE

MAVEN observations of the response of Mars to an interplanetary coronal mass ejection

B. M. Jakosky,[1]* J. M. Grebowsky,[2] J. G. Luhmann,[3] J. Connerney,[2] F. Eparvier,[1] R. Ergun,[1] J. Halekas,[4] D. Larson,[3] P. Mahaffy,[2] J. McFadden,[3] D. L. Mitchell,[3] N. Schneider,[1] R. Zurek,[5] S. Bougher,[6] D. Brain,[1] Y. J. Ma,[7] C. Mazelle,[8,9] L. Andersson,[1] D. Andrews,[10] D. Baird,[11] D. Baker,[1] J. M. Bell,[21] M. Benna,[2] M. Chaffin,[1] P. Chamberlin,[2] Y.-Y. Chaufray,[12] J. Clarke,[13] G. Collinson,[2] M. Combi,[6] F. Crary,[1] T. Cravens,[14] M. Crismani,[1] S. Curry,[3] D. Curtis,[3] J. Deighan,[1] G. Delory,[3] R. Dewey,[1] G. DiBraccio,[2] C. Dong,[6] Y. Dong,[1] P. Dunn,[3] M. Elrod,[2] S. England,[3] A. Eriksson,[10] J. Espley,[2] S. Evans,[15] X. Fang,[1] M. Fillingim,[3] K. Fortier,[1] C. M. Fowler,[1] J. Fox,[16] H. Gröller,[17] S. Guzewich,[2] T. Hara,[3] Y. Harada,[3] G. Holsclaw,[1] S. K. Jain,[1] R. Jolitz,[3] F. Leblanc,[12] C. O. Lee,[3] Y. Lee,[6] F. Lefevre,[12] R. Lillis,[3] R. Livi,[3] D. Lo,[17] M. Mayyasi,[13] W. McClintock,[1] T. McEnulty,[1] R. Modolo,[12] F. Montmessin,[12] M. Morooka,[1] A. Nagy,[6] K. Olsen,[6] W. Peterson,[1] A. Rahmati,[14] S. Ruhunusiri,[4] C. T. Russell,[7] S. Sakai,[14] J.-A. Sauvaud,[8,9] K. Seki,[18] M. Steckiewicz,[8,9] M. Stevens,[19] A. I. F. Stewart,[1] A. Stiepen,[1] S. Stone,[17] V. Tenishev,[6] E. Thiemann,[1] R. Tolson,[20] D. Toublanc,[8,9] M. Vogt,[13] T. Weber,[1] P. Withers,[13] T. Woods,[1] R. Yelle[17]

Coupling between the lower and upper atmosphere, combined with loss of gas from the upper atmosphere to space, likely contributed to the thin, cold, dry atmosphere of modern Mars. To help understand ongoing ion loss to space, the Mars Atmosphere and Volatile Evolution (MAVEN) spacecraft made comprehensive measurements of the Mars upper atmosphere, ionosphere, and interactions with the Sun and solar wind during an interplanetary coronal mass ejection impact in March 2015. Responses include changes in the bow shock and magnetosheath, formation of widespread diffuse aurora, and enhancement of pick-up ions. Observations and models both show an enhancement in escape rate of ions to space during the event. Ion loss during solar events early in Mars history may have been a major contributor to the long-term evolution of the Mars atmosphere.

Quantifying the role that escape of gas to space played throughout martian history will help to determine whether it was an important mechanism for driving the climate change observed in the geological record (*1*, *2*). Determining the effects that discrete solar storms have had on the structure of the upper atmosphere, ionosphere, and magnetosphere, and on the loss rate to space, is an important component of this, owing to the increased occurrence of storms in early martian history and their potential contributions to the total loss.

The Mars Atmosphere and Volatile Evolution (MAVEN) mission to Mars was designed to study the upper atmosphere, ionosphere, and magnetosphere of Mars, the response to solar and solar-wind input, and the ability of atmospheric molecules and atoms to escape to space (*3*). MAVEN was launched on 18 November 2013, and went into orbit around Mars on 21 September 2014. After a 2-month commissioning phase, it began its one-Earth-year primary science mission on 16 November 2014. MAVEN is in an elliptical orbit with periapsis altitude of ~150 km and apoapsis altitude of ~6200 km. This orbit allows a combination of in situ measurements throughout the entire region of interest and remote-sensing measurements that provide quasi-global coverage. The nine science instruments provide a combination of measurements of the solar and solar-wind energetic input into the upper atmosphere, the composition and structure of the upper atmosphere and ionosphere, the topology of the interactions of the solar wind with the planet, and the composition and energetics of atomic and molecular ions interacting with and escaping from the system (*3*, *4*).

We report here on observations from MAVEN that show the integrated effects of an interplanetary coronal mass ejection (ICME) with the planet, the consequences for the upper atmosphere, and the impact on escape to space. We both present the observations made by MAVEN of the ICME and Mars atmospheric response, and use the observations to validate a global model of the martian atmosphere interaction with the solar wind during the ICME. The model is then used to estimate the global response of the system, which MAVEN samples only locally during the event. These observations complement studies of the structure of the upper atmosphere and ionosphere and the overall behavior of the martian system, along with the initial look at the chain of events from energetic drivers to response of the upper atmosphere and then leading to escape to space (*4*–*7*).

Energetic inputs into the system

MAVEN has been making observations nearly continuously since November 2014. The strongest solar event observed to date occurred on 8 March 2015. MAVEN measurements during the entire time period from 25 February to 13 March 2015 exhibited disturbed interplanetary conditions, as shown in Fig. 1. The solar irradiance time series from the perspective of Mars (Fig. 1, top panel) shows the flare activity detected by the MAVEN extreme ultraviolet (EUV) detector. The flare event (F4) occurring on 6 March ~05:00 UT was likely associated with the major interplanetary disturbance of this period. Major flares are often related to eruptions of coronal material known as coronal mass ejections (CMEs, best known for causing geomagnetic storms at Earth) (*8*). White light coronagraph images from the Solar Heliospheric Observatory (SOHO) showed that multiple CMEs erupted in the general direction of Mars during this time.

We used orbital ephemerides and Magnetometer (MAG) (*9*) and Solar Wind Ion Analyzer (SWIA) (*10*) measurements to select periods during which we had unambiguous measurements of the upstream solar wind outside of the martian bow shock and foreshock. The solar-wind density, velocity, and interplanetary magnetic field (IMF) were averaged over the upstream interval, for each MAVEN orbit for which they could be determined. The most disturbed period analyzed here spanned about three ~4.5-hour MAVEN orbits.

The upstream solar-wind data set shows four major density enhancements (labeled S1 to S4) associated with a series of ICMEs. During the last of these events (S4) on 8 March, the solar wind reached a peak flow speed of 825 km/s, with a corresponding peak ram pressure of 15 nPa, and magnetic-field strength of ~20 nT, all the highest values observed by MAVEN to date. For comparison, the peak pressure observed at Mars during the Halloween 2003 ICME event was ~33 nT, and the average pressure during this period was ~7 nPa (*11*); the event reported here is one of the strongest ever observed at Mars. The average upstream solar

[1]University of Colorado, Boulder, CO, USA. [2]NASA/Goddard Space Flight Center, Greenbelt, MD, USA. [3]University of California at Berkeley, Berkeley, CA, USA. [4]University of Iowa, Iowa City, IA, USA. [5]Jet Propulsion Laboratory, California Institute of Technology, Pasadena, CA, USA. [6]University of Michigan, Ann Arbor, MI, USA. [7]University of California at Los Angeles, Los Angeles, CA, USA. [8]CNRS–Institut de Recherche en Astrophysique et Planétologie (IRAP), Toulouse, France. [9]University Paul Sabatier, Toulouse, France. [10]Swedish Institute of Space Physics, Uppsala, Sweden. [11]NASA/Johnson Space Center, Houston, TX, USA. [12]Laboratoire atmosphères, milieux et observations spatiales (LATMOS)–CNRS, Paris, France. [13]Boston University, Boston, MA, USA. [14]University of Kansas, Lawrence, KS, USA. [15]Computational Physics, Inc., Boulder, CO, USA. [16]Wright State University, Dayton, OH, USA. [17]University of Arizona, Tucson, AZ, USA. [18]Nagoya University, Nagoya, Japan. [19]Naval Research Laboratory, Washington, DC, USA. [20]North Carolina State University, Raleigh, NC, USA. [21]National Institute of Aerospace, Hampton, VA, USA.
*Corresponding author. E-mail: bruce.jakosky@lasp.colorado.edu

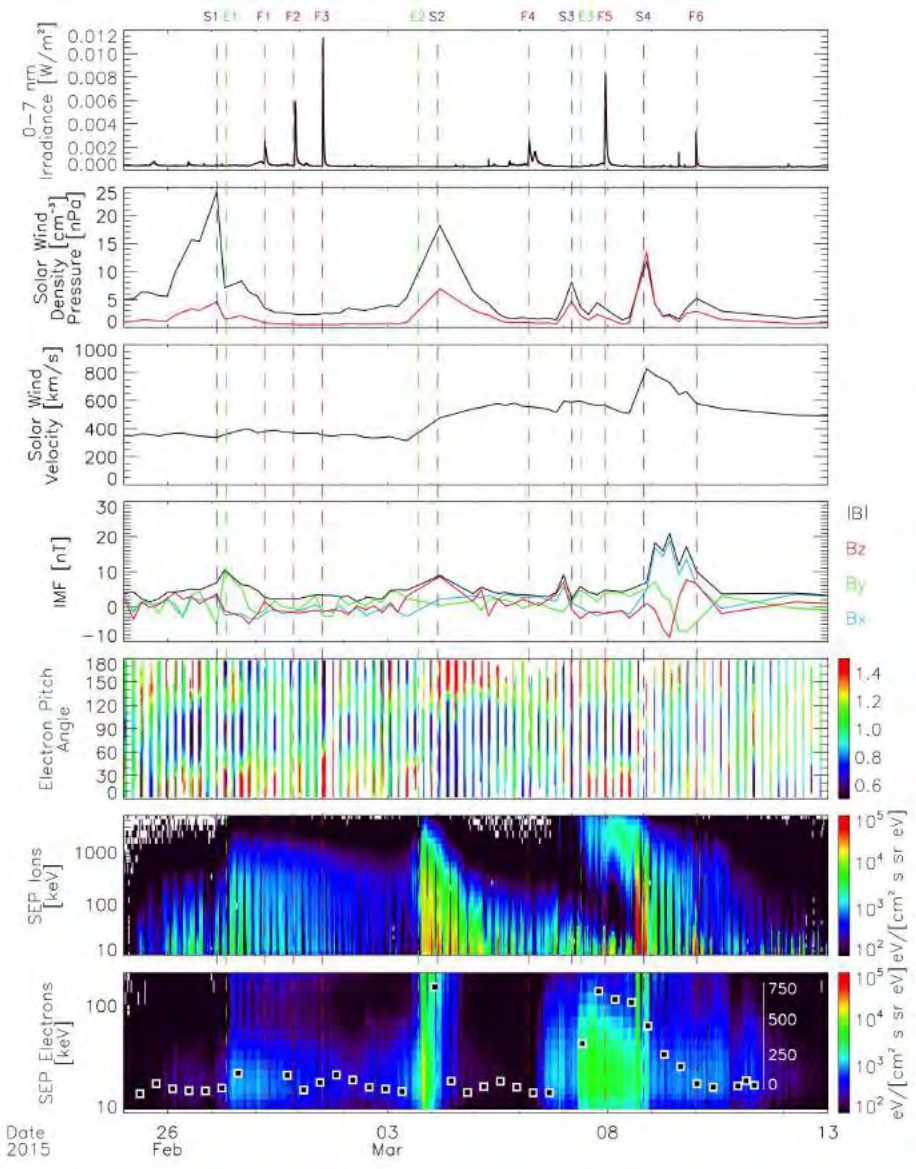

Fig. 1. Energy inputs to the martian system. The seven panels show flare irradiance from EUVM, solar-wind density (black) and ram pressure (red), velocity, and interplanetary magnetic field computed from SWIA and MAG data averaged over the portion of the orbit when the spacecraft was upstream from the bow shock, electron pitch-angle distributions at 110 to 140 eV from SWEA, and energetic ion and electron differential energy flux spectra from SEP. The intensities of CO_2^+ UV doublet auroral emission at 289 nm from the Mars nightside are plotted over the energetic electrons, using the inset scale; values below 50 to 100 Rayleighs are attributed to instrumental noise.

wind values measured by MAVEN from late November 2014 to late March 2015 were ~1 nPa for the ram pressure and 4 nT for the magnetic-field strength. The detailed MAG data from within the induced magnetosphere (discussed below) indicates that at ~15:20 UT 8 March, a strong magnetic rotation and compression associated with the arrival of the major ICME of the interval (event S4) were seen. The IMF returned to a more typical level within 48 hours after this signature. Major ICME events often have durations of up to a few days.

The Solar Wind Electron Analyzer (SWEA) (*12*) instrument measured suprathermal electron pitch-angle distributions (Fig. 1, fourth panel) upstream of the Mars bow shock. These reveal the magnetic topology associated with this series of events. The topology leading up to the final series of events (S3, S4) is complex, with electron beaming reversals and counterstreaming, suggesting that magnetically "closed" topologies are present almost every orbit. Such interplanetary field topologies, which are characteristic of ICME drivers and complex space-weather events, also affect the solar-wind interaction with Mars by altering the details of external field reconnection with the Mars crustal fields.

Solar energetic particle (SEP) events (*13*) (E1 to E3) were seen in conjunction with the multiple ICME passages, as shown in Fig. 1 (last two panels). The highest SEP ion fluxes at lower energies (<1 MeV) peaked around the ICME shock arrival times (S2 and S4), consistent with energetic storm particle (ESP) enhancements that occur when an ICME makes a direct strike. The most energetic ions (>1 MeV) in the strong event (E3) reached Mars at ~08:00 UT 7 March, ahead of the ICME disturbance (S4). This is the classical velocity dispersion, where the most energetic ions arrive first, at least a day before the plasma and field disturbance. The SEP ions gradually diminished in intensity throughout the rest of the ICME disturbance. SEP ion energy deposition in the Mars atmosphere peaked for ICME events S2 and S4, the latter being stronger. The largest energy fluxes occurred below ~300 keV, where most energy is deposited between 100- and 140-km altitude (*14*) and should affect strongly the thermospheric reservoir from which atmospheric escape occurs (*15*). The observed SEP electrons (bottom panel), which arrived early with the most-energetic ions, show a spread in energy at the ICME shock arrival on 8 March and a diminished flux soon after the shock passage.

We used the Wang-Sheeley-Arge (WSA)–ENLIL+Cone model to numerically simulate the interplanetary solar-wind conditions and provide a global heliospheric context for these events at Mars (*16*). Based on the simulation, the 8 March ICME impact of Mars was composed of two individual transients that merged en route to the planet. The first ICME was injected into the inner boundary of the ENLIL solar wind model at 04:49 UT 6 March with an initial radial speed of

900 km/s, whereas the second ICME was injected at 07:12 UT 6 March with a faster speed of 1500 km/s. The southern part of the second ICME interacted with and overtook the first ICME to produce a merged ICME. The model predicted the eastern flank of the merged structure to strike Mars at ~11:40 UT 8 March. Interestingly, the active region that triggered the Mars-directed ICMEs subsequently rotated toward Earth and launched an ICME, to produce one of the strongest geomagnetic storms of the current solar cycle (*17*).

Response of the system

MAVEN observations show that the ICME impact on 8 March 2015 dramatically altered the overall morphology and dynamics of the magnetosphere, affected the ionosphere, and induced auroral emissions from the neutral atmosphere.

Prior to the ICME, SWIA (*10*) measured a solar-wind proton density of 1.8 cm^{-3}, an alpha-particle density of 0.1 cm^{-3}, and flow speed of 505 km/s, corresponding to a ram pressure of 0.9 nPa. MAG (*9*) measured a typical IMF magnitude of ~5 nT. After the passage of the ICME shock, the upstream proton density rose to as high as 11 cm^{-3}, the alpha density to 0.6 cm^{-3}, and the flow speed to 820 km/s, with a ram pressure of 15 nPa, the highest encountered to date during the MAVEN mission. The IMF increased to 14 nT and in succeeding days rose to as high as 20 nT, also the highest value seen so far.

Using these measurements as inputs, we calculated three steady-state cases with a multispecies magnetohydrodynamic (MHD) model (*18*) to provide global context for the observations. The solar-wind conditions are set corresponding to before the ICME arrival (case 1), shortly after the arrival (case 2), and during the later time of the ICME, when the solar-wind dynamic pressure was intensified (case 3). Data-model comparisons are shown in Fig. 2. The orbit prior to arrival of the ICME, with apoapsis near 11:10 UT and periapsis at 13:23 UT, provides a baseline. Given the nominal IMF magnitude and plasma density, but moderately high Mach number of the flow, the observed and modeled magnetospheric boundaries are both asymmetric. The quasi-parallel bow-shock crossing on the outbound portion of the apoapsis segment occurred slightly earlier than expected from its average location (*19*), but the inbound boundaries were close to their nominal positions. MAVEN observed only minor crustal magnetic fields (*20*) of ~10 nT near periapsis, a total magnetic field of ~50 nT in the ionosphere, and few fluctuations.

During the succeeding apoapsis segment, MAVEN encountered extremely unusual plasma, with 10% alpha-particle abundance, a flow speed of 825 km/s with a 150 km/s off-axis component, and a high proton temperature of 130 eV, suggesting

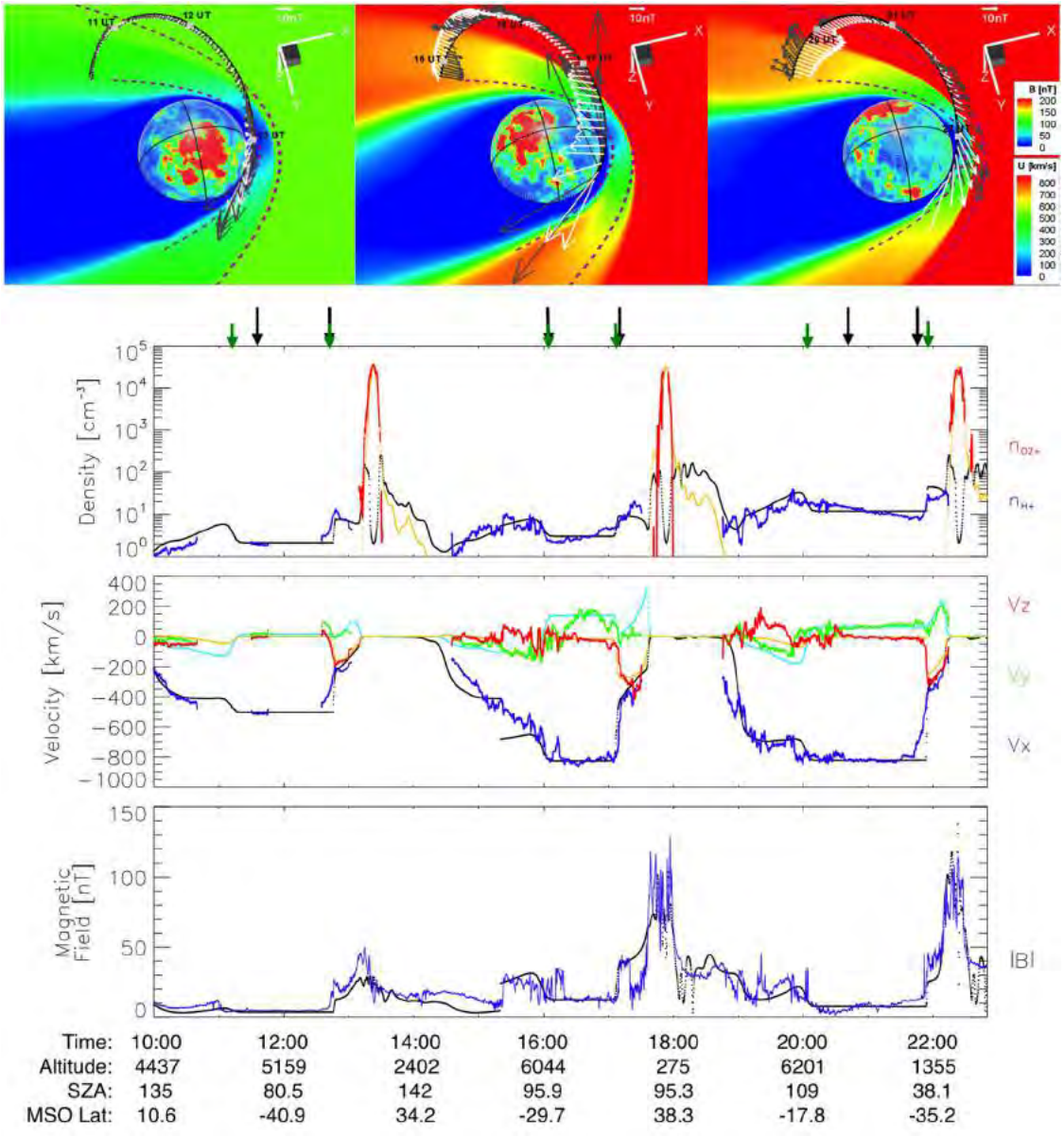

Fig. 2. The response of the martian magnetosphere to the passage of an ICME. The top panel shows predicted magnetospheric structure for three orbits, based on MHD runs utilizing upstream solar-wind conditions. The color contours show plasma flow speed in the equatorial plane (from the south). Black lines indicate the MAVEN orbit, black arrows show measured magnetic fields, and white arrows show model fields. The three-dimensional sphere represents the inner model boundary at 100-km altitude, with colors indicating the crustal magnetic field strength at the time of periapsis. The black dashed lines show nominal ionosphere-magnetosphere boundary and bow shock positions. The bottom three panels show MAG, SWIA, STATIC, and NGIMS (Neutral Gas and Ion Mass Spectrometer) observations (solid lines), with MHD results for comparison (dotted lines). Green and black arrows mark the observed and nominal bow shock locations, respectively.

that MAVEN encountered the sheath region trailing the ICME shock. The combination of high ram pressure and low Mach number conspired to produce boundaries near their normal position, but we observed multiple shock crossings and large magnetic fluctuations during this time period, implying a highly dynamic interaction. Commensurate with the high ram pressure, the average draped field inside the magnetosphere increased to ~90 nT, with a maximum of 130 nT during periapsis. The MHD model matches the overall magnetospheric structure during this period, but the time-stationary model cannot capture the observed variability and fluctuations in magnetic-field direction.

The magnetospheric effects continued and intensified in the succeeding orbit. The magnetic field exhibited large fluctuations, and the draped field remained at ~90 nT. The solar wind flow remained >800 km/s for ~7 hours, and the density increased, producing a solar-wind ram pressure more than an order of magnitude larger than typically observed and resulting in substantial deformation of the bow shock and compression of the entire magnetosphere. The MHD model, which matches the data well during this period, shows these effects globally.

On smaller scales, MAVEN observed sharp isolated magnetic-field enhancements in the martian magnetosheath just after the ICME shock arrival on 8 March. The enhancements are associated with magnetic-field rotations characteristic of magnetic flux ropes (*21*), which are observed to occur in the martian ionosphere and downstream from crustal magnetic fields (*22*, *23*). Suprathermal and Thermal Ion Composition (STATIC) measurements indicate that heavy (i.e., planetary) ions are present in the flux-rope structures, with energies of a few kilo–electron volts. The presence of heavy planetary ions collocated with flux ropes at the 5000-km altitude of the observed structures allows us to infer that the flux ropes formed in the vicinity of the ionosphere. The magnetic-field amplitudes in the flux ropes exceeded 80 nT, which is a few times larger than the typical detached flux ropes seen during nominal solar-wind conditions. Strong-field detached flux ropes observed at high altitudes are unique in the MAVEN observations to date. Moreover, the velocity of the detached flux ropes is estimated to be much faster than usual by a factor of approximately 10, under the assumption that these structures are in magneto-hydrostatic equilibrium (*24*).

The March ICME events also affected the upper atmosphere. MAVEN's Imaging Ultraviolet Spectrograph (IUVS) detected diffuse auroral emissions during the ICME events similar to those observed in December 2014 (*6*). IUVS is a remote-sensing instrument designed to map UV atmospheric emissions with altitude and across the planetary disk (*25*). The most sensitive mode for detection of auroral emission uses limb scans taken near periapsis on Mars' nightside. The vast majority of nightside limb scans show no atmospheric emissions apart from the ubiquitous hydrogen Lyman alpha (*26*) and occasional NO band emissions.

Observations spanning 22 min near periapsis were obtained on alternating orbits at ~9-hour intervals during the period encompassing the ICME. Figure 1 (bottom panel) shows the observed timeline for auroral emission from Mars' nightside during this period. The figure plots emission from the CO_2^+ UV doublet at 289 nm. Fainter emission was also detected from the CO Cameron bands. Both emissions are generated by particle impact on CO_2, which causes ionization, dissociation, and excitation. These emissions have been well studied on Mars' dayside, where they are excited by solar EUV radiation and resulting photoelectrons, and have been observed since the Mariner missions (*27*). The same emissions were observed on the Mars nightside in discrete aurora detected by the SPICAM (Spectroscopy for Investigation of Characteristics of the Atmosphere of Mars) instrument on Mars Express near crustal magnetic fields (*28*), and were seen previously by MAVEN in widespread diffuse aurora far from crustal fields and associated with a solar event (*6*).

IUVS detected three separate episodes of substantial auroral emission. The first occurred on 27 to 28 February and the second in a single orbit on 4 March. On 7 March, emission was observed to rise, peak, and fall over ~50 hours; no data were taken on the orbits immediately preceding the rise or following the decline. Although the seven detections in the third event are limited to ~20-min periods separated by ~9 hours, the repeated detections and relatively smooth variation suggest that it was a widespread, sustained event. The event spanned more than one Mars rotation, indicating that geographic control of this type of auroral emission is weak or nonexistent.

Substantial ion energization and enhancement resulting from the disturbed conditions were observed by SWIA, STATIC, and SEP during the 8 March event, as seen in measurements from a single MAVEN orbit shown in Fig. 3, after the arrival of the ICME shock. Although pickup ions are evident during the entire disturbed period subsequent to the maxima in IMF strength and ram pressure around 14:00 UT, we focus on the orbit spanning ~18:00 to 22:00 on 8 March.

The SWIA instrument (*7*) recorded strong pickup ion enhancements during this orbit (Fig. 3C). The solar wind is evident at high altitudes as a continuous flux of protons with energy per charge of 2 to 5 keV/q and alpha particles with energy per charge of 6 to 9 keV/q. Intermittent periods of higher-energy ion flux (~10 keV and above) appear at high altitudes. The black trace in Fig. 3C illustrates the predicted energy of pickup ions originating from any point directly sunward from the martian subsolar point (*29*) and accelerated entirely by the measured local $\mathbf{V} \times \mathbf{B}$ electric field. The predicted pickup ion energies have good agreement with the observations and correspond to periods where high-energy ion fluxes are observed. This agreement suggests that planetary ions were accelerated to high energies by the local convection electric field.

The STATIC (*30*) instrument also measures ions and can discriminate mass. Figure 3, D and E, show the observed energies [for mass >9 atomic mass units (amu)] and masses of ions during this orbit. Near periapsis, both O_2^+ and CO_2^+ are evident, and as the spacecraft altitude increases, the flux of massive CO_2^+ molecules decreases rapidly, and O^+ fluxes increase. Also present is a probable signature of He^+, most likely produced from charge exchange between solar-wind helium and planetary neutrals, as recently observed by Rosetta (*31*). This population also can be observed during quiet times, but is intensified during this period owing to the high solar-wind flux. Heavy-ion observations at high altitudes are complicated by the substantial solar-wind proton fluxes during the ICME. Internally scattered protons can contaminate higher-mass channels and have been removed via a background subtraction algorithm. Even though the background subtraction errs on the side of subtracting too many counts at high masses, fluxes of high-mass species are distinguishable periodically all the way up to apoapsis, often at energies higher than the predicted pickup ion energy shown in Fig. 3C. A closer look at the period near apoapsis (Fig. 3F) reveals that O^+, O_2^+, and CO_2^+ are all present at energies substantially greater than the solar-wind energy and have been stripped away from the planet.

At even higher energies, the SEP instrument (*13*) detected pick-up oxygen ions that had been produced upstream in the neutral oxygen corona and then accelerated toward Mars; these pick-up ions had energies above ~70 keV. The maximum oxygen pickup ion energy is given by $E_{max} = 2\, m_o\, U_{sw}^2\, \sin^2\theta_{UB}$, where m_o is the mass of atomic oxygen, U_{sw} is the solar-wind speed, and θ_{UB} is the angle between the solar wind and the IMF; after the 8 March ICME arrival, solar-wind velocities in excess of 800 km/s enable acceleration of pickup oxygen to energies as high as 210 keV. Following the method of (*32*), pickup oxygen fluxes are simulated for the first MAVEN apoapsis after the ICME arrival (the orbit prior to the one shown in Fig. 3, A to E, because of more favorable observing geometry during that orbit), and the agreement between the SEP measured and modeled fluxes confirms detection of O^+ by SEP. Figure 3G illustrates MAVEN data for a 45-min time period after 16:20 UT, when MAVEN was in the undisturbed upstream solar wind. For most of this time period, θ_{UB} was ~50°, giving an E_{max} of ~120 keV. The elevated background noise in the SEP data is due to energetic particles associated with the ICME. Oxygen pickup ions detected by SEP during the ICME event have the highest energies observed since MAVEN's arrival at Mars.

Loss to space

We can compare planetary ion fluxes during the ICME event to those observed over many months as a means for assessing the likely impact of the ICME on atmospheric escape rates. In addition, we can calculate the escape rate using MHD models of the interaction of the solar wind with the planet and using measured solar-wind conditions as model inputs. Both show a substantial enhancement in the escape rate during the ICME event.

To determine the measured escape rate, we use STATIC (*30*) observations of heavy-ion fluxes

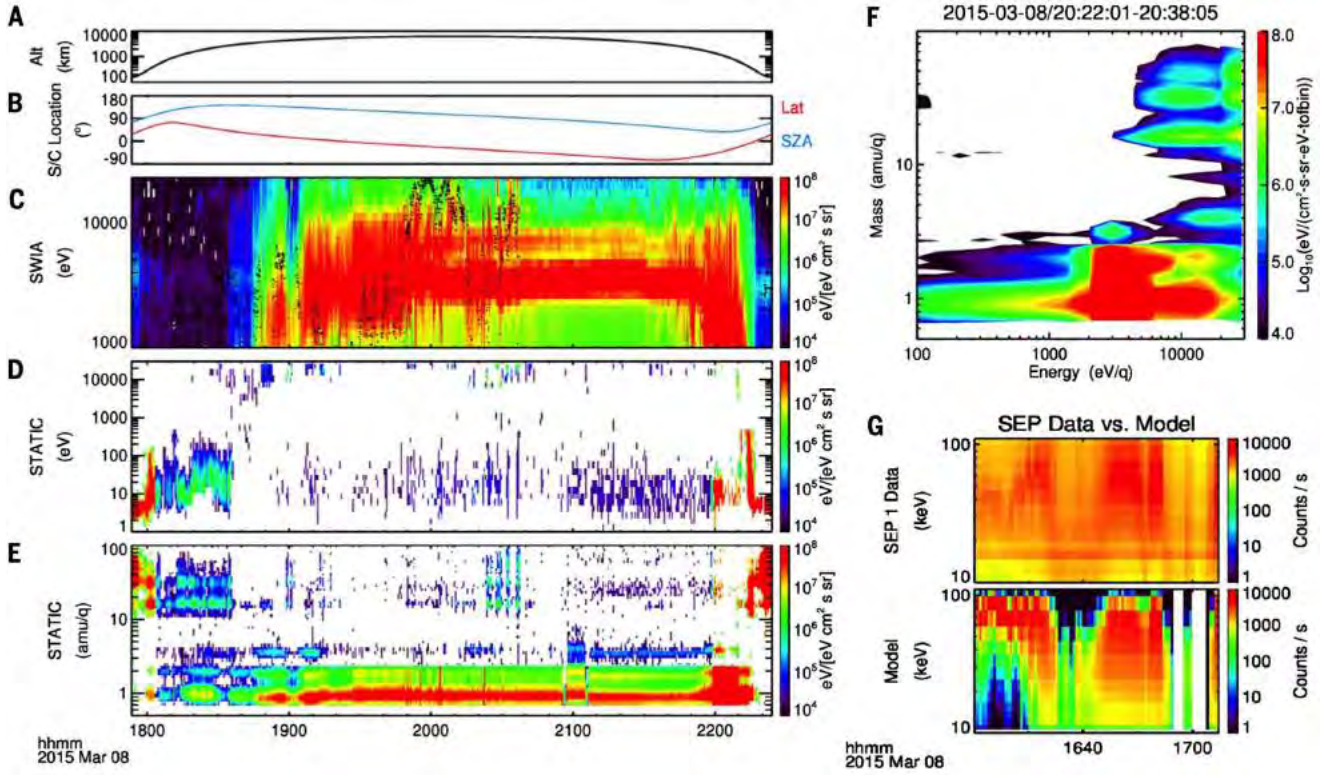

Fig. 3. MAVEN charged-particle observations reveal the presence of pick-up ions during the 8 March 2015 ICME. Observations from a single orbit are shown in (A) to (D). (**A**) Spacecraft altitude. (**B**) Spacecraft location given as latitude and solar zenith angle. (**C**) SWIA observations of ion energy fluxes as a function of energy, with the predicted energy of subsolar pickup ions given by the black trace. (**D**) STATIC observations of high-mass (>9 amu/q) ion energy fluxes as a function of energy. (**E**) STATIC observations of ion energy fluxes as a function of ion mass. (**F**) STATIC observations near periapsis of ion energy fluxes as a function of energy and mass simultaneously, showing both the low-mass solar wind and high-energy, high-mass pickup ions. (**G**) Observed and modeled SEP spectra for ~40 min during the beginning of the ICME passage, on the orbit prior to the one shown in (A) to (D).

during time periods when the spacecraft occupied altitudes between 0.25 and 0.45 planetary radii. At these altitudes, observations cover a large fraction of the sphere enclosing Mars, and the measurements provide a good estimate of the total escape. MAG and SWIA measurements of the IMF and solar-wind velocity, respectively, were used to rotate the spacecraft position into a Mars-Solar-Electric field (MSE) coordinate system, with MSE-x antiparallel to the incident solar-wind flow, MSE-y parallel to the IMF direction projected into the plane perpendicular to the flow, and MSE-z in the direction of the convection electric field given by $-\mathbf{V} \times \mathbf{B}$. Such a coordinate system is frequently used to organize escaping planetary ion fluxes [e.g., (*33*)], which should be strongly influenced by the electric field in the solar wind. Individual observations recorded when the instrument was in "pickup mode" (32 energy bins, 8 mass bins, and 64 look directions) were separated so that ion flux toward and away from the planet were tracked separately. We limit ourselves to energies greater than 25 eV, as the MAVEN data have not been corrected yet for the effects of spacecraft electric potential that can significantly influence the low-energy measurements. Inclusion of low-energy particles will increase both the reported fluxes and escape rates, with the consequence that we present lower limits here. Previous studies (*34*) have shown that reported escape rates depend at least partly on the energy range of ions being considered.

A comparison of fluxes during the ICME event (2015-03-08/16:00 to 2015-03-09/12:00) to median fluxes over a period of approximately 4 months is shown in Fig. 4. Because of uncertainties in the direction of the electric field during the turbulent ICME event, we show the results as a function of solar zenith angle. This comparison is valid independent of the electric-field direction. Most notable is the strong flux of planetary ions away from the planet on the dayside during the ICME, in a region usually dominated by the flow of ions toward the planet. These fluxes are among the strongest observed in this region during the entire mission. Nightside regions sampled during the ICME have fluxes more characteristic for their location, or even lower than is typical.

We cannot reliably provide a global escape rate during the ICME event based on these sparse observations alone, owing to the limited coverage over a short time period. However, it appears that escape rates on the nightside of the planet remained at values during the ICME that were similar to values at other times, and that dayside escape rates of planetary ions were enhanced considerably. Previous measurements of ion escape rates during ICMEs have been reported (*35*) and suggest that total escape rates can be 10 to 100 times greater during solar storm events.

The good agreement described earlier between the MHD model and MAVEN observations during the ICME event gives us confidence to use the model to infer the variations of the ion loss rate during the ICME passage. The integrated ion loss rates are listed in Table 1 using model results of the same three cases described earlier. Before the ICME arrival, the model predicted that the integrated escape rate was of the order of 1.5×10^{24}/s, dominated by O_2^+ ions. As the flow speed of the solar wind increased to more than 800 km/s shortly after the ICME arrival, the solar-wind dynamic pressure was about four times enhanced, and the model predicted that the total ion escape rate would increase to ~10^{25}/s, which is seven times larger than the ion loss rate during nominal conditions. When the solar-wind density and velocity were both enhanced, the corresponding solar-wind dynamic pressure increased to ~15 times, and the escape rate for case 3 reached 3×10^{25}/s, more than an order of magnitude enhancement. The major ions lost to space changed from O_2^+ (in both case 1 and 2) to O^+ ions in case 3. This model prediction is consistent with measurements made by STATIC, which detected a large increase in O^+ ion fluxes during the orbits after the ICME arrival. This increase is likely caused by enhancement of O^+ ion production through augmented electron-impact ionization and charge-exchange reactions

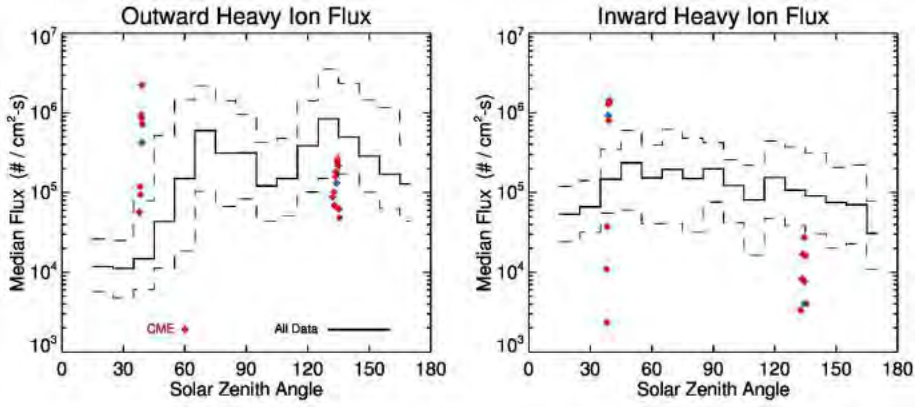

Fig. 4. Comparison of loss during ICME with integrated loss through the mission to date. Planetary heavy ion fluxes (>9 amu) measured by STATIC during the ICME event (red, with median value shown in blue) are shown in comparison to median and first/fourth quartile ion fluxes measured over a ~4 month period (gray traces). Fluxes are evaluated in a spherical shell around Mars from 1.25 to 1.45 R_M (radius of Mars), and the position of MAVEN is rotated into a coordinate system aligned with the solar wind electric field. During the ICME, strong outward flux is observed in regions of typically inward flow.

Table 1. Ion loss rates calculated by the MHD model for the three cases corresponding to three different stages of the ICME. *P*sw is the solar-wind pressure for the model run.

	P_{SW} (nPa)	O^+ (s^{-1})	O_2^+ (s^{-1})	CO_2^+ (s^{-1})	Total (s^{-1})	Total (kg/s)
Case 1	0.9	6.4×10^{23}	7.7×10^{23}	4.9×10^{22}	1.46×10^{24}	0.06
Case 2	3.4	2.6×10^{24}	7.6×10^{24}	3.3×10^{23}	1.06×10^{25}	0.50
Case 3	13.4	1.96×10^{25}	1.32×10^{25}	6.3×10^{23}	3.34×10^{25}	1.27

between solar-wind protons and neutral oxygen atoms, resulting from the intense electron and proton fluxes in the ICME.

Similarly, a multifluid MHD model (*36*, *37*) predicted more than an order-of-magnitude enhancement of the ion loss rates during extreme solar-wind conditions associated with the ICME. The multifluid model results were also used to examine the relative importance of the two major ion loss channels from the planet—energetic-ion loss through the dayside polar plume and cold-ion loss through the nightside plasma-wake region. Escape of ions from the dayside polar plume could be as much as ~30% prior to the ICME arrival. When solar-wind dynamic pressure was drastically intensified, the ratio of escape rates from the polar plume reduced to ~10%, and the cold ions escaping from the plasma wake made up most of the ion loss from the planet.

Both the observations and the model results suggest there are substantial enhancements in the ion loss rates during ICME events. The agreement of the models with the observations reinforces the interpretation and allows a global estimate of the increase of about an order of magnitude to be made. The ion loss reported here is only one means by which gas can be removed from the atmosphere. Particles can also be removed to space as neutrals. Neutral escape may prove to be the dominant loss channel, but observations are more difficult to interpret. These ion loss enhancements can thus be considered a lower limit on the escape enhancement.

The results obtained by MAVEN for this strong ICME event can be compared with previous measurements of ion escape at Mars during disturbed periods. These include case studies (*35*, *38*), and statistical studies during CIR events, solar maximum, and solar minimum periods (*39*–*42*). The compression of the magnetosphere in response to high dynamic pressure is consistent with observations of disturbed conditions presented in the studies cited above. Nearly all of these studies also suggest an increase in ion escape rates during disturbed periods, but differ in the degree to which they change. Our results are consistent with the case study presented by Futaana *et al.* (*35*), which estimated an order-of-magnitude increase in planetary ion fluxes (and thus escape) in response to an ICME event observed by Mars Express. By contrast, our results appear to be inconsistent with a recent statistical reanalysis of Mars Express observations that shows a decrease in escape rates in response to increased solar-wind density (*41*). Though the reason for the discrepancies between previous studies can include differences in data selection and analysis method, it seems likely that different events and different kinds of events induce responses of different magnitude at Mars. Constraining how ICME events influence ion escape is an important component for understanding escape rates from early Mars.

Conclusions and future observations

MAVEN observations show a major impact of the ICME observed in March 2015. The effects through the entire upper-atmosphere–ionosphere–magnetosphere system produced substantially disturbed conditions and appeared to have a major impact on the instantaneous rates of loss of ions to space. Given the likely prevalence of ICME-like conditions earlier in solar-system history (*43*), it is possible that ion escape rates at that time were dominated by storm events. As these early periods may have been the dominant times at which the martian atmosphere experienced loss, the inferred climate change on Mars may have been driven to a large extent by these solar storms.

The MAVEN spacecraft is continuing to collect observations. These ongoing observations will fill in the three-dimensional space surrounding Mars and allow us to better understand the processes occurring in the upper atmosphere and ionosphere and to observe the response to changing external forcing in the form of the changing solar EUV, solar wind, and solar storms. Ongoing observations also will show the response to the changing martian seasons, eventually allowing coverage of a full Mars year and beyond.

REFERENCES AND NOTES

1. M. H. Carr, Water on Mars. *Nature* **326**, 30–35 (1987). doi: 10.1038/326030a0
2. D. J. Des Marais, B. M. Jakosky, B. M. Hynek, Astrobiological implications of Mars surface composition and properties, in *The Martian Surface: Composition, Mineralogy, and Physical Properties*, J. F. Bell III, Ed. (Cambridge Univ. Press, Cambridge, 2008), 599–623.
3. B. M. Jakosky *et al.*, The Mars Atmosphere and Volatile Evolution (MAVEN) Mission. *Space Sci. Rev.* (2015). doi: 10.1007/s11214-015-0139-x
4. B. M. Jakosky, J. M. Grebowsky, J. G. Luhmann, D. A. Brain, Initial results from the MAVEN mission to Mars. *Geophys. Res. Lett.* 10.1002/2015GL065271 (2015).
5. S. Bougher *et al.*, Early MAVEN Deep Dip campaign reveals thermosphere and ionosphere variability. *Science* **350**, aad0459 (2015).
6. N. M. Schneider *et al.*, Discovery of diffuse aurora on Mars. *Science* **350**, aad0210 (2015).
7. L. Andersson *et al.*, Dust observations at orbital altitudes surrounding Mars. *Science* **350**, aad0398 (2015).
8. J. Gosling, The solar flare myth. *J. Geophys. Res.* **98**, 18937–18949 (1993). doi: 10.1029/93JA01896
9. J. E. P. Connerney *et al.*, The MAVEN magnetic field investigation. *Space Sci. Rev.* 10.1007/s11214-015-0169-4 (2015). doi: 10.1007/s11214-015-0169-4
10. J. S. Halekas *et al.*, The solar wind ion analyzer for MAVEN. *Space Sci. Rev.* 10.1007/s11214-013-0029-z (2013). doi: 10.1007/s11214-013-0029-z
11. D. H. Crider *et al.*, Mars Global Surveyor Observations of the Halloween 2003 solar Superstorm's Encounter with Mars. *J. Geophys. Res.* **110**, A09S21 (2005). doi: 10.1029/2004JA010881
12. D. L. Mitchell, C. Mazelle, J. P. McFadden, D. Larson, J. S. Halekas, J. E. P. Connerney, J. Espley, L. Andersson, J. G. Luhmann, R. J. Lillis, M. Fillingim, T. Hara, D. A. Brain, MAVEN observations of the Martian ionosphere and magneotheath [sic]. *Lunar Planet. Sci. Conf.*, abstract 3015, Houston, TX, 2015.
13. D. E. Larson, R. J. Lillis, P. A. Dunn, A. Rahmati, T. E. Cravens, K. Hatch, M. Robinson, D. Glaser, J. Chen, D. W. Curtis, C. Tiu, R. P. Lin, J. G. Luhmann, J. P. McFadden, J. Connerney, J. Halekas, B. M. Jakosky, The Solar Energetic Particle Experiment on MAVEN: First Results. *Lunar Planet. Sci. Conf.*, abstract 2890, Houston, TX, 2015.
14. F. Leblanc, J. G. Luhmann, R. Johnson, E. Chassefiere, Some expected impacts of a solar energetic particle event at Mars. *J. Geophys. Res.* **107**, 1058 (2002). doi: 10.1029/2001JA900178
15. S. W. Bougher, T. E. Cravens, J. Grebowsky, J. Luhmann, The aeronomy of Mars: Characterization by MAVEN of the upper atmospheric reservoir that regulates volatile escape. *Space Sci. Rev.* (2014). doi: 10.1007/s11214-014-0053-7

16. M. L. Mays *et al*., Ensemble modeling of CMEs using the WSA-ENLIL+Cone model. *Sol. Phys.* **290**, 1775–184 (2015). doi: 10.1007/s11207-015-0692-1
17. Y. Kamide, K. Kusano, No major solar flares but the largest geomagnetic storm in the present solar cycle. *Space Weather* **13**, 365–367 (2015). doi: 10.1002/2015SW001213
18. Y. Ma *et al*., Effects of crustal field rotation on the solar wind plasma interaction with Mars. *Geophys. Res. Lett.* **41**, 6563–6569 (2014). doi: 10.1002/2014GL060785
19. D. Vignes *et al*., The solar wind interaction with Mars: Locations and shapes of the bow shock and the magnetic pile-up boundary from the observations of the MAG/ER experiment onboard Mars Global Surveyor. *Geophys. Res. Lett.* **27**, 49–52 (2000). doi: 10.1029/1999GL010703
20. M. H. Acuña *et al*., Magnetic field and plasma observations at Mars: Initial results of the Mars Global Surveyor Mission. *Science* **279**, 1676–1680 (1998). doi: 10.1126/science.279.5357.1676; pmid: 9497279
21. C. T. Russell, R. C. Elphic, Observation of magnetic flux ropes in the Venus ionosphere. *Nature* **279**, 616–618 (1979). doi: 10.1038/279616a0
22. P. A. Cloutier *et al*., Venus-like interaction of the solar wind with Mars. *Geophys. Res. Lett.* **26**, 2685–2688 (1999). doi: 10.1029/1999GL900591
23. D. A. Brain *et al*., Episodic detachment of Martian crustal magnetic fields leading to bulk atmospheric plasma escape. *Geophys. Res. Lett.* **37**, L14108 (2010). doi: 10.1029/2010GL043916
24. T. Hara *et al*., The spatial structure of Martian magnetic flux ropes recovered by the Grad-Shafranov reconstruction technique. *J. Geophys. Res.* **119**, 1262–1271 (2014). doi: 10.1002/2013JA019414
25. W. E. McClintock *et al*., The Imaging Ultraviolet Spectrograph (IUVS) for the MAVEN Mission. *Space Sci. Rev.* 10.1007/s11214-014-0098-7 (2014). doi: 10.1007/s11214-014-0098-7
26. M. S. Chaffin *et al*., Three dimensional structure of the Mars H corona revealed by IUVS on MAVEN. *Geophys. Res. Lett.* 10.1002/2015GL065287 (2015).
27. C. Barth, A. I. Stewart, C. W. Hord, A. L. Lane, Mariner 9 ultraviolet spectrometer experiment: Mars airglow spectroscopy and variations in Lyman alpha. *Icarus* **17**, 457–468 (1972). doi: 10.1016/0019-1035(72)90011-5
28. J.-L. Bertaux *et al*., Discovery of an aurora on Mars. *Nature* **435**, 790–794 (2005). doi: 10.1038/nature03603; pmid: 15944698
29. S. Curry, M. Liemohn, X. Fang, Y. Ma, J. Espley, The influence of production mechanisms on pick-up ion loss at Mars. *J. Geophys. Res.* **118**, 554–569 (2013). doi: 10.1029/2012JA017665
30. J. P. McFadden, R. Livi, J. Luhmann, J. Connerney, D. Mitchell, C. Mazelle, L. Andersson, B. Jakosky, Structure of the martian ionosphere and atmospheric loss: MAVEN STATIC first results. *Lunar Planet. Sci. Conf.*, abstract 2899 (2015).
31. H. Nilsson *et al*., Birth of a comet magnetosphere: A spring of water ions. *Science* **347**, aaa0571 (2015). doi: 10.1126/science.aaa0571; pmid: 25613894
32. A. Rahmati *et al*., Pickup ion measurements by MAVEN: A diagnostic of photochemical oxygen escape from Mars. *Geophys. Res. Lett.* **41**, 4812–4818 (2014). doi: 10.1002/2014GL060289
33. S. Barabash, A. Fedorov, R. Lundin, J. A. Sauvaud, Martian atmospheric erosion rates. *Science* **315**, 501–503 (2007). doi: 10.1126/science.1134358; pmid: 17255508
34. E. Dubinin *et al*., Ion energization and escape on Mars and Venus. *Space Sci. Rev.* **162**, 173–211 (2011). doi: 10.1007/s11214-011-9831-7
35. Y. Futaana *et al*., Mars Express and Venus Express multi-point observations of geoeffective solar flare events in December 2006. *Planet. Space Sci.* **56**, 873–880 (2008). doi: 10.1016/j.pss.2007.10.014
36. D. Najib, A. F. Nagy, G. Tóth, Y. Ma, Three-dimensional, multifluid, high spatial resolution MHD model studies of the solar wind interaction with Mars. *J. Geophys. Res.* **116**, A05204 (2011). doi: 10.1029/2010JA016272
37. C. Dong *et al*., Solar wind interaction with the Mars upper atmosphere: Results from the one-way coupling between the multifluid MHD model and the MTGCM model. *Geophys. Res. Lett.* **41**, 2708–2715 (2014). doi: 10.1002/2014GL059515
38. E. Dubinin *et al*., Ionospheric storms on Mars: Impact of corotating interaction region. *Geophys. Res. Lett.* **36**, L01105 (2009). doi: 10.1029/2008GL036559
39. N. J. T. Edberg *et al*., Pumping out the atmosphere of Mars through solar wind pressure pulses. *Geophys. Res. Lett.* **37**, L03107 (2010). doi: 10.1029/2009GL041814
40. R. Ramstad *et al*., Phobos 2/ASPERA data revisited: Planetary ion escape rate from Mars near the 1989 solar maximum. *Geophys. Res. Lett.* **40**, 477–481 (2013). doi: 10.1002/grl.50149
41. R. Ramstad *et al*., The Martian atmospheric ion escape rate dependence on solar wind and solar EUV conditions: 1. Seven years of Mars Express observations. *J. Geophys. Res.* **120**, 1298–1309 (2015). doi: 10.1002/2015JE004816
42. H. Nilsson *et al*., Heavy ion escape from Mars, influence from solar wind conditions and crustal magnetic fields. *Icarus* **215**, 475–484 (2011). doi: 10.1016/j.icarus.2011.08.003
43. B. Wood, H.-R. Müller, G. P. Zank, J. L. Linsky, S. Redfield, New Mass-loss measurements from Astrospheric Ly-a absorption. *Astrophys. J.* **628**, L143–L146 (2005). doi: 10.1086/432716

ACKNOWLEDGMENTS

The results presented here represent the work of hundreds of scientists and engineers who designed, built, and operated the spacecraft and instruments and carried out the scientific analyses. We are indebted to them beyond words. The MAVEN mission has been funded by NASA through the Mars Exploration Program. Additional support was provided by CNES for the SWEA instrument and analysis, and by the Belgian American Educational Foundation. Part of this research was carried out at the Jet Propulsion Laboratory, California Institute of Technology, under a contract with the National Aeronautics and Space Administration. M. L. Mays and D. Odstrcil provided valuable analysis with the WSA-ENLIL+Cone model. Data from the MAVEN mission have been made available via the Planetary Data System (accessible via http://atmos.nmsu.edu/data_and_services/atmospheres_data/MAVEN/maven_main.html).

15 July 2015; accepted 18 September 2015
10.1126/science.aad0210

MAVEN observations of the response of Mars to an interplanetary coronal mass ejection

B. M. Jakosky, J. M. Grebowsky, J. G. Luhmann, J. Connerney, F. Eparvier, R. Ergun, J. Halekas, D. Larson, P. Mahaffy, J. McFadden, D. L. Mitchell, N. Schneider, R. Zurek, S. Bougher, D. Brain, Y. J. Ma, C. Mazelle, L. Andersson, D. Andrews, D. Baird, D. Baker, J. M. Bell, M. Benna, M. Chaffin, P. Chamberlin, Y.-Y. Chaufray, J. Clarke, G. Collinson, M. Combi, F. Crary, T. Cravens, M. Crismani, S. Curry, D. Curtis, J. Deighan, G. Delory, R. Dewey, G. DiBraccio, C. Dong, Y. Dong, P. Dunn, M. Elrod, S. England, A. Eriksson, J. Espley, S. Evans, X. Fang, M. Fillingim, K. Fortier, C. M. Fowler, J. Fox, H. Gröller, S. Guzewich, T. Hara, Y. Harada, G. Holsclaw, S. K. Jain, R. Jolitz, F. Leblanc, C. O. Lee, Y. Lee, F. Lefevre, R. Lillis, R. Livi, D. Lo, M. Mayyasi, W. McClintock, T. McEnulty, R. Modolo, F. Montmessin, M. Morooka, A. Nagy, K. Olsen, W. Peterson, A. Rahmati, S. Ruhunusiri, C. T. Russell, S. Sakai, J.-A. Sauvaud, K. Seki, M. Steckiewicz, M. Stevens, A. I. F. Stewart, A. Stiepen, S. Stone, V. Tenishev, E. Thiemann, R. Tolson, D. Toublanc, M. Vogt, T. Weber, P. Withers, T. Woods and R. Yelle

(November 5, 2015)
Science **350** (6261), . [doi: 10.1126/science.aad0210]

Editor's Summary

Planetary and Space Science xxx (xxxx) xxx–xxx

Contents lists available at ScienceDirect

Planetary and Space Science

journal homepage: www.elsevier.com/locate/pss

The LatHyS database for planetary plasma environment investigations: Overview and a case study of data/model comparisons

R. Modolo[a,*], S. Hess[b], V. Génot[c], L. Leclercq[a,d], F. Leblanc[e], J.-Y. Chaufray[e], P. Weill[e], M. Gangloff[c], A. Fedorov[c], E. Budnik[f], M. Bouchemit[c], M. Steckiewicz[c], N. André[c], L. Beigbeder[g], D. Popescu[g], J.-P. Toniutti[g], T. Al-Ubaidi[h], M. Khodachenko[h], D. Brain[i], S. Curry[j], B. Jakosky[i], M. Holmström[k]

[a] LATMOS/IPSL, UVSQ Université Paris-Saclay, UPMC University Paris CNRS, Guyancourt, France
[b] ONERA, Toulouse, France
[c] Université de Toulouse, UPS-OMP, IRAP, France
[d] Materials Science and Engineering Department, University of Virginia, Charlottesville, VA22904, USA
[e] LATMOS/IPSL, UPMC University Paris 06 Sorbonne Universités, UVSQ, CNRS, Paris, France
[f] Noveltis, Labege, France
[g] GFI, Toulouse, France
[h] Space Research Institute, Austrian Academy of Science, Austria
[i] LASP, Univ. of Colorado, Boulder, CO, USA
[j] SSL, Univ. of Berkeley, Berkeley, CA, USA
[k] IRF, Kiruna, Sweden

ARTICLE INFO

Keywords:
Mars
Numerical modeling
Solar wind interactions with unmagnetized bodies
Data management

ABSTRACT

We present the Latmos Hybrid Simulation (LatHyS) database, which is dedicated to the investigations of planetary plasma environment. Simulation results of several planetary objects (Mars, Mercury, Ganymede) are available in an online catalogue. The full description of the simulations and their results is compliant with a data model developped in the framework of the FP7 IMPEx project. The catalogue is interfaced with VO-visualization tools such AMDA, 3DView, TOPCAT, CLweb or the IMPEx portal. Web services ensure the possibilities of accessing and extracting simulated quantities/data. We illustrate the interoperability between the simulation database and VO-tools using a detailed science case that focuses on a three-dimensional representation of the solar wind interaction with the Martian upper atmosphere, combining MAVEN and Mars Express observations and simulation results.

1. Introduction

During fifty years of space exploration, several planetary magnetospheres have been explored, leading to a large amount of scientific data. More recently, several space missions, or multi-spacecraft missions, are (or will be) operating simultaneously in the vicinity of various celestial bodies, providing multi-point information. The development of an infrastructure which allows the combination of several data sets from different space missions represents a major step forward for the understanding of the solar wind interaction with planetary environments. The Virtual Observatory (VO) interoperable standards developed for Astronomy by the International Virtual Observatory Alliance (IVOA) can be adapted to Planetary Sciences and give such powerful capabilities.

In addition, modeling efforts have been conducted to support the analysis of space plasma data and to give a three-dimensional context of the observations. A global hybrid simulation model, called LatHyS (Modolo et al., 2016), was developped to describe the interaction between an incoming plasma (the solar wind or a magnetospheric plasma) and planets and moons. Some of the simulation results are described and archived in our simulation database. The simulation database on planetary plasma environments has been developped during the FP7 Integrated Medium for Planetary Exploration - IMPEx project (Khodachenko et al., 2011). The aim of the project is to create an interactive framework where data from planetary missions are interconnected with numerical models providing a variety of possibilities for an external user such as simulating planetary phenomena and interpreting space missions measurements, testing models versus

* Corresponding author.
E-mail address: ronan.modolo@latmos.ipsl.fr (R. Modolo).

http://dx.doi.org/10.1016/j.pss.2017.02.015
Received 30 November 2016; Received in revised form 14 February 2017; Accepted 26 February 2017

experimental data, filling gaps in the measurement by appropriate modeling runs or performing preparation of specific mission operations.

The present paper reports on the description of the simulation database and presents the different steps to perform a model-observation comparison with VO visualization tools. The paper is organized as follow: a brief introduction of the LatHyS model and its simulation database is discussed in Section 2. A science case focusing on the solar wind interaction with the Martian environment is presented in detail in Section 3.

2. The LatHyS model and database

During the last fifteen years, we have conducted a modeling effort to develop, parallelize and implement various physical processes in the global simulation model called LatHyS (Latmos Hybrid Simulation, (Modolo et al., 2016)) to describe the plasma interaction with planetary environments. The model is based on the so called “hybrid” formalism where ions are described by a set of numerical particles (called macro-particles) with adjustable weight while electrons are represented by an inertialess fluid conserving the charge neutrality of the plasma. Ions and electrons are coupled via the electromagnetic field. The temporal evolution of electromagnetic fields and the motion of charged particles are computed self-consistently retaining kinetic effects for ions, which is of prime importance for understanding the interaction of an incident plasma and the upper atmosphere/surface of certain bodies in the solar system (e.g. Modolo et al., 2005). This simulation model describes the dynamic and the structure of the ionized environment in the neighborhood of these bodies and characterizes the atmospheric erosion while distinguishing processes responsible for this escape. The model, initially developed to describe the Martian plasma environment (Modolo et al., 2005, 2006, 2012, 2016), has been adapted to describe Titan (Modolo et al., 2007; Modolo and Chanteur, 2008), Mercury (Richer et al., 2012) and Ganymede's environment (Leclercq et al., 2016) and to model a magnetic cloud interaction with a terrestrial bow shock (Turc et al., 2015).

Besides the kinetic description advantages, this hybrid model stands out for several strengths:

- A multi-species description of the plasma. Such a model allows describing the dynamics of several ion species for both incident and planetary plasmas. These populations differ not only in chemical identity but also from their properties (density, speed, temperature, …).
- The possibility of taking into account the energetic population of Saturn and Jupiter magnetopsheric plasma (i.e. introducing an energetic population which make an important contribution to the magnetospheric total pressure).
- Taking into account self-consistently the charge exchange interaction between neutral and ions.
- The possibility of describing non-Maxwellian velocity distribution functions, for instance related to acceleration processes
- Many physical processes, such as ionosphere conductivities, ionneutral collisions, local production calculation, two electronic fluids,…are taken into account.
- It is a generic multi-object parallelized model.

The hybrid formalism, its hypothesis and limitation, are described in detail in Kallio et al. (2011) and Ledvina et al. (2008).

A project including simulation archiving and dissemination of simulation results has been undertaken in the frame of the FP7 IMPEx IMPEx (#262863, 2011–2015, (Khodachenko et al., 2011) http://impex-fp7.oeaw.ac.at/). Simulation results are publically available on our web-interface (http://impex.latmos.ipsl.fr/LatHyS.htm) and are interoperable with powerfull visualization tools through webservices. Simulation results can be displayed with VO-tools like TOPCAT (http://www.star.bris.ac.uk/~mbt/topcat/), AMDA (http://amda.cdpp.eu/), 3DView (http://3dview.cdpp.eu/), CLweb (http://clweb.irap.omp.eu/) or the IMPEx portal (http://impex-portal.oeaw.ac.at/#/portal).

In this context, the development of a Data Model (i.e. a set of XML dictionary and grammar) has been developped by the IMPEx team (Hess et al., 2013). The Data Model is used to produce metadata which are parsable by automated tools. This Data Model extends the SPASE-Data Model (http://www.spase-group.org/), which is widely used to describe observations and measurements in the solar and space plasma domains and the IMPEx extensions are now fully integrated in the last version of the SPASE data model.

To ensure access to the simulation catalogue and simulation products, we used the IMPEx data model to completely describe the simulations and their results. Two files are required to communicate with visualization tools.

The “Tree.xml” consists of a complete description of each simulation and data files stored in the simulation database (SMDB). It provides all the information required to fully describe simulation runs, inputs, and quantities available as well as the different IMPEx data products.

The LatHyS web interface allows the interactive exploration of the simulation catalogue. It allows parsing the simulation resources to display several information types such as the data products available (3D cubes, 2D cut and 1D time series) for the selected simulation run as well as basic input description concerning the selected run. For all archived simulations, pre-computed products are available. It includes the following simulation results:

- IonComposition (information for density, velocity and temperature of ion species tracked in the simulation)
- MagneticField (3 components of the magnetic field)
- ElectricField (3 components of the electric field)
- ThermalPlasma (electron density, plasma bulk velocity, electron temperature)

“Run Information” is displayed when one simulation product is selected.

Several functionalities are implemented in the LatHyS web interface:

- The ability to download the simulation file
- The ability to activate the SAMP (Simple Application Message Protocol) functionality. This functionality allows transferring a selected 2D or 1D product into visualization tools like AMDA or TOPCAT.
- A “Send” Application which sends the data file as a VOTable into TOPCAT.

The LatHyS webpage provides different information: documentation of the hybrid simulation model, the schema documentation as well as the user's guide for the data model implementation.

In addition to static data products, we developed web services to access quantities/data which are not pre-computed but can be generated with the available simulation runs. The web service technology is a standardized method of machine-to-machine communication over the internet.

The list of web-services available and implemented in SMDB is described in the “Methods.xml” file. This file describes the services that are implemented by the SMDB and gives information about how to request a data set and return a data product. The “Methods.xml” is described in a machine-processable format (WSDL, Web Services Description Language which is an XML language). The interface defines all services (methods) that the server provides along with all necessary input and output format descriptions. The 3D, 2D or 1D data products which are not stored in the LatHyS database, e.g. a 2D cut different from the pre-computed archived 2D cuts, IMPEx tools (AMDA and/or 3DView, CLWeb, IMPEx Portal) can request the information through a

webservice. The eight available webservices are:

1. getFileURL ⇒ This method returns the URL/granule of a data product.
2. getDataPointValue ⇒ This a generic method which can be used to determine and to return a simulated quantity for 0D (a given point), 1D (along a curve/trajectory), 2D (in a plane) or 3D (inside a volume) specified input.
3. getDataPointValueSpacecraft ⇒ This method extracts and returns the physical simulation parameters along a specified spacecraft trajectory.
4. getSurface ⇒ This method (a) generates a 2D regular mesh defined by a specified point and a normal vector, and (b) computes and returns a specified simulated quantity on this mesh.
5. getFieldLine ⇒ This method computes and returns field or flow lines for requested positions or passing through the spacecraft track.
6. getDataPointSpectra ⇒ This method computes and returns ion spectra for a requested positions in 0D (a given point), 1D (along a curve/trajectory).
7. getDataPointSpectraSpacecraft ⇒ This method computes and returns ion spectra along a specified spacecraft track.
8. isAlive ⇒ This method returns the status of the database (alive or not).

An additional web sersice, getMostRelevantRun, will be developped and will help selecting the most relevant simulation according to specified inputs.

Fig. 1 shows a schematical description of one of the web services. A full documentation of LATMOS webservices are provided online as an XML documentation (http://impex.latmos.ipsl.fr/Methods_LATMOS.html) and through the IMPEx technical documentation (http://impex-fp7.oeaw.ac.at/fileadmin/user_upload/pdf/ListofWebservices_for_LATMOS_v1.0.pdf).

3. Science case: comparison of space plasma observations from MAVEN/Mars Express and global hybrid simulation results using VO-tools AMDA, 3DView, TOPCAT

The goal of this science case is to use simultaneous plasma observations from MAVEN and Mars Express in the Martian environment and compare them to modeling results with VO tools.

3.1. Multi-spacecraft space plasma observations at Mars

Mars Express (MEX) has been exploring the Martian environment since December 2003, providing unprecedented results on the Martian plasma environment and its ionized escaping flux (eg Barabash et al., 2007; Nilsson et al., 2011). Recently, with the Mars orbit insertion of Mars Atmosphere Volatile and EvolutioN (MAVEN) in September 2014 (Jakosky et al., 2015), two spacecraft equipped with plasma instruments are probing the different regions and plasma boundaries of the planet. It is therefore a unique opportunity to understand the global structure of the solar wind plasma interaction with the upper atmosphere. As an example we examine here bow shock positions observed by both spacecraft and we compare them with the average BS location determined from an empirical fit (Edberg et al., 2008). To identify bow shock crossings observed by MAVEN and MEX, we use the Automated Multi-Dataset Analysis tool (AMDA, http://amda.cdpp.eu, (Jacquey et al., 2010; Génot et al., 2010)). Among the various functionalities, AMDA allows time series visualization of plasma data sets which are available in national space mission archives like NASA PDS (Planetary Data System), ESA PSA (Planetary Science Archive), and other (observation or modeling) data centers. Fig. 2 presents some of the MAVEN and MEX observations on December 10, 2014. From top to bottom, Fig. 2 shows the total magnetic field measured by MAVEN (Connerney et al., 2015), MAVEN ion spectrograms measured by the Supra-Thermal Analyzer and Thermal Ion Composition-STATIC (McFadden et al., 2015), the distance between Mars and MAVEN/MEX, and the electron and proton spectrograms from MEX (Barabash et al., 2004). During this day, MAVEN has went through five almost identical orbits, exploring different regions such as the solar wind, the magnetosheath, the induced magnetosphere and the ionosphere and crossing plasma boundaries (eg. the bow shock and the induced magnetosphere boundary). Similarly, MEX has perfomed about three equal orbits, exploring the same regions and boundaries. The quasi-periodic signatures are associated to the repeated orbits. Small scale differences are attributed to responses of the Martian environment to external driver variations.

From the MAG measurements, we can easily determine the signature of the bow shock through its sharp jump in the total magnetic field, suggesting a quasi-perpendicular shock. Coincidentally, the bow shock signature on electron and ion spectrograms corresponds to the thermalisation of the charged particles, where electrons/ions temperature goes from a few eV to hundreds of eV (or reciprocally). A list (a time table) of BS crossings from both spacecraft is reported in Table 1. It is possible to store this time table in AMDA and to use it with other VO-tools.

In order to determine if the locations of these BS crossings coincide with their average positions we use the 3DView visualization tool (Génot et al., 2016). This tool provides a 3D orbit visualization in maneuverable scenes but it is also possible to enrich the scene with

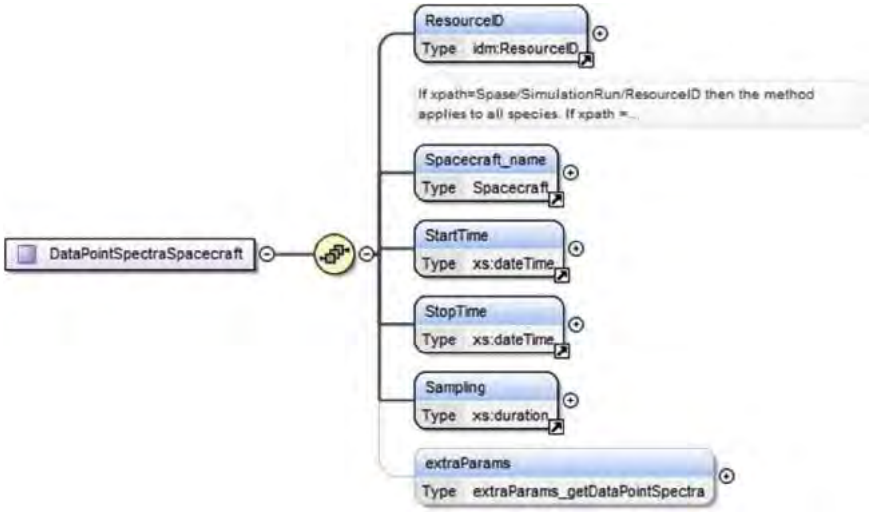

Fig. 1. Diagram representation of the method getDataPointSpectraSpacecraft.

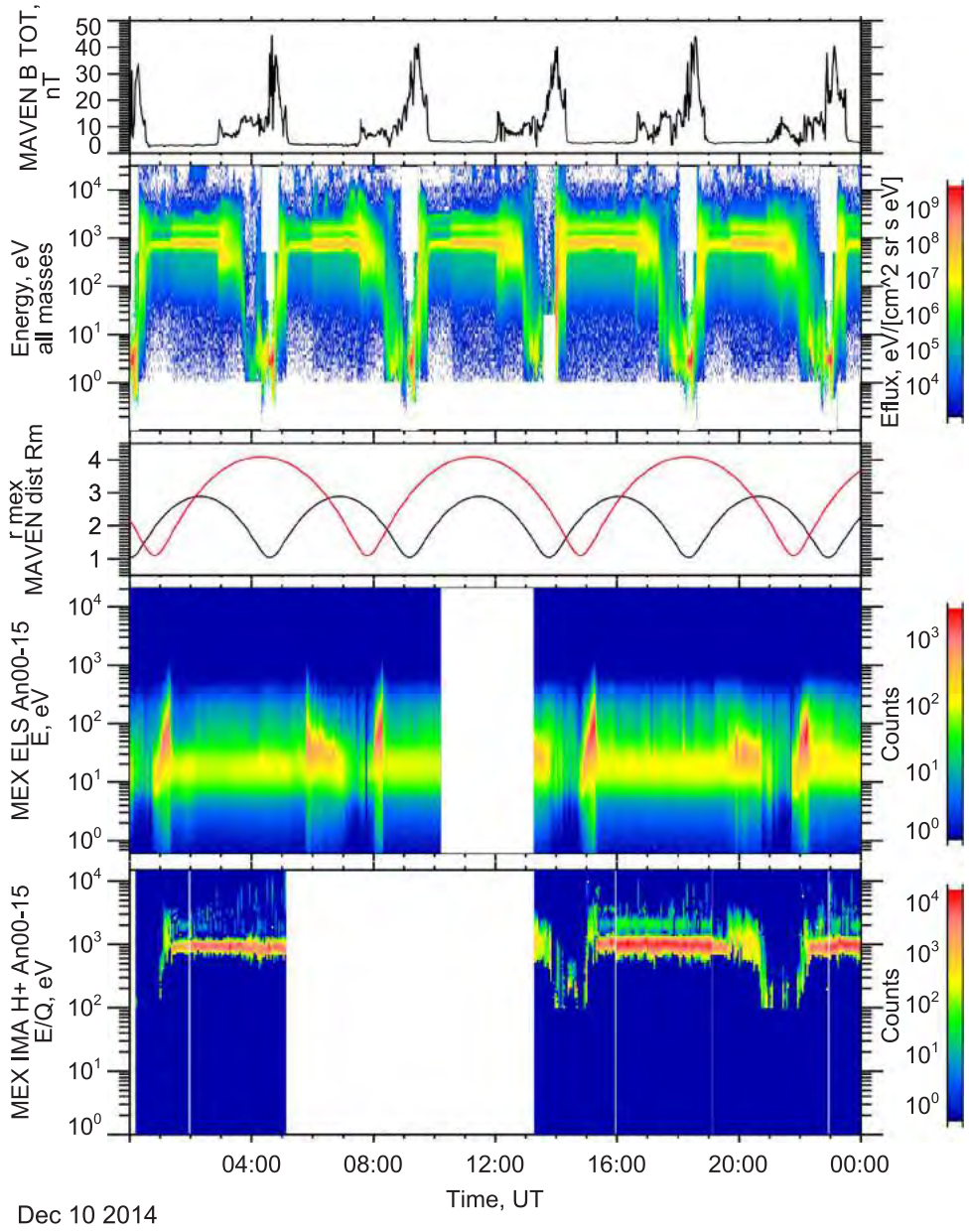

Fig. 2. MAVEN and MEX observations on December 10th, 2014. Panels a and b display MAVEN observations such as the total magnetic field (MAG) and the STATIC ion spectrogram (C0 data product). Panel c indicates the distance between MAVEN (MEX) and Mars in Martian radii (in black, respectively red, curve). Panels d and e presents observations from MEX with electron (ASPERA-ELS) and proton (ASPERA-IMA) spectrograms.

Table 1
Time table (UT) of expected (model) and observed (MAVEN/MEX) bow shock crossings on December 10th, 2014.

MAVEN		MEX	
Obs.	Model	Obs.	Model
~00:31	00:34	~01:19	01:18
~02:56	03:02	~05:47	05:48
~05:08	05:10	~08:18	08:18
~07:34	07:32	~15:16	15:16
~09:45	09:44	~19:52	19:44
~12:08	12:08	~22:16	22:18
~14:18	14:18		
~16:40	16:42		
~18:51	18:54		
~21:22	21:16		
~23:29	23:30		

observations, models and simulation results. Fig. 3 displays such functionality where both spacecraft trajectories are plotted with a 3D representation of the average BS location (Edberg et al., 2008). The intersections between spacecraft orbits and the empirical BS position can be automatically detected and are identified by red dots in Fig. 3. The time evolution of the scene enables the determination of the expected times of BS crossings from both spacecraft. These times are reported in Table 1. Observed and expected times are relatively close each other, suggesting that solar wind parameters were close to average values.

To ease the comparison between observed and expected BS crossings, orbit segments where observed BS crossing occurred are displayed in blue for MEX and green for MAVEN. The visualization of such orbit segments, corresponding to spacecraft positions for the AMDA time tables, are shown in the 3DView menu bar (Science/Remote data), once the user has connected AMDA with 3DView (Interoperability/AMDA login). Fig. 3 shows that orbit segments almost coincide with predicted

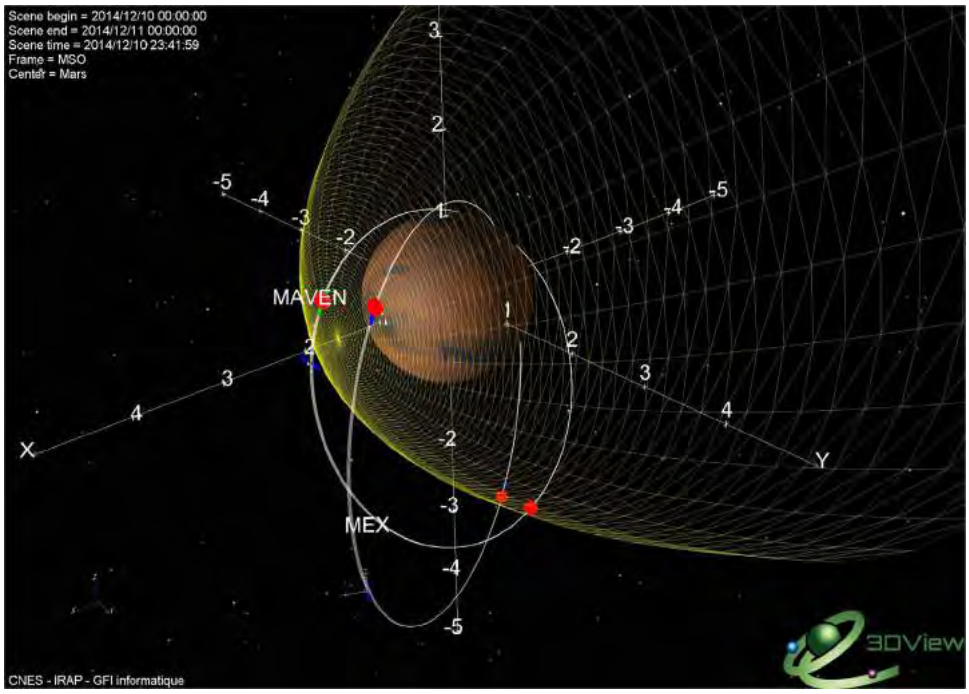

Fig. 3. Three dimensional scene of MAVEN and MEX orbits. The average BS location from Edberg et al. (2008) is identified by the yellow mesh structure. The intersection between the empirical BS and spacecrafts trajectories are indicated by red points. Observed BS locations are displayed by blue (MEX) and green (MAVEN) orbit segments.

BS crossings.

3.2. Comparison of global simulation results with in situ observations

To further investigate the three-dimensional aspect of the solar wind interaction with the Martian environment, simulation results from LatHyS model are used to highlight the context of the observations and to reveal their three-dimensional setting. Comparisons between MAVEN observations and LatHyS simulation results can be quickly obtained from AMDA, 3DView and the LatHyS database. These allow us to perform part of the investigation done by Ma et al. (2015), focusing on a comparison between MHD simulation results and MAVEN observations. The different steps are detailed below.

3.2.1. Finding the most relevant simulation

In order to compare simulation results with observations, we need to determine among the different simulations available in the catalogue the most relevant one (RunID). By relevant we mean the simulation having input conditions as close as possible to the observational conditions. The solar wind parameters (magnetic field direction and amplitude, the bulk velocity and proton density) are probably the most influential at global scales. AMDA and TOPCAT provide useful functionalities to derive average solar wind quantities. On AMDA, the user can select one MAVEN orbit providing the start and stop time, e.g. from 2014/12/10 15:30 to 19:30 UT (orbit 385–386), and plot the magnetic field component (MAG), the solar wind ion density, velocity components and temperature from the Solar Wind Ion Analyzer - SWIA (Halekas et al., 2015) during the selected time interval.

Thanks to the AMDA implementation of the SAMP application (Génot et al., 2014), it is possible to download the data (with all the data in one file) and to send this file to TOPCAT in VOTable format. After the reception of this file in TOPCAT, the user can edit the table and re-arrange the different columns such that each 3-element array becomes 3 scalar columns. This step is required to manipulate and visualize the vector component of the magnetic field, velocity and the diagonal terms of the temperature tensor. TOPCAT enables the creation of new quantities, determined from a combination of columns/quantities. The user is therefore able to create new parameters, for instance the bulk plasma speed and temperature. The determination of average solar wind parameters requires first finding the time period when MAVEN is in the undisturbed solar wind region. An algebraic criterion based on a combination of initial or newly created quantities/columns is used to determine a data subset. As an example, we can consider MAVEN to be in the solar wind region when $|U| > 350$ km/s and $T < 50$ eV. For the time interval considered, and with this solar wind detection criterion, we found that MAVEN has spent 38% of its time in the solar wind. Using the statistical functions of TOPCAT on the solar wind parameters, applied to the solar wind region subset, we can determine the average solar wind conditions (Table 2).

The interplanetary magnetic field direction is quite variable during this orbit (Table 2) therefore a static simulation run would not be able to reproduce the responses of the Martian environment to short scale variations. In addition, due to the rotation of the planet, crustal field locations will change from orbit to orbit while for the simulation the crustal fields are fixed during the simulation. Parsing the simulation catalogue either on the LatHyS web-interface or on AMDA, we can determine the simulation run with input solar wind parameters closest to the MAVEN average solar wind values. The RunID of the identified run is LatHyS_Mars_14_03_14. The solar wind parameters for this simulation run are the following: a solar wind density of 4.2 cm^{-3} with 5% of He^{++}, a bulk speed of 400 km/s along the $-X_{MSO}$ direction ($U_y = U_z = 0$ km/s), and an interplanetary magnetic field

Table 2
Average solar wind parameters for the MAVEN orbit 385–386 (2014/12/10 15:30 - 19:30 UT).

$n_{sw} = 4.0 \pm 0.4$ cm^{-3}	$T_{sw} = 26.8 \pm 2.2$ eV
$\overrightarrow{B_{IMF}} = (-0.9, 2.7, 0.1) \pm (1.6, 1.2, 2.1)$ nT	$\vec{U} = (-409.8, 24.0, -6.6) \pm (12.1, 9.1, 16.0)$ km/s

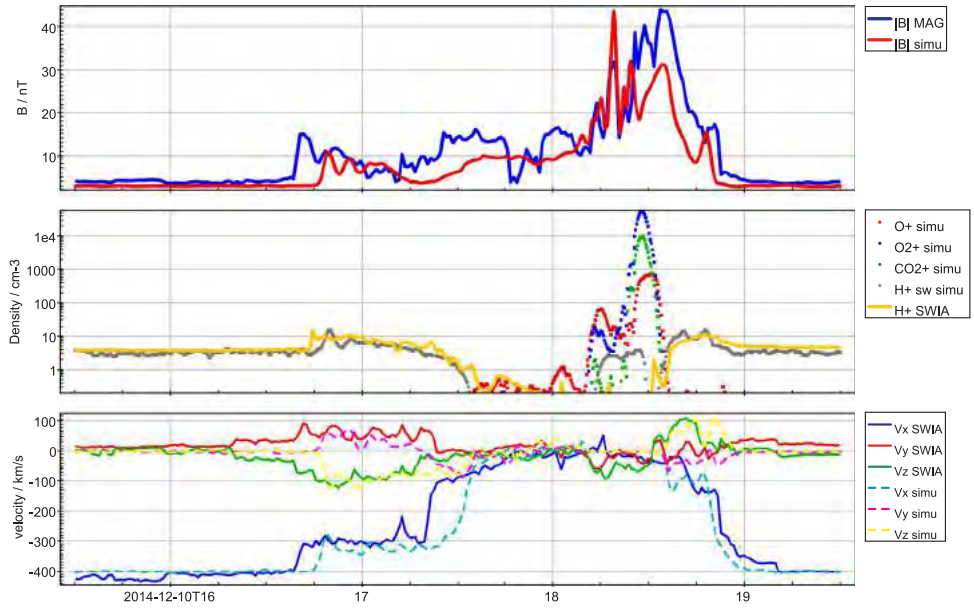

Fig. 4. Comparison between simulations results and MAVEN observations from 15:30 to 19:30 UT. From top to bottom, the first panel displays the total magnetic field, the second panel shows the ion density while the last panel shows the velocity components.

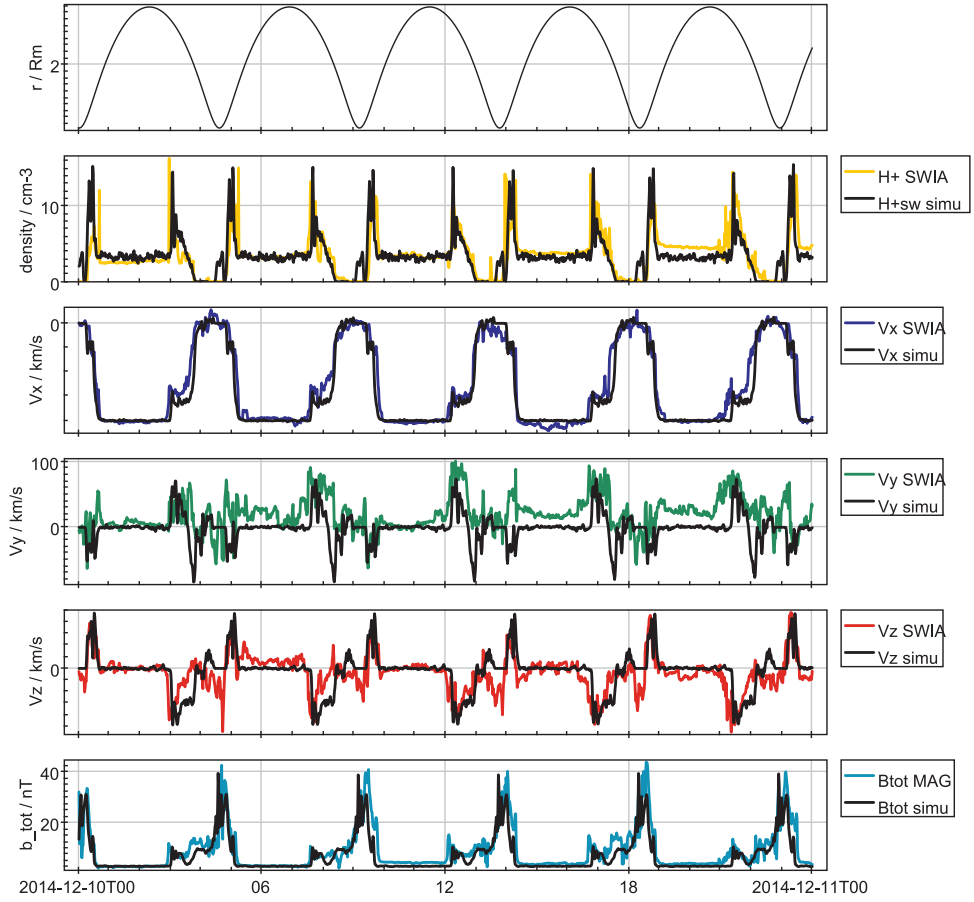

Fig. 5. MAVEN observations and simulation results on December 10th, 2014. From top to bottom: Mars-MAVEN distance in Martian radii, the proton density determined from SWIA (yellow) and the simulated solar wind proton density (black), the next three panels represent the plasma velocity components measured by SWIA (in color) and simulated (in black), and the last panel displays the total magnetic field measured by MAG (in cyan) and simulated (in black).

$\overrightarrow{B_{IMF}} = (-1.6, 2.5, 0)$ nT. The spatial resolution of the simulation is 80 km. The upper atmosphere and exosphere is composed of the CO_2, O and H with a fixed density profile and assuming a spherical symmetry (Brain et al., 2010; Modolo et al., 2016).

3.2.2. Comparing simulation results with MAVEN and MEX

A time series comparison between simulation results and observations can be obtained with AMDA. To achieve it, AMDA uses the web service getDataPointValueSpacecraft. The data can either be visualized in AMDA or sent to TOPCAT. Fig. 4 shows a comparison between

Table 3
Pearson's correlation coefficient determined between MAVEN observation and simulation results for proton density, velocity and total magnetic field.

$r(n_{H^+}) = 0.67$	$r(V_x) = 0.96$
$r(V_y) = 0.36$	$r(V_z) = 0.64$
$r(B_{tot}) = 0.85$	

MAVEN SWIA and MAG observations from 15:30 to 19:30 UT.

The LatHyS model is able to reproduce most of the regions and boundaries explored by the spacecraft and an overall reasonable agreement is found between observations and model results. However the simulated BS is slightly closer to the planet both in the inbound and outbound pass. An inappropriate profile for hydrogen exospheric density might contribute to underestimating the mass loading in the induced magnetosphere region and therefore affect the BS but also the induced magnetosphere boundary location. The simulated BS crossings occurred at 16:45 UT and 18:49 UT. Moreover the simulated magnetic field in the induced magnetosphere region is underestimated by about 25%. Such a difference, although on a different orbit, is also present in Ma et al. (2015). In the ionospheric region, the simulation predict an ionospheric peak of O_2^+ slightly lower than 10^5 cm^{-3}. The bulk velocity observed by SWIA is relatively well reproduced by the simulation.

Such comparisons can be extended to the entire day of December 10, 2014. Fig. 5 shows a comparison between MAVEN SWIA and MAG observations (in color) and the simulations results (in black). The simulation is able to reproduce most of the observations although several differences can be noticed, particularly on the V_y component. Similarly to Ma et al. (2015) we can determine the overall Pearson's correlation coefficient to quantify the comparison. Correlation coefficients for the different parameters are reported in Table 3. We find very high correlation coefficients (≥ 0.85) for the total magnetic field and the V_x component of the velocity, high correlation coefficients for the proton density and the V_z component of the velocity, but relatively low correlation for the V_y component of the velocity. Several factors can contributes to the discrepancy. During the simulation, the input parameters are kept constant, therefore any change in the solar wind conditions will not be reproduced. Secondly, we clearly see in Fig. 5, that for several orbits the solar wind speed has a significant V_y component while in the simulation the solar wind plasma flows only in the $-X_{MSO}$ direction. Finally, as previously said, the simulation is done for a given location of crustal field (here the sub-solar location is local at the Western longitude 180°).

The simulation results can also be compared to MEX observations in other regions. Since MEX was in the solar wind region for the time interval 15:30 - 19h30 UT, the model-observation comparison has been done for the time interval 19:00 - 23:00 UT (Fig. 6). MEX IMA (heavy and proton) ion spectrograms are plotted on the two first panels, while the simulated bulk speed and the total speed for heavy and proton ions are compared in the last panel. As for the MAVEN observations, the LatHyS model reproduce well the MEX observations.

A new way to analyze in situ observations is to combine the multi-point plasma information, measured by MAVEN and MEX, with the simulation results in a 3D interactive scene. The 3DView visualization tool can do this (Fig. 7). In this scene, we loaded a 2D simulated plane (with the bulk speed in the XZ plane passing through the center of the planet) along with the 3D MAVEN and MEX trajectories. The simulated BS is identified upstream of the plasma by an abrupt color change. We can enrich the scene by plotting observational data such the solar wind velocity measured by SWIA (light blue arrows) and predicted plasma velocity from the model (light green arrows). High-level data products are also provided and the user can visualize the draping of the magnetic field around the planet. An example of such field line passing through the MEX trajectory is also shown in Fig. 7.

These functionalities give a three-dimensional context of the in situ observations and present powerfull capabilities to combine multi-point observations and global simulation results.

4. Conclusion

In this paper we have described a simulation database dedicated to planetary plasma investigations which has been developed in the framework of the FP7 IMPEx project. The LatHyS database offers to the community sophisticated simulation results of various planetary plasma environments. A variety of computed data products (1D, 2D and the entire 3D cube) for several plasma quantities (electric field, magnetic field, ion species moments,…) are publically available. The

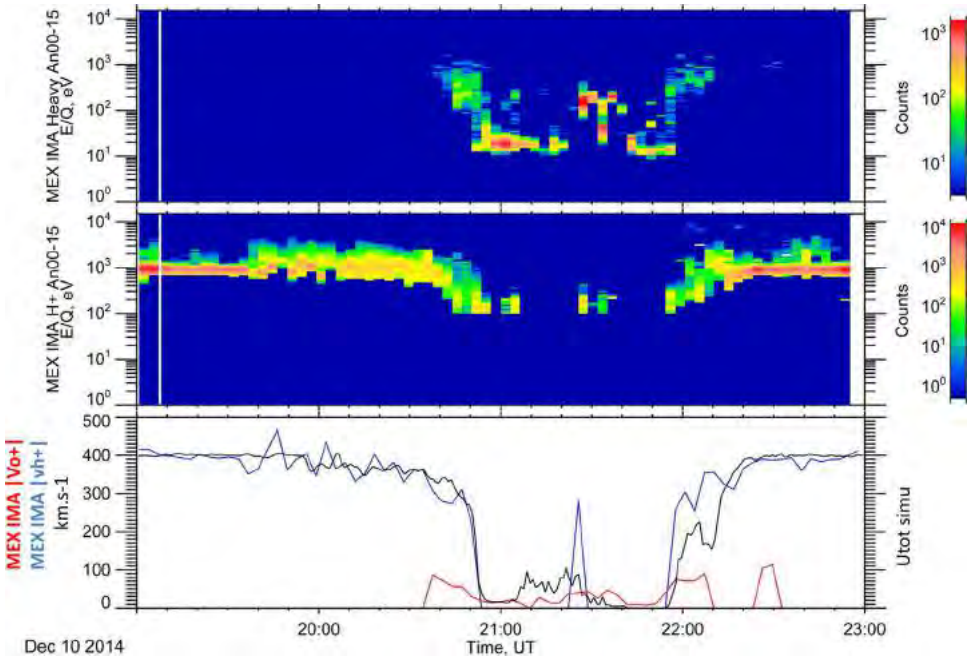

Fig. 6. MEX observations and model comparison from 19:00 to 23:00 UT. Heavy and proton ion spectra from ASPERA IMA are displayed in the top panels. The bottom panel shows a comparison between observed and simulated speed.

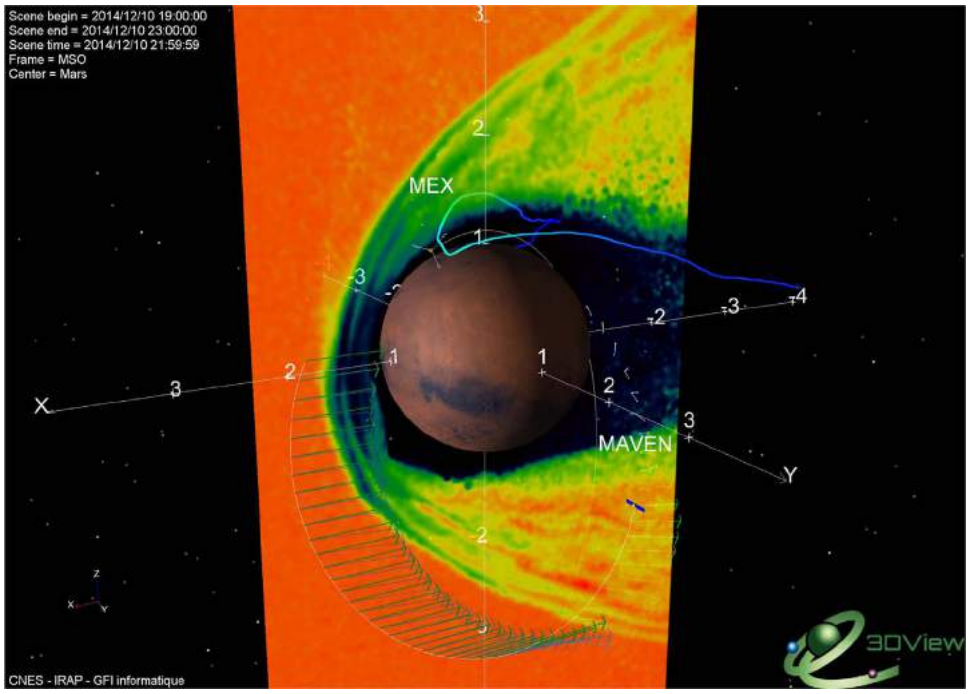

Fig. 7. Three-dimensional scene of the MAVEN, MEX observations and simulation results. Simulated speed is plotted in a 2D XZ plane and along MAVEN track (light green vectors) and compared to MAVEN SWIA velocity observations (light blue vectors). A simulated magnetic field line is displayed at MEX location close to the North pole (at 21:59 UT), with a color code indicating the strength of the magnetic field.

1D and 2D archived simulation results can be visualized with VO tools like TOPCAT thanks to the implementation on the LatHyS web interface of the SAMP functionality (Génot et al., 2014). We have demonstrated interoperability with a number of VO tools. Several web services have been developped to extract high-level simulated data from the archived simulation catalogue. Some of these webservices are implemented in VO tools like AMDA, 3DView, CLweb or IMPEx Portal.

We have also presented a science case focusing on the Martian plasma environment to illustrate the powerfull possibilities of the interoperability between VO tools and the LatHyS database. We have combined multi-spacecraft observations and simulation results to draw three-dimensional pictures of the solar wind interaction with the Martian upper atmosphere.

Additional tutorial/demonstration videos on the LatHyS SMBD have been released and are available at http://impex-fp7.oeaw.ac.at/videos.html. These videos have been presented at the European Planetary Science Congress annual meeting (EPSC 2013) (September 2013) in the Virtual Observatory session and have been the result of a successful collaboration between the Europlanet infrastructure (http://www.europlanet-eu.org/) and IMPEx FP7 projects:

- Interoperability of AMDA, LatHyS and TOPCAT (http://youtu.be/rOh4Me9xTqE)
- AMDA, 3DView and Simulation Databases (SMDBs) (http://youtu.be/8AxJRPho334).

Acknowledgements

The authors are thankful to EU FP7 project IMPEx (contract #262863) for its support in the development of the infrastructure and the simulation database. RM, SH, VG, LL, FL, JYC, PW, MG, AF, MB, MS, NA are indebted to the “Soleil-Heliosphere-Magnetospheres” and “Système Solaire” programs of the French Space Agency CNES for its support. Research at LATMOS has been partly supported by ANR-CNRS through contract ANR-09-BLAN-223 and ANR-13-BS05-0012. Data analysis was performed with the AMDA science analysis system provided by the Centre de Données de la Physique des Plasmas (CDPP) supported by CNRS, CNES, Observatoire de Paris and Université Paul Sabatier, Toulouse. Data used in this study is available on the NASA Planetary Data System, via http://ppi.pds.nasa.gov/project/maven.

References

Barabash, S., Fedorov, A., Lundin, R., Sauvaud, J.-A., 2007. Martian atmospheric erosion rates. Science 315, 501.

Barabash, S., Lundin, R., Andersson, H., Gimholt, J., Holmström, M., Norberg, O., Yamauchi, M., Asamura, K., Coates, A.J., Linder, D.R., Kataria, D.O., Curtis, C.C., Hsieh, K.C., Sandel, B.R., Fedorov, A., Grigoriev, A., Budnik, E., Grande, M., Carter, M., Reading, D.H., Koskinen, H., Kallio, E., Riihela, P., Säles, T., Kozyra, J., Krupp, N., Livi, S., Woch, J., Luhmann, J., McKenna-Lawlor, S., Orsini, S., Cerulli-Irelli, R., Maggi, M., Morbidini, A., Mura, A., Milillo, A., Roelof, E., Williams, D., Sauvaud, J.-A., Thocaven, J.-J., Moreau, T., Winningham, D., Frahm, R., Scherrer, J., Sharber, J., Wurz, P., Bochsler, P., 2004. ASPERA-3: analyser of space plasmas and energetic ions for Mars Express. In: Wilson, A., Chicarro, A. (Eds.), Mars Express: The Scientific Payload 1240. ESA Special Publication, pp. 121–139.

Brain, D., Barabash, S., Boesswetter, A., Bougher, S., Brecht, S., Chanteur, G., Hurley, D., Dubinin, E., Fang, X., Fraenz, M., Halekas, J., Harnett, E., Holmstrom, M., Kallio, E., Lammer, H., Ledvina, S., Liemohn, M., Liu, K., Luhmann, J., Ma, Y., Modolo, R., Nagy, A., Motschmann, U., Nilsson, H., Shinagawa, H., Simon, S., Terada, N., 2010. A comparison of global models for the solar wind interaction with Mars. Icarus 206, 139–151.

Connerney, J.E.P., Espley, J., Lawton, P., Murphy, S., Odom, J., Oliversen, R., Sheppard, D., 2015. MAVEN Magn. Field Investig. 195, 257–291.

Edberg, N.J.T., Lester, M., Cowley, S.W.H., Eriksson, A.I., 2008. Statistical analysis of the location of the Martian magnetic pileup boundary and bow shock and the influence of crustal magnetic fields. J. Geophys. Res. (Space Phys.) 113, 8206.

Génot, V., André, N., Cecconi, B., Bouchemit, M., Budnik, E., Bourrel, N., Gangloff, M., Dufourg, N., Hess, S., Modolo, R., Renard, B., Lormant, N., Beigbeder, L., Popescu, D., Toniutti, J.-P., 2014. Joining the yellow hub: uses of the Simple Application Messaging Protocol in Space Physics analysis tools. Astron. Comput. 7, 62–70.

Génot, V., Beigbeder, L., Dufourg, N., Gangloff, M., Bouchemit, M., Popescu, D., Caussarieu, S., Toniutti, J. P., Durand, J., Modolo, R., André, N., Cecconi, B., Jacquey, C., Pitout, F., Rouillard, A., Pintot, R., Erard, S., Jourdane, N., 2016. Science data visualization in planetary and heliospheric contexts with 3DView. Planet. Space Sci.

Génot, V., Jacquey, C., Bouchemit, M., Gangloff, M., Fedorov, A., Lavraud, B., André, N., Broussillou, L., Harvey, C., Pallier, E., Penou, E., Budnik, E., Hitier, R., Cecconi, B., Dériot, F., Heulet, D., Pinçon, J.-L., 2010. Space Weather applications with CDPP/AMDA. Adv. Space Res. 45, 1145–1155.

Halekas, J.S., Taylor, E.R., Dalton, G., Johnson, G., Curtis, D.W., McFadden, J.P., Mitchell, D.L., Lin, R.P., Jakosky, B.M., 2015. The Solar Wind Ion Analyzer for MAVEN. 195, 125–151.

Hess, S., Modolo, R., Khodachenko, M., al-Ubaidi, T., Topf, F., Kallio, E., Hakkinen, L.,

Jaarvinen, J., Génot, V., Gangloff, M., Budnik, E., Bourrel, N., Alexeev, I., Kalegaev, V., Cecconi, B., 2013. IMPEx Simulation Data Model, a SPASE extension to manage simulations and models. In: Ensuring Long-Term Preservation and Valu Adding to Scientific and Technical Data.

Jacquey, C., Génot, V., Budnik, E., Hitier, R., Bouchemit, M., Gangloff, M., Fedorov, A., Cecconi, B., André, N., Lavraud, B., Harvey, C., Dériot, F., Heulet, D., Pallier, E., Penou, E., Pinçon, J.L., 2010. AMDA, automated multi-dataset analysis: a Web-Based Service Provided by the CDPP. Astrophys. Space Sci. Proc. 11, 239–247.

Jakosky, B.M., Lin, R.P., Grebowsky, J.M., Luhmann, J.G., Mitchell, D.F., Beutelschies, G., Priser, T., Acuna, M., Andersson, L., Baird, D., Baker, D., Bartlett, R., Benna, M., Bougher, S., Brain, D., Carson, D., Cauffman, S., Chamberlin, P., Chaufray, J.-Y., Cheatom, O., Clarke, J., Connerney, J., Cravens, T., Curtis, D., Delory, G., Demcak, S., DeWolfe, A., Eparvier, F., Ergun, R., Eriksson, A., Espley, J., Fang, X., Folta, D., Fox, J., Gomez-Rosa, C., Habenicht, S., Halekas, J., Holsclaw, G., Houghton, M., Howard, R., Jarosz, M., Jedrich, N., Johnson, M., Kasprzak, W., Kelley, M., King, T., Lankton, M., Larson, D., Leblanc, F., Lefevre, F., Lillis, R., Mahaffy, P., Mazelle, C., McClintock, W., McFadden, J., Mitchell, D. L., Montmessin, F., Morrissey, J., Peterson, W., Possel, W., Sauvaud, J.-A., Schneider, N., Sidney, W., Sparacino, S., Stewart, A. I. F., Tolson, R., Toublanc, D., Waters, C., Woods, T., Yelle, R., Zurek, R., 2015. The Mars Atmosphere and Volatile Evolution (MAVEN) Mission.

Kallio, E., Chaufray, J.-Y., Modolo, R., Snowden, D., Winglee, R., 2011. Modeling of Venus. MarsTitan 162, 267–307.

Khodachenko, M.L., Genot, V.N., Kallio, E.J., Alexeev, I.I., Modolo, R., Al-Ubaidi, T., André, N., Gangloff, M., Schmidt, W., Belenkaya, E.S., Topf, F., Stoeckler, R., 2011. Integrated Medium for Planetary Exploration (IMPEx): a new EU FP7-SPACE project. AGU Fall Meeting Abstracts.

Leclercq, L., Modolo, R., Leblanc, F., Hess, S.L.G., Mancini, M., 2016. 3D magnetospheric parallel hybrid multi-grid method applied to planet-plasma interactions. J. Comput. Phys. 309, 295–313.

Ledvina, S.A., Ma, Y.-J., Kallio, E., 2008. Modeling and Simulating Flowing Plasmas and Related Phenomena, 139, 143–189.

Ma, Y.J., Russell, C.T., Fang, X., Dong, Y., Nagy, A.F., Toth, G., Halekas, J.S., Connerney, J.E.P., Espley, J.R., Mahaffy, P.R., Benna, M., McFadden, J.P., Mitchell, D.L., Jakosky, B.M., 2015. MHD model results of solar wind interaction with Mars and comparison with MAVEN plasma observations. Geophys. Res. Lett. 42, 9113–9120.

McFadden, J.P., Kortmann, O., Curtis, D., Dalton, G., Johnson, G., Abiad, R., Sterling, R., Hatch, K., Berg, P., Tiu, C., Gordon, D., Heavner, S., Robinson, M., Marckwordt, M., Lin, R., Jakosky, B., 2015. MAVEN Supra Thermal and Thermal Ion Compostion (STATIC) Instrument, 195, 199–256.

Modolo, R., Chanteur, G.M., 2008. A global hybrid model for Titan's interaction with the Kronian plasma: application to the Cassini Ta flyby. J. Geophys. Res. 113 (1317–+).

Modolo, R., AChanteur, G.M., Dubinin, E., 2012. Dynamic Martian magnetosphere: transient twist induced by a rotation of the IMF. Geophys. Res. Lett. 39, 1106.

Modolo, R., Chanteur, G.M., Dubinin, E., Matthews, A.P., 2005. Influence of the solar EUV flux on the Martian plasma environment. Ann. Geophys. 23, 433–444.

Modolo, R., Chanteur, G.M., Dubinin, E., Matthews, A.P., 2006. Simulated solar wind plasma interaction with the Martian exosphere: influence of the solar EUV flux on the bow shock and the magnetic pile-up boundary. Ann. Geophys. 24, 3403–3410.

Modolo, R., AChanteur, G.M., Wahlund, J.-E., Canu, P., Kurth, W.S., Gurnett, D., Matthews, A.P., Bertucci, C., 2007. Plasma environment in the wake of Titan from hybrid simulation: a case study. Geophys. Res. Lett. 34, L24S07.

Modolo, R., Hess, S., Mancini, M., Leblanc, F., Chaufray, J.-Y., Brain, D., Leclercq, L., Esteban-Hernández, R., Chanteur, G., Weill, P., González-Galindo, F., Forget, F., Yagi, M., Mazelle, C., 2016. Mars-solar wind interaction: LatHyS, an improved parallel 3-D multispecies hybrid model. J. Geophys. Res. (Space Phys.) 121, 6378–6399.

Nilsson, H., Edberg, N.J.T., Stenberg, G., Barabash, S., Holmström, M., Futaana, Y., Lundin, R., Fedorov, A., 2011. Heavy ion escape from Mars, influence from solar wind conditions and crustal magnetic fields. Icarus 215, 475–484.

Richer, E., Modolo, R., Chanteur, G.M., Hess, S., Leblanc, F., 2012. A global hybrid model for Mercury's interaction with the solar wind: case study of the dipole representation. J. Geophys. Res. (Space Phys.) 117, 10228.

Turc, L., Fontaine, D., Savoini, P., Modolo, R., 2015. 3D hybrid simulations of the interaction of a magnetic cloud with a bow shock. J. Geophys. Res. (Space Phys.) 120.

AGU PUBLICATIONS

JGR

Journal of Geophysical Research: Space Physics

RESEARCH ARTICLE
10.1002/2016JA023467

Special Section:
Major Results From the MAVEN Mission to Mars

Martian low-altitude magnetic topology deduced from MAVEN/SWEA observations

Shaosui Xu[1], David Mitchell[1], Michael Liemohn[2], Xiaohua Fang[3], Yingjuan Ma[4], Janet Luhmann[1], David Brain[3], Morgane Steckiewicz[5], Christian Mazelle[5], Jack Connerney[6], and Bruce Jakosky[3]

[1]Space Science Laboratory, University of California, Berkeley, California, USA, [2]Department of Climate and Space Sciences and Engineering, University of Michigan, Ann Arbor, Michigan, USA, [3]Laboratory of Atmospheric and Space Sciences, University of Colorado Boulder, Boulder, Colorado, USA, [4]Department of Earth Planetary and Space Sciences, University of California, Los Angeles, California, USA, [5]IRAP, CNRS and University Paul Sabatier, Toulouse, France, [6]Goddard Space Flight Center, Greenbelt, Maryland, USA

Abstract The Mars Atmosphere and Volatile Evolution mission has obtained comprehensive particle and magnetic field measurements. The Solar Wind Electron Analyzer provides electron energy-pitch angle distributions along the spacecraft trajectory that can be used to infer magnetic topology. This study presents pitch angle-resolved electron energy shape parameters that can distinguish photoelectrons from solar wind electrons, which we use to deduce the Martian magnetic topology and connectivity to the dayside ionosphere. Magnetic topology in the Mars environment is mapped in three dimensions for the first time. At low altitudes (<400 km) in sunlight, the northern hemisphere is found to be dominated by closed field lines (both ends intersecting the collisional atmosphere), with more day-night connections through cross-terminator closed field lines than in the south. Although draped field lines with ~100 km amplitude vertical fluctuations that intersect the electron exobase (~160–220 km) in two locations could appear to be closed at the spacecraft, a more likely explanation is provided by crustal magnetic fields, which naturally have the required geometry. Around 30% of the time, we observe open field lines from 200 to 400 km, which implies three distinct topological layers over the northern hemisphere: closed field lines below 200 km, open field lines with foot points at lower latitudes that pass over the northern hemisphere from 200 to 400 km, and draped interplanetary magnetic field above 400 km. This study also identifies open field lines with one end attached to the dayside ionosphere and the other end connected with the solar wind, providing a path for ion outflow.

Key Points:
- Pitch angle-resolved electron energy shape parameters are used to deduce magnetic topology
- Closed magnetic field lines dominate low altitudes (<400 km) of the northern hemisphere on the dayside
- The 3-D view of the Martian magnetic topology is presented for the first time

Supporting Information:
- Supporting Information S1

Correspondence to:
S. Xu,
shaosui.xu@ssl.berkeley.edu

Citation:
Xu, S., et al. (2017), Martian low-altitude magnetic topology deduced from MAVEN/SWEA observations, *J. Geophys. Res. Space Physics*, *122*, doi:10.1002/2016JA023467.

Received 23 SEP 2016
Accepted 19 JAN 2017
Accepted article online 25 JAN 2017

1. Introduction

One of the most significant findings of the Mars Global Surveyor (MGS) mission was the discovery of strong, localized crustal magnetic fields [*Acuna et al*., 1998]. These fields were partially mapped at altitudes ranging from 100 to 180 km during the 1.4 year aerobraking period, mostly over the North Pole and the sunlit hemisphere. The crustal field was fully sampled during >7 years in the ~400 km altitude, 02:00 A.M./02:00 P.M. circular mapping orbit (Figure 1; from *Connerney et al*. [2005]). These localized crustal fields strongly influence the interaction between solar wind and the Martian space environment, resulting in a complicated and dynamic magnetic topology [e.g., *Brain et al*., 2003; *Harnett and Winglee*, 2005; *Liemohn et al*., 2007; *Y. J. Ma et al*., 2014; *Fang et al*., 2015].

Magnetic topology is essential for understanding the Mars plasma environment, which can be categorized into three types: closed, open, and draped field lines. Closed field lines (both ends intersecting the collisional atmosphere) isolate ionospheric plasma from solar wind plasma and allow transport of ionospheric photoelectrons from one location to another. Open field lines, with one end intersecting the collisional atmosphere and the other end connected to the solar wind, permit particle/energy exchange between the Martian ionosphere and the solar wind. Energetic electron precipitation [e.g., *Lillis and Brain*, 2013; *Xu et al*., 2015a; *Shane et al*., 2016] through open fields can cause ionization [e.g., *Lillis et al*., 2009; *Fillingim et al*., 2007; *Fillingim et al*., 2010], heating [e.g., *Krymskii et al*., 2002, 2004], and excitation (probably aurora [e.g., *Bertaux et al*., 2005; *Brain et al*., 2006; *Liemohn et al*., 2007; *Leblanc et al*., 2008; *Shane et al*., 2016]). Open magnetic field lines attached to the dayside ionosphere also provide possible passages for ion escape [e.g., *Lillis et al*., 2015]. For example, cold ions may be accelerated by the ambipolar electric fields to reach the escape velocity [e.g., *Collinson et al*., 2015], resembling the polar wind at Earth [e.g., *Ganguli*, 1996; *Khazanov et al*., 1997; *Glocer et al*., 2009].

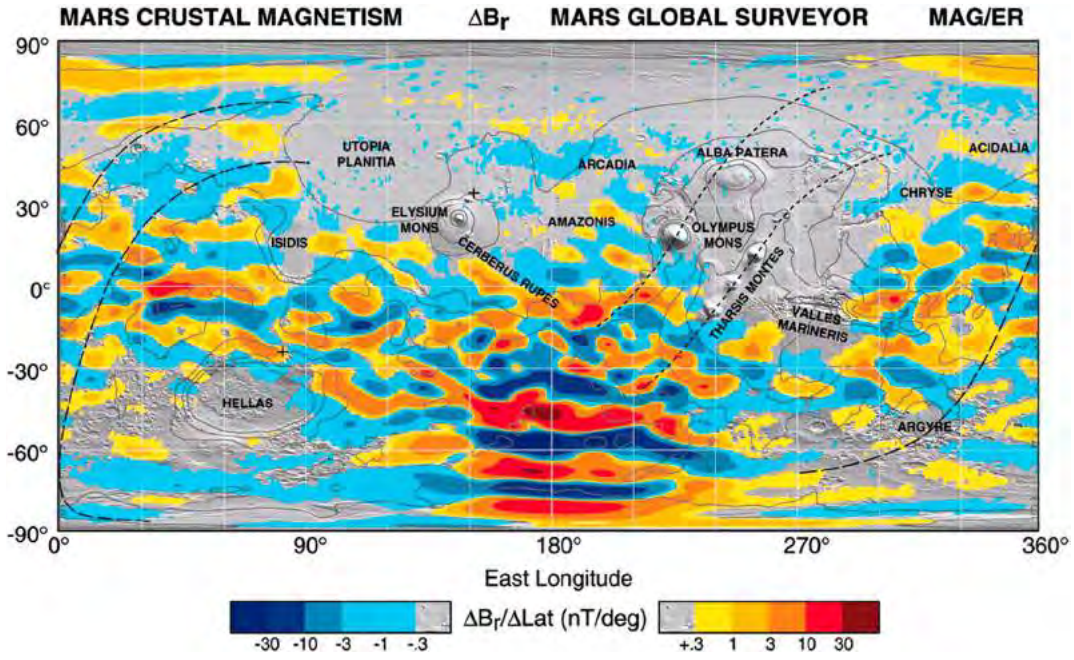

Figure 1. The map of the derivative of the radial magnetic field along the MGS spacecraft track at a nominal 400 km altitude, also Figure 1 of *Connerney et al.* [2005]. Copyright (2005) National Academy of Sciences, USA.

Harada et al. [2016] investigated narrowband whistler mode waves in the Martian magnetosphere observed by Mars Atmosphere and Volatile Evolution (MAVEN), which were generated by cyclotron resonance with anisotropic electrons on open or closed field lines. These waves in return could also cause electron scattering and precipitation. Draped field lines (both ends connected to the solar wind) can dip low enough into the atmosphere to allow energy transfer through collisions [e.g., *Liemohn et al.*, 2006a].

At Mars, superthermal electrons, mainly consisting of ionospheric photoelectrons and solar wind electrons, are typically magnetized (with the gyrocenters of their helical motion constrained to follow magnetic field lines) and are therefore useful for deducing magnetic topology. *Brain et al.* [2007] used electron pitch angle distributions measured by the Magnetometer/Electron Reflectometer (MAG/ER) [*Acuna et al.*, 1992; *Mitchell et al.*, 2001] to determine if a magnetic field is closed, open, or draped. The presence or absence of loss cones, which indicate field line intersection with the collisional atmosphere, was used to infer topology. For example, a one-sided loss cone indicates an open field line; a double-sided loss cone, an isotropic photoelectron spectrum, and a superthermal electron void (extremely low count rate) on the nightside [e.g., *Mitchell et al.*, 2001; *Steckiewicz et al.*, 2015; *Shane et al.*, 2016] are all indicators of closed field lines, and a solar wind spectrum with no loss cones indicates a draped field line. Based on this technique, *Brain et al.* [2007] found that, at ~400 km, the dominant field topology was draped/open in the northern hemisphere and closed over the southern strong crustal field regions with cusps in between, where the field has a large radial component. Additionally, the size of loss cone can be used to derive the crustal field strength at the absorption altitude (~160 km) of these energetic electrons [*Lillis et al.*, 2004; *Liemohn et al.*, 2006a; *Mitchell et al.*, 2007], also known as the superthermal electron exobase [e.g., *Xu et al.*, 2016a].

Another way to infer magnetic topology is to use superthermal electron energy distributions to identify the source(s) of electrons traveling parallel and antiparallel to the field line. For example, *Liemohn et al.* [2006a] and *Frahm et al.* [2006] reported ionospheric photoelectrons in the high-altitude Martian tail, observed by the Analyzer of Space Plasma and Energetic Atoms version 3 experiment [*Barabash et al.*, 2006] on board the Mars Express spacecraft. *Liemohn et al.* [2006b] suggested that these observed high-altitude photoelectrons escape down the tail through open field lines with one end embedded in the dayside ionosphere. *Frahm et al.* [2010] mapped these tail photoelectrons and estimated the escape rate. On the other hand, narrow spikes of electrons fluxes have been observed by

both MGS [e.g., *Mitchell et al*., 2001] and Mars Express [e.g., *Dubinin et al*., 2008] over the strong crustal regions, which are thought to be solar wind electron precipitation along open field lines. Several studies have statistically investigated the dependence of this precipitation on external conditions as well as the effects on the atmospheric target [e.g., *Brain et al*., 2005; *Lillis and Brain*, 2013; *Xu et al*., 2015a; *Shane et al*., 2016].

Electrons can only be used to infer topology where their motion is governed by electric and magnetic fields. We define a "foot point" as the location where a magnetic field line intersects the superthermal electron exobase. Below the foot point, electron motion is dominated by collisions rather than by the magnetic field, so that we can no longer deduce topology from energy-pitch angle distributions. As a specific example, we cannot distinguish between a weak crustal magnetic field line that extends above the electron exobase and a draped solar wind field line that dips below the electron exobase at low solar zenith angles. Additional information, such as the strength and orientation of the magnetic field at the spacecraft, is needed to infer the most likely scenario. In this study, we define magnetic topology based on whether a locally measured flux tube intersects the electron exobase.

Previous missions have greatly improved our understanding of Martian magnetic topology; however, because of limitations in orbit geometry and science instrumentation, there has been no systematic mapping of magnetic topology at altitudes below 300 km until the Mars Atmosphere and Volatile Evolution (MAVEN) mission [*Jakosky et al*., 2015]. MAVEN carries a comprehensive set of plasma and field instruments and has a periapsis as low as ~150 km (~120 km during "deep dips"), which is below the superthermal electron exobase. *Xu et al*. [2016b] reported ionospheric photoelectrons observed in the deep nightside (solar zenith angle (SZA) $>$ 120°) below 150 km by Solar Wind Electron Analyzer (SWEA) [*Mitchell et al*., 2016] onboard MAVEN, which indicated the existence of closed magnetic field lines that straddle the terminator in the northern hemisphere, allowing photoelectron transport from day to night. In this study, we analyze all electron energy/pitch angle distributions obtained to date by SWEA to statistically investigate Mars' magnetic topology down to the superthermal electron exobase over wide ranges of solar zenith angle, local time, longitude, and latitude. The instrumentation is described in section 2. Then, sections 3 and 4 present how to use electron data, from which the pitch angle-resolved shape parameters are obtained, to deduce the magnetic topology, followed by the maps of different field line types in section 5. Sections 6 and 7 are the discussion and conclusions, respectively.

2. Instruments

The MAVEN mission aims to understand the loss of the Mars' atmosphere to space at the current epoch and over the planet's history. MAVEN has an elliptical orbit with an apoapsis of 2.8 Mars radii (R_M) and a periapsis of ~150 km altitude, with several week-long deep dips, which sample key latitudes and local times down to ~120 km altitude. The inclination of the orbit is 74°, and the orbit period is 4.5 h.

SWEA is a symmetric hemispheric electrostatic analyzer with deflectors that measures the energy/angle distributions of electrons from 3 to 2000 eV over ~80% of the sky and electrons from 2000 to 4600 eV with a field of view that shrinks with energy. The 64 logarithmically spaced energy bins provide 12% ($\Delta E/E$) sampling over the full range, which slightly oversamples the instrumental energy resolution of 17%. This is sufficient to distinguish ionospheric photoelectrons from (possibly energized) electrons of solar wind origin. The field view is divided into 96 solid angle bins, providing ~20° resolution. Pitch angle distributions can be obtained from the full energy/angle (3-D) distributions, but these have a low cadence ($>$16 s) because of telemetry rate limitations. The data described here are 2-D cuts (great circles) through the 3-D distributions that are calculated on board using real-time MAG data and designed to provide maximum pitch angle coverage, even as the magnetic field direction varies. This pitch angle distribution (PAD) data product is 6 times smaller than the 3-D product and is provided with a 2–4 s cadence, depending on altitude. See *Mitchell et al*. [2016] for a more detailed description.

The Magnetometer (MAG) is composed of two independent triaxial fluxgate sensors located on extensions ("diving boards") at the ends of the solar panels. Each magnetometer measures the vector field with an accuracy of ~0.1 nT (including corrections for dynamic fields generated on the spacecraft) at a cadence of 1/32 s. More details about the MAG instrument are provided by *Connerney et al*. [2015].

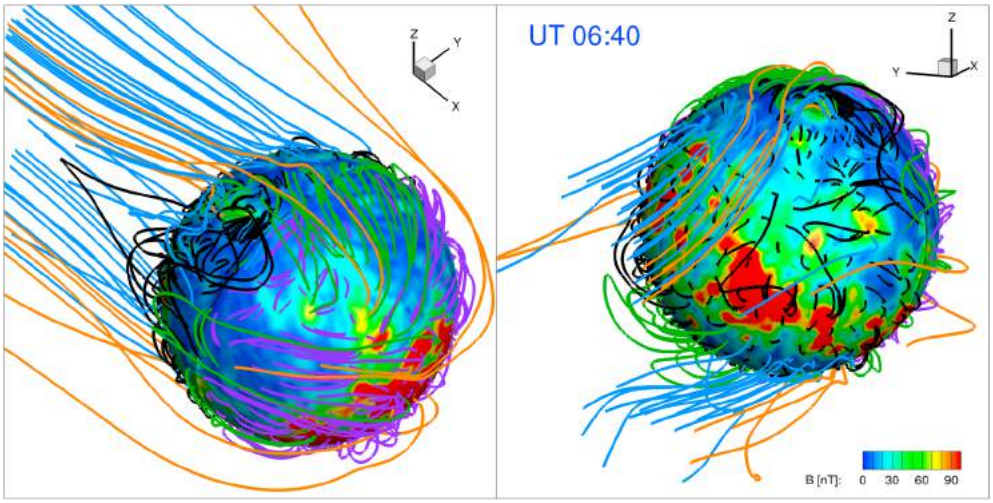

Figure 2. (left and right) Field line tracing at UT 06:40 (the simulation starts at UT 00:00) from two perspectives, with the strong crustal fields on the dayside. The color on the spherical surface is the magnetic magnitude at 150 km. Different types of field lines are highlighted with colors, described in details in the text. The field lines are extracted from the simulation result in *Y. Ma et al.* [2014].

3. Superthermal Electrons and Magnetic Topology

The interaction of solar wind with the Martian ionosphere and crustal anomalies gives rise to several types of magnetic topology. The theoretical prediction of such a complex interaction from a time-dependent multispecies Mars magnetohydrodynamic (MHD) simulation [*Y. Ma et al.*, 2014; *Fang et al.*, 2015] is shown in Figure 2. The multispecies single-fluid MHD [*Ma et al.*, 2004] includes four continuity equations for four ion species, H^+, O_2^+, O^+, and CO_2^+, but assumes that all the ions share the same velocity and temperature. Details of the model are described in *Ma et al.* [2004]. This particular time-dependent run let the planet rotate for 26 h under quiet solar wind conditions, with a solar wind density of $4\,cm^{-3}$, a velocity of 400 km/s, a Parker spiral interplanetary magnetic field (IMF) of -3 nT and 56° in the Mars-centered Solar Orbital (MSO) *x-y* direction, and a plasma temperature of 3.5×10^5 K. The simulation was performed in the MSO coordinates; the *x* axis points from the center of Mars to the Sun, the *y* axis is opposite to the orbital motion of Mars, and the *z* axis is perpendicular to the Mars' orbital plane. Detailed setup of the simulation is described in *Y. Ma et al.* [2014].

Figure 2 shows an example of the field line tracing starting at 150 km in altitude at a specific time point when the strong crustal fields are on the dayside from two perspectives (left view from the Sun and right toward the Sun). The color contour on the spherical surface shows the magnetic magnitude at 150 km altitude. Different types of field lines are highlighted with colors: purple for closed field lines with both foot points on the dayside, black for closed field lines with both foot points on the nightside, green for one foot point on the dayside (solar zenith angle (SZA) $<90°$) and the other on the nightside (SZA $>90°$), orange for open field lines attached to the dayside ionosphere, and blue for open field lines attached to the nightside. Draped field lines are not present in this case because the tracing starts at 150 km, and according to our definition above, we are treating all field lines crossing this altitude (i.e., the electron exobase) as either open or closed. Each type of field lines has access to different electron populations, photoelectrons, or solar wind electrons, in each end. This information of electron populations in return can be utilized to retrieve the magnetic topology.

As mentioned above, SWEA has a fine energy resolution to distinguish ionospheric photoelectrons from solar wind/magnetosheath electrons based on their energy spectral shape. As noted in several studies [e.g., *Mitchell et al.*, 2000; *Liemohn et al.*, 2003; *Frahm et al.*, 2006], the Martian photoelectron energy spectrum has a several distinct features, corresponding to features in solar irradiance [e.g., *Xu et al.*, 2015b; *Peterson et al.*, 2016]: (1) a cluster of sharp peaks from 22 to 27 eV due to ionization of CO_2 and O by the intense He II 30.4 nm (~40 eV) solar line, (2) a sharp drop in flux from 60 to 70 eV (the photoelectron knee) due to a corresponding sharp decrease of solar irradiance at wavelengths shorter than 17 nm, (3) a

Table 1. Criteria for Determining Magnetic Field Topology (Closed, Open, Draped, and Void) Based on Electron Populations Traveling Parallel and Antiparallel to the Magnetic Field on the Dayside and the Nightside, Respectively[a]

	Dayside (SZA $< 90°$)	Nightside (SZA $> 110°$)
Closed	Ph *e*- in both directions (purple)	Ph *e*- traveling toward the planet (green)
Open	Ph *e*- in one direction; SW *e*- in the opposite direction (orange)	Ph *e*- traveling away from the planet; SW *e*- traveling toward the planet (orange)
Draped	SW *e*- in both directions (draped IMF)	SW *e*- in both directions (blue and draped IMF)
Void (closed)	NA	Low omnidirectional electron fluxes (black)

[a]Photoelectron is denoted as "Ph *e*-" and solar wind/sheath electron as "SW *e*-." The colors in the parenthesis indicate the field lines in Figure 2.

peak near 500 eV produced by ionization of oxygen K-shell electrons by soft X-rays (and subsequent relaxation of the resulting excited ion by the emission of photons and Auger electrons), and (4) a second sharp decrease in electron flux at energies just above the Auger peak due to another drop in solar irradiance. In contrast, these features are absent in the energy spectra of solar wind electrons in all regions of the Mars' plasma environment. Although SWEA cannot resolve the cluster of photoelectron peaks from 22 to 27 eV, the energy resolution is sufficient to readily distinguish between photoelectrons and solar wind electrons.

To infer magnetic topology, the basic idea of this study is to examine what electron population, ionospheric photoelectrons versus solar wind electrons, is measured in the parallel and antiparallel directions. The topology criteria are slightly different for the dayside and nightside hemispheres. In this study, we define the dayside as solar zenith angle (SZA) $< 90°$ and the nightside as SZA $> 110°$ to ensure that the ionosphere near and below the electron exobase is in darkness [cf., *Shane et al*., 2016]. On the dayside, a closed field (purple lines in Figure 2) is defined as one on which photoelectrons are being measured in both parallel and antiparallel directions. Closed field lines with both ends intersecting the collisional dayside ionosphere fill with photoelectrons and are simultaneously isolated from solar wind electrons. An open field line (orange lines in Figure 2) is identified as having photoelectrons in one direction and solar wind electrons in the other, as one end of the field is attached to the ionosphere and the other to solar wind; the draped field (not shown in Figure 2) is designated when solar wind/sheath electrons are found in both directions, as the field line connects to the solar wind on both ends.

In the darkness of the nightside ionosphere, there is no photoelectron production, so we use a different set of criteria. There are two types of closed field lines on the nightside: (1) one foot point on the dayside and another on the nightside (a cross-terminator closed field line; green lines in Figure 2) and (2) both foot points on the nightside (black lines in Figure 2). In the first case, photoelectrons are produced on the dayside, travel across the terminator along the field line (above the electron exobase), and precipitate into the nightside. Part of the returning flux is magnetically reflected, while the more field-aligned flux suffers collisions with the neutral atmosphere, forming a loss cone. We denote photoelectrons flowing toward the planet as a closed field line. In the second case, there is no photoelectron production at either foot point and no access for solar wind electrons. Superthermal electron fluxes in both directions are ~2 orders of magnitude lower than typical fluxes of either photoelectron or solar wind electron populations. We define this situation as a superthermal electron void.

For open field lines, one end is connected to the solar wind while the other intersects the electron exobase on either the dayside (orange lines in Figure 2) or the nightside (blue lines in Figure 2). We identify the first case by observing photoelectrons flowing away from the planet and solar wind electrons flowing toward the planet. We identify the second case as measuring solar wind electrons in both directions, which can arise from solar wind electrons traveling toward the planet and magnetically reflected and/or backscattered electrons traveling in the opposite direction. Thus, one drawback of this particular methodology is that we are unable to differentiate the open field lines attached to the nightside from draped solar wind magnetic fields.

On the dayside, we organize our results into three topological categories: closed, open, and draped (Table 1), which correspond with the definitions used by previous authors. However, on the nightside, because we infer topology based on the presence of ionospheric photoelectrons (which are produced in sunlight), we use the following restricted definitions for these categories. "Closed" refers specifically

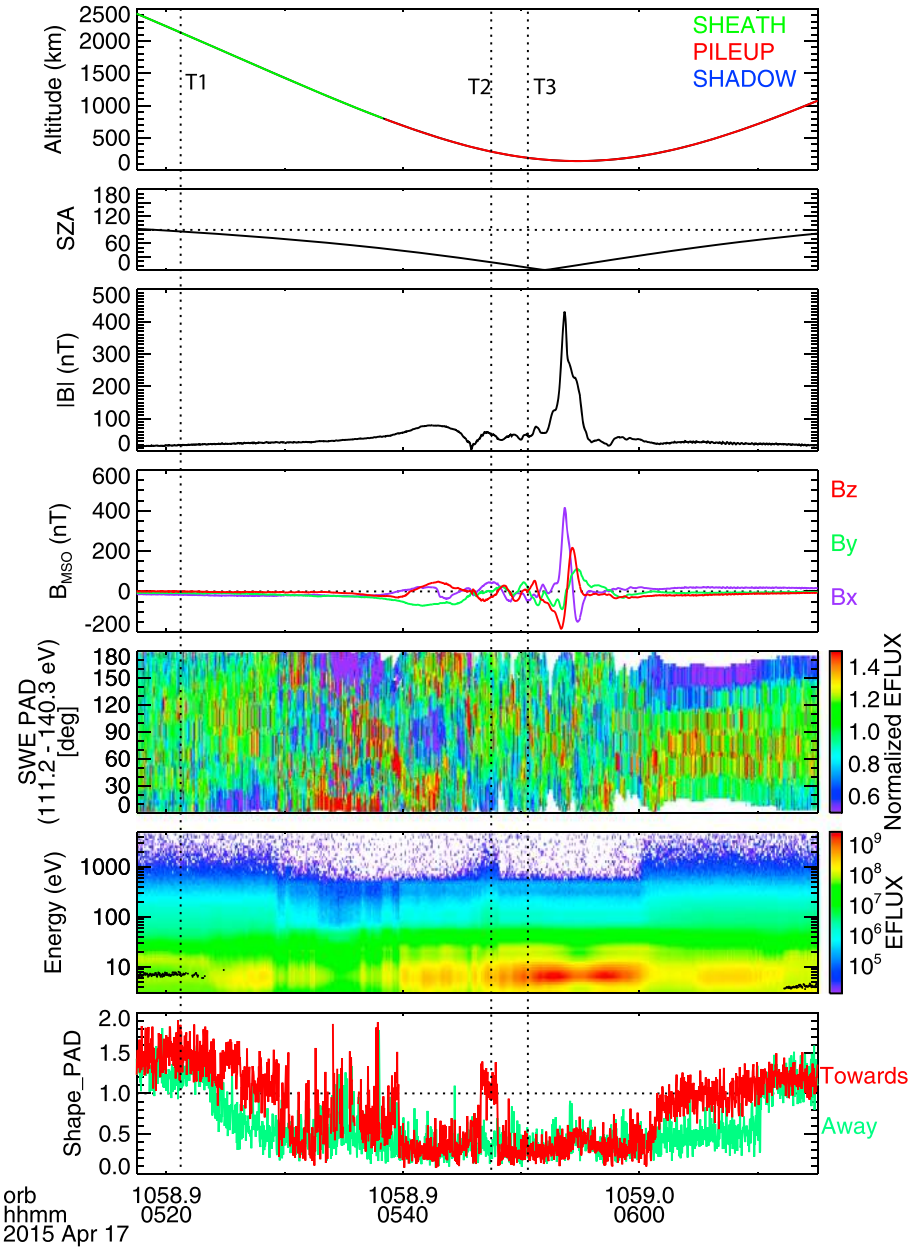

Figure 3. (top to bottom) Time series of the spacecraft altitude, SZA, magnetic field strength, magnetic field components in the MSO coordinates, the normalized pitch angle distribution of 111–140 eV electrons, the energy spectra, and shape parameters for electrons moving toward (red) and away from (green) the planet, respectively. The blue, green, and red colors in the altitude plot highlight the theoretical region for the optical shadow, magnetosheath, and the pileup region based on fittings of the bow shock and the magnetic pileup boundary [*Trotignon et al.*, 2006]. Three dashed vertical lines mark the time of extracted electron energy spectra in Figure 4. The black dots in the electron energy spectrogram plot indicate the spacecraft potential estimated by SWEA.

to transterminator closed field lines, with one foot point on the dayside and the other on the nightside. "Open" refers specifically to field lines with one foot point on the dayside and the other end connected to the IMF. "Draped" refers to field lines that are connected to the IMF on both ends (the normal definition) but also includes open field lines with one foot point on the nightside and the other connected to the IMF. In the latter case, solar wind electrons are observed in both directions because of backscatter and/or magnetic reflection. "Voids" are a second category of closed field line with both foot points on the nightside.

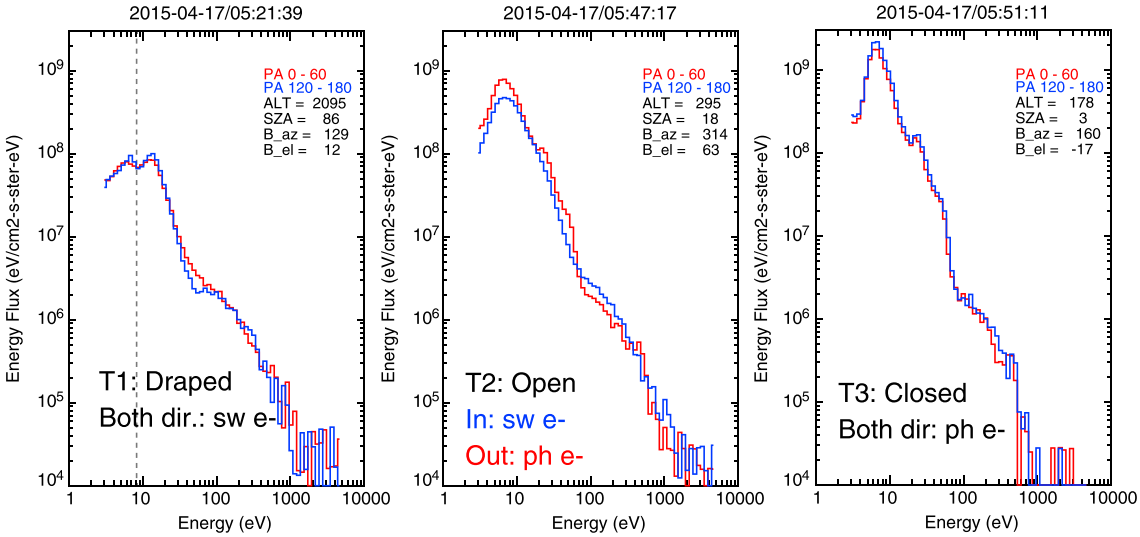

Figure 4. Electron energy spectra for the parallel (red) and antiparallel (blue) directions measured by SWEA. The red spectrum is averaged over pitch angles 0–60° and the blue spectrum over pitch angles 120°–180°. The vertical dashed line in the left plot marks the spacecraft potential. The altitude and SZA of the measurement, as well as the azimuthal (in the horizontal plane) and elevation angles (relative to the horizontal plane) of the local magnetic field, are shown in the top right corner. The three plots corresponding to the time marked out by the three dotted vertical lines in Figure 3.

4. Shape Parameter

To systematically distinguish ionospheric photoelectrons from solar wind electrons, we have designed a shape parameter to identify the He II peaks and the photoelectron knee in the measured energy spectra. We manually selected 60 photoelectron energy spectra and then calculated the derivative of the electron fluxes with respect to energy log space ($d(\log F)/d(\log E)$) using the three-point Lagrangian interpolation for each spectrum. This differentiation removes overall changes in the electron flux caused by variations in solar irradiance [e.g., *Banks and Nagy*, 1970; *Xu and Liemohn*, 2015] and the neutral atmospheric composition [e.g., *Xu et al*., 2014; *Xu et al*., 2015c] and also highlights sharp features in the spectral shape of photoelectrons, such as the He II peaks and the photoelectron knee, which are observed in photoelectrons but not the solar wind. We average the 60 derivatives to produce a template with good counting statistics (Figure S1 in the supporting information, black squares). For any measured electron distribution, we can calculate the electron flux derivatives and compare with the template. We define the shape parameter as the sum of the absolute differences between the measured derivative and the template from 20 eV to 80 eV. The more similar the observed derivative is to the template, the smaller the shape parameter and the more likely that the observed distribution contains photoelectrons. Figure S1 shows how a photoelectron observation (red) follows the template and has a small shape parameter, while a solar wind observation (blue) fails to capture the two sharp photoelectron features and has a large shape parameter. Although the shape parameter is a continuous quantity, since both populations can be present in various proportions on a given field line, we find that a value of unity provides a useful separation of distributions dominated by photoelectrons (shape parameter <1) and those dominated solar wind electrons (shape parameter >1). The shape parameter is calculated separately for the parallel (0°–60° pitch angle) and antiparallel (120°–180° pitch angle) populations. From the local magnetic field direction, we can determine which population is traveling toward the planet and which population is traveling away.

To demonstrate how the shape parameter works, we have selected two orbit examples, for dayside and nightside observations. For the dayside, Figure 3 shows the MAVEN measurements made from 05:17 to 06:15 UT (universal time) on 17 April 2015. The plots from top to bottom are the altitude, solar zenith angle (SZA), magnetic field strength and magnetic field components in MSO coordinates measured by MAG, the normalized 111–140 eV electron pitch angle distribution, and the electron energy spectra measured by SWEA (energy fluxes in units of eV cm^{-2} s^{-1} sr^{-1} eV^{-1}) and shape parameters for electrons moving toward (red) and away from (green) the planet, respectively. The direction of the electrons relative to the planet is determined based on the local magnetic field measurement. During this time range, the spacecraft moves

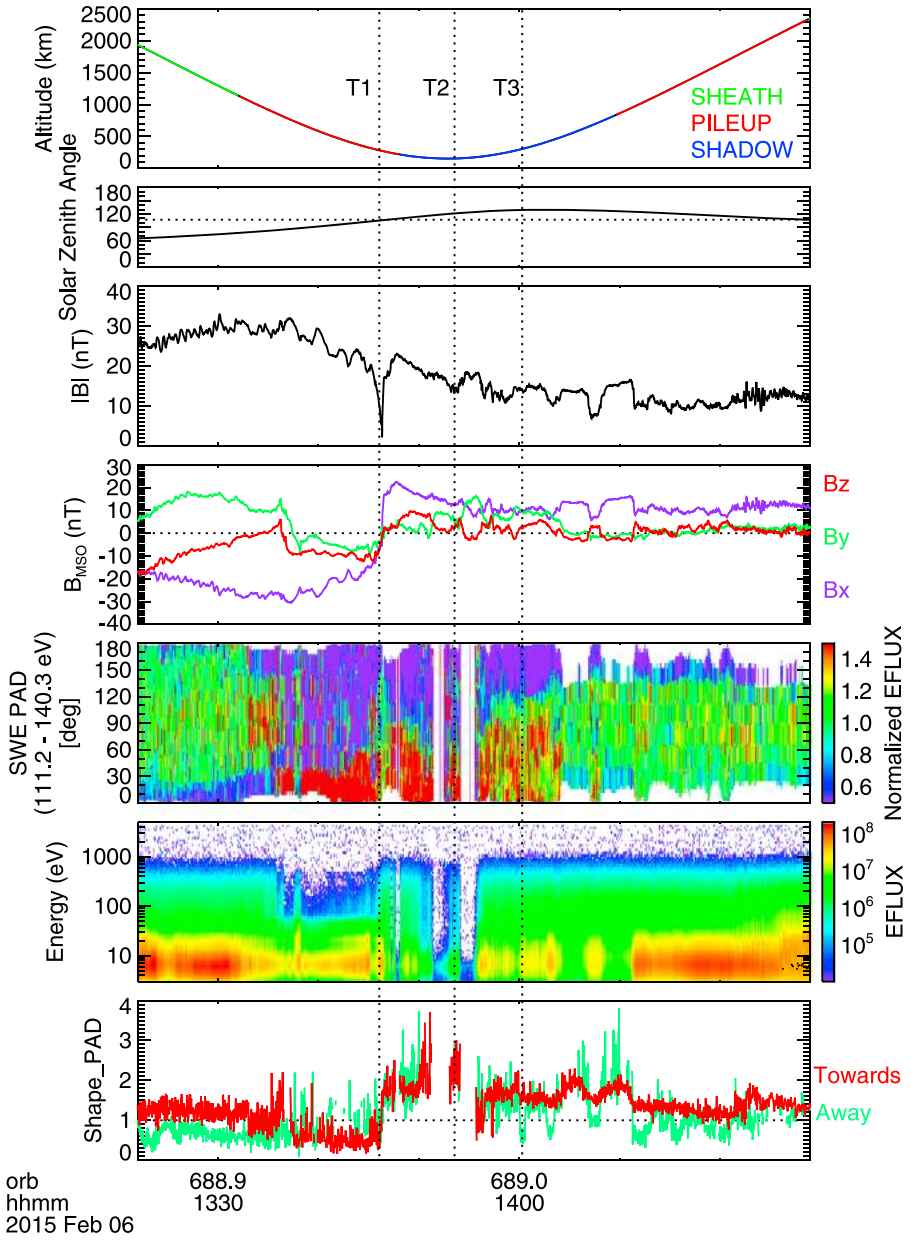

Figure 5. (top to bottom) Time series of the spacecraft altitude, SZA, magnetic field strength, magnetic field components in the MSO coordinates, the normalized pitch angle distribution of 111–140 eV measured, the energy spectra, and shape parameters for electrons moving toward (red) and away from (green) the planet, respectively. Same format as in Figure 3.

from high altitudes, where the magnetic field is weak, through the periapsis, which is dominated by the crustal fields (~05:40–05:56 UT), and then back to high altitudes. The three bottom plots simultaneously exhibit systematic, correlated changes. From 05:17 to 05:24 UT, the pitch angle distribution (PAD) is nearly isotropic, while the shape parameters for both directions are above 1. The left plot of Figure 4 shows the parallel and antiparallel electron spectra obtained at T1, marked by the first dotted vertical line in Figure 3. The electron spectra in both directions are typical solar wind/sheath electron spectra, with no evidence for photoelectron features. The local minimum at ~8 eV is caused by the spacecraft potential (vertical dashed line), which separates spacecraft photoelectrons at lower energies from ambient electrons at higher energies. From 05:30 to 06:00, the electron energy spectrogram (second plot from the bottom) shows one local maximum from 20 to 30 eV, corresponding to the He II feature of the photoelectrons, and another

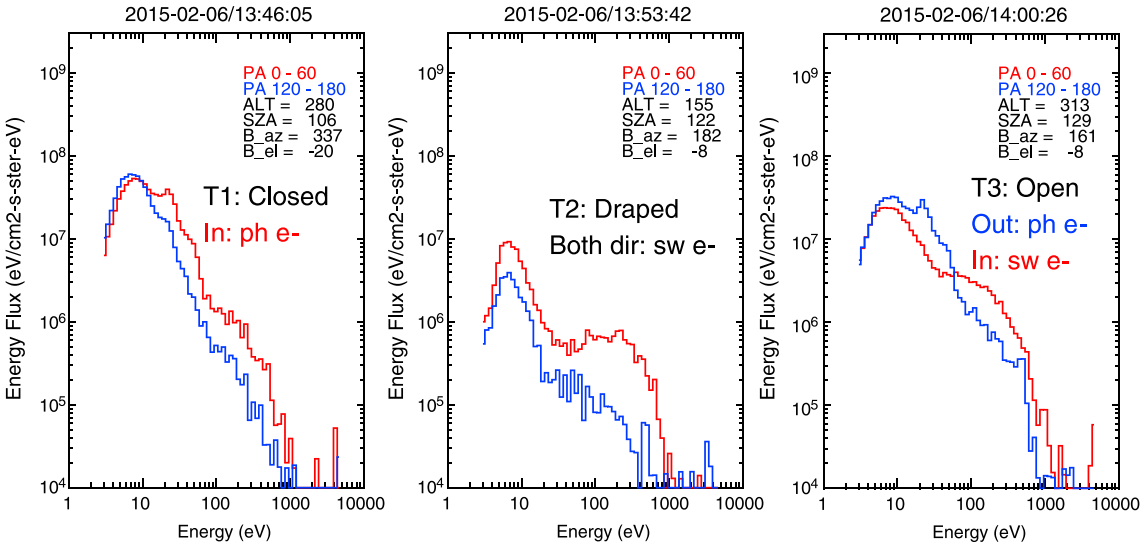

Figure 6. Electron energy spectra for parallel (red) and antiparallel (blue) directions measured by SWEA. The red spectrum is averaged over pitch angle 0–60° and the blue spectrum over pitch angle 120°–180°. The three plots corresponding to the time marked out by the three dotted vertical lines in Figure 5.

one near 500 eV, indicative of Auger electrons. Meanwhile, the shape parameters for both directions are below 1 (except for a brief interval from 05:46 to 05:48 UT, which will be described below). An example of the electron spectra in this region is shown in the right plot of Figure 4. Several photoelectron spectral features are present in both directions, including the He II peaks, the photoelectron knee, and the sharp drop in electron flux above ~500 eV. There are also time periods during which the shape parameter is <1 for electrons traveling away from the planet and >1 for electrons traveling toward the planet, including 05:24–05:30 UT, 05:46–05:48 UT, and 06:02–06:10 UT. During these time intervals, the pitch angle distribution exhibits a one-sided loss cone, which is classified as an indicator for open field lines [see *Brain et al*., 2007]. The parallel and antiparallel electron spectra for this case are shown in the middle plot of Figure 4. The local magnetic field has an elevation angle (relative to the horizontal plane) of 63°, pointing away from the planet; therefore, parallel electrons are flowing away from the planet and antiparallel electrons toward the planet. This conversion from pitch angles to the direction relative to the planet is implied below based on the local magnetic elevation angle. The spectrum for electrons traveling away from the planet (0°–60° pitch angle; red) shows typical photoelectron features, and the spectrum for electrons traveling in the opposite direction (120°–180° pitch angle; blue) is typical for the solar wind. Thus, the pitch angle-resolved shape parameter provides a reliable method for determining the source regions of the parallel and antiparallel electron populations, which we use to infer magnetic topology.

For the nightside, an example orbit on 6 February 2015 is shown in Figure 5, in the same format as in Figure 3. The spacecraft was on the nightside (SZA $>110°$) from 13:47 to 14:28 UT. Three parallel/antiparallel spectral pairs, selected at times marked by the dotted vertical lines in Figure 5, are chosen and shown in Figure 6. For T1, both shape parameters are <1 (Figure 5) and in the left plot of Figure 6. Electrons traveling toward the planet exhibit apparent photoelectron spectral features (Figure 6, left plot, red spectrum), interpreted as photoelectrons precipitating into the nightside on a closed field line that straddles the terminator. The spectra of electrons traveling in the opposite direction (blue) show only faint He II peaks and no clear evidence for a photoelectron knee. This pair of spectra indicates a closed field line with one foot point in the dayside ionosphere and the other foot point in darkness. Photoelectrons produced at the sunlit foot point travel along the field line and precipitate onto the dark foot point. A fraction of the precipitating flux is backscattered, with the photoelectron features washed out mainly by inelastic collisions. This measurement, however, was made near the terminator, and a better example for such a scenario is shown in *Xu et al*. [2016b]. More often than not, the spectrum of backscattered photoelectrons is too washed out to be identified by the shape parameter. Thus, for the nightside, the criterion for a closed field line is only that precipitating electrons have a shape parameter less than 1. For T2, the shape parameters are all >1 and the spectra for both directions (Figure 6, the

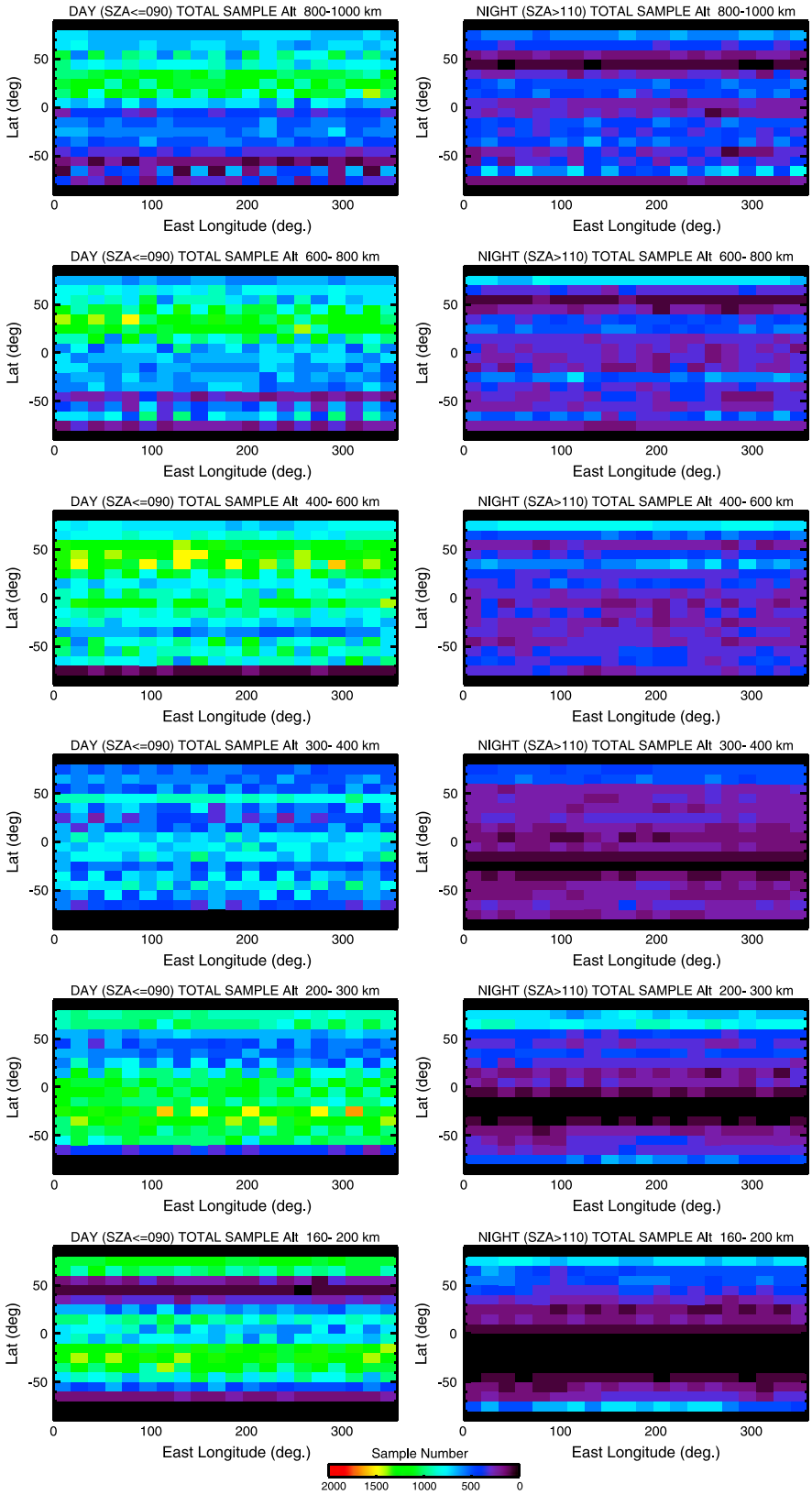

Figure 7. The total sample number against latitude and longitude. (left column) Dayside (SZA $<$ 90°) and (right column) nightside (SZA $>$ 110°). (top to bottom) Each row is for the altitude range of 800–1000 km, 600–800 km, 400–600 km, 300–400 km, 200–300 km, and 160–200 km, respectively.

middle plot) are solar wind/sheath-like. There are several time intervals when the shape parameter for electrons traveling away from the planet dips below 1 and remains above 1 for electrons traveling toward the planet. One example marked as T3 is shown in the right plot of Figure 6. The outflowing flux has a photoelectron spectrum (blue), while precipitating flux has a solar wind/sheath-like spectrum (red). To have access both populations, the field line has to have a foot point on the dayside, is pulled back to the nightside (where the measurement is made), and opens to the solar wind (see the yellow lines in Figure 2). Such open field lines have access to the dayside ionosphere and provide a path for ion escape. The last type of topology, superthermal electron voids, is another example of closed field lines, which exists mostly on the nightside. This can be seen in Figure 5, during the time intervals 13:52–13:53 UT and 13:54–13:56 UT, corresponding to extremely low electron fluxes (at or close to the background level at most energies) as well as the absence of shape parameters in both directions. (Our software tags shape parameters for such intervals as undefined.) A reliable method of identifying these regions is to set an energy flux threshold of $10^5\,\mathrm{eV\,cm^{-2}\,s^{-1}\,sr^{-1}\,eV^{-1}}$ at an energy of 40 eV. Observed fluxes below this threshold are identified as voids.

The two example orbits have demonstrated that the pitch angle-resolved shape parameter is reliable to infer the magnetic topology. However, a complication is that the shape parameter is a gradually increasing, instead of binary, number to represent changing from photoelectrons to solar wind electrons. The threshold of 1 used in this study is reasonable, but we have tested other thresholds, 0.7, 0.8, 1.2, and 1.4. The overall findings of this study stay the same, but the occurrence rate for each type of topology changes with different thresholds, as expected. In particular, when shape parameter is close to 1, it might be a mixed spectrum of both photoelectrons and solar wind/sheath electrons, for example, having both the He II feature and a less prominent flux drop near the photoelectron knee, or a degraded spectrum like the blue line in the left plot in Figure 6. In addition, when the magnetic elevation angle is small, a small perturbation in the magnetic field can change the field line direction, then the classification of away/toward for the shape parameter, consequently the determination of the topology. This is also why we do not distinguish solar wind electron flowing toward or away from the planet for open field lines on the dayside (see Table 1). These complications are important to take into consideration to analyze case studies. For this statistical study, the simple classifications in Table 1 are sufficient to obtain magnetic topology maps below.

5. Maps for Magnetic Topology

Now that we have established the methodology to infer magnetic topology from the pitch angle-resolved shape parameters to determine the magnetic topology, the three-dimensional maps can be created by examining all the available MAVEN data, from 1 December 2014 to 2 May 2016. This study is limited to an altitude range of 160–1000 km to investigate the crustal field control of the Martian magnetic topology. Above 1000 km altitude, the strongest crustal magnetic fields are comparable in strength to the solar wind magnetic field [e.g., *Brain et al*., 2003]. Below 160 km altitude, collisions become important for superthermal electrons [*Xu et al*., 2016a], and the pitch angle distribution becomes isotropic, so that our method for inferring topology is no longer valid.

The data are divided into six altitude ranges: 800–1000 km, 600–800 km, 400–600 km, 300–400 km, 200–300 km, and 160–200 km. For each altitude range, the data are further divided into 18° × 10° geographic longitude-latitude bins. Finally, we divide the data into dayside (SZA < 90°) and nightside (SZA > 110°). Although we present data mapped into geographic longitude and latitude, it is important to note that each bin contains all local times that fall within the SZA range. The total sample number for each bin (Figure 7) is the sum of all cases identified according to Table 1. Because 20% of the sky is outside SWEA's field of view, there is occasionally insufficient pitch angle coverage to calculate the parallel or antiparallel shape parameter. For this reason, 4% of data are excluded on the dayside and 18% on the nightside. The percentage of excluded spectra is higher on the nightside because the magnetic field direction tends to be close to the Mars-Sun line and thus near the edge of SWEA's field of view.

Before calculating the shape parameter, it is necessary to correct the electron data for energy shifts caused by the spacecraft potential (φ_{sc}) shifting the electron energy spectra [*Mitchell et al*., 2016]. When $|\varphi_{sc}| > 4$ V, the shift is large enough that the shape parameter for an uncorrected photoelectron spectrum can exceed 1. Depending on spacecraft orientation and plasma environment, the spacecraft potential is typically in the

range of −20 to +10 V. We have corrected the data for spacecraft potentials estimated from SWEA measurements, ranging from −16 V to −1 V in the ionosphere and > +3 V throughout the Mars environment. There is no need to correct for potentials from −1 to +3 V; however, some data must be excluded when the potential is more negative than −16 V.

Our current understanding of Mars' magnetic environment (based mostly on MGS observations) is that the southern hemisphere is dominated by crustal fields (to an altitude that depends on crustal field strength), while the north is dominated by draped solar wind magnetic fields [*Brain et al.*, 2003, 2006]. For the first time, the MAVEN orbit allows measurements of magnetic topology over wide ranges of local time, longitude, latitude, and altitude (Figure 7). The altitude ranges from the electron exobase (~160 km) to 400 km is of particular interest, because this region was sparsely mapped by MGS, with most of the measurements in the sunlit northern hemisphere.

5.1. Closed Field Lines

Figure 8 presents the occurrence rate of closed field lines on the dayside (left column) and the nightside (right column). The occurrence rate is the number of spectra satisfying the criteria for this category (Table 1) divided by the total sample number. The rows from top to bottom show the results for altitude ranges of 800–1000 km, 600–800 km, 400–600 km, 300–400 km, 200–300 km, and 160–200 km, respectively. Bins with no value (white) occur when the total sample number is less than 50, which applies to Figures 9–11 as well. The gray contours are the modeled crustal magnetic field magnitude at 400 km [*Morschhauser et al.*, 2014]. On the dayside, the most prominent trend is that the occurrence rate of closed field lines increases with decreasing altitude. This trend occurs over regions where the crustal field is relatively strong, as expected; however, it also occurs in the northern hemisphere, with closed field lines eventually dominating below 300–400 km (occurrence rate >50%), even over Hellas and Tharsis, the two most weakly magnetized regions of the crust. In the lowest altitude range, magnetic field lines are actually less likely to be closed in some regions of the southern hemisphere, particularly near longitudes of 20° and 300° and poleward of 40°S. Instead, these regions tend to have a fair amount of open field lines (see section 5.2).

For SZA > 110°, photoelectrons produced in the sunlit ionosphere can travel along closed magnetic field lines above the electron exobase and precipitate onto the nightside atmosphere [*Xu et al.*, 2016b]. The occurrence rate for such a magnetic field configuration is presented in the right column of Figure 8. Overall, the rate is generally below 25% but exceeds 50% in some regions. The occurrence rate drops below 200 km altitude, possibly because of proximity to the electron exobase, where inelastic collisions degrade the photoelectron features. For altitudes above 600 km, the maps are very similar, with regions of relatively high occurrence rates in the northern hemisphere and over the south polar region. Below 600 km, low occurrence rates correspond to the strong crustal fields, suggesting that field lines tend to close more locally in these regions (see section 5.4).

5.2. Open Field Lines

Maps for open field lines are shown in Figure 9, with the same format as in Figure 8 but with a more compressed color scale. On the dayside, different trends can be seen over weak and strong crustal magnetic sources. Over weak sources (mostly in the northern hemisphere), the occurrence rate for open field lines is low above 800 km altitude, increases to ~30–50% in the 300–400 km range, and then falls significantly below 200 km, where closed field lines dominate, as noted above. We will discuss this phenomenon in detail in section 6. Finally, we note that one region of open field lines in the northern hemisphere (50°–60°N, 160°–250°E) does map down to the 160–200 km altitude range. These open field lines may be associated with crustal sources near Arcadia (Figure 1).

At high altitudes (>800 km) over strong sources, open field lines cluster over the strong crustal sources and are likely magnetic cusps that span large angular ranges at this high altitude. These cusps are expected to become narrower with decreasing altitudes as they approach the crustal sources; however, our longitude-latitude grid is too coarse to identify this effect. The high occurrence rate of open field lines over the weakly magnetized regions within 30° of both poles, as well as on the nightside (right top plot), is probably due to open field lines originating from crustal sources and extending to high altitudes over the poles as they flare away from the Mars-Sun line. As the altitude decreases from 800 to 400 km, open field lines become less common over strong crustal sources, as closed field lines become predominant. Below 200 km, the occurrence rate of open field lines

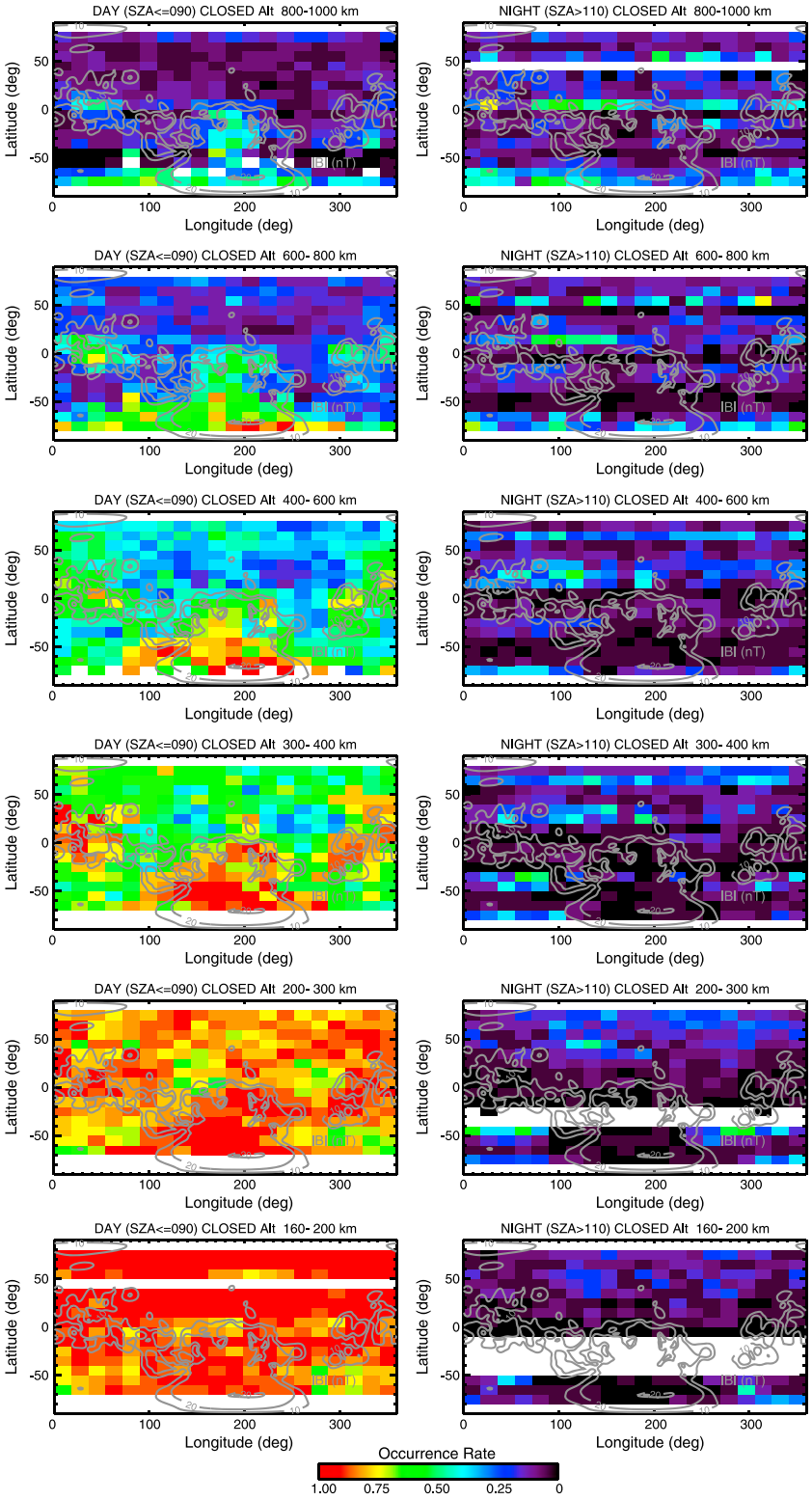

Figure 8. The occurrence rate for closed magnetic field lines (color scale) based on pitch angle-resolved shape parameters is mapped in geographic longitude and latitude. (left column) Maps for the dayside (SZA $< 90°$) and (right column) nightside (SZA $> 110°$) are shown. Representative field line geometries for the left (right) column are the purple (green) lines in Figure 2. (top to bottom) Altitude ranges for each row are 800–1000 km, 600–800 km, 400–600 km, 300–400 km, 200–300 km, and 160–200 km, respectively. The gray contours are the modeled crustal magnetic field magnitude at 400 km [*Morschhauser et al.*, 2014].

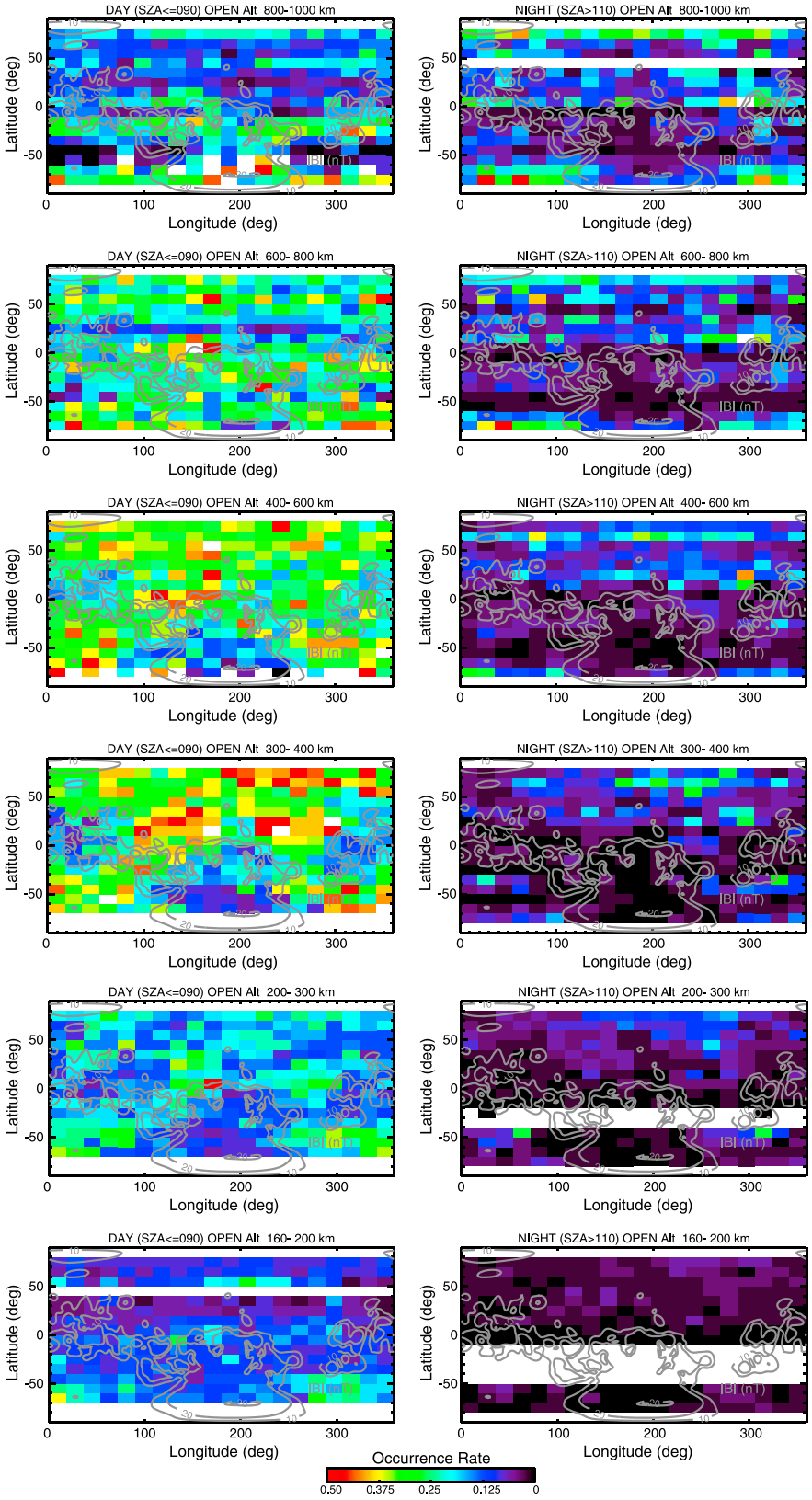

Figure 9. The maps of open field lines, the same format as in Figure 8. The color scale is from 0 (black) to 0.5 (red). (left and right columns) The representative field line geometry is illustrated by the orange field lines in Figure 2. The difference is whether it was observed on the dayside or nightside.

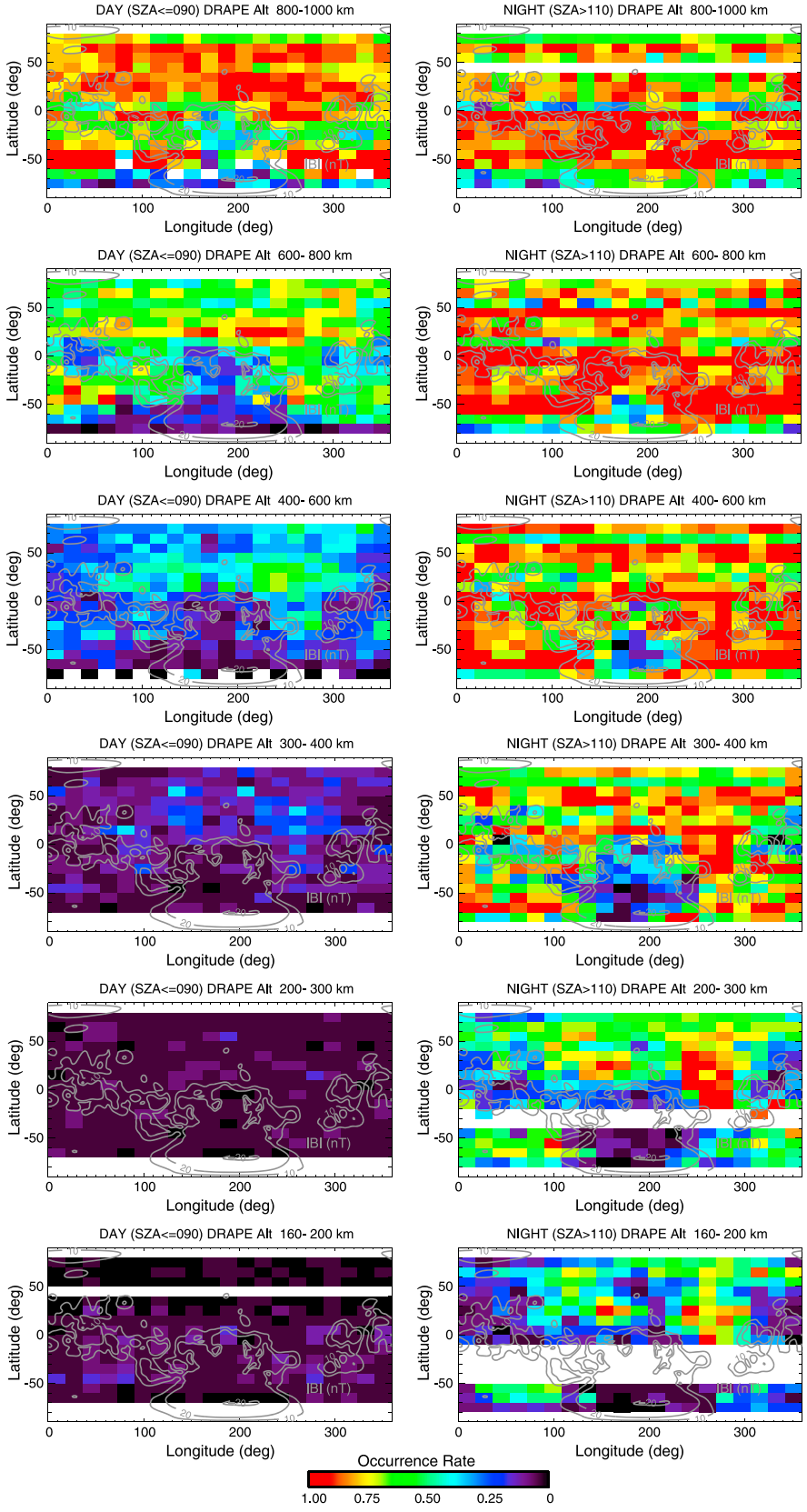

Figure 10. The maps of draped field lines, the same format as in Figure 8. The color scale is from 0 (black) to 1 (red). (right column) Both the draped IMF and open field lines attached to the nightside atmosphere (green lines in Figure 2).

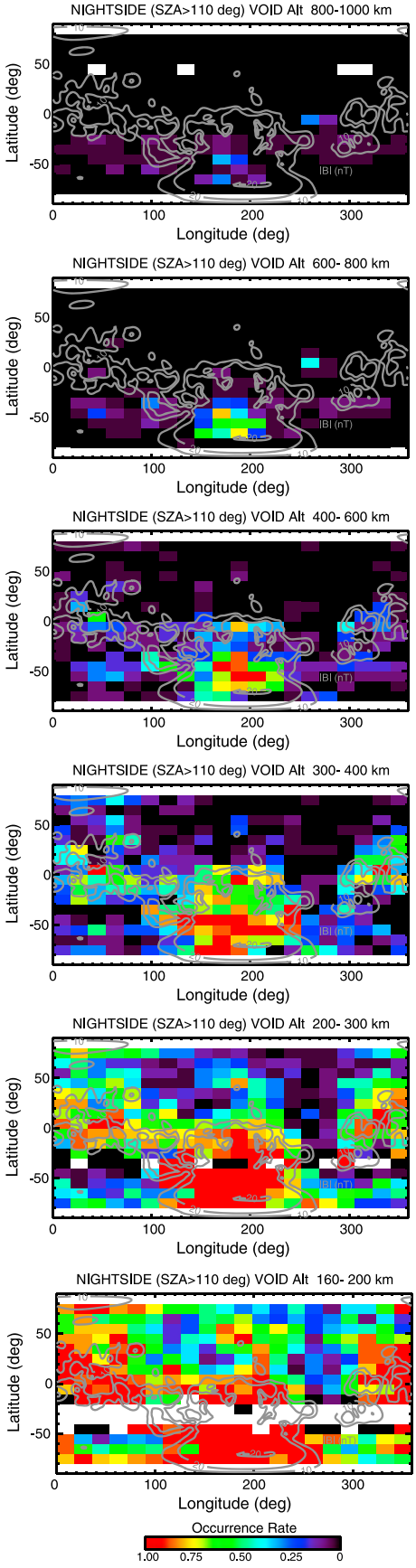

is low over most of the planet, except for Arcadia in the north, as noted above, and for two regions poleward of 40°S and centered near longitudes of 20° and 300°. The two southern regions of open field lines may map to relatively weak crustal magnetic sources around the periphery of the Hellas and Argyre impact basins (Figure 1).

In the northern hemisphere at solar zenith angles greater than 110°, open field lines with access to the dayside ionosphere are rare below 200 km altitude (Figure 9, bottom right plot). This is not unexpected, since open field lines originating in the dayside ionosphere, which become much more common above 200 km in the northern hemisphere, should flare away from the planet with increasing distance. This picture is confirmed by the first appearance of open field lines on the nightside in the 200–300 km altitude bin, with a generally increasing occurrence rate at higher altitudes. The two regions of open field lines at high southern latitudes (>60°S, 20°–120°E and >60°S, 290°–300°E) are likely associated with strong crustal magnetic sources near the South Pole. Interestingly, even for 800–1000 km in altitude, a region of low occurrence rates is seen and resembles the strong crustal regions (Figure 1), suggesting crustal control. While it might imply fewer open field lines resulting from interaction with IMF on the dayside when the strong southern crustal field located on the nightside, it is more likely that the underlying strong crustal fields on the nightside compel surrounding field lines away, which is an indirect proof of crustal control on the nightside extending beyond 1000 km [*Brain et al.*, 2003].

Figure 11. The maps of voids on the nightside (SZA > 110°). The color stands for the occurrence rate. The representative field line geometry is the black lines in Figure 2. (top to bottom) Each plot is for the altitude range of 800–1000 km, 600–800 km, 400–600 km, 300–400 km, 200–300 km, and 160–200 km, respectively. The color scale is from 0 (black) to 1 (red). The gray contours are the modeled crustal magnetic field magnitude at 400 km [*Morschhauser et al.*, 2014].

5.3. Draped Field Lines

Figure 10 shows the occurrence rate for the draped IMF on the dayside (the left column) and the nightside (the right column). On the dayside, the occurrence rate increases with altitude, as expected. Below 400 km altitude, the field lines are mostly closed or open, so that few are draped. Beginning at ~400 km, IMF starts to drape over the northern hemisphere, with an occurrence rate of 20%–50% in the 400–600 km range, >50% in the 600–800 km range, and ~100% above 800 km. In the south, strong crustal field regions can be discerned up to 1000 km with low draping occurrence rates and correspondingly high open and closed rates. A relatively high occurrence rate of draped fields is above 800 km in the 40°–60°S latitude range but avoiding the longitudes of the strongest crustal sources from 160° to 250°E. This latitude band includes the Hellas and Argyre basins, which are the most weakly magnetized regions of the southern hemisphere. Thus, it appears that draped IMF occupies a trough between strong crustal fields to the north and south. This is consistent with the analysis of MGS aerobraking magnetometer data [*Brain et al*., 2003], which indicates that the influence of the strongest crustal fields extends up to ~1000 km altitude on the dayside.

On the nightside, the occurrence rate is mostly higher than on the dayside, because the classification of draped field lines here includes both draped IMF and open field lines with one foot point on the nightside. Since draped field lines are expected to flare away from the Mars-Sun line with distance down the tail, the draped occurrence rate on the nightside is probably dominated by open field lines with foot points in the nightside atmosphere. The low occurrence rates below 800 km over strong crustal sources correspond to the locations of voids (see below).

5.4. Voids

Superthermal electron voids occur on closed crustal magnetic loops with both foot points in the nightside atmosphere, and any trapped electron population has pitch angle scattered into the loss cone or drifted out of the flux tube (Figure 11), so that the omnidirectional flux falls below our threshold (Table 1). Below 200 km, the void occurrence rate is >50% over most of the nightside and nearly unity over the strongest crustal sources. The six altitude ranges reveal the three-dimensional morphology of the voids, which extend up to ~1000 km over the stronger crustal sources. The longitude-latitude resolution of these maps is insufficient to resolve the narrow crustal magnetic cusps separating closed crustal loops of alternating polarity [*Mitchell et al*., 2007; *Lillis et al*., 2008]. These narrow cusps are readily seen in MAVEN time series data (e.g., feature T2 in Figure 4).

The occurrence rate of closed crustal magnetic field lines is generally higher on the dayside (Figure 8, left plots) than on the nightside (Figure 11). One would expect strong crustal fields to be compressed on the dayside by the solar wind interaction, so that closed fields would extend to higher altitudes on the nightside. However, our definition of voids does not include closed crustal field loops with trapped populations; some of which could be identified as draped in Figure 10 (right side).

6. Discussion

This study provides the first three-dimensional map of magnetic field topology from the electron exobase to 1000 km altitude. The electron exobase, which defines the lowest altitude at which electron energy-pitch angle distributions can be used to infer magnetic topology, is not at a fixed altitude but instead depends on the atmospheric density profile and the orientation of the magnetic field with respect to vertical. The lowest altitude bin in this study extends down to 160 km, which is the electron exobase altitude based on electron transport calculations along a vertical magnetic field line. When the field line is not vertical, the electron exobase occurs at a higher altitude. Figure 12a shows how the "collisional depth" τ [*Xu et al*., 2016a] varies with magnetic elevation angle or dip angle. The collisional depth $\tau(h)$, similar to the optical depth, is defined as the integral of the product of neutral or thermal plasma density and collision cross sections along a field line, from a high altitude where collisions are negligible to a given altitude h. For this calculation, we include electron-neutral, electron-electron, and electron-ion collisions [see *Xu et al*., 2016a, equation (2)]. This dimensionless quantity approximates the likelihood that an electron will suffer a collision as it travels from the top of a field line (here is 400 km) to a given altitude or vice versa. The electron exobase is defined to be the altitude where $\tau = 1$, i.e., below 185 km for magnetic elevation angles >10° and ~220 km for elevation angles ~1°. These values are for 20 eV electrons, but *Xu et al*. [2016a] showed that the exobase varies by less than 5 km from 20 to 200 eV.

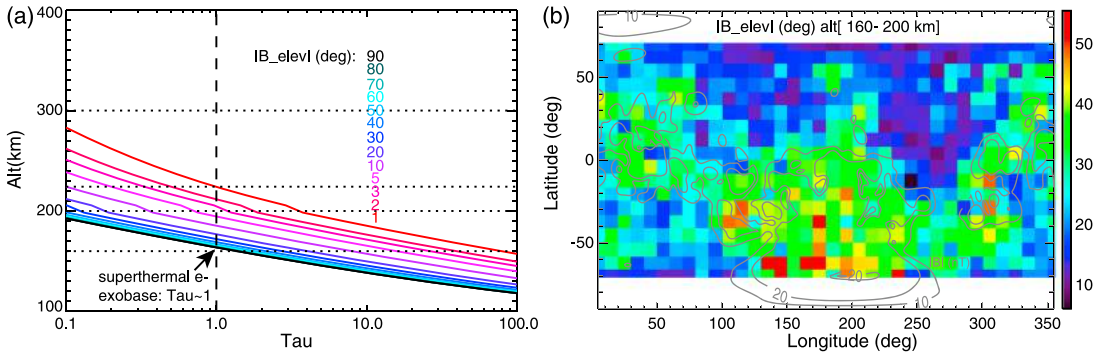

Figure 12. (a) Tau against altitude for different magnetic elevation angles. The vertical dashed line indicates Tau = 1, where the superthermal electron exobase is. (b) The average absolute magnetic elevation angle measured by MAVEN MAG at 160–200 km on the dayside. The gray contours are the modeled crustal magnetic field magnitude at 400 km [*Morschhauser et al*., 2014].

The neutral and plasma density profiles used for this calculation are taken from the simulation results of the Mars thermospheric general circulation model [*Bougher et al*., 1999, 2000], the same as *Xu et al*. [2016a], run at a solar longitude (L_s) of 90° and with an Earth $F_{10.7}$ of 100 solar flux unit (sfu) (~43 sfu at Mars). We assume that the density profiles are the same as SZA = 0° along the path for all the elevation angles, which results in an overestimation for the exobase altitudes in Figure 12a. Figure 12b illustrates the average absolute magnetic elevation angle measured by MAVEN MAG at 160–200 km on the dayside over the same time period as the electron data. For most of the regions, the average elevation angle is greater than 20°, which corresponds to an electron exobase of ~185 km. The higher exobase altitude for more horizontal fields can affect the results in the lowest altitude range, especially over the northern weak crustal regions, but our methodology should be robust above 200 km. This is also supported by the fact that the shape parameters pick up significant amount of open field lines for 200–300 km altitude range, which means that it is distinguishable between solar wind electrons and photoelectrons above 200 km.

Based on extensive observations at 400 km altitude by the MGS MAG/ER, the magnetic topology at 02:00 P.M. over the weakest crustal magnetic field regions in the northern hemisphere (50°–60°N) was found to be dominated by draped IMF [*Brain et al*., 2006]. Our maps show that this is in fact the lowest altitude where draped fields are significant in this region. Closed field lines are found to be dominant below 400 km, even over the weak crustal regions in the northern hemisphere. Although the electron exobase over these weak crustal regions intrudes into the lowest altitude bin, the occurrence rate for closed field lines increases from ~50% in the 300–400 km altitude bin to >75% in the 200–300 km bin, which indicates that closed field lines become increasingly prevalent at low altitudes. Although we have no way of determining field topology below the electron exobase, one possibility is that these closed field lines are of crustal origin. In this case, the closed loops either connect two distant, previously mapped crustal sources (for a possible example, see *Xu et al*. [2016b]) or they are associated with more local, unmapped sources. A second possibility is that an open or draped field line could have a perturbation such that a segment of the line starts below the electron exobase, rises up to the spacecraft altitude, then dips below the electron exobase again. If this is the main explanation, then these perturbations must have a vertical amplitude of approximately hundreds of kilometers, be widespread, and occur much of the time. Note that over the northern weak regions, the elevation angles are small in Figure 12b, which seemingly implies that these field lines are more likely to be draped IMF. However, these can also be large closed field lines connecting distant crustal sources so that they are mostly horizontal over the weak regions. Moreover, over the weak regions, if crustal fields are locally closed, it is likely that we are observing the top of the field lines, which tend to be horizontal as well. We can also use the maps to examine the photoelectron boundary (PEB) [*Mitchell et al*., 2000]. If we define the PEB as the altitude at which there is a 50% probability of observing closed field lines, then we can find that the PEB is located at 300–400 km in the north and ~600 km in the south.

The open field line occurrence rate decreases dramatically from 200–300 km range to 160–200 km range over the north. This could be explained by one or more of the following explanations. First, it could be that the electron exobase over weak crustal sources (more horizontal magnetic fields) intrudes into the lowest

altitude bin enough to bias the probability. Another contributing factor could be that the open field lines converge with decreasing altitude, thus spanning a smaller solid angle and becoming less likely to be observed. The third contributing factor could be that open field lines observed in the northern hemisphere above 200 km intersect the electron exobase at some distant location, most likely near the equator and/or in the south, where strong crustal magnetic sources are present. For such a scenario, open field lines originate from foot points above strong equatorial crustal sources and become more horizontal as they wrap around the planet and extend down the tail. These field lines pass over the northern hemisphere at higher altitudes with a more horizontal orientation. The presence of open field lines, possibly associated with strong crustal sources to the south, beneath the draped IMF would provide an explanation for the asymmetry in the draping direction inferred from MGS observations at 400 km altitude [*Brain et al*., 2006]. The draping pattern is possibly formed by open field lines draping over the northern hemisphere, resulting from the solar wind interaction with crustal fields at low altitudes. This suggests the presence of topological "layers" over the northern hemisphere: closed field lines below 200 km, open field lines with foot points at lower latitudes that pass over the northern hemisphere or closed field lines connecting distant crustal sources for 200–400 km, and draped IMF above 400 km. This suggests that the influence of crustal fields extends over the entire planet, preventing IMF penetration below ~400 km under the typical upstream conditions.

Consider the occurrence rate of low-altitude (160–200 km) closed field lines over the two most weakly magnetized regions in the northern hemisphere, the Utopia basin and the Tharsis rise. When both foot points are on the nightside (superthermal electron voids), the occurrence rate ranges from 10% to 50%. When both foot points are on the dayside (photoelectrons in both directions), the occurrence rate is close to 100%. One possibility is that collisions with the neutral atmosphere in the lower part of this altitude range are limiting our ability to infer topology because electron motion is dominated by collisions rather than by the magnetic field. On the nightside, voids would be caused by collisions and would occur regardless of the magnetic field topology. On the dayside, the spacecraft would be embedded in the ionospheric production region, and photoelectrons would be incident from all directions.

The observations shown in Figures 5 and 6 provide a test of this possibility. On this date, periapsis occurs in darkness at an altitude of 155 km (T2; Figure 5). At this time, the shape parameter analysis indicates a draped topology (Figure 6, middle); however, an alternative and more likely interpretation is an open field line with one foot point on the night hemisphere. The parallel population (red spectrum) is solar wind electrons precipitating onto the atmosphere, and the antiparallel population (blue spectrum) is backscattered electron flux [e.g., *Collinson et al*., 2016]. Both spectra show evidence for significant modification by collisions, including a reduced flux at all energies and a change in the spectral shape compared with solar wind spectra measured at higher altitudes (T3; Figure 6). On either side of the precipitation region at T2, the spacecraft passes through superthermal electron voids at nearly the same altitude. Without a precipitating solar wind flux, the electron populations at these locations have more completely thermalized, with only a residual superthermal population peaking near 7 eV. The intermittent occurrence of a precipitating flux indicates that magnetic topology still plays an important role at these altitudes. Thus, we can confidently interpret voids observed above 160 km as topological, which are closed field lines with both foot points on the nightside.

Since the atmospheric-scale height is smaller on the nightside, the electron exobase should occur at a lower altitude than shown in Figure 12a. Significant superthermal electron depletions caused by collisions with the neutral atmosphere occur below the electron exobase. For example, from the middle plot of Figure 6, we see that the electron flux does not reach the threshold of a void (by our definition) even at the periapsis altitude of 155 km. The occurrence rate of nighttime voids over Utopia and Tharsis is significant (10–50%) but much lower than the ~100% occurrence rate of closed field lines during the day. This difference might be because superthermal electron voids represent only a subset of closed field lines on the nightside. There could also be closed field lines with electrons mirroring above the collisional atmosphere, which would likely be categorized as draped field lines in our scheme (solar wind electrons in both directions). Another possibility is that there might in fact be fewer closed field lines over Utopia and Tharsis on the nightside, if it is more likely for these regions to reconnect with the solar wind in the tail than on the dayside. Now consider the two aforementioned possible closed geometries over the weak crustal regions, draped IMF intersecting the collisional atmosphere twice and closed field lines connecting to crustal source. For the first scenario, it might be that fewer draped IMFs connect twice to the dense atmosphere as they move toward nightside, only intersecting once or not at all. For the closed field lines connecting distant crustal source, i.e., the northern hemisphere

layering, crustal fields on the dayside, opened by reconnection, tend to lay over the weak regions, either just as open field lines or closed up with distant crustal sources. In contrast, on the nightside, crustal fields tend to stretch to down tail and reconnect with solar wind fields, no longer "protecting" the weak regions so that it is easier for IMF to penetrate into low altitudes and form open field lines.

On the nightside, the northern hemisphere is found to be mostly draped according to our selection criteria (Table 1). However, as noted above, our criteria for nightside draped fields also include open field lines with one foot point in the nightside atmosphere. MGS observations show that open field lines are common in the northern hemisphere at 02:00 A.M. local time [*Mitchell et al*., 2007; *Lillis et al*., 2008]. In contrast, electron voids dominate over strong crustal fields in the southern hemisphere and near the equator at low altitudes. The detailed structure of these void regions [see *Mitchell et al*., 2005, Figure 2] is unresolved by our longitude-latitude grid. Such closed field lines prevent superthermal electron precipitation, which is the main source of ionization on the nightside, as well as day-to-night transport above the exobase. Where these closed field lines map to the electron exobase, the ionosphere must be dominated by long-lived ions, such as NO^+, that can survive during the Martian night [*González-Galindo et al*., 2013]. In the north, cross-terminator closed field lines (occurrence rate $<$~25%) can also provide a source of superthermal electrons to the deep nightside [*Xu et al*., 2016b].

All of the magnetic field topologies inferred in this study are present in MHD simulations (e.g., Figure 2). For example, the low-altitude cross-terminator closed field lines are common in both observations and simulations of the northern hemisphere [see also *Xu et al*., 2016b]. Also, the absence of draped field lines below 300 km altitude on the dayside is shown in both model predictions and observations (Figure 10, bottom left plot). Thus, this technique can be used to validate simulation results.

Open field lines can intersect the electron exobase on either the dayside or the nightside. Open field lines connected to the dayside ionosphere provide a path for ion outflow and are thus potentially important for ion escape. These lines occur $<$50% of the time on the dayside and are generally confined to high latitudes on the nightside, with a higher occurrence rate in the northern hemisphere. Open field lines connected to the nightside atmosphere allow precipitation of solar wind electrons and (episodically) solar energetic particle (SEP) electrons, which causes heating, excitation, and ionization, and occasionally observable auroral emissions [e.g., *Schneider et al*., 2015]. These field lines are common on the nightside [e.g., *Mitchell et al*., 2005] but are identified as draped in our study (Figure 10, right side), which is based on the shapes of electron energy spectra and not the presence of one-sided loss cones.

7. Conclusions and Future Work

MAVEN is the first mission to systematically sample the Mars plasma environment down to altitudes of ~150 km over wide ranges of longitude, latitude, local time, and solar zenith angle. We can readily distinguish ionospheric primary photoelectrons from solar wind electrons, and with pitch angle-resolved shape parameters, we deduce the magnetic topology from the electron exobase to 1000 km altitude. For the first time, we are able to determine the topology below 400 km. This study finds that the sunlit hemisphere below 400 km altitude is dominated by closed field lines, even in the northern hemisphere. These maps combined illustrate how the magnetic topology evolves in three dimensions, in particular how one topology connects to another and how crustal control can happen over a large distance. Overall, the results are consistent with many findings from MGS and also qualitatively agree with MHD results. Open field lines attached to the dayside ionosphere can be mapped out by this methodology, which is a key piece to understand ion outflow, and those intersecting the nightside ionosphere allow energetic electron (solar wind electrons and SEP electrons) precipitations, critical to understand the nightside ionosphere dynamics.

This study focuses only on the magnetic topology's dependence on the geographic latitude, longitude, and altitude. One future work would analyze how the topology changes with upstream conditions and the orientation of the crustal magnetic fields with respect to the Mars-Sun line. Our methodology can also be used to analyze the tail magnetic topology as well, especially in the flanks. In addition, the observations qualitatively confirm the predictions of field line types from the multispecies Mars-MHD model. A direct data-model comparison can be performed in the future to further our understanding of the Martian plasma environment from both observational and theoretical points of views.

Acknowledgments
This work was supported by the NASA Mars Scout Program. Work at Michigan was supported by NASA R&A grants. The MAVEN data used in this study are available through Planetary Data System. The BATS-R-US code is publicly available from http://csem. engin.umich.edu/tools/swmf. For distribution of the MHD magnetic field line tracing results used in this study, contact X. Fang (Xiaohua.Fang@lasp.colorado.edu).

References

Acuna, M., et al. (1992), Mars observer magnetic fields investigation, *J. Geophys. Res.*, *97*(E5), 7799–7814, doi:10.1029/92JE00344.
Acuna, M., et al. (1998), Magnetic field and plasma observations at Mars: Initial results of the Mars Global Surveyor mission, *Science*, *279*(5357), 1676–1680, doi:10.1126/science.279.5357.1676.
Banks, P., and A. Nagy (1970), Concerning the influence of elastic scattering upon photoelectron transport and escape, *J. Geophys. Res.*, *75*(10), 1902–1910, doi:10.1029/JA075i010p01902.
Barabash, S., et al. (2006), The analyzer of space plasmas and energetic atoms (aspera-3) for the Mars express mission, *Space Sci. Rev.*, *126*(1–4), 113–164.
Bertaux, J.-L., F. Leblanc, O. Witasse, E. Quemerais, J. Lilensten, S. Stern, B. Sandel, and O. Korablev (2005), Discovery of an aurora on Mars, *Nature*, *435*(7043), 790–794, doi:10.1038/nature03603.
Bougher, S. W., S. Engel, R. Roble, and B. Foster (1999), Comparative terrestrial planet thermospheres: 2. Solar cycle variation of global structure and winds at equinox, *J. Geophys. Res.*, *104*(E7), 16,591–16,611, doi:10.1029/1998JE001019.
Bougher, S. W., S. Engel, R. Roble, and B. Foster (2000), Comparative terrestrial planet thermospheres: 3. Solar cycle variation of global structure and winds at solstices, *J. Geophys. Res.*, *105*(E7), 17,669–17,692, doi:10.1029/1999JE001232.
Brain, D., F. Bagenal, M. Acuna, and J. Connerney (2003), Martian magnetic morphology: Contributions from the solar wind and crust, *J. Geophys. Res.*, *108*(A12), 1424, doi:10.1029/2002JA009482.
Brain, D., J. Halekas, R. Lillis, D. Mitchell, R. Lin, and D. Crider (2005), Variability of the altitude of the Martian sheath, *Geophys. Res. Lett.*, *32*, L18203, doi:10.1029/2005GL023126.
Brain, D., J. Halekas, L. Peticolas, R. Lin, J. Luhmann, D. Mitchell, G. Delory, S. Bougher, M. Acuña, and H. Rème (2006), On the origin of aurorae on Mars, *Geophys. Res. Lett.*, *33*, L01201, doi:10.1029/2005GL024782.
Brain, D., R. Lillis, D. Mitchell, J. Halekas, and R. Lin (2007), Electron pitch angle distributions as indicators of magnetic field topology near Mars, *J. Geophys. Res.*, *112*, A09201, doi:10.1029/2007JA012435.
Collinson, G., et al. (2015), Electric Mars: The first direct measurement of an upper limit for the Martian "polar wind" electric potential, *Geophys. Res. Lett.*, *42*, 9128–9134, doi:10.1002/2015GL065084.
Collinson, G., et al. (2016), Electric Mars: A large trans-terminator electric potential drop on closed magnetic field lines above Utopia Planitia, *J. Geophys. Res. Space Physics*, *121*, doi:10.1002/2016JA023589.
Connerney, J., M. Acuña, N. Ness, G. Kletetschka, D. Mitchell, R. Lin, and H. Reme (2005), Tectonic implications of Mars crustal magnetism, *Proc. Natl. Acad. Sci. U.S.A.*, *102*(42), 14,970–14,975, doi:10.1073/pnas.0507469102.
Connerney, J. E. P., J. Espley, P. Lawton, S. Murphy, J. Odom, R. Oliversen, and D. Sheppard (2015), The MAVEN magnetic field investigation, *Space Sci. Rev.*, *195*(1–4), 257–291, doi:10.1007/s11214-015-0169-4.
Dubinin, E., M. Fraenz, J. Woch, J. Winnigham, R. Frahm, R. Lundin, and S. Barabash (2008), Suprathermal electron fluxes on the nightside of Mars: Aspera-3 observations, *Planet. Space Sci.*, *56*(6), 846–851, doi:10.1016/j.pss.2007.12.010.
Fang, X., Y. Ma, D. Brain, Y. Dong, and R. Lillis (2015), Control of Mars global atmospheric loss by the continuous rotation of the crustal magnetic field: A time-dependent MHD study, *J. Geophys. Res. Space Physics*, *120*, 10,926–10,944, doi:10.1002/2015JA021605.
Fillingim, M., L. Peticolas, R. Lillis, D. Brain, J. Halekas, D. Lummerzheim, and S. Bougher (2010), Localized ionization patches in the nighttime ionosphere of Mars and their electrodynamic consequences, *Icarus*, *206*(1), 112–119, doi:10.1016/j.icarus.2009.03.005.
Fillingim, M. O., L. M. Peticolas, R. J. Lillis, D. A. Brain, J. S. Halekas, D. L. Mitchell, R. P. Lin, D. Lummerzheim, S. W. Bougher, and D. L. Kirchner (2007), Model calculations of electron precipitation induced ionization patches on the nightside of Mars, *Geophys. Res. Lett.*, *34*, L12101, doi:10.1029/2007GL029986.
Frahm, J. R., J. D. Sharber, R. Winningham, M. W. Link, J. U. Liemohn, A. J. Kozyra, D. R. Coates, S. Linder, R. Barabash, and A. F. Lundin (2010), Estimation of the escape of photoelectrons from Mars in 2004 liberated by the ionization of carbon dioxide and atomic oxygen, *Icarus*, *206*(1), 50–63, doi:10.1016/j.icarus.2009.03.024.
Frahm, R., et al. (2006), Carbon dioxide photoelectron energy peaks at Mars, *Icarus*, *182*(2), 371–382, doi:10.1016/j.icarus.2006.01.014.
Ganguli, S. B. (1996), The polar wind, *Rev. Geophys.*, *34*(3), 311–348, doi:10.1029/96RG00497.
Glocer, A., G. Tóth, T. Gombosi, and D. Welling (2009), Modeling ionospheric outflows and their impact on the magnetosphere, initial results, *J. Geophys. Res.*, *114*, A05216, doi:10.1029/2009JA014053.
González-Galindo, F., J.-Y. Chaufray, M. A. López-Valverde, G. Gilli, F. Forget, F. Leblanc, R. Modolo, S. Hess, and M. Yagi (2013), Three-dimensional Martian ionosphere model: I. The photochemical ionosphere below 180 km, *J. Geophys. Res. Planets*, *118*, 2105–2123, doi:10.1002/jgre.20150.
Harada, Y., et al. (2016), MAVEN observations of electron-induced whistler mode waves in the Martian magnetosphere, *J. Geophys. Res. Space Physics*, *121*, 9717–9731, doi:10.1002/2016JA023194.
Harnett, E. M., and R. M. Winglee (2005), Three-dimensional fluid simulations of plasma asymmetries in the Martian magnetotail caused by the magnetic anomalies, *J. Geophys. Res.*, *110*, A07226, doi:10.1029/2003JA010315.
Jakosky, B. M., et al. (2015), The Mars Atmosphere and Volatile Evolution (MAVEN) mission, *Space Sci. Rev.*, *195*(1–4), 3–48, doi:10.1007/s11214-015-0139-x.
Khazanov, G. V., M. W. Liemohn, and T. E. Moore (1997), Photoelectron effects on the self-consistent potential in the collisionless polar wind, *J. Geophys. Res.*, *102*, 7509–7522, doi:10.1029/96JA03343.
Krymskii, A., T. Breus, N. Ness, M. Acuña, J. Connerney, D. Crider, D. Mitchell, and S. Bauer (2002), Structure of the magnetic field fluxes connected with crustal magnetization and topside ionosphere at Mars, *J. Geophys. Res.*, *107*(A9), 1245, doi:10.1029/2001JA000239.
Krymskii, A., N. Ness, D. Crider, T. Breus, M. Acuña, and D. Hinson (2004), Solar wind interaction with the ionosphere/atmosphere and crustal magnetic fields at Mars: Mars Global Surveyor magnetometer/electron reflectometer, radio science, and accelerometer data, *J. Geophys. Res.*, *109*, A11306, doi:10.1029/2004JA010420.
Leblanc, F., et al. (2008), Observations of aurorae by SPICAM ultraviolet spectrograph on board Mars Express: Simultaneous ASPERA-3 and MARSIS measurements, *J. Geophys. Res.*, *113*, A08311, doi:10.1029/2008JA013033.
Liemohn, M. W., D. L. Mitchell, A. F. Nagy, J. L. Fox, T. W. Reimer, and Y. Ma (2003), Comparisons of electron fluxes measured in the crustal fields at Mars by the mgs magnetometer/electron reflectometer instrument with a *b* field-dependent transport code, *J. Geophys. Res.*, *108*(E12), 5134, doi:10.1029/2003JE002158.
Liemohn, M. W., et al (2006a), Numerical interpretation of high-altitude photoelectron observations, *Icarus*, *182*(2), 383–395, doi:10.1016/j.icarus.2005.10.036.

Liemohn, M. W., Y. Ma, R. A. Frahm, X. Fang, J. U. Kozyra, A. F. Nagy, J. D. Winningham, J. R. Sharber, S. Barabash, and R. Lundin (2006b), Mars global MHD predictions of magnetic connectivity between the dayside ionosphere and the magnetospheric flanks, *Space Sci. Rev.*, *126*, 63–76, doi:10.1007/s11214-006-9116-8.

Liemohn, M., Y. Ma, A. Nagy, J. Kozyra, J. Winningham, R. Frahm, J. Sharber, S. Barabash, and R. Lundin (2007), Numerical modeling of the magnetic topology near Mars auroral observations, *Geophys. Res. Lett.*, *34*, L24202, doi:10.1029/2007GL031806.

Lillis, R. J., and D. A. Brain (2013), Nightside electron precipitation at Mars: Geographic variability and dependence on solar wind conditions, *J. Geophys. Res. Space Physics*, *118*, 3546–3556, doi:10.1002/jgra.50171.

Lillis, R. J., D. L. Mitchell, R. P. Lin, J. E. P. Connerney, and M. H. Acuña (2004), Mapping crustal magnetic fields at Mars using electron reflectometry, *Geophys. Res. Lett.*, *31*, L15702, doi:10.1029/2004GL020189.

Lillis, R. J., D. L. Mitchell, R. P. Lin, and M. H. Acuña (2008), Electron reflectometry in the Martian atmosphere, *Icarus*, *194*, 544–561, doi:10.1016/j.icarus.2007.09.030.

Lillis, R. J., M. O. Fillingim, L. M. Peticolas, D. A. Brain, R. P. Lin, and S. W. Bougher (2009), Nightside ionosphere of Mars: Modeling the effects of crustal magnetic fields and electron pitch angle distributions on electron impact ionization, *J. Geophys. Res.*, *114*, E11009, doi:10.1029/2009JE003379.

Lillis, R. J., et al (2015), Characterizing atmospheric escape from Mars today and through time, with MAVEN, *Space Sci. Rev.*, *195*(1–4), 357–422, doi:10.1007/s11214-015-0165-8.

Ma, Y., A. F. Nagy, I. V. Sokolov, and K. C. Hansen (2004), Three-dimensional, multispecies, high spatial resolution MHD studies of the solar wind interaction with Mars, *J. Geophys. Res.*, *109*, A07211, doi:10.1029/2003JA010367.

Ma, Y., X. Fang, C. T. Russell, A. F. Nagy, G. Toth, J. G. Luhmann, D. A. Brain, and C. Dong (2014), Effects of crustal field rotation on the solar wind plasma interaction with Mars, *Geophys. Res. Lett.*, *41*, 6563–6569, doi:10.1002/2014GL060785.

Ma, Y. J., X. Fang, A. F. Nagy, C. T. Russell, and G. Toth (2014), Martian ionospheric responses to dynamic pressure enhancements in the solar wind, *J. Geophys. Res. Space Physics*, *119*, 1272–1286, doi:10.1002/2013JA019402.

Mitchell, D. L., R. J. Lillis, R. P. Lin, J. E. P. Connerney, and M. H. Acuña (2007), A global map of Mars' crustal magnetic field based on electron reflectometry, *J. Geophys. Res.*, *112*, E01002, doi:10.1029/2005JE002564.

Mitchell, D. L., et al. (2016), The MAVEN Solar Wind Electron Analyzer, *Space Sci. Rev.*, *200*(1–4), 495–528.

Mitchell, D., R. Lin, H. Reme, D. Crider, P. Cloutier, J. Connerney, M. Acuña, and N. Ness (2000), Oxygen Auger electrons observed in Mars' ionosphere, *Geophys. Res. Lett.*, *27*(13), 1871–1874, doi:10.1029/1999GL010754.

Mitchell, D., R. Lin, C. Mazelle, H. Reme, P. Cloutier, J. Connerney, M. Acuña, and N. Ness (2001), Probing Mars' crustal magnetic field and ionosphere with the MGS electron reflectometer, *J. Geophys. Res.*, *106*(E10), 23,419–23,427, doi:10.1029/2000JE001435.

Morschhauser, A., V. Lesur, and M. Grott (2014), A spherical harmonic model of the lithospheric magnetic field of Mars, *J. Geophys. Res. Planets*, *119*, 1162–1188, doi:10.1002/2013JE004555.

Peterson, W. K., et al. (2016), Photoelectrons and solar ionizing radiation at Mars: Predictions versus MAVEN observations, *J. Geophys. Res. Space Physics*, *121*, 8859–8870, doi:10.1002/2016JA022677.

Schneider, N. M., et al. (2015), Discovery of diffuse aurora on Mars, *Science*, *350*(6261), aad0313.

Shane, A. D., S. Xu, M. W. Liemohn, and D. L. Mitchell (2016), Mars nightside electrons over strong crustal fields, *J. Geophys. Res. Space Physics*, *121*, 3808–3823, doi:10.1002/2015JA021947.

Steckiewicz, M., et al. (2015), Altitude dependence of nightside Martian suprathermal electron depletions as revealed by MAVEN observations, *Geophys. Res. Lett.*, *42*, 8877–8884, doi:10.1002/2015GL065257.

Trotignon, J., C. Mazelle, C. Bertucci, and M. Acuna (2006), Martian shock and magnetic pile-up boundary positions and shapes determined from the Phobos 2 and Mars Global Surveyor data sets, *Planet. Space Sci.*, *54*(4), 357–369, doi:10.1016/j.pss.2006.01.003.

Xu, S., and M. W. Liemohn (2015), Superthermal electron transport model for Mars, *Earth Space Sci.*, *2*, 47–64, doi:10.1002/2014EA000043.

Xu, S., M. W. Liemohn, D. L. Mitchell, and M. D. Smith (2014), Mars photoelectron energy and pitch angle dependence on intense lower atmospheric dust storms, *J. Geophys. Res. Planets*, *119*, 1689–1706, doi:10.1002/2013JE004594.

Xu, S., M. W. Liemohn, and D. L. Mitchell (2015a), Solar wind electron precipitation into the dayside Martian upper atmosphere through the cusps of strong crustal fields, *J. Geophys. Res. Space Physics*, *119*, 10,100–10,115, doi:10.1002/2014JA020363.

Xu, S., M. W. Liemohn, W. Peterson, J. Fontenla, and P. Chamberlin (2015b), Comparison of different solar irradiance models for the superthermal electron transport model for Mars, *Planet. Space Sci.*, doi:10.1016/j.pss.2015.09.008.

Xu, S., M. Liemohn, S. Bougher, and D. Mitchell (2015c), Enhanced carbon dioxide causing the dust storm-related increase in high-altitude photoelectron fluxes at Mars, *Geophys. Res. Lett.*, *42*, 9702–9710, doi:10.1002/2015GL066043.

Xu, S., M. Liemohn, S. Bougher, and D. Mitchell (2016a), Martian high-altitude photoelectrons independent of solar zenith angle, *J. Geophys. Res. Space Physics*, *121*, 3767–3780, doi:10.1002/2015JA022149.

Xu, S., et al. (2016b), Deep nightside photoelectron observations by MAVEN SWEA: Implications for Martian northern-hemispheric magnetic topology and nightside ionosphere source, *Geophys. Res. Lett.*, *43*, 8876–8884, doi:10.1002/2016GL070527.

AGU PUBLICATIONS

JGR

Journal of Geophysical Research: Space Physics

RESEARCH ARTICLE
10.1002/2017JA024497

Key Points:
- We determined the influence of the main driving parameters on the altitude of the photoelectron boundary (PEB)
- We identified clear plasma and magnetic field characteristics of the PEB and discuss its nature with respect to the ionopause
- We show how the PEB dynamics modifies the tail cross section used for estimating the photoelectrons (and associated ions) escape rate

Correspondence to:
P. Garnier,
philippe.garnier@irap.omp.eu

Citation:
Garnier, P., Steckiewicz, M., Mazelle, C., Xu, S., Mitchell, D., Holmberg, M. K. G., … Jakosky, B. M. (2017). The Martian photoelectron boundary as seen by MAVEN. *Journal of Geophysical Research: Space Physics*, *122*. https://doi.org/10.1002/2017JA024497

Received 21 JUN 2017
Accepted 2 SEP 2017
Accepted article online 11 SEP 2017

The Martian Photoelectron Boundary as Seen by MAVEN

P. Garnier[1], M. Steckiewicz[1], C. Mazelle[1], S. Xu[2,3], D. Mitchell[2], M. K. G. Holmberg[1], J. S. Halekas[4], L. Andersson[5], D. A. Brain[5], J. E. P. Connerney[6], J. R. Espley[6], R. J. Lillis[2], J. G. Luhmann[2], J.-A. Sauvaud[1], and B. M. Jakosky[5]

[1]IRAP, Université de Toulouse, CNRS, UPS, CNES, Toulouse, France, [2]Space Sciences Laboratory, University of California, Berkeley, CA, USA, [3]Department of Climate and Space Sciences and Engineering, University of Michigan, Ann Arbor, MI, USA, [4]NASA Goddard Space Flight Center, Greenbelt, MD, USA, [5]Laboratory for Atmospheric and Space Physics, University of Colorado Boulder, Boulder, CO, USA, [6]Department of Physics and Astronomy, University of Iowa, Iowa City, IA, USA

Abstract Photoelectron peaks in the 20–30 eV energy range are commonly observed in the planetary atmospheres, produced by the intense photoionization from solar 30.4 nm photons. At Mars, these photoelectrons are known to escape the planet down its tail, making them tracers for the atmospheric escape. Furthermore, their presence or absence allow to define the so-called photoelectron boundary (PEB), which separates the photoelectron dominated ionosphere from the external environment. We provide here a detailed statistical analysis of the location and properties of the PEB based on the Mars Atmosphere and Volatile EvolutioN (MAVEN) electron and magnetic field data obtained from September 2014 to May 2016 (including 1696 PEB crossings). The PEB appears as mostly sensitive to the solar wind dynamic and crustal fields pressures. Its variable altitude thus leads to a variable wake cross section for escape (up to $\sim +50\%$), which is important for deriving escape rates. The PEB is not always sharp and is characterized on average by the following: a magnetic field topology typical for the end of magnetic pileup region above it, more field-aligned fluxes above than below, and a clear change of the altitude slopes of both electron fluxes and total density (that appears different from the ionopause). The PEB thus appears as a transition region between two plasma and fields configurations determined by the draping topology of the interplanetary magnetic field around Mars and much influenced by the crustal field sources below, whose dynamics also impacts the estimated escape rate of ionospheric plasma.

1. Introduction

Due to the absence of a strong intrinsic magnetic field, the thin Martian atmosphere directly interacts with the incident solar wind plasma. The ionized part of the atmosphere acts as a conductive obstacle, leading to a draping of the interplanetary magnetic field (IMF) around the planet and the formation of an induced magnetosphere.

Among the numerous processes at work in the Martian environment, the continuous ionization of the atmospheric neutrals by the extreme ultraviolet (EUV) photons from the Sun leads to the production of photoelectrons that play a key role in the heating balance of the atmosphere. In particular, the strong 30.4 nm Helium II line of the solar spectrum ionizes CO_2 and O atmospheric neutrals (Mantas & Hanson, 1979), which can be seen in the energy spectra of electrons at Mars or other bodies such as Titan, Venus, and Earth (Coates et al., 2011) as two peaks between 21 and 24 eV and at 27 eV.

The Mars Global Surveyor (MGS) MAG/ER instrument revealed a strong change of the electron spectra at the external limit of the ionosphere (Mitchell et al., 2000, 2001), with, in particular, a photoelectron boundary (PEB) or ionopause defined by the disappearing of photoelectron features in the 20–50 eV energy range as well as near 500 eV (i.e., Auger electrons) and a change of the slope below 100 eV. These authors already mentioned the possible influence of crustal fields on the altitude of the observed boundary. The finer-energy resolution ($\delta m/m = 7\%$ compared to 25% for MGS) of the Mars Express ASPERA ELS instrument (Barabash et al., 2006) then allowed the two photoelectron peaks in the 20–30 eV range to be resolved and the plasma boundaries at Mars to be investigated in more details (Lundin et al., 2004). Frahm et al. (2006, 2010) also revealed that a portion of the photoelectrons actually escape down to the tail behind the planet along draped open field lines, thus providing an insight into the escape rate of ionospheric plasma, assuming overall neutrality

of the plasma (see also Liemohn et al., 2006, who modeled the magnetic connectivity for Martian photoelectrons from the dayside to the wake). Such photoelectrons are known to be common in planetary atmospheres, such as at Titan, Venus, or Earth (see Coates et al., 2011; Tsang et al., 2015; Wellbrock et al., 2012).

Nevertheless, the definition of the Martian plasma boundaries still raises debates regarding their nature depending on the parameters observed (composition, density gradient, magnetic topology, pressure balance, etc). In particular, the PEB (determined from the disappearance of CO_2 20–30 eV photoelectrons) and the ionopause (determined from electron density gradients or density levels) were often observed at the same locations, but not systematically. Han et al. (2014) used Mars Express MARSIS and ASPERA data from 2005 to 2013 to obtain a median altitude of the ionopause at about 450 km, while the PEB altitude was located 200 km above this. However, no detailed analysis of the boundary characteristics or drivers of influence was performed, except for the solar zenith angle (SZA) variability.

The Mars Atmosphere and Volatile Evolution (MAVEN) mission, designed to study the structure, composition, and variability of the upper atmosphere and ionosphere of Mars, reached Mars in September 2014 (Jakosky et al., 2015). The complete plasma and magnetic field instruments package, combined with the spacecraft's elliptical orbits reaching low altitudes (down to 110 km during deep-dip campaigns), allows us to analyze the Martian plasma environment and the ionosphere in more detail. Recently, Sakai et al. (2015) used a two-stream electron transport code to interpret the photoelectron and Auger electron observations of the MAVEN Solar Wind Electron Analyzer (SWEA) instrument (Mitchell et al., 2016). They showed, in particular, how the solar irradiance, external electron fluxes, and ionospheric thermal electron density control the photoelectron spectrum. Xu, Mitchell, et al. (2016) also showed the presence of photoelectrons in the nightside ionosphere, very likely due to transport along closed crustal magnetic field loops that cross the terminator and extend far into the deep nightside.

In this paper, we use MAVEN electron and magnetic field data to analyze the photoelectron boundary in detail. After a description of the instruments and data set used for the study (section 2), we will discuss the geographical distribution of the boundary crossings (section 3) and the parameters driving its variability (section 4). We will then discuss the influence of the PEB on photoelectron escape (section 5) before we characterize in detail the boundary itself and its near environment through several parameters (section 6) and end with conclusions (section 7).

2. Description of the Data Set

2.1. Description of the Instruments

The MAVEN Solar Wind Electron Analyzer (SWEA) instrument is a symmetric, hemispheric, electrostatic analyzer with deflectors (Mitchell et al., 2016). It is designed to measure the energy and angular distributions of electrons within an energy range of 3 to 4,600 eV, with an energy resolution of $\delta E/E = 17\%$ and maximum time resolution of 2 s (depending on the mode used). MAVEN is not a spinning spacecraft but a three-axis stabilized spacecraft, so that SWEA uses deflectors to sweep the field of view (of $360° \times 7°$ for the hemispheres) to reach a maximum field of view of $360° \times 120°$ (i.e., 87% of the sky).

Moreover, we will use in this study the magnetic field measurements provided by the MAG instrument. It consists of two independent triaxial fluxgate magnetometer sensors, which measure the ambient vector magnetic field at an intrinsic sample rate of 32 vector samples per second over a wide dynamic range (until 65,536 nT per axis) with a maximum resolution of 0.008 nT and an accuracy of better than 0.05% (Connerney et al., 2015).

2.2. The Photoelectron Boundary Data Set

Figure 1 shows an example of a periapsis passage of MAVEN in February 2015, with the SWEA energy spectrograms and orbital parameters. The (X, Y, Z) coordinates are given in the MSO frame, where X points toward the Sun, Y points approximately opposite to Mars orbital angular velocity, and Z completes the right-handed set. The spacecraft was thus, at first, located in the dayside southern magnetosheath (a shocked and heated spectrum typical for the magnetosheath at 02:12 is shown in Figure 1e), with a draping and strong gradient of the magnetic field (not shown) from 02:13 UT, until a large drop of the energetic electron fluxes at about 02:18 UT and the appearance of the strong photoelectron peak at 20–30 eV. The spacecraft thus enters the ionosphere (a typical spectrum at 02:24 UT is shown in Figure 1d) and reaches the terminator region near 02:30 UT. The photoelectron double peak (between 21 and 24 and at 27 eV) appears as a single peak due to the energy

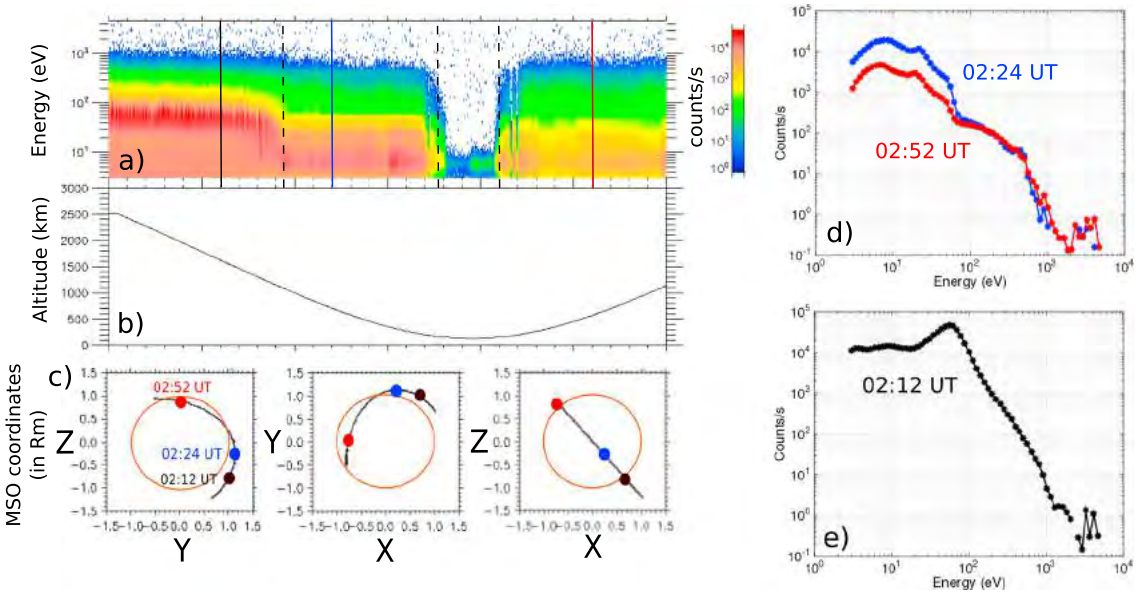

Figure 1. Case study on 12 February 2015. (a) MAVEN SWEA electron energy spectrogram with the color bar giving the omnidirectional counts per second. The dashed black lines show the crossings of the 20–30 eV photoelectron line, while the black/blue/red solid lines correspond to the times of the individual energy spectra given in Figures 1d and 1e. (b) Altitude of the spacecraft. (c) (*X*,*Y*,*Z*) coordinates of the spacecraft in the MSO frame, where *X* points toward the Sun, *Y* points opposite to Mars orbital angular velocity, and *Z* completes the right-handed set. (d) SWEA electron energy spectra typical for the dense ionosphere (blue) or escaping photoelectrons (red) in the tail. (e) Typical magnetosheath SWEA electron spectrum.

resolution of the instrument (except during negative charging events where the line splits into two different lines). Please note that the broad energy peak around 60 eV seen in the magnetosheath spectrum at 02.12 is not associated with photoelectrons but is a typical feature of the heated solar wind particles. A suprathermal electron depletion is then observed around periapsis (02:36 UT to 02:42 UT), since the spacecraft is located in the low-altitude nightside ionosphere where the absorption by CO_2 neutrals depletes almost all suprathermal electrons while the major ionization process—that is, photoionization—is stopped (see Steckiewicz et al., 2015, 2017, for further details). The CO_2 photoelectron line at 20–30 eV thus disappears as the spacecraft moves through the depletion region and reappears at 02:42 UT where it appears again until the end of the period shown, while the spacecraft is located behind the terminator in the tail: these photoelectrons are thus escaping the planet, with a line more diffuse than in the deep ionosphere (see also Coates et al., 2015 and Tsang et al., 2015 for similar observations at Venus).

The three dashed lines in Figure 1 show where the photoelectron line appears or disappears during this case study, corresponding to either the PEB (near 02:19) or to the edges of the electron depletions (at 02:35 and 02:42). We analyzed by hand the SWEA spectrograms and energy spectra from September 2014 to the end of May 2016, and identified 3,022 timings where the photoelectron line appeared or disappeared. An automatic (peak) detection algorithm was used at first, which worked well for large photoelectron peaks below the PEB, but it could hardly detect precisely the faint peaks that often appear close to the PEB (all the more that intermittent photoelectron line crossings are considered as PEB crossings). More than half of the automatic crossings timings had to be corrected by a few minutes, so that we chose to define the crossings manually for a better precision. The automatic algorithm will be, however, discussed in a future paper on a statistical analysis of the ionospheric photoelectrons.

Among these 3,022 crossings, 1,696 correspond unambiguously to dayside PEB crossings, the rest corresponding to edges of electron depletions in the nightside (all suprathermal electron fluxes drop, including the photoelectron fluxes), edges of detached escaping photoelectrons in the wake, or ambiguous crossings below the extreme ultraviolet terminator (here defined by a minimum altitude of 140 km). We thus defined as PEB crossings only the photoelectron line crossings taking place on the dayside ($X > 0$) at altitudes above the EUV terminator (see also Figure 3 later). The timings of the crossings are defined with a precision of ~30 s and define the last (or first) time interval where the photoelectron peak at 20–30 eV is unambiguously observed. The crossings on the dayside are easier to determine, whereas the times where the photoelectron line appears

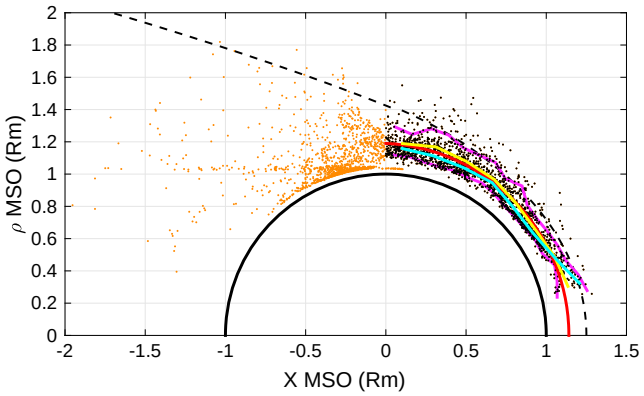

Figure 2. Geographical distribution of the photoelectron line crossings—PEB crossings in black dots, other crossings in orange—in cylindrical coordinates (in the plane (X, ρ) with $\rho = \sqrt{Y^2 + Z^2}$ the distance to the X axis; $1R_M \approx 3{,}390$ km average Martian radius). The dashed black line provides the average location of the magnetic pileup boundary fit by Trotignon et al. (2006). The cyan and yellow solid lines show, respectively, the northern and southern median location of the PEB (for 10° solar zenith angle bins), while the red curve shows the best conic fit for the dayside PEB crossings (see text for more details). The magenta lines show the limits including 80% of the PEB crossings.

or disappears in the tail or nightside ionosphere are much more difficult to define precisely due to the more diffuse structure of the peak. A number of small nightside electron depletions are also not included in the total data set, as well as temporary crossings in the tail where the line is more intermittent, due to the strong plasma dynamics (mixing of several populations, accelerated particles, etc.) occurring in this region. As will be discussed later, the PEB, even on the dayside, can barely be defined with a high precision due to the interpretation of the spectra which often show faint peaks before showing strong unambiguous peaks. The PEB appears as a transition region where the photoelectron flux gradually decreases, more or less sharp depending on the conditions (see section 6).

3. Geographical Distribution of the PEB

3.1. Overall Distribution

Figure 2 shows the geographical distribution of the 3,022 photoelectron line crossings (1,696 PEB crossings) in MSO cylindrical coordinates. No crossing was found at low SZA values (i.e., below 10° SZA) due to the orbital characteristics of MAVEN with few passages at the appropriate altitudes below 10° SZA. The PEB crossings cover a SZA range from ~10° SZA to ~90° SZA. Almost all crossings were confined within the average magnetic pileup boundary fit by Trotignon et al. (2006), determined from the Phobos 2 and Mars Global Surveyor data sets, in a shell of about 0.15–0.2 R_M ($1R_M \approx 3{,}390$ km average Martian radius).

The altitude of the dayside PEB crossings strongly varies between 186 and 1,931 km, with median and average altitudes, respectively, at 528 and 573 km (without including any SZA dependency). This is in close agreement with the Mars Express results by Han et al. (2014), who obtained an average altitude between 553 and 633 km depending on the SZA regime. The suprathermal electrons, thanks to their large mean free path and cross field diffusion in the absence of open draped lines, thus transport vertically to high altitudes (compared to the suprathermal electron exobase at ~145–165 km, see Xu, Liemohn, Bougher, et al., 2016), and are stopped on average before the other plasma boundaries such as the ion composition boundary (ICB), magnetic-pileup boundary (MPB), or pressure β^* boundary (Matsunaga et al., 2015; Xu, Liemohn, Dong, et al., 2016). We can mention that the MPB (named like this by numerous authors, see initially Nagy et al., 2004 or Bertucci et al., 2004) is also often called induced magnetosphere boundary (cf. Brain et al., 2017 or Dubinin et al., 2006), after it was even called at first planetopause (Riedler et al., 1989) or magnetopause (Rosenbauer et al., 1989).

Except near noon (see below for further details), the southern median location (yellow line) of the PEB is always at higher altitudes than the northern one (cyan line), in particular, close to the terminator where the difference reaches ~200 km, presumably due to the influence of the strong crustal magnetic fields of the southern hemisphere, which will be further discussed in section 4. The thickness of the altitude shell (defined by, for example, 80% of the PEB crossings inside the shell, magenta lines) increases from about 230 km at low SZA values until ~800 km near the terminator, as expected from the topology of the draping of the IMF around the planet that is more variable at terminator than at noon (as seen for the MPB location, see Trotignon et al., 2006).

A conic fitting of the dayside PEB crossings—defined by $r = \frac{L}{1+e*\cos(\theta)}$ with r and θ polar coordinates with origin at X_0 referenced to the X axis, and L and e the semilatus rectum and eccentricity; see Edberg et al. (2008) for further details—provides the following results: $(X_0, L, e) = (0R_M, 1.19R_M, 0.0047)$, which is almost identical to the Mars Express (Han et al., 2014) derived results values $(0.01\ R_M, 1.19R_M, 0.005)$. The average location of the PEB is thus very close to a circle (red line) centered on the planet center, as can be expected for the innermost plasma boundary. The closer the boundary, the lower the eccentricity: the MPB and bow shock best conic fits respectively correspond to eccentricities of 0.92/0.90 (Edberg et al., 2008)/(Vignes et al., 2002) and 1.05/1.03 (Edberg et al., 2008)/(Trotignon et al., 2006; Vignes et al., 2002).

3.2. Solar Zenith Angle and Local Time Variability

Figures 3 and 4 show the altitude, solar zenith angle (SZA), and local time (LT) variability of the 3,022 photoelectron line crossings determined during the two first years of the MAVEN mission. The photoelectron line

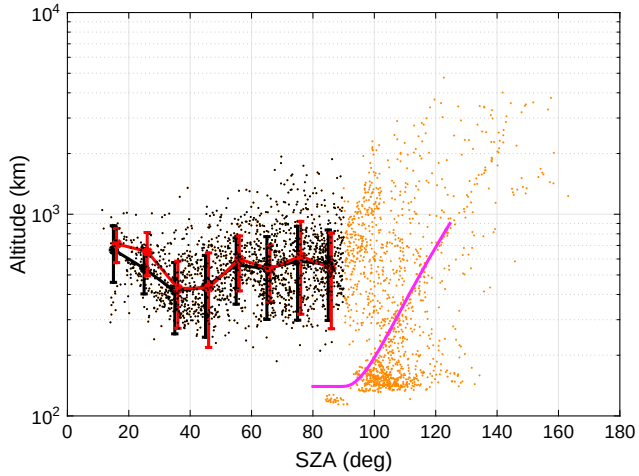

Figure 3. Altitude of the photoelectron line crossings—PEB crossings in black dots, other crossings in orange—as a function of the solar zenith angle (SZA). The magenta solid line provides the extreme ultraviolet terminator limit (where most photons are absorbed) corresponding to a lower limit at 140 km altitude. The black solid line shows the median altitude for SZA bins of 20° with the standard deviation, while the red solid line shows the median and standard deviation altitude for SZA values recalculated after including the aberration angle induced by the solar wind and after rotating the initial MSO frame into the MSE frame (see text for further details).

crossings beyond 90° SZA or below the extreme ultraviolet terminator (for a lower limit altitude of 140 km) are not a priori considered as real PEB crossings, even if some of them could be included as well. Until 30° SZA, the median altitude of the PEB crossings decreases at first, and then increases until a constant value below 600 km from 55° SZA. The increase of the PEB altitude is expected toward the terminator, since the draped field lines induce an increase of the MPB altitude with SZA, but larger altitudes closer to noon are unexpected. Moreover, the median local time variability in the MSO frame shows an unexpected and significant asymmetry, with a minimum altitude displaced with respect to noon, whereas the draping topology can be considered as symmetric. Where do these unexpected features come from? One can mention that a separation of the data sets into northern hemisphere and southern hemisphere observations (not shown) reveals higher altitudes in the south than in the north (presumably due to an enhanced crustal field pressure, see next section), except again near noon (in both SZA and LT) where the trend is reversed.

Since the draping of the IMF around Mars—and the Martian interaction with the solar wind in general—is known to depend significantly on the clock angle of the IMF (Carlsson et al., 2008), the PEB is expected to depend on it as well. Moreover, the solar wind velocity compared to the orbital velocity of the planet around the Sun induces a small but nonnegligible aberration angle (of a few degrees). We thus recalculated the SZA and LT values in the MSE frame that also includes a 4° aberration angle, based on the solar wind velocity and magnetic field parameters provided by the MAVEN SWIA and MAG instruments at each orbit (Halekas et al., 2017). The resulting new LT median variability (red line) shows a much more symmetric behavior: the PEB is thus strongly organized by the solar wind magnetic field direction, whose variability induces a continuous rotation of the draping around the *X* axis and thus a reorganization in terms of local time. One can also mention that the latitudinal variability of the PEB (not shown) is much more homogeneous in this modified MSE frame than in the MSO frame.

However, the SZA variability is obviously only slightly influenced by a small aberration angle, so that the unexpected high-altitude PEB crossings near noon need another explanation. Figure 5 shows the SZA variability of the crustal magnetic field (at a constant altitude of 400 km; Morschhauser et al., 2014) and solar wind dynamic pressure at the times of the photoelectron line crossings. A clear bias thus appears in our data set close to noon, with low solar wind dynamic pressures and high crustal magnetic field values. As will be detailed in the next section, both the solar wind and crustal magnetic field pressures are important drivers for the PEB location, since the pressure will push from above (for the solar wind) or below (for crustal fields) the draping magnetic field topology and modify the location where the upward moving photoelectrons will encounter the draped open field lines to get eventually convected toward the tail. A combination of (relative) low solar wind dynamic pressure and strong crustal field pressure will thus induce high altitudes for the PEB as observed in our data set.

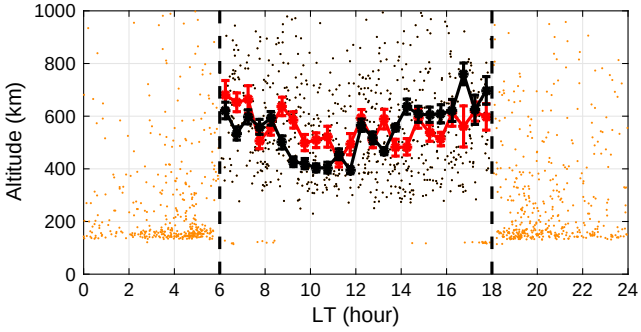

Figure 4. Altitude of the photoelectron line crossings—PEB crossings in black dots, other crossings in orange—as a function of the local time (LT). The dashed lines show the terminator, while the solid lines show the median altitude for LT bins of 0.5 h in the initial MSO frame (black line) and in the MSE frame (red line) that also includes the aberration angle induced by the solar wind (see text for further details).

4. The Parameters of Influence for the PEB: Solar Wind Dynamic and Crustal Magnetic Fields Pressures

The conic fitting of the dayside PEB crossings leads to a nearly circular shape of the boundary. Nonetheless, from now on we will only use the extrapolated terminator distance (i.e., $r_i(1 + e \times \cos(\theta_i))$ or altitude of the PEB to remove the average SZA variability of the PEB altitude, following previous works on the MPB or bow shock (Crider et al., 2003; Edberg et al., 2008).

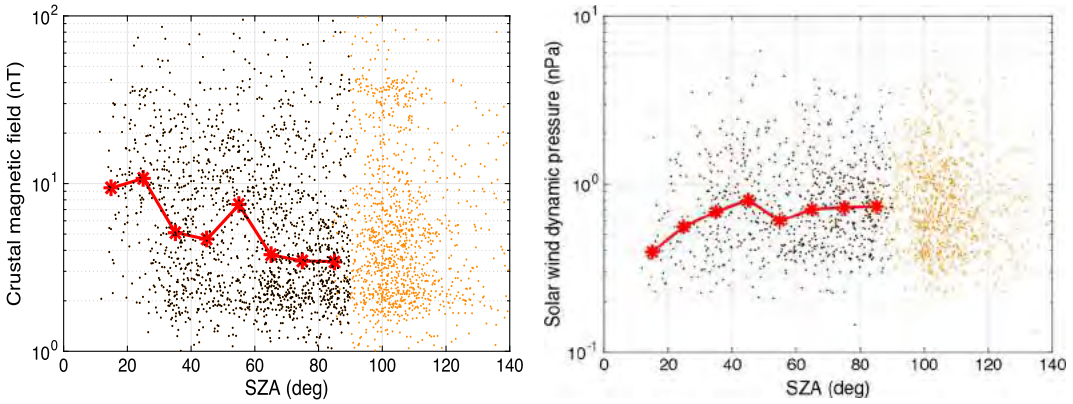

Figure 5. Demonstration of the SZA sampling bias for the PEB crossings data set: SZA variability of (left) the crustal magnetic field and (right) solar wind dynamic pressure at the times of the photoelectron line crossings, with PEB crossings in black dots, other crossings in orange, and the median values in solid red line. The crustal magnetic field is given by the Morschhauser et al. (2014) model at a constant altitude of 400 km.

4.1. The Influence of the Crustal Magnetic Field and Solar Wind Dynamic Pressure

The influence of the crustal field intensity on the PEB altitude is shown in Figure 6, where the estimated terminator altitude is given as a function of the longitude in the geographical IAU frame. This frame is fixed to the planet, with the strongest crustal fields region in the southern hemisphere at longitudes between 120 and 240°. The data set is separated into longitude and latitude regions to separate the strong and weak crustal field regimes, as defined by Edberg et al. (2008), with the strong fields in the following ranges: longitude from 0 to 120° and latitude from −45 to 45°, longitude from 120 to 240° and latitude from −90 to 0°, and longitude from 240 to 360° and latitude from −45 to 45°.

The median altitudes are systematically higher for the strong crustal field regime than for the low crustal field regime, by about 100 km or even 140 km in 120 to 240° longitude region where the strongest crustal fields are located. Edberg et al. (2008) obtained very similar results for the influence of crustal fields on the MPB and bow shock position, with the largest influence in the middle longitude range as well, with an altitude variation, that is, all the larger than the boundary is far: up to ∼400 km and ∼0.48 R_M for, respectively, the MPB and bow shock. One can also note that an IAU mapping of the PEB terminator altitude from our data set gives a good correlation with the location of crustal field sources.

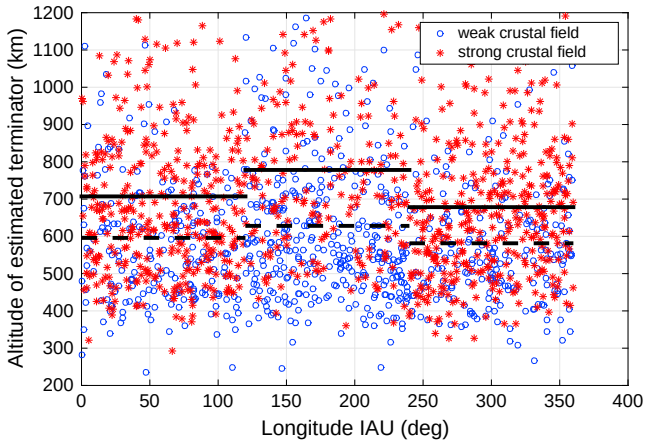

Figure 6. Estimated terminator altitude of the PEB crossings as a function of the longitude in the geographical IAU frame. The data set is separated into longitude and latitude regions to separate the strong and weak crustal field regimes, as defined by Edberg et al. (2008) (see text for more details). The blue circles and red stars correspond to PEB crossings in weak and strong crustal field regions, while the solid and dashed lines correspond to median altitudes for, respectively, strong and weak crustal field conditions in each of the three longitude bins.

The combined influence of the solar wind dynamic pressure and crustal magnetic field is shown in Figure 7. Despite a strong dispersion and a limited number of PEB crossings at high solar wind dynamic pressure values, the PEB terminator altitude clearly decreases while the solar wind dynamic pressure increases, with a median altitude decreasing from ∼700 km to ∼500 km. The separation between weak and strong crustal field crossings is also clear, with few high-altitude crossings located above weak crustal field regions. Power law fits were performed of the form $d_{\mathrm{term_{PEB}}} = a \times P_{\mathrm{SW}}^{b}$ with $d_{\mathrm{term_{PEB}}}$ terminator distance of the PEB in R_M and P_{SW} the solar wind dynamic pressure, for all crossings together (magenta line in the figure) or by separating weak (blue line) and strong (red line) crustal field crossings. The results are the following: $(a, b) \approx (3.60, -0.034)$ for all crossings; $(3.59, -0.034)$ for crossings above weak crustal fields; and $(3.61, -0.039)$ for crossings above weak crustal fields. The influence of the solar wind dynamic pressure is thus on average 40% smaller than on the MPB, for which the power law index value was estimated at about −0.055 (Crider et al., 2003), which is expected since the PEB is located closer to the planet. Even if the dispersion is very large, we may add that the influence of both the solar wind dynamic pressure and crustal magnetic field pressure

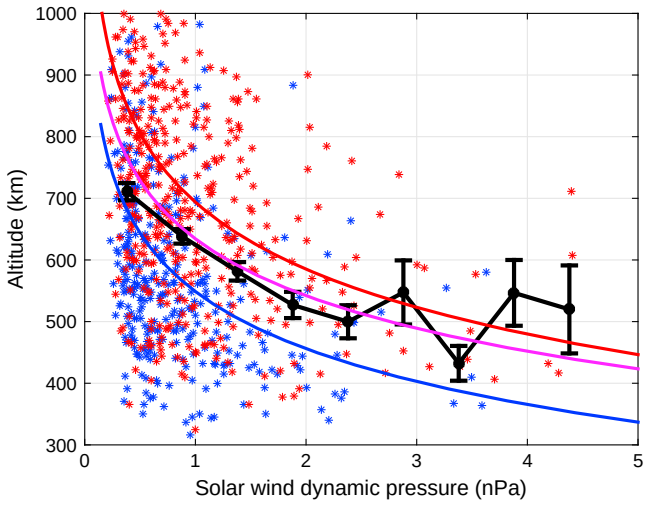

Figure 7. Estimated terminator altitude of the PEB crossings as a function of the solar wind dynamic pressure. The blue and red stars correspond, respectively, to weak and strong crustal field regions (based on the same definition as in Figure 6). The solid black line provides the median altitude (and standard deviation of the median) for 0.5 nPa bins. The magenta/blue/red solid lines give the best power law fits (see section 4.2 for further details) of all/weak crustal field/strong crustal field crossings.

are statistically very significant (assuming power laws), with Fisher tests (Box, 1953) providing risks—that is, probabilities that the influence is not real—of about 10^{-29} and 10^{-18}, respectively. These results are in agreement with a confinement of the atmosphere by the solar wind, which induces a draping of the IMF closer to the planet and thus pushes the PEB to lower altitudes, except when strong crustal fields locally act from below against this incident pressure.

4.2. Comparing the Parameters of Influence

Figure 8 shows the compared influence on the PEB terminator altitude of a number of parameters: extreme ultraviolet fluxes, solar zenith angle, local time, crustal magnetic field pressure, as well as solar wind dynamic pressure, density, velocity, and magnetic field. We shall mention that the EUV fluxes are derived from the FISM model (Chamberlin et al., 2007; available on the CDPP/AMDA database) at the 30.4 nm solar spectrum line which is the source of the 20–30 eV photoelectrons. Each set of parameters was then separated into low (below the median value of the parameter) and high (above the median value of the parameter) subsets of data to allow for a convenient comparison among the various parameters of influence. The median altitudes of the "low" and "high" subsets are then determined for each parameter. The standard deviation of the median value ($\frac{\sigma}{\sqrt{N}}$; σ standard deviation and N number of values) was shown in the figure instead of the classical standard deviation for a better visibility (σ is very large, about 200 km). We shall mention that in this figure we only considered the crossings for which all parameters were available (the solar wind parameters being available for only a part of them), which reduces the data set to 795 PEB crossings. However, the relative importance of the parameters is kept very similar if all crossings are considered for the EUV, LT, SZA, and crustal field parameters.

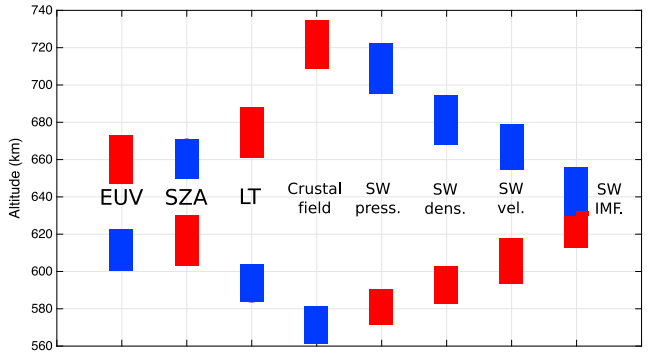

Figure 8. Compared influence of a number of parameters on the PEB terminator altitude: extreme ultraviolet (EUV) fluxes, solar zenith angle (SZA), local time (LT), crustal magnetic field, solar wind (SW), dynamic pressure (press.), density (dens.), velocity (vel.), and magnetic field (IMF). Each set of parameters was separated into low (below the median value of the parameter) and high (above the median value of the parameter) subsets of data. The median and standard deviation of the median are then calculated for the low and high subsets of each parameter, shown by rectangles in the figure (blue/red for the low/high subsets, with the height giving twice the standard deviation of the median). The rectangles of low/high subsets of the solar wind IMF cross each other, since the standard deviations overlap. The EUV fluxes are derived from the FISM model (Chamberlin et al., 2007; available on the CDPP/AMDA database) at the 30.4 nm solar spectrum line which is the source of the 20–30 eV photoelectrons; the crustal magnetic field pressure is calculated from the Morschhauser et al. (2014) model at a constant altitude of 400 km; the solar wind parameters are derived from the MAVEN SWIA and MAG data (Halekas et al., 2017).

The PEB terminator altitude thus increases with (by decreasing importance) increasing crustal magnetic field pressure, decreasing solar wind dynamic pressure, increasing local time, increasing EUV fluxes, and decreasing SZA and IMF. The two major parameters of influence are by far the solar wind dynamic and crustal magnetic field pressures, with a variation reaching 150 km of difference between the low and high median values.

More precisely, the low solar wind density seems even more efficient than a low velocity to cause an increase in the PEB altitude. Ramstad et al. (2015) showed that low solar wind densities lead to larger ion escape rates according to Mars Express ASPERA-3 data, since the atmosphere expands, giving more space and time for ionospheric plasma to accelerate, which leads to larger escape rates during the rarefaction (i.e., low SW density) events following the strong solar wind disturbances. We will discuss in section 5 how the solar wind dynamic pressure will impact the escape rates through the variable PEB altitude.

The influence of the other parameters—EUV, SZAm and LT—is less clear and depends on the frame considered (for the LT influence in MSO versus MSE) or on cross-correlations biases with the major drivers (for SZA near noon, as detailed above), even if the risks of artificial correlations as determined from Fisher's tests are always below 1%, except for the SZA influence (risk of ≈2%). Regarding the EUV influence, we point out that if EUV is a major driver for the photoelectron fluxes (Trantham et al., 2011; Xu et al., 2015) through the production mechanisms, its influence on the PEB should be less strong (e.g., the MGS data could not see any EUV influence

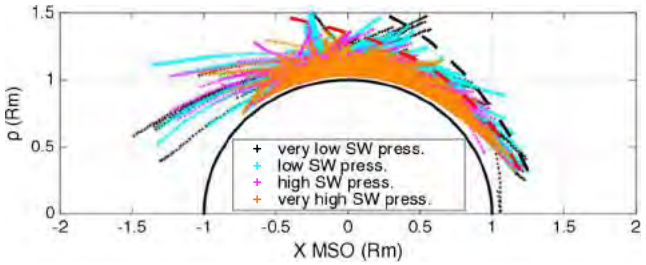

Figure 9. Influence of the solar wind dynamic pressure on the 20–30 eV photoelectron detection location in cylindrical MSO coordinates, assuming a continuous detection between inbound and outbound photoelectron line crossings and four levels of solar wind dynamic pressure conditions: very low corresponds to the P_{SW} <= 25% quantile, low to 25% < P_{SW} <= 50%, high to 50% < P_{SW} <= 75%, very high to P_{SW} > 75%. The two dashed lines represent sketched minimum and maximum altitude shapes for the photoelectron transport (see section 5 for more details).

on the ionopause, Mitchell et al., 2001). The EUV influence corresponds to an enhanced thermal pressure that will act against the solar wind confinement and thus push the draping of the IMF.

5. Discussion on the Photoelectron Escape

The PEB altitude is strongly influenced by the incident solar wind dynamic pressure that confines more or less the Martian ionosphere and that thus drives the location of the IMF draping around the planet. As shown in Figure 9 and explained below, the solar wind will consequently have a strong impact on the transport of the photoelectrons from the dayside to the tail region and eventually on the estimated escape rates derived.

In this figure, we assumed a continuous detection of 20–30 eV photoelectrons from the inbound to outbound crossings of the photoelectron line. This assumption is inaccurate in the nightside region, where a lot of electron depletions are observed, but it is mostly true otherwise, except at intermittent times in the noncollisional regions due to the strong plasma dynamics (mixing of several populations, accelerated particles, etc). We separated the time intervals into four categories, based on the value of the solar wind dynamic pressure at the times considered and superimposed the crossings on the figure in the following order: very low, low, high, and very high. The low and very low SW pressures are hidden behind the high and very high SW pressures close to the planet, but extend further than these. The photoelectron detection thus appears more and more confined close to the planet when higher solar wind dynamic pressure values are observed, not only on the dayside but also at terminator where the photoelectrons are on the way to escape down to the tail.

The PEB altitude is raised by low solar wind dynamic pressure conditions, leading to access to higher altitudes on the dayside for the photoelectrons, and thus transport along draped field lines toward the tail at higher altitudes as well. Overall, the photoelectron escape will not necessarily increase due to low solar wind dynamic pressure conditions, but the tail cross section to be considered for deriving escape rates increases. Frahm et al. (2010) provided the only known escape rates of photoelectrons ($3.14 \pm 1.78 \times 10^{23}$ electrons/s), and thus of corresponding ionospheric ions—assuming they escape at the same rate as the electrons, which may be overestimated if their large gyroradii make them impact the dense atmosphere—based on an average escape flux measured and a constant annular cross section of 1.16×10^{18} cm^2. This annular cross section was derived at $X = -1.5\,R_M$, with a minimum distance to the X axis of 2,850 km (no escaping photoelectrons at Mars were observed closer to the X axis) and an external limit at 6,700 km. However, our results show that the cross section to be considered for deriving escape rates is not a constant and will strongly depend on the PEB altitude on the dayside and thus, in particular, on the solar wind dynamic (and crustal magnetic field) pressure. Assuming sketched limits for low and high PEB altitudes (black and red lines in Figure 9), corresponding to about 200 km of difference near noon, and by extrapolating their shape to the tail until $X = -1.5\,R_M$, this will induce a variation of about 50% of the escape cross section. When escape rates are derived from single point in situ flux measurements, one should thus keep in mind that not only the measured local fluxes vary temporally and spatially but also the escape area (i.e., the cross section to be used) will significantly vary with time and depend on the dayside conditions. We mention that deriving MAVEN escape rates is beyond the scope of this paper, since it needs the quantitative analysis of the photoelectron peaks in the energy spectra (whereas we only focus on the PEB crossings here), but we plan to further investigate this in the future to analyze the variability of the escape rates during the MAVEN mission (with an average value that could be, or not, close to earlier estimates).

6. Characteristics Around the Boundary

Beyond the knowledge of the location and of the variability of the boundary, it is essential to better understand its nature and characteristics; therefore, we examine the evolution of a number of parameters around it. Figure 10 provides the average evolution of the 23–29 eV photoelectron integrated differential fluxes (Figure 10a), electron density (Figure 10c), electron differential fluxes at ~25 and ~130 eV (Figure 10c), as well as information on the pitch angle distributions (Figure 10b) and several magnetic field characteristics (Figures 10d–10f), as a function of the altitude around the boundary. The altitude 0 in the figure thus

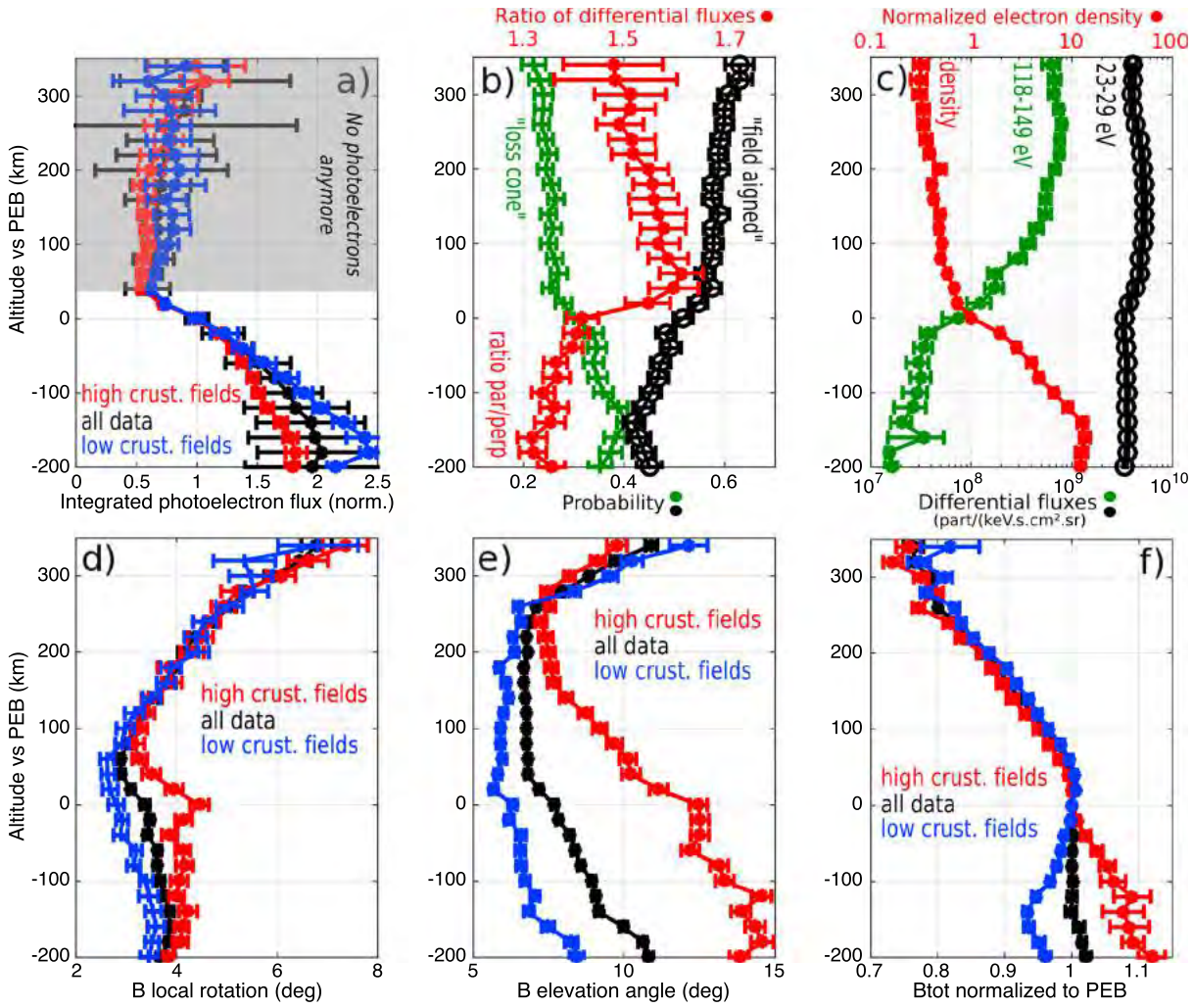

Figure 10. Average evolution of various parameters (eventually normalized, by the value at the PEB) as a function of altitude versus the PEB altitude (0 means the PEB altitude). (a) Normalized integrated 20–30 eV photoelectron flux from SWEA (shadowed part indicates incorrect photoelectron flux values); black/blue/red lines (as in Figures 10d–10f), respectively, correspond to all PEB crossings/only low crustal fields crossings/only high crustal fields crossings (see text). (b) Pitch angle information on 23–29 eV electrons: maximum ratio between parallel and perpendicular differential fluxes, probability of "loss cone" or "field-aligned" pitch angle distributions for the 0–90° range. (c) Mean SWEA differential fluxes of 23–29 eV and 118–149 eV electrons, and thermal electron density by LPW. (d) Local angular rotation, (e) elevation angle, and (f) normalized total magnitude of the in situ magnetic field measured by MAG. See text for more details.

corresponds to the altitude of each individual PEB crossing, while positive and negative values correspond respectively to altitudes above and below the crossing. Such a figure hides the various trajectories of the spacecraft, with, in particular, the altitude variation being different from one orbit to another, but it allows us to compare crossings occurring at different times and altitudes, by normalizing some of the parameters to avoid their strong temporal and/or spatial dynamics to hide the average characteristics of the PEB (e.g., for the electron density or total magnitude of the magnetic field).

We considered all MAVEN SWEA (with ~4 s time resolution) and MAG (with ~2 s time resolution) data at ±300 s around the time of each of the 1,696 PEB crossings available. Median (for Figures 10a, 10d, 10e, and 10f) or average (for Figures 10b and 10c) parameter values were then calculated for each 20 km altitude bin around the crossings, which leads to a maximum altitude range of 700 km. We however removed the data below −200 km since the average altitude actually increases below this limit, which would induce a bias for the interpretation if these data were kept. The standard deviation of the mean ($\frac{\sigma}{\sqrt{N}}$) is also shown for each parameter as an error bar. In Figures 10a, 10d, 10e, and 10f, we also considered three different profiles to identify the influence of the crustal fields: one, for all PEB crossings (black line) and two, for low (blue line) and high (red line) crustal field conditions at the crossings. These low/high conditions are determined by the 25th percentiles

of the crossings with the lowest and highest values of the Morschhauser et al. (2014) modeled crustal magnetic field values at 400 km altitude at the time of crossings.

Figure 10a provides the integrated 20–30 eV photoelectron flux, normalized by the flux at the time of each PEB crossing. Following the approach of Frahm et al. (2010), we integrated, for each time step, the photoelectron flux after removing the background spectrum (i.e., a power law fit) from 17.2 to 34.7 eV to extract the peak photoelectron fluxes only. Several tries were made with various energy ranges considered, leading to no significant qualitative change in the results, and the energy of the peak is very stable on the dayside. Above the PEB, the photoelectrons are by definition essentially absent, so that the fluxes should not be considered from about 50 km above the PEB (gray area), since they correspond to fluxes of magnetosheath electrons. The flux of upward moving photoelectrons gradually decreases when approaching the boundary, before a large drop in a ~100 km altitude shell centered on the PEB location, and ultimately, they disappear. We also find the presence of higher fluxes in the −200 to −100 km range when weak crustal fields are present, which may be related to an easier access of photoelectrons to altitudes above the photoelectron exobase (≈145–165 km altitude, see Xu, Liemohn, Bougher, et al., 2016) in the absence of strong horizontal closed crustal magnetic fields.

The median profiles of the magnetic field characteristics (local rotation every 4 s, Figure 10b; elevation angle, Figure 10c; magnitude of the field measured normalized by the value at the PEB) suggest the following average behavior from above to below the PEB. The magnetic field first drapes (and thus rotates less and less) and piles up (the total field increases) at altitudes above the PEB, which is consistent with the magnetic pileup region (MPR) characteristics, and is consistent with the fact that most data points considered here are located below the nominal magnetic pileup boundary location. The rotation of the field decreases toward lower altitudes, as does the magnetic field elevation angle that reaches a constant minimum value about 250 km above the PEB location. The situation seems, however, different with strong crustal fields: the interaction between upstream and crustal topologies induces on average an increase of the elevation angle ~150 km above the PEB (the influence of crustal fields may also be seen at the same time on the field rotation with a separation between low and high crustal field profiles). At 50 km above the PEB, while the photoelectron fluxes appear and strongly increase, the local rotation of the magnetic field increases slightly and reaches a peak exactly at the PEB in the presence of crustal fields (for this case the PEB marks a transition between two different configurations of the magnetic field, the draped field above and the crustal field below). We note that the absolute values of the rotation are small, which is due to the time resolution considered (4 s, a poorer resolution would lead to larger rotation angles). At the same time (i.e., 50 km or less above the PEB) the magnetic elevation angle slightly increases as well (all the more in the presence of crustal fields) and the total field keeps constant around the boundary (typical for the end of the MPR). Then, below the PEB, the rotation of the field stays small while the elevation angle slightly increases (with a more noisy behavior in the presence of crustal fields, due to the variable local topology) and the field magnitude decreases/increases in the absence/presence of crustal fields.

Figure 10b shows information regarding the pitch angle distribution of 23–29 eV electrons around the PEB (the most appropriate energy bin to investigate 20–30 eV photoelectrons with the pitch angle distribution (PAD) mode of the MAVEN SWEA instrument). The red line provides the ratio between the maximum parallel or antiparallel (maximum value among either the 0–45° or 135–180° pitch angle ranges) and perpendicular (45–135°) differential fluxes. The green and black lines give respectively the probability of "loss cone"and "field-*aligned" pitch angle distributions for the 0–90° range. We defined these categories based on an approach similar to Brain et al. (2007): each half of a PAD is taken separately (0–90° and 90–180°), and the standard deviation of fluxes of each half is calculated among the angular bins; the flux at 90° pitch angle is then compared to the most field-aligned flux for the spectrum (here at least <=30° or > =150° to avoid too narrow PADs); PAD spectra are separated according to whether the perpendicular flux at 90° exceeds the field-aligned flux by more than 1 standard deviation ("loss cone") or whether the field-aligned flux exceeds the perpendicular flux by more than 1 standard deviation ("field-aligned"). The rest of the spectra correspond to either isotropic or conic/anticonic spectra (not shown). We shall mention that only the qualitative behavior is discussed here, since changing the definition of the parameters modifies the absolute probabilities of each configuration.

Globally, the 23–29 eV electrons—that is, essentially photoelectrons below the PEB, magnetosheath electrons above it—PADs are more in a field-aligned configuration than in a loss cone configuration, except at

−140 km below the PEB, where both configurations have a similar probability. From about −200 km below the PEB until the boundary, the loss cone and field-aligned probabilities vary from, respectively, between 0.3 and 0.4 and between 0.4 and 0.5. The loss cone and field-aligned probabilities then abruptly decrease/increase from the PEB (or slightly below it) to about 50 km above it, before they keep stable at, respectively, ≈0.25 and ≈0.6 (with a slight continuous increase though). This change of PAD configuration at the PEB is clearly confirmed by the ratio between the maximum parallel (or antiparallel) and the perpendicular fluxes, which is roughly constant below and above the PEB but strongly increases from the PEB to 50 km above it (from 1.4 to 1.6), revealing an even more field-aligned configuration above than below the boundary (where the PADs are already more field aligned, with a ratio always above 1). As expected, the PADs are more in a field-aligned configuration (thus with more electrons on open field lines, at one end or both) than in a loss cone configuration (closed field lines). We are indeed looking at relatively high altitudes compared to the photoelectron exobase (Xu, Liemohn, Bougher, et al., 2016): 71/86% of the time steps considered correspond to altitudes above 300/400 km, respectively, with an average altitude reaching a minimum of 400 km (at about −150 km below the PEB, which explains the close green and black curves at this location). Moreover, plotting the probability of closed (loss cone + isotropic + conic PADs) and open (field-aligned + anticonic) fields configurations as a function of absolute altitude (not referenced to the PEB level; plot not shown) reveals an expected continuous decrease and increase versus altitude for these respective configurations, with equal probabilities at about 300–400 km. These observations are in agreement with the recent results by Xu et al. (2017) who investigated in details the low altitude topology and electron pitch angle distributions based on the shape parameter technique. This technique (see details in Xu et al., 2017) is based on a parameter whose value determines the nature of the electron spectra (photoelectrons or solar wind) after a comparison between measured spectra and a ionosphere reference spectrum (that includes the 20–30 eV peaks and the sharp drop at 60–70 eV). The authors showed that closed field lines are mostly observed at low altitudes (and above crustal fields), and that above 400 km altitudes the field lines are mostly open and draped around the planet.

Figure 10c shows the mean absolute differential fluxes of 23–29 eV (black lines) and 118–149 eV (green lines) electrons around the PEB, the low energy range corresponding to either photoelectrons (mostly below the PEB) or magnetosheath electrons (mostly above the PEB), while the high energy range corresponds essentially to magnetosheath electrons only and keeps a good signal-to-noise ratio compared to higher energy ranges. The PEB appears as a clear transition between the photoelectron-dominated and magnetosheath electron-dominated regions, with magnetosheath electron fluxes dropping above the PEB (by up to 1 order of magnitude in about 50–100 km for the highest energies), while the photoelectrons fluxes (i.e., 23–29 eV electrons below the PEB) appear and increase below the boundary (since the photoelectron source region is at low altitudes). We shall mention that the profiles are similar for all crustal field conditions. Meanwhile, a strong change in the density profile occurs at the PEB altitude, with a clear and large increase of the gradient with altitude from above to below the PEB. Moreover, one can note that plotting the absolute densities (not normalized to 1 at the PEB; not shown) as a function of altitude versus the PEB confirms our conclusions with the same strong change of slope above the PEB. Finally, in addition to this observation of smaller density gradients above the PEB (and not larger gradients as may be used to define the ionopause), the 1000 cm^{-3} density level used by Han et al. (2014) to define the ionopause level is located in our data set at ∼440 km, which is similar to the Mars Express results (and ∼200 km below our average PEB altitude): these results thus confirm that the PEB and ionopause (as defined by large density gradients or the 1,000 cm^{-3} density level) are not located at the same altitude on average. We shall mention that the normalization of both the density and altitude axes of Figure 10c make it impossible to add the location of the ionopause on the same figure even as defined from a constant density level.

The average variability of plasma and magnetic fields around the PEB altitude thus reveals several characteristics:

1. The 20–30 eV photoelectron flux first gradually decreases from below the PEB, followed by a strong decrease around the PEB over an altitude shell "thickness" of the order of 100 km altitude until photoelectrons disappear.
2. The magnetic field is characteristic for the magnetic pileup region above the PEB, with a strong (decreasing toward the PEB) rotation of the field and a decreasing elevation until the field gets draped; the field magnitude increases linearly until it gets stable around the PEB, where a local increase of rotation and elevation is observed; finally, the crustal fields determine the low-altitude topology (and influence the topology at least until 150 km above the PEB).

3. The pitch angle distributions of 23–29 eV electrons (i.e., photoelectrons below the PEB) show a steep increase of the ratio between parallel (or antiparallel, the maximum value being considered) and perpendicular fluxes at the PEB, and an increase/decrease of the probability for field-aligned/loss cone PADs at the same time, even if the PADs reveal more open field lines than closed field lines at the altitudes considered in our study (in agreement with Xu et al., 2017).
4. The electron fluxes reveal a steep increase of high-energy electrons (i.e., magnetosheath type electrons) above the PEB and a smaller decrease of 25 eV electron fluxes, while the slope of the density profile strongly increases at the PEB; the PEB is thus on average different from an ionopause defined by either a stronger density depletion or by a 1,000 cm^{-3} density level (Han et al., 2014) (which actually also occurs about 200 km below the PEB on the MAVEN data). The PEB thus appears as a flux and density transition region between ionospheric and magnetosheath electrons.

Overall, these characteristics are consistent with the classical picture of the PEB as the location where photoelectrons, after their upward transport above the exobase (modified by the magnetic topology, in particular, crustal fields), encounter open draped field lines, with more field-aligned PADs and get convected toward the tail and eventually escape. However, beyond the coherent average profiles discussed in this section, a large dispersion appears when individual crossings are analyzed. The dispersion (ratio between standard deviation and mean values) is most often above one for all particles parameters (photoelectron flux, electron fluxes and density, and pitch angle profiles) and at all altitudes. The small error bars of Figure 10 actually correspond to the standard deviation of the mean (i.e., much smaller than the nominal standard deviation). In the future, individual crossings will be investigated in more details to better understand the large dynamics beyond the global trends discussed above.

7. Conclusions

The characterization of the plasma boundaries at Mars and their difference has been a matter of debate for many years. In particular, the photoelectron boundary (PEB) discovered by Mars Global Surveyor and defined by the disappearance of ionospheric photoelectrons, still remains poorly understood. We provide in this paper a detailed description of the PEB based on a manual detection of almost 1,700 boundary crossings from MAVEN data before May 2016. We thus determined its shape, its parameters of influence, the variability of several parameters (magnetic field, photoelectron fluxes, etc.) in the vicinity of the boundary, and its influence on the plasma escape fluxes. Our main conclusions are the following.

1. First, the PEB appears approximately as a circular boundary ($e = 0.0047$) with a highly variable altitude that is strongly related to the draping of the IMF around the planet, and mostly depends on the solar wind dynamic and crustal magnetic field pressures (more than extreme ultraviolet fluxes or solar zenith angle and local time). These pressures will push from above (for the solar wind) or below (for the crustal fields) the draping magnetic field topology and thus modify the location where the upward moving photoelectrons will encounter the draped open field lines to get eventually convected toward the tail.
2. Second, we show how the variable PEB altitude on the dayside, due to several drivers, will allow the access of photoelectrons to variable altitudes toward the terminator and thus affect their transport along draped field lines toward the tail and strongly modify (up to ~50%) the tail cross section to be considered for deriving escape rates of photoelectrons (and associated ions assuming neutrality). When escape rates are derived from single-point in situ flux measurements, the temporal and spatial variations of the dayside PEB altitude will thus determine the escape cross section to be considered.
3. Finally, the detailed analysis of plasma and magnetic field characteristics around the PEB crossings shows that the boundary is not always sharp and is characterized on average by the following:
    a. a gradual decrease of the photoelectron flux much before the PEB and a more steep decrease around it over an altitude "thickness" of the order of 100 km;
    b. a magnetic field topology typical for the end of the magnetic pileup region above it, with also a locally increased rotation and elevation angle of the field at the PEB, all the more in the presence of crustal field sources;
    c. more field-aligned fluxes above than below the boundary, despite a more "open" than "closed" field configuration usually much below the PEB; and
    d. a clear change of altitude slopes for both the electron fluxes (in particular, for high-energy electrons) and total density; the density slope indeed decreases from below to above the boundary, the PEB

being thus different from the ionopause if defined by a stronger density slope, and more precisely located ~200 km below the PEB if defined as the 1,000 cm^{-3} density level.

However, beyond these average characteristics of the PEB, a large dispersion appears when individual crossings are analyzed and should be investigated in the future. Furthermore, a more detailed understanding of the various plasma boundaries (MPB/IMB, pressure boundary, ion composition boundary, ionopause, etc.) and of the physical processes linking them will need future common work, by taking advantage of the complete particles and fields package of the MAVEN mission.

Acknowledgments
This work was supported by the French space agency CNES for the observations obtained with the SWEA instrument embarked on MAVEN. The authors acknowledge the support of the MAVEN instrument and science teams, as well as the CDPP/AMDA team (http://amda.cdpp.eu) and Emmanuel Penou for providing support with data analysis tools. The MAVEN data are taken from the Berkeley database with the "spdsoft" software.

References

Barabash, S., Lundin, R., Andersson, H., Brinkfeldt, K., Grigoriev, A., Gunell, H., … Thocaven, J.-J. (2006). The Analyzer of Space Plasmas and Energetic Atoms (ASPERA-3) for the Mars Express mission. *Space Science Reviews*, *126*(1), 113–164. https://doi.org/10.1007/s11214-006-9124-8

Bertucci, C., Mazelle, C., Crider, D. H., Mitchell, D. L., Sauer, K., Acuña, M. H., … Winterhalter, D. (2004). MGS MAG/ER observations at the magnetic pileup boundary of Mars: Draping enhancement and low frequency waves. *Advances in Space Research*, *33*, 1938–1944. https://doi.org/10.1016/j.asr.2003.04.054

Box, G. (1953). Non-normality and tests on variances. *Biometrika*, *40*(3–4), 318–335. https://doi.org/10.1093/ biomet/40.3-4.318

Brain, D. A., Barabash, S., Bougher, S. W., Duru, F., Jakosky, B. M., & Modolo, R. (2017). *Solar Wind Interaction and Atmospheric Escape* (pp. 433–463). Cambridge: Cambridge Planetary Science, Cambridge University Press. https://doi.org/10.1017/9781139060172.015

Brain, D. A., Lillis, R. J., Mitchell, D. L., Halekas, J. S., & Lin, R. P. (2007). Electron pitch angle distributions as indicators of magnetic field topology near Mars. *Journal of Geophysical Research*, *112*, A09201. https://doi.org/10.1029/2007JA012435

Carlsson, E., Brain, D., Luhmann, J., Barabash, S., Grigoriev, A., Nilsson, H., & Lundin, R. (2008). Influence of IMF draping direction and crustal magnetic field location on Martian ion beams. *Planetary and Space Science*, *56*(6), 861–867. https://doi.org/10.1016/j.pss.2007.12.016

Chamberlin, P. C., Woods, T. N., & Eparvier, F. G. (2007). Flare Irradiance Spectral Model (FISM): Daily component algorithms and results. *Space Weather*, *5*, S07005. https://doi.org/10.1029/2007SW000316

Coates, A. J., Tsang, S. M. E., Wellbrock, A., Frahm, R. A., Winningham, J. D., Barabash, S., … Crary, F. J. (2011). Ionospheric photoelectrons: Comparing Venus, Earth, Mars and Titan. *Planetary and Space Science*, *59*, 1019–1027. https://doi.org/10.1016/j.pss.2010.07.016

Coates, A. J., Wellbrock, A., Frahm, R. A., Winningham, J. D., Fedorov, A., Barabash, S., & Lundin, R. (2015). Distant ionospheric photoelectron energy peak observations at Venus. *Planetary and Space Science*, *113*, 378–384. https://doi.org/10.1016/j.pss.2015.02.003

Connerney, J. E. P., Espley, J., Lawton, P., Murphy, S., Odom, J., Oliversen, R., & Sheppard, D. (2015). The MAVEN magnetic field investigation. *Space Science Reviews*, *195*, 257–291. https://doi.org/10.1007/s11214-015-0169-4

Crider, D. H., Vignes, D., Krymskii, A. M., Breus, T. K., Ness, N. F., Mitchell, D. L., … Acuña, M. H. (2003). A proxy for determining solar wind dynamic pressure at Mars using Mars Global Surveyor data. *Journal of Geophysical Research*, *108*, 1461. https://doi.org/10.1029/2003JA009875

Dubinin, E., Fränz, M., Woch, J., Roussos, E., Barabash, S., Lundin, R., … Acuña, M. (2006). Plasma morphology at Mars. Aspera-3 observations. *Space Science Reviews*, *126*, 209–238. https://doi.org/10.1007/s11214-006-9039-4

Edberg, N. J. T., Lester, M., Cowley, S. W. H., & Eriksson, A. I. (2008). Statistical analysis of the location of the Martian magnetic pileup boundary and bow shock and the influence of crustal magnetic fields. *Journal of Geophysical Research*, *113*, A08206. https://doi.org/10.1029/2008JA013096

Frahm, R. A., Sharber, J. R., Winningham, J. D., Link, R., Liemohn, M. W., Kozyra, J. U., … Fedorov, A. (2010). Estimation of the escape of photoelectrons from Mars in 2004 liberated by the ionization of carbon dioxide and atomic oxygen. *Icarus*, *206*, 50–63. https://doi.org/10.1016/j.icarus.2009.03.024

Frahm, R. A., Sharber, J. R., Winningham, J. D., Wurz, P., Liemohn, M. W., Kallio, E., … McKenna-Lawler, S. (2006). Locations of atmospheric photoelectron energy peaks within the Mars environment, *126*, 389–402. https://doi.org/10.1007/s11214-006-9119-5

Halekas, J. S., Ruhunusiri, S., Harada, Y., Collinson, G., Mitchell, D. L., Mazelle, C., … Jakosky, B. M. (2017). Structure, dynamics, and seasonal variability of the Mars-solar wind interaction: MAVEN solar wind ion analyzer in-flight performance and science results. *Journal of Geophysical Research: Space Physics*, *122*, 547–578. https://doi.org/10.1002/2016JA023167

Han, X., Fraenz, M., Dubinin, E., Wei, Y., Andrews, D. J., Wan, W., … Barabash, S. (2014). Discrepancy between ionopause and photoelectron boundary determined from Mars Express measurements. *Geophysical Research Letters*, *41*, 8221–8227. https://doi.org/10.1002/2014GL062287

Jakosky, B. M., Lin, R. P., Grebowsky, J. M., Luhmann, J. G., Mitchell, D. F., Beutelschies, G., … Zurek, R. (2015). The Mars Atmosphere and Volatile EvolutioN (MAVEN) mission. *Space Science Reviews*, *195*, 3–48. https://doi.org/10.1007/s11214-015-0139-x

Liemohn, M. W., Frahm, R. A., Winningham, J. D., Ma, Y., Barabash, S., Lundin, R., … Dierker, C. (2006). Numerical interpretation of high-altitude photoelectron observations. *Icarus*, *182*, 383–395. https://doi.org/10.1016/j.icarus.2005.10.036

Lundin, R., Barabash, S., Andersson, H., Holmström, M., Grigoriev, A., Yamauchi, M., … Bochsler, P. (2004). Solar wind-induced atmospheric erosion at Mars: First results from ASPERA-3 on Mars Express. *Science*, *305*(5692), 1933–1936. https://doi.org/10.1126/science.1101860

Mantas, G. P., & Hanson, W. B. (1979). Photoelectron fluxes in the Martian ionosphere. *Journal of Geophysical Research*, *84*, 369–385. https://doi.org/10.1029/JA084iA02p00369

Matsunaga, K., Seki, K., Brain, D. A., Hara, T., Masunaga, K., McFadden, J. P., … Jakosky, B. M. (2015). Comparison of Martian magnetic pileup boundary with ion composition boundary observed by MAVEN. *American Geophysical Union, Fall Meeting 2015, Abstract P21A-2071*.

Mitchell, D. L., Lin, R. P., Mazelle, C., Rème, H., Cloutier, P. A., Connerney, J. E. P., … Ness, N. F. (2001). Probing Mars' crustal magnetic field and ionosphere with the MGS electron reflectometer. *Journal of Geophysical Research*, *106*, 23,419–23,428. https://doi.org/10.1029/2000JE001435

Mitchell, D. L., Lin, R. P., Rème, H., Crider, D. H., Cloutier, P. A, Connerney, J. E. P., … Ness, N. F (2000). Oxygen auger electrons observed in Mars' ionosphere. *Geophysical Research Letters*, *27*, 1871–1874. https://doi.org/10.1029/1999GL010754

Mitchell, D. L., Mazelle, C., Sauvaud, J.-A., Thocaven, J.-J., Rouzaud, J., Fedorov, A., … Jakosky, B. M. (2016). The MAVEN solar wind electron analyzer. *Space Science Reviews*, *200*, 495–528. https://doi.org/10.1007/s11214-015-0232-1

Morschhauser, A., Lesur, V., & Grott, M. (2014). A spherical harmonic model of the lithospheric magnetic field of Mars. *Journal of Geophysical Research: Planets*, *119*, 1162–1188. https://doi.org/10.1002/2013JE004555

Nagy, A. F, wINTerhalter, D., Sauer, K., Cravens, T. E, Brecht, S., Mazelle, C., … Trotignon, J. G (2004). The plasma environment of Mars. *Space Science Reviews*, *111*, 33–114. https://doi.org/10.1023/B: SPAC.0000032718.47512.92

Ramstad, R., Barabash, S., Futaana, Y., Nilsson, H., Wang, X.-D., & Holmström, M. (2015). The Martian atmospheric ion escape rate dependence on solar wind and solar EUV conditions: 1. Seven years of Mars Express observations. *Journal of Geophysical Research: Planets*, *120*, 1298–1309. https://doi.org/10.1002/2015JE004816

Riedler, W., Schwingenschuh, K., Moehlmann, D., Oraevskii, V. N, Eroshenko, E., & Slavin, J. (1989). Magnetic fields near Mars—First results. *Nature*, *341*, 604–607. https://doi.org/10.1038/341604a0

Rosenbauer, H., Shutte, N., Galeev, A., Gringauz, K., & Apathy, I. (1989). Ions of Martian origin and plasma sheet in the Martian magnetosphere—Initial results of the TAUS experiment. *Nature*, *341*, 612–614. https://doi.org/10.1038/341612a0

Sakai, S., Rahmati, A., Mitchell, D. L., Cravens, T. E., Bougher, S. W., Mazelle, C., … Jakosky, B. M. (2015). Model insights into energetic photoelectrons measured at Mars by MAVEN. *Geophysical Research Letters*, *42*, 8894–8900. https://doi.org/10.1002/2015GL065169

Steckiewicz, M., Garnier, P., André, N., Mitchell, D. L., Andersson, L., Penou, E., … Jakosky, B. M. (2017). Comparative study of the Martian suprathermal electron depletions based on Mars Global Surveyor, Mars Express, and Mars atmosphere and volatile evolution mission observations. *Journal of Geophysical Research: Space Physics*, *122*, 857–873. https://doi.org/10.1002/2016JA023205

Steckiewicz, M., Mazelle, C., Garnier, P., André, N., Penou, E., Beth, A., … Jakosky, B. M. (2015). Altitude dependence of nightside Martian suprathermal electron depletions as revealed by MAVEN observations. *Geophysical Research Letters*, *42*, 8877–8884. https://doi.org/10.1002/2015GL065257

Trantham, M., Liemohn, M., Mitchell, D., & Frank, J. (2011). Photoelectrons on closed crustal field lines at Mars. *Journal of Geophysical Research*, *116*, A07311. https://doi.org/10.1029/2010JA016231

Trotignon, J. G., Mazelle, C., Bertucci, C., & Acuña, M. H. (2006). Martian shock and magnetic pile-up boundary positions and shapes determined from the Phobos 2 and Mars Global Surveyor data sets. *Planetary and Space Science*, *54*, 357–369. https://doi.org/10.1016/j.pss.2006.01.003

Tsang, S. M. E., Coates, A. J., Jones, G. H., Frahm, R. A., Winningham, J. D., Barabash, S., … Fedorov, A. (2015). Ionospheric photoelectrons at Venus: Case studies and first observation in the tail. *Planetary and Space Science*, *113*, 385–394. https://doi.org/10.1016/j.pss.2015.01.019

Vignes, D., Acuña, M. H., Connerney, J. E. P., Crider, D. H., Reme, H., & Mazelle, C. (2002). Factors controlling the location of the bow shock at Mars. *Geophysical Research Letters*, *29*(9), 42–1–42–4. https://doi.org/10.1029/2001GL014513

Wellbrock, A., Coates, A. J., Sillanpää, I., Jones, G. H., Arridge, C. S., Lewis, G. R., … Aylward, A. D. (2012). Cassini observations of ionospheric photoelectrons at large distances from Titan: Implications for Titan's exospheric environment and magnetic tail. *Journal of Geophysical Research*, *117*, A03216. https://doi.org/10.1029/2011JA017113

Xu, S., Liemohn, M., Bougher, S., & Mitchell, D. (2015). Enhanced carbon dioxide causing the dust storm-related increase in high-altitude photoelectron fluxes at Mars. *Geophysical Research Letters*, *42*, 9702–9710. https://doi.org/10.1002/2015GL066043

Xu, S., Mitchell, D., Liemohn, M., Dong, C., Bougher, S., Fillingim, M., … Jakosky, B. (2016). Deep nightside photoelectron observations by MAVEN SWEA: Implications for Martian northern hemispheric magnetic topology and nightside ionosphere source. *Geophysical Research Letters*, *43*, 8876–8884. https://doi.org/10.1002/2016GL070527

Xu, S., Liemohn, M., Bougher, S., & Mitchell, D. (2016). Martian high-altitude photoelectrons independent of solar zenith angle. *Journal of Geophysical Research: Space Physics*, *121*, 3767–3780. https://doi.org/10.1002/2015JA022149

Xu, S., Liemohn, M. W., Dong, C., Mitchell, D. L., Bougher, S. W., & Ma, Y. (2016). Pressure and ion composition boundaries at Mars. *Journal of Geophysical Research: Space Physics*, *121*, 6417–6429. https://doi.org/10.1002/2016JA022644

Xu, S., Mitchell, D., Liemohn, M., Fang, X., Ma, Y., Luhmann, J., … Jakosky, B. (2017). Martian low-altitude magnetic topology deduced from MAVEN/SWEA observations. *Journal of Geophysical Research: Space Physics*, *122*, 1831–1852. https://doi.org/10.1002/2016JA023467

Title: The nightside ionosphere of Mars unveiled by suprathermal electron depletions

Summary:

Nightside suprathermal electron depletions are specific features of the nightside ionosphere of Mars which have been observed at Mars by three spacecraft to date: MGS, MEX and MAVEN. Their study enables the observation of the nightside ionosphere structure and dynamics as well as the underlying neutral atmosphere, the specific Martian magnetic topology, and possible conduits for atmospheric escape, due to the processes leading to their observation on the nightside of Mars.

The main goal of my PhD has been to use the complementarity of the three missions MGS, MEX, and MAVEN to understand the different mechanisms at the origin of suprathermal electron depletions and their implication on the structure and the dynamics of the nightside ionosphere. In this context, three simple criteria adapted to each mission have been implemented to identify suprathermal electron depletions from 1999 to 2017.

Auteur : Morgane Steckiewicz

Titre : L'ionosphère du côté nuit de Mars dévoilée par les déplétions d'électrons suprathermiques

Directeur de thèse : Christian Mazelle

Lieu et date de soutenance : IRAP, Toulouse, le 26 Septembre 2017

Résumé :

Les déplétions d'électrons suprathermiques sont des structures spécifiques de l'ionosphère du côté nuit de Mars, observées jusqu'à présent par trois satellites : MGS, MEX et MAVEN. Leur étude permet aussi bien l'observation de la structure et de la dynamique de l'ionosphère du côté nuit que celle de l'atmosphère neutre, de la topologie magnétique martienne, ainsi que l'étude de l'échappement atmosphérique de Mars, de par les mécanismes à l'origine de leur observation.

Le but principal de ma thèse a été de tirer parties des trois jeux de données offerts par les satellites MGS, MEX et MAVEN pour mieux comprendre les mécanismes à l'origine des déplétions d'électrons suprathermiques observées du côté nuit ainsi que leur impact sur la structure et la dynamique de l'ionosphère du côté nuit. Dans cette optique, trois critères simples adaptés à chaque mission ont été développés pour identifier les déplétions d'électrons suprathermiques dans une base de données allant de 1999 à 2017.

Mots clés : Mars, déplétions d'électrons suprathermiques, MAVEN, MEX, MGS, interaction atmosphère/ionosphère, magnétosphère induite, champ magnétique rémanent

Discipline : Astrophysique, Sciences de l'univers et Astrophysique

Laboratoire de rattachement : IRAP (Institut de Recherche en Astrophysique)
9 avenue du Colonel Roche, 31028 Toulouse Cedex 4